

Smart Material Systems and MEMS: Design and Development Methodologies

Vijay K. Varadan

University of Arkansas, USA

K. J. Vinoy

Indian Institute of Science, Bangalore, India

S. Gopalakrishnan

Indian Institute of Science, Bangalore, India



John Wiley & Sons, Ltd

Copyright © 2006 John Wiley & Sons Ltd, The Atrium, Southern Gate, Chichester,
West Sussex PO19 8SQ, England

Telephone (+44) 1243 779777

Email (for orders and customer service enquiries): cs-books@wiley.co.uk
Visit our Home Page on www.wiley.com

All Rights Reserved. No part of this publication may be reproduced, stored in a retrieval system or transmitted in any form or by any means, electronic, mechanical, photocopying, recording, scanning or otherwise, except under the terms of the Copyright, Designs and Patents Act 1988 or under the terms of a licence issued by the Copyright Licensing Agency Ltd, 90 Tottenham Court Road, London W1T 4LP, UK, without the permission in writing of the Publisher. Requests to the Publisher should be addressed to the Permissions Department, John Wiley & Sons Ltd, The Atrium, Southern Gate, Chichester, West Sussex PO19 8SQ, England, or emailed to permreq@wiley.co.uk, or faxed to (+44) 1243 770620.

Designations used by companies to distinguish their products are often claimed as trademarks. All brand names and product names used in this book are trade names, service marks, trademarks or registered trademarks of their respective owners. The Publisher is not associated with any product or vendor mentioned in this book.

This publication is designed to provide accurate and authoritative information in regard to the subject matter covered. It is sold on the understanding that the Publisher is not engaged in rendering professional services. If professional advice or other expert assistance is required, the services of a competent professional should be sought.

Other Wiley Editorial Offices

John Wiley & Sons Inc., 111 River Street, Hoboken, NJ 07030, USA

Jossey-Bass, 989 Market Street, San Francisco, CA 94103-1741, USA

Wiley-VCH Verlag GmbH, Boschstr. 12, D-69469 Weinheim, Germany

John Wiley & Sons Australia Ltd, 42 McDougall Street, Milton, Queensland 4064, Australia

John Wiley & Sons (Asia) Pte Ltd, 2 Clementi Loop #02-01, Jin Xing Distripark, Singapore 129809

John Wiley & Sons Canada Ltd, 6045 Freemont Blvd, Mississauga, ONT, L5R 4J3

Wiley also publishes its books in a variety of electronic formats. Some content that appears in print may not be available in electronic books.

British Library Cataloguing in Publication Data

A catalogue record for this book is available from the British Library

ISBN-13 978-0-470-09361-0 (HB)

ISBN-10 0-470-09361-7 (HB)

Typeset in 9/11 pt Times by Thomson Digital

Printed and bound in Great Britain by Antony Rowe, Chippenham, Wiltshire

This book is printed on acid-free paper responsibly manufactured from sustainable forestry
in which at least two trees are planted for each one used for paper production.

Contents

<i>Preface</i>	xi
<i>About the Authors</i>	xiii
PART 1: FUNDAMENTALS	1
1 Introduction to Smart Systems	3
1.1 Components of a smart system	3
1.1.1 ‘Smartness’	6
1.1.2 Sensors, actuators, transducers	7
1.1.3 Micro electromechanical systems (MEMS)	7
1.1.4 Control algorithms	9
1.1.5 Modeling approaches	10
1.1.6 Effects of scaling	10
1.1.7 Optimization schemes	10
1.2 Evolution of smart materials and structures	11
1.3 Application areas for smart systems	13
1.4 Organization of the book	13
References	15
2 Processing of Smart Materials	17
2.1 Introduction	17
2.2 Semiconductors and their processing	17
2.2.1 Silicon crystal growth from the melt	19
2.2.2 Epitaxial growth of semiconductors	20
2.3 Metals and metallization techniques	21
2.4 Ceramics	22
2.4.1 Bulk ceramics	22
2.4.2 Thick films	23
2.4.3 Thin films	25
2.5 Silicon micromachining techniques	26
2.6 Polymers and their synthesis	26
2.6.1 Classification of polymers	27
2.6.2 Methods of polymerization	28
2.7 UV radiation curing of polymers	31
2.7.1 Relationship between wavelength and radiation energy	31
2.7.2 Mechanisms of UV curing	32
2.7.3 Basic kinetics of photopolymerization	33

2.8 Deposition techniques for polymer thin films	35
2.9 Properties and synthesis of carbon nanotubes	35
References	40
PART 2: DESIGN PRINCIPLES	43
3 Sensors for Smart Systems	45
3.1 Introduction	45
3.2 Conductometric sensors	45
3.3 Capacitive sensors	46
3.4 Piezoelectric sensors	48
3.5 Magnetostrictive sensors	48
3.6 Piezoresistive sensors	50
3.7 Optical sensors	51
3.8 Resonant sensors	53
3.9 Semiconductor-based sensors	53
3.10 Acoustic sensors	57
3.11 Polymeric sensors	58
3.12 Carbon nanotube sensors	59
References	61
4 Actuators for Smart Systems	63
4.1 Introduction	63
4.2 Electrostatic transducers	64
4.3 Electromagnetic transducers	68
4.4 Electrodynamic transducers	70
4.5 Piezoelectric transducers	73
4.6 Electrostrictive transducers	74
4.7 Magnetostrictive transducers	78
4.8 Electrothermal actuators	80
4.9 Comparison of actuation schemes	82
References	83
5 Design Examples for Sensors and Actuators	85
5.1 Introduction	85
5.2 Piezoelectric sensors	85
5.3 MEMS IDT-based accelerometers	88
5.4 Fiber-optic gyroscopes	92
5.5 Piezoresistive pressure sensors	94
5.6 SAW-based wireless strain sensors	96
5.7 SAW-based chemical sensors	97
5.8 Microfluidic systems	100
References	102
PART 3: MODELING TECHNIQUES	103
6 Introductory Concepts in Modeling	105
6.1 Introduction to the theory of elasticity	105
6.1.1 Description of motion	105
6.1.2 Strain	107

6.1.3 Strain–displacement relationship	109
6.1.4 Governing equations of motion	113
6.1.5 Constitutive relations	114
6.1.6 Solution procedures in the linear theory of elasticity	117
6.1.7 Plane problems in elasticity	119
6.2 Theory of laminated composites	120
6.2.1 Introduction	120
6.2.2 Micromechanical analysis of a lamina	121
6.2.3 Stress–strain relations for a lamina	123
6.2.4 Analysis of a laminate	126
6.3 Introduction to wave propagation in structures	128
6.3.1 Fourier analysis	129
6.3.2 Wave characteristics in 1-D waveguides	134
References	144
 7 Introduction to the Finite Element Method	145
7.1 Introduction	145
7.2 Variational principles	147
7.2.1 Work and complimentary work	147
7.2.2 Strain energy, complimentary strain energy and kinetic energy	148
7.2.3 Weighted residual technique	149
7.3 Energy functionals and variational operator	151
7.3.1 Variational symbol	153
7.4 Weak form of the governing differential equation	153
7.5 Some basic energy theorems	154
7.5.1 Concept of virtual work	154
7.5.2 Principle of virtual work (PVW)	154
7.5.3 Principle of minimum potential energy (PMPE)	155
7.5.4 Rayleigh–Ritz method	156
7.5.5 Hamilton’s principle (HP)	156
7.6 Finite element method	158
7.6.1 Shape functions	159
7.6.2 Derivation of the finite element equation	162
7.6.3 Isoparametric formulation and numerical integration	164
7.6.4 Numerical integration and Gauss quadrature	167
7.6.5 Mass and damping matrix formulation	168
7.7 Computational aspects in the finite element method	171
7.7.1 Factors governing the speed of the FE solution	172
7.7.2 Equation solution in static analysis	173
7.7.3 Equation solution in dynamic analysis	174
7.8 Superconvergent finite element formulation	178
7.8.1 Superconvergent deep rod finite element	179
7.9 Spectral finite element formulation	182
References	184
 8 Modeling of Smart Sensors and Actuators	187
8.1 Introduction	187
8.2 Finite element modeling of a 3-D composite laminate with embedded piezoelectric sensors and actuators	189
8.2.1 Constitutive model	189
8.2.2 Finite element modeling	191

8.2.3 2-D Isoparametric plane stress smart composite finite element	192
8.2.4 Numerical example	194
8.3 Superconvergent smart thin-walled box beam element	196
8.3.1 Governing equation for a thin-walled smart composite beam	196
8.3.2 Finite element formulation	199
8.3.3 Formulation of consistent mass matrix	201
8.3.4 Numerical experiments	202
8.4 Modeling of magnetostrictive sensors and actuators	204
8.4.1 Constitutive model for a magnetostrictive material (Terfenol-D)	204
8.4.2 Finite element modeling of composite structures with embedded magnetostrictive patches	205
8.4.3 Numerical examples	209
8.4.4 Modeling of piezo fibre composite (PFC) sensors/actuators	212
8.5 Modeling of micro electromechanical systems	215
8.5.1 Analytical model for capacitive thin-film sensors	216
8.5.2 Numerical example	218
8.6 Modeling of carbon nanotubes (CNTs)	219
8.6.1 Spectral finite element modeling of an MWCNT	222
References	229
 9 Active Control Techniques	 231
9.1 Introduction	231
9.2 Mathematical models for control theory	232
9.2.1 Transfer function	232
9.2.2 State-space modeling	234
9.3 Stability of control system	237
9.4 Design concepts and methodology	239
9.4.1 PD, PI and PID controllers	239
9.4.2 Eigenstructure assignment technique	240
9.5 Modal order reduction	241
9.5.1 Review of available modal order reduction techniques	242
9.6 Active control of vibration and waves due to broadband excitation	246
9.6.1 Available strategies for vibration and wave control	247
9.6.2 Active spectral finite element model (ASEM) for broadband wave control	248
References	253
 PART 4: FABRICATION METHODS AND APPLICATIONS	 255
 10 Silicon Fabrication Techniques for MEMS	 257
10.1 Introduction	257
10.2 Fabrication processes for silicon MEMS	257
10.2.1 Lithography	257
10.2.2 Resists and mask formation	258
10.2.3 Lift-off technique	259
10.2.4 Etching techniques	260
10.2.5 Wafer bonding for MEMS	261
10.3 Deposition techniques for thin films in MEMS	263
10.3.1 Metallization techniques	264
10.3.2 Thermal oxidation for silicon dioxide	265
10.3.3 CVD of dielectrics	266

10.3.4 Polysilicon film deposition	268
10.3.5 Deposition of ceramic thin films	268
10.4 Bulk micromachining for silicon-based MEMS	268
10.4.1 Wet etching for bulk micromachining	269
10.4.2 Etch-stop techniques	269
10.4.3 Dry etching for micromachining	271
10.5 Silicon surface micromachining	271
10.5.1 Material systems in sacrificial layer technology	273
10.6 Processing by both bulk and surface micromachining	274
10.7 LIGA process	274
References	278
 11 Polymeric MEMS Fabrication Techniques	 281
11.1 Introduction	281
11.2 Microstereolithography	282
11.2.1 Overview of stereolithography	282
11.2.2 Introduction to microstereolithography	284
11.2.3 MSL by scanning methods	285
11.2.4 Projection-type methods of MSL	287
11.3 Micromolding of polymeric 3-D structures	289
11.3.1 Micro-injection molding	290
11.3.2 Micro-photomolding	291
11.3.3 Micro hot-embossing	291
11.3.4 Micro transfer-molding	291
11.3.5 Micromolding in capillaries (MIMIC)	292
11.4 Incorporation of metals and ceramics by polymeric processes	293
11.4.1 Burnout and sintering	293
11.4.2 Jet molding	293
11.4.3 Fabrication of ceramic structures with MSL	294
11.4.4 Powder injection molding	295
11.4.5 Fabrication of metallic 3-D microstructures	296
11.4.6 Metal–polymer microstructures	300
11.5 Combined silicon and polymer structures	300
11.5.1 Architecture combination by MSL	300
11.5.2 MSL integrated with thick-film lithography	301
11.5.3 AMANDA process	301
References	302
 12 Integration and Packaging of Smart Microsystems	 307
12.1 Integration of MEMS and microelectronics	307
12.1.1 CMOS first process	307
12.1.2 MEMS first process	307
12.1.3 Intermediate process	308
12.1.4 Multichip module	308
12.2 MEMS packaging	310
12.2.1 Objectives in packaging	311
12.2.2 Special issues in MEMS packaging	313
12.2.3 Types of MEMS packages	314
12.3 Packaging techniques	315
12.3.1 Flip-chip assembly	315
12.3.2 Ball-grid array	316

12.3.3 Embedded overlay	316
12.3.4 Wafer-level packaging	317
12.4 Reliability and key failure mechanisms	319
12.5 Issues in packaging of microsystems	321
References	322
13 Fabrication Examples of Smart Microsystems	325
13.1 Introduction	325
13.2 PVDF transducers	325
13.2.1 PVDF-based transducer for structural health monitoring	325
13.2.2 PVDF film for a hydrophone	328
13.3 SAW accelerometer	332
13.4 Chemical and biosensors	336
13.4.1 SAW-based smart tongue	337
13.4.2 CNT-based glucose sensor	339
13.5 Polymeric fabrication of a microfluidic system	342
References	344
14 Structural Health Monitoring Applications	347
14.1 Introduction	347
14.2 Structural health monitoring of composite wing-type structures using magnetostriuctive sensors/actuators	349
14.2.1 Experimental study of a through-width delaminated beam specimen	350
14.2.2 Three-dimensional finite element modeling and analysis	352
14.2.3 Composite beam with single smart patch	353
14.2.4 Composite beam with two smart patches	355
14.2.5 Two-dimensional wing-type plate structure	357
14.3 Assesment of damage severity and health monitoring using PZT sensors/actuators	358
14.4 Actuation of DCB specimen under Mode-II dynamic loading	364
14.5 Wireless MEMS-IDT microsensors for health monitoring of structures and systems	365
14.5.1 Description of technology	367
14.5.2 Wireless-telemetry systems	368
References	374
15 Vibration and Noise-Control Applications	377
15.1 Introduction	377
15.2 Active vibration control in a thin-walled box beam	377
15.2.1 Test article and experimental set-up	378
15.2.2 DSP-based vibration controller card	378
15.2.3 Closed-loop feedback vibration control using a PI controller	380
15.2.4 Multi-modal control of vibration in a box beam using eigenstructure assignment	383
15.3 Active noise control of structure-borne vibration and noise in a helicopter cabin	385
15.3.1 Active strut system	387
15.3.2 Numerical simulations	387
References	394
Index	397

Preface

'Smart technology' is a term extensively used in all branches of science and engineering due to its immense potential in application areas of very high significance to mankind. This technology has already been used in addressing several remaining challenges in aerospace, automotive, civil, mechanical, biomedical and communication engineering disciplines. This has been made possible by a series of innovations in developing materials which exhibit features such as electromechanical/magnetomechanical coupling. In other words, these materials could be used to convert one form of energy (say electrical) to another (mechanical, e.g. force, vibration, displacement, etc.). Furthermore, this phenomenon is found to be reciprocal, paving the way for fabricating both sensors and actuators with the same materials. Such a system will also include a control mechanism that responds to the signals from the sensors and determines the responses of the actuators accordingly.

Researchers the world over have devised various ways to embed these components in order to introduce 'smartness' in a system. Originally introduced in larger systems in the bulk form, this science is increasingly leaning towards miniaturization with the popularization of micro electromechanical systems (MEMS). One of the reasons for this is the stringent lightweight constraints imposed on the system design. Although there have been sporadic efforts on various facets of the technology, to the best of these authors' knowledge, there is currently no single book dealing with diverse aspects such as design, modeling and fabrication of both bulk sensors and actuators and MEMS.

The use of MEMS in smart systems is so intensely intertwined that these technologies are often treated as two 'faces of the same coin'. The engineering of smart systems and MEMS are areas for multidisciplinary research, already laden with myriad technological issues of their own. Hence, the books presently available in the literature tend to separate the basic smart concepts, design and modeling of sensors and actuators and

MEMS design and fabrication. Evidently, the books presently available do not address modeling of smart systems as a whole. With smart systems technology branching towards several newer disciplines, it is essential and timely to consolidate the technological advances in selected areas.

In this present book, it is proposed to give a unified treatment of the above concepts 'under a single umbrella'. This book can be used as a reference material/textbook for a graduate level course on Smart Structures and MEMS. It should also be very useful to practicing researchers in all branches of science and engineering and interested in possible applications where they can use this technology. The book will present unified schemes for the design and modeling of smart systems, address their fabrication and cover challenges that may be encountered in typical application areas.

Material for this book has been taken from several advanced short courses presented by the authors in various meetings throughout the world. Valuable comments from the participants of these courses have helped in evolving the contents of this text and are greatly appreciated. We are also indebted to various researchers for their valuable contributions cited in this book. We would like to indicate that this text is a compilation of the work of many people. We cannot be held responsible for the designs and development methods that have been published but are still under further research investigation. It is also difficult to always give proper credit to those who are the originators of new concepts and the inventors of new methods. We hope that there are not too many such errors and will appreciate it if readers could bring the errors that they discover to our attention. We are also grateful to the publisher's staff for their support, encouragement and willingness to give prompt assistance during this book project.

There are many people to whom we owe our sincere thanks for helping us to prepare this book. However, space dictates that only a few of them can receive

formal acknowledgement. However, this should not be taken as a disparagement of those whose contributions remain anonymous. Our foremost appreciation goes to Dr V.K. Aatre, Former Scientific Advisor to the Defence Minister, Defence Research and Development Organization (DRDO), India and to Dr S. Pillai, Chief Controller of Research and Development, DRDO, for their encouragement and support along the way. In addition, we wish to thank many of our colleagues and students, including K.A. Jose, A. Mehta, B. Zhu, Y. Sha, H. Yoon, J. Xie, T. Ji, J. Kim, R. Mahapatra, D.P. Ghosh, C.V.S.

Sastry, A. Chakraborty, M. Mitra, S. Jose, O. Jayan and A. Roy for their contributions in preparing the manuscript for this book. We are very grateful to the staff of John Wiley & Sons, Ltd, Chichester, UK, for their helpful efforts and cheerful professionalism during this project.

Vijay K. Varadan
K. J. Vinoy
S. Gopalakrishnan

About the Authors

Vijay K. Varadan currently holds the 21st Century Endowed Chair in Nano- and Biotechnologies and Medicine and is Distinguished Professor of Electrical Engineering and Distinguished Professor of Biomedical Engineering (College of Engineering) and Neurosurgery (College of Medicine) at the University of Arkansas, USA. He is also the Director of the Institute for Nano-, Micro- and Neuroelectronics, Sensors and Systems and the Director of the High-Density Electronics Center. He has concentrated on the design and development of various electronic, acoustic and structural composites, smart materials, structures and devices, including sensors, transducers, Micro Electromechanical Systems (MEMS), plus the synthesis and large-scale fabrication of carbon nanotubes, Nano Electromechanical Systems (NEMS), microwave, acoustic and ultrasonic wave absorbers and filters. He has developed neurostimulators, wireless microsensors and systems for the sensing and control of Parkinson's disease, epilepsy, glucose in the blood and Alzheimer's disease. He is also currently developing both silicon- and organic-based wireless sensor systems with radio frequency identification (RFID) for human gait analysis and sleep disorders and various neurological disorders. He is an editor of the *Journal of Wave-Material Interaction* and the Editor-in-Chief of the *Journal of Smart Materials and Structures*, as well as being an Associate Editor of the *Journal of Microlithography, Microfabrication and Microsystems*. In addition, he also serves on the editorial board of the *International Journal of Computational Methods*. He has published more than 500 journal papers and 11 books. He holds 12 patents pertinent to conducting polymers, smart structures, smart antennas, phase shifters, carbon nanotubes, implantable devices for Parkinson's patients, MEMS accelerometers and gyroscopes.

K. J. Vinoy is an Assistant Professor in the Department of Electrical Communication Engineering at the Indian Institute of Science, Bangalore, India. He received

an M.Tech degree in Electronics from the Cochin University of Science and Technology, India and a Ph.D. degree in Engineering Science and Mechanics from the Pennsylvania State University, USA, in 1993 and 2002, respectively. From 1994 to 1998, he worked at the National Aerospace Laboratories, Bangalore, India. Following this, he was a research assistant at the Center for the Engineering of Electronic and Acoustic Materials and Devices (CEEAMD) at the Pennsylvania State University from 1999 to 2002. He continued there to carry out postdoctoral research from 2002 to August 2003. His research interests include several aspects of microwave engineering, RF-MEMS and smart material systems. He has published over 50 papers in technical journals and conference proceedings. His other publications include two books, namely *Radar Absorbing Materials: From Theory to Design and Characterization*, and *RF-MEMS and their Applications*. He also holds one US patent.

S. Gopalakrishnan received his Master's Degree in Engineering Mechanics from the Indian Institute of Technology, Madras, Chennai, India and his Ph.D. degree from the School of Aeronautics and Astronautics, Purdue University, USA. He joined the Department of Aerospace Engineering at the Indian Institute of Science, Bangalore, India in November 1997 as Assistant Professor and is currently an Associate Professor in the same department. His areas of interest include structural dynamics, wave propagation, computational mechanics, smart structures, MEMS and nanocomposite structures. He is a Fellow of the Indian National Academy of Engineering and a recipient of the 'Satish Dhawan Young Scientist Award' for outstanding contributions in Aerospace Sciences from the Government of Karnataka, India. He serves on the editorial board of three prime international computational mechanics journals and has published 70 papers in international journals and 45 conference papers.

Part 1

Fundamentals

Introduction to Smart Systems

1.1 COMPONENTS OF A SMART SYSTEM

The area of smart material systems has evolved from the unending quest of mankind to mimic mechanical systems of natural origin. The indispensable common objective in all such initiatives has been to develop technologies to produce non-biological systems that would achieve optimum functionality widely observed in biological systems through emulation of their adaptive capabilities and integrated design.

Smart materials are usually attached or embedded into structural systems to enable these structures to *sense* disturbances, *process* the information and *evoke reaction* at the actuators, possibly to negate the effect of the original disturbance. Thus, smart materials *respond* to environmental stimuli and for that reason are also called *responsive materials*. Since these smart material systems should mimic naturally occurring systems, the general requirements expected in these nonliving systems that integrate the functions sensing, actuation, logic and control include:

- A high degree of reliability, efficiency and sustainability of whole systems
- High security of infrastructures, even in extreme ambience
- Full integration of all functions of the system
- Continuous health and integrity monitoring
- Damage detection and self recovery
- Intelligent operational management system.

As one would notice, the materials involved in implementing this technology are not necessarily novel, but the smart systems technology has been accelerating at a tremendous pace in recent years. This has indeed been inspired by several innovative concepts developed around

the world. The prime movers for this technology have been the military and aerospace industries. Some of the ‘proof-of-concept’ programs have addressed structural health monitoring, vibration suppression, shape control and multifunctional structural aspects for spacecraft, launch vehicles, aircraft and rotorcraft. These demonstrations have focused on showing potential system-level performance improvements using smart technologies in realistic aerospace systems. Civil engineering structures, including bridges, runways and buildings, that incorporate this technology have also been demonstrated. Smart system design envisages the integration of the conventional fields of mechanical engineering, electrical engineering and computer science/information technology at the design stage of a product or a system.

The concept of ‘self-healing materials’ has received wide attention in recent years. For example, self-healing plastics may use materials that have the ability to heal cracks as and when these occur. Shape memory alloys (SMAs) in composites can stop propagating cracks by imposing compressive forces, resulting from stress-induced phase transformation. SMAs have also been used in spectacle frames to repair bends. Current research aims at developing adaptive, ‘self-repairing materials’ and structures that can arrest dynamic crack propagation, heal cracks, restore structural integrity and stiffness and reconfigure themselves to serve even more functions.

Before we head any further with this discussion, some clarifications regarding the terminology is called for. Several of these (e.g. smart, adaptive, intelligent and active) are sometimes used almost interchangeably to represent the type of materials and structures described above. Before we formally define a smart system, we would like to quote (Webster’s) dictionary meanings of these terms [1]:

- Active: producing or involving action or movement.
- Adaptive: showing or having a capacity for or tendency toward adaptation.
- Smart: making one smart; mentally alert; bright, knowledgeable.
- Intelligent: having or indicating a high or satisfactory degree of intelligence and mental capacity; revealing or reflecting good judgment or sound thought; skillful.
- Material: the elements, constituents or substances of which something is composed or can be made.
- Structure: the aggregate of elements of an entity in their relationships to each other.
- System: a group of devices or artificial objects or an organization forming a network especially for distributing something or serving a common purpose.

In the present context, a smart material is one whose electrical, mechanical or acoustic properties or their structure, composition or functions change in a specified manner in response to some stimulus from the environment. This response should be repetitive. However, the means by which the objectives are met could be many. Recall that dimensions of most materials change when heated; but then what distinguishes a smart material from the rest? This is one in which we *design* the material so that such changes occur in a specific manner. In addition, some other objective can also be accomplished based on it. Hence, the main objective in the area of smart materials is to identify materials which would respond to external stimuli that most materials are unresponsive to. Furthermore, one would want to maximize such response, at least one or two orders of magnitude better than the rest of the materials.

Being responsive to external stimuli is probably not sufficient to call a material smart. To define this more precisely, a structure or material system may be considered smart if it somehow evaluates the external stimuli and take some action based on them. This action may be to neutralize the effects of the external stimuli or to perform a function (completely different). This definition requires the system to have sensor(s), a feedback controller and actuator(s). The selection of sensors may be based on the type of stimuli expected, the controller may consist of information processing and storage units, while the actuator may depend on the type of function expected of the system. Materials or material systems that can be ‘programmed’ (possibly by tailoring their

composition) to behave in a certain way in response to an external stimulus may be called smart. These systems should:

- monitor environmental and internal conditions
- process the sensed data according to an internal algorithm
- decide whether to act based on the conditions(s) monitored
- implement the required action (if warranted)
- repeat the steps continuously.

As with any other engineering problem, systems designed with the above objectives should also have a high degree of reliability, efficiency and sustainability [2]. It should be possible to integrate such a system to existing platforms by replacing ‘dumb’ counterparts with little or no modifications to the rest of the platform. Thus, the technology areas that require urgent attention have been in developing new sensing and actuation materials and devices, and control techniques. In addition, another area that holds immense potential is in self-detection, self-diagnostic, self-corrective and self-controlled functions of smart material systems [2].

Some examples of smart system components are given in Table 1.1. These materials are usually embedded in systems to impart smartness. As this list indicates, most materials involved in smart systems are not new, while the smart system technology in itself is new. Smart systems are the result of a design philosophy that emphasizes predictive, adaptive and repetitive system responses. The improvements in the technology and widespread availability of cost-effective digital signal processors (DSPs) and microcontroller chips have a major influence on the accelerated growth in the smart systems market.

Brief descriptions of the materials included in Table 1.1 are given in the following.

Piezoelectric materials These are ceramics or polymers which can produce a linear change of shape in response to an applied electric field. The application of the field causes the material to expand or contract almost instantly. These materials have already found several uses in actuators in various diverse fields of science and technology. The converse effect has also been observed, which has led to their use as sensors.

Electrostrictive materials These materials can also change their dimensions significantly on the application of an electric field; the effect is reciprocal as well. Although the changes thus obtained are not linear in

Table 1.1 Examples of materials used in smart systems.

Development stage	Material type	Examples
<i>Widely commercialized</i>	Shape memory alloys Polymers: piezoelectric electrostrictive	NITINOL PZT-5A, 5H PMN-PT
<i>Early commercialization or under development</i>	Magnetostrictive materials Fiber-optic sensor systems Conductive polymers Chromogenic materials and systems: thermochromic electrochromic Controllable fluids: Electrorheological Magnetorheological	Terfenol-D — — — — — — —
<i>Early research and development</i>	Biomimetic polymers and gels Fullerenes and carbon nanotubes	— —

either direction, these materials have also found widespread application in medical and engineering fields.

Magnetostrictive materials These are quite similar to electrostrictive materials, except for the fact that they respond to magnetic fields. The most widely used magnetostrictive material is TERFENOL-D, which is made from the rarest of the rare earth elements, i.e. terbium. This material is highly non-linear and has the capability to produce large strains, which in turn can produce large ‘block forces’. These materials are also used in similar applications to those of electrostrictive materials.

Rheological materials While the materials described above are all solids, rheological materials are in the liquid phase. These can change state instantly through the application of an electric or magnetic charge. These fluids may find applications in brakes, shock absorbers and dampers for vehicle seats.

Thermoresponsive materials Shape memory alloys (SMAs) are another widely used type of smart materials, which change shape in response to changes in temperature. Once fabricated into a specified shape, these materials can retain/regain their shape at certain operating temperatures. They are therefore useful in thermostats and in parts of automotive and air vehicles.

Electrochromic materials Electrochromism is the ability of a material to change its optical properties (e.g. color) when a voltage is applied across it. These are used as antistatic layers, electrochrome layers in liquid crystal displays (LCDs) and cathodes in lithium batteries.

Fullerenes These are spherically caged molecules with carbon atoms at the corner of a polyhedral structure consisting of pentagons and hexagons. These are usually embedded in polymeric matrices for use in smart systems.

Biomimetic materials Most physical materials available contrast sharply with those in the natural world where animals and plants have the clear ability to adapt to their environment in real time. Some of the interesting features of the natural world include the ability of plants to adapt their shape in real time (for example, to allow leaf surfaces to follow the direction of sunlight) and limping (essentially a real-time change in the load path through the structure to avoid overload of a damaged region). The materials and structures involved in natural systems have the capability to sense their environment, process this data and respond instantly. It is widely accepted that living systems have much to teach us on the design of future man-made materials. The field of biomimetic materials explores the possibility of engineering material properties based on biological materials and structures.

Smart gels These are gels that can shrink or swell by several orders of magnitude (even by a factor of 1000). Some of these can also be programmed to absorb or release fluids in response to a chemical or physical stimulus. These gels are used in areas such as food, drug delivery and chemical processing.

In addition to having sensing and/or actuation properties, smart materials should also have further favorable characteristics [2]:

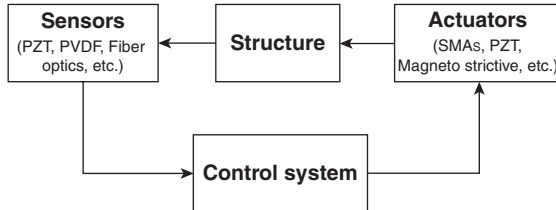


Figure 1.1 Building blocks of a typical smart system.

- Technical properties (e.g. mechanical, behavioral, thermal, electrical).
- Technological properties (e.g. manufacturing, forming, welding abilities, thermal processing).
- Economic aspects (e.g. raw material and production costs, availability).
- Environmental characteristics (e.g. toxicity, pollution, possibility of reuse or recycling).

Similar to a smart material, a smart structure would also require sensors, actuators and a controller, as shown in the schematic given in Figure 1.1. However, unlike smart material systems, the number of possible environmental stimuli monitored in this context is very limited and may include vibrations, cracks, etc. One distinctive feature of smart structures is that actuators and sensors can be embedded at discrete locations

inside the structure. One such example where this can be done is the *laminated composite structure*. Furthermore, in many applications the behavior of the entire structure itself is coupled with the surrounding medium. These factors necessitate a coupled modeling approach to analyze smart structures. The functions and descriptions of the various components of a smart structure are summarized in Table 1.2.

1.1.1 ‘Smartness’

As described above, a smart system is one that can assess a situation, determine if any responses are required and then perform these responses. In this context, ‘smartness’ may be characterized by self-adaptability, self-sensing, memory and decision making. Both active and passive systems have been used in this context. Usually, active sensors and actuators have been favored in designing smart structures. This is based on the requirement to generate the power required to perform responses. In recent years, the concept of *passive smartness* has come to the fore. Some characteristics of passive smartness are that it is pervasive and continuous in the structure, and there is no need for external intervention, and in addition, there is no requirement for a power source. This has a particular relevance to large-scale civil engineering infrastructures. Passive smartness can be derived from

Table 1.2 Purposes of the various components of a smart structure (adapted from Akhras [2]).

Unit	Equivalent in biological systems	Purpose	Description
Sensor	Tactile sensing	Data acquisition	Collect the required raw data needed for appropriate sensing and monitoring
Data bus 1	Sensory nerves	Data transmission	Forward the raw data to the local and/or central command and control units
Control system	Brain	Command and control unit	Manage and control the whole system by analyzing the data, reaching the appropriate conclusion and determining the actions required
Data bus 2	Motor nerves	Data instructions	Transmit the decisions and the associated instructions to the members of the structure
Actuator	Muscles	Action devices	Take the action by triggering the controlling devices/units

the unique intrinsic properties of the material used to build the structure. One common example is an SMA embedded in aerospace composites. Such structures are designed to prevent crack propagation.

We will now try to define smartness by borrowing some definitions from the observations of the Research Theory and Development – Smart Adaptive Systems (RTD – SAS) Technology Committee and the European Network on Intelligent Technologies (EUNITE) for Smart Adaptive Systems in the context of artificial intelligence, that ‘smart’ implies that intelligent techniques must be involved in the adaptation of a system for it to be considered a ‘smart adaptive system’ [3]. According to this, the accepted formal definition of ‘adaptive’ has three-levels of meanings, as follows:

- (1) Adaptation to a changing environment
- (2) Adaptation to a similar setting without explicitly being ‘ported’ to it
- (3) Adaptation to a new/unknown application.

In the first case, the system must adapt itself to a drifting (over time, space, etc.) environment, applying its intelligence to recognize the changes and react accordingly. This is probably the easiest concept of adaptation for which examples abound, e.g. control of non-stationary systems (drifting temperature).

In the second case, the emphasis is more on the change of the environment itself rather than on a drift of some features of the environment. Examples include systems that must be ported from one situation to another without explicitly changing any of their main parameters. Another example could be aerospace structures built to prevent crack formations and civil engineering structures that can withstand earthquakes.

The third level is the most futuristic one, but several of its research objectives have been addressed. For example, in the ‘machine-learning’ field, starting from very little information on the problem, it is now possible to build a system through incremental learning. Although this may

be the ultimate aim of most smart systems, such a level of smartness has not been observed in any man-made system.

1.1.2 Sensors, actuators, transducers

As discussed previously, smart systems should respond to internal (intrinsic) and environmental (extrinsic) stimuli. To do this, they should have sensors and actuators embedded in them. Let’s first look at the dictionary meaning of these terms (Merriam Webster’s Dictionary online [1]):

- **Transducer** A device that is actuated by power from one system and supplies power, usually in another form, to a second system.
- **Sensor** A device that responds to a physical stimulus (as heat, light, sound, pressure, magnetism or a particular motion) and transmits a resulting impulse (as for measurement or operating a control).
- **Actuator** One that actuates, e.g. a mechanical device for moving or controlling something.

Some of these devices commonly encountered in the context of smart systems are listed in Table 1.3.

1.1.3 Micro electromechanical systems (MEMS)

The emphasis here is to reduce the overall size of the system. Miniaturization can result in faster devices with improved thermal management. Energy and materials requirements during fabrication can be reduced significantly, thereby resulting in cost/performance advantages. Arrays of devices are possible within a small space. This has the potential for improved ‘redundancy’. Another important advantage of miniaturization is the possibility of integration with electronics, thereby simplifying systems and reducing the power requirements. Microfabrication employed for realizing such devices has improved reproducibility. The devices thus produced will have

Table 1.3 Some examples of sensors and actuators used in smart systems.

Device	Physical quantity	Example	Technology
<i>Sensor</i>	Acceleration	Accelerometer	PZT MEMS
	Angular rate	Gyroscope	Fiber optic
	Position	LVDT	Electromagnetic
<i>Transducer</i>	Crack detection	Ultrasonic transducer	PZT
	Movement	Thermal	Shape memory alloy

increased selectivity and sensitivity, a wider dynamic range and improved accuracy and reliability.

Smart micro electromechanical systems (MEMS) refer to collections of microsensors and actuators which can sense their environments and have the ability to react to changes in such environments with the use of a micro-circuit control. They include, in addition to conventional microelectronics packaging, integrating antenna structures for command signals into micro electromechanical structures for desired sensing and actuating functions. These systems may also need micro-power supply, micro-relay and micro-signal processing units. Micro-components make the systems faster, more reliable, cheaper and capable of incorporating more complex functions.

At the beginning of the 1990s, micro electromechanical systems (MEMS) emerged with advancements made in the development of integrated circuit (IC) fabrication processes, by which sensors, actuators and control functions are co-fabricated in silicon. Since then, remarkable progress has been achieved in MEMS under strong capital promotions from both government and industries. In addition to the commercialization of some less-integrated MEMS devices, such as micro-accelerometers, inkjet printer heads, micro-mirrors for projection, etc., the concepts and feasibility of more complex MEMS devices have been proposed and demonstrated for applications in such varied fields as microfluidics, aerospace, biomedical, chemical analysis, wireless communications, data storage, display, optics, etc. [4,5]. Some branches of MEMS, appearing as micro-optoelectromechanical systems (MOEMS), micro-total analysis systems (μ TAS), etc., have attracted a great deal of research interests since their potential applications market. By the end of the 1990s, most of the MEMS devices with various sensing or actuating mechanisms were fabricated by using silicon bulk micromachining, surface micromachining and LIGA¹ processes [6,7]. Three-dimensional microfabrication processes incorporating more materials have been recently presented for MEMS when some specific application requirements (e.g. biomedical devices) and micro-actuators with higher output powers were called for [4,8,9].

Micromachining has become the fundamental technology for fabrication of MEMS devices and, in particular, miniaturized sensors and actuators. Silicon micromachining is the most mature of the micromachining

technologies and allows for the fabrication of MEMS that have dimensions in the sub-millimeter range. It refers to fashioning microscopic mechanical parts out of a silicon substrate or on a silicon substrate, making the structures three-dimensional and bringing new principles to the designers. By employing materials such as crystalline silicon, polycrystalline silicon and silicon nitride, etc., a variety of mechanical microstructures, including beams, diaphragms, grooves, orifices, springs, gears, suspensions and a great diversity of other complex mechanical structures, has been conceived.

Silicon micromachining has been the key factor for the fast progress of MEMS in the last decade of the 20th Century. This refers to the fashioning of microscopic mechanical parts out of silicon substrates and, more recently, other materials. It is used to fabricate such features as clamped beams, membranes, cantilevers, grooves, orifices, springs, gears, suspensions, etc. These can be assembled to create a variety of sensors. Bulk micromachining is the most commonly used method but it is being replaced by surface micromachining which offers the attractive possibility of integrating the machined device with microelectronics which can be patterned and assembled on the same wafer. Thus, power supply circuitry and signal processing using ASICs (Application Specific Integrated Circuits) can be incorporated. It is the efficiency of creating several such complete packages using existing technology that makes this an attractive approach.

Micro devices can also be fabricated by using stereo lithography of polymeric multifunctional structures. Stereo lithography is a ‘poor man’s’ LIGA for fabricating high-aspect-ratio MEMS devices in UV-curable semiconducting polymers. With proper doping, a semiconducting polymer structure can be synthesized. By using stereo lithography, it is now possible to make three-dimensional microstructures of high aspect ratio. Ikuta and Hirowatari [10] demonstrated that a three-dimensional microstructure of polymers and metal is feasible by using a process named the *IH Process*, also known as Integrated Harden Polymer Stereo Lithography. Using a UV light source, an XYZ-stage, a shutter, lens and microcomputer, they have shown that micro devices, such as spring, various valve and electrostatic microactuators, can be fabricated. In the case of difficulty with the polymeric materials, some of these devices can be micromachined in silicon and the system architecture can be obtained by photoforming or hybrid processing [11–13]. Photoforming or photofabrication employs an optical method, such as stereo lithography, a photo mask layering process and the IH process which involves

¹LIGA – German acronym for Lithographie, Galvanoformung, Abformung (lithography, galvanoforming, molding).

solidification of the photochemical resin by light exposure. Takagi and Nakajima [14] proposed new concepts of ‘combined architecture’ and ‘glue mechanism’ by using the photoforming process to fabricate complicated structures by combining components, each of them made by its best fabrication process. Batch processing of such hybrid silicon and polymer devices thus seems feasible.

The combined architecture may also result in sheets of smart skins with integrated sensors and actuators at the μm to mm scale. For some applications (say airfoil surfaces), the smart skin substrate has to be flexible to conform to the airfoil shape and at the same time it has to be compatible with the IC processing for sensor and smart electronics integration. It has been proposed by Carraway [15] that polyimide is an excellent material for use as the skin because of its flexibility and IC processing compatibility. The control loop between the sensors and actuators employs multifunctional materials which provide electrical functionality at selected locations using conductive polymers and electrodes that are connected to on-site antennas communicating with a central antenna. A related and difficult problem, and one which has been largely unaddressed is the method for telemetry of the data. In some applications, stresses and strains to which the structure is subjected to may pose a problem for conventional cabling. In others, environmental effects may affect system performance. Advances in conformal antenna technology coupled with MEMS sensors/actuators appear to be an efficient solution. The integration of micromachining and microelectronics on one chip results in so-called smart sensors. In the latter, small sensor signals are amplified, conditioned and transformed into a standard output format. They may include a micro controller, digital signal processor, application specific integrated circuit (ASIC), self test, self-calibration and bus interface circuits simplifying their use and making them more accurate and reliable.

Many basic MEMS devices have a diaphragm, microbridge or cantilever structure. Special processing steps, commonly known as micromachining, are needed to fabricate these. For a given application, it may be necessary to have integrated MEMS employing one or more of the basic structures. These three structures provide some feasible designs for microsensors and actuators that eventually perform the desired task in most smart structures. However, the main issues with respect to implementing these structures are the choice of materials and the micromachining technologies to fabricate such devices.

To address the first issue, we note that in all of the three structures proposed the sensing and actuation occur

as a result of exciting a piezoelectric layer by the application of an electric field. This excitation brings about sensing and actuation in the form of expansion in the diaphragm, or in the free-standing beam in the microbridge structure, or in the cantilever beam. In the former two cases, the expansion translates into upward curvature in the diaphragm or in the free-standing beam, hence resulting in a net vertical displacement from the unexcited equilibrium configuration. In the cantilever case, however, upon the application of an electric field the actuation occurs by a vertical upward movement of the cantilever tip. Evidently, in all three designs the material system structure of the active part (diaphragm, free-standing beam or cantilever beam) in the microactuator must comprise at least one piezoelectric layer as well as conducting electrodes for the application of an electric field across this layer. Piezoelectric force is used for actuation for many of the applications mentioned above. Micromachining is employed to fabricate the membranes, cantilever beams and resonant structures.

1.1.4 Control algorithms

As mentioned earlier, a smart system consists of a sensor, an actuator and a control system. The desired operations on a smart system are performed by an actuator by taking the instructions given by the control systems. These instructions are given to the actuator using a suitable control law that is driven by a set of control algorithms. The main objective of the control system is to inject a control force onto the system to perform the desired operation. These control forces can be injected into the system by using the coupling characteristics of smart materials. That is, for example, if we use a PZT actuator, in the absence of any mechanical disturbance, the passing of a voltage on the actuator causes the smart system to expand (or contract). These strains can be converted into forces to perform the desired operations such as vibration reductions in structural systems, shape control of aerofoil cross-sections in an aircraft, etc. The control algorithms necessarily direct the type of operations that a system has to perform to get the desired results.

The control law that drives a smart system could be ‘open-loop’ or ‘closed-loop’. In an open-loop system, the system is injected with a known parameter (for example, a known voltage in the case of a PZT actuator or a known value of AC current in the case of a magnetostrictive actuator) to generate the control forces for meeting the target application. Such a control system is not suitable in the real-world, wherein the uncertainties are so much that

it is not always possible to quantify the value of the parameter that is required to meet the control objective. As opposed to the open-loop control, closed-loop control to a great extent can work better in a non-deterministic framework. The closed-loop control can be of two categories, namely the ‘feed forward’ and ‘feed back’, wherein the later is more easily realizable and hence extensively used in real-world application.

A closed-loop control system can be designed in many ways. The most common design essentially takes the sensed response and feeds it back to the actuator to obtain the desired control objective. The responses that are fed back to the actuator in structural applications could be displacements, velocities or accelerations. Such a controller design is called a Proportional, Proportional-Integral (PI) or Proportional-Integral-Differential (PID) controller.

1.1.5 Modeling approaches

The development of mathematical model for analysis depends on the following:

- The size of the smart system – Macro or micro system.
- The type of applications, such as vibration control, structural health monitoring etc.
- The constitutive behavior of the smart material, namely linear or non-linear.
- The frequency content of the input loading, that is, low-frequency or high-frequency loading.
- Small-deformation and large-deformation problems.

The most common method of modeling the macro structure is by the well-established Finite Element Method (FEM). This method can also handle effectively the material and geometrical non-linearities. However, FEM is limited to problems wherein the frequency content of input excitation is band-limited. However for problems involving, say, the structural health monitoring of smart laminated composite structures, one has to inject a pulse having a very high frequency content (of the order of kHz and higher) to detect the presence of small damages. This problem essentially transforms from a dynamics to a wave-propagation problem. For such problems, FEM is unsuitable from a computational viewpoint due to the limitation that the element size should be of the order of the wavelengths. In such situations, one can use wave-based Spectral Element Modeling (SEM). The main disadvantage with SEM, however, is that it is not as versatile as FEM in modeling arbitrary geometries.

Hence, one has to judiciously choose the type of modeling to suit the problem on hand.

Modeling of a microsystem can also be handled by FEM. Many researchers have designed many new MEMS by using FEM. Modeling through techniques such as FEM are based on a continuum analysis. However, one has to clearly understand that beyond a certain size of the system, the continuum analysis assumption breaks down. In most MEMS devices that are reported in the literature, the sizes are such that the continuum assumption does hold and hence one can still use FEM to model these devices.

1.1.6 Effects of scaling

For the modeling of nano-scale devices, one has to bring in the effect of scale. Nano-scale devices are of the order of 10–100 nanometers in size. In most cases, at these sizes the continuum assumptions break down. A classic example is the analysis of single-wall or multi-wall carbon nanotubes. Analysis of such systems can be performed either by molecular dynamic modeling or quasi-continuum modeling, although there are a few reports that state that the results of continuum modeling are reasonable.

The effects of scale become more profound when these nanotubes are embedded in, say, composites. It is well known that these nanotubes have enormous stiffness and hence can resist the deformation significantly. This cannot be effectively captured if one resorts to single-scale modeling. Therefore, one should adopt a multi-scale modeling approach. That is, in a small region of the nanotubes, one has to adopt a nano-scale modeling approach, such as a molecular dynamics model, and ‘lump’ the effects of this onto a macro-model of the composites. Multi-scale modeling is an open area of research worldwide and many researchers are working towards breaking the size barrier and to come up with an effective way of incorporating the effects of scale on the modeling technique.

1.1.7 Optimization schemes

Optimization schemes forms an essential part in the modeling of a smart system. These schemes are necessary whenever constraints arise in designing a smart system. Most of the smart sensors/actuators are very expensive and these have to be located judiciously on the system, keeping cost in mind and at the same time maximizing the efficiency of the system by meeting the required control objective.

For all optimization problems, an objective function is required. For example, for the placement of sensors and actuators in a structure, the main objective is to increase the sensitivity of the sensors. This sensitivity can be increased if it can effectively measure higher strains (and hence the stresses). Thus, the objective function for this problem will be to locate regions of higher strains and minimum stress gradients.

There are two major optimization schemes that are reported in the literature. One is the gradient-based optimization, where the assumption is made that the optimal solution to the problem lies in a space wherein the gradient of a variable (such as displacement, strains, stress, etc.) is minimum. This is the most common approach. The second approach is based on a genetic algorithm, wherein all probable solutions are assumed and eliminated by using the concept of Darwin's Theory of Evolution, namely 'survival of the fittest'.

1.2 EVOLUTION OF SMART MATERIALS AND STRUCTURES

The field of smart materials and structures is interdisciplinary between science and technology and combines the knowledge of physics, mathematics, chemistry, computer sciences, with material, electrical and mechanical engineering. It implements human creativity and innovative ideas to serve human society for such tasks as making a safer car, a more comfortable airplane, a self-repair water pipe, etc. Smart structures can help us to control the environment better and to increase the energy efficiency of devices.

Smart structures are usually systems containing multifunctional components that can perform sensing, control and actuation. Key materials used to construct these structures are called smart materials. The 'smartness' of these is gauged by their responsiveness (large change in amplitude) and agility (speed of response). Materials used in these applications may include single-phase or functional composite materials, and smart structures.

Single-phase materials used in this context have one or more large anomalies associated with phase-transition phenomena. Functional composites are generally designed to use nonfunctional materials to enhance functional materials or to combine several functional materials to make a multifunctional composite. Examples include donor-doped BaTiO₃ ceramics that are typically used for sensing temperature.

A magnetic probe is a multifunctional composite in which a magnetostrictive material is integrated with a piezoelectric material to produce a large magnetoelectric effect. The magnetostrictive material will produce shape deformation under a magnetic field, and this shape deformation produces a stress on the piezoelectric material which generates electric charge.

As mentioned earlier, smart structures involve sensors, actuators and a control system. Apart from the use of better functional materials as sensors and actuators, an important part of a 'smarter' structure is to develop an optimized control algorithm that could guide the actuators to perform required functions after sensing changes.

Active damping is one of the most studied areas using smart structures. A number of active damping schemes with guaranteed stability have been developed by using collocated actuators and sensors (i.e. physically located at the same place and energetically conjugated, such as force and displacement). These schemes are categorized on the basis of feedback type in the control procedure, i.e. velocity, displacement or acceleration.

Although several natural materials (such as piezoelectric, electrostrictive and magnetostrictive materials) are classified as smart materials, these usually have limited amplitude responses and must be operated in a limited temperature range. Chemical and mechanical methods may be used to tailor their properties for a particular smart structure design.

The **shape memory effect** in materials was first observed in the 1930s by Arne Olander while working with an alloy of gold and cadmium. This Au–Cd alloy was plastically deformed when cold but returned to its original configuration when heated. The shape memory properties of nickel–titanium alloys were discovered in the early 1960s. Although pure nickel–titanium has very low ductility in the martensitic phase, the properties can be modified significantly by the addition of a small amount of a third element. These groups of alloys are known as NitinolTM (Nickel–Titanium–Naval–Ordnance–Laboratories). Ni–Ti SMAs are less expensive, easier to work with and less hazardous than previous SMAs.

Commercial products based on SMAs began to appear in the 1970s. Initial applications for these materials were in static devices such as pipe fittings. Later SMA devices have also been used in sensors and actuators. In order to perform well in these devices, the SMA must experience a cycle of heating, cooling and deformation within a short time span.

Ferroelectric SMAs offer the possibility of introducing strain magnetically. This effect was discovered in the 1990s on SMAs with high magnetocrystalline anisotropy and high magnetic moment (e.g. Ni₂MnGa). These materials produce strain of up to 6 % at room temperature.

The **piezoelectric effect** was initially observed by Pierre and Jacques Curie in 1880. They discovered a connection between the macroscopic piezoelectric phenomena and the crystallographic structure in crystals of sugar and Rochelle salt. The reverse effect of materials producing strain when subjected to an electric field was first mathematically deduced from fundamental thermodynamic principles by Lippmann in 1881. Several naturally occurring materials were shown to display these effects. Nickel sonar transducers using this effect came to be used in the World War I.

This application triggered intense research and development into a variety of piezoelectric (ceramic) formulations and shapes. Since then, several sonar transducers, circuits, systems and materials have been reported. The second generation of piezoelectric applications was developed during World War II. It was discovered that certain ceramic materials, known as ‘ferroelectrics’, showed dielectric constants up to 100 times larger than common-cut crystals and exhibited similar improvements in piezoelectric properties. Soon, the barium titanate and lead zirconate titanate families of piezoceramics were developed. Some of these began to be used in structural health monitoring and vibration damping. Polymeric materials, such as poly (vinylidene fluoride) (PVDF), have also been shown to exhibit similar characteristics. Intense research is still going on to produce useful and reasonably priced actuators, which are low in power consumption and high in reliability and environmental ruggedness.

The **electrostrictive effect** is similar to piezoelectricity and converts the electrical pulse into a mechanical output; yet electrostriction is caused by electric polarization and has a quadratic dependence. The main difference between electrostrictive and piezoelectric materials is that the former doesn’t show spontaneous polarization and hence no hysteresis, even at very high frequencies. Electrostriction occurs in all materials, but the induced strain is usually too small to be utilized practically. Electrostrictive ceramics, based on a class of materials known as ‘relaxor ferroelectrics’, show strains comparable to those of piezoelectric materials (strain ~0.1 %) and have already found application in many commercial systems. New materials such as carbon nanotubes

have also been shown to have significant electrostrictive properties.

The **magnetostrictive effect** was first reported in iron in the 1840s by James P. Joule. The inverse effect was discovered later by Villari. Other materials, such as cobalt and nickel, also showed small strains. Some of the first sonars were built on this principle. Large-scale commercialization of this effect began with the discovery of ‘giant’ magnetostriction in rare-earth alloys during the 1960s. These showed 0.2–0.7 % strain, which is two orders of magnitude higher than nickel. An alloy of these materials, ‘Terfenol-D’ (named after its constituents, terbium, iron and dysprosium, and place of invention, the Naval Ordnance Laboratory (NOL) exhibits relatively large strains (0.16–0.24 %) at room temperature and at relatively small applied fields. Terfenol-D has now become the leading magnetostrictive material for engineering use. The development of polymer matrix Terfenol-D particulate composites has further overcome some of the limitations of ‘pure’ Terfenol-D.

‘Field-responsive’ fluids were also known to exist since the 19th Century. The effective viscosity of some pure insulating liquids was found to increase when an electric field is applied. This phenomenon, originally termed the ‘electro-viscous effect’, later came to be called the **electro-rheological (ER) effect**. These materials usually consist of suspensions of solid semiconducting materials (e.g. gelatin) in low-viscosity insulating oils (e.g. silicone oil).

In some ER compositions, both Coulomb and viscous damping can be achieved so that a vibration damper can be fabricated. The limitations of most ER fluids include the relative low yield stress and its temperature-dependence, the sensitivity of ER fluids to impurities (which may alter the polarization mechanisms) and the need for high-voltage power supplies (which are relatively expensive).

The **magnetorheological (MR) effect** was discovered by J. Rabinow in the late 1940s. However, due to some difficulties in using MR fluids in actual applications, these have not yet become popular. One of the difficulties was the low ‘quality’ of the early MR fluids which caused the inability of the particles to remain suspended in the carrier liquid. Recently, MR fluids have found new potential in engineering applications (e.g. vibration control), due to their higher yield stress and the lower voltage requirement (compared to ER fluids). These have also been commercially exploited for an active suspension system for automobiles and controllable fluid brakes for fitness equipment.

1.3 APPLICATION AREAS FOR SMART SYSTEMS

Developments in the areas of smart materials and structural systems have centered around the natural human instinct of 'mimicking nature'. Although the technology is yet far from this goal, several systems with consumer, aerospace and military applications have been produced in recent years. As one can imagine, new possibilities emerge as time goes by. Hence, readers are cautioned that the items described below should not be construed as representing an exhaustive list.

Reduction of vibrations in sporting goods. To increase the users' comfort, several new smart sporting goods (e.g. tennis rackets, golf clubs, baseball bats, skis, etc.) are available on the market.

Noise control in vehicles. Composites of piezoelectric ceramic fibers are used to reduce noise in vehicles, shaking in helicopter rotor blades or vibrations in air conditioner fans and automobile dashboards.

Aerospace applications. Demonstrated aerospace applications of smart structures include the spatial high accuracy position encoding and control system (SHAPE-CONS) and Frangibolt (used to deploy solar arrays, antennas and satellites from a launch vehicle) in the Clementine mission.

In addition, *several military applications* have been envisaged for smart materials and structures. In the battlefield, soldiers may wear clothing made of special tactile material that can detect signals from the human body to determine bullet wounds. This information can then be used to analyze the nature of the wound, decide on the urgency to react and possibly take some action to stabilize the situation.

There are several potential locations for the use of smart materials and structures in aircraft. Ground, marine or space smart vehicles will be a feature of future military operations. These manned or unmanned carriage systems, equipped with sensors, actuators and sophisticated controls, can improve surveillance and target identification and improve battlefield awareness. These smart vehicles could even be constructed using stealth technologies for their own protection. The B-2 stealth bomber or the F-117 stealth fighter are good examples of this technology. Smart systems are also needed for the quick and reliable identification of space or underwater stealth targets. Smart systems may also be used to improve the performance of otherwise 'dumb' systems. Examples of applications in many diverse areas are presented in Table 1.4.

In the future, it may even be possible to develop structures that are smart enough to communicate directly

with the human brain using MEMS-based devices. Smart noses, tongues, etc. have already been developed by various groups. Newer sensors may even extend human sensing capabilities, such as by enabling us to detect more scents, hear beyond our normal frequency range, and see what we cannot normally see (using IR). There is also significant scope for developing newer capabilities in the domain of smart structures. It can be expected that we will see further smarter materials and structures being developed in the near future.

1.4 ORGANIZATION OF THE BOOK

This book is divided into fifteen chapters, describing fundamentals, design principles, modeling techniques, fabrication methods and applications of smart material systems and MEMS. The first two chapters of the book deal with the fundamental concepts of smart systems and their constituent components. Preliminary concepts of these materials will be introduced, along with important characteristics expected of them, in Chapter 2.

In the second part of the book, the design principles for sensors and actuators are discussed in detail. Here, we first begin with the design philosophy behind some commonly available sensors, such as accelerometers, gyroscopes, pressure sensors and chemical and biosensors. The design issues of bulk sensors made from piezoelectric, magnetostrictive and ferroelectric materials are also given in Chapter 3. This is followed (Chapter 4) by the basic design principles of several actuators. Chapter 5 is devoted to examples describing the design principles of sensors and actuators, wherein the principles behind developing components with SMAs, piezoelectric, electrostrictive and magnetostrictive materials are given.

Chapters 6–9 dwell on a detailed account of modeling of smart systems. First, the theory of elasticity and composites are introduced, which serve as prerequisites for the advanced techniques that follow. Next, the complete theory and application of finite element (FE) modeling is given, including an introduction to variational methods, various element formulations and equation solutions for both discretized statics and dynamics equations of motion in Chapter 7. Following this, the basic concepts of wave propagation and spectral finite element modeling is introduced, which are used to study wave propagation in isotropic and composite structures. This is followed, in Chapter 8, by the modeling of smart sensors and actuators, where the approach is demonstrated by using a number of examples. The last chapter

Table 1.4 Applications of smart systems in various areas.

Application	System	Use
Machine tools	Piezoceramic transducers	To control ‘chatter’ and thereby improve precision and increase productivity
Photolithography	Vibration control during the process using piezoceramic transducers	In the manufacture of smaller microelectronic circuits
Process control	Shape memory alloys	For shape control, e.g. in aerodynamic surfaces
Health Monitoring	Fiber-optic sensors	To monitor the ‘health’ of fiber-reinforced ceramics and metal–matrix composites and in structural composites
Consumer electronics	Piezoceramic and MEMS accelerometers and rotation-rate sensors; quartz, piezoceramic and fiber-optic gyros; piezoceramic transducers	For shake-stabilization of hand-held video cameras
Helicopters and aircraft	Piezoceramic stack actuators; PZT and MEMS accelerometers; magnetostrictive mounts	Vibration and twist control of helicopter rotor blades and adaptive control of aircraft control surfaces
	Piezoceramic pick-ups and error sensors; PZT audio resonators and analog voice coils; digital signal processor chips	Active noise control
Submarines	Piezoceramic actuators	Acoustic signature suppression of submarine hulls
Automotive	Electrochromics (sol-gel, sputtered and vacuum-evaporated oxides; solution-phase reversible organic redox systems); suspended particles; dispersed liquid crystals; reversible electrodeposition Piezo yaw-axis rotation sensors (antiskid, antilock braking); ceramic ultrasonic ‘radar’ (collision avoidance, parking assist); MEMS accelerometers (air bag controls); electronic stability controls (four-wheel independent auto braking) Piezopolymer IR sensors; rain monitors; occupant identification; HVAC sensors; air pollution sensors (CO and NO _x)	Chromogenic mirrors and windows Smart comfort control systems
In Buildings	IR, vision and fiber-optic sensors and communications systems	For improved safety, security and energy control systems; smart windows to reduce heating, ventilation and air conditioning costs

Table 1.4 (Continued)

Application	System	Use
Biomechanical and biomedical systems	Shape memory alloys and polymer gels	To develop artificial muscles; active control of <i>in vivo</i> drug-delivery devices (insulin pumps)
	Piezoceramic and other ultrasonic sensors and actuators	Catheter guide wires; surgical tools; imaging devices
Computer industry	Piezoceramic and MEMS accelerometers and rotation rate sensors; quartz, piezoceramic and fiber-optic gyros	For smart read/write head micropositioners in next-generation data storage devices
	bimorph-type piezo-positioner and asperity-detector arms	For high-density disk drives
	Piezo-accelerometers to provide error-anticipating signals	To correct for head-motion-related read/write errors

in this part (Chapter 9) deals with control techniques required for smart actuation.

Next, we present a complete ‘bird’s eye view’ of the various fabrication techniques used for both bulk and microsensors and actuators. Building on the fundamental concepts from the earlier chapters, details of the bulk and surface micromachining concepts for the silicon-based processing of MEMS sensors and actuators are presented in Chapter 10. The techniques used to fabricate polymer-based systems, such as microstereolithography and micromolding, are also included in Chapter 11, opening up new opportunities, especially with regard to 3-dimensional microstructures. Due to their delicate nature, these microstructures are required to be packaged and integrated with the electronics. Chapter 12 is devoted entirely to these aspects. In addition, several examples of sensors and actuators fabricated by the above routes are included in Chapter 13.

The last two chapters of this book deal with some practical applications where smart technologies including microsystems are used to solve some real-world problems. Implementation issues in structural, vibration and noise-control applications are described in Chapters 14 and 15.

REFERENCES

1. Merriam Webster’s Dictionary: [Website: <http://www.m-w.com/cgi-bin/mwwod.pl>]
2. G. Akhras, ‘Smart materials and smart systems for the future’, *Canadian Military Journal*, 1(3), 25–31 (Autumn 2000).
3. EUNITE: [Website: <http://www.eunite.org/eunite.index.htm>]
4. H. Fujita, ‘Future of actuators and microsystems’, *Sensors and Actuators*, **A56**, 105–111 (1996).
5. H. Fujita, ‘Microactuators and micromachines’, *Proceedings of the IEEE*, **86**, 1721–1732 (1998).
6. G.T.A. Kovacs, N.I. Maluf and K.E. Petersen, ‘Bulk micromachining of silicon’, *Proceedings of the IEEE*, **86**, 1536–1551 (1998).
7. J.M. Bustillo, R.T. Howe and R.S. Muller, ‘Surface micromachining for microelectromechanical systems’, *Proceedings of the IEEE*, **86**, 1552–1574 (1998).
8. V.K. Varadan, X. Jiang, and V.V. Varadan, *Microstereolithography and other Fabrication Techniques for 3D MEMS*, John Wiley & Sons (2001).
9. G. Thornell and S. Johansson, ‘Microprocessing at the fingertips’, *Journal of Micromechanics and Microengineering*, **8**, 251–262 (1998).
10. K. Ikuta and K. Hirowatari, ‘Real three-dimensional micro-fabrication using stereolithography and metal molding’, in *Proceedings of the IEEE: MEMS’93*, IEEE, Piscataway, NJ, USA, pp. 42–47 (1993).
11. V.K. Varadan (Ed.), *Smart Electronics: SPIE Proceedings*, Vol. 2448, Bellingham, WA, USA (1995).
12. J. Tani and M. Esashi (Eds), *Proceedings of the International Symposium on Microsystems, Intelligent Materials and Robots*, Tohoku University, Japan (1995).
13. V.K. Varadan, and V.V. Varadan, ‘Three-dimensional polymeric and ceramic MEMS and their applications’, *Proceedings of SPIE*, **2722**, 156–164 (1996).
14. T. Tatagi and N. Nakajima, ‘Photoforming applied to fine machining’, in *Proceedings of the IEEE: MEMS’93*, IEEE, Piscataway, NJ, USA, pp. 173–178 (1993).
15. D.L. Carraway, ‘The use of silicon microsensors in smart skins for aerodynamic research’ in *Proceedings of the International Congress on Instrumentation in Aerospace Simulation Facilities*, IEEE, Piscataway, NJ, USA, pp. 413–422 (1991).

Processing of Smart Materials

2.1 INTRODUCTION

Smart microsystems are a collection of microsensors and actuators which can sense their environment and have the ability to react to changes in that environment with the use of a microcircuit control. The system may also need micro-power supply and microelectronics for signal processing. These components make the system efficient, faster, more reliable, cheaper, less power consuming and capable of incorporating more complex functions. Yet, the critical functional components of smart systems are sensors and actuators. A number of novel materials have been developed in recent years for use in these components.

Silicon-based micro-fabrication has been the key factor for the rapid developments in MEMS. During the 1980s, micro electromechanical systems (MEMS) spun off from the developments in integrated circuit (IC) fabrication processes, enabling co-fabrication of sensors, actuators and control functions on silicon chips. Since then, remarkable research advances have been made in this area. Presently, most MEMS devices are fabricated by bulk micromachining, surface micromachining, and LIGA processes on silicon wafers [1–3]. Three-dimensional micro-fabrication processes, incorporating layers of more materials, were recently reported for MEMS in some specific application areas (e.g. biomedical devices) and micro-actuators with higher output powers [4–9]. Many micro devices are also fabricated by using semiconductor processing technologies or stereo lithography on the polymeric multifunctional structures [10,11]. The combined architecture may also result in sheets of ‘smart skins’ with integrated sensors and actuators at the μm to mm scale. For example, in airfoil surfaces, the smart skin substrate has to be flexible enough to conform to the airfoil shape and at the same time

compatible with the IC processing procedure for sensor and smart electronics integration.

A knowledge of the relevant properties of materials is essential in establishing their role in various devices. MEMS materials include metals, semiconductors, ceramics, polymers and composites. Some of the common materials which are used are listed in Table 2.1. In several MEMS devices, substrates are primarily used for mechanical support only. In many others, these facilitate IC compatibility. Thin film materials can have several roles in micro systems. For example, they could form structural or sacrificial layers in surface micromachined components. Dielectric thin films are usually polymeric, ceramic or silicon-based materials. In general, these thin film materials can have multiple functions. For example, ‘poly-silicon’ and metal films are used as *conductors* (layouts/electrodes), as well as *structural layers*. Sometimes, the same material may have opposing functions in different devices. For example, SiO_2 is usually used as a *sacrificial material* but it is also used as a structural or *etch stop layer* in other cases. Some of these terminologies will be defined later in this chapter, while the chapter in general focuses on introducing some well-known processing approaches for these materials.

2.2 SEMICONDUCTORS AND THEIR PROCESSING

Semiconductor substrates are essential starting points in the fabrication of MEMS-based smart microsystems. Their electrical properties are essential in ‘building’ the necessary electronics, while their mechanical properties allow fabrication of several structural components. Semiconductors are commonly inorganic materials, often made from elements in the fourth column (Group IV)

Table 2.1 Materials used in MEMS and microelectronics.

Functional class	Type of material	Example
<i>Substrate</i>	Semiconductor	Si, GaAs, InP
	Ceramic	MgO, alumina, sapphire
	Plastic	Plexiglass
	Glass	—
<i>Thin films</i>	Dielectric	SiO ₂ , Si ₃ N ₄ , PMMA
	Metal	Al, Au, Ag, Pd, Pt, Cu, Ti; alloys
	Functional ceramic	PZT, STO, BST
	Semiconductor	Si
<i>Packages</i>	Poly-silicon	—
	Plastic	—
	Ceramic	—
Metal	—	—

of the Periodic Table. The most important among these elements is silicon, since this can be modified in several ways to change its electrical, mechanical and optical properties. The use of silicon in solid-state electronics and microelectronics has shown a spectacular growth since the early 1970s. Other semiconductor materials, from Group IV elements in the Periodic Table, are germanium and carbon (diamond). Semiconductor materials can also be made from a combination of elements from either Group III and Group V or Group II and Group VI. Examples of these ‘compound semiconductors’ are gallium arsenide and zinc telluride.

The name ‘semiconductor’ is given to these materials because at certain regimes of temperatures they are able to exhibit good electrical conduction properties, while outside of these temperature regimes they behave as insulators. The crystal structures of semiconductors are explained based on the *cubic crystalline system*. In the diamond lattice, each atom has four nearest neighbors. In GaAs, one of the two arrays is composed entirely of Ga atoms, while the other array is composed of As atoms. This particular class of the diamond structure is called the *zinc blende structure*. In both elemental and compound semiconductors, there is an average of four valence electrons per atom. Each atom is thus held in the crystal by four covalent bonds with two electrons participating in each bond. In a ‘perfect’ semiconductor crystal at a temperature of absolute zero, the number of available electrons would exactly fill the inner atomic shells and the covalent bonds. At temperatures above absolute zero, some of these electrons gain enough thermal energy to break loose from these covalent bonds and become *free electrons*. The latter are responsible for electrical conduction across the semiconductor crystal. The physical properties of some selected semiconductor crystals are given in Table 2.2.

By themselves, these semiconductors are of little use in electronics and are usually doped with donor and acceptor impurities for the fabrication of active components and circuits. Semiconductor materials are said to be ‘doped’ when traces of impurities are added to them. These doped semiconductors are referred to as *extrinsic* semiconductors, in contrast to *intrinsic* (undoped) semiconductor materials. Diffusion and ion implantation are the two key processes used to introduce controlled amounts of dopants into semiconductors. These two processes are used to selectively dope the semiconductor substrate to produce either an *n*-type or a *p*-type region.

Table 2.2 Typical physical properties of some common semiconductors.

Property	Crystalline silicon	Poly-silicon	Germanium	GaAs
Density (kg/m ³)	2330	2320	5350	5316
Melting point (°C)	1410	—	937	1238
Electrical conductivity (10 ³ × S/cm)	4 × 10 ⁻³	1	3 × 10 ⁻⁵	~10 ⁻⁵
Energy band gap (eV)	1.1	1.1	0.67	1.35
Thermal conductivity (W/m/K)	168	150	60	370
Dielectric constant	11.7	—	16.3	12
Young’s modulus (GPa)	190	161	—	—

Table 2.3 Electrical, mechanical and thermal properties of crystalline silicon.

Property	Parameter	Value
<i>Electrical</i>	Minority-carrier lifetime	30–300 µs
	Resistivity (B-doped)	0.005–50 Ω cm
	Resistivity (P-doped)	1–50 Ω cm
	Resistivity (Sb-doped)	0.005–10 Ω cm
<i>Mechanical</i>	Density	2.3 gm/cm ³
	Dislocations	< 500/cm ²
	Yield strength	7 × 10 ⁹ N/m ²
<i>Thermal</i>	Young's modulus	1.9 × 10 ¹¹ N/m ²
	Thermal conductivity	1.57 W/cm °C
	Thermal expansion	2.33 × 10 ⁻⁶ /°C

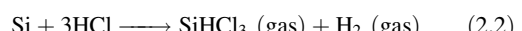
Apart from being the most important material for microelectronics and integrated circuit technology, silicon and its compounds and their technologies are the ‘cornerstones’ for MEMS and nanofabrication. For this reason, we will be concentrating on silicon and using it to demonstrate the general properties of semiconductor materials. Table 2.3 lists the relevant mechanical, electrical and thermal properties of single-crystalline silicon. It may be recalled that silicon has several sensory properties. For example, it exhibits piezo resistivity, thermal variation and optical properties. In addition, silicon also has excellent mechanical properties. For example, Si has a better yield strength than steel, a lower density than aluminum, a better hardness than steel, and a Young's modulus approaching that of steel.

2.2.1 Silicon crystal growth from the melt

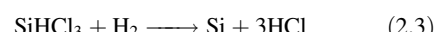
To demonstrate the methods of growing semiconductors, we will consider the crystal growth of silicon in detail first. Basically, the technique used for silicon crystal growth from the melt is the *Czochralski technique*. This starts from a pure form of sand (SiO_2), known as quartzite, which is placed in a furnace with different carbon-releasing materials, such as coal and coke. Several reactions then take place inside the furnace and the net reaction that results in silicon is as follows:



The silicon so-produced is known as metallurgical-grade silicon (MGS) which contains up to 2% of impurities. Subsequently, the silicon is treated with hydrogen chloride to form trichlorosilane (SiHCl_3):



SiHCl_3 is a liquid at room temperature. Fractional distillation of the SiHCl_3 removes the impurities and the purified liquid is reduced in a hydrogen atmosphere to yield electronic-grade silicon (EGS) by the following reaction:



EGS is a polycrystalline material of remarkably high purity and is used as the raw material for preparing high-quality Si wafers. The Czochralski technique employs the apparatus shown in Figure 2.1. To grow a crystal, the EGS is placed in the crucible and the furnace is heated above the melting temperature of silicon. An appropriately oriented seed crystal (e.g. [100]) is suspended over the crucible in a seed holder. The seed is then lowered into the melt. Part of it melts but the tip of the remaining seed crystal still touches the liquid surface. The seed is next gently withdrawn, and progressive freezing at the

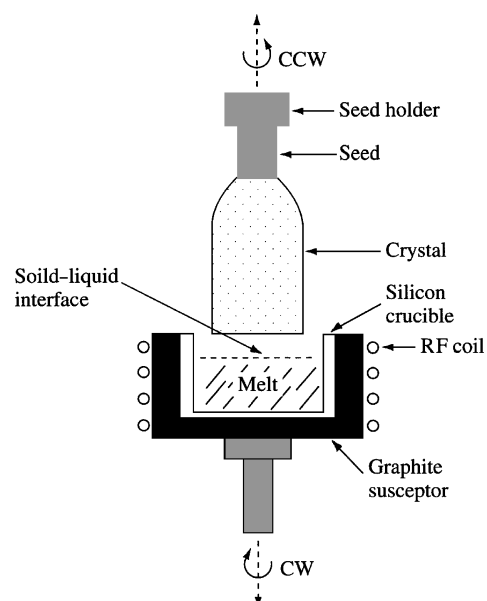


Figure 2.1 Schematic of the Czochralski crystal puller: CW, clockwise; CCW, counter-clockwise.

solid–liquid interface yields a large single crystal. Absolute control of temperatures and pull rate is required for high-quality crystals. A typical pull rate is a few millimeters per minute.

High-resistivity silicon can only be produced by using the *float-zone* crystal growth method, which does not use a crucible during crystal growth. However, the Czochralski method *does* use a quartz crucible during crystal growth and oxygen from the crucible unintentionally dopes the material. The oxygen dopant behaves as an *n*-type impurity and impedes high resistivity. The float-zone method is usually carried out in an inert gaseous atmosphere, keeping a polycrystalline rod and a seed crystal vertically face-to-face. Both are partially melted by high-frequency inductive heating at the (molten-zone) liquid phase. This molten zone is gradually moved upwards while rotating the seed crystal until the entire polycrystalline rod has been converted into a single crystal. This process has the advantage that there is no physical contact with the crucible. This method is difficult to carry out for producing large wafer sizes and is thus less used.

After a crystal is grown, the seed is removed from the other end of the ingot, which is then left to solidify. Next, the surface is ground so that the diameter of the material is defined. After this, one or more flat regions are ground along the length of the ingot to mark the specific crystal orientation of the ingot and the ‘conductivity type’ of the material (Figure 2.2). Finally, the ingot is sliced by a diamond saw into wafers. Such slicing determines four wafer parameters, i.e. surface orientation, thickness, taper (which is defined as the variation in wafer thickness from one end to another) and bow (i.e. surface curvature of the wafer, measured from the center of the wafer to its edge).

2.2.2 Epitaxial growth of semiconductors

In many situations, it may not be feasible to start with a silicon substrate to build a smart system. Instead, one

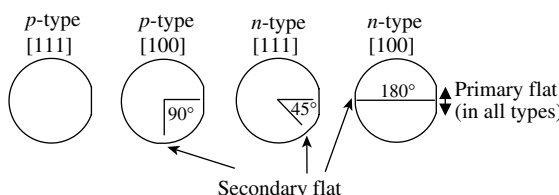


Figure 2.2 Crystal orientation and dopant types in commercial silicon wafers.

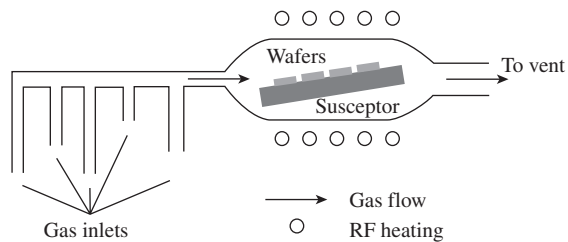
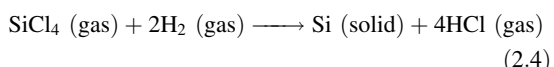


Figure 2.3 Schematic of the vapour phase epitaxy process used to produce silicon layers.

could start with other possibilities and grow silicon films on the substrate by epitaxial deposition to ‘build the necessary electronics’. The method for growing a silicon layer on a substrate wafer is known as an *epitaxial* process where the substrate wafer acts as the seed crystal. Epitaxial processes are different from crystal growth from the melt in that the epitaxial layer can be grown at a temperature much lower than the melting point. Among various epitaxial processes, vapor phase epitaxy (VPE) is the most common.

A schematic of the VPE apparatus is given in Figure 2.3, and shows a horizontal susceptor made from graphite blocks. The susceptor mechanically supports the wafer and being an induction-heated reactor it also serves as the source of thermal energy for the reaction.

Several silicon sources can be used, e.g. silicon tetrachloride (SiCl_4), dichlorosilane (SiH_2Cl_2), trichlorosilane (SiHCl_3) and silane (SiH_4). The typical reaction temperature for silicon tetrachloride is $\sim 1200^\circ\text{C}$. The overall reaction, in the case of silicon tetrachloride, is reduction by hydrogen, as follows:



A competing reaction which occurs simultaneously is:



In Equation (2.4), silicon is deposited on the wafer, whereas in Equation (2.5) silicon is removed (etched). Therefore, if the concentration of SiCl_4 is excessive, etching rather than growth of silicon will take place.

An alternative epitaxial process for silicon layer growth is *molecular beam epitaxy* (MBE) which is an epitaxial process involving the reaction of a thermal beam of silicon atoms with a silicon wafer surface under ultra-high vacuum conditions ($\sim 10^{-10}$ torr). MBE can achieve precise control in both chemical composition and impurity profiles when introduced intentionally. Single-crystal multilayer

structures with dimensions of the order of atomic layers can be made by using MBE. The solid source materials are placed in evaporation cells to provide an angular distribution of atoms or molecules in a beam. The substrate is heated to the necessary temperature and is often continuously rotated to improve the growth homogeneity.

2.3 METALS AND METALLIZATION TECHNIQUES

Metals are used in MEMS and microelectronics due to their good conductivities, both thermal and electrical. Metals are somewhat strong and ductile at room temperature and maintain good strength, even at elevated temperatures. Hence, they could also be used to form useful structures.

While thin metal films have been used in IC chips for a long time (primarily due to their electrical conductivities), thick metal film structures are required for some MEMS devices [12]. Thick metal films are generally used as structural materials in MEMS devices or as mold inserts for polymers in ceramic micromolding. Micro-electroplating and photoforming are used to build such thick metal structures [13,14]. Nickel, copper and gold can be electroplated to form these thick films, while three-dimensional stainless steel micro-parts can be fabricated by a process known as photoforming [8]. However, in most instances a layer of metal is first deposited by a process known as metallization.

Metallization is a process whereby metal films are formed on the surface of a substrate. These metallic films are used for interconnections, ohmic contacts, etc. Hence, their continuity, uniformity and surface properties are critical in the device performance. Metal films can be formed by using various methods, with the most important being *physical vapor deposition* (PVD). The latter is performed under vacuum by using either an evaporation or sputtering technique. In these, physical mechanisms, such as evaporation or impact, are used as the means of deposition – unlike in CVD where a chemical reaction is taking place under ‘favorable conditions’. In evaporation, atoms are removed from the source by thermal energy while in sputtering, the impact of gaseous ions is the cause of such removal.

The evaporation rate is a function of the vapor pressure of the metal. Hence, metals that have a low melting point (e.g. 660 °C for aluminum) are easily evaporated, whereas refractory metals require much higher temperatures (e.g. 3422 °C for tungsten) and can cause damage to

polymeric or plastic samples. In general, evaporated films are highly disordered and have large residual stresses; thus, only thin layers of the metal can be evaporated. The chemical purity of the evaporated films depends on the level of impurities in the source and contamination of the source from the heater, crucible or support materials and are also due to residual gases within the chamber [14]. In addition, the deposition process is relatively slow – at a few nanometers per second.

Sputtering is a physical phenomenon involving the acceleration of ions via a potential gradient and the bombardment of a ‘target’ or cathode. Through momentum transfer, atoms near the surface of the target metal become volatile and are transported as a vapor to a substrate. A film grows at the surface of the substrate via deposition. Sputtered films tend to have better uniformity than evaporated ones and the high-energy plasma overcomes the temperature limitations of evaporation. Most elements from the Periodic Table can be sputtered, as well as inorganic and organic compounds. Refractory materials can be sputtered with ease. In addition, materials from more than one target can be sputtered at the same time. This process is referred to as ‘co-sputtering’ and can be used to form ‘compound thin films’ on the substrate. The sputtering process can, however, be used to deposit films with the same stoichiometric composition as the source and hence allows the utilization of alloys as targets [14]. Sputtered thin films have better adhesion to the substrate and a greater number of grain orientations than evaporated films.

The structures of sputtered films are mainly amorphous and their stress and mechanical properties are sensitive to specific sputtering conditions. Some atoms of the inert gas can be trapped in the film, hence causing anomalies in the mechanical and structural characteristics. Therefore, the exact properties of a thin film vary according to the precise conditions under which it was grown. The deposition rate is proportional to the square of the current density and is inversely proportional to the spacing between the electrodes.

Metallo-organic chemical vapor deposition (MOCVD) is a relatively low temperature (200–800 °C) process for the epitaxial growth of metals on semiconductor substrates. Metallo-organics are compounds where each atom of the element is bound to one or many carbon atoms of various hydrocarbon groups. For precise control of the deposition, high-purity materials and very accurate controls are necessary [15]. However, due to the high cost, this approach is used only where high-quality metal films are required.

In addition to several elemental metals, various alloys have also been developed for MEMS. CoNiMn thin films have been used as permanent magnet materials for magnetic actuation. NiFe permalloy thick films have been electroplated on silicon substrates for magnetic MEMS devices, such as micromotors, micro-actuators, microsensors and integrated power converters [14]. TiNi shape memory alloy (SMA) films have been sputtered onto various substrates in order to produce several well-known SMA actuators [16]. Similarly, TbFe and SmFe thin films have also been used for magnetostrictive actuation [17].

2.4 CERAMICS

Ceramics are another major class of materials widely used in smart systems. These generally have better hardness and high-temperature strength. The thick ceramic film and three-dimensional (3D) ceramic structures are also necessary for MEMS for special applications. Both crystalline as well as non-crystalline materials are used in the context of MEMS. For example, ceramic pressure microsensors have been developed for pressure measurement in high-temperature environments [16], silicon carbide MEMS for harsh environments [18], etc. In addition to these structural ceramics, some functional ceramics, such as ZnO and PZT, have also been incorporated into smart systems.

New functional microsensors, micro-actuators and MEMS can be realized by combining ferroelectric thin films, having prominent sensing properties such as pyroelectric, piezoelectric and electro-optic effects, with micro devices and microstructures. There are several such ferroelectric materials including oxides and non-oxides and their selection depends on a specific application. Generally, ferroelectric oxides are superior to ferroelectric non-oxides for MEMS applications. One useful ferroelectric thin film studied for microsensors and RF-MEMS is barium strontium titanate [19]. Hence, as a typical example, we will concentrate on this material and its preparation method in this section.

Barium strontium titanate (BST) is of interest in bypass capacitors, dynamic random access memories and phase shifters for communication systems and adaptive antennas because of its high dielectric constant. The latter can be as high as 2500 at room temperature. For RF-MEMS applications, the loss tangent of such materials should be very low. The loss tangent of BST can be reduced to 0.005 by adding a small percentage (1–4 %)

of Fe, Ni and Mn to the material mixture [20–22]. The (Ba–Sr)TiO₃ series, (Pb–Sr)TiO₃ and (Pb–Ca)TiO₃ materials and similar titanates, having their Curie temperatures in the vicinity of room temperature, are well suited for MEMS phase shifter applications. The relative phase shift is obtained from the variation of the dielectric constant with DC biasing fields.

Ferroelectric thin films of BST have usually been fabricated by conventional methods, such as RF sputtering [23], laser ablation [24], MOCVD [25] and hydro-thermal treatment [25]. Even though sputtering is widely used for the deposition of thin films, it has the potential for film degradation by neutral and negative-ion bombardment during film growth. For BST, this ‘re-sputtering’ can lead to ‘off-stoichiometric’ films and degradation of its electrical properties. In a recent study, Cukauskas *et al.* [26] have shown that inverted cylindrical magnetron (ICM) RF sputtering is superior for BST. This fabrication set-up is discussed in the next section.

2.4.1 Bulk ceramics

As a high dielectric constant and low loss tangent are the prime characteristics of ceramic materials such as barium strontium titanate (BST), a ceramic composite of this material is usually fabricated as the bulk material. It is known that the Curie temperature of BST can be changed by adjusting the Ba:Sr ratio. Sol–gel processing is sometimes adopted to prepare Ba_{1-x}Sr_xTiO₃ for four values of *x*, i.e. 0.2, 0.4, 0.5 and 0.6. The sol–gel method offers advantages over other fabrication technique for better mixing of the precursors, homogeneity, purity of phase, stoichiometry control, ease of processing and controlling composition. The sol–gel technique is one of the most promising synthesis methods and is now being extensively used for the preparation of metal oxides in ‘bulk’, ‘thin film’ and ‘single crystal’ forms. The advantage of the sol–gel method is that metal oxides can easily be doped accurately to change their stoichiometric composition because the precursors are mixed at the ‘molecular level’ [27].

Titanium tetraisopropoxide (Ti(O–C₃H₇)₄) and catalyst are mixed in the appropriate molar ratio with methoxyethanol solvent and refluxed for 2 h at 80°C. Separate solutions of Ba and Sr are prepared by dissolving the 2,4-pentadionate salts of Ba and Sr in methoxyethanol. Mild heating is required for complete dissolution of the salts. The metal salt solution is then slowly transferred to the titania sol and the solution is refluxed for another 6 h. The sol is then hydrolyzed to

4 M concentration in water. It is important to note that direct addition of water leads to precipitation in the sol. Therefore, a mixture of water/solvent has to be prepared and then added to the sol drop-by-drop. The resultant sol is refluxed for 2 h to complete the hydrolysis. This sol was kept in an oven at 90 °C to obtain the xerogel and then heated at 800 °C for 30 min in air to obtain the BST powder. If necessary, the latter can be mixed at an appropriate wt % with metal oxides e.g. Al₂O₃ and MgO, in an ethanol slurry. Then, 3 wt % of a binder (e.g. an acrylic polymer) is added to the slurry and the mixture ball-milled using a zirconia grinding medium. Ball-milling is performed for 24 h and the material is then air-dried and properly sieved to avoid any agglomeration. The final powder is pressed at a pressure of 8 tonnes in a suitable sized mold. The composites are then fired under air, initially at 300 °C for 2 h and finally at 1250 °C for 5 h. The heating and cooling rate of the furnace is typically 1 °C/min. The structure of the Ba_{1-x}Sr_xTiO₃ is determined by using X-ray diffraction (XRD) so that a pure phase of the BST can be analyzed. The dielectric constants were measured at 1 MHz at room temperature by a two-probe method using an impedance analyzer (HP 4192A).

Metal oxides are used to fabricate composites of Ba_{1-x}Sr_xTiO₃ in order to vary its electronic properties. Investigations, carried out by varying the weight ratio of BST from 90 to 40 % in its composites with Al₂O₃ and MgO, indicate that the dielectric constant decreases with increasing metal oxide content. The dielectric constant of a BST composite with MgO is observed to be higher than its composite with Al₂O₃. It is assumed that the addition of metal oxides plays an important role in affecting the grain boundaries of Ba_{1-x}Sr_xTiO₃, which leads to an increase in dielectric loss. The composite of Ba_{1-x}Sr_xTiO₃ with alumina offers a low dielectric constant and low loss in comparison to MgO and hence is usually preferred for low-loss applications. It is concluded from these measurements that if we select a weight of metal oxide less than 10 %, then the loss tangent and the dielectric constant can be ‘tailored’ for the desired range [21].

2.4.2 Thick films

Tape casting is a basic fabrication process which can produce materials that are the backbone of the electronics industries where the major products are capacitor dielectrics, thick and thin film substrates, multilayer circuitry (ceramic packing) and piezoelectric devices. Particles

can be formed into dense, uniformly packed ‘green-ware’ by various techniques, such as sedimentation, slip casting, (doctor-blade) tape casting and electrophoretic deposition. Tape casting is used to form sheets – thin, flat ceramic pieces that have large surface areas and low thickness. Therefore, tape casting is a very specialized ceramic fabrication technique.

The doctor-blade process basically consists of suspending finely divided inorganic powders in aqueous or non-aqueous liquid systems composed of solvents, plasticizers and binders to form a slurry that is then cast onto a moving carrier surface. For a given stacking sequence, the strength is controlled by critical micro-cracks, whose severity is very sensitive to casting parameters such as the particle size of the powder, the organic used and the temperature profile. In this forming method, a large volume of binder (up to 50%) has to be added to the ceramic powder to achieve rheological properties appropriate for processing. This large volume of binder has to be removed before the final sintering can take place. There is usually a difference in firing shrinkage between the casting direction and the cross-casting direction for the tape.

Titanium tetrakisopropoxide (Ti(O—C₃H₇)₄) (1 mol) and triethanolamine (TEA) (molar ratio of 1 with respect to Ti(O—C₃H₇)₄) were mixed in appropriate molar ratios with methoxyethanol solvent (100 ml) and refluxed for 2 h at 80 °C. Separate solutions of 0.65 mol of Ba and 0.35 mol of Sr were prepared by dissolving the 2,4-pentadionate salts of Ba and Sr in methoxyethanol to achieve x = 0.35. Mild heating was required for complete dissolution of the salts. The metal salt solution was then slowly transferred to the titania sol, and the solution refluxed for another 6 h. The sol was then hydrolyzed with a particular concentration of water (molar ratio of 2 with respect to Ti(O—C₃H₇)₄). A water/solvent mixture has to be prepared and then added to the sol drop-by-drop to avoid precipitation. The resultant sol was refluxed for another 6 h to allow complete hydrolysis. This sol was then kept in an oven at 90 °C for 6–7 days in order to obtain the xerogel. Finally, the xerogel was calcined at 900 °C for 30 min in air.

BST powder can also be prepared by a ‘conventional’ method. In this approach, oxides of barium, strontium and titanate were used at appropriate molar ratios for achieving a value of x of 0.35. These oxides were mixed with 100 ml of ethyl alcohol in a plastic container and ball-milled for 24 h with zirconia balls. The slurry from the container was transferred into a beaker and dried in an oven at 80 °C for 2 days in

air. The dried powder was calcined at 900 °C for 30 min.

A tape-casting technique is used to fabricate ceramic multilayered BST tape. BST powder obtained by one of the above methods was mixed with 10 wt% of ethanol and 10 wt% of methyl ethyl ketone (MEK); 1 wt% of fish oil was then added to the mixture. Calvert *et al.* [28] have reported that fish oil is far superior than triglycerides due to the polymeric structure induced by oxidation. The mixture is ball-milled in a plastic jar with a zirconia

medium for 24 h. ‘Santicizer’ (4 wt%), used as a plasticizer, was added to the resultant slurry, followed by 4 wt% of Carbowax 400 (poly(ethylene glycol)) along with 0.73 wt% of cyclohexanone. ‘Acryloid’ (13.9 wt%) was added to the slurry as a binder. The slurry was ball-milled for another 24 h and then tape-cast and ‘de-aired’. The tape-cast BST was punched and stacked to produce multiple layers. The tapes were then pressed at a pressure of 35 MPa and a temperature of 70 °C for 15 min. A schematic of this process is shown in Figure 2.4

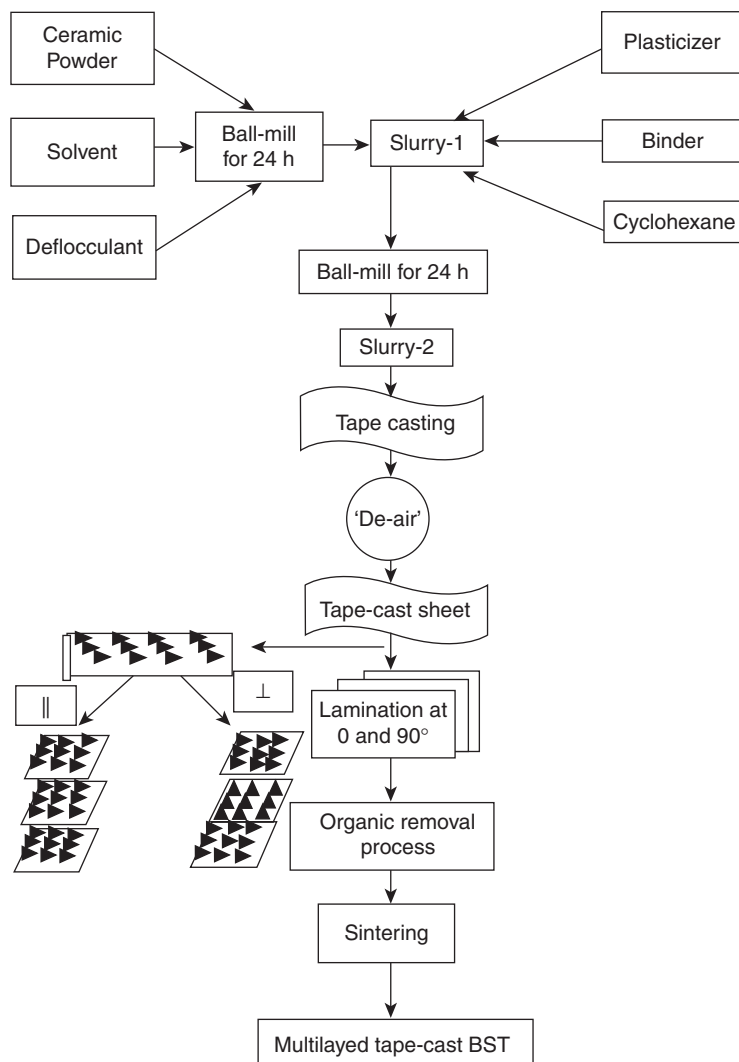


Figure 2.4 Flow chart for thick film fabrication using the doctor-blade process.

2.4.3 Thin films

Thin films of ceramic materials can be fabricated by using several different approaches. In this section, we will first describe RF sputtering. Due to its similarity with the thick film and bulk processing techniques described above, the sol–gel process for thin films is also presented here.

2.4.3.1 Inverted cylindrical magnetron (ICM)

RF sputtering

Figure 2.5 illustrates the ICM sputter gun set-up [26]. This consists of a water-cooled copper cathode, which houses the hollow cylindrical BST target, surrounded by a ring magnet concentric with the target. A stainless steel thermal shield is mounted to shield the magnet from the thermal radiation coming from the heated table. The anode is recessed in the hollow-cathode space. The latter aids in collecting electrons and negative ions, hence minimizing ‘re-sputtering’ the growing film. Outside the deposition chamber, a copper ground wire is attached between the anode and the stainless steel chamber. A DC bias voltage could be applied to the anode to alter the plasma characteristics in the cathode/anode space. The sputter gas enters the cathode region through the space surrounding the table.

By using the above set-up, Cukauskas *et al.* [26] were able to deposit BST films at temperatures ranging from 550 to 800 °C. The substrate temperature was maintained by two quartz lamps, a type-K thermocouple and a temperature controller. The films were deposited at 135 W to a film thickness of 7000 Å and cooled to room temperature at 1 atm of oxygen before removing them from the deposition unit. This was then followed by

annealing the films in 1 atm of flowing oxygen at a temperature of 780 °C for 8 h in a tube furnace.

2.4.3.2 Sol–gel processing technique

The sputtering techniques described above and other methods, such as laser ablation, MOCVD and hydro-thermal treatment, require much work, time and high costs of instrumentations, which lead to a high cost for the final product. However, large areas of homogenous films can be obtained by relatively low temperature heat treatment. The sol–gel method is a technique for producing inorganic thin films without processing in vacuum, and offers high purity and ensures homogeneity of the components at the ‘molecular level’ [29].

In the sol–gel method, the precursor solution of barium strontium titanates is prepared from barium 2-ethyl hexanoate, strontium 2-ethyl hexanoate and titanium tetraisopropoxide (TTIP). Methyl alcohol is used as a solvent, along with acetyl acetone. A known amount of barium precursor is dissolved in 30 ml of methyl alcohol and refluxed at a temperature of about 80 °C for 5 h. Strontium 2-ethyl hexanoate is added to this solution and refluxed for a further 5 h to obtain a yellow-colored solution. Acetylacetone is added to the solution as a chelating agent, which prevents any precipitation. This solution is stirred and refluxed for another 3 h. Separately, a solution of titanium isopropoxide (TTIP) is prepared in 20 ml of methyl alcohol; this solution is added to the barium strontium solution drop-by-drop and finally refluxed for 4 h at 80 °C. Water is added to the BST solution drop-by-drop in order to initiate hydrolysis. This solution is refluxed for another 6 h with vigorous stirring under a nitrogen atmosphere.

For thin-film deposition and characterization, one could use a substrate such as platinized silicon or a ceramic. The substrate is immersed in methanol and dried by nitrogen gas to remove any dust particles. The precursor solution is coated on the substrate by *spin coating*. The latter is carried out by using a spinner rotated at a rate of 3100 rpm for 30 s. After coating on the substrate, the films are kept on a hot plate for 15 min to dry and pyrolyze the organics. This process can be repeated to produce multilayer films if needed. In such cases repeated heating after every spin coat is required in order to successfully ‘burn off’ the organics trapped in the films. This improves the crystallinity and leads to a dense sample after multiple coating. To obtain thicker films, many depositions are required. The films are then annealed at 700 °C for 1 h in air. The annealing temperature and duration has a significant effect in the film orientation and properties [30,31].

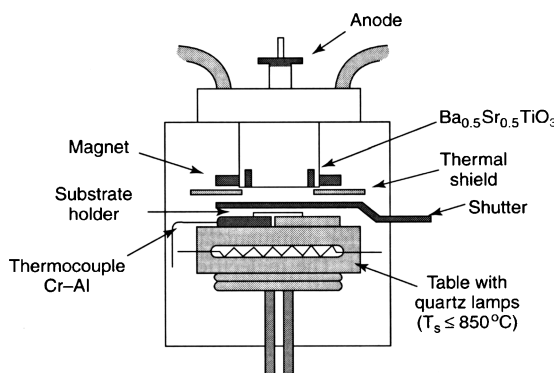


Figure 2.5 Schematic of the ICM sputter gun set-up [26].

2.5 SILICON MICROMACHINING TECHNIQUES

Micromachining is the fundamental technology for the fabrication of micro electromechanical (MEMS) devices, in particular, miniaturized sensors and actuators having dimensions in the sub-millimeter range. Silicon micromachining is the most mature of the micromachining technologies. This process refers to the fashioning of microscopic mechanical parts out of a silicon substrate or on a silicon substrate, thus making the structures three dimensional and hence bringing in new avenues to designers. By employing materials such as crystalline silicon, polycrystalline silicon and silicon nitride, a variety of mechanical microstructures, including beams, diaphragms, grooves, orifices, springs, gears, suspensions and numerous other complex mechanical structures, have been fabricated [32–36].

Silicon micromachining has been a key factor for the vast progress of MEMS towards the end of the 20th Century. Silicon micromachining comprises two technologies: bulk micromachining, in which structures are etched into a silicon substrate, and surface micromachining in which the micromechanical layers are formed from layers and films deposited on the surface. Yet another but less common method, i.e. LIGA 3D micro-fabrication, has been used for the fabrication of high-aspect ratio and three dimensional microstructures for MEMS.

Bulk micromachining, which originated in the 1960s, has matured as the principal silicon micromachining technology and has since been used in the successful fabrication of many microstructures. Presently, bulk micromachining is employed to fabricate the majority of commercial devices – pressure sensors, silicon valves and acceleration sensors. The term ‘bulk micromachining’ arises from the fact that this type of micromachining is used to realize micromechanical structures within the bulk of a single-crystal silicon wafer by selectively removing the wafer material. The microstructures fabricated by using bulk micromachining may vary in thickness from sub-microns to the full thickness of a wafer (200 to 500 μm), with the lateral size ranging from microns to the full diameter of a wafer (usually 75 to 200 mm).

The bulk micromachining technique allows selective removal of significant amounts of silicon from a substrate to form membranes on one side of the wafer, a variety of trenches, holes or other structures. In addition to an etch process, bulk micromachining often requires *wafer bonding* and *buried-oxide-layer* technologies [37]. However the use of the latter in bulk micromachining is still in its infancy. In recent years, a vertical-walled bulk

micromachining techniques, known as single crystal reactive etching and metallization (SCREAM) which is a combination of anisotropic and isotropic plasma etching, has also been used [36].

Since the beginning of the 1980s, significant interest has been directed towards micromechanical structures fabricated by a technique called *surface micromachining*. This approach does not shape the bulk silicon, but instead builds structures on the surface of the silicon by depositing thin films of ‘sacrificial layers’ and ‘structural layers’ and by eventually removing the sacrificial layers to release the mechanical structures. More details on the processing steps involved in the fabrication of MEMS components using these techniques will be discussed in Chapter 10. The dimensions of these surface-micromachined structures can be several orders of magnitude smaller than bulk-micromachined structures. The resulting ‘2½-dimensional’ structures are mainly located on the surface of the silicon wafer and exist as a thin film – hence the ‘half dimension’. The main advantage of surface-micromachined structures is their easy integration with IC components, since the same wafer surface can also be processed for IC elements. Surface micromachining can therefore be used to build monolithic MEMS devices.

2.6 POLYMERS AND THEIR SYNTHESIS

Polymers are very large molecules (macromolecules) made up of a number of small molecules. These small molecules which connect with each other to build up the polymer are referred to as monomers and the reaction by which they connect together is called polymerization. Recently, a considerable effort is being focused on the use of polymers in microelectronics and micro electro-mechanical systems (MEMS). Features that make them particularly attractive are moldability, conformability, ease in deposition in the form of thin and thick films, semiconducting and even metallic behavior in selected polymers, a choice of widely different molecular structures and the possibility of piezoelectric and pyroelectric effects in the polymer side-chain.

For several MEMS devices, the polymers need to have conductive and possibly piezoelectric or ferroelectric properties. For these polymers to be used for polymeric MEMS, they should have the following:

- Strong interfacial adhesion between the various polymer layers.
- Suitable elastic moduli to support the deformation required in MEMS.

- Excellent overall dimension stability.
- Long-term environmental stability.

In addition, their processing should help attachment of nanoceramics and/or conductive phases and formation of a uniform coating layer. Furthermore, many of these polymers provide a large strain under an electric field and thus can be used as actuators for MEMS-based devices such as micro pumps.

Polymer processing techniques include photopolymerization, electrochemical polymerization and vacuum polymerization, either stimulated by electron bombardment or initiated by ultraviolet irradiation, or microwave-assisted polymerization. These methods are also widely used for processing and curing thin and thick polymer films on silicon-based electronic components.

Two types of polymers are employed for micromachining polymeric MEMS devices: structural polymers and sacrificial polymers. The structural polymer is usually a UV-curable polymer with a urethane acrylate, epoxy acrylate or acryloxy silane as the main ingredient. Its low viscosity allows easy processing through automatic equipment or by manual methods without the need to add solvents or heat to reduce the viscosity. It also complies with all volatile organic compound (VOC) regulations. It has excellent flexibility and resistance to fungus, solvents, water and chemicals. The structural polymer may be used as a backbone structure for building the multifunctional polymer described below.

It should be pointed out here that the above structural polymers can also be used to construct sensing and actuating components for MEMS. Polymer strain gauges and capacitors can serve as sensing elements for piezo-resistive and capacitive microsensors [38]. Another important point is that as the wafer polymer micro-fabrication process is being developed for polymer micro devices, the batch fabrication of polymereric MEMS will not be a serious concern.

The sacrificial polymer is an acrylic resin containing 50% silica and is modified by adding crystal violet, as given in Varadan and Varadan [38]. This composition is UV-curable and can be dissolved with 2 mol/l of caustic soda at 80 °C. In principle, this process is similar to the surface micromachining technique used for silicon devices. However, the process yields 3D structures.

Since only limited sensing and actuation mechanisms can be obtained using structural polymers by themselves, a large variety of functional polymers have been used for MEMS [39]. Some of these functional polymers are listed in Table 2.4. Such polymers used in smart systems may contain several functional groups. A ‘Functional group’ is

Table 2.4 Functional polymers for MEMS.

Polymer	Functional property	Application
PVDF	Piezoelectricity	Sensor/actuator
Polypyrrole	Conductivity	Sensor/actuator/electric/connection
Fluorosilicone	Electrostrictivity	Actuator [40]
Silicone	Electrostrictivity	Actuator [40]
Polyurethane	Electrostrictivity	Actuator [40]

defined as the atom or group of atoms that defines the structure of a particular family of organic compounds and, at the same time, determines their properties. Some examples of functional groups are the double bond in alkenes, triple bond in alkynes, the amino ($-NH_2$) group, the carboxyl ($-COOH$) group, the hydroxyl ($-OH$) group, etc. ‘Functionality’ can be defined as the number of such functional groups per molecule of the compound.

Many polymers used in MEMS are biocompatible and are thus useful for many medical devices. Applications of these include implanted medical delivery systems, chemical and biological instruments, fluid delivery in engines, pump coolants and refrigerants for local cooling of electronic components.

Functional polymer-solid powder composites with magnetic and magnetostrictive properties have also been developed for micro devices. For example, the polymer-bonded Terfenol-D composites showed excellent magnetostrictivity, useful for micro-actuation [41]. The polyimide-based ferrite magnetic composites have been used as polymer magnets for magnetic micro-actuators [42].

In addition to being used as sensing and actuating materials, polymers have also been used for electronics materials. Polymer transistors have been developed. Therefore, integrating polymer sensors, actuators and electronics into polymeric MEMS will be practical for some special applications.

2.6.1 Classification of polymers

Polymers can be classified, based on their structure (linear, branched or cross-linked), by the method of synthesis, physical properties (thermoplastic or thermoset) and by end-use (plastic, elastomer, fiber or liquid resin).

A linear polymer is made up of identical units arranged in a linear sequence. This type of polymer has only two functional groups. Branched polymers are those

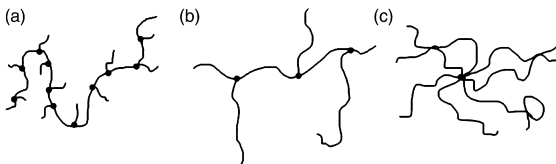


Figure 2.6 The various kinds of branching in polymers: (a) short; (b) long; (c) star.

in which there are many side-chains of lined monomers attached to the main polymer chain at various points. These side-chains could be either short or long (Figure 2.6). When polymer molecules are linked with each other at points, other than their ends, to form a network, the polymers are said to be cross-linked (Figure 2.7). Cross-linked polymers are insoluble in all solvents, even at elevated temperatures.

Based on their physical properties, polymers may be classified as either thermoplastic or thermoset. A polymer is said to be a *thermoplastic* if it softens (flows) when it is squeezed, or pulled, by a load, usually at a high temperature, and hardens on cooling. This process of reshaping and cooling can be repeated several times. High-density polyethylene (HDPE) or low-density polyethylene (LDPE), poly(vinyl chloride) (PVC) and nylon are some examples of thermoplastic polymers.

Thermoset polymers, on the other hand, can flow easily and can be molded when initially produced. Once they are molded in to their shape, usually by applying heat and pressure, these materials become very hard. This process of the polymer becoming an infusible and insoluble mass is called ‘curing’. Reheating such a thermosetting polymer just results in the degradation of the polymer and will distort the object made. Epoxy and phenol formaldehyde are some examples of thermosetting polymers.

Depending upon their final use, polymers can be classified as plastic, elastomer, fiber or liquid resin. When a polymer is formed into hard and tough articles by the application of heat and pressure, then it is used as

a *plastic*. When a polymer is vulcanized into rubbery materials, which show good strength and elongation, it is used as an *elastomer*. *Fibers* are polymers drawn into long filament-like materials, whose lengths are at least 100 times their diameters. When the polymer is used in the liquid form, such as in sealants or adhesives, they are called *liquid resins*.

2.6.2 Methods of polymerization

There are basically two methods by which polymers can be synthesized, namely ‘addition’ or ‘chain’ polymerization and ‘condensation’ or ‘step-growth’ polymerization. When molecules just add on to form the polymer, the process is called ‘addition’ or ‘chain’ polymerization. The monomer in this case retains its structural identity, even after it is converted into the polymer, i.e. the chemical repeat unit in the polymer is the same as the monomer. When molecules react with each other (with the elimination of small molecules such as water, methane, etc.), instead of simply adding together, the process is called step-growth polymerization. In this case, the chemical repeat unit is different from the monomer.

2.6.2.1 Addition polymerization

Compounds containing a reactive double bond usually undergo addition polymerization, also called chain polymerization. In this type of polymerization process, a low-molecular-weight monomer molecule with a double bond breaks the double bond so that the resulting free valencies will be able to bond to other similar molecules to form the polymer. This polymerization takes place in three steps, namely, initiation, propagation and termination. This can be induced by a free-radical, ionic or coordination mechanism. Depending on the mechanism, there are therefore three types of chain polymerization, namely, free radical, ionic (cationic and anionic) and coordination polymerization. The coordination polymerization mechanism is excluded in this present discussion due to its specialized nature.

2.6.2.2 Free-radical polymerization

There are three steps in polymerization: initiation, propagation and termination. In this type of polymerization, the *initiation* is brought about by the free radicals produced by the decomposition of initiators, where the latter break down to form free radicals. Each component has an unpaired (lone) electron and is called a free

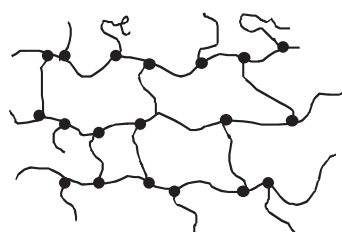
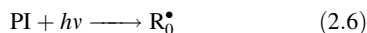


Figure 2.7 Illustration of cross-linking in polymers.

radical. This radical adds to a molecule of the monomer and in doing so generates another free radical. This radical adds to another molecule of the monomer to generate a still larger radical, which in turn adds to yet another molecule of monomer, and the process continues.

The decomposition of the initiator to form these free radicals can be induced by heat, light energy or catalysts. Peroxides, many azo compounds, hydroperoxides and peracids are the most commonly used initiators. The latter can also be decomposed by UV light. The rate of decomposition in this case depends mainly on the intensity and wavelength of radiation and not so much on the temperature. A polymerization reaction initiated by UV light falls under the category of *photoinitiated* polymerization. The reaction in such a case may be expressed as follows

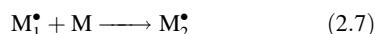


where PI represents the photoinitiator, and R_0^\bullet is the reactive intermediate from the UV cleavage of PI.

UV curing is therefore based on photoinitiated polymerization which is mediated by photoinitiators. These photoinitiators are required to absorb light in the UV-visible spectral range, generally 250–550 nm, and convert this light energy into chemical energy in the form of reactive intermediates, such as free radicals and reactive cations, which subsequently initiates the polymerization.

During the *propagation* step, the radical site on the first monomer unit reacts with the double bond of a ‘fresh’ monomer molecule, which results in the linking up of the second monomer unit to the first and the transfer of the free radical onto the second monomer molecule. This process, involving the attack on a fresh monomer molecule, which in turn keeps adding to the growing chain, is called propagation. The chain keeps propagating as far as the monomer is available. This step can also end when the free-radical site is ‘killed’ by some impurities or by the termination process.

The propagation step can be represented as follows:



where M represents the monomer molecule, and $\text{M}_1^\bullet \dots \text{M}_n^\bullet$ represent reactive molecules.

The last step in the polymerization reaction is called *termination*. In this step, any further addition of the monomer units to the growing chain is stopped and the growth of the polymer chain is inhibited. The decomposition of the initiator results in the formation of a large number of

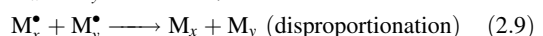
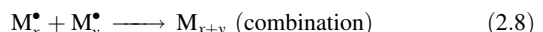
Table 2.5 Examples of monomers polymerized by using free-radical polymerization.

Monomer	Structure
Ethylene	$\text{CH}_2=\text{CH}_2$
Butadiene	$\text{CH}_2=\text{CH}-\text{CH}=\text{CH}_2$
Styrene	$\text{CH}_2=\text{CH}-\text{C}_6\text{H}_5$
Vinyl chloride	$\text{CH}_2=\text{CH}-\text{Cl}$
Vinylidene chloride	CH_2-CCl_2
Acrylic acid	$\text{CH}_2=\text{CH}-\text{COOH}$
Methyl methacrylate	$\text{CH}_2-\text{C}(\text{CH}_3)\text{COOCH}_3$

free radicals. Depending on factors such as temperature, time and monomer and initiator concentrations, there exists a chance when the growing chains collide against each other. This can occur in two ways:

- Termination by combination – the chain terminates by the simple formation of a bond between two radicals.
- Termination by disproportionation – a proton is transferred and a double bond is formed.

These reactions can be represented as follows:



where M_{x+y} is the stable polymer molecule containing $x+y$ monomer units, while M_x and M_y are also stable polymer molecules with x and y monomer units, respectively.

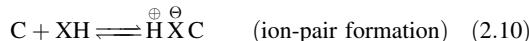
Some common monomers that can be polymerized by using free-radical polymerization are listed in Table 2.5.

2.6.2.3 Cationic polymerization

Ionic polymerization involves the breaking down of the π -electron pair of the monomer. This is not done by free radicals but by either a positive or negative ion. If the active site has a positive charge (i.e. a carbonium ion), then it is called *cationic polymerization*. Monomers which have an electron-donating group are the most suitable for cationic polymerization, for example, alkyl vinyl ethers, vinyl acetals, isobutylene, etc.

Initiation in this case can be achieved by using protic acids and Lewis acids. The latter usually require a ‘co-catalyst’ such as water or methyl alcohol. Here, a proton is introduced into the monomer. This proton pulls the π -electron pair towards it and this is how the positive

charge moves to the other end of the monomer, hence resulting in the formation of a carbonium ion:

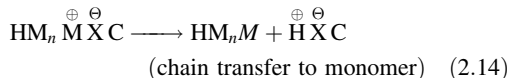
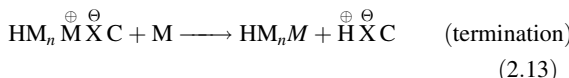


where C is the catalyst, XC the co-catalyst and M the monomer.

Propagation of the cationic polymerization reaction occurs as the carbonium ion attacks the π -electron pair of the second monomer molecule. The positive charge is then transferred to the farther end of the second monomer, and thus a chain reaction is started:



Termination can occur by anion–cation recombination, resulting in an ester group. Termination can also occur by splitting of the anion. This occurs by reaction with trace amounts of water:

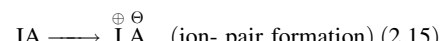


2.6.2.4 Anionic polymerization

If the active site has a negative charge (i.e. a carbanion), then the process is called anionic polymerization. Monomers capable of undergoing anionic polymerization are isoprene, styrene and butadiene.

Initiation takes place in the same way as in cationic polymerization, except that here a carbanion is formed. The general initiators used in this case are the alkyl and aryl derivatives of alkali metals such as triphenyl methyl potassium and ethyl sodium. *Propagation* then proceeds with the transfer of the negative charge to the end of the monomer molecule. Termination is not always a spontaneous process, and unless some impurities are present or some strongly ionic substances are added, termination does not occur. So, if an inert solvent is used and if impurities are avoided, the reaction proceeds up until all of the monomer is consumed. Once this is achieved, the carbanions at the end of the chain still remain active and are considered as ‘living’; polymers synthesized by using this method are known

as ‘living polymers’. This technique is useful for producing block copolymers.



where IA is the initiator and HA is a protonating agent,

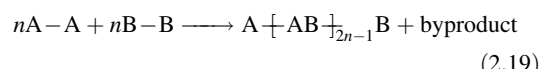
2.6.2.5 Step-growth polymerization

Step polymerizations are carried out by the stepwise reaction between the functional groups of the monomers. In such polymerizations, the size of the polymer chains increases at a relatively slow rate from monomer to dimer, trimer, tetramer and so on:

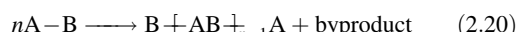
Monomer + Monomer	(Dimer)
Dimer + Monomer	(Trimer)
Dimer + Dimer	(Tetramer)
Trimer + Dimer	(Pentamer)
Trimer + Trimer	(Hexamer)

Any two molecular species can react with each other throughout the course of the polymerization until, eventually, large polymer molecules consisting of large numbers of monomer molecules have been formed. These reactions take place when monomers containing more than two reactive functional groups react. Typical condensation polymers include polyamides, polyesters, polyurethanes, polycarbonates, polysulfides, phenol formaldehyde, urea formaldehyde and melamine formaldehyde.

When a pair of bifunctional monomers (dicarboxylic acid/diamine or dialcohol/dihalide) undergoes polycondensation, it is called an AA–BB-type polycondensation:



When a single bifunctional monomer undergoes self-condensation, it is known as an A-B type polycondensation.



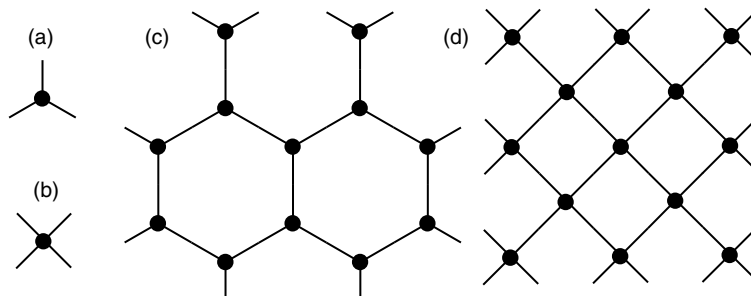


Figure 2.8 Illustration of the formation of networks in polymers with a functionality greater than two: (a,b) functional groups are at the ends of the line segments; (c) a chain of a trifunctional polymer; (d) a network of a tetrafunctional polymer.

If in the AA–BB type of polycondensation, one of the monomers has a functionality of three or more, it forms a 3D network. Figure 2.8 illustrates the formation of networks in polymers with a functionality of three or higher, while Table 2.6 shows some examples of functionality in monomer compounds.

Some of the common monomers that can be polymerized by using step-growth polymerization are listed in Table 2.7.

2.7 UV RADIATION CURING OF POLYMERS

Radiation curing refers to radiation as an energy source to induce the rapid conversion of specially formulated 100% reactive liquids into solids by polymerizing and cross-linking functional monomers and oligomers (usually liquid) into a cross-linked polymer network (usually solid) [43].

The radiation energy could be from electron beams, X-rays, γ -rays, plasmas, microwaves and, more commonly, ultraviolet (UV) light. UV radiation curing has also been extensively used in MEMS, photoresist patterning and building flexible polymer structures (both planar and

three-dimensional) (UV-LIGA, microstereolithography, etc.). Advantages of using radiation curing include the following:

- It has a high processing speed and hence a high productivity.
- The processes are very convenient and economical, plus since most comprise ‘one pack compositions’, they can be dispensed automatically.
- There is very low heat generation and so heat-sensitive substrates can be used.
- Lower energy and space requirements than conventional curing systems.
- Since the organic emission levels are very low, this treatment is ‘eco-friendly’.
- Low capital costs, especially if UV is used as the curing ‘stimulant’.

2.7.1 Relationship between wavelength and radiation energy

Typical average energies from the homolytic cleavage of selected chemical bonds in organic molecules are shown in Table 2.8 [44]. The radiation wavelengths that can potentially break these bonds are given by Planck’s theory.

Table 2.6 Functionality of some monomer compounds.

Compound	Chemical formula	Functional group	Number of functional groups	Functionality
Ethyl alcohol	$\text{CH}_3\text{CH}_2\text{OH}$	–OH	1	Monofunctional
Hexamethylene diamine	$\text{H}_2\text{NCH}_2(\text{CH}_2)_4\text{CH}_2\text{NH}_2$	–NH ₂	2	Bifunctional
Maleic acid	$\text{HOOCCH}_2\text{CH}(\text{OH})\text{COOH}$	–COOH, –OH	3	Trifunctional
Gallic acid	$\text{HOOC}_6\text{H}_2(\text{OH})_3$	–COOH, –OH	4	Tetrafunctional

Table 2.7 Some of the polymers that can be prepared by using step-growth polymerization.

Polymer	Chemical formula
Nylon 6	$\left[\text{NH}-\overset{\text{O}}{\underset{\text{ }}{\text{C}}}-(\text{CH}_2)_5 \right]_n$
Polycarbonate	$\left[\text{O} \text{---} \text{C}_6\text{H}_4 \text{---} \overset{\text{CH}_3}{\underset{\text{CH}_3}{\text{C}}} \text{---} \text{C}_6\text{H}_4 \text{---} \overset{\text{O}}{\underset{\text{ }}{\text{C}}} \right]_n$
Poly(butylene terephthalate)	$\left[(\text{CH}_2)_4 \text{---} \overset{\text{O}}{\underset{\text{ }}{\text{C}}} \text{---} \text{C}_6\text{H}_4 \text{---} \overset{\text{O}}{\underset{\text{ }}{\text{C}}} \right]_n$

Table 2.8 Energies and corresponding wavelengths for the homolytic fission of typical chemical bonds [44].

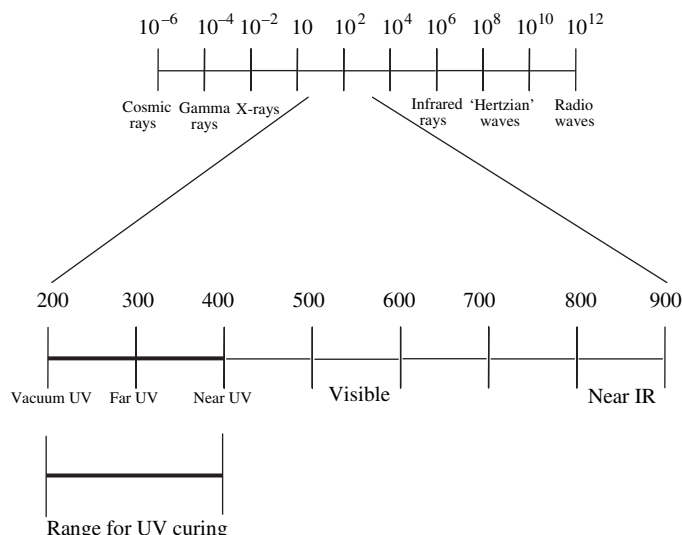
Bond	Energy kcal/mol	λ (nm)
C=C	160	179
C-C	85	336
C-H	95–100	286–301
C-O	80–100	286–357
C-Cl	60–86	332–477
C-Br	45–70	408–636
O-O	35	817
O-H	85–115	249–336

Planck developed his theory of ‘black-body radiation’ on the basis of a postulate that radiation possessed particulate properties and that the particles, or photons, of radiation of a specific frequency, v , had associated with them a fixed energy, ε , given by the relationship $\varepsilon = hv$, where h is known as the Planck constant ($6.626\,076 \times 10^{-34}$ J s) and $v = c/\lambda$, in which c is the speed of light (3×10^8 m/s) and λ is the wavelength. Figure 2.9 illustrates the relevant ranges in the electromagnetic spectrum. This shows that photons at wavelengths within the UV range possess enough energy to break the bonds listed in the table and these undergo rearrangements to form polymer networks [45].

2.7.2 Mechanisms of UV curing

UV curing is based on photoinitiated polymerization, which is mediated by photoinitiators. These absorb UV light and convert (light) energy into chemical energy in the form of reactive intermediates, such as free radicals and reactive cations, which subsequently initiate the polymerization. Typical photopolymer formulations contain a photoinitiator system, monomers and oligomers (or a polymer or polymers) to provide specific physical and/or processing properties. They may also contain a variety of additives to modify the physical properties of the light-sensitive compositions or the final properties of the cured photopolymers.

The photopolymerization reactions fall into two categories, i.e. radical photopolymerization and cationic

**Figure 2.9** The electromagnetic spectrum (wavelengths in nanometers) [11].

photopolymerization. Generally, acrylates are associated with free-radical polymerization while epoxies are typical of cationic curing. The most commonly used reactive monomeric materials are low-molecular-weight unsaturated acrylate or methacrylate monomers that can be made to cross-link with the use of a radical-generating photoinitiator. The practical applications of cationic-initiated cross-linking of monomeric materials with epoxy and/or vinyl ether functionalities have significantly increased with the development of new UV-sensitive, high-efficiency photoinitiators which generate cationic species (e.g. strong acids). Table 2.9 gives a comparison of the characteristics of cationic and free-radical curing, showing their relative merits and demerits. In this table, *moisture inhibition* refers to the ability of a formulation to cure in the presence of atmospheric moisture, while *post-irradiance cure* refers to curing taking place after the light source has been removed. For free-radical curing in air, surface curing lags behind bulk curing, which is known as 'oxygen inhibition'. This lag results from competition at the surface between oxygen molecules and free radicals for the monomer sites. A through cure of cationic systems is recommended since free radicals have a limited lifetime.

Once the photoinitiator (PI) absorbs light, it is raised to an electronically excited state, PI^* . The lifetimes of the PI^* states are short, generally less than 10^{-6} s. During this time, the PI^* state may be affected by the one of the following possibilities: (i) it may decay back to the PI state with the emission of light and/or heat; (ii) it may attain a (further) excited state following quenching by oxygen, monomer or other quenching agents; (iii) it may disintegrate by a chemical reaction, yielding the initiator species, R_0 [46].

Table 2.9 Comparison of free-radical curing versus cationic curing [45].

Property	Free-radical curing	Cationic curing
Cure speed	Faster	Slower
Oxygen inhibition	Yes	No
Adhesion	'Problems'	Excellent
Toxicity	Skin irritation	Acceptable
Moisture inhibition	No	Yes
Post-irradiation cure	No	Yes
Formulation latitude	Good	Limited
Through cure	Fair	Good
Viscosity	Higher	Lower
Cost	Moderate	Higher

The rate of initiation (R_i) is expressed as the rate of formation of PI^* , which corresponds to the number of photons absorbed by the PI per unit time:

$$R_i = I_{\text{abs}} F f \quad (2.21)$$

where the term I_{abs} corresponds to the intensity of light absorbed by the PI, F is the fraction of PI^* that yields initiator species, and f is the fraction of initiator which initiates polymerization. I_{abs} is related to the incident light intensity (I_0), the number of photons incident to the system per unit time and area and the absorbance (A) of the PI, according to the Beer-Lambert law:

$$I_{\text{abs}} = I_0 (1 - e^{-A}) \quad (2.22)$$

where $A = \varepsilon d c$

where d is the pathlength of light (or film thickness), ε is the molar absorptivity of the PI and c is the PI concentration.

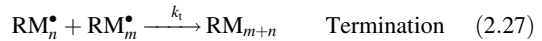
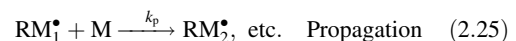
It is desirable that the rate of initiation, R_i , be uniform throughout the system and to be high enough for efficient utilization of the light energy. For example, internal stresses arising from non-uniform cross-linking adversely affect adhesion to the substrate and mechanical properties, such as tensile strength. From Equation (2.22), one can also see that the non-uniformity of the absorption increases with the absorbance A . Therefore, the appropriate PI concentration, molar absorptivity of PI and the value of absorbance of the system are very important in order to optimize a monomer system for UV curing [46].

2.7.3 Basic kinetics of photopolymerization

Since the rate of polymerization is an important parameter in characterizing polymer curing, the curing profile can be predicted from this. The kinetics of photopolymerization presented below should prove helpful in understanding how to calculate the rate of polymerization.

2.7.3.1 Radical photopolymerization

Radical photopolymerization is a chain reaction which proceeds according to the following steps:



where PI represents the photoinitiator, RM_{m+n} is the stable polymer molecule and k_i , k_p and k_t are the rate constants for initiation, propagation and termination, respectively.

The rate of photochemical initiation is expressed as follows:

$$R_i = 2\Phi I_{abs} \quad (2.28)$$

where I_{abs} is the intensity of absorbed light in moles of light quanta per liter and second and Φ , referred to as the quantum yield for initiation, is the number of propagating chains initiated per light photon absorbed. The factor of '2' indicates that two radicals are produced per molecule undergoing photolysis. The maximum value of Φ is 1 for all photoinitiated polymerizations.

Monomers are consumed by the initiation reaction, as well as by propagation reactions. The rate of change in monomer concentration by polymerization is expressed as follows:

$$-\frac{d[M]}{dt} = R_i + R_p \quad (2.29)$$

where R_i and R_p are the rates of initiation and propagation, respectively. For a process producing high-molecular-weight polymers, the number of monomers reacting in the initiation step is far less than that in the propagation step. Thus, Equation (2.29) can be simplified as follows:

$$-\frac{d[M]}{dt} = R_p \quad (2.30)$$

Assume that the rate constants for all of the propagation steps are the same, the polymerization rate can be expressed by the following:

$$R_p = k_p[M][M^\bullet] \quad (2.31)$$

where $[M]$ is the monomers concentration and $[M^\bullet]$ is the total concentration of all chain radicals.

The polymerization rate cannot be directly obtained from Equation (2.31) since it is difficult to measure the radical concentrations quantitatively, which are very low ($\sim 10^{-8} M$). In order to eliminate $[M^\bullet]$ from Equation (2.31), we use a steady-state assumption that the concentration of radicals increases initially but then reaches a constant steady-state value within a very short time. This means that the rates of initiation, R_i , and termination, R_t , of the radicals are equal, or:

$$R_i = R_t = 2k_t[M^\bullet]^2 \quad (2.32)$$

where the factor of '2' in the above equation represents the fact that the radicals are 'destroyed' in pairs. By rearranging Equation (2.32), the concentration of the radicals is given by:

$$[M^\bullet] = \left(\frac{R_i}{2k_t} \right)^{1/2} \quad (2.33)$$

and then by substituting Equation (2.33) into Equation (2.31), we obtains:

$$R_p = k_p[M] \left(\frac{R_i}{2k_t} \right)^{1/2} \quad (2.34)$$

A combination of Equations (2.28) and (2.34) then yields:

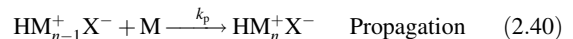
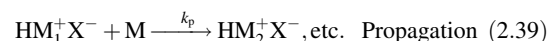
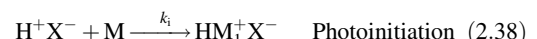
$$R_p = k_p[M] \left(\frac{\Phi I_{abs}}{k_t} \right)^{1/2} \quad (2.35)$$

and by using Equation (2.22), the expression for R_p becomes:

$$R_p = k_p[M] \left[\frac{\Phi I_0 (1 - 10^{-edc})}{k_t} \right]^{1/2} \quad (2.36)$$

2.7.3.2 Cationic photopolymerization

The process of cationic photopolymerization can be generalized as follows:



The reaction rates for initiation, propagation and termination are expressed as follows:

$$R_i = \Phi I_{abs} \quad (2.42)$$

$$R_p = k_p[\text{HM}^+ \text{X}^-][\text{M}] \quad (2.43)$$

$$R_t = k_t[\text{HM}^+ \text{X}^-] \quad (2.44)$$

where $[\text{HM}^+ \text{X}^-]$ is the total concentration of the reactive centers. Supposing that the steady-state assumption is

also valid for cationic photopolymerization, one can get the following:

$$[HM^+X^-] = \frac{\Phi I_{\text{abs}}}{k_t} \quad (2.45)$$

A combination of Equations (2.43) and (2.45) yields:

$$R_p = \frac{k_p \Phi I_{\text{abs}} [M]}{k_t} \quad (2.46)$$

This is the rate of polymerization for cationic photopolymerization. R_p can also be expressed in terms of I_0 , which is as follows:

$$R_p = k_p [M] \frac{\Phi I_0 (1 - 10^{-edc})}{k_t} \quad (2.47)$$

2.8 DEPOSITION TECHNIQUES FOR POLYMER THIN FILMS

A brief list of the polymeric materials commonly used in the context of various microsystems is presented in Table 2.10. Polypyrrole is one candidate for a sorbent thin-film material. Chemical oxidation as a means of depositing these conducting polymers onto host membranes has been shown to be useful [47]. In this method, the host PVDF film is ‘pre-wet’ in a 50 % ethanol solution and then dipped into the monomer (pyrrole) solution. The ‘superficial’ solution is ‘blot dried’ with filter paper. This coated material is then dipped in an oxidant solution (e.g. ferric chloride hexahydrate) for chemical polymerization. A similar approach has been reported by de Lacy Costello *et al.* [48], where ferric nitrate solution was used for polymerization.

To deposit polymer thin films without affecting their chemical integrity and physico-chemical properties, the pulsed laser deposition technique has been recently used [49]. A patterned deposition is possible by incorporating an $x-y$ positioning stage in this approach. These authors [49] have deposited a fluoroalcoholpolysiloxane (SXFA) polymer under vacuum onto piezoelectric substrates in this way. In yet another instance, UV-induced graft copolymerization with 4-vinylpyridine has been used for surface modification of PVDF for the electroless deposition of nickel [50]. This method enhanced the adhesion of nickel to the PVDF by interfacial charge-transfer interactions between the grafted polymer chains and the deposited metals, the spatial distribution of the

grafted chains into the metal matrix and the covalent ‘tethering’ of the grafted chains on the PVDF surface. Processing techniques involved in the fabrication of polymer MEMS are described in Chapter 11.

2.9 PROPERTIES AND SYNTHESIS OF CARBON NANOTUBES

Over the last few years there has been an increasing trend to further miniaturize the sensors/actuators from the micro to the nano scale. This is due to some outstanding properties that these nano-scale materials can offer over conventional bulk materials. One such nano-scale material is the carbon nanotube (CNT). From their unique electronic properties and thermal conductivities higher than diamond to mechanical properties where the stiffness, strength and resilience exceed any current material, carbon nanotubes offer tremendous opportunities for the development of fundamentally new material systems. In particular, the exceptional mechanical properties of carbon nanotubes, combined with their low density, offer much scope for the development of nanotube-reinforced composite materials. The potential for nanocomposites, reinforced with carbon nanotubes, having extraordinary specific stiffness and strength properties, represent tremendous opportunities for applications in the 21st Century.

The research towards exploring the various special properties of carbon began in the mid-1980s, when Smalley and coworkers discovered the fullerenes [51], which are cage-like structures of carbon atoms having hexagonal and pentagonal faces. The first closed convex structure formed is the C_{60} ‘buckyball’ structure. The other forms of carbon-based materials that can exist in different forms are ‘Diamond’ and the ‘graphite’ sheets. In 1991, Iijima [52] discovered yet another form of carbon-based material, which he named as ‘carbon nanotubes’. All of these forms are shown in Figure 2.10.

CNTs, due to their superior properties, have immense potential for use in many structural applications. A single layer of CNTs can achieve 50 times the tensile strength of conventional steel [53], while the mass density of CNTs is only 1/6 that of steel. These properties highlight the promising role of CNTs in applications involving nanomaterials and nanodevices. Theoretically, the tensile modulus and strength of a graphene layer can reach up to 1 TPa and 200 GPa, respectively.

In addition to the exceptional mechanical properties associated with carbon nanotubes, they also possess superior thermal and electric properties. They are thermally stable up to 2800 °C in vacuum, have a thermal

Table 2.10 Polymeric materials commonly used in various microsystems.

Polymer	Acronym	Chemical formula	General properties
Polyethylene	PE	$\left[-\text{CH}_2-\text{CH}_2\right]_n$	Excellent chemical resistance, low cost, good electrical insulation properties, clarity of thin films, easy processability
Poly(vinyl chloride)	PVC	$\left[-\text{CH}\left(\text{Cl}\right)-\text{CH}_2\right]_n$	Excellent electrical insulation over a range of frequencies, good fire-retardant properties, resistance to weathering
Poly(vinylidene fluoride)	PVDF	$\left[-\text{C}\left(\text{F}\right)-\text{CH}_2\right]_n$	Piezoelectric and pyroelectric properties, excellent resistance to 'harsh' environments
Polytetrafluoroethylene	PTFE	$\left[-\text{C}\left(\text{F}\right)_2-\text{C}\left(\text{F}\right)_2\right]_n$	High heat resistance, high resistance to chemical agents and solvents, high 'anti-adhesiveness', high dielectric properties, low friction coefficient non-toxic.
Poly(vinyl acetate)	PVAC	$\left[-\text{CH}-\text{CH}_2\right]_n$	Good adhesive properties.
Poly(vinyl alcohol)	PVAL	$\left[-\text{CH}-\text{CH}_2\right]_n$	Good adhesive properties, water absorption, heat resistance, electrical insulation
Polyamide	Nylon 6	$\left[-\text{NH}-\text{C}=\text{O}-\text{CH}_2\right]_n$	Very good abrasion resistance, excellent resistance to hydrocarbons
Poly(styrene)	PS	$\left[-\text{CH}-\text{CH}_2\right]_n$	Optical properties (transparency), ease of coloring and processing
Polybutyleneterephthalate	PBT	$\left[-\text{(CH}_2\text{)}_4-\text{O}-\text{C}_6\text{H}_4-\text{C}(=\text{O})\text{O}\right]_n$	Good dimensional stability in water, high mechanical strength, low water absorption

Poly(ether ether ketone)	PEEK		Hydrolysis resistance, good resistance to acids
Polycarbonate	PC		High impact strength, low moisture absorption, good heat resistance, good rigidity and electrical properties, high light transmission, high creep resistance
Poly(methyl methacrylate)	PMMA		Excellent weatherability, combination of stiffness, density and moderate toughness, elasticity, optical properties
Polyimide	PI		Elasticity
Silicone rubber			Elasticity
Polysulfone	PSU		Good for molding
Polypyrrole	PPy		Electroactive, conducting
Polydimethylsiloxane	PDMS		Elasticity and biomedical compatibility
Polyaniline	PANI		Electroactive, conducting

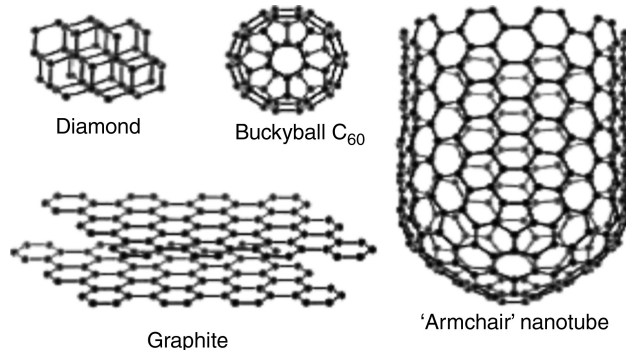


Figure 2.10 Different forms of carbon-based materials. Reprinted from Composites Part B Engineering, vol 35 (2), pp. 95–101, Copyright 2004, with permission from Elsevier

conductivity about twice as high as diamond and an electric-current-carrying capacity 1000 times higher than copper wire. These exceptional properties have been investigated for devices such as field-emission displays, scanning probe microscopy tips and microelectronic devices.

The size, mechanical strength and electrical properties of nanotubes are highly dependent on the atomic architecture. It has been reported that *armchair* nanotubes exhibit better ductility and electrical conductivity than *zigzag* nanotubes. Schematics of these two forms are CNTs shown in Figure 2.11 exist in two different forms. A *single-walled carbon nanotube* (SWCNT) has a hollow structure formed by covalently bonded carbon atoms and can be imagined as a rectangular graphene sheet rolled from one side of its longest edge to form a cylindrical tube. Hemispherical caps seal both ends of the tube as shown in Figure 2.10. For *multi-walled*

carbon nanotubes (MWCNTs), a number of graphene layers are co-axially rolled together to form a cylindrical tube (Figure 2.11). The spacing between the graphene layers is about 0.34 nm. In other words, an MWCNT is thought to be made up of nested shells of cylinders with weak interlayer interactions. These values have been widely used to interpret the mechanical properties of single-walled and multi-walled nanotubes. The typical dimensions of SWCNTs are shown in Table 2.11.

It has also been observed that the majority of carbon nanotubes exhibit chirality [54] (Figure 2.12). In other words, the hexagonal carbon orientation with respect to the tubular axis could be different for different carbon nanotubes. The properties of CNTs depend largely on their diameters and chirality. Carbon nanotubes have extraordinary mechanical, thermal and electrical properties due to their unique carbon structure, as well as their nano-size scale [55]. Wong *et al.* [56] reported the average Young's modulus value of MWCNTs, determined by atomic force microscopy (AFM) measurements, to be 1.28 ± 0.59 TPa, which is the largest of any known material. Wildöer *et al.* used scanning tunnelling microscopy (STM) to measure the conductivities of individual carbon nanotubes and found that these depend on the chiral angle and diameter [55].

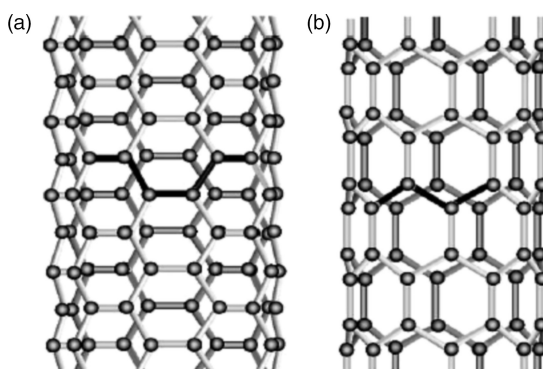


Figure 2.11 Different forms of carbon nanotubes: (a) armchair; (b) zig-zag. Reprinted from Composite Science & Technology, 61, 1899–1912, Copyright 2001, with permission from Elsevier

Table 2.11 Key geometric parameters of single-walled carbon nanotubes.

Parameter	Range of values
Thickness	0.0066–0.34 nm
Diameter	0.40–100 nm
Length	1 nm–1 μ m

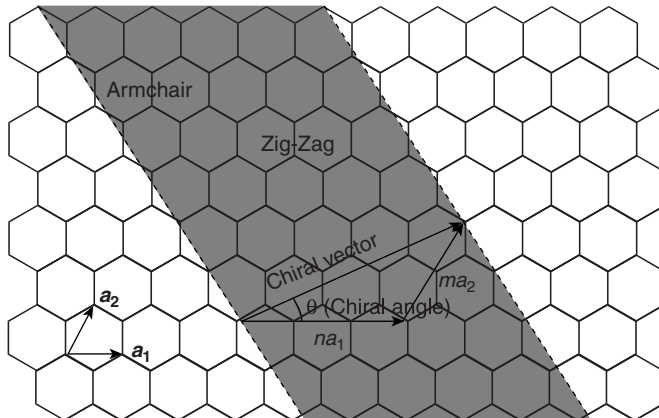


Figure 2.12 Schematic showing the formation of a carbon nanotube from a rolled graphite sheet. Reprinted from Composite Science & Technology, 61, 1899–1912, Copyright 2001 with permission from Elsevier

The features (size, single- or multi-walled, helicity, etc.) of carbon nanotubes are also determined by the method of preparation. There are several methods for the synthesis of carbon nanotubes. Arc discharge and laser vaporization of a graphite electrode in the presence of metal catalysts were the earliest methods used to synthesize CNTs [57]. However, both of these methods require reaction temperatures higher than 3000 °C, which is incompatible with modern IC fabrication. Another limitation is the high production cost due to the complex equipment required and the low deposition rate [58]. In recent years, pyrolysis of hydrocarbon (e.g. acetylene, methane, etc.) vapors over transition metals incorporated on a catalyst support has attracted much research interest because of the simplicity of the equipment and reproducibility of the product in comparison with other methods.

Another method to produce high-quality carbon nanotubes is the use of microwave CVD. Compared with the conventional thermal filament CVD method, microwave CVD has much faster heating and cooling times and higher yields of nanotubes. By optimization, this approach is expected to result in up to 90 % yields and a large-scale production capability [59]. Techniques for the purification and functionalization of nanotubes for nanocomposites and MEMS have also been developed [59].

Carbon nanotubes are regarded as promising filler materials for a new generation of high-performance nanocomposites because of their exceptionally high Young's modulus [60], bending strength and low density. The use of physical bonding and chemical bonding represent two approaches for preparing composites of nanotubes. In the former method, the CNTs are added to a solvent, e.g. chloroform, toluene, ethanol, etc. and a

high-power ultrasonic probe is used to disperse the system. Then, the dispersed nanotubes are blended with the host material. Composite films can be deposited by drop- and spin-coating on various substrates. In this method, the carbon nanotubes are only physically bonded to the host material. Because of the pure carbon composition and their stable structures, carbon nanotubes are insoluble in all organic solvents. This makes it extremely difficult to explore their properties and applications. Furthermore, because the high surface energies make carbon nanotubes easy to agglomerate (due to their nano-size dimensions, composite processing is still limited to bench-top levels and has been hampered by the high viscosities of available matrix materials, lack of good dispersion techniques and excessive porosity [61].

To overcome this problem, chemical modification by functionalization of the carbon nanotube surface has been pursued [62]. It has been reported that functionalized nanotubes can form stable and uniform colloidal dispersions with some solvents. This can be explained by the electrostatic repulsion resulting from the functional groups attached to the surfaces of the nanotubes. Thus, well-dispersed colloidal systems are required for *in situ* polymerization. The functional groups attached to the surfaces of the nanotubes are able to react with functional monomers to form a chemically bonded UV-curable polymer. The 'functionalization yield' can be enhanced by using a phase-transfer catalyst at room temperature [63]. A UV-curable polymer with chemically bonded nanotubes can be synthesized by a three-step *in situ* polymerization. Since UV curing is one of the preferred methods of MEMS fabrication, especially by microstereolithography, those materials are likely to have many

potential applications. Design modeling and fabrication of CNT based microsystems will be presented in later chapters.

REFERENCES

- G.T.A. Kovacs, N.I. Maluf and K.E. Petersen, 'Bulk micro-machining of silicon', *Proceedings of the IEEE*, **86**, 1536–1551 (1998).
- J.M. Bustillo, R.T. Howe and R.S. Muller, 'Surface micro-machining for microelectromechanical systems', *Proceedings of the IEEE*, **86**, 1552–1574 (1998).
- H. Guckel, 'High-aspect-ratio micromachining via deep X-ray lithography', *Proceedings of the IEEE*, **86**, 1586–1593 (1998).
- Y. Xia and G.M. Whitesides, 'Soft lithography', *Angewandte Chemie, International Edition*, **37**, 550–575 (1998).
- V.K. Varadan and V.V. Varadan, 'Three dimensional polymeric and ceramic MEMS and their applications', *Proceedings of SPIE*, **2722**, 156–164 (1996).
- K. Ikuta and K. Hirowatari, 'Real three dimensional micro-fabrication using stereo lithography and metal molding', in *Proceedings of the IEEE: MEMS'93*, IEEE, Piscataway, NJ, USA, pp. 42–47, (1993).
- T. Katagi and N. Nakajima, 'Photoforming applied to fine machining', in *Proceedings of the IEEE: MEMS'93*, IEEE, Piscataway, NJ, USA, 173–178, (1993).
- C.S. Taylor, P. Cherkas, H. Hampton, J.J. Frantzen, B.O. Shah, W.B. Tiffany, L. Nanis, P. Booker, A. Salahieh and R. Hansen, 'A spatial forming – a three dimensional printing process', in *Proceedings of the IEEE: MEMS'94*, IEEE, Piscataway, NJ, USA, pp. 203–208 (1994).
- G. Thornell and S. Johansson, 'Microprocessing at the fingertips', *Journal of Micromechanical and Microengineering*, **8**, 251–262 (1998).
- J.W. Gardner, V.K. Varadan and O.O. Awadelkarim, *Micro-sensors MEMS and Smart Devices*, John Wiley & Sons, Ltd, London, UK (2002).
- V.K. Varadan, X. Jiang and V.V. Varadan, *Microstereolithography and other Fabrication Techniques for 3D MEMS*, John Wiley & Sons, Ltd, London, UK (2001).
- L.E. Larson, 'Microwave MEMS technology for next-generation wireless communications', *IEEE MTT-S International Symposium Digest*, **3**, 1073–1076 (1999).
- L.T. Romankiw, 'A path: from electroplating through lithographic masks in electronics to LIGA in MEMS', *Electrochimica Acta*, **42**, 2985–3005 (1997).
- C.H. Ahn and M.G. Allen, 'Micromachined planar inductors on silicon wafers for MEMS applications', *IEEE Transactions on Industrial Electronics*, **45**, 866–876 (1998).
- H.O. Pierson, *Handbook of Chemical Vapor Deposition (CVD): Principles, Technology and Applications*, 2nd Edn, Noyles Publications, New York, NY, USA (1999).
- A. Ohta, S. Bhansali, I. Kishimoto and A. Umeda, 'Development of TiNi shape memory alloy film deposited by sputtering from separate Ti and Ni targets', *Proceedings of SPIE*, **3512**, 138–145 (1998).
- T. Honda, K.I. Arai and M. Yamaguchi, 'Basic properties of magnetostrictive actuators using Tb–Fe and Sm–Fe thin films', *IEICE Transactions on Electronics*, **E80-C**, 232–238 (1997).
- L.C. Chin, V.V. Varadan and V.K. Varadan, 'Hybrid finite element formulation for periodic piezoelectric arrays subjected to fluid loading', *International Journal of Numerical Methods in Engineering*, **37**, 2987–3003 (1994).
- V.K. Varadan, K.J. Vinoy and K.A. Jose, *RF MEMS and their Applications*, John Wiley & Sons, Ltd, London, UK (2002).
- V.K. Varadan, F. Selmi and V.V. Varadan, 'Voltage tunable dielectric ceramics which exhibit low dielectric constants and applications thereof to antenna structure', *US Patent*, 5 557 286 (1996).
- S.B. Herner, F.A. Selmi, V.V. Varadan and V.K. Varadan, 'The effect of various dopants on the dielectric properties of barium strontium titanate', *Materials Letters*, **15**, 317–324 (1993).
- V.K. Varadan, D.K. Ghodgaonkar, V.V. Varadan, J.F. Kelly and P. Glikerdas, 'Ceramic phase shifters for electronically steerable antenna systems', *Microwave Journal*, **38**, 116–127 (1992).
- J.H. Won, H. Paek, Y.S. Huang, K.K. Kim and Y.S. Cho, 'Phase formation and characteristics of RF sputtering of barium strontium titanate thin films on various bottom layers', *Journal of Materials Science: Materials in Electronics*, **6**, 161–164 (1995).
- S. Saha and S.B. Krapanidhi, 'Study of the electrical properties of pulsed laser ablated $(BaO_0.5SrO_0.5)TiO_3$ thin films', *Materials Science and Engineering: Solid-State Materials for Advanced Technologies*, **B57**, 135–146 (1999).
- I. Levin, R.D. Leapman and D.L. Kaiser, 'Microstructure and chemistry of non-stoichiometric $(Ba,Sr)TiO_3$ ', thin films deposited by metalorganic chemical vapor deposition', *Journal of Materials Research*, **15**, 1433–1436 (2000).
- E.J. Cukauskas, S.W. Kirchoefer and J.M. Pond, 'Low-loss $BaO_0.5SrO_0.5TiO_3$ thin films by inverted magnetron sputtering', *Journal of Applied Physics*, **88**, 2830–2835, (2000).
- M. Sedlar, M. Sayer and L. Weaver, 'Sol-gel processing and properties of cerium doped barium strontium titanate thin films', *Journal of Sol-Gel Science and Technology*, **5**, 201–210 (1995).
- P.D. Calvert, E.S. Tormey and R.L. Pober, 'Fish oil and triglycerides as dispersants for alumina', *American Ceramics Society Bulletin*, **65**, 669–672 (1986).
- A. Nazeri, M. Khan and T. Kidd, 'Strontium barium titanate thin films by Sol-Gel processing', *Journal of Materials Science: Letters*, **14**, 1085–1088 (1995).
- S.B. Majumdar, M. Jain, A. Matinez, R.S. Katiyar, F.W. van Keuls and F.A. Miranda, 'Sol-Gel derived grain oriented barium strontium titanate thin films for phase shifter applications', *Journal of Applied Physics*, **90**, 896–903 (2001).
- C.L. Canedy, S. Aggarwal, H. Li, T. Venkatesan, R. Ramesh, F.W. van Keuls, R.R. Romanofsky and F.A. Miranda,

- 'Structural and dielectric properties of epitaxial $\text{Ba}_{1-x}\text{Sr}_x\text{TiO}_3/\text{Bi}_4\text{Ti}_3\text{O}_12/\text{ZrO}_2$ heterostructures grown on silicon', *Journal of Applied Physics*, **77**, 1523–1525 (2000).
32. S. Middelhoek and S.A. Audet, *Silicon Sensors*, Academic Press, London, UK (1989).
 33. K.E. Peterson, 'Silicon as a mechanical material', *Proceedings of the IEEE*, **70**, 420–457 (1982).
 34. J. Bryzek, K. Petersen and W. McCulley, 'Micromachines on the march', *IEEE Spectrum*, **31**(5), 20–31 (May 1994).
 35. L.-S. Fan, Y.-C. Tai and R.S. Muller, 'Integrated movable micromechanical structures for sensors and actuators', *IEEE Transactions: Electron Devices*, **35**, 724–730 (1988).
 36. K.A. Shaw, Z.L. Zhang and N.C. MacDonald, 'SCREAM 1: a single mask, single-crystal silicon process for microelectromechanical structures', in *Proceedings of the IEEE: MEMS'93*, IEEE, Piscataway, NJ, USA, pp. 155–160 (1993).
 37. W.H. Ko, J.T. Suminto and G.J. Yeh, 'Bonding techniques for microsensors', *Studies in Electrical and Electronic Engineering*, **20**, 41–61 (1985).
 38. V.K. Varadan, and V.V. Varadan, 'Three-dimensional polymeric and ceramic MEMS and their applications', *Proceedings of SPIE*, **2722**, 156–164 (1996).
 39. D.L. Carraway, 'The use of silicon microsensors in smart skins for aerodynamic research', in *Proceedings of the International Congress on Instrumentation in Aerospace Simulation Facilities*, IEEE, Piscataway, NJ, USA, pp. 413–422 (1991).
 40. R. Pelrine, R. Kornbluh, J. Joseph and S. Chiba, 'Electrostriction of polymer films for microactuators', in *Proceedings of the IEEE: MEMS'97*, IEEE, Piscataway, NJ, USA, pp. 238–243 (1997).
 41. L. Ruiz de Angulo, J.S. Abell and I.R. Harris, 'Magnetostrictive properties of polymer bonded Terfenol-D', *Journal of Magnetism and Magnetic Materials*, **157–158**, 508–509 (1996).
 42. L.K. Lagorce and M.G. Allen, 'Micromachined polymer magnets', in *Proceedings of ISAF'96*, IEEE, Piscataway, NJ, USA, pp. 85–90 (1996).
 43. J.P. Fouassier, *Photoinitiation, Photopolymerization and Photocuring: Fundamentals and Applications*, Hanser/Gardener, Munich, Germany (1995).
 44. J. Kagan, *Organic Photochemistry: Principles and Applications*, Academic Press, London, UK (1993).
 45. C.L. Haertling, 'Patterned ceramics for multilayer packaging using ultraviolet curable pastes', *M.Sc. Thesis*, Pennsylvania State University, State College, PA, USA (1989).
 46. S.P. Pappas (Ed.), *Radiation Curing: science and Technology*, Plenum Press, New York, NY, USA (1992).
 47. J. Mansouri and R.P. Burford, 'Characterization of PVDF-PPy composite membranes', *Polymer*, **38**, 6055–6069 (1997).
 48. B.P.J. de Lacy Costello, P. Evans, N. Guernion, N.M. Ratcliffe, P.S. Sivanand and G.C. Teare, 'The synthesis of a number of 3-alkyl and 3-carboxy substituted pyrroles; their chemical polymerization onto poly(vinylidene fluoride) membranes and their use as gas sensitive resistors', *Synthetic Metals*, **114**, 181–188 (2000).
 49. A. Piqué, R.C.Y. Auyeung, J.L. Stepnowski, D.W. Weir, C.B. Arnold, R.A. McGill and D.B. Chrisey, 'Laser processing of polymer thin films for chemical sensor applications', *Surface and Coatings Technology*, **163–164**, 293–299 (2003).
 50. G.H. Yang, C. Lim, Y.P. Tan, Y. Zhang, E.T. Kang and K.G. Neoh, 'Electroless deposition of nickel on fluoropolymers modified by surface graft copolymerization', *European Polymer Journal*, **38**, 2153–2160 (2002).
 51. H.W. Kroto, J.R. Heath, S.C. O'Brien, R.F. Curl and R.E. Smalley, ' C_{60} : Buckminsterfullerene', *Nature (London)*, **318**, 162–163 (1985).
 52. S. Iijima, 'Helical microtubules of graphitic carbon', *Nature (London)*, **354**, 56–58 (1991).
 53. M.F. Yu, O. Lourie, M.J. Dyer, K. Moloni, T.F. Kelly and R.S. Ruoff, 'Strength and breaking mechanism of multiwalled carbon nanotubes under tensile load', *Science*, **287**, 637–640 (2000).
 54. M.S. Dresselhaus, G. Dresselhaus and R. Saito, 'Physics of carbon nanotubes', *Carbon*, **33**, 883–891 (1995).
 55. J.W.G. Wildöer, L.C. Venema, A.G. Rinzler, R.E. Smalley and C. Dekker, 'Electronic structure of atomically resolved carbon nanotubes', *Nature (London)*, **391**, 59–62 (1998).
 56. E.W. Wong, P.E. Sheehan and C.M. Lieber, 'Nanobeam mechanics: elasticity, strength, and toughness of nanorods and nanotubes', *Science*, **277**, 1971–1974 (1997).
 57. V. Ivanov, J.B. Nagy, P. Lambin, A. Lucas, X.B. Zhang, X.F. Zhang, D. Bernaerts, G.V. Tendeloo, S. Amelinckx and J.V. Landuyt, 'The study of carbon nanotubes produced by a catalytic method', *Chemical Physics Letters*, **223**, 329–335 (1994).
 58. V.K. Varadan and J. Xie, 'Large scale manufacturing of functionalized carbon nanotubes and their applications to EMI shielding, microfuel cells, batteries and structural components', *US Patent*, pending (2002).
 59. J. Xie, N. Zhang, M. Guers and V.K. Varadan, 'Ultraviolet-curable polymer composites with chemically bonded carbon nanotubes for microelectromechanical system applications', *Smart Materials and Structures*, **11**, 575–580 (2002).
 60. M.M.J. Treacy, T.W. Ebbesen and J.M. Gibson, 'Exceptionally high Young's modulus observed for individual carbon nanotubes', *Nature (London)*, **381**, 678–680 (1996).
 61. E.V. Barrera, 'Key methods for developing single-wall nanotube composites', *Journal of the Minerals, Metals and Materials Society*, **52**, 38–42 (2000).
 62. M.S.P. Shaffer, X. Fan and A.H. Windle, 'Dispersion and packing of carbon nanotubes', *Carbon*, **36**, 1603–1612 (1998).
 63. N. Zhang, J. Xie, M. Guers and V.K. Varadan, 'Functionalization of carbon nanotubes by potassium permanganate with the help of a phase transfer catalyst', *Smart Materials and Structures*, **11**, 962–965 (2002).

Part 2

Design Principles

3

Sensors for Smart Systems

3.1 INTRODUCTION

Various microsensing and micro-actuation mechanisms have been developed for diverse smart system applications [1,2], including chemical sensors, gas sensors, optical sensors, biosensors, thermal sensors, mechanical sensors, etc. Some of the major sensing mechanisms for mechanical microsensors are introduced in this chapter.

First, let's consider some terminology regarding sensor performance. The *transfer function* of a sensor is the functional relationship between the physical input signal and electrical output signal. The *sensitivity* is a relationship indicating how much output one obtains per unit input. The sensitivity is usually taken as the ratio between a change in the electrical signal corresponding to a change in the physical signal. Hence, the sensitivity of the sensor is generally defined as the slope of the output characteristic curve. Furthermore, in some sensors, the sensitivity is defined as the input parameter change required to produce a standardized output change.

The *span* or *dynamic range* is specified as the range over which other performance characteristics described in the data sheets are expected to apply. The *accuracy* of a sensor is the largest expected error between actual and ideal output signals. Accuracy is often expressed as the percentage of the full range output.

Often, the relationship between input and output is assumed to be linear over the working range. The *error* is the maximum deviation from a linear transfer function over the specified dynamic range, while the *resolution* of a sensor is defined as the minimum detectable signal fluctuation. The *stability* of a sensor is its ability to give the same output when measuring a constant input, measured over a period of time. The change that occurs is referred to as *drift*.

All sensors have a finite response time when subjected to an instantaneous change in the physical signal. In addition, many sensors have decay times, which represent the time after a step change in physical signal that the sensor output takes to decay to its original value. The reciprocals of these times correspond to the upper and lower cutoff frequencies, respectively. The *bandwidth* of a sensor is the frequency range between these two frequencies.

We now proceed to describe various sensor principles applicable to smart systems.

3.2 CONDUCTOMETRIC SENSORS

When pressure is applied on a section of a conductor its dimension changes, causing a change in its resistance. This change, although it is usually very small in magnitude, can be detected by using a resistance bridge circuit, and the detected output is the differential voltage which is proportional to the applied pressure. Conventional examples of such resistive (conductometric) sensors include film resistors, strain gauges, metal alloys and polycrystalline semiconductors.

A very popular example of such a sensor is the strain gauge shown in Figure 3.1. When pressure is applied to the structure attached to the strain gauge, the lengths of the metal strips increase and their widths decrease. Both of these changes cause an increase in the resistance. Although this change in resistance is usually too small to measure directly, it can be determined with reasonable sensitivity by including the strain gauge as an arm of a Wheatstone bridge. The bridge is excited with a stabilized DC supply, and the output is 'zeroed' at the null point of measurement by additional conditioning electronics. As stress is applied to the bonded strain gauge(s),

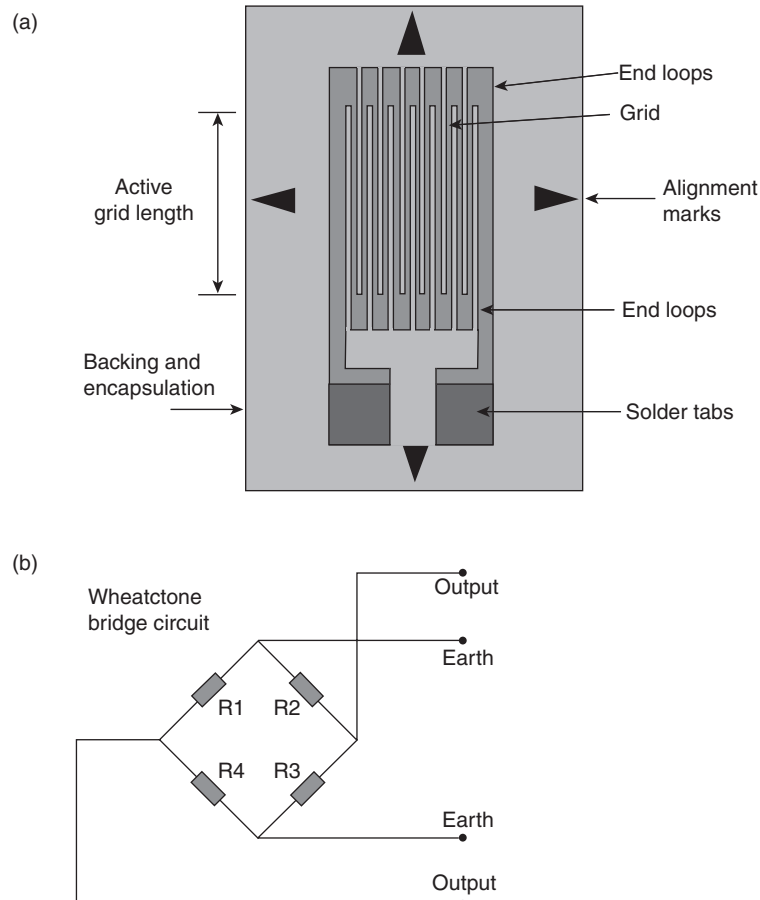


Figure 3.1 (a) Schematic of a typical strain gauge. (b) Schematic of the Wheatstone bridge circuit used in connection with a strain gauge to measure change in resistance.

the resistive changes caused by this unbalances the bridge and this results in a signal output.

Strain gauges have been in use for several years as pressure sensors, load cells, torque sensors and position sensors. With the popularization of micromachining technologies, their small-sized counterparts have also been developed. In these, usually a bulk micromachined silicon diaphragm is patterned with micro-sized strain gauges.

3.3 CAPACITIVE SENSORS

Capacitive sensors consist of a pair of electrodes arranged in such a way that one of the electrodes moves when the input variable (pressure, acceleration or rate) is applied. While the simplest configuration

consists of capacitors with two parallel plate electrodes, capacitors with interdigitated fingers (Figure 3.2) have gained wide acceptance as inertial sensors, as they allow for larger linear sensing ranges.

In a parallel plate capacitor, the capacitance C is given by:

$$C = \frac{\epsilon A}{d} \quad (3.1)$$

where ϵ is the permittivity of the gap, A is the area of the electrodes and d is the separation between the electrodes. For a circular diaphragm sensor, the capacitance under deflection is as follows:

$$C = \int \int \frac{\epsilon}{d - w(r)} r dr d\theta \quad (3.2)$$

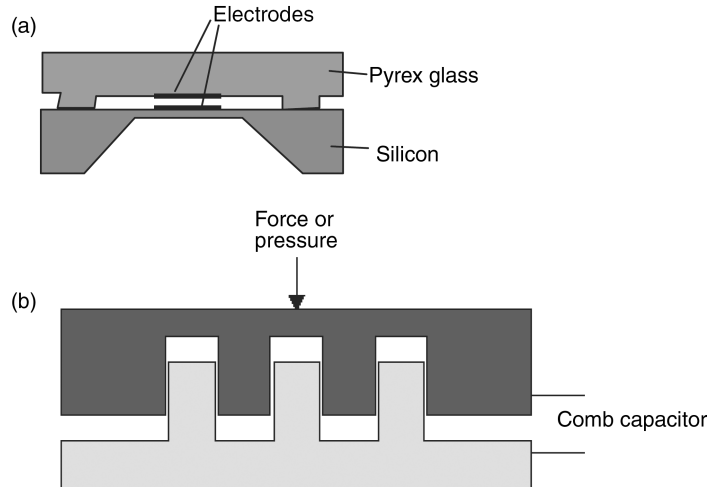


Figure 3.2 Two arrangements for capacitive sensing: (a) parallel plate; (b) comb structure.

where $w(r)$ is the deflection of the diaphragm given by:

$$w(r) = \frac{Pa^4}{64D} \left[1 - \left(\frac{r}{a} \right)^2 \right]^2 \quad (3.3)$$

in which r is the radial distance from the center of the diaphragm, a is the diaphragm radius and P is the applied pressure. The flexural rigidity, D , is given by:

$$D = \frac{Eh^3}{12(1-v^2)} \quad (3.4)$$

where E , h and v are the Young's modulus, thickness and Poisson's ratio of the diaphragm, respectively.

Capacitive sensing utilizes the capacitance change induced by the deformation of the diaphragm to convert the sensory information (pressure, force, etc.) into electrical signals (such as changes in oscillation frequency, time, charge and voltage). A schematic of a typical capacitive microsensor is given in Figure 3.2(a), showing an electrode on the flexible diaphragm and another on the substrate constructing the sensing capacitor. Capacitive microsensors can be used for measuring pressure, force, acceleration, flow rate, displacement, position, orientation measurement, etc.

In capacitive microsensors, the capacitance change is not usually linear with respect to diaphragm deformation. The small capacitance (generally 1–3 pF) requires the measurement circuit to be integrated on the chip. However, capacitive sensing has been found to have potential for higher performance than piezoresistive sensing in applications requiring high sensitivity, low pressure

ranges and high stability [2]. Comb-type electrostatic sensing is made possible by micromachining technologies. In this case, the area between the plates is made to vary as the overlap between the 'fingers' change. Hence, this type of sensor has a much broader linear range than the parallel-plate type.

Two modifications have been suggested to increase the linearity of the sensing arrangement shown in Figure 3.2(a). These are the contact mode sensor and the use of bossed diaphragms, as indicated in Figure 3.3 [3]. In the former, the capacitance is proportional to the contact area and hence is linear with respect to the applied pressure at the expense of decreased sensitivity. In the latter, the shape of the center boss does not distort appreciably when pressure is applied, while in the non-uniform bossed diaphragm, the thicker center portion contributes to most of the capacitance but is stiffer than the outer area.

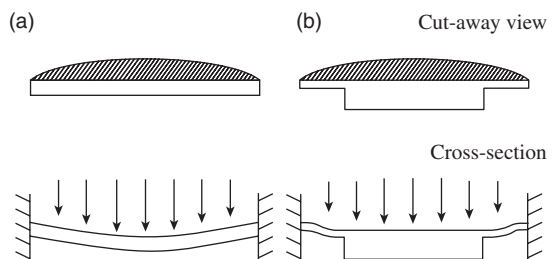


Figure 3.3 Comparison of deflection shape in (a) normal and (b) bossed diaphragms [3]. W.P. Eaton and J.H. Smith, Micro-machined pressure sensors- Review and recent developments, Smart Materials & Structures, vol. 6, 1997 © IOP



Figure 3.4 A typical structure for a piezoelectric sensing device.

3.4 PIEZOELECTRIC SENSORS

These sensors are based on the piezoelectric effect observed in some materials. In this, an electrical charge change is generated when a mechanical stress is applied across the face of a piezoelectric film. The converse effect is also observed in such materials. Piezoelectricity is attributed to an asymmetry in the unit cell and the resultant generation of electric polarization dipoles due to the mechanical distortion. Examples of such materials include lead zirconate titanate (more popularly known by the acronym PZT), lead metaniobate, lead titanate and their modifications. Above the Curie temperature, a phase change occurs in these materials as their crystal structures change from piezoelectric to non-piezoelectric.

For a piezoelectric disk of thickness t , the voltage (V) generated across the electrode disk (Figure 3.4), when subjected to a stress (T), is given by:

$$V = gtT \quad (3.5)$$

where g is the piezoelectric voltage coefficient, defined as the ratio of the field developed to the applied mechanical stress.

The piezoelectric substrate forms an important element which influences the performance of the sensor. The relationship between the dipole moment and the mechanical deformation is expressed by the following constitutive relationships:

$$\sigma = cS - eE \quad (3.6)$$

and:

$$D = \epsilon_0 E + eS \quad (3.7)$$

where σ is the mechanical stress, S is the strain, E is the electric field, D is the flux density, c is the elastic constant, e is the piezoelectric constant and ϵ_0 is the permittivity of free space. It may be noticed that in the absence of piezoelectricity these relationships reduce to Hooke's law and the constitutive relationship for dielectric materials, respectively.

The effectiveness of a piezoelectric material is best expressed in terms of its electromechanical coupling coefficient, K^2 . By definition, this is related to other material parameters used in the above constitutive equations by the following:

$$K^2 = \frac{e^2}{ce} \quad (3.8)$$

Piezoelectric devices have several advantages over other sensing mechanisms. Since this sensor generates its own voltage, it does not require power for operation. Therefore, for applications where power consumption is a significant constraint, piezoelectric devices can be used. Furthermore, the piezoelectric effect is scalable to small devices and several micro-fabricated sensors have been reported in the literature, e.g. Lee *et al.* [4]. One disadvantage of piezoelectric sensing is that it is sensitive only to time-varying signals and hence static quantities such as weight cannot be measured by using this approach.

While bulk ceramic substrates have been in use for this application for a long time now, their micro-sized counterparts with a ceramic thin film deposited on another substrate material have also been developed recently. Piezoelectric sensing is widely used in pressure and force sensors, accelerometers, hydrophones, microphones, etc. A schematic of a micromachined piezoelectric force sensor is shown in Figure 3.5.

3.5 MAGNETOSTRICTIVE SENSORS

Certain ferromagnetic materials show deformation when subjected to a magnetic field. This phenomenon, commonly known as magnetostriiction, is reversible and is also called the 'Joule and Villari effects'. In their demagnetized forms, domains in a ferromagnetic material are randomly oriented. However, when a magnetic field is applied these domains become oriented along the direction of the field. This orientation results in microscopic forces between these domains, hence resulting in deformation of the material. By reciprocity, mechanical deformation can cause orientation of the domains, so resulting in induction at the macroscopic level [5]. The elongation is quadratically related to the induced magnetic field and hence is strongly non-linear.

Apart from the ferroelectric bar, a magnetostrictive transducer consists of a coil and a magnet [5] (Figure 3.6(a)). It is now possible to translate this electrical equivalent circuit to a electromechanical circuit, as shown in Figure 3.6(b). This has electrical and mechanical

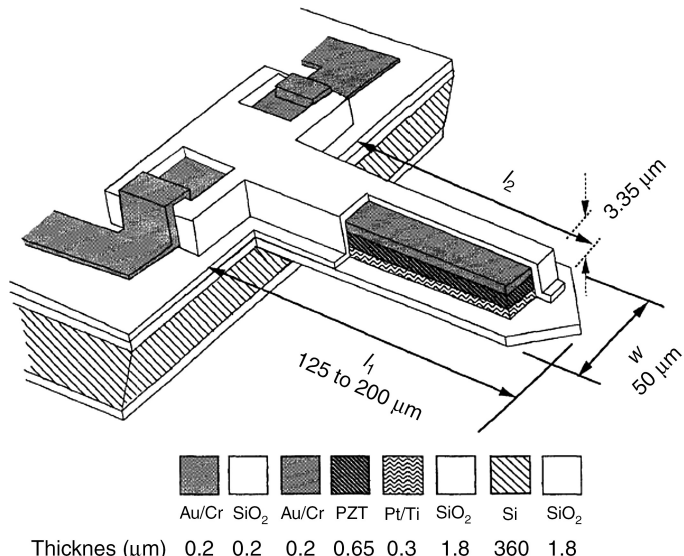


Figure 3.5 Schematic of a micromachined piezoelectric force sensor [4]. C. Lee, T. Itoh, and T. Suga, “Micromachined piezoelectric force sensors based on PZT thin films,” IEEE Trans Ultrasonics, Ferroelectrics & Freq. Control, vol. 43, © 1996 IEEE

components connected to an electromechanical transformer. The ratio of the ‘turns’ of this transformer is decided by the amount of coupling. The electromechanical coupling coefficient is defined as the ratio of the energy stored in the mechanical circuit to the total input energy.

The electromechanical coupling for the magnetostrictive transducer shown in Figure 3.6(a) relates the induced voltage V at the terminals of the coil with the rate of change in displacement at the free end of the bar:

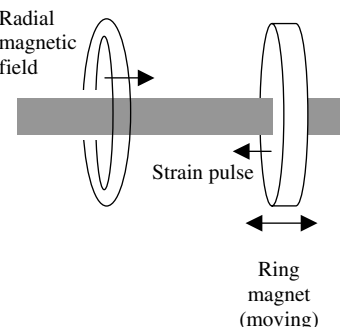
$$V = \frac{g\Delta EN}{R_m} \dot{x} \quad (3.9)$$

where $g\Delta$ is the magnetostrictive strain modulus, E is the Young’s modulus of the material, R_m is the total ‘reluctance’ of the magnetic circuit and N is the number of turns in the coil. The ratio on the right-hand side of Equation (3.9) represents the electromechanical coupling.

Ferrites, and metallic alloys such as ‘Permalloy’ (45 % Ni + 55 % Fe), ‘Alfer’ (13 % Al + 87 % Fe) and ‘Alcofer’ (12 % Al + 2 % Co + 86 % Fe), are some of the common materials used in magnetostrictive transducers. These materials can also be deposited as thin films, thus making it possible to fabricate micro-actuators and sensors by using them. In addition, amorphous thin films, such as $TbFe_2$, $Tb_{0.3}Dy_{0.7}Fe_2$ and $DyFe_2$, have been reported in the literature [6]. The realization of such thin films is more process-dependent than their bulk

counterparts, as the preparation conditions affect the homogeneity and growth process of the films, as well as their stoichiometry.

(a) Schematic



(b) Equivalent circuit

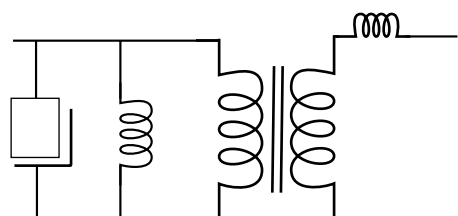


Figure 3.6 Schematics of (a) a magnetostrictive transducer and (b) the equivalent electromechanical circuit [5].

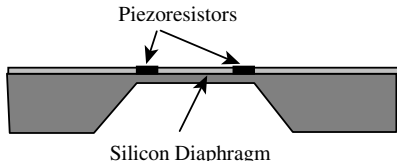


Figure 3.7 A typical structure for a piezoresistive sensing device.

3.6 PIEZORESISTIVE SENSORS

Apart from the electronic and mechanical properties of silicon, discussed in Chapter 2, piezoresistivity is another of its important characteristics which has resulted in the widespread utilization of this material for sensors. The piezoresistive effect, first reported by Smith [7] in 1954, *in silicon*, produces an approximately two orders of magnitude larger resistance change than that due to the dimension change under an applied stress in a typical conductor. For example, if the material is elongated 0.1 % by stretching, the typical metallic resistors used for strain gauges would change by about 0.2 %, but the resistance of silicon would change by about 10 %. Piezoresistive sensors fabricated on micromachined diaphragms (Figure 3.7) dominate pressure, acceleration and force sensing applications. For small deflections of thin diaphragms, the change in resistance is linear with the applied pressure [3]. Silicon obeys the Hooke's law up to 1 % strain, much higher a range than most metals alloys.

The key processes involved in the fabrication of these sensors include wet etching, ion implantation and anodic bonding. Wet etching (discussed in Chapter 10, Section 10.4) is required to form the diaphragm. Strain gauges are formed on the single crystal silicon by ion implantation. Recall that by this process, the majority of carriers are injected into the intrinsic material, thereby increasing its conductivity 'selectively'. The uniformity and con-

centration of doping can be better controlled by ion implantation than by other methods, such as diffusion. Anodic bonding (for details, see Chapter 10, Section 10.2.5) can be used to attach the silicon wafer to Pyrex glass for improved ruggedness. Since these are commonly used batch processing methods used in the IC industry, the resulting sensors are of low cost.

A typical structure for a piezoresistive microsensor is shown in Figure 3.7. Notice that the resistor is built on a silicon diaphragm. The deflection of the diaphragm leads to the dimensional change of the resistors, hence resulting in the resistance changing due to the piezoresistive effect in silicon.

$$\frac{\Delta R}{R} = (1 + 2\nu) \frac{\Delta l}{l} + \frac{\Delta \rho}{\rho} \quad (3.10)$$

where ΔR is the change of the resistance, R is the original resistance, ν is the Poisson ratio, Δl is the length change of the resistor, l is the original length of the resistor and $\Delta \rho$ and ρ represent the resistivity change and resistivity of the resistor, respectively. It is easily found that the resistance of the resistors used for these types of piezoresistive microsensors is proportional to the external pressure when the resistivity change is ignored, since the dimensional change is proportional to the applied pressure. Typically, four piezoresistors are connected into a Wheatstone bridge configuration to reduce temperature errors (Figure 3.8).

Another piezoresistive-type microsensor is shown in Figure 3.9, where a semiconductor polymer foil is formed on inter-digitated transducer (IDT) electrodes. If a voltage is applied to the electrodes and there is no pressure applied, the resistance is at the level of megohms (Mohm). When a force is applied, the resistance decreases due to the current that flows across the 'shunting' polymer foil [9]. Here, the sensing resistance is inversely proportional to the applied pressure.

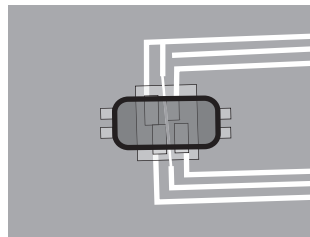
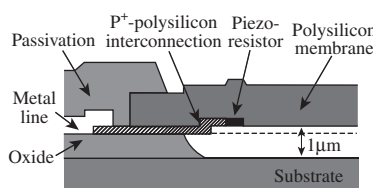


Figure 3.8 A schematic and illustration of a micromachined sensor using the piezoresistive properties of a polysilicon membrane [8]. T. Liseck, M. Kreutzer, and B. Wagner, "Surface micromachined piezoresistive pressure sensors with step-type bent and flat membrane structures," IEEE Trans. Electron. Dev., vol. 43, © 1996 IEEE

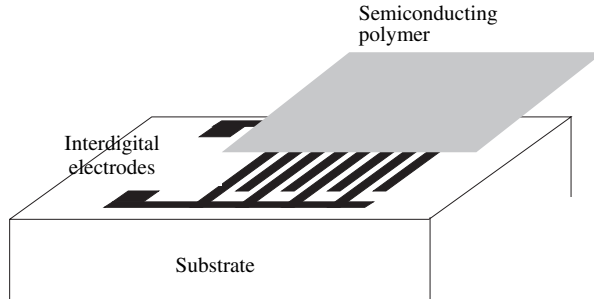


Figure 3.9 Illustration of a piezoresistive sensing device combining inter-digitated transducers (IDTs) and a semiconducting polymer [9].

The performance of piezoresistive microsensors varies with temperature and pressure. The sensitivities of the sensors decrease as the temperature increases, while any residual stress generated during the fabrication will also influence the sensitivities of the sensors. A non-linear deflection of the diaphragm occurs when the high pressure induced a deflection which is over 10% of the diaphragm thickness.

3.7 OPTICAL SENSORS

Optical sensors are based on measuring either the intensity change in one or more light beams or phase changes in the light beams caused by their interaction or interference. Thus, optical sensors can be grouped as either *intensity* sensors or *interferometric* sensors. The techniques used in the case of intensity sensors include light scattering (both Rayleigh and Raman), spectral transmission changes (i.e. simple attenuation of transmitted light due to absorption), microbending or radiative losses, reflectance changes and changes in the modal properties of the fiber [10]. Interferometric sensors, on the other hand, are based on the magneto-optic, the laser-Doppler or the Sagnac effects.

The simplest optical sensor is a photodetector. In a reverse-biased P–N junction detector, electron–hole pairs generated by the incident optical energy increases the carrier density. PIN and avalanche-type photodiodes are also used in several applications.

Interferometric techniques, such as Mach–Zehnder interferometry and Fabri–Pérot interferometry, can be used in conjunction with diaphragms to sense pressure, force and related quantities. The deflection of the diaphragm varies linearly with the applied pressure. Some optical sensors are based on measuring quantum-well spectrum deformation.

Temperature sensors based on Fabri–Pérot interferometry can measure the change in optical pathlength of a short piece of material whose thermal expansion coefficient and refractive index as a function of temperature are known. When improved selectivity is needed, multiple wavelengths can be used to null secondary effects, such as strain or pressure, in the material being measured. Materials used in such sensors include glass, calcite or zinc selenide (ZnSe).

In a fiber-optic interferometer (Figure 3.10), the interference occurs at the partially reflecting surface of the fiber and an external mirror. The size of the sensitive element based on this principle can be as small as diameter of the fiber. A low-coherence optical source is usually used in this system. The prime advantage of this interferometer is its simple configuration.

The radiation of the laser diode is coupled into the fiber and propagates partially through the coupler towards the mirror. At the tip of the fiber, a part of the radiation is internally reflected and the other part goes out, gets reflected by the mirror and is picked up again by the fiber. These two optical beams interfere with each other and as a result the intensity of the optical radiation at the photodetector is periodically changed, depending on the distance x_0 between the fiber and mirror. The displacement of the mirror by $\lambda/2$ changes the pathlength difference of the interfering rays by 2π , resulting in one period variation of the radiation intensity at the photodetector.

Generally, the intensities of the interfering rays are different. In such a case, 100% ‘visibility’ of the interference cannot be achieved, even at a zero pathlength difference of the interfering rays. The detected signal intensity is given by the following

$$I = I_1 + I_2 + 2\gamma\sqrt{I_1 I_2} \cos \varphi \quad (3.11)$$

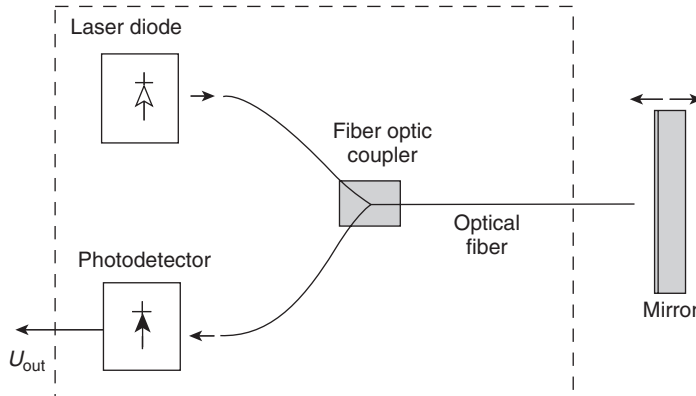


Figure 3.10 Schematic of a fiber-optic interferometric sensor.

where φ is the phase difference of the interfering rays, I_1 and I_2 are the intensities of the two rays and γ is the degree of coherence of the beam.

In a fiber optic Fabry–Pérot interferometer;

$$I_1 = R_1 I_0 \quad (3.12)$$

and:

$$I_2 = (1 - R_1)^2 R I_0 \quad (3.13)$$

where I_0 is the intensity of the laser diode radiation coupled into the fiber, R_1 is the reflectivity of the end face of the fiber and R is the reflectivity of the external mirror. Thus, when the distance between the interferometer mirrors equals x_0 , the light intensity detected by the photodetector is:

$$I = I_0 \left[R_1 + (1 - R_1)^2 R + 2(1 - R_1)\sqrt{R_1 R_2} \times \left(\frac{\sin \theta}{\theta}\right) \cos\left(\frac{4\pi}{\lambda}x_0\right) \right] \quad (3.14)$$

where:

$$\theta = \pi \frac{l}{l_c}$$

in which l and l_c are the path difference and coherence length of two rays in a non-coherent system. When the distance between the fiber and mirror is smaller than the coherence length, interference occurs and the intensity of the light in the interferometer changes with the mirror displacements. The ‘visibility’ of interference increases when the distance between the mirror and fiber is decreased.

Another possibility is to use fiber Bragg grating (FBG) devices, e.g. for temperature sensing. The challenge here is to fabricate a device that responds only to temperature. In one reported example, two identical FBGs have been interferometrically monitored [11]. By incorporating these in a bimetallic beam, the temperature was reliably measured independent of other effects, with $\pm 1\%$ linearity achieved over the range 25 to 65°C, and with a possible resolution of ± 0.006 °C. Germanium–silica fibers, fabricated as a fiber Bragg grating [12], can be used for higher temperatures up to 650°C.

Two types of optical rotation sensors have been developed based on the Sagnac effect; i.e. the ring laser gyroscope and the fiber-optic gyroscope. When two light beams propagate in opposite directions around a common path, they experience a relative phase shift, depending upon the rotation rate of the plane of the path. The actual direction is obtained by integrating the output. In the case of the ring laser gyroscope, this phase change produces a change in the oscillation frequency of a laser that is integral to the path. In the case of the fiber-optic gyroscope, the phase difference is detected by ‘interfering’ the two beams outside the path. The fiber-optic gyroscope is a simpler device and can achieve the required performance at a lower cost than with ring laser or mechanical gyroscope technology.

The fiber-optic gyroscope consists of a loop of a single-mode optical fiber and related coupler components, a semiconductor laser and signal-processing electronics. The coupler components are generally fabricated in proton-exchanged LiNbO₃ integrated-optic circuits due to their ability to modulate the light beam for improved detection.

As seen from the above, nearly all physical quantities of relevance to smart systems may be measured by using optical sensors. These include temperature, pressure, flow, displacement, velocity, acceleration, etc. Optical sensors usually have high sensitivity, fast response, low noise and high reliability. They are also free of electromagnetic interference. However, the main disadvantages are the cost involved in accurately aligning and calibrating the sensors and issues associated with temperature sensitivity.

3.8 RESONANT SENSORS

Resonant sensors are based on measuring the resonant frequency of the mechanical vibration of beams or diaphragms. The applied strain causes changes in the resonant frequency (similar to a guitar string), enabling measurement of input variables such as pressure, acceleration, rate and temperature. Resonant frequency pickup can use any of the sensing technologies discussed previously. Resonant sensing is easily understood based on the change in the natural frequency of a string with the tensile force. In a resonant microsensor developed based on this principle, the strain caused by pressure on the diaphragm leads to variation of its natural frequency. By picking up the natural frequency variation of the resonator, the physical information which caused the strain will be sensed.

As an example, the natural resonant frequency of a flexure resonator with both ends fixed can be obtained from the following [13]:

$$f = \frac{4.73^2 h}{2\pi l^2} \left\{ \frac{E}{12\rho} [1 + 0.2366(l/h)^2 \epsilon]^{1/2} \right\} \quad (3.15)$$

where f is the natural frequency of the fundamental oscillating mode, l the resonator length, h the resonator thickness, E the Young's modulus, ρ the density of the diaphragm material and ϵ the strain generated inside the resonator structure. Comparing resonant sensing with piezoresistive sensing, the resonator acts as a kind of strain gauge – the resonant strain gauge – which relates the strain with the resonant frequency. Therefore, the gauge factor of the above resonant strain gauge can be determined as:

$$k_{gf} = \frac{1}{2} \left[\frac{0.2366(l/h)^2}{1 + 0.2366(l/h)^2 \epsilon} \right] \quad (3.16)$$

and:

$$\frac{\Delta f}{f} = k_{gf} \epsilon \quad (3.17)$$

If the strain is 100 ppm, for a 1.2 mm long, 20 μm wide and 5 μm thick resonator strain gauge, the gauge factor can be as high as 3000, while the piezoresistive strain gauge factor is only about 2. Since the gauge factor relates directly to the sensitivity of the sensor, resonant sensing can be used to obtain high-sensitive micro sensors. However, as resonant sensing usually requires a more complex sensor structure than piezoresistive sensing, resonant strain gauges need to be encapsulated from the fluid [14].

The resonant microbeam system shown in Figure 3.11 acts as a sensitive strain gauge [15]. In Figure 3.11(b), when the pressure P_1 exceeds P_2 , the diaphragm bends downward, increasing the resonance frequency of the microbeam, represented by the line in the middle of the figure. In Figure 3.11(c), an upward acceleration deflects the proof mass downward, hence causing a frequency increase. The microbeam is sealed in an integral vacuum enclosure to prevent gas damping (Figure 3.11(a)). Changes in the stress state of the diaphragm cause changes in the tension in the embedded structure, which in turn result in changes in its resonant frequency. The structure is usually driven into resonance by electrostatic excitation by applied AC voltages and the resonant frequency is sensed by piezoresistive sensing. For open-loop tests, the beam electrode is driven by an external oscillator at the test frequency. The differential amplifier amplifies the AC signal from the piezoresistive sense resistor. For closed-loop operation, an automatic gain control (AGC) circuit is used to maintain a constant amplitude and prevent 'over driving' the beam. Open-loop tests disable the AGC, measure the gain = (V_{out}/V_{in}) versus frequency and drive amplitude. Closed-loop tests enable the AGC, connect the beam drive and measure frequency versus strain and temperature.

Capacitive sensing may also be employed in a similar arrangement. Alternately, the structure can be optically excited by a laser and sensed by a photodetector. Resonant sensors have better sensitivity than simple piezoresistive sensors. It may also be noted that the output is frequency, and hence is inherently more immune to noise than analog signals in the case of piezoresistive or capacitive sensors.

3.9 SEMICONDUCTOR-BASED SENSORS

There are several sensor configurations making use of the interesting properties of semiconductor devices. In the following example, a field effect transistor (FET) is modified with its gate electrode suspended with micro-machined beams. Changes in the positions of the beams, caused by the measurand quantity, affect the FET output and can be used as a sensing mechanism.

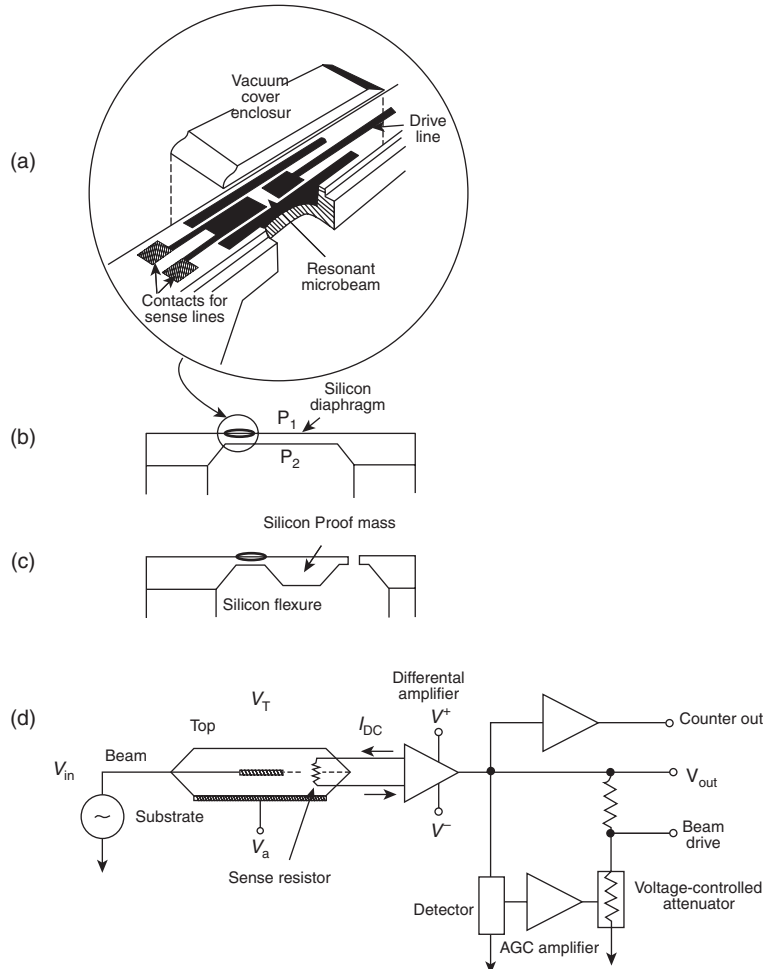


Figure 3.11 Resonant microbeam system (a) showing cross-sectional views of the polysilicon beam attached to a silicon diaphragm (b) or silicon flexure (c), along with (d) a schematic of the related microbeam test circuit [15]. Reprinted from Sensors Actuators A, 35, Zook J D, Burns D W, Guckel H, Sniegowski J J, Engelstad R L and Feng Z, Characteristics of polysilicon resonant microbeams, pp. 51–59, Copyright 1992, with permission from Elsevier

First, we will discuss an accelerometer consisting of a proof mass suspended over an FET, with the gate electrode of the device attached to the suspended structure. The anchors of the ‘meander’ support are elevated to suspend the beam above the gate region (Figure 3.12). This arrangement provides a gap between the gate and the insulator layer, thus keeping the threshold voltage for the FET constant [16]. The meander beams attached to this system are configured such that the electrode moves in the direction shown in Figure 3.12.

This motion of the gate electrode changes the transistor drain current without affecting the current density through the channel. The sensitivity S of this device is given by the following:

$$S = \frac{\delta I_D}{\delta W} \quad (\text{A/m}) \quad (3.18)$$

where δI_D is the change in drain current and δW is the change in the depth to which the gate is overlapping the channel.

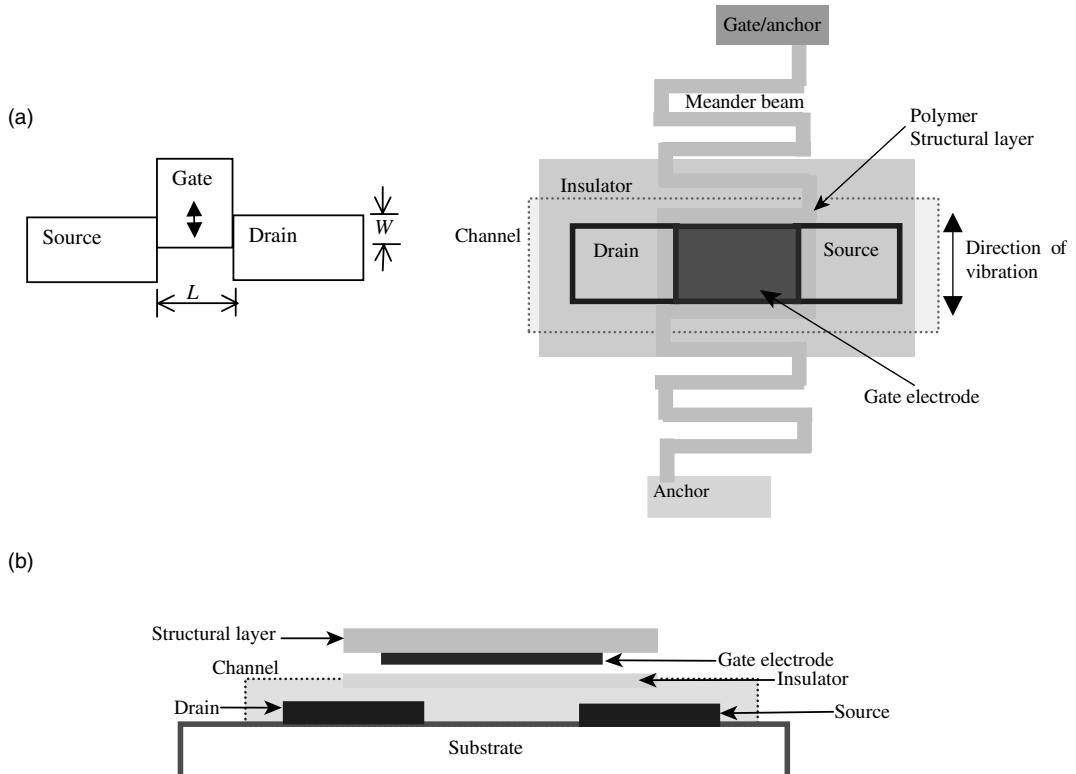


Figure 3.12 Schematics of a movable-gate field effect transistor: (a) top view; (b) cross-sectional view.

For a typical n -channel FET, the drain current is given by:

$$I_D = \frac{C_g \mu W}{2L} [2(V_{GS} - V_T)V_{DS} - V_{DS}^2] \quad \text{for } V_{DS} < V_{GS} - V_T \quad (3.19)$$

and:

$$I_D = \frac{C_g \mu W}{2L} (V_{GS} - V_T)^2 \quad \text{for } V_{DS} \geq V_{GS} - V_T \quad (3.20)$$

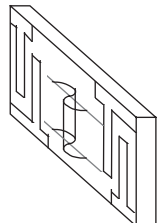
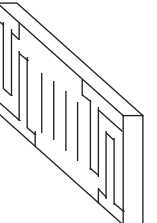
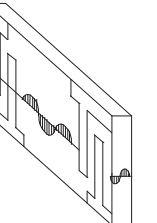
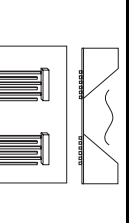
where V_{GS} and V_{DS} are the gate-to-source and drain-to-source voltages, V_T is the threshold voltage at which the channel begins to conduct, C_g is the gate capacitance per unit gate area, μ is the majority carrier mobility for the channel and W and L are the width and length of the channel, respectively. These equations show a linear relationship between the drain current and the channel width W .

The threshold voltage for the FET is as follows:

$$V_T = V_{FB} - \frac{Q_D}{C_i} - \frac{\sqrt{2q\epsilon N_D(V_{bi} - V_{BS})}}{C_i} \quad (3.21)$$

where Q_D is the dose of the n-type impurity, N_D is the doping concentration, ϵ is the dielectric constant of the semiconductor and V_{FB} , V_{bi} and V_{BS} are the flat-band voltage, built-in potential of the channel junction and substrate bias, respectively; C_i is the capacitance of the gate, which is a series combination of the capacitance due to the air gap and that due to the insulator layer. For very thin insulator layers, this capacitance can be approximated to that due to air alone. Thus, the configuration presented here results in a linear relationship for the device current to the mechanical motion. Furthermore, the lateral motion permits larger amplitudes of variation. The inertial force of the mass causes the lateral movement when the device can be used as an accelerometer.

Table 3.1 Structures of Love, SAW, SH-SAW, SH-APM and FPW devices and comparison of their operation [17,18]. M. Hoummady, A. Campitelli and W. Włodarski, “Acoustic wave sensors: design, sensing mechanisms and applications,” Smart Mater. Struct. 6 1997, © IOP

Device type	Substrate	Typical frequency	Structure	Particle displacement relative to wave propagation	Transverse component relative to sensing surface	Sensing medium/quantity
Love	ST-quartz	95–130 MHz		Transverse	Parallel	Ice, liquid
Rayleigh SAW	ST-quartz	80 MHz–1 GHz		Transverse parallel	Normal	Strain, gas
SH-SAW	LiTaO ₃	90–150 MHz		Transverse	Parallel	Gas, liquid
SH-APM	ST-quartz	160 MHz		Transverse	Parallel	Gas, liquid, chemical
Lamb/FPW	Si _x N _y /ZnO	1–6 MHz		Transverse parallel	Normal	Gas, liquid

3.10 ACOUSTIC SENSORS

Acoustic sensors operate by converting electrical energy into acoustic waves, the propagation characteristics of which could be influenced by the physical parameter being measured, and then converting this back to electrical energy for further processing. Various configurations of acoustic wave devices are possible for sensor applications. The important characteristics of some of these devices are summarized in Table 3.1. The type of acoustic wave generated in a piezoelectric material depends mainly on the substrate material properties, the crystal cut and the structure of the electrodes utilized to transform the electrical energy into mechanical energy.

A *Rayleigh wave* has both a surface-normal component and a surface-parallel component in the direction of propagation. The wave velocity is determined by the substrate material and the crystal cut. Most *surface acoustic wave (SAW)* devices operate under this mode and will be discussed further below. The energies of the SAW are confined to a zone close to the surface a few wavelengths thick [19]. *Love waves* are guided acoustic modes which propagate in a thin layer deposited on a substrate. The acoustic energy is concentrated in this guiding layer and results in a high-mass sensitivity. This wave mode is typically employed in gases, biochemical or viscosity sensors.

The selection of a different crystal cut can yield *shear horizontal (SH)* surface waves instead of Rayleigh waves. The particle displacements of this wave are transverse to the wave propagation direction and parallel to the plane of the surface. The frequency of operation is determined by the inter-digitated transducer (IDT) finger spacing and the shear horizontal wave velocity for the particular substrate material. These have shown considerable promise in applications such as sensors in liquid media and biosensors [20–22]. In general, SH-SAWs are sensitive to mass loading, viscosity, conductivity and permittivity of the adjacent liquid.

The configuration of SH-APM devices is similar to the Rayleigh SAW devices, but the wafer is thinner, typically a few acoustic wavelengths. SH waves excited by the transducer propagate in the bulk of the substrate, at an angle to the surface. These waves reflect between the plate surfaces as they travel in the plate between the input and output transducers. The frequency of operation is determined by the thickness of the plate and the design of the transducer. SH-APM devices are mainly used in liquid sensing and offer the advantage of using the back surface of the plate as the sensing active area.

Lamb waves, also known as flexural plate waves (FPWs), are elastic waves that propagate in plates of finite thickness and are used for the health monitoring of structures and for flow sensors: as the fluid passes through a channel above the acoustic path, it affects the properties of the acoustic waves propagating on the substrate.

Surface acoustic wave (SAW)-based sensors form an important part of the sensor family and in recent years have seen diverse applications ranging from gas and vapor detection to strain measurement [19]. SAW devices were first used in radar and communication equipment as filters and delay lines and were recently found to have several applications in sensors for various physical variables, including temperature, pressure, force, electric field and magnetic field, as well as chemical compounds. A SAW device consists of a piezoelectric wafer, IDTs and reflectors on its surface. The IDT is the ‘cornerstone’ of SAW technology, converting the electrical energy into mechanical energy, and vice versa, and hence are used for exciting as well as detecting the SAW.

An IDT consists of two metal comb-shaped electrodes placed on a piezoelectric substrate (Figure 3.13). An electric field, created by the voltage applied to the electrodes, induces dynamic strains in the piezoelectric substrate, which in turn launches elastic waves. These waves contain, among others, the Rayleigh waves which run perpendicular to the electrodes with velocity V_R .

If a harmonic voltage, $v = v_0 \exp(j\omega t)$, is applied to the electrodes, the stress induced by a finger pair travels along the surface of the crystal in both directions. To ensure constructive interference and in-phase stress, the distance between two neighboring fingers should be equal to half the elastic wavelength, λ_R .

$$d = \lambda_R/2 \quad (3.22)$$

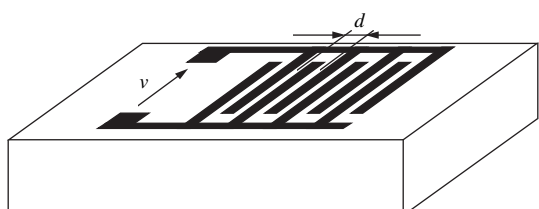


Figure 3.13 Finger spacings and (d) and their role in determination of the acoustic wavelength (v) in an inter-digitated transducer [23].

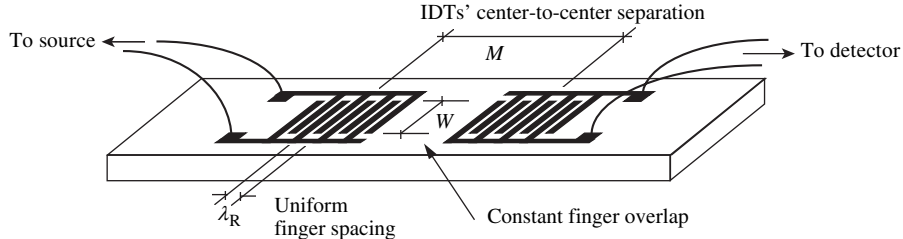


Figure 3.14 Schematic of a SAW device with IDTs metallized onto the surface [23].

The associated frequency is known as the *synchronous* frequency and is given by the following:

$$f_0 = V_R / \lambda_R \quad (3.23)$$

At this frequency, the transducer efficiency in converting electrical energy to acoustical, or vice versa, is maximized. The width of each electrode finger is generally chosen as half the period. Its length determines the acoustic beamwidth and hence is not as significant in this preliminary design. The number of pairs of fingers are however critical in choosing the device bandwidth. The impulse response of the basic IDT is a rectangle. The Fourier transform of a rectangle is a sinc function whose bandwidth in the frequency domain is proportional to the length of the rectangular window in the space domain. As a result, a narrow bandwidth requires the IDT to have a large number of fingers. A schematic of a SAW device with IDTs metallized onto the surface is shown in Figure 3.14 [23].

The exact calculation of the piezoelectric field driven by the inter-digital transducer is rather elaborate [19]. For simplicity, analysis of the IDT is carried out by means of numerical models. The frequency response of a single IDT can be simplified by the delta-function model [19]. The SAW velocity on the substrate depends on its density and elastic and piezoelectric constants. The principle of SAW sensors is based on the fact that the SAW traveling time between the IDTs changes with variation in the physical variables.

Acoustic sensors offer a rugged and relatively inexpensive platform for the development of wide-ranging sensing applications. A unique feature of acoustic sensors is their direct response to a number of physical and chemical parameters, such as surface mass, stress, strain, liquid density, viscosity, dielectric and conductivity properties [24]. Furthermore, the anisotropic nature of piezoelectric crystals allows for various angles of cut, with each cut having unique properties. Applications, such as, for example, a SAW-based accelerometer utilize a

quartz crystal with an ST-cut, which has an effective zero temperature coefficient [25], with a negligible frequency shift through changes in temperature. Again, depending on the orientation of the crystal cut, various SAW sensors with different acoustic modes may be constructed, with a mode ideally suited towards a particular application. Other attributes include very low internal loss, uniform material density and elastic constants and advantageous mechanical properties [26].

The principal means of detection of the physical property change involves the transduction mechanism of a SAW acoustic transducer, which involves transfer of signals from the mechanical (acoustic wave) to the electrical domain [19]. Small perturbations affecting the acoustic wave would manifest themselves as large changes when converted to the electromagnetic (EM) domain because of the difference in velocity between the two waves. Given that the velocity of propagation of the SAW on a piezoelectric substrate is 3488 m/s and the AC voltage is applied to the IDT at a synchronous frequency of 1 MHz, the SAW wavelength is given by $\lambda = v/f = 3.488 \times 10^{-3}$ m. The EM wavelength in this case is $\lambda c = c/f$, where $c = (3 \times 10^8$ m/s) is the velocity of light. Thus, $\lambda c = 30$ m, and the ratio of the wavelengths ($\lambda/\lambda c$) = 1.1×10^{-5} .

3.11 POLYMERIC SENSORS

Several well-known sensing mechanisms have been discussed so far in this chapter. This and the next section will dwell on two material systems that have not been explored to their fullest potential.

The advancement of silicon-based micro systems is intimately intertwined with developments in silicon semiconductor processing technology. Accordingly, various processing approaches have been established for the integration of silicon-based micro systems with standard complimentary metal oxide semiconductor (CMOS) processing. For precision devices, and for devices requiring

integrated electronics, silicon is presently unrivaled. However, it is not necessarily the best material for all applications. For example, structures fabricated on this is limited to 2-D or very limited 3-D systems, unpackaged silicon devices are incompatible with many chemical and biological substances and fabrication requires sophisticated, expensive equipment operated in a clean-room environment. These often limit the low-cost potential of silicon-based micro systems. Polymer-based micro systems are rapidly gaining momentum due to their potential for conformability and other special characteristics not available with silicon. In general, polymer-based devices may not be as small or as complex as those with silicon. However, polymers are often flexible, chemically and biologically compatible, available in many varieties and can be fabricated in truly 3-D shapes. Most of these materials and their fabrication processes are inexpensive. Perhaps one of the most important advantages of sensors using polymeric materials, in the context of smart systems, is their potential for being distributed over a large area.

Polymer sensors are particularly advantageous in ‘moderate-performance’ devices which are low cost or disposable [27]. Unlike many silicon devices that are often packaged inside polymers, sensors built with polymers can even be ‘self-packaged’. Active polymer components can take advantage of several functional polymers to increase their functionality. Polymer sensors may be divided into two categories. The first uses the piezoelectric properties observed in some functional polymers while the second uses the change in conductivity of some other polymers when exposed to changing environmental conditions.

Since the discovery of strong piezoelectricity in poly(vinylidene fluoride) (PVDF) in 1969, piezoelectric polymers have been extensively investigated for various applications [28]. There are some unique features of piezoelectric polymers that make them attractive for use as sensing elements, including their relatively low acoustic impedance, broadband acoustic performance, flexible form and availability in large area films, and ability to be dissolved and coated onto various substrates. In the successful applications of piezoelectric polymer technology, these characteristics have prevailed over their inherent disadvantages of relatively weak piezoelectric properties, large dielectric and elastic losses, and low dielectric constants. In addition to its piezoelectric properties, PVDF also offers pyroelectric properties [17].

PVDF is a semicrystalline high-molecular-weight polymer formed by the linking together of simple 1,1-difluoroethylene (VDF) molecules. Under precisely controlled

reaction conditions, a molecular structure of PVDF with a 90% head-to-tail arrangement (i.e. $\text{CH}_2\text{--CF}_2\text{--}(\text{CH}_2\text{--CF}_2)_n\text{--CH}_2\text{--CF}_2$) [29] can be obtained. PVDF is approximately half crystalline and half amorphous. The most common polymorph form of PVDF, the α -phase, is produced by crystallization from the melt or solution. The α -phase can be transformed into the polar form, the β -phase, by mechanically stretching or rolling at elevated temperatures. Since all of the dipole moments become perpendicular to the chain axes, microscopically, each crystallite has a net dipole moment and is piezoelectric. However, on the macroscopic scale, there is no polarization within the polymer due to the random orientation of the dipole moments of the crystallites. In order to render the PVDF film piezoelectric, poling is required, which involves the application of an electric field. This step preferentially aligns the dipoles of the crystallites in the direction of the applied electric field and thus produces a net polarization. In the copolymer (P(VDF-TrFE)), the increased number of the relatively large fluorine atoms prevents the formation of tg + tg-conformation. This extends the polymer chains to crystallize directly into the β -phase. The copolymer also needs a final poling step to make it fully piezoelectric. The two main poling techniques are conventional two-electrode poling (also referred to as thermal poling) and corona poling. A listing of the properties of poled PVDF and its copolymer P(VDF-TrFE) is provided in Table 3.2 [30].

Several standard processes are available for the deposition of polymer thin films. Some films which are used for gas sensing employing SAW devices are listed in Table 3.3. These could be deposited on a substrate by deposition methods such as spin coating, dip coating and *in situ* polymerization.

3.12 CARBON NANOTUBE SENSORS

After carbon nanotubes (CNTs) were first discovered by Iijima in 1991 [31], several researchers have reported excellent mechanical, electrical and thermal properties for these materials, both theoretically and experimentally. In recent years, such nanotubes have been introduced into microelectronics and micro electromechanical systems (MEMS). These nanotubes are also regarded as promising materials for nanotechnology and nano electromechanical systems (NEMS).

Fundamentally, CNTs can be considered as rolled-up cylinders of graphite sheets of sp₂-bonded carbon atoms with diameters less than 100 nm. The length of an individual carbon nanotube could typically vary from

Table 3.2 Comparison of typical properties of PVDF and P(VDF-TrFE) [30].

Property	PVDF	P(VDF-TrFE)
<i>Coupling coefficient</i>		
k_{31}	0.12	0.20
k_t	0.14	0.25–0.29
<i>Piezoelectric strain constant</i> (10^{-12} m/V or C/N)		
d_{31}	23	11
d_{33}	−33	−38
<i>Piezoelectric stress constant</i> (10^{-3} V m/N)		
g_{31}	216	162
g_{33}	−330	−542
<i>Pyroelectric coefficient, P</i> ($10^{-6} \text{ C}/(\text{m}^2 \text{ K})$)	30	40
<i>Young's modulus, Y</i> (10^9 N/m^2)	2–4	3–5
<i>Relative permittivity, ϵ/ϵ_0</i>	12–13	7–8
<i>Mass density, ρ</i> (10^3 kg/m^3)	1.78	1.82
<i>Speed of sound, c</i> (10^3 m/s)	2.2	2.4
<i>Acoustic impedance, Z</i> (MRa)	3.92	4.37
<i>Loss tangent, $\tan \delta_e$</i> (at 1 kHz)	0.02	0.015
<i>Temperature range</i> ($^\circ\text{C}$)	−40 to 80	−40 to 115

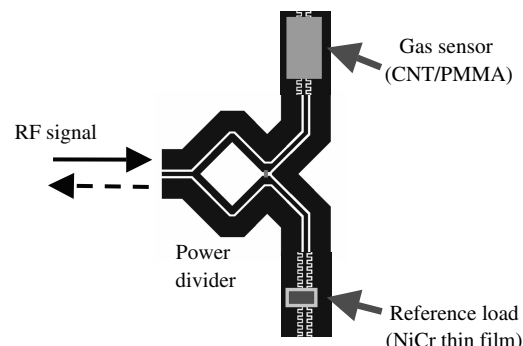
tens of nanometers to several microns. Caps have always been observed at both ends of these cylinders, which could be hemispheres of a fullerene, such as C_{60} . Carbon nanotubes can be divided into two categories, i.e. single-walled nanotubes (SWNTs) and multi-walled nanotubes (MWNTs), according to the number of graphene layers.

Some properties of CNTs, such as conductivity variation and the electrostrictive effect, have been used in implementing sensors using them. The design of such sensors follow the principles discussed earlier in this chapter. In the following, we present a somewhat different approach that makes use of the variation in electro-

magnetic properties of a transmission line coated with a layer of a CNT [32]. Based upon the change in this electrical property in composite thin films of carbon naotubes (as the vapor concentration varies), monitoring of the reflection phase at radio frequencies has been proposed for real-time wireless sensing applications. The reflection phase of electromagnetic waves reflected from a load was determined by load impedance. For this purpose, composite thin films with funtionalized carbon nanotubes (f-CNTs) were coated onto an interdigital coplanar waveguide, as shown in Figure 3.15, and the phase change of the reflected waves due to the presence of an organic gas was evaluated.

Table 3.3 Typical examples of polymer thin films used in gas sensors.

Measurand	Coating
Hydrogen	Palladium
SO_2	Triethanolamine
NO_2	Lead phthalocyanine
Toluene	Polydimethylsiloxane
Water vapor/humidity	Polymide, SiO_2 , cellulose acetate
H_2S	WO_3
CO	Metal phthalocyanine
CO_2	Polyethyleneimine
CH_4	Metal phthalocyanine
NH_3	Platinum

**Figure 3.15** Schematic of a sensor based on the phase changes in a transmission line coated with a carbon nanotube composite.

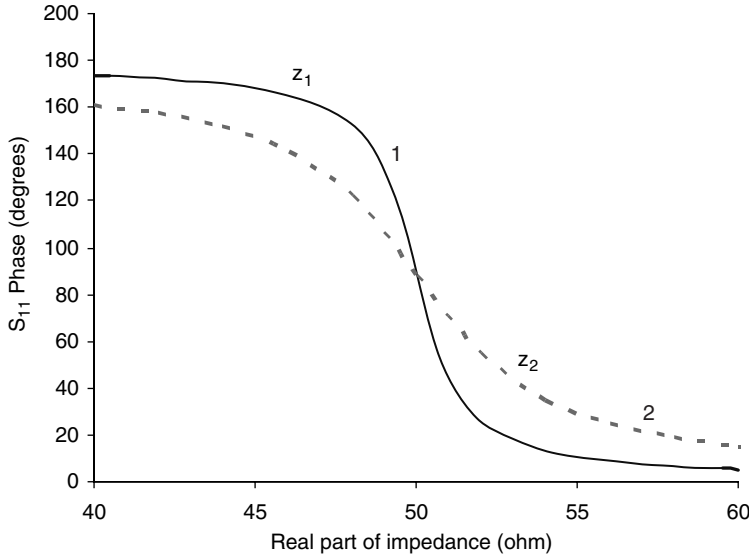


Figure 3.16 Relationship of the reflection (S_{11}) phase to the real and imaginary parts of the load impedance ($Z_L = a + jb$), with $z_1 = a + j1$ and $z_2 = a + j2$.

When a reflected wave exists on a ‘lossless’ transmission line terminated with a load impedance, $Z_L = a + jb$, the voltage across T the line is given by the following:

$$V = V^+ e^{-j\beta z} + V^- e^{j\beta z} \quad (3.24)$$

where V^+ and V^- are the amplitude constants of the incident and reflected waves, respectively, and β is the phase constant for the ‘lossless’ line. The voltage reflection coefficient, Γ_L , is described by the ratio of V^- to V^+ as follows [33].

$$\Gamma_L = \frac{V^-}{V^+} = \frac{Z_L - Z_c}{Z_L + Z_c} \quad (3.25)$$

and the voltage at any point on the transmission line ($z < 0$) is given by the following:

$$V = V^+ \left(e^{-j\beta z} + |\Gamma_L| e^{j(\theta + \beta z)} \right) \quad (3.26)$$

where:

$$\Gamma_L = |\Gamma_L| e^{j\theta} \quad (3.27)$$

and:

$$|\Gamma_L| = \sqrt{\frac{[(a^2 - Z_c^2) + b^2] + 4b^2 Z_c^2}{[(a + Z_c^2) + b^2]^2}} \quad (3.28)$$

plus:

$$\theta = \tan^{-1} \left[\frac{2bZ_c}{(a^2 - Z_c^2) + b^2} \right] \quad (3.29)$$

where Z_c is the characteristic impedance of the transmission line.

According to Equation (3.29), the phase of the reflected waves in a transmission line is determined by load impedance. Typical changes in the phase of the reflected waves with respect to the load impedance of a transmission line are illustrated in Figure 3.16. As long as the *imaginary* part of the load impedance (b) is low, the reflected wave phase exhibits a large phase shift with a small change in the *real* part of the load impedance (a) near the characteristic impedance. The basic schematic of phase monitoring in this newly designed sensor employs a variable resistor with a small imaginary impedance as a load terminating a coplanar waveguide (Figure 3.15).

REFERENCES

1. S. Fatikow and U. Rembold, *Microsystem Technology and Microrobotics*, Springer-Verlag, Berlin, Germany (1997).
2. P. Rai-Choudhury (Ed.), *Handbook of Microlithography, Micromachining and Microfabrication*, Vol. 2, *Micromachining and Microfabrication*, SPIE Optical Engineering Press, Bellingham, WA, USA (1997).

3. W.P. Eaton and J.H. Smith, 'Micromachined pressure sensors – review and recent developments', *Smart Materials and Structures*, **6**, 530–539 (1997).
4. C. Lee, T. Itoh and T. Suga, 'Micromachined piezoelectric force sensors based on PZT thin films', *IEEE Transactions: Ultrasonics, Ferroelectrics and Frequency Control*, **43**, pp. 553–559 (1996).
5. M. Rossi, *Acoustics and Electroacoustics*, Artech House, Norwood, MA, USA (1988).
6. C. Body, G. Reyne and G. Meunier, 'Modeling of magnetostrictive thin films: application to a micromembrane', *Journal de Physique (France), Part III*, **7**, 67–85 (1997).
7. C.S. Smith, 'Piezoresistance effect in germanium and silicon', *Physical Review*, **94**, 42–49 (1954).
8. T. Liseec, M. Kreutzer and B. Wagner, 'Surface micromachined piezoresistive pressure sensors with step-type bent and flat membrane structures', *IEEE Transactions on Electronics Developments*, **43**, 1547–1552 (1996).
9. M. Witte and H. Gu, 'Force and position sensing resistors: an emerging technology', in *Proceedings of the International Conference on New Actuators*, VDI/VDE – Technologiezentrum Informationstechnik, Berlin, Germany, pp. 168–170 (1992).
10. Website: [http://www.wtec.org/loyola/opto/c6_s3.htm].
11. Y.J. Rao and D.A. Jackson, 'Prototype fibre-optic-based fizeau medical pressure and temperature sensor system using coherence reading', *Measurement Science and Technology*, **5**, 741–746, (1994).
12. W.W. Morey, G. Meltz and J.M. Weiss, 'Recent advances in fiber-grating sensors for utility industry applications', *Proceedings of SPIE*, **2594**, 90–98, (1996).
13. K. Ikeda, H. Kuwayama, T. Kobayashi, T. Watanabe, T. Nishikawa, T. Yoshida and K. Harada, 'Silicon pressure sensor integrates resonant strain gauge on a diaphragm', *Sensors and Actuators*, **A21–23**, 146–150 (1990).
14. K. Harada, K. Ikeda, H. Kuwayama and H. Murayama, 'Various applications of a resonant pressure sensor chip based on 3-D micromachining', *Sensors and Actuators*, **A73**, 261–266 (1999).
15. J.D. Zook, D.W. Burns, H. Guckel, J.J. Sniegowski, R.L. Engelstad and Z. Feng, 'Characteristics of polysilicon resonant microbeams', *Sensors and Actuators*, **A35**, 51–59 (1992).
16. X. Wang and P.K. Ajmera, 'Laterally movable gate field effect transistor for microsensors and microactuators', *US Patent* 6 204 544 (2001).
17. M.J. Vellekoop, 'Acoustic wave sensors and their technology', *Ultrasonics*, **36**, 7–14 (1998).
18. M. Hoummady, A. Campitelli and W. Włodarski, 'Acoustic wave sensors: design, sensing mechanisms and applications', *Smart Materials and Structures*, **6**, 647–657 (1997).
19. C. Campbell, *Surface Acoustic Wave Devices and their Signal Processing Applications*, Academic Press, London, UK (1998).
20. N. Nakamura, M. Kazumi and H. Shimizu, 'SH-type and Rayleigh type surface waves on rotated Y-cut LiTaO₃', in *Proceedings of the IEEE Ultrasonics Symposium*, IEEE, Piscataway, NJ, USA, pp. 819–822, (1977).
21. S. Shiokawa and T. Moriizumi, 'Design of an SAW sensor in a liquid', *Japanese Journal of Applied Physics*, **27**(Suppl. 1), 142–144 (1988).
22. J. Kondoh, Y. Matsui and S. Shiokawa, 'New bio sensor using a shear horizontal surface acoustic wave device', *Japanese Journal of Applied Physics*, **32**, 2376–2379 (1993).
23. V.K.Varadan and V.V. Varadan, 'Microsensors, actuators, MEMS and electronics for smart structures', in *Handbook of Microlithography, Micromachining and Microfabrication*, Vol. 2, *Micromachining and Microfabrication*, P. Rai-Choudhury (Ed.), SPIE Optical Engineering Press, Bellingham, WA, USA, pp. 617–688 (1997).
24. J.W. Grate, S.J. Martin and R.M. White, 'Acoustic wave microsensors, Part 1', *Analytical Chemistry*, **65**, 940–948 (1993).
25. V.K. Varadan and V.V. Varadan, 'IDT, SAW and MEMS Sensors for measuring deflection, acceleration and ice detection of aircraft', *Proceedings of SPIE*, **3046**, 209–219 (1996).
26. J.W. Grate, S.J. Martin and R.M. White, 'Acoustic wave microsensors, Part 1I', *Analytical Chemistry*, **65**, 987–996 (1993).
27. V.K. Varadan, X. Jiang and V.V. Varadan, *Microstereolithography and other Fabrication Techniques for 3D MEMS*, John Wiley & Sons, London, UK (2001).
28. Y. Roh, V.K. Varadan and V.V. Varadan, 'Characterization of all of the elastic, dielectric and piezoelectric constants of uniaxially oriented poled PVDF films', *IEEE Transactions: Ultrasonics, Ferroelectrics and Frequency Control*, **49**, 836–847 (2002).
29. Pennwalt Corporation, *KYNARTM Piezo Film Technical Manual*, Technical Brochure 10-M-11-83-M, Pennwalt Corporation, King of Prussia, PA, USA (1983).
30. Website: http://www.msiusa.com/piezo_download_listing.htm#PART1-INT.pdf.
31. S. Iijima, 'Helical microtubules of graphitic carbon', *Nature (London)*, **354**, 56–58, (1991).
32. H. Yoon, B. Philip, J.K. Abraham, T. Ji and V.K. Varadan, 'Nanowire sensor array for wireless detection and identification of bio-hazards', *Proceedings of SPIE*, **5763**, 326–332 (2005).
33. R.E. Collin, *Foundations for Microwave Engineering*, McGraw-Hill, New York, NY, USA (1992).

4

Actuators for Smart Systems

4.1 INTRODUCTION

In this chapter, the basic principles of common electro-mechanical actuators are briefly discussed. The energy conversion schemes presented here include piezoelectric, electrostrictive, magnetostrictive, electrostatic, electromagnetic, electrodynamic and electrothermal. Most of the schemes are reciprocal and hence these devices are generally referred to as *transducers*. Although some of these schemes are not quite amenable for smart micro-mechanical systems, they do have the potential for being used in such systems in the foreseeable future.

One important step in the design of these mechanical systems is obtaining their electrical equivalent circuits from analytical models. This remains the main focus of this chapter. However, relevant examples of fabricated prototypes from the published literature are also included wherever necessary. In what follows we extensively make use of electromechanical analogies to arrive at electrical equivalent circuits of transducers. These equivalent circuits are neither unique nor exact, but would serve as an easily understood tool in transducer design. The use of these electrical equivalent circuits would also facilitate use of the vast resources available for modern optimization programs for electrical circuit design into transducer designs.

A list of useful electromechanical analogies is given in Table 4.1 [1]. These are known as mobility analogies. These analogies become useful when one needs to replace mechanical components with electrical components which behave similarly, forming the equivalent circuit. As a simple example, the development of an electrical equivalent circuit of a mechanical transmission line component is discussed here [1]. The variables in such a system are force and velocity. The input and output variables of a section of a ‘lossless’ transmission

line can be conveniently related by an ABCD matrix form as follows:

$$\begin{bmatrix} \dot{x}_1 \\ F_1 \end{bmatrix} = \begin{bmatrix} \cos \beta x & jZ_0 \sin \beta x \\ j \frac{Z_0}{\rho} \sin \beta x & \cos \beta x \end{bmatrix} \begin{bmatrix} \dot{x}_2 \\ F_2 \end{bmatrix} \quad (4.1)$$

where:

$$Z_0 = \frac{1}{A\sqrt{\rho E}} \sqrt{\frac{C_1}{M_1}} \quad (4.2)$$

and:

$$\beta = \frac{\omega}{v_p} \quad (4.3)$$

and:

$$v_p = \sqrt{\frac{E}{\rho}} = \frac{1}{\sqrt{C_1 M_1}} \quad (4.4)$$

In these equations, A is the cross-sectional area of the mechanical transmission line, E its Young’s modulus and ρ the density; C_1 and M_1 are the compliance and mass per unit length of the line, respectively. Now, looking at the electromechanical analogies in Johnson [1], the expression for an equivalent electrical circuit can be obtained in the same form as Equation (4.1) above:

$$\begin{bmatrix} V_1 \\ I_1 \end{bmatrix} = \begin{bmatrix} \cos \beta x & jZ_0 \sin \beta x \\ j \frac{Z_0}{\rho} \sin \beta x & \cos \beta x \end{bmatrix} \begin{bmatrix} V_2 \\ I_2 \end{bmatrix} \quad (4.5)$$

In Equation (4.5), the quantities in the components of the matrix are also represented by equivalent electrical parameters as follows:

$$Z_0 = \sqrt{\frac{\mu}{\epsilon}} = \sqrt{\frac{L_1}{C_1}} \quad (4.6)$$

Table 4.1 Electromechanical mobility analogies [1].

Feature	Mechanical parameter	Electrical parameter
<i>Variable</i>	Velocity, angular velocity	Voltage
	Force, torque	Current
<i>Lumped network element</i>	Damping	Conductance
	Compliance	Inductance
	Mass, mass moment of inertia	Capacitance
<i>Transmission line</i>	Compliance/unit length	Inductance/unit length
	Mass/unit length	Capacitance/unit length
	Characteristic mobility	Characteristic impedance
<i>Immitance</i>	Mobility	Impedance
	Impedance	Admittance
	Clamped point	Short circuit
	Free point	Open circuit
<i>Source immitance</i>	Force	Current
	Velocity	Voltage

$$v_p = \frac{1}{\sqrt{\mu\epsilon}} = \frac{1}{\sqrt{L_1 C_1}} \quad (4.7)$$

In Equations (4.6) and (4.7) L_1 and C_1 represent the inductance and capacitance per unit length of the line, respectively.

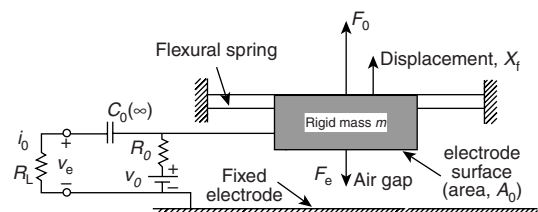
Apart from the above mobility analogy, a direct analogy is also followed at times to obtain the equivalence between electrical and mechanical circuits. These result from the similarity of integro-differential equations governing the electrical and mechanical components [2]. A brief list of these analogies is presented in Table 4.2. A brief description of the operational principles of some of the common transduction mechanisms used in electromechanical systems is provided below.

4.2 ELECTROSTATIC TRANSDUCERS

Electrostatic actuation is the most common type of electromechanical energy conversion scheme in micro-mechanical systems. This is a typical example of an energy storage transducer. Such transducers store energy when either mechanical or electrical work is done on them [3]. Assuming that the device is lossless, this stored energy is conserved and later converted to the other form of energy. The structure of this type of transducer commonly consists of a capacitor arrangement, where one of the plates is movable by the application of a bias voltage. This produces displacement, a mechanical form of energy. A schematic of a practical electrostatic transducer is shown in Figure 4.1. The transfer matrix for this transducer can be derived following [2].

Table 4.2 Direct analogy of electrical and mechanical domains [2].

Mechanical quantity	Electrical quantity
Force	Voltage
Velocity	Current
Displacement	Charge
Momentum	Magnetic flux linkage
Mass	Inductance
Compliance	Capacitance
Viscous damping	Resistance

**Figure 4.1** Schematic of a practical electrostatic transducer. H.A.C. Tilmans, "Equivalent circuit representation of electro-mechanical transducers: I. Lumped parameter systems", J. Micromech. Microeng., vol. 6, 1996 © IOP

We use the electromechanical force in a simple (fixed) parallel plate capacitor:

$$F = \frac{1}{2} v^2 \frac{\epsilon A}{x^2} \quad (4.8)$$

In more complicated systems, it is difficult to calculate this directly. Instead, we start with the basic energy balance equation:

$$dW_e + dW_m = dW_t \quad (4.9)$$

This expression indicates that the force balance is between the electrostatic and mechanical forces. Substituting for the appropriate values of work done:

$$VIdt + Fdx = d\left(\frac{1}{2} CV^2\right) \quad (4.10)$$

It may be noted that the capacitance of the arrangement cannot be considered a constant. Furthermore, we can eliminate I by the following:

$$I = \frac{dQ}{dt} = \frac{d(CV)}{dt} = C \frac{dV}{dt} + V \frac{dC}{dt} \quad (4.11)$$

The first term on the right-hand side is for a fixed capacitor, while the second term results from the physical motion of the movable plate. Obviously, this is zero for a fixed plate capacitor.

Substituting this in Equation (4.10):

$$VCdV + V^2dC + Fdx = CVdV + \frac{1}{2} V^2dC \quad (4.12)$$

$$Fdx = -\frac{1}{2} V^2dC \quad (4.13)$$

$$F = -\frac{1}{2} V^2 \frac{dC}{dx} \quad (4.14)$$

Observe that dC/dx is negative for a parallel plate capacitor. Furthermore, the force depends on the square of the voltage and hence does not depend on its polarity or rate of change:

$$VCdV + V^2dC + Fdx = CVdV + \frac{1}{2} V^2dC \quad (4.15)$$

When both plates of the capacitor are fixed, there is no mechanical motion, and hence no work is done:

$$VCdV + 0 + 0 = CVdV + 0 \quad (4.16)$$

and so the term $CVdV$ represents the energy stored!!

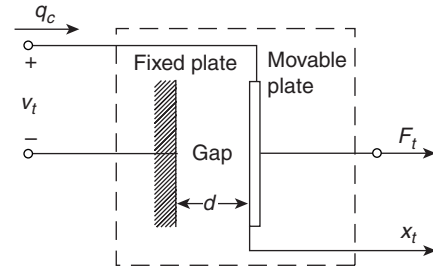


Figure 4.2 Schematic of a simplified case for an electrostatic transducer [2]. H.A.C. Tilmans, “Equivalent circuit representation of electromechanical transducers: I. Lumped parameter systems,” J. Micromech. Microeng., vol. 6, 1996 © IOP

By cancelling this term from Equation (4.15), we obtain the energy transfer caused entirely by motion:

$$V^2dC + Fdx = \frac{1}{2} V^2dC \quad (4.17)$$

By comparing Equations (4.17) and (4.13), we see that the electrical source contributes twice as much energy as the mechanical source.

Based on the simplified schematic of the transducer shown in Figure 4.2, constitutive equations can be derived; the state variables of this are the displacement x_t and charge q_t . Since all variables are dependent on time, these are omitted here for convenience. The electrical energy contained in the transducer is given by the following:

$$W_e = W_e(q_t, x_t) = \frac{q_t^2}{2C(x_t)} = \frac{q_t^2(d + x_t)}{2\epsilon_0 A_e} \quad (4.18)$$

We use $C(x_t) = \epsilon_0 A_e / (d + x_t)$ and d , the spacing of the plates when uncharged.

The total differential of W_e is:

$$dW_e = \left(\frac{\partial W_e}{\partial q_t} \right)_{x_t=\text{constant}} dq_t + \left(\frac{\partial W_e}{\partial x_t} \right)_{q_t=\text{constant}} dx_t \quad (4.19)$$

In thermodynamic equilibrium, the energy put into the transducer through the electric and mechanical ports is given by:

$$dW_e = v_t dq_t + F_t dx_t \quad (4.20)$$

Equating the terms on the right-hand sides of Equations (4.19) and (4.20), we get:

$$v_t(q_t, x_t) \equiv \frac{\partial W_e(q_t, x_t)}{\partial q_t} \Big|_{x_t = \text{constant}} = \frac{q_t(d + x_t)}{\epsilon_0 A_e} \quad (4.21)$$

$$F_t(q_t, x_t) \equiv \frac{\partial W_e(q_t, x_t)}{\partial x_t} \Big|_{q_t = \text{constant}} = \frac{q_t^2}{2\epsilon_0 A_e} \quad (4.22)$$

The above equations define the terminal voltage and the force as being the effort variables at the respective ports. The equilibrium values are given by the partial derivatives of W_e with respect to the corresponding state variable. Note that F_t is the externally applied force necessary to achieve equilibrium. Its magnitude is equal to the electrostatic Coulomb force between plates of a charged capacitor (opposite in direction).

This force has a quadratic dependence with charge. To make it linear, we assume small signal state variables. So:

$$x_t = x_0 + x(t) \quad (4.23)$$

$$q_t = q_0 + q(t) \quad (4.24)$$

There Equation (4.23) becomes:

$$\begin{aligned} v(q, x) &= \frac{\partial v_t}{\partial q_t} \Big|_0 q + \frac{\partial v_t}{\partial x_t} \Big|_0 x = \frac{(d + x_0)}{\epsilon_0 A_e} q + \frac{q_0}{\epsilon_0 A_e} x \\ &= \frac{1}{C_0} q + \frac{v_0}{x_0} x \end{aligned} \quad (4.25)$$

while similarly, Equation (4.24) becomes:

$$F(q, x) = \frac{\partial F_t}{\partial q_t} \Big|_0 q + \frac{\partial F_t}{\partial x_t} \Big|_0 x = \frac{q_0}{\epsilon_0 A_e} q + 0x = \frac{v_0}{x_0} q + 0x \quad (4.26)$$

Note that bias signals are independent of time since they define static equilibrium. It is rather easy to show that the plate illustrated in Figure 4.3(a) is not in equilibrium. To keep the plate in place we need to provide an external force. This requires a spring constant term, correspond-

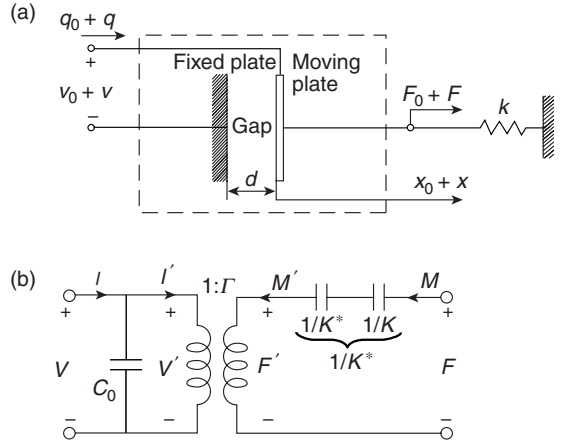


Figure 4.3 Schematic (a) and equivalent circuit (b) of an electrostatic actuator with a spring attached to the movable plate for stability [2]. H.A.C. Tilmans, “Equivalent circuit representation of electromechanical transducers: I. Lumped parameter systems,” J. Micromech. Microeng., vol. 6, 1996 © IOP

ing to the mechanical energy at the spring, added to Equation (4.18):

$$\begin{aligned} W_{em} &= W_{em}(q_t, x_t) = \frac{q_t^2}{2c(x_t)} + \frac{1}{2}k(x_t - x_r)^2 \\ &= \frac{q_t^2(d + x_t)}{2\epsilon_0 A_e} + \frac{1}{2}k(x_t - x_r)^2 \end{aligned} \quad (4.27)$$

This changes Equations (4.24) and (4.26) to the following [2]:

$$F_t(q_t, x_t) \equiv \frac{\partial W_{em}(q_t, x_t)}{\partial x_t} \Big|_{q_t = \text{constant}} = \frac{q_t^2}{2\epsilon_0 A_e} + kx_t \quad (4.28)$$

$$F(q, x) = \frac{\partial F_t}{\partial q_t} \Big|_0 q + \frac{\partial F_t}{\partial x_t} \Big|_0 x = \frac{q_0}{\epsilon_0 A_e} q + kx = \frac{v_0}{x_0} q + kx \quad (4.29)$$

Note that Equations (4.25) and (4.29) express voltage and force in terms of displacement and charge. It is usually required to have voltage and displacement as the independent variables. This makes:

$$\begin{aligned} q(v, x) &= \frac{\epsilon_0 A_e}{d + x_0} v - \frac{q_0}{d + x_0} x \\ &= \frac{\epsilon_0 A_e}{d + x_0} v - \frac{\epsilon_0 A_e v_0}{(d + x_0)^2} x \end{aligned} \quad (4.30)$$

$$\begin{aligned} F(v, x) &= \frac{q_0}{d+x_0} v + \left(k - \frac{q_0^2}{\epsilon_0 A_e (d+x_0)} \right) x \\ &= \frac{\epsilon_0 A_e v_0}{(d+x_0)^2} v + \left(k - \frac{\epsilon_0 A_e v_0^2}{(d+x_0)^3} \right) x \end{aligned} \quad (4.31)$$

Note that the system is in equilibrium as long as the second term on the right-hand side of Equation (4.31) is negative.

$$k < k', \quad \text{where } k' = \frac{\epsilon_0 A_e v_0^2}{(d+x_0)^3}$$

The matrix form of Equations (4.25) and (4.31) is:

$$\begin{bmatrix} v \\ F \end{bmatrix} = \begin{bmatrix} d+x_0 & q_0 \\ \frac{\epsilon_0 A_e}{d+x_0} & \frac{\epsilon_0 A_e}{d+x_0} \\ \frac{q_0}{\epsilon_0 A_e} & k \end{bmatrix} \begin{bmatrix} q \\ x \end{bmatrix} \quad (4.32)$$

The static capacitance and transduction factor are:

$$C_0 = \frac{\epsilon_0 A_e}{d+x_0}; \quad \Gamma = \frac{q_0}{d+x_0}$$

Therefore, Equation (4.32) becomes [2]:

$$\begin{bmatrix} v \\ F \end{bmatrix} = \begin{bmatrix} 1 & \Gamma \\ \frac{C_0}{\Gamma} & \frac{C_0}{d+x_0} \\ \frac{C_0}{d+x_0} & k \end{bmatrix} \begin{bmatrix} q \\ x \end{bmatrix} \quad (4.33)$$

The 2×2 matrix in Equation (4.33) is the constitutive matrix for the electrostatic transducer. The coupling factor K is an important characteristic of an electromechanical transducer. This gives the electromechanical energy conversion for a lossless transducer:

$$K = \sqrt{\frac{\Gamma^2}{kC_0}} \quad (4.34)$$

It may be noticed that a stable equilibrium state exists for $0 < K < 1$. The typical values for K are between 0.05 and 0.25.

Transduction may also be expressed in such a way as to connect between electrical variables (on the left-hand side) and mechanical variables (on the right-hand side). The transfer matrix relates force and velocity with voltage and current.

We start with rewriting the second part of Equation (4.33) with q on the left-hand side and taking the time derivative for current:

$$I = j\omega \frac{C_0}{\Gamma} F - \frac{kC_0}{\Gamma} U \quad (4.35)$$

We assume time-harmonic variations in the force and substitute velocity for the time derivative of displacement. Substituting this into the first part of Equation (4.33):

$$\begin{aligned} v &= \frac{1}{C_0} \left(\frac{C_0}{\Gamma} F - \frac{kC_0}{\Gamma} x \right) + \frac{\Gamma}{C_0} x \\ &= \frac{1}{\Gamma} F + \left(\frac{\Gamma^2}{C_0} - k \right) \frac{U}{j\omega \Gamma} \end{aligned} \quad (4.36)$$

$$\begin{bmatrix} v \\ I \end{bmatrix} = \begin{bmatrix} \frac{1}{\Gamma} & \frac{1}{j\omega \Gamma} \left(\frac{\Gamma^2}{C_0} - k \right) \\ j\omega \frac{C_0}{\Gamma} & -\frac{kC_0}{\Gamma} \end{bmatrix} \begin{bmatrix} F \\ U \end{bmatrix} \quad (4.37)$$

This 2×2 matrix is known as the *transfer matrix*. This transfer can be split as follows to conveniently express the equivalent circuit for the transducer [2]:

$$\begin{bmatrix} \frac{1}{\Gamma} & \frac{1}{j\omega \Gamma} \left(\frac{\Gamma^2}{C_0} - k \right) \\ j\omega \frac{C_0}{\Gamma} & -\frac{kC_0}{\Gamma} \end{bmatrix} = \begin{bmatrix} 1 & 0 \\ j\omega C_0 & 1 \end{bmatrix} \times \begin{bmatrix} \frac{1}{\Gamma} & 0 \\ 0 & -\Gamma \end{bmatrix} \begin{bmatrix} 1 & \frac{1}{j\omega} \left(\frac{\Gamma^2}{C_0} - k \right) \\ 0 & 1 \end{bmatrix} \quad (4.38)$$

This network is an exact representation for the transfer matrix. This, however, may not be a unique way of expressing an equivalent circuit for this transducer.

As noted earlier, the spring is represented in the circuit by a capacitor. The corresponding ‘impedance’ of the spring (= force/velocity) is $k/j\omega$. The spring has a negative stiffness, as follows:

$$-k' = -\frac{\Gamma^2}{C_0} = -\frac{\epsilon_0 A_e v_0^2}{(d+x_0)^3} = -K^2 k \quad (4.39)$$

This is a result of the electromechanical coupling, leading to a lowering of the overall dynamic spring constant.

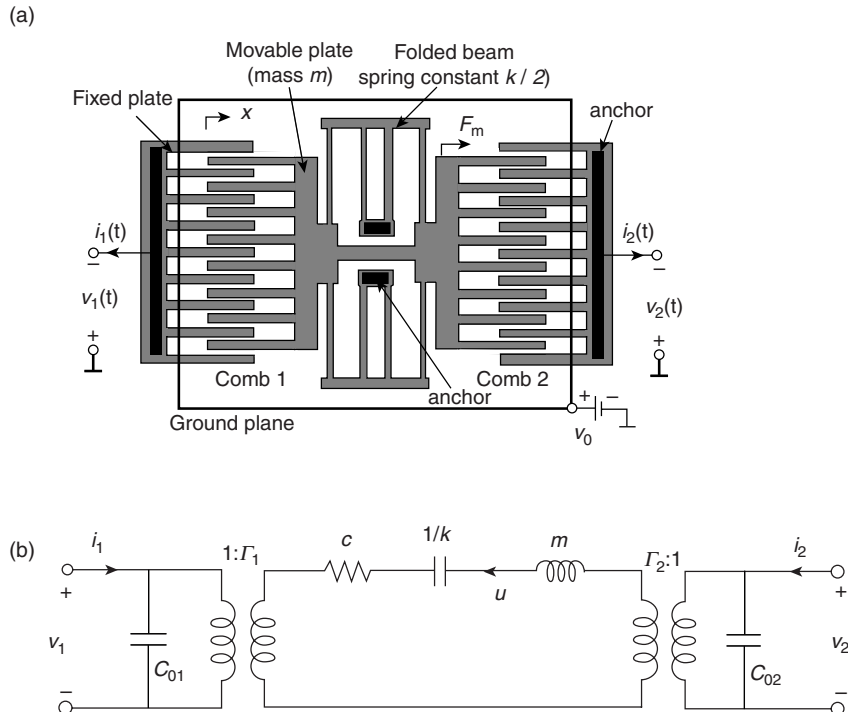


Figure 4.4 Schematic (a) and equivalent circuit (b) of a comb-type electrostatic resonator. CTA Nguyen and RT Howe, CMOS micromechanical resonator oscillator, IEEE Electron Devices Meeting, © 1993 IEEE

If we combine the two springs, the combined spring constant is:

$$k^* = k(1 - K^2) \quad (4.40)$$

Recall that the system is mechanically stable as long as this spring constant is positive, i.e. $K < 1$. If the coupling K is zero ($K = 0$), $k^* = k$. Therefore, k^* is the measured stiffness when the electrical port is short-circuited and k is the stiffness when it is open-circuited.

A similar approach may be followed to obtain the equivalent circuit for an in-plane electrostatic actuator of the comb type, as shown in Figure 4.4.

Fabrication of micro-sized devices with an electrostatic actuation scheme is relatively easy as it is usually independent of the properties of the material systems. Therefore, the electrostatic actuation scheme is the most preferred one for micro-actuators. Both parallel-plate and comb drive mechanisms are popular in these devices.

4.3 ELECTROMAGNETIC TRANSDUCERS

The magnetic counterpart of a moving plate capacitor is a moving coil inductor. This is yet another energy-storing transducer, the difference in this case being that the forms of energy are magnetic and mechanical. A simplified illustration of such a transducer is shown in Figure 4.5 [4]. When a current i flows through the coil, the magnetic flux is ϕ_t . Neglecting non-idealities such as electrical capacitance and resistance, and mechanical mass and friction, the constitutive relationships for this device can be derived for the current and

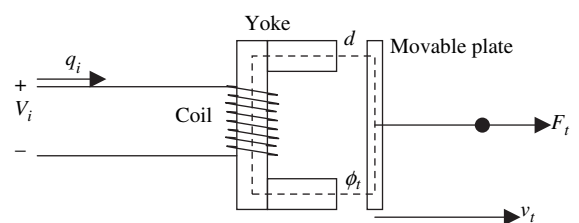


Figure 4.5 Schematic of an electromagnetic transducer.

force, in terms of displacement and flux linkage [3]. The conversion of energy takes place due to interactions between these electrical and mechanical quantities in such a circuit.

In the transducer shown in Figure 4.5, the fixed armature has N turns of winding, while the armature and the moving part are made of ferromagnetic materials.

The magnetic flux in the core (ϕ_t) is related to the current through the coil by:

$$\phi_t = L(x_t)i_t \quad (4.41)$$

The magnetic energy stored in the transducer when an input is applied to it is given by:

$$W_M = \frac{1}{2}L(x_t)i_t^2 \quad (4.42)$$

where $L(x_t)$ is the inductance of the driving coil when the moving coil is at $x = x_t$. Therefore:

$$L(x_t) = \frac{N\mu A_e}{d + x_t} \quad (4.43)$$

where N is the number of turns, μ is the permeability and A_e is the effective area of the movable plate.

By substituting Equation (4.43) into Equation (4.41):

$$W_M = \frac{1}{2} \frac{\phi_t^2}{L(x_t)} = \frac{\phi_t^2(d + x_t)}{2N^2\mu A_e} \quad (4.44)$$

This shows that W_M is a function of ϕ_t and x_t . Therefore we can write:

$$dW_M = \left. \frac{\partial W_M}{\partial \phi_t} \right|_{x_t=\text{constant}} d\phi_t + \left. \frac{\partial W_M}{\partial x_t} \right|_{\phi_t=\text{constant}} dx_t$$

$$dx_t = i_t d\phi_t + F_t dx_t \quad (4.45)$$

From this, we can get

$$i_t(\phi_t, x_t) = \frac{\partial W_M(\phi_t, x_t)}{\partial \phi_t} = \frac{\phi_t(d + x_t)}{N^2\mu A_e} \quad (4.46)$$

$$F_t(\phi_t, x_t) = \frac{\partial W_M(\phi_t, x_t)}{\partial x_t} = \frac{\phi_t^2}{N^2\mu A_e} \quad (4.47)$$

Note that the force-to-flux relationship here is quadratic. To linearize this, we assume small signal conditions:

$$x_t = x_0 + x(t) \quad (4.48)$$

$$\phi_t = \phi_0 + \phi(t) \quad (4.49)$$

Therefore:

$$i(\phi, x) = \left. \frac{\partial i_t}{\partial \phi_t} \right|_{x=0} \phi + \left. \frac{\partial i_t}{\partial x_t} \right|_{\phi=0} x = \frac{d + x_0}{N^2\mu A_e} \phi + \frac{\phi_0}{N^2\mu A_e} x \quad (4.50)$$

Similarly:

$$F(\phi, x) = \left. \frac{\partial F_t}{\partial \phi_t} \right|_{x=0} \phi + \left. \frac{\partial F_t}{\partial x_t} \right|_{\phi=0} x = \frac{\phi_0}{N^2\mu A_e} \phi + 0x \quad (4.51)$$

These are the constitutive relationships for the transducer. As discussed in the case of the electrostatic transducer, an additional element is required to keep the plate in a stable equilibrium. The spring element for this purpose is attached to the movable plate, as shown in Figure 4.5. The modified energy-balance equation is:

$$W'_M = W'_M(\phi_t, x_t) = \frac{\phi_t^2}{2L(x_t)} + \frac{1}{2}k(x_t - x_r)^2 \quad (4.52)$$

The first term on the right-hand side of the above equation is the energy stored in the coil due to the current flow while the second term accounts for the energy stored in the spring. The rest position of the spring is denoted by x_r .

$$F_t(\phi_t, x_t) = \left. \frac{\partial W'_M(\phi_t, x_t)}{\partial x_t} \right|_{\phi_t=\text{constant}} = \frac{\phi_t^2}{2N^2\mu A_e} + kx_t \quad (4.53)$$

Based on the constitutive relationship (Equation (4.46)), this becomes:

$$F(\phi, x) = \left. \frac{\partial F_t}{\partial \phi_t} \right|_0 q + \left. \frac{\partial F_t}{\partial x_t} \right|_0 x = \frac{\phi_0}{N^2\mu A_e} \phi + kx \quad (4.54)$$

The other constitutive relationship can be rewritten as:

$$i(\phi, x) = \frac{\phi}{L_0} + \frac{i_0 x}{x_0} \quad (4.55)$$

with:

$$L_0 = \frac{\mu N^2 A_e}{d + x_0}; \quad i_0 = \frac{\phi_0}{\mu N^2 A_e}$$

and where i_0 is the bias current; $\phi_0 = L_0 i_0$.

$$F(\phi, x) = \frac{i_0 \phi}{x_0} + kx \quad (4.56)$$

The constitutive matrix can be written in the form:

$$\begin{bmatrix} i \\ F \end{bmatrix} = \begin{bmatrix} \frac{1}{L_0} & \Psi \\ \frac{\Psi}{L_0} & k \end{bmatrix} \begin{bmatrix} \phi \\ x \end{bmatrix} \quad (4.57)$$

where:

$$\Psi = \frac{N^2 \mu A_e}{d + x_0} i_0$$

This may also be rearranged to obtain the Ψ transfer matrix. Rewriting the second part in Equation (4.57):

$$\phi = \frac{L_0}{\Psi} F - \frac{L_0 k}{\Psi} x \quad (4.58)$$

$$V = \frac{d\phi}{dt} = \frac{L_0}{\Psi} \frac{dF}{dt} - \frac{L_0 k}{\Psi} \frac{dx}{dt} \quad (4.59)$$

Assuming time-harmonic inputs and writing F in the form $A e^{j\omega t}$:

$$V = \frac{L_0}{\Psi} j\omega F - \frac{L_0 k}{\Psi} v \quad (4.60)$$

From the constitutive relationship:

$$\begin{aligned} i &= \frac{\phi}{L_0} + \frac{\Psi}{L_0} x = \frac{1}{\Psi} F + \left(\frac{\Psi}{L_0} - \frac{k}{\Psi} \right) x \\ &= \frac{1}{\Psi} F - \frac{1}{j\omega \Psi} \left(k - \frac{\Psi^2}{L_0} \right) v \end{aligned} \quad (4.61)$$

Therefore:

$$\begin{bmatrix} i \\ V \end{bmatrix} = \begin{bmatrix} \frac{1}{\Psi} & \frac{-1}{j\omega \Psi} \left(k - \frac{\Psi^2}{L_0} \right) \\ \frac{j\omega L_0}{\Psi} & \frac{L_0 k}{\Psi} \end{bmatrix} \begin{bmatrix} F \\ v \end{bmatrix} \quad (4.62)$$

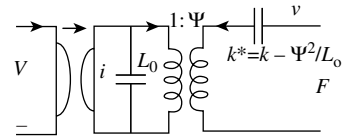


Figure 4.6 Equivalent circuit of the electromagnetic transducer shown in Figure 4.5.

In order to obtain an equivalent circuit, this transfer matrix may be split into several sub-matrices:

$$\begin{bmatrix} \frac{1}{\Psi} & \frac{-1}{j\omega \Psi} \left(k - \frac{\Psi^2}{L_0} \right) \\ \frac{j\omega L_0}{\Psi} & \frac{L_0 k}{\Psi} \end{bmatrix} = \begin{bmatrix} 0 & 1 \\ 1 & 0 \end{bmatrix} \begin{bmatrix} 1 & 0 \\ j\omega L_0 & 1 \end{bmatrix} \times \begin{bmatrix} \frac{1}{\Psi} & 0 \\ 0 & -\Psi \end{bmatrix} \begin{bmatrix} 1 & \frac{1}{j\omega} \left(\frac{\Psi^2}{L_0} - k \right) \\ 0 & 1 \end{bmatrix} \quad (4.63)$$

The matrices on the right-hand side of Equation (4.63) represent a gyrator, a shunt capacitor, a transformer and a series impedance, as shown in Figure 4.6.

Miniaturization of electromagnetic actuators requires the fabrication of magnetic thin films and current-carrying coils. Although few attempts have been made in this direction, the overall sizes of the devices developed so far are not very small. Coupled with this is the difficulty in isolating the magnetic field between adjacent devices, which makes fabrication of integrated micro devices rather challenging.

4.4 ELECTRODYNAMIC TRANSDUCERS

These are one of the most common types of electro-mechanical actuation schemes. The primary component is a current-carrying moving coil such as the one commonly used in loudspeakers. A schematic of such an actuator is shown, in Figure 4.7. For simplicity in analysis, a small segment of the coil is shown, along with the directions of the field quantities in Figure 4.8. The element of length dl , carrying a current i , is further characterized by its velocity v and induction B . By Lenz's law for the electromotive force e :

$$de = (v \times B)dl \quad (4.64)$$

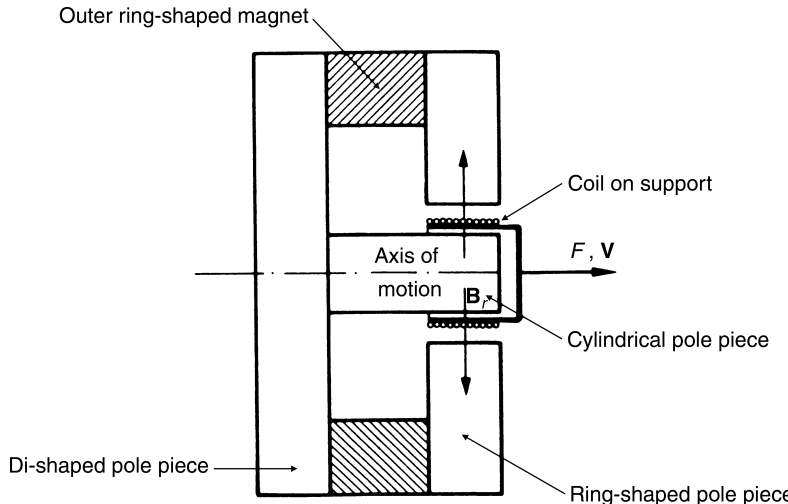


Figure 4.7 Schematic for an electrodynamic actuator. Reproduced by permission from M. Rossi, *Acoustics and Electroacoustics*, Norwood, MA: Artech House, Inc., 1988, © 1988 by Artech House, Inc

The magnetic force is given by Laplace's law:

$$dF_{\text{mag}} = idl \times B \quad (4.65)$$

In this analysis, flux linkages and displacement may be taken as the state variables. Although these are functions of time in the dynamic analysis, for the sake of convenience, this dependence is omitted here.

The energy stored in the magnetic field is given by:

$$W_m = \frac{1}{2} L_0 i^2 \quad (4.66)$$

where L_0 is the series inductance of the coil. The emf induced in the coil is:

$$e = Bl\dot{x}_t + \dot{\lambda}_t \quad (4.67)$$

where B is the magnetic flux due to the biasing magnet. The second term on the right-hand side of the above equation denotes the dynamically induced emf, due to changes in flux linkages.

$$i = \frac{1}{L_0} \int edt = \frac{Blx_t + \lambda_t}{L_0} \quad (4.68)$$

Therefore:

$$W_m = \frac{1}{2} \frac{(Blx_t + \lambda_t)^2}{L_0} \quad (4.69)$$

Taking the total derivative:

$$dW_m = \left. \frac{\partial W_m}{\partial \lambda_t} \right|_{x_t = \text{constant}} d\lambda_t + \left. \frac{\partial W_m}{\partial x_t} \right|_{\lambda_t = \text{constant}} dx_t \quad (4.70)$$

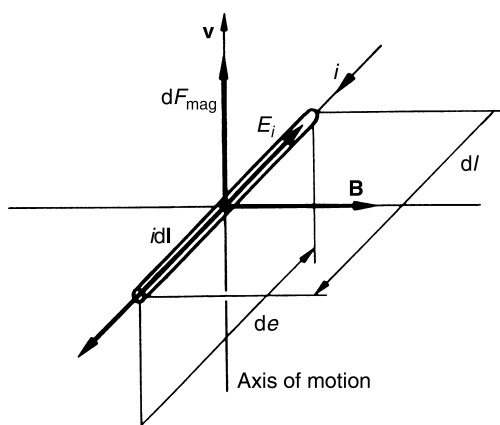


Figure 4.8 Field directions for a section of the coil shown in Figure 4.7. Reproduced by permission from M. Rossi, *Acoustics and Electroacoustics*, Norwood, MA: Artech House, Inc., 1988, © 1988 by Artech House, Inc

for a transducer in thermodynamic equilibrium, the energy put into the transducer through the electrical and mechanical ports is given by:

$$dW_m = i_t d\lambda_t + F dx_t \quad (4.71)$$

Therefore:

$$i_t(\lambda_t, x_t) = \frac{\partial W_m}{\partial \lambda_t} \Big|_{x_t=\text{constant}} = \frac{B_0 l x_t + \lambda_t}{L_0} \quad (4.72)$$

$$\begin{aligned} F_t(\lambda_t, x_t) &= \frac{\partial W_m}{\partial x_t} \Big|_{\lambda_t=\text{constant}} = \frac{B_0 l (B_0 l x_t + \lambda_t)}{L_0} \\ &= \frac{(B_0 l)^2 x_t}{L_0} + \frac{B_0 l \lambda_t}{L_0} \end{aligned} \quad (4.73)$$

Small signal variations in the effort and state variables are obtained by defining a bias point (x_0, λ_0) :

$$i(\lambda, x) = \frac{\partial i_t}{\partial \lambda_t} \Big|_0 \lambda + \frac{\partial i_t}{\partial x_t} \Big|_0 x = \frac{\lambda}{L_0} + \frac{B_0 l x}{L_0} \quad (4.74)$$

$$F(\lambda, x) = \frac{\partial F_t}{\partial \lambda_t} \Big|_0 \lambda + \frac{\partial F_t}{\partial x_t} \Big|_0 x = \frac{B_0 l \lambda}{L_0} + \frac{(B_0 l)^2 x}{L_0} \quad (4.75)$$

These are the constitutive relationships for an electrodynamic transducer. Recall that the model of the transducer shown in Figure 4.7 is not stable since there is no mechanism to hold in place the movable plate. A mechanical spring with a spring constant k may be attached to the plate to introduce stability.

With this, the energy equation needs to be modified as follows:

$$W_m = \frac{1}{2} \frac{(Blx_t + \lambda_t)^2}{L_0} + \frac{1}{2} k(x_t - x_r)^2 \quad (4.76)$$

where x_r denotes the rest position of the plate. The above constitutive relationships for $i(\lambda, t)$ is not affected by this. However, the relationship for $F(\lambda, t)$ should be modified as:

$$\begin{aligned} F_t(\lambda_t, x_t) &= \frac{\partial W_m(\lambda_t, x_t)}{\partial x_t} \Big|_{\lambda_t=\text{constant}} \\ &= \frac{(B_0 l)^2 x_t}{L_0} + \frac{B_0 l \lambda_t}{L_0} + 2k(x_t - x_r) \end{aligned} \quad (4.77)$$

$$F(\lambda, x) = \frac{\partial F_t(\lambda_t, x_t)}{\partial \lambda_t} \Big|_0 \lambda + \frac{\partial F_t(\lambda_t, x_t)}{\partial x_t} \Big|_0$$

$$x = \frac{B_0 l \lambda}{L_0} + \frac{(B_0 l)^2 x}{L_0} + kx \quad (4.78)$$

The constitutive matrix may therefore be formed as:

$$\begin{bmatrix} i(t) \\ F(t) \end{bmatrix} = \begin{bmatrix} \frac{1}{L_0} & \frac{\Psi}{L_0} \\ \frac{\Psi}{L_0} & k + \frac{\Psi^2}{L_0} \end{bmatrix} \begin{bmatrix} \lambda(t) \\ x(t) \end{bmatrix} \quad (4.79)$$

In the above matrix, $\Psi (= B_0 l)$ is the transduction factor. To obtain the transfer matrix, we proceed by rearranging the equations:

$$F(t) = \frac{\Psi}{L_0} \lambda(t) + \left(K + \frac{\Psi^2}{L_0} \right) x(t) \quad (4.80)$$

Therefore:

$$\lambda(t) = \frac{L_0}{\Psi} F(t) - \frac{k}{\Psi} \left(L_0 + \frac{\Psi^2}{k} \right) x(t) \quad (4.81)$$

The voltage induced, $v(t) = \dot{\lambda}(t)$. Therefore:

$$v(t) = \frac{j\omega L_0}{\Psi} F(t) - \frac{k}{\Psi} \left(L_0 + \frac{\Psi^2}{k} \right) u(t) \quad (4.82)$$

where $u(t)$ denotes velocity. In addition:

$$i(t) = \frac{\lambda(t)}{L_0} + \frac{\Psi}{L_0} x(t) \quad (4.83)$$

$$\begin{aligned} i(t) &= \frac{1}{L_0} \left[\frac{L_0}{\Psi} F(t) - \frac{k}{\Psi} \left(L_0 + \frac{\Psi^2}{k} \right) x(t) \right] + \frac{\Psi}{L_0} x(t) \\ &= \frac{1}{\Psi} F(t) - \frac{k}{j\omega \Psi} v(t) \end{aligned} \quad (4.84)$$

The transduction equation in the matrix form is as follows:

$$\begin{bmatrix} i(t) \\ v(t) \end{bmatrix} = \begin{bmatrix} \frac{1}{\Psi} & \frac{-k}{j\omega \Psi} \\ \frac{j\omega L_0}{\Psi} & \frac{-k}{j\omega \Psi} \left(L_0 - \frac{\Psi^2}{k} \right) \end{bmatrix} \begin{bmatrix} F(t) \\ u(t) \end{bmatrix} \quad (4.85)$$

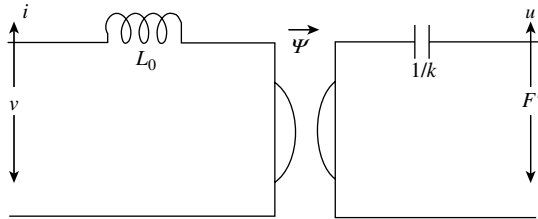


Figure 4.9 Equivalent circuit for an electrodynamic transducer.

The transfer matrix may be modified as follows to obtain the equivalent circuit (Figure 4.9):

$$\begin{bmatrix} \frac{1}{\Psi} & \frac{-k}{j\omega\Psi} \\ \frac{j\omega L_0}{\Psi} & \frac{-k}{j\omega\Psi} \left(L_0 - \frac{\Psi^2}{k} \right) \end{bmatrix} = \begin{bmatrix} 1 & 0 \\ j\omega L_0 & 1 \end{bmatrix} \quad (4.86)$$

$$\times \begin{bmatrix} \frac{1}{\Psi} & 0 \\ 0 & -\Psi \end{bmatrix} \begin{bmatrix} 1 & \frac{jk}{\omega} \\ 0 & 1 \end{bmatrix}$$

As mentioned earlier, a very common form of electrodynamic transducer is found in loudspeakers. However, due to the requirements of the coil and magnetic field, they are not so popular at the micro-scale. Electrodynamic micromotors have been successfully fabricated in reasonably smaller sizes (7 mm × 15 mm × 0.4 mm) [5]. The resonant frequency of such a system is given as:

$$f_0 = \frac{1}{2\pi} \left(\frac{BJ\eta_m}{\rho s} \right)^{1/2} \quad (4.87)$$

where η_m is the utilization factor of the rotor, ρ is the density of the material of the wire, J is the current density and s is the maximum displacement of the rotor.

As with the electromagnetic actuation schemes discussed previously, these devices also require fabrication of small-sized magnets and current-carrying coils. In this case, however, the coil is also movable. This remains a fabrication challenge, as miniaturized components are required for MEMS applications.

4.5 PIEZOELECTRIC TRANSDUCERS

When subjected to mechanical stress, certain anisotropic crystalline materials generate charge. This phenomenon,

discovered in 1880 by Jaques and Pierre Curie, is known as *piezoelectricity*. This effect is widely used in ultrasonic transducers. Lead zirconate titanates (PZTs) are the most common ceramic materials used in piezoelectric transducers. These crystals contain several randomly oriented domains, if no electric potential is applied during the fabrication process of the material. This results in small changes in the dipole moment of such a material when a mechanical stress is applied. However, if the material is subjected to an electric field during the cooling-down process of its fabrication, these domains would be aligned in the direction of the field. When an external stress is applied to such a material, the crystal lattices get distorted, causing changes in the domains and a variation in the charge distribution within the material. The converse effect of producing strain is caused when these domains change shape by the application of an electric field.

The direction of vibration of the piezoelectric material depends on the dimensions of the slab. If $l \gg b$ and h , the slab will vibrate along the length direction. On the other hand, if l and $b \gg h$, the slab will vibrate in the thickness direction. Hence, for the thin slab shown in Figure 4.10(a) the vibrations are in the thickness direction. The piezoelectric vibrations are given by:

$$v = \frac{\beta_{33}^s h}{bl} q + h_{33} w \quad (4.88)$$

$$F = \frac{C_{33}^D Q bl}{\tan Q h} w + h_{33} q \quad (4.89)$$

where C_{33}^D is the elastic stiffness of the piezoelectric material at constant electric displacement, h_{33} is the piezoelectric strain constant and Q is the phase constant.

By defining the static capacitance C_0 , the transfer factor Γ and the spring constant k as follows:

$$C_0 = \frac{bl}{\beta_{33}^s h}; \quad G = h_{33} \frac{bl}{\beta_{33}^s h}; \quad k = \frac{C_{33}^D bl}{h}$$

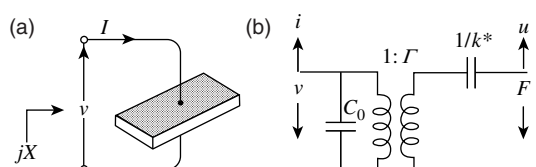


Figure 4.10 Schematic (a) and equivalent circuit (b) of a piezoelectric transducer.

we can simplify the above expressions for v and F and write the constitutive matrix in the following form:

$$\begin{bmatrix} v \\ F \end{bmatrix} = \begin{bmatrix} \frac{1}{C_0} & \frac{\Gamma}{C_0} \\ \frac{\Gamma}{C_0} & \frac{kwh}{\tan \frac{wh}{v_t^D}} \end{bmatrix} \begin{bmatrix} q \\ x \end{bmatrix} \quad (4.90)$$

Furthermore, the transfer matrix can be obtained as:

$$\begin{bmatrix} v \\ i \end{bmatrix} = \begin{bmatrix} \frac{1}{\Gamma} & \frac{-1}{j\omega\Gamma} \left(\frac{\frac{kwh}{v_t^D}}{\tan \frac{wh}{v_t^D}} - \frac{\Gamma^2}{C_0} \right) \\ j\omega C_0 & \frac{-kwh}{\tan \frac{wh}{v_t^D} \Gamma} \end{bmatrix} \begin{bmatrix} F \\ u \end{bmatrix} \quad (4.91)$$

The transfer matrix may be split as follows to obtain a convenient electrical equivalent circuit for the transducer (Figure 4.10(b)):

$$\begin{bmatrix} \frac{1}{G} & \frac{-1}{j\omega G} \left(\frac{\frac{kwh}{v_t^D}}{\tan \frac{wh}{v_t^D}} - \frac{\Gamma^2}{C_0} \right) \\ j\omega C_0 & \frac{-kwh}{\tan \frac{wh}{v_t^D} \Gamma} \end{bmatrix} = \begin{bmatrix} 1 & 0 \\ j\omega C_0 & 1 \end{bmatrix}$$

$$\times \begin{bmatrix} \frac{1}{\Gamma} & 0 \\ 0 & \Gamma \end{bmatrix} \begin{bmatrix} 1 & \frac{1}{j\omega X} \\ 0 & 1 \end{bmatrix} \quad (4.92)$$

where:

$$\frac{1}{X} = \left(\frac{\frac{kwh}{v_t^D}}{\tan \frac{wh}{v_t^D}} - \frac{\Gamma^2}{C_0} \right)$$

PZT thin films have been developed using standard thin-film deposition techniques such as sputtering and physical or chemical vapor deposition. Their use in

sensors and actuators is inherently limited by the quality and ‘repeatability’ of the thin films obtained by using these techniques. Compared to bulk-material processing techniques, the thin film performance is severely hampered by the properties of the surface where the film is deposited [6]. Non-ferroelectric AlN thin films have also been explored for sensor applications where voltage output is required. However, PZT thin films are still preferred in actuators. Compared to other electromechanical conversion schemes, these require a low voltage input but generally have a low electromechanical conversion efficiency.

4.6 ELECTROSTRRICTIVE TRANSDUCERS

Electrostriction is the phenomenon of mechanical deformation of a material due to an applied electric field. This is a fundamental phenomenon which is present to varying degrees in all materials and occurs due to the presence of polarizable atoms and molecules. An applied electric field can distort the charge distribution within the material, resulting in modifications to bond length, bond angle or electron distribution functions, which in turn affects the macroscopic dimensions of the material.

Lead magnesium niobate (PMN) is an electrostrictive ceramic which exhibits an order of magnitude more strain than most piezoceramics for the same electric field strength.

To develop an equivalent circuit [3,7], we start with the basic laws of electromagnetism that should be obeyed. The electric field displacement due to an applied field is given by:

$$D = \epsilon E + P \quad (4.93)$$

A planar slab with electrodes on either side would exhibit a zero electric field when the electrodes are shorted together and if ‘fringing fields’ are neglected.

An isolated specimen containing no free charges must exhibit a zero electric displacement field if the fringing fields are neglected. The generalized model of electrostriction under stress-free conditions is:

$$P = P_0 + \frac{\epsilon_0(\epsilon - 1)}{\sqrt{1 + aE^2}} E \quad (4.94)$$

where P_0 is the remnant polarization, ϵ is the relative permittivity of the dielectric material and a is the saturation parameter. For large values of a , the polarization

saturates at modest field strengths. Therefore:

$$\mathbf{D} = \epsilon\mathbf{E} + \mathbf{P}_0 + \frac{\epsilon_0(\epsilon - 1)\mathbf{E}}{\sqrt{1 + a\mathbf{E}^2}} \quad (4.95)$$

For non-zero stress in the thickness direction of the slab:

$$E_3 = \alpha_1 D_3 + \alpha_2 D_3^2 + \alpha_3 D_3 T_3 \quad (4.96)$$

and:

$$s_3 = \beta_1 T_3 + \beta_2 D_3^2 \quad (4.97)$$

where the subscript '3' represents the thickness direction; E_3 is the electric field, D_3 is the electric displacement field, s_3 is the strain and T_3 is the stress. In addition α_1 , α_2 , α_3 , β_1 , and β_2 are constants resulting from series expansions, where β_1 is the compliance and β_2 is equivalent to the electrostriction constant denoted by Q .

Recalling that the permittivity of electrostrictive materials such as PMN is of the order of 2000:

$$\mathbf{D} \approx \mathbf{P}_0 + \frac{\epsilon_0 \epsilon \mathbf{E}}{\sqrt{1 + a\mathbf{E}^2}} \quad (4.98)$$

Solving for E :

$$E_3 = \frac{D_3 - P_0}{\sqrt{\epsilon_0^2 E^2 - a(D_3 - P_0)^2}} \quad (4.99)$$

with the restriction that $D_3 - P_0 < (0.99\epsilon_0\epsilon/\sqrt{a})$. Generalizing this one-dimensional nonlinear model to three dimensions:

$$E_1 = \frac{D_1 - P_0^{(1)}}{\sqrt{(\epsilon_0 \epsilon_{11}^T)^2 - a(\epsilon_{11}^T)^2 w}} - 2Q_{33} T_1 D_1 - 2Q_{13} T_2 D_1 - 2Q_{13} T_3 D_1 - 4Q_{44} T_6 D_2 - 4Q_{44} T_5 D_3 \quad (4.100)$$

$$E_2 = \frac{D_2 - P_0^{(2)}}{\sqrt{(\epsilon_0 \epsilon_{22}^T)^2 - a(\epsilon_{22}^T)^2 w}} - 4Q_{44} T_6 D_1 - 2Q_{33} T_2 D_2 - 2Q_{13} T_3 D_2 - 2Q_{13} T_1 D_2 - 4Q_{44} T_4 D_3 \quad (4.101)$$

$$E_3 = \frac{D_3 - P_0^{(3)}}{\sqrt{(\epsilon_0 \epsilon_{33}^T)^2 - a(\epsilon_{33}^T)^2 w}} - 4Q_{44} T_5 D_1 - 4Q_{44} T_4 D_2 - 2Q_{33} T_3 D_3 - 2Q_{13} T_1 D_3 - 2Q_{13} T_2 D_3 \quad (4.102)$$

$$s_1 = s_{11}^D T_1 + s_{12}^D T_2 + s_{13}^D T_2 + Q_{33} D_1^2 + Q_{13} D_2^2 + Q_{13} D_3^2 \quad (4.103)$$

$$s_2 = s_{12}^D T_1 + s_{11}^D T_2 + s_{13}^D T_3 + Q_{13} D_1^2 + Q_{33} D_2^2 + Q_{13} D_3^2 \quad (4.104)$$

$$s_3 = s_{13}^D T_1 + s_{13}^D T_2 + s_{33}^D T_3 + Q_{13} D_1^2 + Q_{13} D_2^2 + Q_{33} D_3^2 \quad (4.105)$$

$$s_4 = s_{44}^D T_4 + 4Q_{44} D_2 D_3 \quad (4.106)$$

$$s_5 = s_{44}^D T_5 + 4Q_{44} D_1 D_3 \quad (4.107)$$

$$s_6 = s_{66}^D T_6 + 4Q_{44} D_1 D_2 \quad (4.108)$$

where $P_0^{(1)}$, $P_0^{(2)}$ and $P_0^{(3)}$ are components of the remnant polarization vector \mathbf{P}_0 and $w = \sum_{j=1}^3 [(D_j - P_0^{(j)})/\epsilon_{jj}^T]^2$. For permanently poled ferroelectrics, only two physically independent permittivities, ϵ_{11}^T and ϵ_{33}^T , exist and $P_0^{(1)} = P_0^{(2)} = 0$ and $P_0^{(3)} = P_0$ -- thus $\epsilon_{11}^T = \epsilon_{22}^T$.

It should be noted that s_{66}^D is not an independent elastic constant, and is related to other elastic constants according to the following:

$$s_{66}^D = \begin{cases} 2(s_{11}^D - s_{12}^D) & \text{(piezoelectric ceramics, biased PMN)} \\ s_{44}^D & \text{(unbiased PMN)} \end{cases}$$

Components (1) to (3) are each subject to a limitation of the field strength of the form:

$$\sum_{j=1}^3 [(D_j - P_0^{(j)})/\epsilon_{jj}^T]^2 < 0.99\epsilon_0/\sqrt{a} \quad (4.109)$$

A bar with electrodes on its ends, poled along its length and lying along the z -direction may be considered to obtain the model for a typical electrostrictive transducer. Solving the three-dimensional equations for E_3 and s_3 , subject to the following conditions:

$$T_1 = T_2 = T_4 = T_5 = T_6 = 0$$

and:

$$D_1 = D_2 = 0$$

we get:

$$E_3 = \frac{D_3 - P_0}{\sqrt{\varepsilon_0^2 E^2 - a(D_3 - P_0)^2}} - 2\beta_2 T_3 D_3 \quad (4.110)$$

and:

$$s_3 = \beta_1 T_3 + \beta_2 D_3^2 \quad (4.111)$$

where $\beta_1 = s_{33}^D$ and $\beta_2 = Q_{33}$. The equivalent circuit for this bar may be obtained by linearizing the theory for the expansion of the bar. To do this, the displacement field may be written as:

$$D = \frac{Q_0}{A} + \frac{q}{A} \quad (4.112)$$

where q is the first-order charge and Q_0 is the fixed charge on the electrodes, each of area A , arising either from a fixed polarization P_0 , or a bias voltage V_0 , or a combination of both.

The strain is written in the form $s = s^{(0)} + s^{(1)}$ where $s^{(0)}$ is a fixed strain and $s^{(1)}$ is the first-order strain. Similarly, the electric field is expressed as $E = E^{(0)} + E^{(1)}$.

To obtain the functional dependence about Q_0 , the voltage and force are taken as the *effort* variables, the charge (q) and displacement (x) are taken as the *state* variables and the current (i) and velocity (u) are taken as the *flow* variables.

The ‘actuation’ of the transducer is assumed to consist of stacks of active material, where each element of each stack acts electrically in parallel but mechanically in series. Each stack contains n_e elements and several such stacks are combined appropriately to drive the transducer face. There are m_s such mechanically parallel stacks.

The voltage due to the first order charge q is:

$$v_1 = \frac{q}{C_1} \quad (4.113)$$

where C_1 is the blocked capacitance given by:

$$C_1 = \frac{m_s n_e}{Gd}$$

and d is the plate separation. In the above expression, G is:

$$G = \frac{(\varepsilon_0 \varepsilon_{33}^T)^2}{A \left[(\varepsilon_0 \varepsilon_{33}^T)^2 - a(Q_0/4 - P_0)^2 \right]^{3/2}} + 4 \frac{\beta_2^2 Q_0^2}{\beta_1 A^3}$$

The voltage due to the fixed charge Q_0 is:

$$v_2 = \frac{-x}{dn_e} \left(\frac{2\beta_2 Q_0 d}{\beta_1 A} - V_0 \right) \quad (4.114)$$

A capacitive term C_0 is defined as follows:

$$C_0 = \frac{-n_e Q_0}{(2\beta_2 Q_0 d / \beta_1 A) - V_0} \quad (4.115)$$

The transduction factor N is defined as:

$$N = \frac{C_1 Q_0}{C_0 d} \quad (4.116)$$

Therefore:

$$v_2 = \frac{xN}{C_1} \quad (4.117)$$

where x is the displacement. Hence, the total voltage is given by the following:

$$v = v_1 + v_2 = \frac{q}{C_1} + \frac{xN}{C_1} \quad (4.118)$$

To derive the force equation, we need to combine the electrostatic and electrostrictive forces. The electrostrictive forces are:

$$F_1 = \frac{-2\beta_2 Q_0}{\beta_1 A \eta_e}; \quad F_2 = \frac{qV_0}{d \eta_e}$$

The opposing force due to the loading mass, i.e. the motional resistance of the material, is:

$$F_3 = u \left[j\omega L_M + R_M + \frac{1}{j\omega C_M} \right] \\ = u \left[j\omega M + \frac{m_s}{\eta_e} r_M + \frac{m_s A}{j\omega \eta_e \beta_1 d} \right] \quad (4.119)$$

where $L_M (= M)$ is the total motional mass which, includes the loading mass, r_M is the motional resistance of a single element, ω is the angular frequency and u is the velocity.

By assuming time-harmonic motion:

$$F_3 = j\omega x \left[j\omega M + \frac{m_s}{\eta_e} r_M + \frac{m_s A}{j\omega \eta_e \beta_1 d} \right] = j\omega x Z_M \quad (4.120)$$

where x is the displacement and Z_M is the motional impedance. Hence, the effective force is:

$$F = F_1 + F_2 + F_3 = \frac{Nq}{C_1} - j\omega Z_M x \quad (4.121)$$

In the matrix form, the constitutive relationship for the transducer is:

$$\begin{bmatrix} v \\ F \end{bmatrix} = \begin{bmatrix} \frac{1}{C_1} & \frac{N}{C_1} \\ \frac{N}{C_1} & -j\omega Z_M \end{bmatrix} \begin{bmatrix} q \\ x \end{bmatrix} \quad (4.122)$$

This relationship shows that the total strain in a material is the sum of the elastic strain and the polarization-induced strain. By rearranging, we obtain the transfer matrix relationship in following form:

$$\begin{bmatrix} v \\ i \end{bmatrix} = \begin{bmatrix} \frac{1}{N} & \frac{N}{j\omega C_1} + \frac{C_1 Z_M}{N} \\ \frac{j\omega C_1}{N} & \frac{-j\omega C_1 Z_M}{N} \end{bmatrix} \begin{bmatrix} F \\ u \end{bmatrix} \quad (4.123)$$

This transfer matrix may be split conveniently as follows:

$$\begin{bmatrix} \frac{1}{N} & \frac{N}{j\omega C_1} + \frac{C_1 Z_M}{N} \\ \frac{j\omega C_1}{N} & \frac{-j\omega C_1 Z_M}{N} \end{bmatrix} = \begin{bmatrix} 1 & 0 \\ j\omega C & 1 \end{bmatrix} \begin{bmatrix} 1 & -1 \\ j\omega C_1 & 1 \end{bmatrix} \times \begin{bmatrix} \frac{1}{N} & 0 \\ 0 & -N \end{bmatrix} \begin{bmatrix} 1 & Z_M \\ 0 & 1 \end{bmatrix} \quad (4.124)$$

This results in the equivalent circuit shown in Figure 4.11. In this model, the total impedance Z_M is:

$$Z_M = j\omega M + R_M + 1/j\omega C_M$$

where C_M , the total motional capacitance is given by:

$$C_M = \frac{\eta_e \beta_1 d}{m_s A};$$

In addition, L_M is the total motional inductance (= effective mass, M), R_M is the total motional resistance (= $m_s r_M / \eta_e$), r_M is the motional resistance for a single element, C_1 is the total capacitance (= $m_s \eta_e / Gd$) and N is the electromechanical transformation ratio (= $(C_1 / C_0) (Q_0 / d)$).

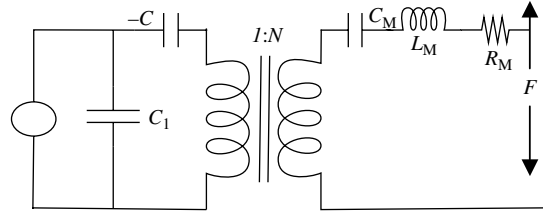


Figure 4.11 Equivalent circuit of an electrostrictive transducer.

The coupling coefficient κ is calculated in terms of the circuit capacitances:

$$\kappa^2 = \frac{\beta_1}{d^2 G A} \left[\frac{2\beta_2 Q_0 d}{\beta_1 A} - V_0 \right]^2 \quad (4.125)$$

The phenomenon of electrostriction is very similar to piezoelectricity. One of the fundamental difference between the two, however, is the closeness of the transition temperature of the material to the operating temperatures. This accounts for the improved strain and hysteresis properties for electrostrictive materials. However, a larger number of coefficients are required to model electromechanical coupling for electrostriction. The polarization in piezoelectric materials is spontaneous, while that in electrostrictive materials is field-induced. The properties of electrostrictive materials are more temperature-dependent, with the operating temperature ranges for these materials being narrower than those of piezoelectrics [8].

Material compositions based on lead magnesium niobate ($Pb(Mg_{0.33},Nb_{0.67})O_3$ or PMN) are commonly used in electrostrictive transducers. Their properties have been studied extensively [9]. However, practical thin-film transducers using this approach are yet to be realized. However, polymeric thin-film materials with compliant graphite electrodes have been shown to have excellent electrostrictive properties [10]. These materials are capable of efficient and fast responses with high strains, good actuation pressures (up to 1.9 MPa) and high specific energy densities. In this case, the electrostriction phenomenon is not due to molecular dipole realignment [11]. In these silicone film actuators, the strain results from external forces caused by electrostatic attraction of their graphite compliant electrodes. Although their mechanism is electrostatics-based, these actuators have been shown to produce a much larger effective actuation pressure than conventional air-gap electrostatics with similar electric fields.

4.7 MAGNETOSTRICTIVE TRANSDUCERS

While the characteristic property of electrostrictive materials is the production of strain on the application of an electric field, in magnetostrictive materials mechanical strain is produced by the application of a magnetic field. In addition, like ordinary materials, strains may also originate from applied stresses. Their magnetization changes are due to applied mechanical stresses as well as applied magnetic fields. Mathematically, these relationships may be summarized as follows:

$$S = S(T, H) \quad (4.126)$$

$$B = B(T, H) \quad (4.127)$$

Therefore:

$$dS_i = \left. \frac{\partial S_i}{\partial T_j} \right|_H dT_j + \left. \frac{\partial S_i}{\partial H_k} \right|_T dH_k \quad (4.128)$$

$$dB_i = \left. \frac{\partial B_m}{\partial T_j} \right|_H dT_j + \left. \frac{\partial B_m}{\partial H_k} \right|_T dH_k \quad (4.129)$$

In these equations, $i = (1, \dots, 6)$ denote the components of the engineering strains, while $m = 1, 2$ and 3 . The elastic compliances at constant H are:

$$\left. \frac{\partial S_i}{\partial T_j} \right|_H = s_{ij}^H \quad (4.130)$$

while the magnetic permeabilities at constant T are:

$$\left. \frac{\partial B_m}{\partial H_k} \right|_T = \mu_{mk}^T \quad (4.131)$$

For small variations in dT and dH , the constitutive relationships may be linearized as follows:

$$S_i = S_{ij}^H T_j + d_{ki} H_k \quad (i = 1, \dots, 6) \quad (4.132)$$

$$B_m = d_{mj} T_j + \mu_{mk}^T H_k \quad (m = 1, 2, 3) \quad (4.133)$$

where d_{mi} ($= d_{im}$) are the magnetostrictive constants.

$$\begin{bmatrix} S_1 \\ S_2 \\ S_3 \\ S_4 \\ S_5 \\ S_6 \end{bmatrix} = \begin{bmatrix} s_{11}^H & s_{12}^H & s_{13}^H & 0 & 0 & 0 \\ s_{12}^H & s_{11}^H & s_{13}^H & 0 & 0 & 0 \\ s_{13}^H & s_{13}^H & s_{33}^H & 0 & 0 & 0 \\ 0 & 0 & 0 & s_{44}^H & 0 & 0 \\ 0 & 0 & 0 & 0 & s_{55}^H & 0 \\ 0 & 0 & 0 & 0 & 0 & s_{66}^H \end{bmatrix} \\ \begin{bmatrix} T_1 \\ T_2 \\ T_3 \\ T_4 \\ T_5 \\ T_6 \end{bmatrix} + \begin{bmatrix} 0 & 0 & d_{31} \\ 0 & 0 & d_{31} \\ 0 & 0 & d_{33} \\ 0 & d_{15} & 0 \\ d_{15} & 0 & 0 \\ 0 & 0 & 0 \end{bmatrix} \begin{bmatrix} H_1 \\ H_2 \\ H_3 \end{bmatrix} \quad (4.134)$$

$$\begin{bmatrix} B_1 \\ B_2 \\ B_3 \end{bmatrix} = \begin{bmatrix} 0 & 0 & 0 & 0 & d_{15} & 0 \\ 0 & 0 & 0 & d_{15} & 0 & 0 \\ d_{31} & d_{31} & d_{33} & 0 & 0 & 0 \end{bmatrix} \\ \begin{bmatrix} T_1 \\ T_2 \\ T_3 \\ T_4 \\ T_5 \\ T_6 \end{bmatrix} + \begin{bmatrix} \mu_{11}^T & 0 & 0 \\ 0 & \mu_{22}^T & 0 \\ 0 & 0 & \mu_{33}^T \end{bmatrix} \begin{bmatrix} H_1 \\ H_2 \\ H_3 \end{bmatrix} \quad (4.135)$$

Assuming linear relationships between B and H and between S and H , the internal energy may be written as follows:

$$\begin{aligned} U &= \frac{1}{2} S_i T_i + \frac{1}{2} H_m B_m \\ &= \frac{1}{2} T_i s_{ij}^H T_j + \frac{1}{2} T_i d_{mi} H_m + \frac{1}{2} H_m d_{mi} T_i + \frac{1}{2} H_m \mu_{mk}^T H_k \\ &= U_e + 2U_{me} + U_m \end{aligned} \quad (4.136)$$

Here, U_e and U_m are the pure elastic magnetic energies and U_{me} is the magnetoelastic energy of the system. These quantities may be used to arrive at an important figure of merit, called *the magnetomechanical coupling coefficient*, k , as:

$$k = \frac{U_{me}}{\sqrt{U_e U_m}} \quad (4.137)$$

Usually magnetostrictive materials operate in the longitudinal mode. This reduces the stresses strains, and magnetic field components in the direction with subscript

'3', while all others are zero. These conditions simplify the magnetomechanical coupling coefficient to:

$$k_{33}^2 = \frac{d_{33}^2}{\mu_{33}^T s_{33}^H} \quad (4.138)$$

After the subscript '3' is dropped, Equations (4.132) and (4.133) then become:

$$S = s^H T + dH \quad (4.139)$$

$$B = dT + \mu^T H \quad (4.140)$$

By rearranging to change the variables, we then obtain:

$$T = \frac{1}{s^B} S - \lambda B \quad (4.141)$$

$$H = -\lambda S + \frac{1}{\mu^S} B \quad (4.142)$$

where the constant λ is given by:

$$\lambda = \frac{d}{\mu^T s^B} \quad (4.143)$$

By assuming sinusoidal variation (with angular frequency ω) for all quantities, the strain along the rod under 'quasi-static' conditions is related to the phase velocities on the rod by:

$$S = \frac{v_2 - v_1}{j\omega l_r} \quad (4.144)$$

From Equation (4.141), the force on the rod is given by:

$$F = -TA_r = -\frac{A_r}{s^B} \frac{v_2 - v_1}{j\omega l_r} + \lambda A_r B \quad (4.145)$$

The magnetizing field from a thin solenoid with N turns and $l_r \gg r$ is given by:

$$H = \frac{NI}{l_r} \quad (4.146)$$

By substituting Equations (4.146) and (4.142) into Equation (4.145), we obtain:

$$F = -\frac{v_2 - v_1}{j\omega C^H} + \frac{\lambda A_r N}{s^H l_r} I \quad (4.147)$$

where:

$$C^H = \frac{s^H l_r}{A_r}; \quad C^B = \frac{s^B l_r}{A_r}$$

By Faraday's law, the induction through a solenoid can be related to the voltage across the terminals by:

$$B = \frac{V}{j\omega N A_r} \quad (4.148)$$

By substituting Equation (4.148) into Equation (4.142), we obtain:

$$\frac{NI}{l_r} = -\lambda \frac{v_2 - v_1}{j\omega l_r} + \frac{V}{j\omega N A_r \mu^S} \quad (4.149)$$

Rewriting Equation (4.149), we obtain:

$$V = j\omega L^S I + \frac{dA_r N}{s^H l_r} (v_2 - v_1) \quad (4.150)$$

where the clamped and free inductances of the magnetizing coil are:

$$L^S = \frac{\mu^S N^2 A_r}{l_r} \quad \text{and} \quad L^T = \frac{\mu^T N^2 A_r}{l_r}$$

By rearranging Equations (4.147) and (4.150), we can obtain the transfer matrix as follows:

$$\begin{bmatrix} V \\ I \end{bmatrix} = \begin{bmatrix} \frac{j\omega L^S}{\Gamma} & \frac{1}{j\omega C^H \Gamma} \\ \frac{1}{\Gamma} & \frac{L^S}{C^H \Gamma} + \frac{d\Gamma}{\lambda} \end{bmatrix} \begin{bmatrix} F \\ u \end{bmatrix} \quad (4.151)$$

where:

$$\Gamma = \frac{\lambda A_r N}{s^H l_r}$$

Correspondingly, the equivalent circuit takes the form shown in Figure 4.12.

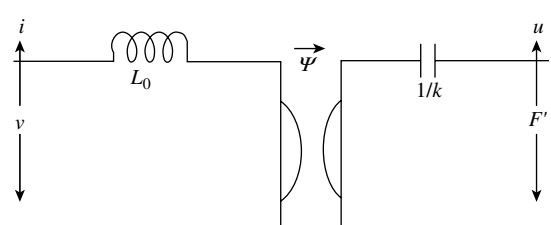


Figure 4.12 Equivalent circuit of a magnetostrictive transducer.

4.8 ELECTROTHERMAL ACTUATORS

In electrothermal actuators, heat is applied to a ‘bimorph’ beam, the expansion of which is used to generate the mechanical moment required for the actuation. Large deflections and greater energy densities are achievable with this scheme. However, electrothermal transducers are generally very slow. Several configurations have been reported in the literature for this kind of actuator. In general, these consist of two transduction mechanisms – the first an irreversible electrothermal process and the second, a reversible thermomechanical transduction. The configuration of an audio frequency filter with such an actuator is shown in Figure 4.13 [12]. This consists of a thermally isolated thin diaphragm, fabricated by ‘back-side etching’, and a pair of metal resistors for the actuator (heater) and sensor, patterned by a ‘lift-off’ process.

Several other configurations of micromachined thermal actuators have also been reported in the literature [13,14].

In Huang and Lee [14], for example, the difference in electrical resistances of a wide and a narrow arm in a bimorph structure (Figure 4.14) is used to generate the necessary deflection. This difference causes variation in the heat produced and hence thermal expansion of the two arms. In Figure 4.14, in-plane motion is made possible by the asymmetrical thermal expansion of the microstructure having different cross-sections for its arms. As an electric current is fed through the ‘anchors’, the higher current density in the ‘hot arm’ generates heat and causes it to expand more than the ‘cold arm’. Since

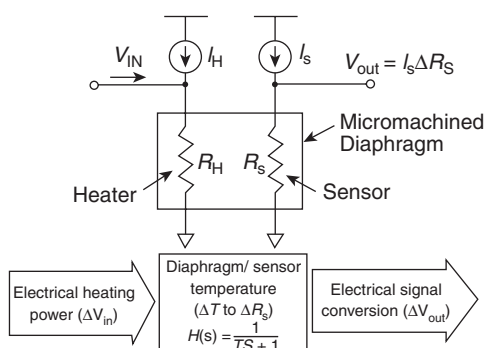


Figure 4.13 Principles of an electrothermal transducer [12]. K.H. Lee, H.J. Byun, H.K. Lee, I.J. Cho, J.U. Bu, and E. Yoon, “An audio frequency filter application of micromachined thermally-isolated diaphragm structures,” 13th Annual Inter. Confer. Micro Electro Mechanical Systems MEMS 2000, © 2000 IEEE

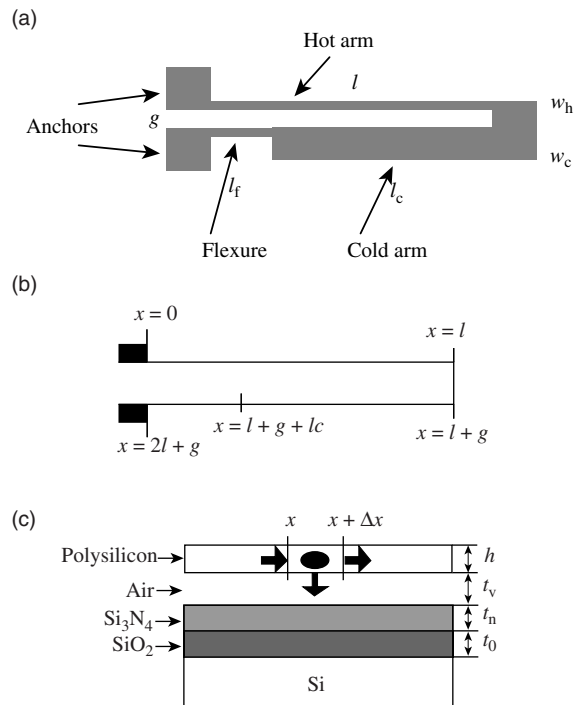


Figure 4.14 Schematics of a ‘bimorph’ electrothermal transducer: (a) top view; (b) equivalent one-dimensional coordinate system; (c) cross-sectional view [14]. Q.A. Huang and N.K.S. Lee, Analysis and design of polysilicon thermal flexure actuator, J. Micromech. Microeng., vol. 9, 1999, © IOP

the arms are joined at the free end, the actuator tip moves laterally along an arc in the direction of the cold arm.

This electrothermal transducer is irreversible, since even though the electrical energy can produce mechanical motion, energy transport in the opposite direction is not possible. Hence, this cannot be modeled with a reciprocal electrical network. The deflection of the actuator can be derived to be:

$$u = \frac{l^2}{6EI_h} (x_1 l - 3x_3) \quad (4.152)$$

where I_h is the moment of inertia of the hot arm, E is the Young’s modulus of the arm, x_1 is the horizontal force in the arm and x_3 is the coupling force on it. The equivalent force acting on this may be obtained as follows:

$$F = \frac{1}{2L} (x_1 l - 3x_3) \quad (4.153)$$

Hence, the force acting is dependent on the temperature changes which are produced due to different current densities in these arms. The corresponding spring constant is:

$$K = \frac{3EI}{L^3} \quad (4.154)$$

By choosing that the displacement y_t and charge q_t are the state variables, the mechanical energy confined in the transducer is as follows:

$$W_T = \frac{1}{2}kq_t y_t^2 \quad (4.155)$$

The total differential of W_T is given by:

$$dW_T = \left. \frac{dW_T}{dq_t} \right|_{y_t=\text{constant}} dq_t + \left. \frac{dW_T}{dy_t} \right|_{q_t=\text{constant}} dy_t \quad (4.156)$$

In thermodynamic equilibrium, the electrical energy fed into the transducer is transferred to the mechanical port, while the remaining energy is stored in the transducer:

$$dW_T = v_t dq_t - F_t dy_t \quad (4.157)$$

Therefore:

$$V_t(q_t, x_t) = \left. \frac{dW_T}{dq_t} \right|_{y_t=\text{constant}} = \frac{1}{2} y_t^2 \frac{dk(q_t)}{dq_t} \quad (4.158)$$

$$F_t(q_t, x_t) = -\left. \frac{dW_T}{dy_t} \right|_{q_t=\text{constant}} = y_t k q_t \quad (4.159)$$

It may, however, be pointed out that due to the non-linear nature of these expressions, development of an equivalent circuit in the form described elsewhere is not possible for an electrothermal transducer.

Another thermoresponsive transducer is based on the class of materials known as shape memory alloys (SMAs), which includes certain alloys (Ni-Ti, Cu-Al-Zn, etc.) that undergo large strains. These can recover their initial configurations spontaneously or by heating without any residual deformation. These properties of SMAs are associated with a solid-solid phase transformation which can be thermal- or stress-induced. SMAs are mainly used in medical sciences, electrical, aerospace, civil and mechanical engineering.

Important properties of SMAs include the following:

- Compact powerful actuators with high work output per volume.
- Large actuation displacement and recovery force.
- Medium operational voltage (below 40 V).
- Hysteresis may be put to use in large energy absorption and damping capacity.
- SMA-active elements transform into their original parent phases/shapes, even after several years.
- Repeated absorption of large amounts of strain energy and fatigue resistance under loading without any permanent deformation.
- Possibility for obtaining a wide cyclic behavior by varying the number and/or the characteristics of the SMA components.
- Usable strain range of 70 %.
- Smooth operation of the transducer.

Based on the above, these materials are used in several structural applications, such as in active and passive control structures, as smart material tags, in self-stressing and self-healing structures and in structural health monitoring.

As mentioned previously, SMAs undergo a solid-to-solid phase transition. Because of this, they can have two different crystalline lattice structures, depending on both the applied stress and the temperature. As result of this solid-to-solid phase transition, SMAs show three special properties: the shape memory effect (SME), the pseudoelastic effect and the ‘martensitic deformability’.

Martensite is the crystallographic description of the low-temperature phase of an SMA, formed during cooling. The martensitic crystalline structure is thermodynamically more stable below a certain transition temperature. Martensite evolves from austenite crystals in various directions and can therefore have many different lattice arrangements, depending on the local stress field. In addition, the structure can appear as twinned or ‘de-twinned’. In this phase, the SMA can be deformed easily due to the mobility of the twinned boundaries. A plateau stress is present in the stress-strain curve of the SMA in the martensite phase.

Typically, a phase transition is induced by a change in temperature. The temperature at which the SMA starts to transform into the martensite phase is the ‘martensite start-temperature’. This transformation is completed when the temperature falls below the ‘martensite finish-temperature’. However, the transformation of austenite to martensite can also be induced at higher temperatures during loading; this is known as ‘strain induced martensite’ (SIM).

Table 4.3 Properties of an Ni–Ti shape memory alloy.

Property	Value	
Density (g/cm^3)	6.45–6.7	
Maximum energy density (J/m^3)	106–107	
Ultimate tensile strength (MPa)	≤ 1900	
Poisson ratio	0.33	
Shape memory effect (%)	~ 8	
Elongation at failure (%)	≤ 50	
Response speed (time to heat/cool) (Hz)	≤ 10	
Power supply (typical) (V, A)	< 40 V; \leq several kA	
Operational temperature range ($^\circ\text{C}$)	< 250	
Transition temperature ($^\circ\text{C}$)	–200 to +110	
<i>Properties that change between two phases</i>		
Property	Phase	
	Austenite	Martensite
Yield strength (MPa)	195–690	70–140
Young's modulus (GPa)	90–100	28–41
Coefficient of thermal expansion ($^\circ\text{C}^{-1}$)	$10\text{--}11 \times 10^{-6}$	6.7×10^{-6}
Thermal conductivity ($\text{W}/(\text{m}\text{°}\text{C})$)	18	8.5–9.0

The second crystalline lattice structure is austenite, which is the strong, high-temperature phase of an SMA. The molecular arrangement of the austenite structure is cubic and because of this symmetrical structure the alloy shows a high modulus of elasticity. This austenitic structure has the characteristic stress-strain curve of typical metals and is much stronger than the martensitic structure. The austenite phase starts to form out of the martensite phase at the ‘austenite start-temperature’. This transformation is completed when the temperature rises above the ‘austenite finish-temperature’. However, above this temperature, the SMA element can still be in the martensitic phase due to an applied load (SIM). The specific transformation temperatures can vary significantly with the chemical composition of the SMA.

Heating of an SMA to induce the phase change can be achieved by actually providing heat. External heating elements are usually bulky, not very efficient and may cause internal stresses. Usually, resistive heating is used to deform the SMA by passing an electric current through it. The time needed for complete shape recovery is directly related to the time required to heat the element to above a certain temperature. The time needed to relax depends on the cooling rate of the

material. This cooling process cannot be accelerated very easily, but the transformation back to the martensite state can also be induced by means of an applied stress or strain. The response time of an SMA can be minimized by reducing the actuator size and maximizing the heat transfer. The latter can be achieved with a moving liquid, or by making the contact surface as large as possible.

Sun and Sun [15] used a thermomechanical approach to develop a constitutive relationship for the bending of a composite beam with continuous SMA fibers embedded eccentric to the neutral axis. These authors concluded that SMAs can be successfully used for active structural vibration control.

Table 4.3 lists the properties of a representative shape memory alloy, i.e. Ni–Ti.

4.9 COMPARISON OF ACTUATION SCHEMES

A brief comparison of some of the electromechanical transducers discussed previously is presented in Table 4.4. Due to its simplicity, electrostatic actuation is the most preferred, especially in micro devices. The

Table 4.4 Comparison of the properties of electromechanical transducers [16]. Reproduced with permission of IEE.

Actuator	Fractional stroke (%)	Maximum energy density (J/cm ³)	Efficiency	Speed
Electrostatic	32	0.004	High	Fast
Electromagnetic	50	0.025	Low	Fast
Piezoelectric	0.2	0.035	High	Very fast
Magnetostrictive	0.2	0.07	Low	Very fast
Electrostrictive	4	0.032	High	Fast
Thermal	50	25.5	Low	Slow

control signal here is voltage, which is easy to manipulate in electrical circuits. However, these devices require greater environmental protection as electrostatic fields are prone to attract dust, which could affect the performance of associated complementary metal oxide semiconductor (CMOS) circuits. Electromagnetic and electrodynamic actuators are based on Lorentz force effects. The current-carrying coil is stationary in the former case, while in the latter it is moving. These are ideally suited when large currents are possible, even if with lower voltages. However, they are prone to problems with power dissipation, but are tolerant to dust and humidity.

Actuators based on piezoelectricity, magnetostriction and electrostriction depend on changes in strain produced by an applied electric or magnetic field in some special materials used. The achievable strain is at a maximum for electrostrictive materials but the force generated is at a maximum in magnetostrictive materials. Both electrostrictive and piezoelectric materials deform with the application of an electric field, but while the relationship between the force produced and applied field is linear in piezoelectrics, it is quadratic in electrostrictive materials.

Most of these transduction schemes are non-linear. That is, the transfer function between electrical (voltage or current) and mechanical (force or displacement) is not linear. Such non-linearities distort the ‘sensed signal’, and may cause loss of ‘fidelity’. One approach to overcome this difficulty is to restrict the signal to very small variations about a DC bias. It is fairly reasonable to assume that the responses to these small signal variations are linear.

REFERENCES

- R.A. Johnson, *Mechanical Filters in Electronics*, John Wiley & Sons, Inc., New York, NY, USA (1983).
- H.A.C. Tilmans, ‘Equivalent circuit representation of electromechanical transducers: I. Lumped parameter systems’, *Journal of Micromechanical and Microengineering*, **6**, 157–176 (1996).
- S.H. Crandall, D.C. Karnopp, E.F. Kurtz, Jr and D.C. Pridmore-Brown, *Dynamics of Mechanical and Electromechanical Systems*, McGraw-Hill, New York, NY, USA (1968).
- M. Rossi, *Acoustics and Electroacoustics*, Artech House, Norwood, MA, USA (1988).
- T. Frank, ‘Two-axis electrodynamic micropositioning devices’, *Journal of Micromechanical and Microengineering*, **8**, 114–118 (1998).
- P. Muralt, ‘PZT thin films for microsensors and actuators: Where do we stand?’ *IEEE Transactions: Ultrasonics, Ferroelectrics and Frequency Control*, **47**, 903–915 (2000).
- J.C. Piquette and S.E. Forsythe, ‘Generalized material model for lead magnesium niobate (PMN) and an associated electromechanical equivalent circuit’, *Journal of the Acoustical Society of America*, **104**, 2763–2772, (1998).
- J. Chen and T.R. Gururaja, ‘DC-biased electrostrictive materials and transducers for medical imaging’ in *Proceedings of the IEEE Ultrasonics Symposium*, IEEE, Piscataway, NJ, USA, pp. 1651–1658 (1997).
- S. M. Pilgrim, ‘Electrostrictive ceramics for low-frequency active transducers’, *IEEE Transactions: Ultrasonics, Ferroelectrics and Frequency Control*, **47**, 861–876 (2000).
- R.E. Pelrine, R.D. Kornbluh and J.P. Joseph, ‘Electrostriction of polymer dielectrics with compliant electrodes as a means of actuation’, *Sensors and Actuators: Physical*, **A64**, 77–85 (1998).
- R. Heydt, R. Kornbluh, R. Pelrine and V. Mason, ‘Design and performance of an electrostrictive-polymer-film acoustic actuator’, *Journal of Sound and Vibration*, **215**, 297–311, (1998).
- K.H. Lee, H.J. Byun, H.K. Lee, I.J. Cho, J.U. Bu and E. Yoon, ‘An audio frequency filter application of micromachined thermally isolated diaphragm structures’, in *Proceedings of the 13th Annual International Conference on Micro*

- Electromechanical Systems: MEMS' 2000*, IEEE, Piscataway, NJ, USA, pp. 142–147 (2000).
13. W. Riethmuller and W. Benecke, ‘Thermally excited silicon microactuators’, *IEEE Transactions: Electron Devices*, **35**, 758–763 (1988).
 14. Q.A. Huang and N.K.S. Lee, ‘Analysis and design of polysilicon thermal flexure actuator’, *Journal of Micromechanical and Microengineering*, **9**, 64–70, (1999).
 15. G. Sun and C.T. Sun, ‘Bending of shape-memory alloy-reinforced composite beam’, *Journal of Materials Science*, **30**, 5750–5754 (1995).
 16. D. Wood, J.S. Burdess and A.J. Harris, ‘Actuators and their mechanisms in microengineering’, in *Proceedings of the Colloquium on Actuator Technology: Current Practice and New Developments*, No. 110, IEE, London, UK, pp. 7/1–7/3 (1996).

5

Design Examples for Sensors and Actuators

5.1 INTRODUCTION

The principles of several sensors and actuators have been discussed in Chapters 3 and 4. Several of these devices are employed in numerous applications in civil, military, aerospace and biological areas, as will be demonstrated in Part 4 of this text. This chapter is intended to provide the basic understanding of the design of some of these sensors and actuators. Examples of sensors presented here include the piezoelectric and piezoresistive types. A chemical sensor based on the surface acoustic wave (SAW) principles is described. A fiber-optic gyroscope represents the optical segment of sensors in this chapter. In addition, the design of microvalves and pumps required in several biomedical applications is also included here.

5.2 PIEZOELECTRIC SENSORS

Lead zirconate titanate (commonly known by the acronym PZT) is arguably the most widely used component in smart systems. The importance of this material comes from the fact that it exhibits significant piezoelectric properties. Piezoelectricity refers to the phenomenon in which forces applied to a slab of a material result in the generation of electrical charges on the surfaces of the slab. This is due to the distribution of electric charges in the unit cell of a crystal when force is applied.

In these crystals, the force applied along one axis of the crystal leads to the appearance of positive and negative charges on opposite sides of the crystal along another axis. The strain induced by the force leads to a physical displacement of the charge within the unit cell. This polarization of the crystal leads to an accumulation of charge:

$$Q = \mathbf{d}F \quad (5.1)$$

In the above equation, the piezoelectric coefficient \mathbf{d} is a 3×3 matrix. In general, forces in the x, y, z directions contribute to charges produced in any of the x, y, z directions. Values of the piezoelectric coefficients of these materials are usually made available by the manufacturer. Typical values of the piezoelectric charge coefficients are 1–100 pC/N. Some of the other properties of PZT are listed in Table 5.1. Once the charge is known, the voltage across the plate of the piezoelectric material can be determined by:

$$V = Q/C \quad (5.2)$$

where the parallel plate capacitance of this configuration is:

$$C = \frac{\epsilon_0 \epsilon_r A}{d} \quad (5.3)$$

Thus, in order to produce a larger voltage one can resort to reducing the area of the sensor. However, it must be cautioned that piezoelectrics are not generally good dielectrics. These materials have substantial leakage losses. In other words, the charge across a pair of electrodes may vanish over time. Therefore, there is a time constant for retention of voltage on the piezoelectric after the application of a force. This time constant depends on the capacitance of the element, and the leakage resistance. Typical time constants are of order of 1 s. Because of this effect, piezoelectrics are not used for static measurements such as weight.

The reversible effect is used in piezoelectric actuators. Application of a voltage across such a material results in dimensional changes in the crystal. The coefficients involved are exactly the same as in

Table 5.1 Electromechanical properties of PZT.

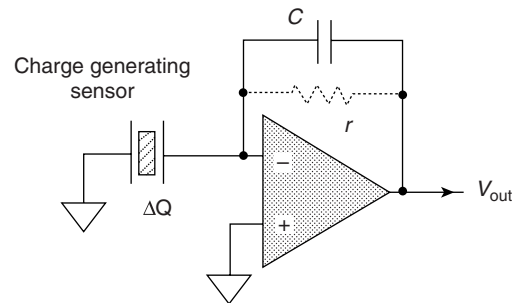
Property	Value
Density (g/cm^3)	7.7–8.1
Maximum energy density (J/m^3)	102
Young's modulus (GPa)	60–120
Tensile strength (MPa)	25 (dynamic); 75 (static)
Compressive strength (MPa)	520
Curie temperature ($^\circ\text{C}$)	160–350
Operational temperature range ($^\circ\text{C}$)	–273 to 80
Inducible strain (1–2 kV/m) at ($\mu\text{m}/\text{m}$)	1–2
Response time	Very fast (typically kHz, up to GHz)

Equation (5.1). The change in length per unit applied voltage is given by:

$$\frac{dL}{V} = \frac{\left(\frac{FL}{EA}\right)}{\left(\frac{d_{11}FL}{\varepsilon_0\varepsilon_r A}\right)} = \frac{\varepsilon_0\varepsilon_r}{Ed_{11}} \quad (5.4)$$

The strain in the above expression depends only on the piezoelectric coefficient, the dielectric constant and Young's modulus. Therefore, it may be inferred that objects of a given piezoelectric material, irrespective of their shape, would undergo the same fractional change in length upon the application of a given voltage.

Most sensors using the piezoelectric effect require a charge-amplifying preamplifier. A simple circuit for this purpose is shown in Figure 5.1. Another recently developed material with sizeable piezoelectric properties is poly(vinylidene fluoride) (PVDF). This can usually be treated during fabrication to have a good piezoelectric coefficient in the direction of interest. Being polymeric, films of this material can be made at low cost. A related copolymer P(VDF-TrFE) also shows significant piezoelectric properties. The properties of PVDF and P(VDF-TrFE) are given in Table 5.2. Both of these materials are used in acoustic sensors because of their strong piezoelectricity, low acoustic impedance (useful in underwater applications, since there are only small mismatches with those of water) and flexibility (which permits applications on curved surfaces). Therefore, transducers with wide operating bandwidths can be easily designed using PVDF. This also results in improvements in the overall performance of sensors such as hydrophones used for sensing acoustic fields. As the sensor size decreases, it

**Figure 5.1** Schematic of a piezoelectric sensor which uses a charge preamplifier.

becomes necessary to provide an amplifier or buffer in close proximity to overcome the sensitivity loss due to interconnected capacitances. This calls for the concept of sensors integrated with electronics. The discussion below shows the integration of a sensor where an on-chip MOSFET is implemented in which the sensor is placed over the extended gate metal electrode of the MOSFET. The MOSFET amplifier takes care of the loss of the sensor signal due to the finite capacitances of the cables that are used to drive the signal to the signal processing unit.

A schematic of the device structure is shown in Figure 5.2 [3]. This is fabricated using six levels of photo masks. The device consists of a sensing part and an amplifying part. A PVDF film is used as the sensing material and an *n*-channel MOSFET with an extended aluminum gate is used as the electronic interface to the PVDF sensor. The basic structure is fabricated using a standard NMOS process. Transistors with large *W/L*

Table 5.2 Properties of PZT, PVDF and P(VDF-TrFE) [1,2]. F. S. Foster, K. A. Harasiewicz and M. D. Sherar, "A History of Medical and Biological Imaging with Polyvinylidene Fluoride (PVDF) Transducers," IEEE Trans. Ultrasonics Ferroelectrics Freq. Control, UFFC-47, © 2000 IEEE

Property	PZT-5A	PVDF	P(VDF-TrFE)
Thickness mode coupling coefficient	0.49	0.14	0.25–0.29
Relative permittivity, ε_r	1200	12–13	7–8
Density (g/cm^3)	7.75	1.78	1.88
Acoustic impedance, Z (MRa)	33.7	3.92	4.37
Maximum temperature ($^\circ\text{C}$)	365	80	115–145

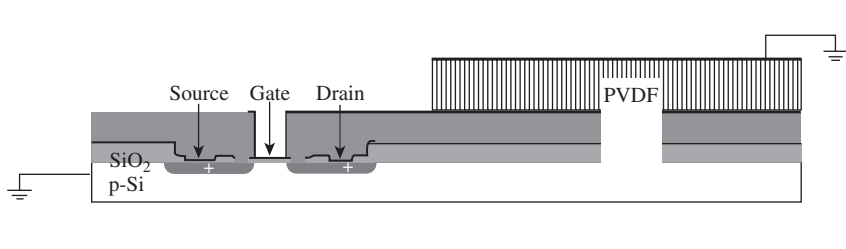


Figure 5.2 Schematic of the cross-section of PVDF–MOSFET hydrophone device [3].

ratios are preferred in order to obtain a large transconductance, g_m , and low noise. Hence, MOSFETs with different W/L ratios are preferred for this application.

The operating principle of this device can be explained as follows. The incident acoustic signal initiates the charge redistribution on the surfaces of the PVDF film that, in turn, changes the charge on the gate of an n -type MOSFET. The shift in gate voltage is used to modulate the drain current in a common source configuration. Since the FET is an important component in these sensors, its electrical characteristics are important in determining the behavior of these sensors. They also help to determine the operating point for the integrated sensors.

In a MOSFET, the drain current I_D is produced when electrons flow from source to drain. So, the existence of the channel is the cause of current flow. If V_{GS} is the gate-source voltage of the MOSFET and V_T the threshold voltage, then the condition for a channel to exist is that $V_{GS} > V_T$. With source and substrate terminals at ground potential, the threshold voltage V_T is given by [4]:

$$V_T = V_{T_mos} + V_{FB} \quad (5.5)$$

where V_{T_mos} is the threshold voltage of the MOS capacitor and V_{FB} is the flat band voltage:

The threshold voltage of the MOS capacitor V_{T_mos} is given by:

$$V_{T_mos} = 2\phi(b) + \frac{Q_b}{C_{ox}} \quad (5.6)$$

where $\phi(b)$ is the bulk potential, Q_b is the maximum space charge density per unit area of the depletion region and C_{ox} is the gate oxide capacitance. From these relations, it is evident that V_T is a function of the material properties of the gate conductor and insulation, the thickness of the gate insulator, the channel doping and the impurities at the silicon–insulator interface.

If N_a is the acceptor atom concentration and N_i is the intrinsic concentration, then the bulk potential $\Phi(b)$ is given by:

$$\phi(b) = \frac{KT}{q} \ln\left(\frac{N_a}{N_i}\right) \quad (5.7)$$

If ϵ_{si} is the permittivity of the silicon substrate, then the maximum space charge density Q_b is given by:

$$Q_b = \sqrt{4\epsilon_{si}qN_a\phi(b)} \quad (5.8)$$

The flat band voltage V_{FB} is given by:

$$V_{FB} = \phi_{ms} - \frac{Q_{fc}}{C_{ox}} \quad (5.9)$$

where ϕ_{ms} is the work function at the metal–semiconductor interface, Q_{fc} is the surface charge state and C_{ox} is the gate oxide capacitance.

If E_g is the band gap energy and $\Phi(b)$ the bulk potential, then the work function ϕ_{ms} is given by:

$$\phi_{ms} = \frac{-E_g}{2q} + \phi(b) \quad (5.10)$$

To operate the MOSFET as an amplifier, it must be biased at a point in the saturation region where the transconductance is proportional to the applied gate voltage but is independent of the drain voltage. For the MOSFET to operate in the linear region, the drain source voltage $V_{DS} < (V_{GS} - V_T)$. Then the drain source current I_{ds} is given by:

$$I_{ds} = \frac{W\mu_n C_{ox}}{2L} (V_{GS} - V_T)^2 \quad (5.11)$$

where L is the length, W the width and μ_n the surface mobility of the carriers in the channel of the MOSFET.

Hence the length L , the width W and the gate insulator thickness of the MOSFET are decided based on the above equations. The channel length of these devices is

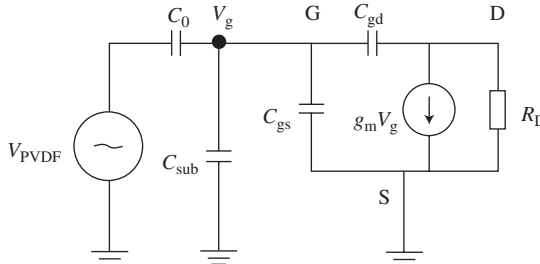


Figure 5.3 Equivalent small-signal model of a PVDF–MOSFET device.

designed as $10\text{ }\mu\text{m}$. From the I – V characteristic curves, the carrier mobility μ_n was obtained as about 600 – $700\text{ cm}^2/(\text{Vs})$. The threshold voltages for both the devices are within -0.5 to 0.3 V , which means the devices are ‘depletion-mode’ n -channel MOSFETs.

Since the resistance of the MOSFET is quite small and the equivalent output impedance of the PVDF transducer is simply a capacitor (C_0), the ideal PVDF–MOSFET structure may be modeled as shown in Figure 5.3. In the equivalent circuit, V_g is the signal voltage reaching the gate of the MOSFET (induced gate voltage), C_0 is the ‘clamped’ capacitance of the PVDF film, C_{sub} is the extended gate electrode-to-substrate capacitance, C_{gs} and C_{gd} are the gate-to-source and gate-to-drain capacitances, respectively, g_m is the transconductance and R_D is the resistance of the resistor connected to the drain of the MOSFET.

From the equivalent circuit, it is easy to get:

$$\frac{V_g}{V_{\text{PVDF}}} = \frac{C_0}{C_0 + C_{\text{sub}} + C_{\text{gs}} + C_{\text{gd}}(1 + g_m R_D)} \quad (5.12)$$

where C_0 is related to the thickness of the PVDF film. In the design shown here, the PVDF film has a thickness of $110\text{ }\mu\text{m}$. The values of C_{sub} , C_{gs} and C_{gd} can be calculated from the structural and geometrical parameters of the MOSFET (Table 5.3). Equation (5.12) shows that the

Table 5.3 Structural and geometrical parameters of a fabricated MOSFET (all values in μm).

Parameter	Value
Field oxide thickness	1
Gate oxide thickness	30.0
Metal thickness	0.25
n^+ junction depth	0.5
p-Type substrate thickness	250
SU-8 thickness	11

induced gate voltage can be improved by minimizing C_{sub} , C_{gs} and C_{gd} . When an acoustic signal reaches the PVDF transducer, a small voltage is generated and partially transmitted to the gate of the MOSFET. The small variation of the gate voltage in turn induces the voltage variation across R_D . The voltage gain is:

$$\frac{V_0}{V_g} = -g_m R_D = -\frac{W \mu_n C_g}{L} (V_{GS} - V_T) R_D \quad (5.13)$$

The sensitivity of the sensor with the electronics built in can be obtained as:

$$\frac{V_0}{P_1} = \left(\frac{V_0}{V_g} \right) \left(\frac{V_g}{V_{\text{PVDF}}} \right) \left(\frac{V_{\text{PVDF}}}{P_1} \right) \quad (5.14)$$

5.3 MEMS IDT-BASED ACCELEROMETERS

The concept and design principles underlying an MEMS–IDT (inter-digitized transducer)-based accelerometer are based on the use of surface acoustic waves (SAWs). This unique concept is a departure from the conventional comb-driven MEMS accelerometer design. By designing the seismic mass of the accelerometer to float just above a high-frequency Rayleigh surface acoustic wave sensor, it is possible to realize the accuracy and versatility required for the measurement of a wide range of accelerations. Another unique feature of this device is that because the SAW device operates at radiofrequencies (RFs), it is easier to be able to connect the 1DT device to a planar antenna and read the acceleration remotely by wireless transmission and reception. This unique combination of technologies results in a novel accelerometer that can be remotely sensed by an RF communication system, with the advantage of no power requirements at the sensor site.

In the device described here, a conductive seismic mass is placed close to the substrate (at a distance of less than one acoustic wavelength). This serves to alter the electrical boundary condition as discussed above. Programmable tapped delay lines have used the principle of air gap coupling between the SAW substrate and a silicon ‘superstrate’ to form individual MOS capacitors. These capacitors are then used to control the amount of RF coupling from the input IDT on the SAW substrate to the output terminal on the silicon chip [5]. This principle has also been successfully implemented in the realization of SAW ‘convolvers’ [6].

The seismic mass consists of a micromachined silicon structure which incorporates reflectors and flexible beams. The working of the device is as follows. The

IDT generates a Rayleigh wave, and the array of reflectors reflect this wave back to the IDT. The phase of the reflected wave is dependent on the position of the reflectors. If the positions of the reflectors are altered, then the phase of the reflected wave is also changed. The reflectors are part of the seismic mass. In response to acceleration, the beam flexes, so causing the reflectors to move. This can be measured as a phase shift of the reflected wave. By calibrating the phase shift measured with respect to the acceleration, the device can be used as an acceleration sensor. Alternatively, the measurement can be done in the time-domain, in which case the delay time of the reflection from the reflectors is used to sense the acceleration. A schematic of an MEMS-IDT-based accelerometer is shown in Figure 5.4. For waves propagating in the piezoelectric medium, there are two sets of equations, namely the mechanical equation of motion and Maxwell's equation for the electrical behavior. The equation of motion is as follows:

$$\rho \frac{\partial^2 u_i}{\partial t^2} = \sum_{j=1}^3 \frac{\partial T_{ij}}{\partial x_j} \quad (5.15)$$

where ρ is the density of the material, u_i is the wave displacement in the i th direction and T_{ij} is the stress. This equation is intercoupled by the constitutive relation:

$$T_{ij} = \sum_k \sum_l c_{ijkl}^E S_{kl} - \sum_k e_{kij} E_k \quad (5.16)$$

where c_{ijkl}^E is the stiffness tensor for a constant electric field, i.e. if the electric field (E) is held constant, this tensor relates changes in T_{ij} to changes in S_{kl} . The electric

displacement (D) is determined by the field E and the permittivity tensor ε_{ij} . In a piezoelectric material, the electric displacement is also related to the strain:

$$D_i = \sum_j \varepsilon_{ij}^S E_j + \sum_j \sum_k e_{kij} S_{jk} \quad (5.17)$$

where ε_{ij}^S is the permittivity tensor for constant strain and e_{kij} is the coupling constant between the elastic and electric fields.

The constitutive equations for piezoelectric materials relating the stress T , strain S , electric field E and electric displacement D are given by Equations (5.15) and (5.16). It can be seen that the electric field and the electric field displacement are coupled in this set of equations. For a non-piezoelectric material, $e_{kij} = 0$ and there is no coupling between the elastic and electric fields. The symmetric strain tensor is given by:

$$S_{ij} = \frac{1}{2} \left(\frac{\partial u_i}{\partial x_j} + \frac{\partial u_j}{\partial x_i} \right) \quad (5.18)$$

where u is the wave displacement.

The electromagnetic quasi-static approximation:

$$E_i = - \frac{\partial \phi}{\partial x_i} \quad (5.19)$$

$$\nabla D = 0 \quad (5.20)$$

for an electric potential ϕ can be used here to make further simplifications. The rotational part of the electric field due to the existence of a moving magnetic field is neglected. This approximation (Equation (5.19)) is valid as the acoustic velocity is small when compared to that of the electromagnetic wave.

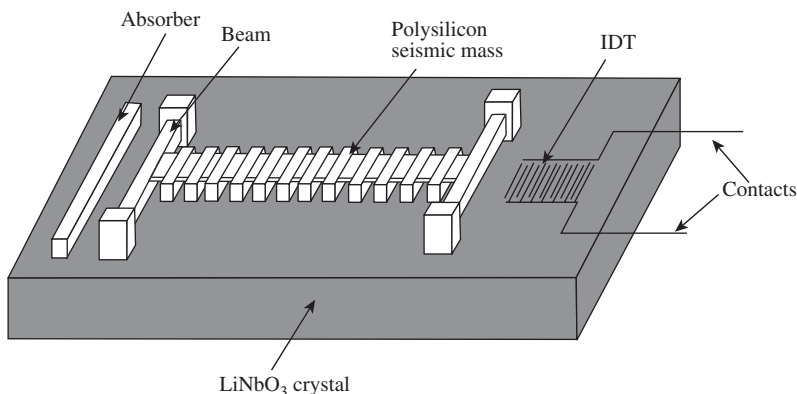


Figure 5.4 Schematic of an MEMS-IDT-based accelerometer.

By incorporating Equations (5.17)–(5.19) in Equation (5.20) results in a system of four coupled equations relating the electric potential with three components of displacement in a piezoelectric crystal:

$$\rho \frac{\partial^2 u_i}{\partial t^2} = \sum_j \sum_k \left(e_{kij} \frac{\partial^2 \phi}{\partial x_j \partial x_k} + \sum_l c_{ijkl}^E \frac{\partial^2 u_k}{\partial x_j \partial x_l} \right) \quad (5.21)$$

$$\sum_i \sum_j \left(\varepsilon_{ij}^S \frac{\partial^2 \phi}{\partial x_i \partial x_j} - \sum_l e_{ijk} \frac{\partial^2 u_j}{\partial x_i \partial x_k} \right) = 0. \quad (5.22)$$

where i, j and k vary from 1 to 3. The problem of wave propagation on anisotropic substrates can be solved by the method of partial waves. Plane wave solutions of the form:

$$u_j^m = \alpha_j^m e^{ikb^m x_3} e^{ik(x_1 - vt)} \quad (5.23)$$

$$\phi^m = \alpha_4^m e^{ikb^m x_3} e^{ik(x_1 - vt)} \quad (5.24)$$

are considered where $j = 1\text{--}3$ and $m = 1\text{--}4$. The coordinate system is aligned to the substrate such that the propagation is along x_1 and the surface normal is in the x_3 direction. Therefore, the surface wave decays along the x_3 direction. In Equations (5.23) and (5.24), k is the wave number, b is the decay factor and v is the phase velocity. The partial wave solutions are substituted into Equations (5.21) and (5.22). The weighing coefficients of these plane waves are chosen to satisfy the mechanical and electrical boundary conditions at the surface of the crystal.

In equations of motion, the material parameters are expressed in terms of axes which are selected for convenient boundary conditions and excitation requirements. The tabulated values of these material parameters are expressed according to the crystalline axes. It is necessary to transform the material parameters to match the coordinate system of the problem. In certain cases, this is a mere interchange of the coordinate axes (as in YZ lithium niobate). For more complex situations (128° YZ lithium niobate) the parameters are transformed using an appropriate transformation matrix. The elements of this matrix are the direction cosines between the crystalline axis and the ‘problem’ axis.

A YZ lithium niobate crystal is usually the material of choice in the design of devices of this type as it has the highest electromechanical coupling efficiency. The basic principle of the device depends on the strength of the piezoelectric coupling. ‘YZ lithium niobate’ indicates that the x_3 axis is parallel to the crystal axis Y, and x_1 is parallel to the crystal axis Z. The orientation of x_3 is called the ‘cut’ of the crystal. For YZ lithium niobate, the

crystal is Y-cut and Z-propagating. Since the material tensors, permittivity and piezoelectric tensors are specified with reference to the crystal axes, they need to be transformed into a frame defined by x_1, x_2, x_3 . The rotated material parameters are:

$$C = \begin{bmatrix} c_{33} & c_{13} & c_{13} & 0 & 0 & 0 \\ c_{13} & c_{11} & c_{12} & 0 & c_{14} & 0 \\ c_{13} & c_{12} & c_{11} & 0 & -c_{14} & 0 \\ 0 & 0 & 0 & c_{66} & 0 & c_{14} \\ 0 & c_{14} & -c_{14} & 0 & c_{44} & 0 \\ 0 & 0 & 0 & c_{14} & 0 & c_{44} \end{bmatrix} \quad (5.25)$$

$$e = \begin{bmatrix} e_{33} & e_{31} & e_{31} & 0 & 0 & 0 \\ 0 & 0 & 0 & -e_{22} & 0 & e_{15} \\ 0 & -e_{22} & e_{22} & 0 & e_{15} & 0 \end{bmatrix} \quad (5.26)$$

$$\epsilon = \begin{bmatrix} \epsilon_{33} & 0 & 0 \\ 0 & \epsilon_{11} & 0 \\ 0 & 0 & \epsilon_{11} \end{bmatrix} \quad (5.27)$$

The partial wave solutions (Equations (5.23) and (5.24)) are substituted into Equations (5.21) and (5.22), after the material parameters have been rotated to match the coordinate system defined for the problem, to get:

$$\begin{bmatrix} m_{11} - \rho V^2 & m_{12} & m_{13} & m_{14} \\ m_{12} & m_{22} - \rho V^2 & m_{23} & m_{24} \\ m_{13} & m_{23} & m_{33} - \rho V^2 & m_{34} \\ m_{14} & m_{24} & m_{34} & m_{44} - \rho V^2 \end{bmatrix} \times \begin{bmatrix} \alpha_1 \\ \alpha_2 \\ \alpha_3 \\ \alpha_4 \end{bmatrix} = 0 \quad (5.28)$$

where:

$$\begin{aligned} m_{11} &= c_{55}b^2 + 2c_{15}b + c_{11} \\ m_{12} &= c_{45}b^2 + (c_{14} + c_{56})b + c_{16} \\ m_{13} &= c_{35}b^2 + (c_{13} + c_{55})b + c_{15} \\ m_{14} &= e_{35}b^2 + (e_{15} + e_{31})b + e_{11} \\ m_{22} &= c_{44}b^2 + 2c_{46}b + c_{66} \\ m_{23} &= c_{34}b^2 + (c_{36} + c_{45})b + c_{56} \\ m_{24} &= e_{34}b^2 + (e_{14} + e_{36})b + e_{16} \\ m_{33} &= c_{33}b^2 + 2c_{35}b + c_{55} \\ m_{34} &= e_{33}b^2 + (e_{13} + e_{35})b + e_{15} \\ m_{44} &= -(\epsilon_{33}b^2 + 2\epsilon_{13}b + \epsilon_{11}). \end{aligned}$$

For YZ lithium niobate, m_{12} , m_{23} and $m_{24} = 0$. For non-trivial solutions, the determinant of the coefficients of α must vanish. For a given value of the phase velocity, setting this determinant equal to zero results in an eighth-order equation in the decay constant (b). These roots of b are purely real or conjugate pairs. Only values with negative imaginary parts are admissible as these roots lead to waves that decay with depth (i.e. surface waves). There exist four such roots of b . For each of the four roots, the corresponding eigenvalues and the eigenvectors are determined. A linear combination of the partial waves is then formed:

$$U_j = \left(\sum_m C_m \alpha_j^m e^{ikb^m x_3} \right) e^{ik(x_1 - vt)} \quad (5.29)$$

$$\phi = \left(\sum_m C_m \alpha_4^m e^{ikb^m x_3} \right) e^{ik(x_1 - vt)} \quad (5.30)$$

These are then substituted into the boundary conditions in the mechanical and electrical domains of the problem. The mechanical boundary condition states that the surface of the crystal is ‘mechanically free’. There is no component of force in the x_3 direction on the surface ($x_3 = 0$). This further implies that T_{31} , T_{32} and $T_{33} = 0$.

In the electrical domain, since a conductive plate is placed at a height h above the substrate, the potential goes to zero at $x_3 = h$. The potential above the surface satisfies Laplace’s equation. The potential and the electric displacement (D) in the direction normal to the substrate are continuous at $x_3 = 0$. This boundary condition is represented by the following equations. The potential in the air gap is given by:

$$\phi_1(x_3) = (Be^{kx_3} + Ce^{-kx_3}) e^{ik(x_1 - vt)} \quad (5.31)$$

The potential at $x_3 = h$ is zero. Therefore:

$$\begin{aligned} \phi_1(h) &= (Be^{kh} + Ce^{-kh}) e^{ik(x_1 - vt)} \\ C &= -Be^{2kh} \end{aligned} \quad (5.32)$$

The potential given by Equation (5.27) is equal to the potential given by the plane wave solution at the surface ($x_3 = 0$). Equating these results in an expression for the unknown constant B :

$$\phi_1(0) = B(1 - e^{2kh}) e^{ik(x_1 - vt)} = \phi(0) \quad (5.33)$$

$$\phi(0) = \left(\sum_m c_m \alpha_4^m \right) e^{ik(x_1 - vt)} \quad (5.34)$$

$$B = \frac{\sum_m c_m \alpha_4^m}{1 - e^{2kh}} \quad (5.35)$$

The electric displacement in the air gap is given by:

$$D_3 = -\epsilon_0 \frac{\partial \phi_1(x_3)}{\partial x_3} \quad (5.36)$$

The electric displacement on the surface of the crystal is given by:

$$D_3(x_3 = 0) = -k\epsilon_0 \frac{\sum_m c_m \alpha_4^m}{1 - e^{2kh}} (1 + e^{2kh}) e^{ik(x_1 - vt)} \quad (5.37)$$

This equation is obtained from the potential equation in Equation (5.25). The expression for the electric field displacement from the plane wave solution of potential is similarly obtained and is given by:

$$D_3(x_3 = 0) = \sum_j \epsilon_{3j}^E E_j + \sum_j \sum_k e_{3jk} S_{jk} \quad (5.38)$$

From the above equations, the relevant electrical boundary conditions can be obtained.

The choice of the suspension for the seismic mass determines the linearity of motion and the sensitivity to residual strain. A single support is the simplest and lowest spring constant design, but allows substantial offline motion and rotation in the suspended mass. Two parallel supports remove the rotation component of the motion, but still introduce offline motion due to curvature of the beams (arclength is preserved, while vertical distance is not). A two-sided support removes that problem but greatly increases the sensitivity to residual stress.

In addition to launching surface waves, the IDT can also generate bulk acoustic waves. These waves can propagate in any direction within the body of the substrate material. In this design, the principal effect of the generation of bulk waves is reduction of the power available for the generation of surface waves. The following strategies may be useful to minimize the generation of bulk waves:

- (a) The bottom surface of the piezoelectric substrate is roughened and coated with a soft conductor like silver epoxy.
- (b) Use substrate geometries that are not rectangular in shape.
- (c) Choice of the right number of IDT fingers. The input power is converted into bulk wave energy and surface wave energy as $P = P_S + P_B$, where P_S represents the power in the excited SAW wave and P_B the component that is radiated as bulk waves. The ratio

of P_S to P_B decreases drastically as the number of finger pairs in the exciting IDT is reduced. For YZ lithium niobate, the amount of input power converted into transverse bulk waves increases almost exponentially as the number of IDT fingers is reduced below five.

5.4 FIBER-OPTIC GYROSCOPES

Fiber-optic gyroscopes are miniature solid-state optical devices for the precise measurements of mechanical rotation in inertial space. Conventionally used mechanical gyroscopes involve a spinning mass and ‘gimballed’ mountings. Optical gyroscopes are free of such moving parts and may be used for a wide range of applications, for example, navigation, exploration and in the manufacturing and defence industries.

The basic theory of rotation sensing by optical means is known as the *Sagnac effect*, since this possibility was first demonstrated by G. Sagnac in 1913. The type of interferometer used to measure rotation is known as the Sagnac interferometer (Figure 5.5). Two identical light beams traveling in opposite directions around a closed path experience a phase difference when the loop is rotated about its axis, and this phase difference is proportional to the rotation rate [7]. Consider the interferometer shown in Figure 5.5. Here, a light beam is split by using a beam splitter and the two beams (B_1 and B_2) are made to travel in a circular path. When the interferometer is at rest in an inertial frame of reference, the pathlength of the counter-propagating waves are equal since light travels at the same speed in both directions around the loop.

The time taken by the beam B_1 to complete the circular path is:

$$\tau_1 = \frac{2\pi r}{c} \quad (5.39)$$

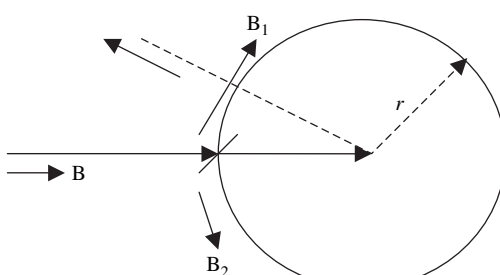


Figure 5.5 Schematic of a Sagnac interferometer.

where r is the radius of the circular path. Similarly, the time taken by the beam B_2 is also of the same value. Therefore:

$$\tau_1 = \tau_2 = \tau \quad (5.40)$$

If the interferometer is rotating at a speed of Ω m/s in the clockwise direction and the observer is motionless in the original inertial frame, the time taken by B_1 to complete the circular path is less than B_2 . In this case, the time taken by B_1 to complete the circular path is given by:

$$\tau_1 = \frac{2\pi r}{c} + \frac{\Omega \tau r}{c} \quad (5.41)$$

Similarly, the time taken by B_2 to complete the circular path is:

$$\tau_2 = \frac{2\pi r}{c} - \frac{\Omega \tau r}{c} \quad (5.42)$$

Therefore, the difference between the propagation times of the two waves is:

$$\Delta\tau = \tau_1 - \tau_2 = \frac{2\Omega \tau r}{c} = \frac{4\pi r^2 \Omega}{c^2} \quad (5.43)$$

Obviously, B_2 will reach its destination before B_1 . For a continuous wave of frequency ω , this corresponds to a phase shift:

$$\Delta\phi = \omega \Delta\tau = \frac{4\pi r^2 \Omega}{c^2} \omega = \frac{4\omega}{c^2} A \Omega \quad (5.44)$$

where A is the area of the circular path. It may also be noted that this result would remain unchanged even when the interferometer is filled with a medium of refractive index n because of the *Fresnel–Fizeau* drag effect due to the movement of the medium compensating for the increased optical pathlengths.

The advantage of using an optical-fiber coil to form the interferometer is that the Sagnac phase difference increases with the number of turns or length of the fiber. In this special case, Equation (5.44) can be rewritten as:

$$\Delta\phi = 2\pi \frac{LD}{\lambda c} A \Omega \quad (5.45)$$

where L is the length of the fiber and D is the diameter of the coil.

Fiber-optic gyroscopes are broadly classified into two types. The first type is an open-loop fiber-optic gyroscope

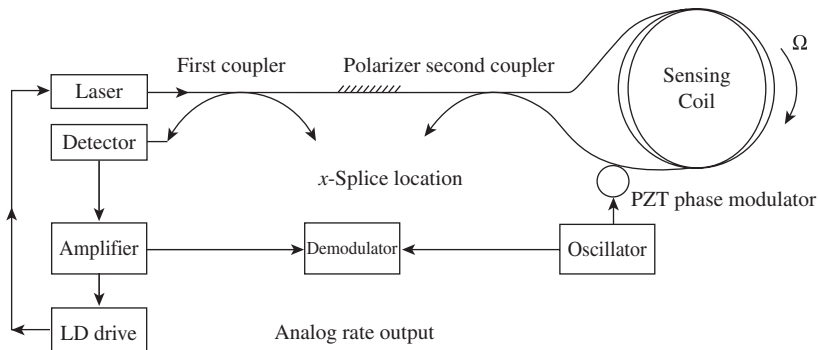


Figure 5.6 Schematic of a fiber-optic gyroscope in the open-loop configuration [8]. Reproduced with permission of KVH Industries Inc

with a dynamic range of the order of 1000 to 5000, with a scale-factor accuracy (inclusive of non-linearity and hysteresis effects) of about 0.5 %, and sensitivities that vary from less than 0.01 degrees/h to 100 degrees/h and higher. These fiber-optic gyroscopes are generally used for low-cost applications where dynamic range and linearity are not crucial. The second type is the closed-loop fiber-optic gyroscope that may have a dynamic range of 10^6 and a scale-factor linearity of 10 ppm or better. These types of fiber-optic gyroscopes are primarily targeted at medium- to high-accuracy navigation applications that have high turning rates and require high linearity and large dynamic ranges.

Figure 5.6 illustrates the open-loop configuration. This consists of a fiber coil, two directional couplers, a polarizer, an optical source and a detector. A piezo-electric (PZT) device wound with a small length at one end of the fiber coil applies a non-reciprocal phase modulation. Light from the laser traverses the first directional coupler, polarizer and then the second directional coupler where it is split into two signals of equal intensity that travel around the coil in opposite directions. The light recombines at the coupler, returning through the polarizer, and half of the light is directed by the first coupler into a photo detector. This configuration permits measuring the difference in phase between the two signals to one part in 10^{16} . This is possible due to the principle of reciprocity. Light passing from the laser through the polarizer is restricted to a single state of polarization, and the directional couplers and coil are made of special polarization-maintaining fibers to ensure a single-mode path. Beams of light in both directions travel through the same pathlength. Almost all environmental conditions (except rotation) have the same effects on both beams and are canceled out. Hence, this gyroscope

is sensitive only to rotation about the axis perpendicular to the plane of the coil. The light intensity returning from the coil to the polarizer is a raised cosine function, having a maximum value when there is no rotation and a minimum when the optical phase difference is $\pm \pi$ (half an optical wavelength). This effect can be shown to be independent of the shape of the optical path and of the propagation medium. Modulating PZT with a sinusoidal voltage impresses a differential optical phase shift between the two light beams at the modulating frequency. The interferometer output when there is no rotation of the coil exhibits the periodic behavior shown in Figure 5.7, whose frequency spectrum comprises *Bessel* harmonics of the modulation frequency. Since the phase modulation is symmetrical, only even harmonics are present; the ratio of the harmonic amplitudes depends on the extent of phase modulation. When the coil is rotated, the modulation occurs about the shifted position of the interferometer response. The modulation is unbalanced, and the fundamental and odd harmonics will also be present (Figure 5.8). The amplitudes of the fundamental and odd harmonics are proportional to the sine of the angular rotation rate, while the even harmonics have a cosine relationship. The simplest demodulation scheme synchronously detects the signal at the fundamental frequency.

Further improvements in dynamic range and linearity can be obtained by using a closed-loop configuration where the phase shift induced by rotation is compensated by an equal and opposite artificially imposed phase shift. One way to accomplish this is to introduce a frequency shifter into the loop, as shown in Figure 5.9. The relative frequency difference of the light beams propagating in the fiber loop can be controlled, resulting in a net phase difference that is proportional to the length of the fiber coil and the frequency shift. In

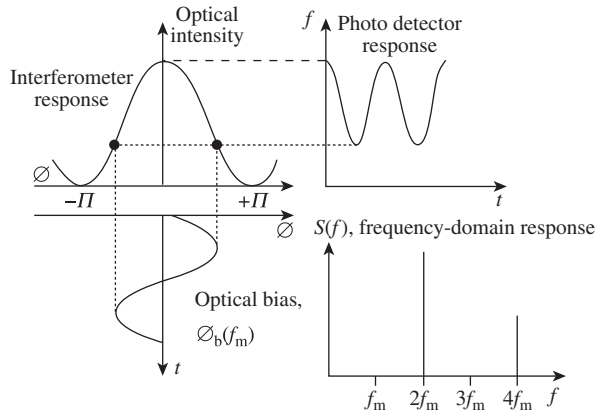


Figure 5.7 Sagnac interferometer response for stationary open-loop gyroscope configuration [8]. Reproduced with permission of KVH Industries Inc

Figure 5.9, this is done by using a modulator in the fiber-optic coil to generate a phase shift at a rate of ω . When the coil is rotated, the first harmonic signal modifies the phase, in a manner similar to that for open-loop fiber-optic gyroscopes. By using the rotationally induced first harmonic as an error signal, the frequency shift can be adjusted by using a synchronous demodulator with a detector to translate the first harmonic signal into a corresponding voltage. This voltage is applied to a voltage-controlled oscillator whose output frequency is fed into the frequency shifter in the loop so that the phase relationship between the counter-propagating light beams is locked into a single value.

5.5 PIEZORESISTIVE PRESSURE SENSORS

A pressure sensor can consist of a micromachined silicon wafer bonded onto a glass substrate. Strain gauges are patterned onto the micromachined diaphragm area. To analyze its operation, if we first consider a circular plate of thickness h , where the deflection of the plate w , under a uniformly distributed pressure (p), is assumed to be smaller than $h/5$, the differential equation describing the elastic behavior of the middle plane of a thin plate is obtained from the elementary theory of plates [9]:

$$\nabla^4 w = \frac{p}{D} \quad (5.46)$$

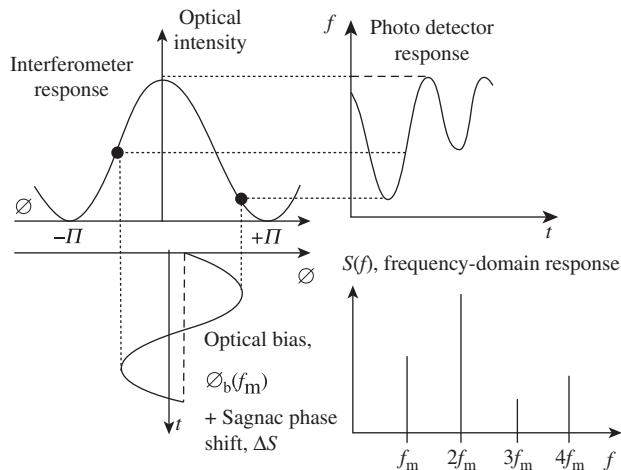


Figure 5.8 Sagnac interferometer response for rotating open-loop gyroscope configuration [8]. Reproduced with permission of KVH Industries Inc

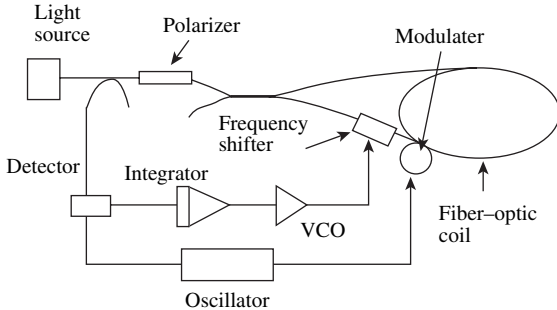


Figure 5.9 Schematic of a fiber-optic gyroscope in the closed-loop configuration [8].

where D is the stiffness of the plate, ($D = Eh^3/[12(1 - v^2)]$); here, E is the Young's modulus of the plate and v is the Poisson ratio. In the case of a simply supported edge, w is solved as follows:

$$w = \frac{p(a^2 - r^2)}{64D} \left[\left(\frac{5+v}{1+v} \right) a^2 - r^2 \right] \quad (5.47)$$

where a is the radius of the plate and r is measured in a coordinate system fixed to the center of the plate.

The radial strain (ε_r) is given by:

$$\begin{aligned} \varepsilon_r(r, z) &= -\frac{Dz}{Eh^3/12} \left(\frac{d^2w}{dr^2} + \frac{v dw}{r dr} \right) \\ &= \frac{3}{8} \left[\frac{pa^2(h_p - h_m)(3+v)}{E(h_p + h_m)^3} \right] \left(1 - \frac{r^2}{a^2} \right) \end{aligned} \quad (5.48)$$

while the tangential strain (ε_t) is given by:

$$\begin{aligned} \varepsilon_t(r, z) &= -\frac{Dz}{Eh^3/12} \left(v \frac{d^2w}{dr^2} + \frac{1}{r} \frac{dw}{dr} \right) \\ &= \frac{3}{8} \left[\frac{pa^2(h_p - h_m)(3+v)}{E(h_p + h_m)^3} \right] \left[1 - \left(\frac{3v+1}{3+v} \right) \left(\frac{r^2}{a^2} \right) \right] \end{aligned} \quad (5.49)$$

where z is the vertical coordinate from the middle plane to the boundary lamina of the plate and the thickness h consists of the plate thickness, h_p , and the membrane thickness, h_m .

As the pressure-induced strains are functions of the radius, the mean radial strain is given by:

$$\bar{\varepsilon}_r = \frac{\int_{r_i}^{r_0} \varepsilon_r(r) dr}{\int_{r_i}^{r_0} dr} = \varepsilon_0 \left[1 - \frac{1}{3a^2} \left(\frac{r_0^3 - r_i^3}{r_0 - r_i} \right) \right] \quad (5.50)$$

while the mean tangential strain is:

$$\bar{\varepsilon}_t = \frac{\int_{\rho_i}^{\rho_0} \varepsilon_t(r) dr}{\int_{\rho_i}^{\rho_0} dr} = \varepsilon_0 \left[1 - \frac{1}{3a^2} \left(\frac{3v+1}{3+v} \right) \left(\frac{\rho_0^3 - \rho_i^3}{\rho_0 - \rho_i} \right) \right] \quad (5.51)$$

where r_0 and r_1 represent the outer and inner diameters of radial strain, ρ_0 and ρ_1 are the outer and inner diameters of tangential strain and ε_0 is the maximum strain acting in the center of the circular plate, given by:

$$\varepsilon_0 = \frac{3}{8} \left[\frac{pa^2(h_p - h_m)(3+v)}{E(h_p + h_m)^3} \right] \quad (5.52)$$

A Wheatstone bridge is widely used to pick up variation in the electrical resistances of the strain gauges. When the bridge is balanced, there is no voltage output (when there is no resistance change from its balance value) but the bridge indicates a voltage output if the resistance is varied from its nominal value. This resistance variation depends on the strain generated in the resistor and the change in resistivity:

$$\frac{\Delta R}{R} = (1+2v)\varepsilon + \frac{\Delta\rho}{\rho} \quad (5.53)$$

where ΔR is the resistance change, R is the original resistance to achieve the Wheatstone bridge balance, ε is the strain, v is the Poisson ratio of the resistor material, $\Delta\rho$ is the resistivity change and ρ is the original resistivity of the resistor materials. Usually, the resistivity change can be ignored, considering that resistors are made from homogeneous materials. The linear relationship between the resistance change and strain is obtained as follows:

$$\frac{\Delta R}{R} = (1+2v)\varepsilon \quad (5.54)$$

Here, $k_{gf} (= 1+2v)$ is called the *gauge factor* which directly reflects the relationship between resistance change and strain.

If four gauges are placed on the flexible plate, two of them for radial-strain sensing and the other two for tangential-strain measurement, all four gauges have the same nominal resistance so that the Wheatstone bridge is in the 'balance state' and there is no voltage output. The radial- and tangential-resistance changes due to the radial

and tangential strains, respectively, are obtained by considering the temperature-shift-induced strain:

$$\frac{\Delta R_r}{R} = k_{gf}(\bar{\epsilon}_r + \epsilon_{temp}) \quad (5.55)$$

$$\frac{\Delta R_t}{R} = k_{gf}(\bar{\epsilon}_t + \epsilon_{temp}) \quad (5.56)$$

The voltage output due to the resistance change is calculated from:

$$V_{out} = V_0 \frac{\left(\frac{\Delta R_r}{R} - \frac{\Delta R_t}{R} \right)}{\left(2 + \frac{\Delta R_r}{R} + \frac{\Delta R_t}{R} \right)} \quad (5.57)$$

By considering the fact that $\Delta R_r/R \ll 1$ and $\Delta R_t/R \ll 1$ and combining Equations (5.55)–(5.57), the voltage output of the circuit is given by:

$$V_{out} = \frac{V_0}{2} k (\bar{\epsilon}_r - \bar{\epsilon}_t) = \frac{k}{16} \frac{(h_p - h_m)(3 + v)}{E(h_p + h_m)^3} \times \left[\left(\frac{3v + 1}{3 + v} \right) \left(\frac{\rho_0^3 - \rho_i^3}{\rho_0 - \rho_i} \right) - \left(\frac{r_0^3 - r_i^3}{r_0 - r_i} \right) \right] p \quad (5.58)$$

where V_0 is the DC supply voltage of the Wheatstone bridge. If the voltage output of this pressure transducer is V_{out} when it is exposed to a pressure p , the sensitivity of the transducer is then calculated as:

$$S = \frac{1}{V_0} \frac{dV_{out}}{dp} = \frac{k}{16} \frac{(h_p - h_m)(3 + v)}{E(h_p + h_m)^3} \times \left[\left(\frac{3v + 1}{3 + v} \right) \left(\frac{\rho_0^3 - \rho_i^3}{\rho_0 - \rho_i} \right) - \left(\frac{r_0^3 - r_i^3}{r_0 - r_i} \right) \right] \quad (5.59)$$

It may be interesting to note from the above equation that pressure transducers with high sensitivities can be obtained by using flexible materials with low Young's modulus values.

5.6 SAW-BASED WIRELESS STRAIN SENSORS

In this section, a surface acoustic wave (SAW)-based strain sensor is described. This sensor has recently been proposed for studying the deflection and strain of a 'flexbeam'-type structure for a helicopter blade [10]. The basic design principles of operation of SAW sensors have been discussed in Chapter 3. The system presented here consists of a remotely readable passive MEMS sensor and a microwave-reader system, as shown in Figure 5.10. The microwave-reading system used in this system employs a frequency-modulated (FM) radar-device. The FM signal sent by the system antenna is:

$$S(t) = A \cos \left(\omega_0 + \frac{\mu t}{2} \right) t \quad (5.60)$$

where ω_0 is the start frequency of the FM signal, μ is the rate of modulation and t is time. The echoes from the reflectors, $S_1(t)$ and $S_2(t)$, are the same as the transmitted signal $S(t)$ but with time delays t_1 and t_2 respectively. These are written as:

$$S_1(t) = S_1 \cos \left(\omega_0 + \frac{\mu t}{2} \right) (t - t_1) \quad (5.61)$$

and:

$$S_2(t) = S_2 \cos \left(\omega_0 + \frac{\mu t}{2} \right) (t - t_2) \quad (5.62)$$

where $t_1 = 2d_1/v + \tau_e$ and $t_2 = 2d_2/v + \tau_e$. Here, v is the SAW velocity, d_1 and d_2 are the distances from the IDT transducer to the reflectors 1 and 2, respectively, and

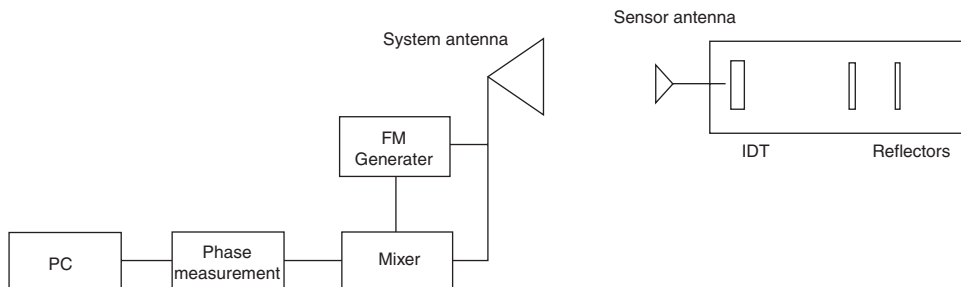


Figure 5.10 Schematic diagram of a remote-reading sensor system with a passive SAW sensor.

τ_e is the total of other delays, such as the electromagnetic wave traveling time and the delay in the electronic circuit and devices, which is the same for both echoes. Through the mixer, which uses the transmitted signal as the reference, and low-pass filter, the frequency differential signals are obtained as:

$$E_1(t) = E_1 \cos[\mu t_1 + (\omega_0 t_1 - \mu t_1^2)] = E_1 \cos(\omega_1 t + \phi_1) \quad (5.63)$$

and:

$$E_2(t) = E_2 \cos[\mu t_2 + (\omega_0 t_2 - \mu t_2^2)] = E_2 \cos(\omega_2 t + \phi_2) \quad (5.64)$$

It may be observed that both the frequencies and phases of these two signals depend on the delay times. The two signals can be separated in the frequency domain. Since ω_0 is usually much greater than μ , the phase shift is more sensitive to the variation of the delay time than that of the frequency. The difference of the two phases can be written as:

$$\phi = \phi_1 - \phi_2 = \left[\omega_0 - \frac{\mu}{2}(t_1 + t_2) \right] (t_2 - t_1) \quad (5.65)$$

where the extra delay time of the second echo with reference to the first is equal to the ‘round-trip’ time for the acoustic wave traveling from the first reflector to the second, and is $t_2 = t_2 - t_1 = 2d/v$, where d is the distance between the two reflectors. The phase difference is sensitive to the change in delay times. The variation of the phase difference due to the change in delay times is expressed as:

$$\Delta\phi = \left[\omega_0 - \frac{\mu}{2}(t_1 + t_2) \right] \Delta\tau \quad (5.66)$$

Since ω_0 is usually much larger than $\mu(t_1 + t_2)/2$, we get $\Delta\phi = \omega_0 \Delta\tau$.

The wave traveling time t is proportional to the distance between the two reflectors and inversely proportional to the velocity. If we neglect the possible velocity variation

of the SAW under strain and take into account only the direct effect, the distance change is given as:

$$\Delta\phi = \omega_0 \frac{2ed}{v} = \omega_0 \varepsilon \tau_0 \quad (5.67)$$

where ε is the strain and τ_0 is the traveling time when the strain is zero. The sensitivity of this remote-sensor system depends on the operating frequency and the round-trip traveling time between the two reflectors of the SAW. The phase shift of the signal therefore varies linearly with the strain on the structure to which the sensor is attached. Strain can therefore be monitored at the reader unit.

5.7 SAW-BASED CHEMICAL SENSORS

Acoustic microsensors are also used to detect/identify/estimate many liquids and gases based on variations in the electroacoustic properties. Their responses can be easily related to physical quantities, such as mass density and viscosity. These sensors offer a number of advantages over traditional sensors, including real-time electronic read-out, small size, robustness and low-cost fabrication. By employing so-called chemical interfaces, the interaction of a chemical analyte with the sensor surface results in a change in the propagation characteristics of the wave. While Rayleigh surface acoustic wave (SAW) sensors are most commonly used in gas-sensing applications, shear horizontal (SH) polarized waves are more suitable for liquid sensing [11]. However, improved sensitivity can be obtained by using Lamb waves (flexural plate waves) [12–15]. These sensors can be fabricated on piezoelectric substrates. This approach is used for simultaneous measurements of both mechanical and electrical parameters of the fluid. The basic principles of operation of a SH-SAW sensor in a single free delay-line configuration are shown in Figure 5.11. In this, the input and output IDTs are connected to the source and the load

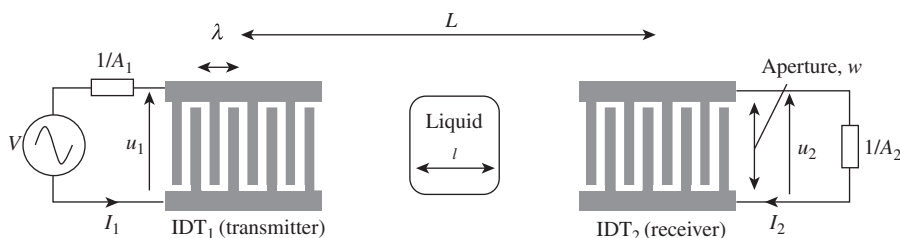


Figure 5.11 Schematic of a delay-line arrangement with inter-digitized transducers on a piezoelectric substrate.

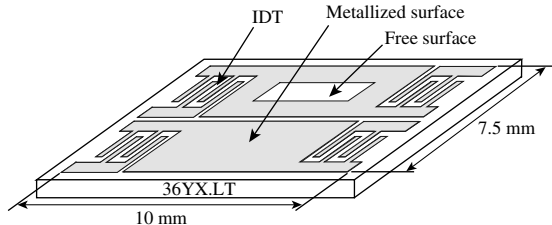


Figure 5.12 Schematic of a dual-delay-line SH-SAW microsensor.

with admittances A_1 and A_2 , respectively. The basic design considerations are identical to those used for Rayleigh SAWs. The design of the IDTs for the generation and detection of SH-SAWs uses the delay-line configuration often employed for SAW filters [11]. The sensor consists of two adjacent delay lines, as shown in Figure 5.12, consisting of an uncoated metallized (reference) surface and an electrically free delay line. The basic operating principles utilized in the design of these liquid-sensing devices is that the perturbations which affect SH-SAW propagation on a metallized and electrically shorted surface are associated with the mechanical properties of the adjacent liquid, while the SH-SAWs propagating on a free surface are associated with both the mechanical and electrical properties of the adjacent liquid [12]. Common environmental interactions arise from both delay lines and can be removed by comparison between the two signals. The design is made by considering analysis and prediction of the sensor response, which requires that the sensor effect is accounted for in the device response. The sensor effect can be incorporated into the device unperturbed transfer function, to allow for the variations of delay time (related to phase shift) and attenuation. When applying a voltage across the two bus bars of the transmitter IDT, which are connected to identical finger pairs, a current enters the electrodes. This current is determined by the static capacitances of the electrodes and the acoustic admittances of the IDTs caused by generation of the SH-SAWs.

The SH-SAWs which propagate on the surfaces of piezoelectric substrates have associated electric fields that will propagate typically several micrometers into a liquid. This electrical interaction (also known as the acoustoelectric interaction) with the liquid affects the velocity and/or attenuation of SH-SAW propagation and is utilized in sensing the dielectric properties of liquids [15]. SH-SAW sensors thus can exhibit some specificity in detecting the electrical properties of an adjacent liquid [16,17].

The piezoelectric potential becomes zero for the electrically shorted surface and hence the mechanical properties, including viscosity and density of a liquid, can be detected because the horizontally polarized shear wave can interact with it. On the other hand, since the piezoelectric potential at the free space extends into the liquid, the electrical properties, and hence the wave propagation, will change due to an acoustoelectric interaction known as ‘electrical perturbation’. The potential that is associated with the SH-SAW will be affected by the electrical properties of the adjacent liquid.

The complex unperturbed acoustic admittance transfer function for transmitter to receiver can be approximated as follows: [15,18]

$$A_{12}(\omega) = G(\omega)\alpha e^{-\frac{j2\pi L}{\lambda}} \quad (5.68)$$

where α is the attenuation coefficient of the acoustic wave, λ is the acoustic wavelength, L is the distance between the centers of the IDTs and $G(\omega) = G_0(\sin\omega/\omega)^2$, with $\omega = \pi N(\omega - \omega_0)/\omega_0$ and $G_0 = 2.25\omega_0 N^2 W(\varepsilon_0 + \varepsilon_p^T)K^2/2$. In the latter, G_0 is the conductance at the center frequency, N is the number of fingers pairs, W is the aperture of the electrodes, ε_0 is the permittivity of a vacuum, ε_p^T is the effective permittivity of the piezoelectric substrate and K^2 is the electromechanical coupling coefficient of the substrate, which depends on the crystal cut, frequency ω_0 and the mechanical properties and thickness of the IDT metallization [18].

The presence of a liquid causes a variation in the delay time and attenuation of the SH wave. These should be included in this admittance transfer function as an additional phase shift and attenuation. Therefore, the perturbed admittance transfer function for the liquid sensor is:

$$A_{12}(\omega) = G(\omega)\alpha e^{-\frac{j2\pi L}{\lambda}} e^{\frac{j2\pi\delta t}{\lambda}} e^{-al} \quad (5.69)$$

where ($= \Delta v/v$) is the fractional velocity change of the SH-SAW due to the sensing effect, l is the length of the liquid contact area and a is the attenuation of the SH-SAW due to the sensor effect along the region of liquid contact.

If the conductivity of the unperturbed liquid (reference liquid) is zero, the electrical properties of the liquid, in terms of permittivity and conductivity, can be written as:

$$\varepsilon_l = \varepsilon_r \varepsilon_0 \quad (5.70)$$

where ε_l , ε_r and ε_0 are the permittivity and dielectric constant of the liquid, and the permittivity of free space,

respectively. The electrical property after perturbation, ϵ'_l , in terms of the conductivity σ , is:

$$\epsilon'_l = \epsilon'_r \epsilon_0 - j \frac{\sigma}{\omega} \quad (5.71)$$

Using the perturbation theory, the acoustoelectrical interaction relations of velocity and attenuation of SH waves in the presence of a liquid can be written as follows [14]:

$$\frac{\Delta v}{v} = - \frac{K_s^2 (\sigma'/\omega)^2 + \epsilon_0 (\epsilon'_r - \epsilon_r) (\epsilon'_r \epsilon_0 + \epsilon_p^T)}{(\sigma'/\omega)^2 + (\epsilon'_r \epsilon_0 + \epsilon_p^T)^2} \quad (5.72)$$

where ϵ_p^T is the effective permittivity of the crystal, ϵ_r is the permittivity of the reference liquid and ϵ'_r and σ' are the permittivity and conductivity, respectively, related to loss of the measurand. The change in attenuation due to the presence of the liquid can be written as follows [14]:

$$\frac{\Delta \alpha}{k} = \frac{K_s^2}{2} \frac{(\sigma'/\omega)(\epsilon_r \epsilon_0 + \epsilon_p^T)}{(\sigma'/\omega)^2 + (\epsilon'_r \epsilon_0 + \epsilon_p^T)^2} \quad (5.73)$$

where K_s^T is the electromechanical coupling coefficient and k is the wave number. By using Equations (5.71) and (5.72), Equation (5.73) can be rewritten as follows:

$$\left(\frac{\Delta v}{v} + \frac{K_s^2}{2} \right)^2 + \left[\frac{\Delta \alpha}{k} - \left(\frac{K_s^2}{4} \frac{\epsilon_r \epsilon_0 + \epsilon_p^T}{\sigma'/\omega^2} \right) \right]^2 = \left(\frac{K_s^2}{4} \frac{\epsilon_r \epsilon_0 + \epsilon_p^T}{\sigma'/\omega} \right)^2 \quad (5.74)$$

The SAW that propagates on the metallized surface is affected only by the mechanical properties of the adjacent liquid. However, the SAW that propagates on the free surface is affected by both the mechanical and electrical properties of the liquid. The above Equations (5.73) and (5.74) can be used to determine the permittivity and conductivity of the liquid under test [17]. These may be solved by graphical means.

These sensors can be used in ‘smart tongues’. Taste is comprised of five basic qualities, namely sourness, bitterness, saltiness, sweetness and umani. A taste sensor should be able to measure these effects and discriminate between them for recognition and identification applications. Acoustic microsensors can detect different physical properties such as mass, temperature, strain, torque, pressure and viscosity of liquids and gases. These microsensors, together with an oscillatory circuit, can give a real-time electronic read-out with smaller size and very

low unit cost. SAW microsensors are a unique class of devices that have been used as electronic ‘tongues’ and ‘noses’ because the propagating acoustic waves can effectively couple with the medium placed in contact with the device surface. The interactions between acoustic waves and mass density, elastic stiffness and electric/dielectric properties of the propagating medium can give the sensing responses. Any changes in the above properties can be measured as changes in the phase or amplitude of the propagating waves.

It is highly desirable in the food industry for the development of a taste sensor with high sensitivity, stability and selectivity. The main goal of a taste sensor is to reproduce five kinds of human senses, which is quite difficult. The importance of knowing the quality of beverages and drinking water has been recognized as a result of the increase in concern in environmental pollution issues. However, no accurate measuring system, appropriate for the quality evaluation of beverages, is yet available.

A similar approach can be extended for the sensing of gases. However, here the acoustic wave is guided through a channel of the piezomaterial, with its top surface coated with a sensitive polymer thin film. In such a case, the gas–polymer partition coefficient, K (the interaction between vapor and polymer molecules), and the solvation equation (modeling physio-chemical and biochemical processes) are expressed by a linear solvation energy relationship (LSER) [19]:

$$\log K = c + rR_2 + s\pi_2^H + a\alpha_2^H + b\beta_2^H + l\log L^{16} \quad (5.75)$$

where R_2 is the excess molar refraction (which models the polarizability contributions from n and p electrons), π_2^H is the depolarity/polarizability, α_2^H is the hydrogen-bond acidity, β_2^H is the hydrogen-bond basicity and L^{16} is the gas–liquid partition coefficient for *n*-hexadecane. These coefficients are obtained by regression analysis. The change in the relative phase velocity ($\Delta v/v_0$) and attenuation per wave number ($\Delta \alpha/k_0$) of the acoustic wave for an acoustically thin, viscoelastic and isotropic film is given by the following [20]:

$$\frac{\Delta v}{v_0} \cong -\omega h \left[\rho_f (c_1 + c_2 + c_3) - \left(\frac{c_1 + 4c_3}{v_0} \right) G' \right] \quad (5.76)$$

$$\frac{\Delta \alpha}{k_0} = (c_1 + 4c_3) \frac{\omega h}{v_0^2} G'' \quad (5.77)$$

where c_i represents the substrate specific material constants, h is the film thickness, ρ_f is the film density, v_0 is the unperturbed Rayleigh wave velocity, G' and G'' are the real and imaginary parts of the shear modulus of the polymer film, respectively, and ω is the radian frequency.

When the polymer is exposed to a vapor, the total mass increases due to adsorption and diffusion and there is an additional change in the shear modulus due to swelling and softening. The change in the resonant frequency of a SAW-based gas sensor can be derived as follows [21]:

$$\Delta f = -(k_1 + k_2)f_0^2 h \rho_f + k_2 f_0^2 h \left[\frac{4\mu(\lambda + \mu)}{v_0^2(\lambda + 2\mu)} \right] \quad (5.78)$$

where k_1 and k_2 are the substrate material constants, f_0 is the unperturbed SAW resonant frequency, μ is the shear modulus of the film and λ is the Lame constant of the film. The second term in the above equation may be neglected in most cases. As the polymer film absorbs vapor, the change in resonant frequency is due to mass loading, as well as changes in its shear characteristics. The change in resonant frequency due to vapor absorption (Δf_v) in this case is given by the following [20]:

$$\Delta f_v = \frac{4\Delta f C_v K}{\rho_f} \quad (5.79)$$

where K is defined in Equation (5.75) above.

For soft viscoelastic materials with low shear acoustic velocities, the maximum layer thickness, h_0 , to ensure monomode operation is given by the following [22]:

$$h_0 = \frac{V_S V_L}{2f \sqrt{V_S^2 - V_L^2}} \quad (5.80)$$

where f is the operational frequency and V_S and V_L are the acoustic velocities on the substrate and the deposited polymer layer, respectively.

5.8 MICROFLUIDIC SYSTEMS

Compared to the number of microsensors discussed above, far fewer micro-actuators have been commercialized. One of the reasons for this is the fact that the deflection, force or power generated by micro-actuators is usually low. In this section, the design of various microfluidic systems is presented.

Microvalves is a primary component of microfluidic systems, which have wide applications in areas of the

automotive industry, refrigeration and home appliances, control, medical and biomedical sciences, chemical analysis, the aeronautical industry, etc. Basically, micro-valves are divided into passive valves and active valves, but both of these share the same flow characteristics. As an example, an analytical static-flow model of a diaphragm microvalve is presented here for us to understand why flexible diaphragm microvalves are desired in some applications. A cross-sectional view of a typical diaphragm microvalve is shown in Figure 5.13, containing both a diaphragm and a valve seat. As the viscosity flow through diaphragm microvalves can be considered as a viscosity flow through a slot with a varying gap resistance, the volume flow rate through the microvalve can be calculated as follows [23]:

$$Q = f(w, l) \times d^3 \times \Delta P / \eta \quad (5.81)$$

where $f(w, l)$ is a function related to the width (w) and the length (l), d is the height of the gap, ΔP is the fluid pressure drop through the gap and η is the viscosity of the fluid. One can see that the height of the gap is an important parameter affecting the valve flow characteristics. Basically, the gap height of the diaphragm microvalve is proportional to the pressure drop applied to the diaphragm:

$$d = f(w_d, t_d, l_d) \times \Delta F / E \quad (5.82)$$

where w_d, t_d and l_d are the width, thickness and length, respectively, of the diaphragm where the pressure drop is applied, ΔF is the net force applied on the diaphragm and E is the Young's modulus of the material used for the diaphragm. It should be pointed out have that the net force acting on the diaphragm is related to the inlet and outlet fluid pressures in the case of a 'passive' valve, while the actuating force needs to be accounted for in the calculation in the case of an 'active' valve. It is easy to see that with a fixed force, pressure drop and geometric parameters, the volume fluid flow rate increases significantly with the decreasing Young's modulus of the diaphragm material. Specifically, in the case of a passive

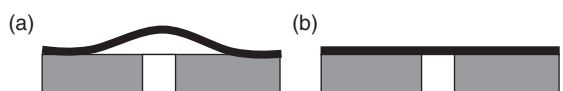


Figure 5.13 Cross-sectional views of a microvalve containing both a diaphragm and valve seat: (a) opened; (b) closed.

microvalve, the same pressure drop through the microvalves will generate larger flow rates or with smaller pressure drops the desired flow rate can be achieved when the diaphragm is made of a low-Young's-modulus material. In the case of an active microvalve, a smaller actuating force can be used to generate the designed flow rate. In addition to the high flow rate which is practical with a low Young's modulus, a large deflection of the valve diaphragm will ensure a lower 'leakage' of the valve [24]. The above general analysis can also be applied to a gas-flow microvalve [25]. Hence, materials with low Young's moduli and their fabrication processes are also important for microvalves in applications with large flow rates and low leakage requirements.

Micropumps are further primary components for microfluidic systems. Several micropumps have been developed with various actuation principles and designs [26]. Reciprocating diaphragm micropumps are one of the most extensively studied types of micropumps. A typical diaphragm micropump consists of an actuating diaphragm, two microvalves (or nozzles/diffusers [27]), micropump cavities, etc. (Figure 5.14). During the initial state, the actuation is off, both inlet and outlet valves are closed and there is no fluid flow in or out. Once the actuation is on and assuming that the actuation diaphragm can move upwards, the cavity volume will be expanded, hence resulting in the inside pressure being decreased. The inlet valve is then opened and the fluid flows into the pump cavity until the inside pressure is increased to its original level. Then, the actuation diaphragm moves downwards and the shrinkage of the pump cavity leads to the inside pressure increasing; the outlet valve is then opened and the fluid flows out of the pump cavity. By repeating the above steps, a continuous fluid flow can be realized by the micropump.

A static analytical model for diaphragm micropumps is given below in order to provide a better understanding

of the working behavior of micropumps. By considering a 'square actuation' diaphragm with a side length of $2a$, the deflection expression of the diaphragm can be written as follows:

$$\begin{aligned} w(x, y) &= \frac{49\Delta p a^4}{2304D} F(x, y) \\ F(x, y) &= \left(1 - \frac{x^2}{a^2}\right)^2 \left(1 - \frac{y^2}{a^2}\right)^2 \end{aligned} \quad (5.83)$$

where Δp is the net applied pressure on the diaphragm, $F(x, y)$ is a polynominal which satisfies the boundary conditions, D is the stiffness of the diaphragm (defined by $Eh^3/12(1 - v^2)$, where h is the diaphragm thickness), E is the Young's modulus of the diaphragm and v is the Poisson ratio. The 'stroke volume' of the diaphragm can be obtained from:

$$\Delta V = \int_{-a}^a \int_{-a}^a w(x, y) dx dy \quad (5.84)$$

It can be observed that the 'stroke volume' of the pump, ΔV , is inversely proportional to the Young's modulus, E , indicating that with the same conditions, a lower E will lead to a larger 'stroke volume' for the micropump. From the static model, the 'stroke volume' of the micropump is directly related to the pump flow rate. In addition, the 'stroke volume' is important for realizing a *self-priming* micropump which requires a large ratio between the 'stroke volume' and the dead volume, $\varepsilon(\equiv \Delta V/V_0)$ [26]. Therefore, a flexible actuation diaphragm for micropumps is expected in such applications which require a high pump flow rate and an excellent 'priming' performance. A micropump, fabricated using polymeric materials, is shown in Figure 5.15.

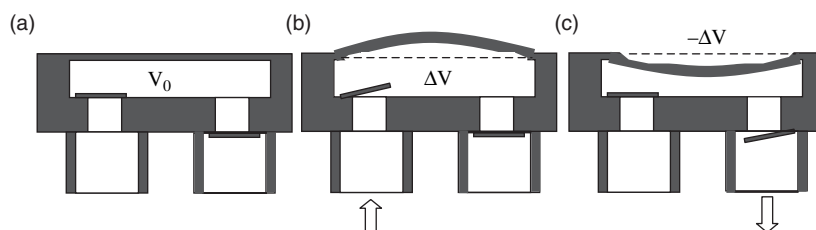


Figure 5.14 Working principle for a diaphragm micropump: (a) initial state; (b) supply mode; (c) pumping mode.

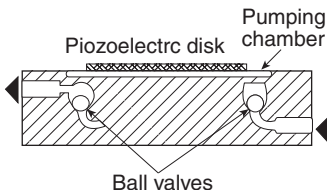


Figure 5.15 Schematic (cross-sectional view) of a polymer micropump fabricated using the microstereolithography (MSL) process [28]. M. C. Carrozza, N. Croce, B. Magnani, and P. Dario, ‘A piezoelectric-driven stereolithography-fabricated micropump’, *J. Micromech. Microeng.*, **5**, 1995, © IOP

REFERENCES

1. F.S. Foster, K.A. Harasiewicz and M.D. Sherar, ‘A history of medical and biological imaging with polyvinylidene fluoride (PVDF) transducers’, *IEEE Transactions: Ultrasonics, Ferroelectrics and Frequency Control*, **47**, 1363–1371 (2000).
2. Website: [http://www.msiusa.com/piezo_download_listing.htm#PART1-INT.pdf].
3. B. Zhu, ‘Design and development of PVDF based MEMS micro acoustic sensor and accelerometer’, *Ph.D. Dissertation*, Department of Engineering Science and Mechanics, Pennsylvania State University, State College, PA, USA (2001).
4. D.A. Neamen, *Semiconductor Physics and Devices*, McGraw-Hill, New Delhi, India (2002).
5. D.E. Oates, D.L. Smythe and J.B. Green, ‘SAW/FET programmable transversal filter with 100 MHz bandwidth and enhanced programmability’, in *Proceedings of the 1985 Ultrasonics Symposium*, IEEE, Piscataway, NJ, USA, pp. 124–129 (1985).
6. I. Yao and S.A. Reible, ‘Wide bandwidth acoustoelectric convolvers’, in *Proceedings of the 1979 Ultrasonics Symposium*, IEEE, Piscataway, NJ, USA, pp. 701–705 (1979).
7. R.A. Bergh, H.C. Lefevre and H.J. Shaw, ‘An overview of Fiber-optic gyroscopes’, *Journal of Lightwave Technology*, **LT-2**, 91–107 (1984).
8. S. Bennett, S. Emge and R. Dyott, ‘Fiber optic gyros for robotics’. Available online at: [http://www.kvh.com/pdf/fog_robots.pdf].
9. J. Martin, W. Bacher, O.F. Hagena and W. K. Schomburg, ‘Strain gauge pressure and volume-flow transducers made by thermoplastic molding and membrane transfer’, in *Proceedings of IEEE: MEMS’98*, IEEE, Piscataway, NJ, USA, pp. 361–366 (1998).
10. V.K. Varadan and V.V. Varadan, ‘Microsensors, microelectromechanical systems (MEMS) and electronics for smart structures and systems’, *Smart Materials and Structures*, **9**, 953–972 (2000).
11. M.J. Vellekoop, ‘Acoustic wave sensors and their technology’, *Ultrasonics*, **36**, 7–14 (1998).
12. J.A. Chilton and M.T. Goosney (Eds), *Special Polymers for Electronics and Optoelectronics*, Chapman & Hall, London, UK (1995).
13. J.S. Kim, ‘Wireless structural health monitoring using a PVDF interdigital transducer’, *Masters Thesis*, Pennsylvania State University, State College, PA, USA (2002).
14. J.D.N. Cheeke and Z. Wang, ‘Acoustic wave gas sensors’, *Sensors and Actuators: Chemical*, **B59**, 146–153 (1999).
15. J. Kondoh, K. Saito, S. Shiokawa and H. Suzuki, ‘Simultaneous measurements of liquid properties using shear horizontal surface acoustic wave sensors’, *Japan Journal of Applied Physics*, **35**(1, No. 5B), 3093–3096 (1996).
16. J. Kondoh and S. Shiokawa, ‘New application of shear horizontal surface acoustic wave sensors to identifying fruit juices’, *Japanese Journal of Applied Physics*, **33**(1, No. 5B), 3095–3099 (1994).
17. M. Cole, G. Sehra, J.W. Gardner and V.K. Varadan, ‘Development of smart tongue devices for measurement of liquid properties’, *IEEE Sensors Journal*, **4**, 543–550 (2004).
18. A. Leidl, I. Oberlack, U. Schaber, B. Mader and S. Drost, ‘Surface acoustic wave devices and applications in liquid sensing’, *Smart Material and Structures*, **6**, 680–688 (1997).
19. M. Rapp, J. Reibel, S. Stier, A. Voigt and J. Bahlo, ‘SAGAS: gas analyzing sensor systems based on surface acoustic wave devices – an issue of commercialization of SAW sensor technology’, in *Proceedings of the 1997 IEEE International Frequency Control Symposium*, IEEE, Piscataway, NJ, USA, pp. 129–132 (1997).
20. J.W. Grate, S.J. Patrash and S.N. Kaganove, ‘Inverse least-squares modeling of vapor descriptors using polymer-coated surface acoustic wave sensor array responses’, *Analytical Chemistry*, **73**, 5247–5259 (2001).
21. B.A. Auld, *Acoustic Fields and Waves in Solids*, 2nd Edn, Kreiger, Melbourne, FL, USA (1990).
22. E. Gizeli, A.C. Stevenson, N.J. Goddard and C.R. Lowe, ‘A novel Love-plate acoustic sensor utilizing polymer overlayers’, *IEEE Transactions: Ultrasonics, Ferroelectrics and Frequency Control*, **39**, 657–659 (1992).
23. R. Rossberg and H. Sandmaier, ‘Portable micro liquid dosing system’, in *Proceedings of IEEE: MEMS’98*, IEEE, Piscataway NJ, USA, pp. 526–531 (1998).
24. X. Yang, C. Grosjean, Y.C. Tai and C.M. Ho, ‘A MEMS thermopneumatic silicone rubber membrane valve’, *Sensors and Actuators: Physical*, **A64**, 101–108 (1998).
25. A.K. Henning, ‘Microfluidic MEMS’, in *Proceedings of the IEEE Aerospace Applications Conference*, Vol. **1**, Piscataway, NJ, USA, pp. 471–486 (1998).
26. M. Ritcher, R. Linnemann and P. Woias, ‘Robust design of gas and liquid micropumps’, *Sensors and Actuators: Physical*, **A68**, 480–486 (1998).
27. X.N. Jiang, Z.Y. Zhou, X.Y. Huang, Y. Li, Y. Yang and C.Y. Liu, ‘Micronozzle/diffuser flow and its application in micro valveless pumps’, *Sensors and Actuators: Physical*, **A70**, 81–87 (1998).
28. M.C. Carrozza, N. Croce, B. Magnani and P. Dario, ‘A piezoelectric-driven stereolithography-fabricated micropump’, *Journal of Micromechanical and Microengineering*, **5**, 177–179 (1995).

Part 3

Modeling Techniques

6

Introductory Concepts in Modeling

One of the fundamental concepts involved in mathematical modeling is to first generate the governing differential equation of the system. There are two ways of doing this. In the first method, the system is broken at the continuum level and a small block of this continuum is isolated as a free body and the 3-D state of stress, acting on the block, is written. Writing the equilibrium equation of this free body essentially gives the equation governing the system. 2-D and 1-D approximations can further be obtained from the 3-D equations of motion by converting the stresses into stress resultants through integration of the equation of motion in the directions where condensation of the dimension is desired. The method described above is the *Theory of Elasticity* procedure of obtaining the governing equation. One can see that, in this method, one has to deal with tensors and vectors. This chapter will give a complete bird's eye view of this method.

An alternate way of generating the governing equations is by the *energy method*, wherein minimization of the energy functional, will not only yield the desired governing equations but also their associated boundary conditions. This is the most widely used method in discrete modeling techniques (described in Chapter 7), where obtaining an approximate solution to the governing equation is the main goal. This chapter gives complete details of obtaining the energy functional from the continuum modeling and the associated energy theorems for obtaining an approximate solution to the governing equation.

The ease of embedding smart sensors and actuators in laminated composites has increased their popularity as structural materials. In addition to having low weight and high strength, laminated constructions enable the structures to become 'active' by placing the smart sensors and actuators at any desired location. Hence, one can find a variety of applications for the use of smart materials in

laminated composites reported in the literature. These structures are orthotropic in construction and hence their behavior is quite complex compared to metallic structures. Hence, the second part of this chapter deals with the basic theory related to the behavior of laminated composite structures.

Many analysis tools are required to study the functionality of the designed smart structures. The *Finite Element Method* (FEM) is extensively used for this purpose. However, when the frequency content of the load is very high (which is very relevant in the case of impact-related problems) or when one is addressing *Structural Health Monitoring* (SHM) in composites (here, for small flaw sizes, only the higher modes get altered), FEM may lead to enormous problem sizes due to the small element size requirement. Hence, the FE solution may be computationally prohibitive. In such a situation, wave-based techniques are extensively used. Hence, the last part of this chapter gives the introductory concepts of wave propagation. The details of FE and wave modeling are given in Chapter 7.

6.1 INTRODUCTION TO THE THEORY OF ELASTICITY

6.1.1 Description of motion

Consider a body undergoing deformation to some applied loading (Figure 6.1). Let u_i^0 be its position at the time $t = 0$ (undeformed) configuration and u_i^t its position after some time $t = t$. In terms of the unit vectors e_i , they can be expressed as follows:

$$\begin{aligned} \text{Undeformed position : } & u^0 = u_i^0 e_i \\ \text{Deformed position : } & u = u_i^t e_i \end{aligned}$$

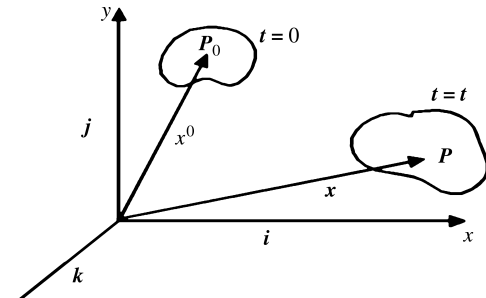


Figure 6.1 Undefomed and deformed configurations of a body.

Hence, the motion can be expressed as:

$$u_i = u_i(x^0, y^0, z^0, t) \quad \text{or} \quad u_i^0 = u_i^0(x, y, z, t) \quad (6.1)$$

The former represents the Eulerian coordinates, which are normally used to represent a fluid in motion. Here, the independent variables are the position vector u_i at a given instant. The latter is called the *Lagrangian variable*, where quantities are expressed in terms of the initial position vector u_i^0 and time. The difference between these two motion descriptions can be stated as:

- **Langragian:** If we put a rectangular grid on an undefomed body and visualize this grid after deformation, it will look like that shown in Figure 6.2(a).
- **Eulerian:** If we put a rectangular grid on a deformed body and visualize it in the undefomed state, it will look like that shown in Figure 6.2(b).

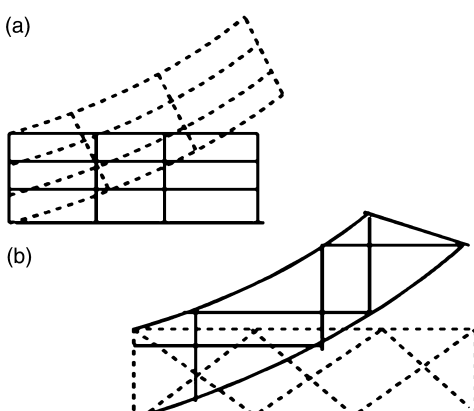


Figure 6.2 Grids describing (a) Lagrangian and (b) Eulerian motions.

Due to the above definitions, evaluation of the material derivatives will defer. For example, in the Langrangian frame of reference, the derivative of $u(x^0, y^0, z^0, t)$ is given by:

$$\frac{du}{dt} = \frac{\partial u}{\partial t} + \frac{\partial u}{\partial x} \frac{dx}{dt} + \frac{\partial u}{\partial y} \frac{dy}{dt} + \frac{\partial u}{\partial z} \frac{dz}{dt} \quad (6.2)$$

In the Eulerian frame of reference, the derivative of $u(x, y, z, t) = u(x^0, y^0, z^0, t)$ is given by:

$$\begin{aligned} \frac{du}{dt} &= \frac{\partial u}{\partial t} + \frac{\partial u}{\partial x} \frac{dx}{dt} + \frac{\partial u}{\partial y} \frac{dy}{dt} + \frac{\partial u}{\partial z} \frac{dz}{dt} \\ &= \frac{\partial u}{\partial t} + v_x \frac{\partial u}{\partial x} + v_y \frac{\partial u}{\partial y} + v_z \frac{\partial u}{\partial z} \end{aligned} \quad (6.3)$$

where v_x , v_y and v_z are the convective velocities in the three material directions. Deformation is defined as the comparison of two states, namely the initial and the final configurations. The motion of the particle is defined in terms of its coordinates attached to the particle, while displacement is defined as the shortest distance traveled when a particle moves from one location to the other. That is, if the position vectors of two points are r_1 and r_2 , the displacement vector u is given by:

$$\begin{aligned} u &= r_2 - r_1 = (x_2 i + y_2 j + z_2 k) - (x_1 i + y_1 j + z_1 k) \\ &\quad \text{or} \\ u &= (x_2 - x_1)i + (y_2 - y_1)j + (z_2 - z_1)k \end{aligned} \quad (6.4)$$

The deformation gradient is an important parameter which is extensively used in the theory. Let us now compute the deformation gradients. These relate the behaviors of the neighboring particles. Consider points P_0 and P'_0 at time $t = 0$, which are at a distance given by the vector $d\hat{r}_0 = dx^0 i + dy^0 j + dz^0 k$ (Figure 6.3). At some time t , if

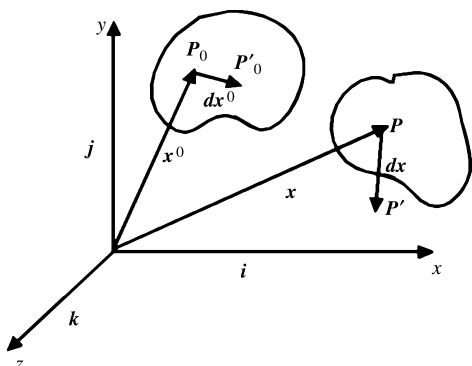


Figure 6.3 Deformation of neighboring points.

these two points move to the new locations P and P' the new distance between them is given by the vector $\hat{r} = dx_i + dy_j + dz_k$. The location of P' , with respect to P is now given by $\hat{r} + d\hat{r} = (x + dx)i + (y + dy)j + (z + dz)k$. Now consider the first term in the vector, namely $(x + dx)$. Expanding this term in a Taylor series with respect to the variables corresponding to time $t = 0$, we get:

$$x + dx = x + \frac{\partial x}{\partial x^0} dx^0 + \frac{\partial x}{\partial y^0} dy^0 + \frac{\partial x}{\partial z^0} dz^0 \dots \quad (6.5)$$

This gives the relation:

$$dx = \frac{\partial x}{\partial x^0} dx^0 + \frac{\partial x}{\partial y^0} dy^0 + \frac{\partial x}{\partial z^0} dz^0$$

Similarly, one can write:

$$\begin{aligned} dy &= \frac{\partial y}{\partial x^0} dx^0 + \frac{\partial y}{\partial y^0} dy^0 + \frac{\partial y}{\partial z^0} dz^0 \text{ and} \\ dz &= \frac{\partial z}{\partial x^0} dx^0 + \frac{\partial z}{\partial y^0} dy^0 + \frac{\partial z}{\partial z^0} dz^0 \end{aligned}$$

These relations can be written in tensorial notations as:

$$dx_i = \frac{\partial x_i}{\partial x_j^0} dx_j^0 \quad i, j = 1, 2 \text{ and } 3 \quad (6.6)$$

where i and j correspond to the three coordinate directions, namely x , y and z . Similarly, the motion of the particles at time $t = 0$ can be expressed in terms of the current time t as:

$$dx_i^0 = \frac{\partial x_i^0}{\partial x_j} dx_j \quad i, j = 1, 2 \text{ and } 3 \quad (6.7)$$

The quantities $\partial x_i / \partial x_j^0$ and $\partial x_i^0 / \partial x_j$ are called the deformation gradients and form the basis of description of any deformation. Equations (6.6) and (6.7), when expanded and written in the matrix form, become:

$$\begin{aligned} \{dx\} &= [J_0]\{dx^0\} \\ &= \begin{Bmatrix} dx \\ dy \\ dz \end{Bmatrix} = \begin{bmatrix} \frac{\partial x}{\partial x^0} & \frac{\partial x}{\partial y^0} & \frac{\partial x}{\partial z^0} \\ \frac{\partial y}{\partial x^0} & \frac{\partial y}{\partial y^0} & \frac{\partial y}{\partial z^0} \\ \frac{\partial z}{\partial x^0} & \frac{\partial z}{\partial y^0} & \frac{\partial z}{\partial z^0} \end{bmatrix} \begin{Bmatrix} dx^0 \\ dy^0 \\ dz^0 \end{Bmatrix} \quad (6.8) \end{aligned}$$

$$\begin{Bmatrix} dx^0 \\ dy^0 \\ dz^0 \end{Bmatrix} = \begin{bmatrix} \frac{\partial x^0}{\partial x} & \frac{\partial x^0}{\partial y} & \frac{\partial x^0}{\partial z} \\ \frac{\partial y^0}{\partial x} & \frac{\partial y^0}{\partial y} & \frac{\partial y^0}{\partial z} \\ \frac{\partial z^0}{\partial x} & \frac{\partial z^0}{\partial y} & \frac{\partial z^0}{\partial z} \end{bmatrix} \begin{Bmatrix} dx \\ dy \\ dz \end{Bmatrix} \quad (6.9)$$

The determinant of the matrices $[J]$ and $[J_0]$ is defined as the Jacobian. Since the deformation is continuous, it requires that the value of the Jacobian not be equal to zero. Since no region of finite volume can be deformed into a region of zero or infinite volume, it is required that they follow the following conditions:

$$0 < J_0 < \infty, \quad 0 < J < \infty \quad (6.10)$$

This condition is very useful to check and see if the deformation is physically possible. From the above results, it is straightforward to write the deformation of *lines*, *areas* and *volumes*. A line along the x -axis before deformation is represented by a vector $dx^0 = dx^0 i + dy^0 j + dz^0 k = dx_i^0$. After deformation, this line becomes:

$$d\hat{x} = \frac{\partial x}{\partial x^0} dx^0 i + \frac{\partial y}{\partial x^0} dx^0 j + \frac{\partial z}{\partial x^0} dx^0 k \quad (6.11)$$

Even though the initial vector is horizontal, the deformed configuration will have components in all three directions. Similarly, one can write the deformation of areas and volumes as:

$$dA_k = J_0 \frac{\partial x_p^0}{\partial x_k} dA_p^0, \quad dV = J_0 dV^0 \quad (6.12)$$

where J_0 is Jacobian with respect to the horizontal direction, dA_p^0 is the initial area vector and dA_k is the final area vector. In addition, dV^0 is the volume before deformation, while dV represent the same parameter after deformation. Here, the Jacobian is a function of two coordinates for area transformation and all three coordinates for volume transformation.

6.1.2 Strain

Strain is a measure of the relative displacement of particles within a body and is an essential ingredient for the description of the constitutive behavior of the materials. There are three different measures of strain.

These can be described on a specimen of original and final length L_0 and L as:

- Engineering strain, $\varepsilon = \frac{\text{Change in length}}{\text{Original length}} = \frac{\Delta L}{L_0}$
- True strain, $\varepsilon^T = \frac{\text{Change in length}}{\text{Final (current) length}} = \frac{\Delta L}{L} = \frac{\Delta L}{L_0 + \Delta L}$
- Logarithmic strain, $\varepsilon^N = \int_{L_0}^L \text{True strain} = \int_{L_0}^L \frac{dL}{L} = \ln\left(\frac{L}{L_0}\right)$

Using the above definitions, the final length L can be written in terms of these strains as:

- Engineering strain $L = L_0 + \Delta L = L_0 + L_0\varepsilon = L_0(1 + \varepsilon)$
- True strain $L = L_0 + \Delta L = L_0 + \frac{\varepsilon^T L_0}{(1 - \varepsilon^T)} = \frac{L_0}{(1 - \varepsilon^T)}$
- Logarithmic strain $L = L_0 \exp(\varepsilon^N)$

Using the basic definitions of the above strain measures, we can also write the relationship among them as:

$$\varepsilon^T = \frac{\varepsilon}{1 + \varepsilon}, \quad \varepsilon^N = \ln(1 + \varepsilon)$$

Strain measures are normally established by considering the change in the distance between two neighboring material particles. Consider two material particles having coordinates (x^0, y^0, z^0) and $(x^0 + dx^0, y^0 + dy^0, z^0 + dz^0)$. After the motion, these particles will have the coordinates (x, y, z) and $(x + dx, y + dy, z + dz)$. The initial and final distances between these neighboring particles are given by:

$$ds_0^2 = (dx^0)^2 + (dy^0)^2 + (dz^0)^2 \quad (6.13)$$

$$ds^2 = (dx)^2 + (dy)^2 + (dz)^2 \quad (6.14)$$

Using Equation (6.8) in Equation (6.14) we get:

$$ds^2 = \{dx\}^T \{dx\} = \{dx^0\}^T [J_0]^T [J_0] \{dx^0\} \quad (6.15)$$

In the event of deformation, ds^2 is different from ds_0^2 . That is:

$$\begin{aligned} ds^2 - ds_0^2 &= \{dx^0\}^T [J_0]^T [J_0] \{dx_0\} - \{dx^0\}^T \{dx^0\} \\ &= \{dx^0\}^T \left[[J_0]^T [J_0] - [I] \right] \{dx^0\} \\ &= 2\{dx^0\}^T [E] \{dx^0\} \end{aligned} \quad (6.16)$$

The above measure gives the relative displacements between the two material particles, which is insensitive

to the rotations. If the Eulerian frame of reference is used, then the relative displacement is given by:

$$\begin{aligned} dS^2 - dS_0^2 &= \{dx\}^T \{dx\} - \{dx\}^T [J]^T [J] \{dx\} \\ &= \{dx\}^T \left[[I] - [J]^T [J] \right] \{dx\} \\ &= 2\{dx\}^T [e] \{dx\} \end{aligned} \quad (6.17)$$

In Equations (6.16) and (6.17), the matrices $[E]$ and $[e]$ are the Lagrangian and Eulerian strain tensors. In tensorial form, they are given by:

$$E_{ij} = \frac{1}{2} \left(\frac{\partial x_m}{\partial x_{0i}} \frac{\partial x_m}{\partial x_{0j}} - \delta_{ij} \right), \quad e_{ij} = \frac{1}{2} \left(\delta_{ij} - \frac{\partial x_{0m}}{\partial x_i} \frac{\partial x_{0m}}{\partial x_j} \right) \quad (6.18)$$

The physical significance of E_{ij} and e_{ij} can be established by considering a line element of length $dx^0 = dS_0$. The deformation of the line element is given by dS . The extension of the line element per unit length (E_1) is given by:

$$E_1 = \frac{dS - dS_0}{dS_0} \quad \text{or} \quad dS = (1 + E_1)dS_0 \quad (6.19)$$

From equation (6.16), we have:

$$ds^2 - ds_0^2 = 2E_{11}dS_0^2$$

Combining the above, we can establish the relationship between E_1 and E_{11} as:

$$E_{11} = E_1 + \frac{1}{2}E_1^2 \quad \text{or} \quad E_1 = \sqrt{1 + 2E_{11}} - 1 \quad (6.20)$$

Expanding the right-hand term by binomial expansion, we get:

$$\begin{aligned} E &= (1 + E_{11} - \frac{1}{2}E_{11}^2 + \dots) - 1 \\ &= E_{11} - \frac{1}{2}E_{11}^2 \end{aligned} \quad (6.21)$$

For very small E_{11} , $E_1 = E_{11}$, which simply says that E_{11} can be interpreted as an elongation per unit length only when the extension is very small. Similarly, we can write:

$$E_2 = \sqrt{1 + 2E_{22}} - 1, \quad E_3 = \sqrt{1 + 2E_{33}} - 1 \quad (6.22)$$

for line elements in the other two directions.

6.1.3 Strain–displacement relationship

In most of the analysis methods to follow, it is customary to deal with the displacement and displacement gradients rather than deformation gradients. If u , v and w are the three displacements in the three coordinate directions, then, we can write:

$$\begin{aligned} x &= x^0 + u, \quad y = y^0 + v, \quad z = z^0 + w \\ \text{or } x^0 &= x - u, \quad y^0 = y - v, \quad z^0 = z - w \end{aligned} \quad (6.23)$$

The derivatives of these can be written as follows:

$$\begin{aligned} \frac{\partial x}{\partial x^0} &= 1 + \frac{\partial u}{\partial x^0}, \quad \frac{\partial y}{\partial x^0} = \frac{\partial v}{\partial x^0}, \quad \frac{\partial z}{\partial x^0} = \frac{\partial w}{\partial x^0} \\ \frac{\partial x}{\partial y^0} &= \frac{\partial u}{\partial y^0}, \quad \frac{\partial y}{\partial y^0} = 1 + \frac{\partial v}{\partial y^0}, \quad \frac{\partial z}{\partial y^0} = \frac{\partial w}{\partial y^0} \\ \frac{\partial x}{\partial z^0} &= \frac{\partial u}{\partial z^0}, \quad \frac{\partial y}{\partial z^0} = \frac{\partial v}{\partial z^0}, \quad \frac{\partial z}{\partial z^0} = 1 + \frac{\partial w}{\partial z^0} \end{aligned}$$

In tensorial form, we can write the above equations as:

$$\frac{\partial x_m}{\partial x_i^0} = \frac{\partial u_m}{\partial x_i^0} + \delta_{im} \quad (6.24)$$

Similarly, one can write:

$$\begin{aligned} \frac{\partial x^0}{\partial x} &= 1 - \frac{\partial u}{\partial x}, \quad \frac{\partial y^0}{\partial x} = -\frac{\partial v}{\partial x}, \quad \frac{\partial z^0}{\partial x} = -\frac{\partial w}{\partial x} \\ \frac{\partial x^0}{\partial y} &= -\frac{\partial u}{\partial y}, \quad \frac{\partial y^0}{\partial y} = 1 - \frac{\partial v}{\partial y}, \quad \frac{\partial z^0}{\partial y} = -\frac{\partial w}{\partial y} \\ \frac{\partial x^0}{\partial z} &= -\frac{\partial u}{\partial z}, \quad \frac{\partial y^0}{\partial z} = -\frac{\partial v}{\partial z}, \quad \frac{\partial z^0}{\partial z} = 1 - \frac{\partial w}{\partial z} \end{aligned}$$

In tensorial form, the above equations become:

$$\frac{\partial x_{0m}}{\partial x_i} = \delta_{im} - \frac{\partial u_m}{\partial x_i} \quad (6.25)$$

where, δ_{ij} is the *Kronecker delta*. Substituting Equations (6.24) and (6.25) in the Lagrangian and Eulerian strain tensors (Equation (6.18)), we get after some simplification:

$$\begin{aligned} E_{ij} &= \frac{1}{2} \left[\frac{\partial u_i}{\partial x_j^0} + \frac{\partial u_j}{\partial x_i^0} + \frac{\partial u_m}{\partial x_i^0} \frac{\partial u_m}{\partial x_j^0} \right] \\ e_{ij} &= \frac{1}{2} \left[\frac{\partial u_i}{\partial x_j} + \frac{\partial u_j}{\partial x_i} + \frac{\partial u_m}{\partial x_i} \frac{\partial u_m}{\partial x_j} \right] \end{aligned} \quad (6.26)$$

The first two terms in the above two equations represent the linear part of the strain tensors, while the last term

represents the non-linear part. Both these tensors are symmetric. When the displacement gradients are very small, we can neglect the non-linear parts of the above tensors. Thus, infinitesimal strain components have direct interpretations as extensions or changes of angles. Furthermore, the magnitudes of the strains are very small compared to unity, which means that the deformations are very small. Hence, we can conclude for very small deformations:

$$E_{ij} = \varepsilon_{ij} = e_{ij}$$

Expanding the linear part of Equation (6.26), we get:

$$\begin{aligned} \varepsilon_{11} &= \frac{\partial u}{\partial x^0}, \quad \varepsilon_{12} = \frac{1}{2} \left[\frac{\partial u}{\partial y^0} + \frac{\partial v}{\partial x^0} \right], \quad \varepsilon_{13} = \frac{1}{2} \left[\frac{\partial u}{\partial z^0} + \frac{\partial w}{\partial x^0} \right] \\ \varepsilon_{22} &= \frac{\partial v}{\partial y^0}, \quad \varepsilon_{23} = \frac{1}{2} \left[\frac{\partial v}{\partial z^0} + \frac{\partial w}{\partial y^0} \right], \quad \varepsilon_{33} = \frac{\partial w}{\partial z^0} \end{aligned} \quad (6.27)$$

In addition, for small deformations, following condition is normally true. That is:

$$\frac{u_i}{L} \ll 1$$

where L is the smallest dimension of the body. If the above condition is true, then we can conclude that $x_i^0 = x_i$. That is, we do not differentiate between Eulerian and Lagrangian coordinates. Hence, the functional form of displacement and its components become identical in these two frames of reference. Henceforth, we will use ε_{ij} to denote both the Eulerian and Lagrangian strain tensors and x_i to represent their coordinates. We will extensively use Equation (6.27) in the later chapters on composites, finite element analysis and wave propagation.

In terms of displacements, the rotation terms can be written in tensorial form as:

$$\omega_{ij} = \frac{1}{2} \left(\frac{\partial u_j}{\partial x_i} - \frac{\partial u_i}{\partial x_j} \right) \quad (6.28)$$

This is a second-order tensor that is antisymmetric. In matrix form, the diagonal term is always zero. In the 2-D case, there is only one non-vanishing component of the above tensor, which is given by

$$\omega_{xy} = \frac{1}{2} \left(\frac{\partial v}{\partial x} - \frac{\partial u}{\partial y} \right) \quad (6.29)$$

6.1.3.1 Stress

Strains (deformations) are normally caused by forces or moments exerted on the mass of the continuum or through the contacts contained in the mass. The contact forces are normally referred to as *surface tractions* as their effects occur on the surface of the continuum. The different types of forces or moments can be *Extrinsic*, *Mutual* or *Contact-type*, depending upon the way these act on a body. Extrinsic forces are the external forces that act outside the body under consideration, such as gravity loads, magnetic loads, etc. Mutual forces are those that arise within the body. The most general type of forces encountered in many phenomena is the contact type of force that generates what we call *Stress* or *Pressure*.

To explain the concept of stress, let us consider a small surface element of area ΔA in the deformed configuration, as shown in Figure 6.4. The forces and moments should be acting in this small elemental area such that they cancel each other out, or in other words, the elemental area should be in equilibrium. These forces can be thought of as contact forces although they act inside a body. Let \hat{n} be the unit vector, which is perpendicular to the surface of the elemental area, and let $\Delta \hat{f}$ be the resultant force exerted for the other part of the surface element. In the limiting case of ΔA becoming very small, we get what is called the *Traction Vector*, which is given by:

$$\hat{t}^{(n)} = \frac{d\hat{f}}{dA} = \lim_{\Delta A \rightarrow 0} \frac{\Delta \hat{f}}{\Delta A} \quad (6.30)$$

The above limit is possible due to the assumption that the material is continuous. This traction vector has a unit of force per unit area acting on the surface. Note that the use

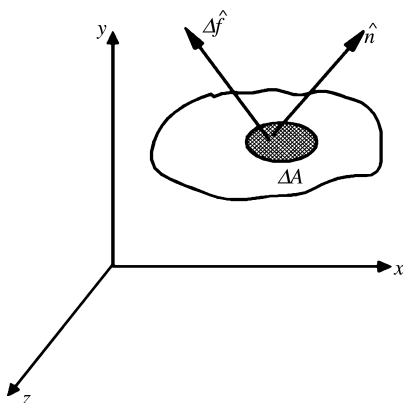


Figure 6.4 A section of an arbitrary continuum.

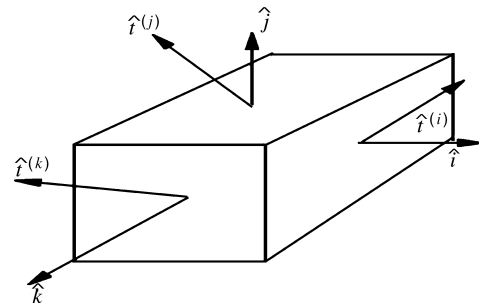


Figure 6.5 Stress cube with stress vectors and an outward unit normal.

of \hat{n} is to remind the reader that these traction vectors are dependent on the orientation of the area. To give an explicit representation of the traction vector, let us consider a cube, as shown in Figure 6.5. Let us now write the components of the vector on this cube on three faces as shown. On face 1, we have:

$$\hat{n} = i, \quad \hat{t}^{(n)} = \hat{t}^{(i)} = t_i \hat{e}_i = t_x^{(i)} i + t_y^{(i)} j + t_z^{(i)} k$$

While on face 2, we have:

$$\hat{n} = j, \quad \hat{t}^{(n)} = \hat{t}^{(j)} = t_j \hat{e}_j = t_x^{(j)} i + t_y^{(j)} j + t_z^{(j)} k$$

The above definitions can be simplified by introducing the following notation, $\sigma_{ij} = t_j^{(e_i)}$. That is, $\sigma_{xx} = t_x^{(i)}$, $\sigma_{xz} = t_z^{(i)}$, $\sigma_{zx} = t_x^{(k)}$, ..., etc. Hence, it can be said that the projections of the traction vector $\hat{t}^{(n)}$ on the faces are the normal stress components, σ_{xx} , σ_{yy} and σ_{zz} , while the projections perpendicular to the outward normal \hat{n} are the shear stress components, σ_{xy} , σ_{yz} , σ_{zx} , σ_{yx} , σ_{zy} and σ_{xz} . Thus, unlike deformations, stress is a second-order tensor having both direction and a plane of application. The matrix containing the elements of the stress components $[\sigma_{ij}]$, in all 9, is called *Cauchy's Stress Tensor*. It will be shown later that this tensor is symmetric, meaning $\sigma_{ij} = \sigma_{ji}$. Next, we can establish the relation between the traction vector \hat{t} and the outward normal \hat{n} . For this purpose, consider an arbitrary surface of a tetrahedron, as shown in Figure 6.6.

On the faces perpendicular to the coordinates, the components of the three stress vectors are denoted by the respective stress components (σ_{ij}) on the plane in which they are acting. These are the following:

- The stresses acting on the x -axis face: σ_{xx} , σ_{xy} and σ_{xz} .
- The stresses acting on the y -axis face: σ_{yx} , σ_{yy} and σ_{yz} .
- The stresses acting on the z -axis face: σ_{zx} , σ_{zy} and σ_{zz} .

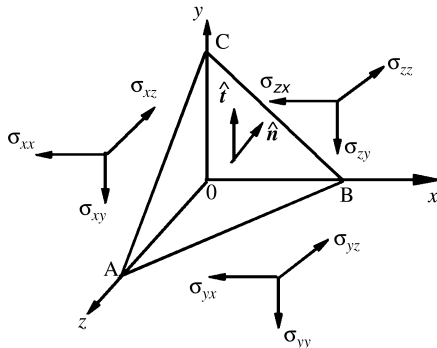


Figure 6.6 Stresses acting on an arbitrary surface of a tetrahedron.

The stress vector acting on the inclined surface ABC is \hat{t} and the unit normal vector \hat{n} . The equilibrium of the tetrahedron requires that the resultant force acting on it must vanish.

Writing the equilibrium along the x -direction, we get:

$$t_x dA - \sigma_{xx} dA_x - \sigma_{yx} dA_y - \sigma_{zx} dA_z + b_x \rho dV = 0$$

where b_x is the x -component of the body force vector \hat{b} , which has a unit of force per unit volume. Here, t_x is the x -component of the stress vector, dA_x , dA_y and dA_z are the areas of the faces perpendicular to the coordinate axes x , y and z and dA is the area of the inclined surface. In addition, we have $dV = (1/3)hdA$ as the volume of the tetrahedron, where h is the smallest distance from any point to the inclined surface ABC. Furthermore, the outward normal vector can be written in terms of unit vectors along the three coordinate directions as $\hat{n} = n_x i + n_y j + n_z k$. The elemental areas, dA_i , can now be written in terms of the components of the unit normal vector as:

$$dA_x = n_x dA, \quad dA_y = n_y dA, \quad dA_z = n_z dA$$

and letting $dA \rightarrow 0$, we get:

$$t_x = \sigma_{xx} n_x + \sigma_{yx} n_y + \sigma_{zx} n_z \quad (6.31)$$

Similarly, equilibrium of the forces in y and z will give:

$$t_y = \sigma_{xy} n_x + \sigma_{yy} n_y + \sigma_{zy} n_z, \quad t_z = \sigma_{xz} n_x + \sigma_{yz} n_y + \sigma_{zz} n_z \quad (6.32)$$

Hence, we can write these equations in tensorial notation as:

$$t_i = \sigma_{ji} n_j \quad (6.33)$$

The above relation is valid for any value of the outward normal vector \hat{n} and in any coordinate system. Hence, it can be concluded that the state of stress in a body is completely known if the stress tensor σ_{ij} is given. In other words, given any surface with the unit normal vector \hat{n} , it will be possible to determine the stress vector (force intensity) acting on that surface if the stress tensor is known.

6.1.3.2 Principal stress

It is established now that the stress vector acting on a surface depends on the direction \hat{n} and in general this is not parallel to \hat{n} . Now, we will attempt to find \hat{n} such that the stress vector is acting in the direction of \hat{n} . That is:

$$t_i = \lambda n_i \quad (6.34)$$

where λ is a scalar representing the magnitude of the stress vector. The direction n_i that satisfies the above condition is the principal direction and λ is called the principal stress. Substituting Equation (6.33) in to Equation (6.34), we get:

$$\sigma_{ji} n_j = \lambda n_i$$

The above equation can be written in the matrix form as

$$[\sigma] - \lambda [I] \{n\} = 0 \quad (6.35)$$

In other words, the above problem reduces to a standard eigenvalue problem of size 3×3 with eigenvectors giving the principal directions n_1, n_2 and n_3 and the eigenvalues giving the principal stresses λ_1, λ_2 and λ_3 . This problem can be solved by equating the determinant of the matrix $[\sigma] - \lambda [I]$ to zero, as done in conventional eigenvalue problems. When the determinant of the above matrix is expanded, we get the following cubic polynomial equation in λ :

$$\lambda^3 - I_1 \lambda^2 + I_2 \lambda - I_3 = 0 \quad (6.36)$$

Here, I_1, I_2 and I_3 are the stress invariants, that is, their values do not change with the coordinate system being used. They can be written both in terms of the components of the stress tensor σ_{ij} or the principal stresses λ_i as:

$$I_1 = \sigma_{xx} + \sigma_{yy} + \sigma_{zz} = \sigma_{ii} = \lambda_1 + \lambda_2 + \lambda_3$$

$$I_2 = \frac{1}{2} (I_1^2 - \sigma_{ij} \sigma_{ij}) = \lambda_1 \lambda_2 + \lambda_2 \lambda_3 + \lambda_3 \lambda_1$$

$$I_3 = \frac{1}{3} (3I_1 I_2 - I_1^3 + \sigma_{ij} \sigma_{jk} \sigma_{kl}) = \lambda_1 \lambda_2 \lambda_3 \quad (6.37)$$

In addition, the principal directions n_i will have to satisfy the relation:

$$n_1^2 + n_2^2 + n_3^2 = 1 \quad (6.38)$$

From the theorem relating to eigenvalue analysis, it can be easily shown that the eigenvalues are always real since the stress tensor is symmetric (which will be shown later) and hence the principal directions are mutually orthogonal.

6.1.3.3 Normal stress

To obtain normal stresses from Cauchy's stress tensor, we define the normal stress σ_n as the component of the stress vector in the direction of unit normal \hat{n} to the surface of interest. This is obtained by taking the dot product of the stress vector and the normal vector, that is:

$$\sigma_n = t_i n_i = \sigma_{ij} n_i n_j$$

If the coordinate axes are chosen such that they are aligned in the direction of principal stresses, then Cauchy's stress tensor becomes diagonal with:

$$\sigma_{xx} = \lambda_1, \quad \sigma_{yy} = \lambda_2, \quad \sigma_{zz} = \lambda_3$$

Hence, the normal stress can be evaluated from the expression:

$$\sigma_n = \lambda_1 n_1^2 + \lambda_2 n_2^2 + \lambda_3 n_3^2 \quad (6.39)$$

If $\lambda_1 > \lambda_2 > \lambda_3$, then by using Equation (6.38) in Equation (6.39) we can conclude that $\lambda_1 > \sigma_n > \lambda_3$, from which we get that λ_1 and λ_3 are the maximum and minimum normal stresses, respectively, at the point under consideration.

6.1.3.4 Shear stress

We can also extract the shear stresses from Cauchy's stress tensor. Projection of the stress vector on any surface of interest will give the shear stress vector $\hat{\tau}$. Mathematically, this can be represented as follows. The stress vector equation can be split in terms of normal and shear stress tensors as:

$$\hat{t} = \sigma_n \hat{n} + \hat{\tau}, \quad \text{or} \quad \hat{\tau} = \hat{t} - \sigma_n \hat{n} \quad (6.40)$$

The magnitude of the shear stress τ can be written as:

$$\tau^2 = |\hat{\tau}|^2 - \sigma_n^2 = t_i t_i - \sigma_n^2 = t_x^2 + t_y^2 + t_z^2 - \sigma_n^2$$

where $|\hat{\tau}|$ is the magnitude of the stress vector. In arriving at the above relation, we have used the relation $|\hat{n}| = 1$. If we assume that the coordinate axes coincide with the principal direction, then we have:

$$t_x = \lambda_1 n_x, \quad t_y = \lambda_2 n_y, \quad t_z = \lambda_3 n_z \quad (6.41)$$

Using Equation (6.41), we can write the magnitude of the stress vector $|\hat{\tau}|^2$ as:

$$|\hat{\tau}|^2 = t_i t_i = t_x^2 + t_y^2 + t_z^2 = \lambda_1^2 n_x^2 + \lambda_2^2 n_y^2 + \lambda_3^2 n_z^2 \quad (6.42)$$

Using Equation (6.42), the magnitude of the shear stress can now be written as:

$$\begin{aligned} \tau^2 &= \lambda_1^2 n_x^2 + \lambda_2^2 n_y^2 + \lambda_3^2 n_z^2 - \lambda_1 n_x^2 + \lambda_2 n_y^2 + \lambda_3 n_z^2 \\ &= n_x^2 (1 - n_x^2) \lambda_1^2 + n_y^2 (1 - n_y^2) \lambda_2^2 + n_z^2 (1 - n_z^2) \lambda_3^2 \\ &\quad - 2\lambda_1 \lambda_2 n_x^2 n_y^2 - 2\lambda_2 \lambda_3 n_y^2 n_z^2 - 2\lambda_3 \lambda_1 n_z^2 n_x^2 \end{aligned}$$

Using Equation (6.38) in the above equation to replace the terms in parentheses, for example, $1 - n_1^2 = n_2^2 + n_3^2$, we can write the magnitude of the shear stress as:

$$\begin{aligned} \tau^2 &= n_1^2 n_2^2 (\lambda_1 - \lambda_2)^2 + n_2^2 n_3^2 (\lambda_2 - \lambda_3)^2 \\ &\quad + n_3^2 n_1^2 (\lambda_3 - \lambda_1)^2 \end{aligned} \quad (6.43)$$

From this relation, it is clear that the magnitude of the shear stress is zero on the surfaces with:

$$\begin{aligned} n_1 &= 1, & n_2 &= n_3 = 0, & n_2 &= 1, \\ n_1 &= n_3 = 0, & n_3 &= 1, & n_1 &= n_2 = 0 \end{aligned}$$

On these surfaces, the normal stresses σ_n are either minimum or maximum values. For example, consider the surface that contains the y -axis with $n_2 = 0$. From Equation (6.43), the magnitude of the shear stress becomes:

$$\tau^2 = n_3^2 n_1^2 (\lambda_3 - \lambda_1)^2 = (1 - n_1^2) n_1^2 (\lambda_3 - \lambda_1)^2$$

The maximum value of the shearing stress occurs at:

$$\frac{\partial(\tau^2)}{\partial n_1} = 0 = (2n_1 - 4n_1^3)(\lambda_3 - \lambda_1)^2$$

which gives $n_1 = \pm 1/\sqrt{2} = n_3$. That is, the maximum shearing stress occurs on the surfaces bisecting the angle

between the x - and z -axes. The corresponding value of the shearing stress is:

$$\tau_{\max}^2 = \frac{1}{4}(\lambda_3 - \lambda_1)^2$$

The above expression, which is normally found in many elementary ‘Strength of Materials’ textbooks, is true if $\lambda_1 > \sigma_n > \lambda_3$ is true.

6.1.4 Governing equations of motion

There are a number of ways to derive the governing differential equations of a continuum. The most common method is to draw the free-body diagram of an isolated volume of the continuum and establish the equilibrium of forces in all of the three coordinate directions to get the required governing equations. However, here we will use Newton’s Second Law of Motion for not only deriving the governing equation, but to also establish the symmetry of Cauchy’s stress tensor.

Consider a body of density ρ and volume V , as shown in Figure 6.7. Let the body be subjected to a surface traction $\hat{t} = t_x i + t_y j + t_z k$ and a body force per unit volume $\hat{b} = b_x i + b_y j + b_z k$. Newton’s Laws of Motion relating to force and moment equilibrium for a body of mass m and having acceleration \hat{a} is given by:

$$\sum \hat{F} = m\hat{a}, \quad \sum \hat{M} = m\hat{x} \times \hat{a}$$

where \hat{F} is the resultant force vector, \hat{M} is the resultant moment vector and $\hat{x} = xi + yj + zk$ is the position vector of the resultant force. Applying these two laws to the

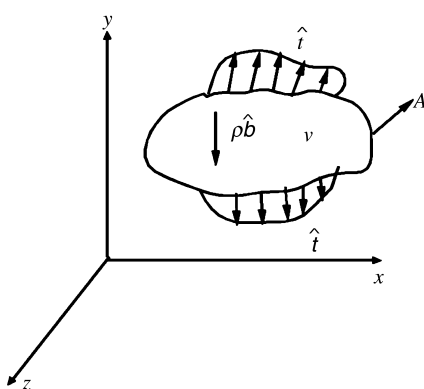


Figure 6.7 Arbitrary small volume under the action of forces.

elemental volume shown in Figure 6.7, we get

$$\int_A \hat{i} dA + \int_V \rho \hat{b} dV = \int_V \rho \hat{u} dV \quad (6.44)$$

$$\int_A \hat{x} \times \hat{i} dA + \int_V \hat{x} \times \rho \hat{b} dV = \int_V \hat{x} \times \rho \hat{u} dV \quad (6.45)$$

Here, \hat{t} is the traction vector on the boundary surface of area A . In tensor notation, these can be rewritten as:

$$\int_A t_i dA + \int_V \rho b_i dV = \int_V \rho \ddot{u}_i dV \quad (6.46)$$

$$\int_A \varepsilon_{ijk} x_j t_k dA + \int_V \varepsilon_{ijk} x_j b_k \rho dV = \int_V \varepsilon_{ijk} x_j \rho \ddot{u}_k dV \quad (6.47)$$

Here, ε_{ijk} is the permutation tensor used to represent a cross-product of any two vectors. By using Equation (6.33) in Equations (6.46) and (6.47), and using the Divergence Theorem [1]:

$$\int_A t_i dA = \int_A \sigma_{pi} n_p dA = \int_V \frac{\partial \sigma_{pi}}{\partial x_p} dV$$

we get:

$$\begin{aligned} & \int_V \left[\frac{\partial \sigma_{pi}}{\partial x_p} + \rho b_i - \rho \ddot{u}_i \right] dV \\ & \int_V \left[\frac{\partial}{\partial x_k} (\varepsilon_{ijk} x_j \sigma_{pk}) + \rho \varepsilon_{ijk} x_j b_k - \rho \varepsilon_{ijk} x_j \ddot{u}_k \right] dV \end{aligned} \quad (6.48)$$

The first term in the second equation can be written as:

$$\frac{\partial}{\partial x_p} (x_j \sigma_{pk}) = \sigma_{jk} + x_j \frac{\partial \sigma_{pk}}{\partial x_p}$$

Using the above equation in Equation (6.48), we can obtain the governing equilibrium equations as:

$$\frac{\partial \sigma_{pi}}{\partial x_p} + \rho b_i = \rho \ddot{u} \quad (6.49)$$

$$\varepsilon_{ijk} \sigma_{jk} = 0 \quad (6.50)$$

While the first equation (Equation (6.49)) gives the governing differential equation of a continuum in terms of stresses, the second equation states that Cauchy’s stress tensor σ_{ij} is symmetric, that is, $\sigma_{ij} = \sigma_{ji}$. Expanding

Equation (6.49), we get the following three differential equations of motion:

$$\frac{\partial \sigma_{xx}}{\partial x} + \frac{\partial \tau_{yx}}{\partial y} + \frac{\partial \tau_{zx}}{\partial z} + \rho b_x = 0 \quad (6.51)$$

$$\frac{\partial \tau_{xy}}{\partial x} + \frac{\partial \sigma_{yy}}{\partial y} + \frac{\partial \tau_{zy}}{\partial z} + \rho b_y = 0 \quad (6.52)$$

$$\frac{\partial \tau_{xz}}{\partial x} + \frac{\partial \tau_{yz}}{\partial y} + \frac{\partial \sigma_{zz}}{\partial z} + \rho b_z = 0 \quad (6.53)$$

The above equations will form the heart of many analyses which will be reported later in this book. It is also worth mentioning that out of nine stress components in Cauchy's stress tensor, only six are independent, which is the outcome of the symmetry of the tensor. The derived equations of equilibrium are valid for both small and large deformation analyses.

6.1.5 Constitutive relations

In the theory of elasticity, constitutive relations are important components in the analysis and basically they relate the stresses developed with the strains. In normal materials, the stresses and strains are related through a material matrix. In the case of smart materials, the constitutive law has two parts, one due to mechanical loading and the other due to either electrical loading (in cases of piezoelectric or electrostrictive materials) or magnetic loading (in the case of magnetostrictive material). That is, the second part denotes the existence of the coupling between the mechanical motion and the motion due to electrical or magnetic fields. This material law is normally called the *actuation law*. It is this coupling strain that gives the required control force for a host of applications, such as vibration control, noise control, etc. which are reported in the last chapter of this book. In addition to the actuation law, smart materials, such as piezoelectric or magnetostrictive materials, exhibit a second constitutive law, called the *sensing law*, which relates the electric/magnetic fluxes to the mechanical stresses and the electric/magnetic fields. This law is normally used in Structural Health Monitoring (SHM) applications to sense the presence of any damage. In this section, we will mention the constitutive relations for 'normal' materials only. Constitutive relations for smart materials will be dealt with separately in Chapter 8.

Returning back to 'normal' materials, the constitutive relations are normally established under certain assumptions. These can be summarized as the following:

- The stress at a point depends on geometric changes that take place in the immediate vicinity.
- There are no history effects – the present state of stress will give the strain. Hence, the presence of material non-linearity is assumed negligible.
- The structure under loading will 'bounce' back to its original shape on its removal.
- Temperature changes only cause a change in shape or volume but otherwise do not directly affect the stresses.
- The material is homogeneous, that is, the material properties are not a function of spatial coordinates.
- Displacements and hence the strains are very small compared to unity.

The constitutive relations can be developed by two different methods – one is based on the second assumption, which we call the *Hookean Elastic Solid*, while the second method is by the use of the *Principle of Virtual Work* (which we will dwell on in more detail in Chapter 7). The constitutive law obtained based on the above theorem is called *Green's Elastic Solid*. Both of these methods will essentially give the same material matrix for an elastic solid.

6.1.5.1 Hookean elastic solid

This constitutive model is normally referred to as *Hooke's Law*. It is based on the assumption that for an elastic body, the stress depends only on deformation and not on the history of deformation. This can be mathematically expressed as:

$$\sigma_{ij} = f_{ij}(\varepsilon_{ij}) \quad (6.54)$$

Expanding the above term by a Taylor series about the initial configuration ($t = 0$), we get:

$$\sigma_{ij} = f_{ij}(0) + \left[\frac{\partial f_{ij}(0)}{\partial \varepsilon_{kl}} \right] \varepsilon_{kl} + \frac{1}{2} \left[\frac{\partial^2 f_{ij}(0)}{\partial \varepsilon_{kl} \partial \varepsilon_{mn}} \right] \varepsilon_{kl} \varepsilon_{mn} + \dots \quad (6.55)$$

If the assumption of zero initial stress is true, then we require $\sigma_{ij} = 0$ when $\varepsilon_{ij} = 0$. This condition leads to $f_{ij}(0) = 0$. The second term in Equation (6.55) is the linear term and all other terms in the expression are non-linear. Retaining only the linear term due to a small-strain assumption, we can write Equation (6.55) as:

$$\sigma_{ij} = C_{ijkl} \varepsilon_{kl} \quad \text{with} \quad C_{ijkl} = \left[\frac{\partial f_{ij}(0)}{\partial \varepsilon_{kl}} \right] \quad (6.56)$$

Equation (6.56) is called *Hooke's Law*, which states that the stress tensor is linearly related to the strain tensor.

The term in Equation (6.56), C_{ijkl} , is a fourth-order tensor of elastic constants, which are independent of either stress or strain. The tensorial quality of the constants C_{ijkl} follows the quotient rule, according to which, for a fourth-order tensor, it should have $3^4 = 81$ elements. Due to symmetry of the stress tensor ($\sigma_{ij} = \sigma_{ji}$), we should have $C_{ijkl} = C_{jikl}$. Furthermore, since the strain tensor is also symmetric ($\varepsilon_{kl} = \varepsilon_{lk}$), we have $C_{ijkl} = C_{ijlk}$. Under these conditions, the fourth-order tensor C_{ijkl} will have only 36 independent constants. Hence, the total number of elastic constants cannot exceed 36, since the maximum independent elements in the stress and strain tensors are only 6 each. With these reductions, the generalized Hook's law can be written in the matrix form as:

$$\begin{Bmatrix} \sigma_{xx} \\ \sigma_{yy} \\ \sigma_{zz} \\ \tau_{yz} \\ \tau_{xz} \\ \tau_{xy} \end{Bmatrix} = \begin{bmatrix} C_{11} & C_{12} & C_{13} & C_{14} & C_{15} & C_{16} \\ C_{21} & C_{22} & C_{23} & C_{24} & C_{25} & C_{26} \\ C_{31} & C_{32} & C_{33} & C_{34} & C_{35} & C_{36} \\ C_{41} & C_{42} & C_{43} & C_{44} & C_{45} & C_{46} \\ C_{51} & C_{52} & C_{53} & C_{54} & C_{55} & C_{56} \\ C_{61} & C_{62} & C_{63} & C_{64} & C_{65} & C_{66} \end{bmatrix} \begin{Bmatrix} \varepsilon_{xx} \\ \varepsilon_{yy} \\ \varepsilon_{zz} \\ \gamma_{yz} \\ \gamma_{xz} \\ \gamma_{xy} \end{Bmatrix} \quad (6.57)$$

where all of the τ 's represent the shear stresses in their respective planes and all of the γ 's are the corresponding shear strains. For most elastic solids, the number of elastic constants can further be reduced by exploiting the material symmetry about different reference planes.

6.1.5.2 Green's elastic solid

An alternate method of deriving the constitutive relationship is by using the work and energy principles. This method is normally referred to as *Green's Elastic Solid*. For elastic materials, it will give the same material matrix as that of the Hookean Solid approach. This method is based on the assumption that the work done by the elastic forces is completely transformed into potential energy and furthermore the potential energy is entirely due to the deformation a body undergoes due to applied tractions (forces). We begin by considering the total forces acting on a body, which is given by Equation (6.44). Total incremental (virtual) work done by the forces (acting on a surface S) of a body of volume V in displacing by an incremental (virtual) displacement of du_i is given by:

$$dW_e = \int_S t_i du_i dA + \int_V \rho b_i du_i dV \quad (6.58)$$

Using the Divergence Theorem, the surface integral can be converted to the volume integral and the above equation becomes:

$$dW_e = \int_V \sigma_{ij} d \left(\frac{\partial u_i}{\partial x_j} \right) dV = \int_V \sigma_{ij} d\varepsilon_{ij} dV \quad (6.59)$$

The change in the potential energy (also called the *Strain Energy*) is given by:

$$dU^* = \int_V dU dV \quad (6.60)$$

where U is the potential energy per unit volume (which is also called the strain energy density function). Assuming that U is a function of only deformations (strains), which is the basic hypothesis on which this material model is based, we can write:

$$dU = dU(\varepsilon_{ij}) = \frac{\partial U}{\partial \varepsilon_{ij}} d\varepsilon_{ij}$$

Using the above in Equation (6.60), we get:

$$dU^* = \int_V \frac{\partial U}{\partial \varepsilon_{ij}} d\varepsilon_{ij} dV \quad (6.61)$$

Comparing Equations (6.61) and (6.59), we can say:

$$dW_e = dU^* \quad \text{or} \quad \int_V \sigma_{ij} d\varepsilon_{ij} dV = \int_V \frac{\partial U}{\partial \varepsilon_{ij}} d\varepsilon_{ij} dV \quad (6.62)$$

Since the volume is arbitrary, we can equate the integrands and in doing so we get:

$$\sigma_{ij} = \frac{\partial U}{\partial \varepsilon_{ij}} \quad (6.63)$$

Equation (6.62) is the famed *Principle of Virtual Work* (PVW), which is the heart of many numerical methods, such as the Finite Element Method (FEM). We will again deal with this principle in more detail in Chapter 7 on FEM. Returning to the constitutive modeling, Equation (6.63) can be expanded by using Taylor series as:

$$\begin{aligned} \sigma_{ij} = \frac{\partial U}{\partial \varepsilon_{ij}} &= \left[\frac{\partial U(0)}{\partial \varepsilon_{ij}} \right] + \left[\frac{\partial^2 U(0)}{\partial \varepsilon_{ij} \partial \varepsilon_{kl}} \right] \varepsilon_{kl} + \dots \\ &= \sigma_{ij}^0 + E_{ijkl} \varepsilon_{kl} \end{aligned} \quad (6.64)$$

Assuming that the stress is zero when the strains are zero, the above equation reduces to:

$$\sigma_{ij} = E_{ijkl}\varepsilon_{kl}$$

which is the same as what we derived earlier. Because of the symmetry of both stress and strain tensors, the number of independent constants in the E_{ijkl} tensor is 36. Since:

$$E_{ijkl} = \left[\frac{\partial^2 U(0)}{\partial \varepsilon_{ij} \partial \varepsilon_{kl}} \right] = \left[\frac{\partial^2 U(0)}{\partial \varepsilon_{kl} \partial \varepsilon_{ij}} \right] = E_{klji}$$

This additional symmetry reduces the number of independent constants to 21.

6.1.5.3 Elastic symmetry

A material having all of the 36 unknown material constants is said to be a highly *Anisotropic* material (Triclinic System). However, if the internal composition of a material possesses symmetry of any kind, then symmetry can also be observed in the elastic properties. The presence of symmetry reduces the number of independent constants. Such simplification in the generalized Hooke's law can be obtained as follows. Let x , y , and z be the original coordinate system of the body and let x' , y' and z' be the second coordinate system, which is symmetric to the first system in accordance with the form of elastic symmetry. Since the directions of similar axes of both systems are equivalent with respect to elastic properties, the equations of the generalized Hooke's law will have the same form in both coordinate systems and the corresponding constants should be identical.

6.1.5.4 Monoclinic system: one elastic symmetric plane

Supposing that the material system is symmetric about the z -axis, the second coordinate system x' , y' and z' can be described by the following base unit vectors:

$$\hat{e}_1 = \{1, 0, 0\}, \quad \hat{e}_2 = \{0, 1, 0\}, \quad \hat{e}_3 = \{0, 0, -1\}$$

Using this, we can construct a transformation matrix by having the base vectors as the column of the transformation matrix. For the above case, the transformation matrix and the stress tensor in a 'primed' coordinate

system becomes:

$$[T] = \begin{bmatrix} 1 & 0 & 0 \\ 0 & 1 & 0 \\ 0 & 0 & -1 \end{bmatrix},$$

$$[\sigma'_{ij}] = [T]^T [\sigma_{ij}] [T] = \begin{bmatrix} \sigma_{xx} & \tau_{xy} & -\sigma_{xz} \\ \tau_{yx} & \sigma_{yy} & -\tau_{yx} \\ -\sigma_{zx} & -\tau_{zy} & \sigma_{zz} \end{bmatrix}$$

Similarly, transforming the strains in the 'primed' coordinate system will give:

$$[\varepsilon'_{ij}] = \begin{bmatrix} \varepsilon_{xx} & \gamma_{xy} & -\varepsilon_{xz} \\ \gamma_{yx} & \varepsilon_{yy} & -\gamma_{yz} \\ -\varepsilon_{zx} & -\gamma_{zy} & \varepsilon_{zz} \end{bmatrix}$$

The elastic symmetry requires that:

$$\begin{aligned} \{\sigma'_{xx} & \sigma'_{yy} & \sigma'_{zz} & \tau'_{yz} & \tau'_{xz} & \tau'_{xy}\}^T \\ &= [C_{ij}] \{\varepsilon'_{xx} & \varepsilon'_{yy} & \varepsilon'_{zz} & \gamma'_{yz} & \gamma'_{xz} & \gamma'_{xy}\}^T \end{aligned}$$

Using the above relations, the constitutive law in the original coordinate system becomes:

$$\begin{aligned} \left\{ \begin{array}{c} \sigma_{xx} \\ \sigma_{yy} \\ \sigma_{zz} \\ \tau_{yz} \\ \tau_{xz} \\ \tau_{xy} \end{array} \right\} &= \begin{bmatrix} C_{11} & C_{12} & C_{13} & -C_{14} & -C_{15} & C_{16} \\ C_{21} & C_{22} & C_{23} & -C_{24} & -C_{25} & C_{26} \\ C_{31} & C_{32} & C_{33} & -C_{34} & -C_{35} & C_{36} \\ -C_{41} & -C_{42} & -C_{43} & C_{44} & C_{45} & -C_{46} \\ -C_{51} & -C_{52} & -C_{53} & C_{54} & C_{55} & -C_{56} \\ C_{61} & C_{62} & C_{63} & -C_{64} & -C_{65} & C_{66} \end{bmatrix} \\ &\times \left\{ \begin{array}{c} \varepsilon_{xx} \\ \varepsilon_{yy} \\ \varepsilon_{zz} \\ \gamma_{yz} \\ \gamma_{xz} \\ \gamma_{xy} \end{array} \right\} \end{aligned}$$

Comparing the above matrix with the general matrix (Equation (6.57)) leads to the conclusion $C_{14} = C_{15} = C_{24} = C_{25} = C_{34} = C_{35} = C_{46} = C_{56} = 0$. Hence, the material matrix for a monoclinic system becomes:

$$\begin{bmatrix} C_{11} & C_{12} & C_{13} & 0 & 0 & C_{16} \\ C_{12} & C_{22} & C_{23} & 0 & 0 & C_{26} \\ C_{13} & C_{23} & C_{33} & 0 & 0 & C_{36} \\ 0 & 0 & 0 & C_{44} & C_{45} & 0 \\ 0 & 0 & 0 & C_{45} & C_{55} & 0 \\ C_{16} & C_{26} & C_{36} & 0 & 0 & C_{66} \end{bmatrix} \quad (6.65)$$

Hence, in the case of a monoclinic system, 13 independent constants require to be determined to define the material matrix.

6.1.5.5 Orthotropic system: three orthogonal planes of symmetry

The most common example of the orthotropic system is the lamina of a laminated composite structure, which is dealt with in great detail in Section 6.2. Here, the original coordinate system of the body is perpendicular to the three planes. The orthotropy assures that no change in mechanical behavior will be incurred when the coordinate directions are reversed. Following the procedure described for the *monoclinic* system, the material matrix for an orthotropic system is given by:

$$\begin{bmatrix} C_{11} & C_{12} & C_{13} & 0 & 0 & 0 \\ C_{12} & C_{22} & C_{23} & 0 & 0 & 0 \\ C_{13} & C_{23} & C_{33} & 0 & 0 & 0 \\ 0 & 0 & 0 & C_{44} & 0 & 0 \\ 0 & 0 & 0 & 0 & C_{55} & 0 \\ 0 & 0 & 0 & 0 & 0 & C_{66} \end{bmatrix} \quad (6.66)$$

The number of elastic constants that requires to be determined is 9. The relationship of these constants with the elastic constants can be found in Jones [2].

6.1.5.6 Hexagonal system: transversely isotropic system

This system has a plane of symmetry in addition to an axis of symmetry perpendicular to the plane. If the plane of symmetry coincides with the x - y plane, then the axis of symmetry is along the z -axis. Thus, any pair of orthogonal axes (x' , y') lying in the x - y plane are similar to (x, y) . Hence, the stress-strain relations with respect to (x', y', z') where $z' = -z$, should remain identical to those with respect to the (x, y, z) system. Following the procedure given for a monoclinic system, we can derive the material matrix. The material matrix for this case is given by:

$$\begin{bmatrix} C_{11} & C_{12} & C_{13} & 0 & 0 & 0 \\ C_{12} & C_{22} & C_{23} & 0 & 0 & 0 \\ C_{13} & C_{23} & C_{33} & 0 & 0 & 0 \\ 0 & 0 & 0 & C_{44} & 0 & 0 \\ 0 & 0 & 0 & 0 & C_{55} & 0 \\ 0 & 0 & 0 & 0 & 0 & \frac{1}{2}(C_{11} - C_{12}) \end{bmatrix} \quad (6.67)$$

For the transversely isotropic system, the number of independent material constants required to describe the system is 5.

6.1.5.7 Isotropic system: infinite plane of symmetry

This is the most commonly occurring material system for structural materials. For this case, every plane is a plane of symmetry and every axis is an axis of symmetry. It turns out that there are only two elastic constants which require to be determined and the material matrix is given by:

$$\begin{bmatrix} C_{11} & C_{12} & C_{12} & 0 & 0 & 0 \\ C_{12} & C_{11} & C_{12} & 0 & 0 & 0 \\ C_{12} & C_{12} & C_{11} & 0 & 0 & 0 \\ 0 & 0 & 0 & \frac{1}{2}(C_{11} - C_{12}) & 0 & 0 \\ 0 & 0 & 0 & 0 & \frac{1}{2}(C_{11} - C_{12}) & 0 \\ 0 & 0 & 0 & 0 & 0 & \frac{1}{2}(C_{11} - C_{12}) \end{bmatrix} \quad (6.68)$$

where:

$$C_{11} = \lambda + 2G, \quad C_{12} = \lambda$$

The constants λ and G are the *Lamé* constants. The stress-strain relations for isotropic materials are usually expressed in the form:

$$\sigma_{ij} = \lambda \varepsilon_{kk} \delta_{ij} + 2G \varepsilon_{ij}, \quad 2G \varepsilon_{ij} = \sigma_{ij} - \frac{\lambda}{3\lambda + 2G} \sigma_{kk} \delta_{ij} \quad (6.69)$$

Note that except for an isotropic material, the coefficients are given with respect to a particular coordinate system.

In practice, the elastic constants for an isotropic material are K , E and v . These are called the *Bulk modulus*, *Young's modulus* and *Poisson's ratio*, respectively. They are related to the Lamé constants in the following manner:

$$K = \frac{1}{3}(3\lambda + 2G), \quad v = \frac{\lambda}{2(\lambda + 2G)} \quad (6.70)$$

Some relationships among the constants are as follows:

$$\lambda = \frac{vE}{(1+v)(1-2v)}, \quad G = \frac{E}{2(1+v)}, \quad K = \frac{E}{3(1-2v)} \quad (6.71)$$

6.1.6 Solution procedures in the linear theory of elasticity

The developments in the last subsections form the basis of field equations of the theory of elasticity. In this

subsection, these are reformulated to make them convenient for solving boundary value problems. The fundamental assumptions adopted here are the following:

- (a) All the deformations are small.
- (b) The constitutive relations are linear. For metallic structures, the material behavior can be idealized as isotropic. However, for composite structures, the material behavior is assumed anisotropic.

In 3-D elasticity, there are 15 unknowns, namely the 6 stress components, 6 strain components and 3 displacements. Hence, for complete solution, we require 15 equations, which come from:

- 3 equations of equilibrium (Equation (6.49)).
- 6 stress-strain relations (Equation (6.57)).
- 6 strain-displacement relations (Equation (6.27)) or 6 compatibility conditions (to be introduced later). Either of these conditions will be used depending on the choice of solution schemes to be used.
- In addition, for the solution to be unique it has to satisfy the boundary conditions on the surface S , which has two parts, that is, surface S_u on which the boundary conditions in terms of the displacements u_i are prescribed and surface S_t on which the traction boundary condition $t_i = \sigma_{ij}n_j$ is prescribed.

Historically, there are two different solution philosophies, one based on assuming displacements as the basic unknowns, while the other approach is based on assuming stresses as the basic unknowns. In the former, the compatibility of the displacements is ensured as we begin the analysis with displacements as the basic unknowns. However, the equilibrium is not ensured and hence they are enforced in the solution process. In the latter, since the stresses are the basic unknowns, the equilibrium is ensured and the compatibility is not ensured and hence enforced during the solution process. In the next few paragraphs, for both of these methods, we will derive the basic equations and their solution.

6.1.6.1 Displacement formulation: Navier's equation

In this approach, the displacements are taken as the basic unknowns, that is, at each point, there are three unknown functions u , v and w . These must be determined subject to the constraint that the stresses derived from them are equilibrated, or in other words, by enforcing equilibrium. For this, the stresses are first expressed in terms of displacements. That is, first the strains are expressed in

terms of displacements using strain-displacement relations (Equation (6.27)) and then these are later converted to stresses. For isotropic solids, these can be written as:

$$\sigma_{ij} = G \left(\frac{\partial u_i}{\partial x_j} + \frac{\partial u_j}{\partial x_i} \right) + \lambda \frac{\partial u_k}{\partial x_k} \delta_{ij} \quad (6.72)$$

Substituting this into the equilibrium equation (Equation (6.49)), we get:

$$G \frac{\partial^2 u_i}{\partial x_k \partial x_k} + (\lambda + G) \frac{\partial^2 u_k}{\partial x_i \partial x_k} + \rho b_i = 0 \quad (6.73)$$

These are known as Navier's equations, with three displacements as unknowns. The above equations should satisfy the following boundary conditions in terms of displacements:

On S_u : u_i specified

On S_t : $\lambda \frac{\partial u_k}{\partial x_k} n_i + G \left(\frac{\partial u_i}{\partial x_j} + \frac{\partial u_j}{\partial x_i} \right) n_j = t_i$ specified

Note that the traction boundary conditions are a set of inhomogeneous differential equations. These are very difficult to solve directly. The most common way to solve the above equation is to express the displacement field in terms of scalar potential (Φ) and vector potential (H) by using Helmholtz's theorem. The displacement field takes the following form:

$$u_i = \frac{\partial \Phi}{\partial x_i} + \varepsilon_{ijk} \frac{\partial H_k}{\partial x_j}, \quad \frac{\partial H_k}{\partial x_k} = 0 \quad (6.74)$$

where, ε_{ijk} is the permutation symbol. If the body force is absent, then Navier's equations can be expressed as:

$$(\lambda + 2G) \frac{\partial}{\partial x_i} \nabla^2 \Phi + G \varepsilon_{ijk} \nabla^2 H = 0 \quad (6.75)$$

This equation will be satisfied if:

$$\nabla^2 \Phi = \text{constant}, \quad \nabla^2 H = \text{constant} \quad (6.76)$$

Thus, the problem reduces to solving a set of Poisson's equations in terms of potentials, which are easier to solve than the original Equation (6.73). The displacements are later obtained from differentiation.

6.1.6.2 Stress formulation: Beltrami–Mitchell equations

In this approach, the stresses are assumed as basic unknowns. That is, at each point in the body, there are

6 unknown functions, namely, $\sigma_{xx}, \sigma_{yy}, \sigma_{zz}, \tau_{xy}, \tau_{yz}$ and τ_{zx} . These stresses obviously have to satisfy the equilibrium equations. However, there are only 3 equations of equilibrium. The rest of the conditions come from the requirement that the strains must be *compatible*.

The assumed stress fields can be converted to strain fields by using the generalized Hooke's law, which in turn can be converted to displacement fields by using strain displacement relationships. In doing so, we get 6 independent partial differential equations for displacements with prescribed strains ε_{ij} . For arbitrary values of ε_{ij} , there may not exist unique solutions for the displacement fields. Hence, for getting unique solutions for displacements, it is necessary to place some restriction on the strains ε_{ij} . By differentiating twice, the strain-displacement relations (Equation (6.27)), we get:

$$\frac{\partial^2 \varepsilon_{ij}}{\partial x_k \partial x_l} = \frac{1}{2} \left(\frac{\partial^3 u_i}{\partial x_j \partial x_k \partial x_l} + \frac{\partial^3 u_j}{\partial x_i \partial x_k \partial x_l} \right) \quad (6.77)$$

Interchanging the subscripts and with some manipulation leads to the following relation:

$$\frac{\partial^2 \varepsilon_{ij}}{\partial x_k \partial x_l} + \frac{\partial^2 \varepsilon_{kl}}{\partial x_i \partial x_j} - \frac{\partial^2 \varepsilon_{ik}}{\partial x_j \partial x_l} - \frac{\partial^2 \varepsilon_{jl}}{\partial x_i \partial x_k} = 0 \quad (6.78)$$

There are 81 equations in the above relation, out of which some are identically satisfied and some of them are repetitions. Only 6 equations are nontrivial and independent and in expanded notation, these equations are the following:

$$\begin{aligned} \frac{\partial^2 \varepsilon_{xx}}{\partial y \partial z} &= \frac{\partial}{\partial x} \left(-\frac{\partial \varepsilon_{yz}}{\partial x} + \frac{\partial \varepsilon_{zx}}{\partial y} + \frac{\partial \varepsilon_{xy}}{\partial z} \right) & \frac{\partial^2 \varepsilon_{xy}}{\partial x \partial y} &= \frac{\partial^2 \varepsilon_{xx}}{\partial y^2} + \frac{\partial^2 \varepsilon_{yy}}{\partial x^2} \\ \frac{\partial^2 \varepsilon_{yy}}{\partial z \partial x} &= \frac{\partial}{\partial y} \left(-\frac{\partial \varepsilon_{xz}}{\partial y} + \frac{\partial \varepsilon_{xy}}{\partial z} + \frac{\partial \varepsilon_{yz}}{\partial x} \right) \text{ and} & \frac{\partial^2 \varepsilon_{yz}}{\partial y \partial z} &= \frac{\partial^2 \varepsilon_{yy}}{\partial z^2} + \frac{\partial^2 \varepsilon_{zz}}{\partial y^2} \\ \frac{\partial^2 \varepsilon_{zz}}{\partial x \partial y} &= \frac{\partial}{\partial z} \left(-\frac{\partial \varepsilon_{xy}}{\partial z} + \frac{\partial \varepsilon_{yz}}{\partial x} + \frac{\partial \varepsilon_{zx}}{\partial y} \right) & \frac{\partial^2 \varepsilon_{zx}}{\partial z \partial x} &= \frac{\partial^2 \varepsilon_{zz}}{\partial x^2} + \frac{\partial^2 \varepsilon_{yy}}{\partial z^2} \end{aligned} \quad (6.79)$$

These 6 relations are collectively known as *compatibility equations*. The bodies can be simply or multiply connected, as shown in Figure 6.8. For simply connected bodies, equations of compatibility are necessary and sufficient for their solution. However, for multiply connected bodies, they are necessary, but no longer sufficient. Additional conditions need to be imposed to ensure that the displacements are single-valued.

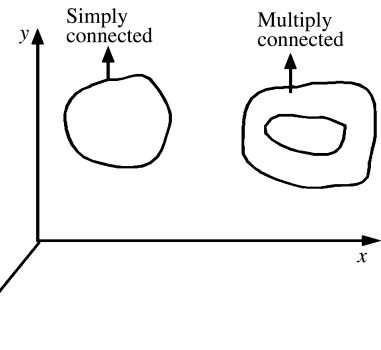


Figure 6.8 Simply and multiply connected bodies.

The general solution procedure in stress formulation is as follows. We first transform the strains into stresses by using Hooke's law (for isotropic solids) of the form:

$$\varepsilon_{ij} = \frac{1+v}{E} \sigma_{ij} - \frac{v}{E} \sigma_{kk} \delta_{ij}$$

By substituting for strains in the compatibility equations (Equation (6.79)) and with some simplification (that is, by using equations of equilibrium), we get:

$$\begin{aligned} \frac{\partial^2 \sigma_{ij}}{\partial x_k \partial x_l} + \left(\frac{1}{1+v} \right) \frac{\partial^2 \sigma_{kk}}{\partial x_i \partial x_j} + \left(\frac{v}{1-v} \right) \rho \frac{\partial b_k}{\partial x_k} \delta_{ij} \\ + \rho \left(\frac{\partial b_i}{\partial x_j} + \frac{\partial b_j}{\partial x_i} \right) = 0 \end{aligned} \quad (6.80)$$

The stress field should satisfy the above equation along with the equilibrium equation (Equation (6.49)) in order to be admissible. In addition, it has to satisfy the following boundary conditions:

On S_i : $\sigma_{ij} n_j = t_i$ = given and on S_u : u_i = given

Note that the second set of boundary conditions are obtained by integrating the strain-displacement relations in conjunction with the stress-strain relations.

6.1.7 Plane problems in elasticity

The 3-D equations and their associated boundary conditions are extremely difficult to solve and solutions only exist for very few problems. Hence, in most cases some approximations are made to reduce the complexity of the problem. One such reduction is to reduce the dimension of the problem from three to two. This can be made for certain types of problems, which falls under two different

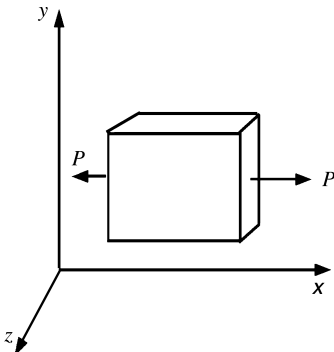


Figure 6.9 A thin plate under plane-stress conditions.

categories, namely the *Plane Stress* problems and the *Plane Strain* problems. A typical plane stress problem is a thin plate loaded along its plane, as shown in Figure 6.9. In this case, the stress perpendicular to the plane of the plate (σ_{zz}) can be assumed to be zero. In addition, the corresponding shear in the x - z and y - z planes (τ_{yz} and τ_{xz}) can also be assumed zero. In the process, the equations get simplified considerably.

The following are the equations required for solution of the plane stress problem:

- Equations of equilibrium.

$$\frac{\partial \sigma_{xx}}{\partial x} + \frac{\partial \tau_{xy}}{\partial y} + b_x = \rho \frac{\partial^2 u}{\partial t^2},$$

$$\frac{\partial \tau_{xy}}{\partial x} + \frac{\partial \sigma_{yy}}{\partial y} + b_y = \rho \frac{\partial^2 v}{\partial t^2}$$

- Strain-displacement relations.

$$\varepsilon_{xx} = \frac{\partial u}{\partial x}, \quad \varepsilon_{yy} = \frac{\partial v}{\partial y}, \quad \gamma_{xy} = \frac{\partial u}{\partial y} + \frac{\partial v}{\partial x}$$

- Stress-strain relations. This is obtained by inserting $\sigma_{zz} = 0$, $\tau_{xz} = 0$, $\tau_{yz} = 0$ in the generalized Hooke's law (Equation (6.57)) and solving the resulting equation after substituting for strains in terms of displacements. After substitution, we get:

$$\sigma_{xx} = \frac{E}{(1 - v^2)} \left(\frac{\partial u}{\partial x} + v \frac{\partial v}{\partial y} \right),$$

$$\sigma_{yy} = \frac{E}{(1 - v^2)} \left(\frac{\partial v}{\partial y} + v \frac{\partial u}{\partial x} \right), \quad \tau_{xy} = G \gamma_{xy}$$

This we call plane stress reduction in the x - y plane. Note that a similar reduction of stresses in the other plane is also possible.

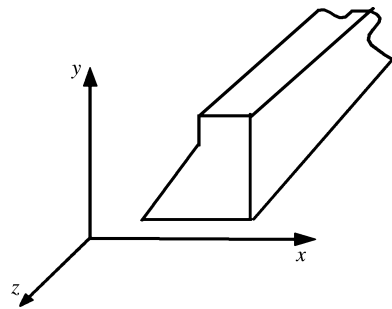


Figure 6.10 A dam-type structure under plane-strain conditions.

- If one has to use the stress-based approach for the solution, then only one compatibility equation requires to be enforced, which is given by:

$$2 \frac{\partial^2 \gamma_{xy}}{\partial x \partial y} = \frac{\partial^2 \varepsilon_{xx}}{\partial y^2} + \frac{\partial^2 \varepsilon_{yy}}{\partial x^2}$$

Note that although the normal stress σ_{zz} is zero in the plane stress case, the normal strain ε_{zz} is non-zero and its value can be computed from the 3-D constitutive law. The second type of reduction is called the plane strain reduction, where the body perpendicular to the plane of loading is assumed rigid, that is, the displacement w and hence the strains, $\varepsilon_{zz} = \varepsilon_{xz} = \varepsilon_{yz} = 0$, can be inserted in the 3-D constitutive model and the resulting equations can be solved to get the stress-strain relations, as was done for the plane stress case. A typical example of a plane strain case is the dam structure shown in Figure 6.10, wherein the structure is assumed rigid in the z -direction.

6.2 THEORY OF LAMINATED COMPOSITES

6.2.1 Introduction

Laminated composites have found extensive use as aircraft structural materials due to their high strength-to-weight and stiffness-to-weight ratios. Their popularity stems from the fact that they are extremely lightweight and the laminate construction enables the designer to tailor the strength of the structure in any required direction depending upon the loading environment to which the structure is subjected. In addition to aircraft structures, they have found application in many automobile and building structures. In addition to better strength, stiffness and lower weight properties, they have better corrosion resistance and wear resistance and

thermal and acoustic insulation properties over metallic structures.

A laminated composite structure consists of many laminas (plies) stacked together to form the structure. The number of plies or laminas depends on the strength that the structure is required to sustain. Each lamina contains fibers oriented in the direction where the maximum strength is required. These fibers are bonded together by a matrix material. These laminated composite structures derive their strength from the fibers. The most commonly used fibers include the following: carbon fibers, glass fibers, Kevlar fibers and boron fibers. The most commonly used matrix material is epoxy resin. These materials are orthotropic at the lamina level, while at the laminate level they exhibit a high level of anisotropic behavior. The anisotropic behavior results in *stiffness coupling*, such as bending-axial-shear coupling in beams and plates, bending-axial-torsion coupling in aircraft thin-walled structures, etc. These coupling effects make the analysis of laminated composite structures very complex.

With the advent of smart materials, the usage of composites is increasing due to the possibility of embedding smart sensors and actuators anywhere in the structures, for potential applications such as structural health monitoring, vibration and noise control, shape control, etc. This is because many of the smart materials are available either in powder form (magnetostrictive materials, such as Terfenol-D) or in thin-film form (PVDF sheets or PZT films), which can be readily integrated into the host composite structure. This increases the possibility of building on-line health monitoring or vibration monitoring systems with built-in sensors, actuators and processors. Laboratory-level models of such systems are already in place at Stanford University [3] and a few other places.

The basic theory and modeling aspects of laminated composite structures are introduced in this section, while detailed modeling and analysis of smart composites are introduced in Chapter 8. Readers who are already familiar with the basic theory of composites can skip the following.

This section is organized as follows. First, the micromechanical aspects of laminas are described. This is followed by the macromechanics of laminas and the complete analysis of laminates.

6.2.2 Micromechanical analysis of a lamina

A lamina is a basic element of a laminated composite structure, constructed with the help of fibers that are bonded together with the help of a matrix resin. The strength of the lamina and hence the laminate depends on

the type of fiber, its orientation and also the volume fraction of the fiber in relation to the overall volume of the lamina. Since the lamina is a heterogeneous mixture of fibers dispersed in the matrix, determination of the material properties of the lamina, which are assumed to be orthotropic in character, is a very involved process. The methods involved in determination of the lamina material properties constitute micromechanical analysis. According to Jones [2], micromechanics are the study of composite material behavior, wherein the interaction of the constituent materials is examined in detail as part of the definition of the behavior of the heterogeneous composite material.

Hence, the objective of micromechanics is to determine the elastic modulus of a composite material in terms of the elastic moduli of the constituent materials, namely, the fibers and matrix. Hence, the property of a lamina can be expressed as:

$$Q_{ij} = Q_{ij}(E_f, E_m, v_f, v_m, V_f, V_m) \quad (6.81)$$

where E_f and E_m are the elastic moduli of the fiber and the matrix, v_f and v_m are the Poisson's ratios of the fiber and matrix and V_f and V_m are the volume fractions of fiber and matrix, respectively. The volume fraction of the fiber is determined from the expression:

$$V_f = \frac{\text{Volume of the fibers}}{\text{Total volume of the lamina}}$$

Similarly, one can determine the volume fraction of the matrix. There are two basic approaches to determining the material properties of the lamina. These can be grouped under the following: (1) *Strength of Materials* approach and (2) *Theory of Elasticity* approach. The first method gives the experimental way of determining the elastic moduli. The second method actually gives the upper and lower bounds of the elastic moduli and not their actual values. In fact, there are many papers available in the literature that deal with the theory of elasticity approach to determine the elastic moduli of composites. In this section, only the first method is presented. There are several classic textbooks on composites, such as Jones [2] and Tsai [4], which dwell on this in detail.

6.2.2.1 Strength-of-material approach to determination of the elastic moduli

The material properties of a lamina are determined by making some assumptions as regards its behavior. The fundamental assumption is that the fiber is the strongest

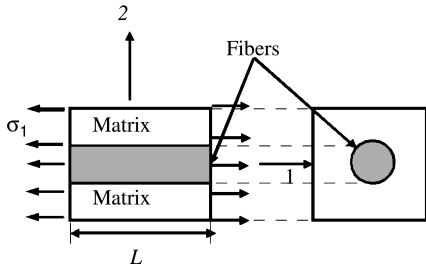


Figure 6.11 Representative volume (RV) for determination of the longitudinal material properties.

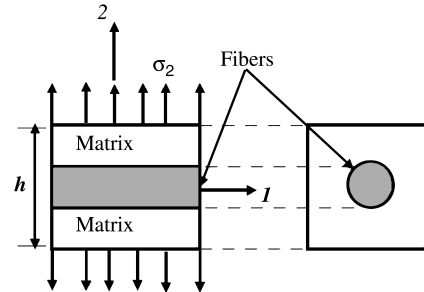


Figure 6.12 Representative volume (RV) for determination of the transverse material properties.

constituent of a composite lamina, and hence is the main load-bearing member, and the matrix is weak and its main function is to protect the fibers from severe environmental effects. In addition, the strains in the matrix as well as in the fiber are assumed to be the same. Hence, the plane sections before being stressed ‘remain plane’ after the stress is applied. In this present analysis, we consider a unidirectional, orthotropic composite lamina for deriving the expressions for the elastic moduli. In doing so, we limit our analysis to a small volume element, which is small enough to show the microscopic structural details, yet large enough to represent the overall behavior of the composite lamina. Such a volume is called the *Representative Volume* (RV). A simple RV is a fiber surrounded by a matrix, as shown in Figure 6.11.

First, the procedure for determining the elastic modulus E_1 is given. In Figure 6.11, the strain in the ‘1-direction’ is given by $\varepsilon_1 = \Delta L/L$, where this strain is felt both by the matrix and the fiber, according to our basic assumption. The corresponding stresses in the fiber and the matrix are given by:

$$\sigma_f = E_f \varepsilon_1, \quad \sigma_m = E_m \varepsilon_1 \quad (6.82)$$

Here, E_f and E_m are the elastic moduli of the fiber and matrix, respectively. The cross-sectional area of the RV, A , is made up of the area of the fiber, A_f , and the area of the matrix, A_m . If the total stress acting on the cross-section of the RV is σ_1 , then the total load acting on the cross-section is:

$$P = \sigma_1 A = E_1 \varepsilon_1 A = \sigma_f A_f + \sigma_m A_m \quad (6.83)$$

From the above expression, we can write the elastic moduli in the ‘1-direction’ as:

$$E_1 = E_f \frac{A_f}{A} + E_m \frac{A_m}{A} \quad (6.84)$$

The volume fractions of the fiber and the matrix can be expressed in terms of the areas of the fiber and matrix as:

$$V_f = \frac{A_f}{A}, \quad V_m = \frac{A_m}{A} \quad (6.85)$$

Using Equation (6.85) in (6.84), we can write the modulus in the ‘1-direction’ as:

$$E_1 = E_f V_f + E_m V_m \quad (6.86)$$

Equation (6.86) is the well known *rule of mixtures* for obtaining the equivalent modulus of the lamina in the direction of the fibers.

The equivalent modulus, E_2 , of the lamina is determined by subjecting the RV to a stress σ_2 perpendicular to the direction of the fiber, as shown in Figure 6.12. This stress is assumed to be same in both the matrix as well as the fiber. The strains in the fiber and matrix due to this stress are given by:

$$\varepsilon_f = \frac{\sigma_2}{E_f}, \quad \varepsilon_m = \frac{\sigma_2}{E_m} \quad (6.87)$$

If h is the depth of the RV (see Figure 6.12), then this total strain ε_2 gets distributed as a function of volume fraction as:

$$\varepsilon_2 h = V_f \varepsilon_f h + V_m \varepsilon_m h \quad (6.88)$$

Substituting Equation (6.87) into (6.88), we get:

$$\varepsilon_2 = V_f \left(\frac{\sigma_2}{E_f} \right) + V_m \left(\frac{\sigma_2}{E_m} \right) \quad (6.89)$$

However, we have:

$$\sigma_2 = E_2 \varepsilon_2 = E_2 \left(V_f \frac{\sigma_2}{E_f} + V_m \frac{\sigma_2}{E_m} \right) \quad (6.90)$$

From the above relation, the equivalent modulus in the transverse direction is given by:

$$E_2 = \frac{E_f E_m}{V_f E_m + V_m E_f} \quad (6.91)$$

The major Poisson's ratio v_{12} is determined as follows. If the RV of width W and depth h is loaded in the direction of the fiber, then both the strains ε_1 and ε_2 will be induced in the '1' and '2' directions. The total transverse deformation, δ_h , is the sum of the transverse deformation in the matrix and the fiber and is given by:

$$\delta_h = \delta_{hf} + \delta_{hm} \quad (6.92)$$

The major Poisson's ratio is also defined as the ratio of the transverse strain to the longitudinal strain and is mathematically expressed as:

$$v_{12} = -\frac{\varepsilon_2}{\varepsilon_1} \quad (6.93)$$

The total transverse deformation can also be expressed in terms of depth h as:

$$\delta_h = -h\varepsilon_2 = h v_{12} \varepsilon_1 \quad (6.94)$$

Following the procedure adopted for the determination of the transverse modulus, the transverse displacement in the matrix and fiber can be expressed in terms of their respective volume fractions and Poisson's ratios as:

$$\delta_{hf} = h V_f v_f \varepsilon_1, \quad \delta_{hm} = h V_m v_m \varepsilon_1 \quad (6.95)$$

Using Equations (6.94) and (6.95) in Equation (6.92), we can write the expression for the major Poisson's ratio as:

$$v_{12} = v_f V_f + v_m V_m \quad (6.96)$$

By adopting a similar procedure to that used in the determination of the transverse modulus, we can write the shear modulus in terms of its constituent properties as:

$$G_{12} = \frac{G_f G_m}{V_f G_m + V_m G_f} \quad (6.97)$$

The next important property of the composite that requires determination is the density. For this, we begin with the total mass of the lamina, which is the sum of the masses of the fiber and the matrix. That is, the total mass

M can be expressed in terms of the densities (ρ_f and ρ_m) and volumes (V_f and V_m) as:

$$M = M_f + M_m = \rho_f V_f + \rho_m V_m \quad (6.98)$$

The density of the composite can then be expressed as:

$$\rho = \frac{M}{V} = \frac{\rho_f V_f + \rho_m V_m}{V} \quad (6.99)$$

Once the properties of the lamina are determined, then one can proceed to a macromechanical analysis of the lamina to characterize its constitutive model and behavior, which is described in the next subsection.

6.2.3 Stress-strain relations for a lamina

Determination of the overall constitutive model for a lamina of a laminated composite constitutes the macromechanical study of composites. Unlike the micro-mechanical study where the composite is treated as a heterogeneous mixture, here the composite is presumed to be homogenous and the effects of the constituent materials are accounted for only as an averaged apparent property of the composite. The following are the basic assumptions used in deriving the constitutive relations:

- The composite material is assumed to behave in a linear (elastic) manner. That is, Hooke's law, as well as the principle of superposition, are valid.
- At the lamina level, the composite material is assumed to be homogenous and orthotropic. Hence, the material has two planes of symmetry, one coinciding with the fiber direction and the other perpendicular to the fiber direction.
- The state of stress in a lamina is predominantly plane stress.

Consider the lamina shown in Figure 6.13 with its principle axes, which we denote as '1', '2' and '3'. That is, axis '1' corresponds to the direction of the fiber while axis '2' is the axis transverse to the fiber. The lamina is assumed to be in a 3-D state of stress with six stress components, given by $\{\sigma_{11}, \sigma_{22}, \sigma_{33}, \tau_{23}, \tau_{31}, \tau_{12}\}$. The generalized Hooke's law for an orthotropic material has already been derived in the previous section.

This is given by Equation (6.66). For the 3-D state of stress, nine engineering constants require to be determined. The macromechanical analysis will begin from

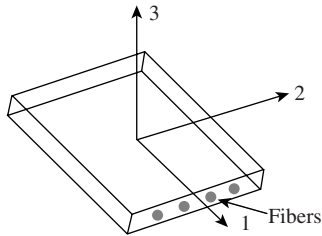


Figure 6.13 Principal axes of a lamina.

here. Inverting Equation (6.66), we get:

$$\begin{Bmatrix} \varepsilon_{11} \\ \varepsilon_{22} \\ \varepsilon_{33} \\ \gamma_{23} \\ \gamma_{31} \\ \gamma_{12} \end{Bmatrix} = \begin{bmatrix} S_{11} & S_{12} & S_{13} & 0 & 0 & 0 \\ S_{12} & S_{22} & S_{23} & 0 & 0 & 0 \\ S_{13} & S_{23} & S_{33} & 0 & 0 & 0 \\ 0 & 0 & 0 & S_{44} & 0 & 0 \\ 0 & 0 & 0 & 0 & S_{55} & 0 \\ 0 & 0 & 0 & 0 & 0 & S_{66} \end{bmatrix} \begin{Bmatrix} \sigma_{11} \\ \sigma_{22} \\ \sigma_{33} \\ \tau_{23} \\ \tau_{31} \\ \tau_{12} \end{Bmatrix} \quad (6.100)$$

Here, S_{ij} are the material compliances. Their relationships with the engineering constants are given in Jones [2]; ν_{ij} , the Poisson's ratio for transverse strain in the j th direction when the stress is applied in the i th direction, is given by:

$$\nu_{ij} = -\frac{\varepsilon_{jj}}{\varepsilon_{ii}} \quad (6.101)$$

The above condition is for $\sigma_{jj} = \sigma$, with all other stresses being equal to zero. Since the stiffness coefficients $C_{ij} = C_{ji}$, from this it follows that the compliance matrix is also symmetric, that is, $S_{ij} = S_{ji}$. This condition enforces the relation among the Poisson's ratios as:

$$\frac{\nu_{ij}}{E_i} = \frac{\nu_{ji}}{E_j} \quad (6.102)$$

Hence, for a lamina under the 3-D state of stress, only three Poisson's ratios, namely ν_{12} , ν_{23} and ν_{31} , require to be determined. Other Poisson's ratios can be obtained from Equation (6.102).

For most of our analysis, we will assume the condition of plane stress. Here, we derive the equations assuming that the condition of plane stress exists in the 1–2 plane (see Figure 6.14 below). However, if one has to carry out an analysis of a laminated composite beam, which is essentially a 1-D member, the condition of plane stress will

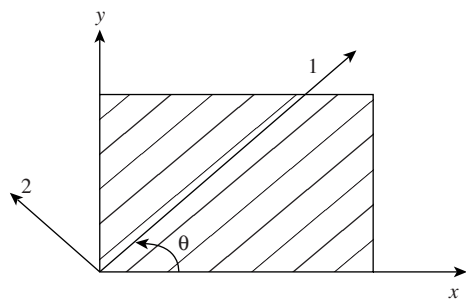


Figure 6.14 Principal material axes of a lamina, plus the 'global' x - y axes.

exist in the 1–3 plane and a similar procedure could be followed.

For the plane-stress condition in the 1–2 plane, we set the following stresses equal to zero in Equation (6.100), that is, $\sigma_{33} = \tau_{23} = \tau_{31} = 0$. The resulting constitutive model under the plane-stress condition can be written as:

$$\begin{Bmatrix} \varepsilon_{11} \\ \varepsilon_{22} \\ \gamma_{12} \end{Bmatrix} = \begin{bmatrix} \frac{1}{E_1} & \frac{-\nu_{12}}{E_1} & 0 \\ \frac{-\nu_{21}}{E_2} & \frac{1}{E_2} & 0 \\ 0 & 0 & \frac{1}{G_{12}} \end{bmatrix} \begin{Bmatrix} \sigma_{11} \\ \sigma_{22} \\ \tau_{12} \end{Bmatrix} \quad (6.103)$$

Note that the strain ε_{33} also exists, which can be obtained from the third constitutive equation:

$$\varepsilon_{33} = S_{13}\sigma_{11} + S_{23}\sigma_{22}$$

From this equation, it also means that the Poisson's ratios ν_{13} and ν_{23} should also exist. Inverting Equation (6.103), we can express the stresses in terms of strains, which are given by:

$$\begin{Bmatrix} \sigma_{11} \\ \sigma_{22} \\ \tau_{12} \end{Bmatrix} = \begin{bmatrix} Q_{11} & Q_{12} & 0 \\ Q_{12} & Q_{22} & 0 \\ 0 & 0 & Q_{66} \end{bmatrix} \begin{Bmatrix} \varepsilon_{11} \\ \varepsilon_{22} \\ \gamma_{12} \end{Bmatrix} \quad (6.104)$$

where Q_{ij} are the reduced stiffness coefficients, which can be expressed in terms of the elastic constants as:

$$Q_{11} = \frac{E_1}{1 - \nu_{12}\nu_{21}}, \quad Q_{12} = \frac{\nu_{21}E_1}{1 - \nu_{12}\nu_{21}} = \frac{\nu_{12}E_2}{1 - \nu_{12}\nu_{21}},$$

$$Q_{22} = \frac{E_2}{1 - \nu_{12}\nu_{21}}, \quad Q_{66} = G_{12} \quad (6.105)$$

6.2.3.1 Stress-strain relations for a lamina of arbitrary orientation

In most cases, the orientations of the global axes, which we call the $x-y$ axes, which are geometrically ‘natural’ for solution of the problem, do not coincide with the lamina principle axes, which we have already designated as the 1–2 axes. The lamina principal axes and the global axes are shown in Figure 6.14. A small element in the lamina of area dA is taken and the free-body diagram (FBD) is drawn as shown in Figure 6.15. Consider the free body A. Summing all of the forces in the direction of the 1-axis, we get:

$$\begin{aligned}\sigma_{11}dA - \sigma_{xx}(\cos\theta dA)(\cos\theta) - \sigma_{yy}(\sin\theta dA)(\sin\theta) \\ - \tau_{xy}(\sin\theta dA)(\cos\theta) - \tau_{xy}(\cos\theta dA)(\sin\theta) = 0\end{aligned}\quad (6.106)$$

On simplification, the above equation can be written as:

$$\sigma_{11} = \sigma_{xx}\cos^2\theta + \sigma_{yy}\sin^2\theta + 2\tau_{xy}\sin\theta\cos\theta \quad (6.107)$$

Similarly, by summing up all the forces along the 2-axis (free body A), we get:

$$\begin{aligned}\tau_{12}dA - \sigma_{xx}(\cos\theta dA)(\sin\theta) - \sigma_{yy}(\sin\theta dA)(\cos\theta) \\ - \tau_{xy}(\sin\theta dA)(\sin\theta) + \tau_{xy}(\cos\theta dA)(\cos\theta) = 0\end{aligned}\quad (6.108)$$

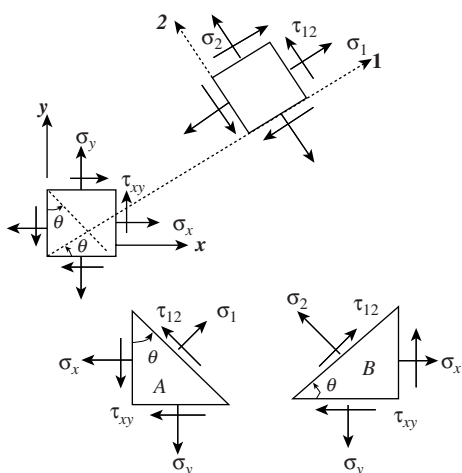


Figure 6.15 Lamina and laminate coordinate system and the free-body diagram (FBD) of a stressed element.

Simplifying the above equation, we get:

$$\tau_{12} = -\sigma_{xx}\sin\theta\cos\theta + \sigma_{yy}\sin\theta\cos\theta + \tau_{xy}(\cos^2\theta - \sin^2\theta) \quad (6.109)$$

Following the same procedure and summing up all the forces in the 2-direction in the free body B, we can write:

$$\sigma_{22} = \sigma_{xx}\sin^2\theta + \sigma_{yy}\cos^2\theta - 2\tau_{xy}\sin\theta\cos\theta \quad (6.110)$$

Equations (6.2.107), (6.2.109) and (6.2.110) can be written in the matrix form as

$$\begin{Bmatrix} \sigma_{11} \\ \sigma_{22} \\ \tau_{12} \end{Bmatrix} = \begin{bmatrix} C^2 & S^2 & 2CS \\ S^2 & C^2 & -2CS \\ -CS & CS & (C^2 - S^2) \end{bmatrix} \begin{Bmatrix} \sigma_{xx} \\ \sigma_{yy} \\ \tau_{xy} \end{Bmatrix},$$

$$C = \cos\theta, S = \sin\theta$$

or

$$\{\sigma\}_{1-2} = [T]\{\sigma\}_{x-y} \quad (6.111)$$

In a similar manner, the strains from the 1–2 axis can be transformed to the $x-y$ axis by a similar transformation. Note that by having the same transformation, shear strains are to be divided by two. Without going into much too detail, they can be written as:

$$\begin{Bmatrix} \varepsilon_{11} \\ \varepsilon_{22} \\ \frac{\gamma_{12}}{2} \end{Bmatrix} = \begin{bmatrix} C^2 & S^2 & 2CS \\ S^2 & C^2 & -2CS \\ -CS & CS & (C^2 - S^2) \end{bmatrix} \begin{Bmatrix} \varepsilon_{xx} \\ \varepsilon_{yy} \\ \frac{\gamma_{xy}}{2} \end{Bmatrix}$$

$$\text{or } \{\bar{\varepsilon}\}_{1-2} = [T]\{\bar{\varepsilon}\}_{x-y} \quad (6.112)$$

Inverting Equations (6.111) and (6.112), we can express the stresses and strains in terms of global coordinates as:

$$\begin{Bmatrix} \sigma_{xx} \\ \sigma_{yy} \\ \tau_{xy} \end{Bmatrix} = \begin{bmatrix} C^2 & S^2 & -2CS \\ S^2 & C^2 & 2CS \\ CS & -CS & (C^2 - S^2) \end{bmatrix} \begin{Bmatrix} \sigma_{11} \\ \sigma_{22} \\ \tau_{12} \end{Bmatrix},$$

$$\{\sigma\}_{x-y} = [T]^{-1}\{\sigma\}_{1-2} \quad (6.113)$$

$$\begin{Bmatrix} \varepsilon_{xx} \\ \varepsilon_{yy} \\ \frac{\gamma_{xy}}{2} \end{Bmatrix} = \begin{bmatrix} C^2 & S^2 & -2CS \\ S^2 & C^2 & 2CS \\ CS & -CS & (C^2 - S^2) \end{bmatrix} \begin{Bmatrix} \varepsilon_{11} \\ \varepsilon_{22} \\ \frac{\gamma_{12}}{2} \end{Bmatrix},$$

$$\{\bar{\varepsilon}\}_{x-y} = [T]^{-1}\{\bar{\varepsilon}\}_{1-2} \quad (6.114)$$

The actual strain vectors in both the 1–2 and $x-y$ axes, $\{\varepsilon\}_{1-2}$ and $\{\varepsilon\}_{x-y}$, can be related to $\{\bar{\varepsilon}\}_{1-2}$ and $\{\bar{\varepsilon}\}_{x-y}$

through a transformation matrix as:

$$\begin{cases} \varepsilon_{11} \\ \varepsilon_{22} \\ \gamma_{12} \end{cases} = \begin{bmatrix} 1 & 0 & 0 \\ 0 & 1 & 0 \\ 0 & 0 & 2 \end{bmatrix} \begin{cases} \bar{\varepsilon}_{11} \\ \bar{\varepsilon}_{22} \\ \frac{\gamma_{12}}{2} \end{cases}, \quad \text{and}$$

$$\begin{cases} \varepsilon_{xx} \\ \varepsilon_{yy} \\ \gamma_{xy} \end{cases} = \begin{bmatrix} 1 & 0 & 0 \\ 0 & 1 & 0 \\ 0 & 0 & 2 \end{bmatrix} \begin{cases} \bar{\varepsilon}_{xx} \\ \bar{\varepsilon}_{yy} \\ \frac{\gamma_{xy}}{2} \end{cases}$$

$$\{\varepsilon\}_{1-2} = [R]\{\bar{\varepsilon}\}_{1-2}, \quad \{\varepsilon\}_{x-y} = [R]\{\bar{\varepsilon}\}_{x-y} \quad (6.115)$$

Now, the constitutive equation of a lamina in its principal directions (Equation (6.104)) can now be written as:

$$\{\sigma\}_{1-2} = [\mathcal{Q}]\{\varepsilon\}_{1-2} \quad (6.116)$$

Substituting Equations (6.111), (6.112) and (6.115) into Equation (6.116), we get:

$$\begin{aligned} [T]\{\sigma\}_{x-y} &= [\mathcal{Q}][R]\{\bar{\varepsilon}\}_{1-2} = [\mathcal{Q}][R][T]\{\bar{\varepsilon}\}_{x-y} \\ &= [\mathcal{Q}][R][T][R]^{-1}\{\varepsilon\}_{x-y} \end{aligned}$$

Hence, the constitutive relation in the global $x-y$ axes can now be written as:

$$\{\sigma\}_{x-y} = [\bar{\mathcal{Q}}]\{\varepsilon\}_{x-y} = [T]^{-1}[\mathcal{Q}][R][T][R]^{-1}\{\varepsilon\}_{x-y} \quad (6.117)$$

Here, the matrix $[\bar{\mathcal{Q}}]$ is a fully populated matrix. Hence, although the lamina in its own principal direction is orthotropic, in the transformed coordinate it represents complete anisotropic behavior, that is, the normal stresses are coupled to the shear strains and vice versa. The elements of the $[\bar{\mathcal{Q}}]$ matrix is given by:

$$\begin{aligned} \bar{Q}_{11} &= Q_{11}C^4 + 2(Q_{12} + 2Q_{66})S^2C^2 + Q_{22}S^4 \\ \bar{Q}_{12} &= (Q_{11} + Q_{22} - 4Q_{66})S^2C^2 + Q_{12}(S^4 + C^4) \\ \bar{Q}_{16} &= (Q_{11} - Q_{12} - 2Q_{66})SC^3 + (Q_{12} - Q_{22} + 2Q_{66})S^3C \\ \bar{Q}_{22} &= Q_{11}S^4 + 2(Q_{12} + 2Q_{66})S^2C^2 + Q_{22}C^4 \\ \bar{Q}_{26} &= (Q_{11} - Q_{12} - 2Q_{66})S^3C + (Q_{12} - Q_{22} + 2Q_{66})SC^3 \\ \bar{Q}_{66} &= (Q_{11} + Q_{22} - 2Q_{12} - 2Q_{66})S^2C^2 + Q_{66}(S^4 + C^4) \end{aligned} \quad (6.118)$$

Equation (6.118) gives the constitutive equation of a lamina under plane stress in the $1-2$ plane.

6.2.4 Analysis of a laminate

A laminate is one in which two or more laminas are bonded together to form an integral structural element. Different laminas in the laminate have different principal directions and as a consequence, a laminate does not have any defined principal direction. In addition, different fiber orientations will enable resisting loads in different directions. The goal of the analysis is to use the determined properties of the laminas from micro- and macromechanical analysis to find the stress resultants acting on the laminate. The heart of the present analysis here is based on the Classical Lamination Theory (CLT).

6.2.4.1 Classical lamination theory (CLT)

The approach used in the CLT is to first write the lamina constitutive relations for each laminate. Based on the mechanics of the structure, a suitable displacement field is assumed from which the strains and the stresses in each lamina are found. These are then integrated over the thickness to get the overall stress resultants. In this process, we will also obtain the coupling stiffness matrices at the laminate level, which are normally called the $[A]$, $[B]$ and $[D]$ matrices. Matrix $[B]$ determines the extent of stiffness coupling in the laminate.

The lamina constitutive relation was derived earlier and is given in Equation (6.117). For the k^{th} lamina in a laminate, the stress strain relation can be written as:

$$\{\sigma\}_k = [\bar{\mathcal{Q}}_k]\{\varepsilon\}_k \quad (6.119)$$

Next, the stress resultants for the laminate are established. For this, consider the laminate shown in Figure 6.16.

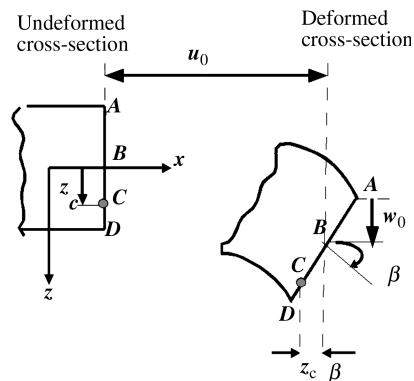


Figure 6.16 Deformation of a laminate in the $x-y$ plane.

Assuming no shear deformation and the condition of plane stress, the laminate displacement fields can be assumed as:

$$\begin{aligned} u(x, y, z) &= u_0(x, y) - z \frac{\partial w_0}{\partial x}, \\ v(x, y, z) &= v_0(x, y) - z \frac{\partial w_0}{\partial y}, \\ w(x, y, z) &= w_0(x, y) \end{aligned} \quad (6.120)$$

Here, u_0 , v_0 and w_0 are the mid-plane displacements. The second term in the u and v displacement fields represents the respective slopes of a laminate. From these displacement fields, the strains can be evaluated as:

$$\begin{aligned} \varepsilon_{xx} &= \frac{\partial u}{\partial x} = \frac{\partial u_0}{\partial x} - z \frac{\partial^2 w_0}{\partial x^2}, \quad \varepsilon_{yy} = \frac{\partial v}{\partial y} = \frac{\partial v_0}{\partial y} - z \frac{\partial^2 w_0}{\partial y^2} \\ \gamma_{xy} &= \frac{\partial u}{\partial y} + \frac{\partial v}{\partial x} = \frac{\partial u_0}{\partial y} + \frac{\partial v_0}{\partial x} - 2z \frac{\partial^2 w_0}{\partial x \partial y} \end{aligned} \quad (6.121)$$

The above strain fields can be written as:

$$\begin{aligned} \begin{Bmatrix} \varepsilon_{xx} \\ \varepsilon_{yy} \\ \gamma_{xy} \end{Bmatrix} &= \begin{Bmatrix} \varepsilon_{xx}^0 \\ \varepsilon_{yy}^0 \\ \gamma_{xy}^0 \end{Bmatrix} + z \begin{Bmatrix} \kappa_{xx} \\ \kappa_{yy} \\ \kappa_{xy} \end{Bmatrix}, \\ \begin{Bmatrix} \varepsilon_{xx}^0 \\ \varepsilon_{yy}^0 \\ \gamma_{xy}^0 \end{Bmatrix} &= \begin{Bmatrix} \frac{\partial u_0}{\partial x} \\ \frac{\partial v_0}{\partial y} \\ \frac{\partial u_0}{\partial y} + \frac{\partial v_0}{\partial x} \end{Bmatrix}, \quad \begin{Bmatrix} \kappa_{xx} \\ \kappa_{yy} \\ \kappa_{xy} \end{Bmatrix} = \begin{Bmatrix} \frac{\partial^2 w_0}{\partial x^2} \\ \frac{\partial^2 w_0}{\partial y^2} \\ \frac{\partial^2 w_0}{\partial x \partial y} \end{Bmatrix} \end{aligned} \quad (6.122)$$

The first term represents the normal strain, while the second term represents the curvature. As in the case of beams, the strain varies linearly over the depth. The stress-strain relation for the k^{th} laminate is written by inserting the above strain field in Equation (6.119), which is given by:

$$\begin{Bmatrix} \sigma_{xx} \\ \sigma_{yy} \\ \tau_{xy} \end{Bmatrix}_k = \begin{bmatrix} \bar{Q}_{11} & \bar{Q}_{12} & \bar{Q}_{16} \\ \bar{Q}_{12} & \bar{Q}_{22} & \bar{Q}_{26} \\ \bar{Q}_{16} & \bar{Q}_{26} & \bar{Q}_{66} \end{bmatrix} \left\{ \begin{Bmatrix} \varepsilon_{xx}^0 \\ \varepsilon_{yy}^0 \\ \gamma_{xy}^0 \end{Bmatrix} + z \begin{Bmatrix} \kappa_{xx} \\ \kappa_{yy} \\ \kappa_{xy} \end{Bmatrix} \right\} \quad (6.123)$$

On a laminate, there are three force resultants, namely N_x , N_y and N_{xy} and three moment resultants namely

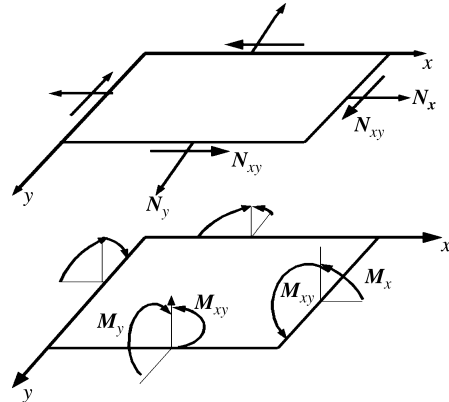


Figure 6.17 Force and moment resultants on a laminate.

M_x , M_y and M_{xy} (shown in Figure 6.17). The resultant forces and moments are obtained by integration of the stresses in each lamina through the laminate thickness. These can be written for an N -ply laminate as:

$$\begin{Bmatrix} N_x \\ N_y \\ N_{xy} \end{Bmatrix} = \int_{-h/2}^{h/2} \begin{Bmatrix} \sigma_{xx} \\ \sigma_{yy} \\ \tau_{xy} \end{Bmatrix}_k dz = \sum_{k=1}^N \int_{z_{k-1}}^{z_k} \begin{Bmatrix} \sigma_{xx} \\ \sigma_{yy} \\ \tau_{xy} \end{Bmatrix}_k dz \quad (6.124)$$

and

$$\begin{Bmatrix} M_x \\ M_y \\ M_{xy} \end{Bmatrix} = \int_{-h/2}^{h/2} \begin{Bmatrix} \sigma_{xx} \\ \sigma_{yy} \\ \tau_{xy} \end{Bmatrix}_k z dz = \sum_{k=1}^N \int_{z_{k-1}}^{z_k} \begin{Bmatrix} \sigma_{xx} \\ \sigma_{yy} \\ \tau_{xy} \end{Bmatrix}_k z dz \quad (6.125)$$

Here, h is the laminate thickness and z_{k-1} and z_k represent the ply depths from the middle plane – shown in Figure 6.18. Substituting for the stresses from Equation (6.123) in Equation (6.125) and designating:

$$A_{ij} = \sum_{k=1}^N (\bar{Q}_{ij})_k (z_k - z_{k-1}) \quad (6.126)$$

$$B_{ij} = \frac{1}{2} \sum_{k=1}^N (\bar{Q}_{ij})_k (z_k^2 - z_{k-1}^2) \quad (6.127)$$

$$D_{ij} = \frac{1}{3} \sum_{k=1}^N (\bar{Q}_{ij})_k (z_k^3 - z_{k-1}^3) \quad (6.128)$$

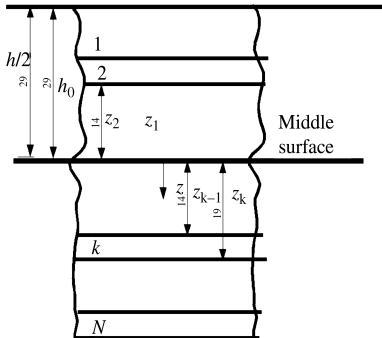


Figure 6.18 Depth coordinates for an N -layered laminate.

we can write the stress resultants as

$$\begin{Bmatrix} N_x \\ N_y \\ N_{xy} \end{Bmatrix} = \begin{bmatrix} A_{11} & A_{12} & A_{16} \\ A_{12} & A_{22} & A_{26} \\ A_{16} & A_{26} & A_{66} \end{bmatrix} \begin{Bmatrix} \varepsilon_{xx}^0 \\ \varepsilon_{yy}^0 \\ \gamma_{xy}^0 \end{Bmatrix} + \begin{bmatrix} B_{11} & B_{12} & B_{16} \\ B_{12} & B_{22} & B_{26} \\ B_{16} & B_{26} & B_{66} \end{bmatrix} \begin{Bmatrix} \kappa_{xx} \\ \kappa_{yy} \\ \kappa_{xy} \end{Bmatrix} \quad (6.129)$$

$$\begin{Bmatrix} M_x \\ M_y \\ M_{xy} \end{Bmatrix} = \begin{bmatrix} B_{11} & B_{12} & B_{16} \\ B_{12} & B_{22} & B_{26} \\ B_{16} & B_{26} & B_{66} \end{bmatrix} \begin{Bmatrix} \varepsilon_{xx}^0 \\ \varepsilon_{yy}^0 \\ \gamma_{xy}^0 \end{Bmatrix} + \begin{bmatrix} D_{11} & D_{12} & D_{16} \\ D_{12} & D_{22} & D_{26} \\ D_{16} & D_{26} & D_{66} \end{bmatrix} \begin{Bmatrix} \kappa_{xx} \\ \kappa_{yy} \\ \kappa_{xy} \end{Bmatrix} \quad (6.130)$$

Equations (6.129) and (6.130) can be combined and written as:

$$\begin{Bmatrix} \{N\} \\ \{M\} \end{Bmatrix} = \begin{bmatrix} [A] & [B] \\ [B] & [D] \end{bmatrix} \begin{Bmatrix} \{\varepsilon^0\} \\ \{\kappa\} \end{Bmatrix} \quad (6.131)$$

Equation (6.131) represents the stiffness equation for a laminate. Here, A_{ij} represents the axial stiffness and D_{ij} represents the bending stiffness of the laminate. B_{ij} is the coupling stiffness matrix and exists only for an unsymmetric ply lay up. In other words, the complete stiffness coupling is represented by this matrix B_{ij} .

6.3 INTRODUCTION TO WAVE PROPAGATION IN STRUCTURES

In this section, we present some introductory concepts of wave propagation in structures. The question that one

may be asking is why this part is necessary in the first place in a book dealing with smart materials, structures and MEMS. The reason is quite simple. Today, there is a new class of analytical (numerical) techniques available for modeling, which is based on wave propagation theories. This method, which is described in detail in the next chapter, and used extensively in many examples in this book, is called the *Spectral Finite Element Method* (SFEM). Some applications presented in the last part of the book are based on wave solutions. Some of the modeling and control aspects dealt with in Chapters 7, 8 and 9 derive their origin from the governing wave equation. Hence, it becomes necessary for the reader to understand the rudiments of wave propagation before he/she attempts to understand some of the topics given in the later part of this book.

A structure, when subjected to dynamic loads, will experience stresses of varying degree of severity depending upon the load magnitude and its duration. If the temporal variation of load is of a large duration (of the order of seconds), the intensity of the load felt by the structure will usually be of lower severity and such problems falls under the category of *Structural Dynamics*. For such problems, there are two parameters which are of paramount importance in the determination of its response, namely the natural frequency of the system and its normal modes (mode shapes). The total response of the structure is obtained by the superposition of the first few normal modes. A large duration of the load makes it low on the frequency content and hence the load will excite only the first few modes. Hence, the structure could be idealized with fewer unknowns (which we call the degrees of freedom, a terminology which we will introduce in the next chapter). However, when the duration of the load is small (of the order of microseconds), stress waves are set up, which start propagating in the medium with certain velocities. Hence, the response is necessarily transient in nature and in this process many normal modes will get excited. Hence, the model sizes will be many orders larger than what is required for the structural dynamics problem. Such problems come under the category of *Wave Propagation*. The key factors in the wave propagation are the propagating velocity, level of attenuation of the response and its wavelengths. Hence, phase information is one of the most important parameters, which is of no concern in the structural dynamics problems.

Since wave propagation is a multi-modal phenomenon, the analysis becomes quite complex when the problem is solved in the time domain. This is because the problem by its very nature is a high-frequency-content problem. Hence, the analysis methods based on the frequency

domain are highly suited for such problems. That is, all of the governing equations, boundary conditions and variables are transformed to the frequency domain using any of the integral transforms available. The most common transformation for transforming the problem to the frequency domain is *Fourier Transform*. This transform has a discrete representation and hence is amenable for numerical implementation, which makes it very attractive for its usage in wave propagation problems. By transforming the problem into the frequency domain, the complexity of the governing partial differential equation is reduced by removing the time variable out of the picture, thus making the solution of the resulting Ordinary Differential Equation (ODE) much simpler than the original equation. In wave propagation problems, two parameters are very important, namely the wavenumber and the speeds of the propagation. There are many types of waves that can be generated in a structure. Wavenumbers reveal the type of waves that are generated. These give us two important relations, namely the *Spectrum Relation*, which is a plot of the wavenumber with the frequency and the *Dispersion Relation*, which is a plot of wave velocity with the frequency. These relations reveal the characteristics of different waves that are generated in a given structure.

In this subsection, first the basic Fourier theory is discussed, which forms the ‘backbone’ of all our wave analysis to follow. Next, the spectral analysis of motion is discussed, wherein the determination of wavenumbers and speeds is given. This will be followed by a subsection on wave propagation in all commonly occurring structural elements.

6.3.1 Fourier analysis

The time signal encountered in wave mechanics has two extreme bounds in the temporal axis, that is, from $-\infty$ to $+\infty$ and is assumed to persist at all times. This signal can be represented in the Fourier domain in three possible ways, namely the *Continuous Fourier Transforms* (CFTs), the *Fourier Series* (FS) and the *Discrete Fourier Transforms* (DFTs). In this section, only brief definitions of the above transforms are given. The interested reader is encouraged to refer to many classic textbooks, such as Chatfield [5] and Sneddon [6], available on this subject for greater detail.

6.3.1.1 Continuous Fourier Transforms

Consider any time signal $F(t)$. The inverse and the forward CFT, which are normally referred to as a transform pair,

are given by:

$$F(t) = \frac{1}{2\pi} \int_{-\infty}^{\infty} \hat{F}(\omega) e^{i\omega t} d\omega, \quad \hat{F}(\omega) = \int_{-\infty}^{\infty} F(t) e^{-i\omega t} dt \quad (6.132)$$

where, $\hat{F}(\omega)$ is the CFT of the time signal, ω is the angular frequency and $i = \sqrt{-1}$. $\hat{F}(\omega)$ is necessarily complex and a plot of the amplitude of this function with the frequency will give the frequency content of the time signal. As an example, consider a rectangular time signal of pulse width d . Mathematically, this function can be represented as:

$$\begin{aligned} F(t) &= F_0 & -d/2 \leq t \leq d/2 \\ &= 0 & \text{otherwise} \end{aligned}$$

This time signal is symmetric about the origin. If this pulse is substituted in Equation (6.132), we get:

$$\hat{F}(\omega) = F_0 d \left\{ \frac{\sin(\omega d/2)}{\omega d/2} \right\} \quad (6.133)$$

The CFT in this case is real only and as seen from Figure 6.19, it is symmetric about $\omega = 0$. The term

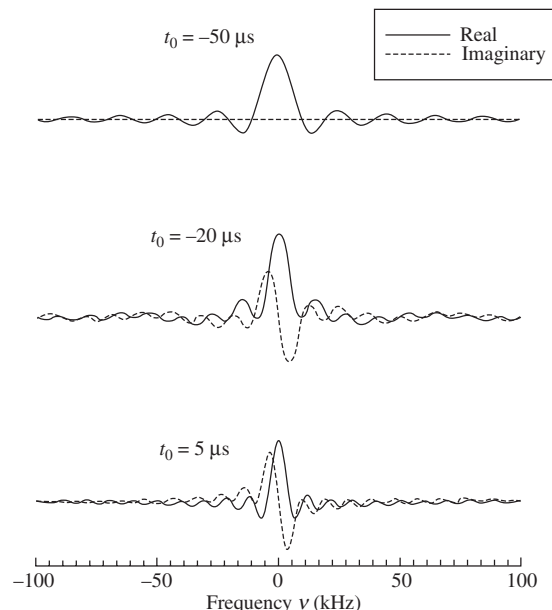


Figure 6.19 Continuous Fourier transforms for various pulse widths.

inside the brace is called the *sinc function*. In addition, the value of the CFT at $\omega = 0$ is equal to the area under the time signal.

Now, if the pulse is allowed to propagate in the time domain by an amount t_s seconds, mathematically such a signal can be written as:

$$\begin{aligned} F(t) &= F_0 & t_s \leq t \leq t_s + d \\ &= 0 & \text{otherwise} \end{aligned}$$

Substituting the above function into Equation (6.132) and integrating, we get:

$$\hat{F}(\omega) = F_0 d \left\{ \frac{\sin(\omega d/2)}{\omega d/2} \right\} e^{-i\omega(t_s+d/2)} \quad (6.134)$$

The above CFT has both real and imaginary parts. These are again plotted in Figure 6.19. From Equations (6.133) and (6.134), we see that the magnitudes of both of these transforms are the same; however, the second transform has phase information built into it. Furthermore, we see that propagation of the signal in the time domain is associated with the change of phase in the frequency domain. Wave-propagation problems are always associated with the phase changes occurring as the signal propagates.

Based on the CFT, one can also determine the spread of the signal both in the time and frequency domains. For this, one has to look at the frequencies at which the CFT is zero. This occurs when:

$$\begin{aligned} \sin\left(\frac{\omega_n d}{2}\right) &= 0, \quad \text{or} \quad \frac{\omega_n d}{2} = n\pi \quad \text{or} \quad \omega_n = \frac{2n\pi}{d} \\ \omega_2 - \omega_1 &= \Delta\omega = \frac{2\pi}{d} \end{aligned}$$

That is, if the spread of the signal in the time domain is d , then the spread in the frequency domain is $\Delta\omega = 2\pi/d$. In other words, if the spread in the time domain is small, then the spread in the frequency domain gets larger. Here, $\Delta\omega$ represents the frequency bandwidth. Hence, a *Dirac Delta function*, which has infinitesimal width in the time domain, will have infinite bandwidth in the frequency domain. This aspect has greater implications in choosing the mesh sizes, when one resorts to the Finite Element technique to solve the wave-propagation problem. The following are some of the properties of the CFT:

- **Linearity:** Consider two time functions $F_1(t)$ and $F_2(t)$. The CFTs of these functions are given by $\hat{F}_1(\omega)$ and $\hat{F}_2(\omega)$ and then the Fourier transform of the combined function $F_1(t) + F_2(t) \Leftrightarrow \hat{F}_1(\omega) + \hat{F}_2(\omega)$.

Here, the symbol ‘ \Leftrightarrow ’ is used to denote the CFT of a time signal.

Implications in wave propagation: Here, $F_1(t)$ and $F_2(t)$ can be thought of as the incident and reflected waves, respectively. The linearity property states that the combined transforms of the incident and reflected waves are equal to the individual transform of these obtained separately.

- **Scaling:** If a time signal $F(t)$ is multiplied by a factor k to become $F(kt)$, the CFT of this time signal is given by $F(kt) \Leftrightarrow 1/k\hat{F}(\omega/k)$.

Implications in wave propagation: Time-domain compression is the frequency-domain expansion. That is, this property fixes the frequency bandwidth of the given time signal.

- **Time shifting:** If a given time signal $F(t)$ is shifted by an amount t_s to become $F(t - t_s)$, the CFT of the shifted signal is given by $F(t - t_s) \Leftrightarrow \hat{F}(\omega)e^{-i\omega t_s}$.

Implications in wave propagation: Propagation in the time domain is accompanied by the phase changes in the frequency domain.

- **The CFT is always complex:** Any given time function $F(t)$ can be split up into symmetric and antisymmetric functions, $F_s(t)$ and $F_a(t)$. Furthermore, by using the property of the linearity of the CFT, we can show that:

$$F_s(t) = \text{Real } (\hat{F}(\omega)) \text{ and } F_a(t) = i \text{Imag } (\hat{F}(\omega)).$$

Implications in wave propagation: Since the time signals encountered in wave mechanics are neither symmetric (even) or antisymmetric (odd) in nature, the CFT is necessarily complex in nature. Hence, wave-propagation problems are always associated with phase changes.

- **Symmetric property of the CFT:** Since the CFT of a time signal $F(t)$ is complex, it can be split up into real and imaginary parts as $\hat{F}(\omega) = \hat{F}_R(\omega) + i\hat{F}_I(\omega)$. Substituting this in the first equation of Equation (6.132) and expanding the complex exponential in terms of sine and cosine functions, we can write the real and imaginary parts of the transform as:

$$\hat{F}_R = \int_{-\infty}^{\infty} F(t) \cos(\omega t) dt, \quad \hat{F}_I = \int_{-\infty}^{\infty} F(t) \sin(\omega t) dt$$

The first integral is the even function and the second is the odd function, that is, $\hat{F}_R(\omega) = \hat{F}_R(-\omega)$ and $\hat{F}_I(\omega) = -\hat{F}_I(-\omega)$. Now, if we consider the CFT about a point $\omega = 0$ (origin), the transform on the right of the origin can be written as $\hat{F}(\omega) = \hat{F}_R(\omega) + i\hat{F}_I(\omega)$. Similarly, the transforms to the left of the origin

can be written as $\hat{F}(-\omega) = \hat{F}_R(-\omega) + i\hat{F}_I(-\omega) = \hat{F}_R(\omega) - i\hat{F}_I(\omega) = \hat{F}^*(\omega)$, which is the complex conjugate of the transform on the right side of the origin. The zero frequency point about which this happens is called the *Nyquist Frequency*.

Implication in wave propagation: The Nyquist frequency is an important parameter in wave propagation analysis, especially in the context of using a *Fast Fourier Transform* (to be introduced later), since it is only up to this frequency that all of the analysis can be performed.

- **Convolution:** This is a property relating to the product of two time signals $F_1(t)$ and $F_2(t)$. The CFT of the product of these two functions can be written as:

$$\hat{F}_{12}(\omega) = \int_{-\infty}^{\infty} F_1(t)F_2(t)e^{-i\omega t} dt$$

Now, substituting Equation (6.132) for both of these functions in the above equation, we can write:

$$\begin{aligned}\hat{F}_{12}(\omega) &= \int_{-\infty}^{\infty} \hat{F}_1(\bar{\omega}) \int_{-\infty}^{\infty} F_2(t)e^{-i(\omega-\bar{\omega})t} dt d\bar{\omega} \\ &= \int_{-\infty}^{\infty} \hat{F}_1(\bar{\omega}) \hat{F}_2(\omega - \bar{\omega}) d\bar{\omega} \quad \text{or} \\ F_1(t)F_2(t) &\Leftrightarrow \int_{-\infty}^{\infty} \hat{F}_1(\bar{\omega}) \hat{F}_2(\omega - \bar{\omega}) d\bar{\omega}\end{aligned}$$

The above form of the CFT is called the *Convolution*. Conversely, we can also write:

$$\hat{F}_1(\omega)\hat{F}_2(\omega) \Leftrightarrow \int_{-\infty}^{\infty} F_1(\tau)F_2(t-\tau) d\tau$$

Implication in wave propagation: The first property of using the product of two time domain signals has its use in understanding the signal-processing aspects. For example, a truncated signal in the time domain is equal to the product of the original signal and the truncated signal. The second (or the converse) property is of great utility in wave-propagation analysis. That is, all of the responses (output) of mechanical waveguides to applied loadings can be represented as the frequency-domain product of the input times the system transfer function. Thus, the time responses are

obtained by convolving the transfer functions with the load spectrum.

6.3.1.2 Fourier series

Both forward and inverse CFTs require mathematical descriptions of the time signals, as well as their integration. In most cases, the time signals are ‘point-data’ acquired during experimentation. Hence, what we require is the numerical representation for the transform pair (Equation (6.132)), which is called the *Discrete Fourier Transform* (DFT). This is introduced in great detail in the next subsection. The *Fourier Series* (FS) is inbetween the CFT and the DFT, wherein the inverse transform is represented by a series, while the forward transform is still in the integral form as in the CFT. That is, one still needs a mathematical description of the time signal for getting these transforms.

The FS of a given time signal can be represented as:

$$F(t) = \frac{a_0}{2} + \sum_{n=1}^{\infty} \left[a_n \cos\left(2\pi n \frac{t}{T}\right) + b_n \sin\left(2\pi n \frac{t}{T}\right) \right] \quad (6.135)$$

where,

$$\begin{aligned}a_n &= \frac{2}{T} \int_0^T F(t) \cos\left(2\pi n \frac{t}{T}\right) dt, \\ b_n &= \frac{2}{T} \int_0^T F(t) \sin\left(2\pi n \frac{t}{T}\right) dt, \quad n = 0, 1, 2, \dots\end{aligned} \quad (6.136)$$

Equation (6.135) corresponds to the inverse transform of the CFT, while Equation (6.136) corresponds to the forward transforms of the CFT. Here, T is the period of the time signal. That is, the discrete representation of a continuous time signal, $F(t)$, introduces periodicity to the time signal. The FS given in Equation (6.135) can also be written in terms of complex exponentials, which can give a one-to-one comparison with the CFT. That is, Equations (6.135) and (6.136) can be rewritten as:

$$\begin{aligned}F(t) &= \frac{1}{2} \sum_{-\infty}^{\infty} (a_n - b_n) e^{i\omega_n t} = \sum_{-\infty}^{\infty} \hat{F}_n e^{i\omega_n t} \\ n &= 0, \pm 1, \pm 2, \dots \\ \hat{F}_n &= \frac{1}{T} (a_n - b_n) = \frac{1}{T} \int_0^T F(t) e^{-i\omega_n t} dt, \quad \omega_n = \frac{2\pi n}{T} \quad (6.137)\end{aligned}$$

Because of the enforced periodicity, the signal repeats itself after every T seconds. Hence, we can define the fundamental frequency either in radians per second (ω_0) or Hertz ($f_0 = \omega_0/2\pi = 1/T$).

We can now express the time signal in terms of the fundamental frequency as:

$$F(t) = \sum_{-\infty}^{\infty} \hat{F}_n e^{i2\pi n f_0 t} = \sum_{-\infty}^{\infty} \hat{F}_n e^{in\omega_0 t} \quad (6.138)$$

From Equation (6.138), it is clear that, unlike in the CFT, the transform given by the FS is discrete in frequency. To understand the behavior of the FS as opposed to the CFT, the same rectangular time signal used earlier is again considered here. The FS coefficients (or transform) are obtained by substituting the time-signal variation in Equation (6.137). This is given by:

$$\hat{F}_n = \frac{F_0}{T} \left[\frac{\sin\left(\frac{\pi n d}{T}\right)}{\frac{n\pi d}{T}} \right] e^{-i(t_s+d/2)2\pi n/T} \quad (6.139)$$

The plot of transform amplitude obtained from the CFT and FS are shown in Figure 6.20. This figure shows that the value of the transform obtained by the FS at discrete

frequencies falls exactly on the transform obtained by the CFT. This figure also shows the transform values for different time periods T . We see from this figure that the larger the time period, then the more close are the frequency spacings. Hence, if the period tends to infinity, the transform obtained by the FS will be exactly equal to the transform obtained by the CFT.

6.3.1.3 Discrete Fourier transforms

The *Discrete Fourier Transform* (DFT) is the other alternate way of mathematically representing the CFT in terms of summations. Here, both the forward and inverse CFT given in Equation (6.132) are represented by summations. This will completely do away with all of the complex integration involved in computation of the CFT. In addition, it is not necessary to represent the time signals mathematically and the great advantage of this is that one can use the time data obtained from experimentation. Numerical implementation of the DFT is done by using the famous *Fast Fourier Transform* (FFT) algorithm.

We begin here with Equation (6.137), which is the FS representation of the time signal. The main objective here is to replace the integral involved in computation of the Fourier coefficients by summation. For this, the plot of

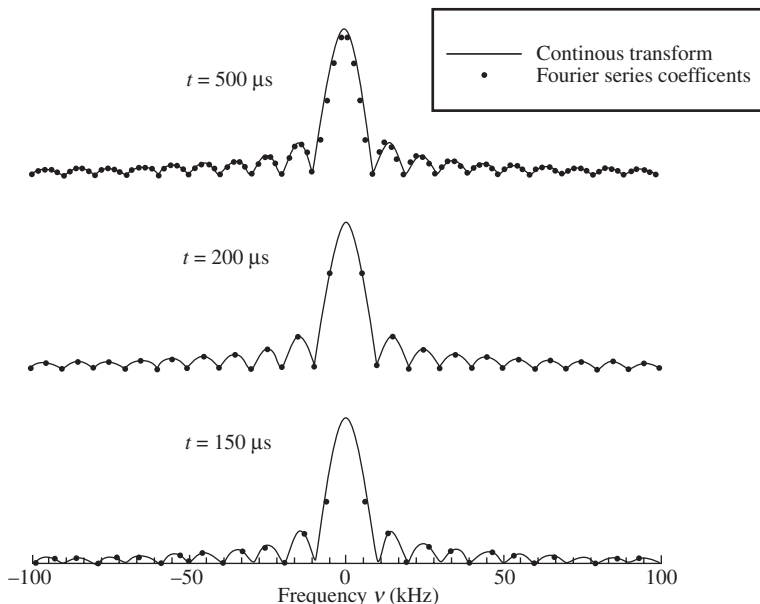


Figure 6.20 Comparison of Fourier series with continuous Fourier transforms.

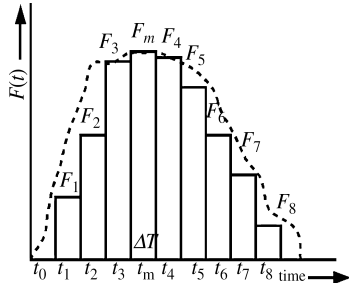


Figure 6.21 Time-signal digitization for discrete Fourier transforms (DFTs).

the time signal shown in Figure 6.21 is considered. The time signal is divided into M piecewise constant rectangles, whose height is given by F_m and the width of these rectangles is equal to $\Delta T = T/M$. We have derived earlier that the continuous transform of a rectangle is a *sinc* function. By rectangular idealization of the signal, the DFT of the signal will be the summation of M *sinc* functions of pulse width ΔT and hence the second integral in Equation (6.137) can now be written as:

$$\hat{F}_n = \Delta T \left[\frac{\sin(\omega_n \Delta T / 2)}{(\omega_n \Delta T / 2)} \right] \sum_{m=0}^M F_m e^{-i\omega_n t_m} \quad (6.140)$$

Let us now look at the *sinc* function in Equation (6.140). Its value depends on the width of the rectangle ΔT . That is, as the width of the rectangle becomes smaller, the term inside the bracket of Equation (6.140) tends to reach a unit value. This will happen for all values of $n < M$. It can be easily shown that for values of $n \geq M$, the values of the transform is approximately equal to zero. Hence, the DFT transform pairs can now be written as:

$$\begin{aligned} F_m &= F(t_m) = \frac{1}{T} \sum_{n=0}^{N-1} \hat{F}_n e^{i\omega_n t_m} = \frac{1}{T} \sum_{n=0}^{N-1} \hat{F}_n e^{i2\pi nm/N} \\ \hat{F}_n &= \hat{F}(\omega_n) = \Delta T \sum_{m=0}^{N-1} F_m e^{-i\omega_n t_m} \\ &= \Delta T \sum_{m=0}^{N-1} F_m e^{-i2\pi nm/N} \end{aligned} \quad (6.141)$$

Here, both m and n range from 0 to $N - 1$.

The periodicity of the time signal is necessary for the DFT as we begin from FS representation of the time signal. Now, we can probe a little further to see whether the signal has any periodicity in the frequency domain. For this, we can look at the summation term in Equation

(6.140). Hypothetically, let us assume that $n > M$. Hence, we can write $n = M + \bar{n}$. Then, the exponential term in the equation becomes:

$$\begin{aligned} e^{-i\omega_n t_m} &= e^{-in\omega_0 t_m} = e^{-iM\omega_0 t_m} e^{-i\bar{n}\omega_0 t_m} \\ &= e^{-i2\pi m} e^{-i\bar{n}\omega_0 t_m} = e^{-i\bar{n}\omega_0 t_m} \end{aligned}$$

Hence, the summation term in Equation (6.140) becomes:

$$\Delta T \sum_{m=0}^{M-1} F_m e^{-i\bar{n}\omega_0 t_m}$$

This term shows that the above summation evaluates the same value when $n = \bar{n}$. For example, if $M = 6$, then for $n = 9, 11$ and 17 evaluate the same as $n = 3, 5$ and 11 , respectively. Two aspects are very clear from this analysis. First $n > M$ is not important and the second is that there is forced periodicity in both the time and frequency domains in using the DFT. This periodicity occurs about a frequency where the transform goes to zero. This frequency can be obtained if one looks at the *sinc* function given in Equation (6.140). That is, the argument of the *sinc* function is given by:

$$\frac{\omega_n \Delta T}{2} = \pi n \Delta T = \frac{\pi n}{M}$$

where, we have used the relation $\Delta T = T/M$ in the above.

Here, we see that the *sinc* function goes to zero when $n = M$. It is at this value of n that the periodicity is enforced and the frequency corresponding to this value is called the *Nyquist* frequency. As mentioned earlier, this happens due to the time signal being real only and the transform beyond the Nyquist frequency is the complex conjugate of the transform before this frequency. Thus, N real points are transformed to $N/2$ complex points. Knowing the sampling rate ΔT , we can compute the Nyquist frequency from the expression:

$$f_{\text{Nyquist}} = \frac{1}{2\Delta T} \quad (6.142)$$

Numerical implementation of the DFT is the *Fast Fourier Transform* (FFT). There are a number of issues in numerical implementation of the DFT. These are not discussed here. However, the interested reader is encouraged to refer to many classic textbooks, such as Chatfield [5] and Sneddon [6], to obtain more information on these aspects. In all of the wave-propagation examples given in

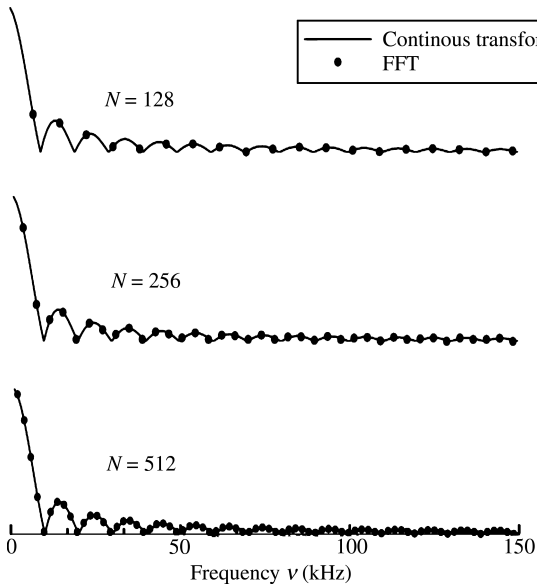


Figure 6.22 Comparison of the fast-Fourier transform (FFT) and a continuous transform for a sampling rate ΔT of $1 \mu\text{s}$.

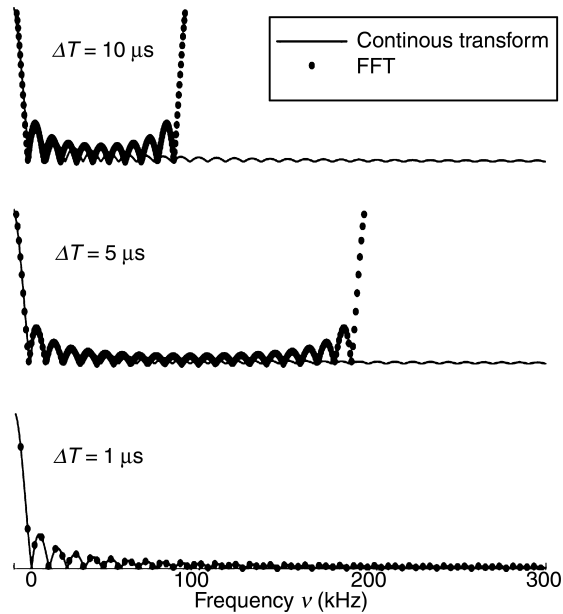


Figure 6.23 Comparison of the fast-Fourier transform (FFT) and a continuous transform for various sampling rates.

this text book, the FFT is used to transform the signal back and forth between time and the frequency.

In order to see the differences in the different transform representations, the same rectangular pulse is again used here. There are two parameters on which the accuracy of the transforms obtained from the DFT depends, namely the sampling rate ΔT and the time window parameter N . Figures 6.22 and 6.23 show the transforms obtained for various sampling rates ΔT and the time window parameter N . From these figures, we can clearly see the periodicity about the Nyquist frequency. For a given time window N , the figures show that the frequency spacing increases with the decrease in the sampling rate. In addition, the Nyquist frequency shifts to a higher value. Next, for a given sampling rate ΔT , the time window is varied through the parameter N . In this case, the Nyquist frequency does not change. However, for larger N , the frequency spacing becomes smaller and hence we get a denser frequency distribution.

6.3.2 Wave characteristics in 1-D waveguides

In this section, we will describe the different types of waves that are associated with 1-D waveguides. The general procedure to determine the wave characteristics is to first establish the governing partial differential equation of motion. This equation is transformed to the

Fourier domain by using a forward FFT. The resulting equation is then solved to determine the wave parameters, such as wavenumbers, phase speeds and group speeds. Determination of these parameters will eventually lead to the solutions for displacements, velocities and accelerations. Before outlining the procedure in greater detail, first a few wave propagation terminologies are introduced:

- Waveguide.** Any structural element is called a waveguide as it guides the wave in a particular manner. For example, a rod essentially supports only the axial motion and hence it is called an *axial* or *longitudinal* waveguide. In the case of a beam, only a bending motion is possible and hence the beam is called a *flexural* waveguide. In the case of shafts, the only possible motion is a ‘twist’ and hence they are known as *torsional* waveguides. In the case of a laminated composite beam, due to the stiffness coupling both axial and flexural motions are possible. In general, if there are n highly coupled governing partial differential equations, then such a waveguide can support n different motions.
- Wavenumber.** This is a frequency-dependent parameter which determines the following: (1) whether the wave is propagating or non-propagating or will

propagate after a certain frequency; (2) the type of wave – *dispersive* or *non-dispersive*. Non-dispersive waves are those that retain their shapes as they propagate, while dispersive waves completely change their shapes as they propagate. That is, if the wavenumber (k) is expressed as a linear function of frequency (ω), say $k = a\omega$, then the waves will be non-dispersive in nature. Wavenumber in rods and in general for most second-order systems will be of this form and hence the waves in such waveguides will be non-dispersive in nature. However, if the wave number is of the form $k = a\omega^n$, the waves will essentially be dispersive. Such a behavior can be seen in higher-order systems such as beams and plates. The plot of wavenumber with frequency is usually referred to as a *spectrum relation*.

- (c) **Phase speeds.** These are the speeds of the individual particles that propagate in the structure. They are related to the wavenumber through the relation $C_p = \omega/k$. If the waves are non-dispersive in nature (that is, $k = a\omega$), then the phase speeds are constant and independent of frequency. Conversely, if the phase speeds are constant, then such a system is a non-dispersive system.
- (d) **Group speeds.** During the propagation of waves, groups of particles travel in bunches. The speeds of each of these groups are called the group speeds of the wave. They are mathematically expressed as $C_g = d\omega/dk$. Again here, for a non dispersive system, the group speeds are constant and independent of frequency. The time of arrival of all of the waves will be based on this speed. The plot of phase/group speeds with frequency is called the *dispersion relation*.

6.3.2.1 Wave equation for a generalized higher-order anisotropic laminated composite beam

For characterization of the waves, it is first necessary to obtain the wave equation for the waveguide under consideration. Here, we derive the wave equation for the most complicated 1-D structure, namely the unsymmetric higher-order laminated composite beam. From this equation, various simplifications can be made to obtain the governing wave equations for different waveguide models, such as elementary isotropic rods and beams, higher-order rods and beams, elementary laminated composite beams and higher-order laminated composite beams.

There are different methods of obtaining the governing wave equation for a given waveguide. Here, we resort to using energy methods for deriving the wave equation.

This is because the energy methods, through Hamilton's Principle, will not only give the required wave equation but also the associated force boundary conditions. Although this method is explained in greater detail in Chapter 7 (Section 7.5.5), here we will just mention the procedure and obtain the governing differential equation. We make the following assumptions for deriving the governing equations: (1) the structure is assumed to behave linearly and the deformations are assumed to be small; (2) the structural material is also assumed to behave linearly; (3) the material is homogenous. Developing the governing equations from Hamilton's Principle requires the energy associated with the motion, namely the strain energy and kinetic energy, to be expressed in terms of displacements. For this, it is required to make some assumptions on the displacement field, based on the physics of the problem. Since the higher-order laminated composite beam is used as an example for deriving the governing equation of motions, one can expect a high degree of axial–flexural shear coupling in the member. Without loss of any generality, we can assume the displacement field for a laminated composite beam as:

$$\begin{aligned} u(x, t) &= u_0(x, t) - z\phi(x, t) \\ w(x, t) &= w_0(x, t) + z\psi(x, t) \end{aligned} \quad (6.143)$$

Here, u_0 and w_0 are the mid-plane axial and transverse displacements of the laminate, x and z are the axial and depthwise coordinates, ϕ is the slope and ψ represents the lateral motion due to the Poisson's ratio effect. These displacements are pictorially represented in Figure 6.24. Next, strains are calculated by using the strain displacement relations (Equation 6.27). These are given by:

$$\varepsilon_{xx} = \frac{\partial u_0}{\partial x} - z \frac{\partial \phi}{\partial x}, \quad \varepsilon_{zz} = \psi, \quad \gamma_{xz} = -\phi + \frac{\partial w_0}{\partial x} + z \frac{\partial \psi}{\partial x} \quad (6.144)$$

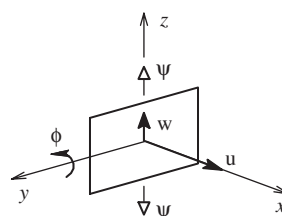


Figure 6.24 Cross-section of a beam and its degrees of freedom.

The stresses are then expressed in terms of displacement by using the plane-stress-reduced constitutive law in the $x-z$ plane as:

$$\begin{aligned}\sigma_{xx} &= \bar{Q}_{11}\varepsilon_{xx} + \bar{Q}_{13}\varepsilon_{zz} = \bar{Q}_{11}\left(\frac{\partial u_0}{\partial x} - z\frac{\partial\phi}{\partial x}\right) + \bar{Q}_{13}\psi \\ \sigma_{zz} &= \bar{Q}_{13}\varepsilon_{xx} + \bar{Q}_{33}\varepsilon_{zz} = \bar{Q}_{13}\left(\frac{\partial u_0}{\partial x} - z\frac{\partial\phi}{\partial x}\right) + \bar{Q}_{33}\psi \\ \tau_{xz} &= \bar{Q}_{55}\left(-\phi + \frac{\partial w_0}{\partial x} + z\frac{\partial\psi}{\partial x}\right)\end{aligned}\quad (6.145)$$

Here, \bar{Q}_{ij} are the plane stress reduced material constants that depend on the Young's modulus and the Poisson's ratio. For the present problem in question, they are given by:

$$\begin{aligned}\bar{Q}_{11} &= 4Q_{66}\cos^2\theta\sin^2\theta + \cos^2\theta(Q_{11}\cos^2\theta + Q_{12}\sin^2\theta) \\ &\quad + \sin^2\theta(Q_{12}\cos^2\theta + Q_{22}\sin^2\theta) \\ \bar{Q}_{13} &= (Q_{13}\cos^2\theta - Q_{23}\sin^2\theta), \quad \bar{Q}_{33} = Q_{33}, \\ \bar{Q}_{55} &= (Q_{55}\cos^2\theta + Q_{44}\sin^2\theta)\end{aligned}\quad (6.146)$$

The strain energy stored in the structure is evaluated by using a volume integral given by

$$U = \frac{1}{2} \int_V (\sigma_{xx}\varepsilon_{xx} + \sigma_{zz}\varepsilon_{zz} + \tau_{xz}\gamma_{xz}) dV \quad (6.147)$$

where V is the volume of the structure. In a similar manner, we can write the kinetic energy as:

$$T = \frac{1}{2} \int_V \rho(\dot{u}^2 + \dot{w}^2) dV = \frac{1}{2} \int_V \rho[(\dot{u}_0 - z\dot{\phi})^2 + (\dot{w}_0 + z\dot{\psi})^2] dV \quad (6.148)$$

where all quantities with a 'dot' on their heads represent the time derivatives. Hamilton's principle, which states that the minimization of the net energy gives the alternate statement of equilibrium, is mathematically represented as follows (more details are given in the next chapter):

$$\delta \int_{t_1}^{t_2} (T - U) dt = 0 \quad (6.149)$$

Substituting the energies given in Equations (6.147) and (6.148) into Equation (6.149) and minimizing, we get the following four highly coupled partial differential

equations corresponding to four degrees of freedom, namely u_0, w_0, ϕ and ψ . These are given by:

$$\begin{aligned}I_0 \frac{\partial^2 u_0}{\partial t^2} - I_1 \frac{\partial^2 \phi}{\partial t^2} - A_{11} \frac{\partial^2 u_0}{\partial x^2} + B_{11} \frac{\partial^2 \phi}{\partial x^2} - A_{13} \frac{\partial \psi}{\partial x} &= 0 \\ I_0 \frac{\partial^2 w_0}{\partial t^2} + I_1 \frac{\partial^2 \psi}{\partial t^2} - A_{55} \left(\frac{\partial^2 w_0}{\partial x^2} - \frac{\partial \phi}{\partial x} \right) - B_{55} \frac{\partial^2 \psi}{\partial x^2} &= 0 \\ I_2 \frac{\partial^2 \phi}{\partial t^2} - I_1 \frac{\partial^2 u_0}{\partial t^2} - A_{55} \left(\frac{\partial w_0}{\partial x} - \phi \right) - B_{55} \frac{\partial \psi}{\partial x} \\ + B_{11} \frac{\partial^2 u_0}{\partial x^2} - D_{11} \frac{\partial^2 \phi}{\partial x^2} + B_{13} \frac{\partial \psi}{\partial x} &= 0 \\ I_2 \frac{\partial^2 \psi}{\partial t^2} + I_1 \frac{\partial^2 w_0}{\partial t^2} + A_{13} \frac{\partial u_0}{\partial x} - B_{13} \frac{\partial \phi}{\partial x} + A_{33} \psi \\ - B_{55} \left(\frac{\partial^2 w_0}{\partial x^2} - \frac{\partial \phi}{\partial x} \right) - D_{55} \frac{\partial^2 \psi}{\partial x^2} &= 0\end{aligned}\quad (6.150)$$

Here, I_0, I_1 and I_2 represent the inertial constants, while A_{ij}, B_{ij} and D_{ij} represent the stiffness constants, given by:

$$\begin{aligned}[A_{ij}, B_{ij}, D_{ij}] &= \sum_i \int_{z_i}^{z_{i+1}} \bar{Q}_{ij}[1, z, z^2] b dz, [I_0, I_1, I_2] \\ &= \sum_i \int_{z_i}^{z_{i+1}} \rho[1, z, z^2] b dz\end{aligned}\quad (6.151)$$

The above highly coupled equations represent a complicated set of partial differential equations that are very difficult to solve in the time domain. This complexity is due to the material construction of the laminate which represents all possible stiffness and inertial couplings, namely the axial-shear-bending-lateral contraction. However, we will not try to solve this equation straightaway. We will reduce the above equations to a simpler isotropic waveguide devoid of stiffness or inertial coupling and get an insight of the wave behavior before analyzing the above system. This will also enable us to compare the behavior of waves in elementary waveguides as opposed to higher-order waveguides.

6.3.2.2 Wave propagation in elementary isotropic rods

Rods are structural waveguides that support only the axial motion $u(x, t)$. Equation (6.150) can be reduced to a wave equation governing the motion of rods by assuming the following:

$$E_1 = E_2 = E, \quad v_{12} = v_{21} = v, \quad \theta = 0, \quad \psi = -v \frac{\partial u}{\partial x}$$

On substituting the above into Equations (6.146 and 6.151), the material constants and the stiffness coefficients become:

$$\begin{aligned}\bar{Q}_{11} &= Q_{11} = \frac{E}{1 - v^2}, \quad \bar{Q}_{13} = Q_{13} = \frac{vE}{1 - v^2}, \\ \bar{Q}_{55} &= Q_{55} = \frac{E}{2(1 + v)} \\ A_{11} &= \frac{EA}{1 - v^2}, \quad A_{13} = \frac{vEA}{1 - v^2} = A_{33}, \\ B_{11} &= B_{55} = B_{13} = 0 \\ I_0 &= \rho A, \quad I_1 = I_2 = 0, \quad D_{55} = 0, \quad D_{11} = EI\end{aligned}$$

Here, E and ρ are the Young's modulus and density of the material and A and I are the area and moment of inertia of the cross-section. In substituting these into Equation (6.150), the bending and axial motions are decoupled and we get the following equations:

$$\begin{aligned}\rho A \frac{\partial^2 u_0}{\partial t^2} - EA \frac{\partial^2 u_0}{\partial x^2} &= 0 \\ u_0(x, t) &= \sum_{n=1}^N \hat{u}_n(x, \omega_n) e^{i\omega_n t}\end{aligned}\quad (6.152)$$

$$\rho A \frac{\partial^2 w_0}{\partial t^2} - A_{55} \left(\frac{\partial^2 w_0}{\partial x^2} - \frac{\partial \phi}{\partial x} \right) = 0 \quad (6.153)$$

$$-A_{55} \left(\frac{\partial w_0}{\partial x} - \phi \right) - EI \frac{\partial^2 \phi}{\partial x^2} = 0 \quad (6.154)$$

Differentiating Equation (6.154) with respect to x and substituting this into Equation (6.153) and using $\phi = \partial w_0 / \partial x$, we get the following governing differential equation for the elementary beam:

$$\rho A \frac{\partial^2 w_0}{\partial t^2} + EI \frac{\partial^4 w_0}{\partial x^4} = 0 \quad (6.155)$$

For wave analysis in elementary rods, we will use only Equation (6.152). We begin the analysis by transforming the governing wave equation to the Fourier domain by using the forward DFT. This can be done by assuming the solution for axial displacement in the spectral form as:

$$u_0(x, t) = \sum_{n=1}^N \hat{u}_n(x, \omega_n) e^{i\omega_n t} \quad (6.156)$$

In the above equation, \hat{u}_n are the frequency-dependent Fourier coefficients and are also a function of the spatial coordinates. In the rest of the sections in this part, the

quantities with a "hat" represent the frequency-domain quantity; ω_n is the circular frequency and $i = \sqrt{-1}$. Equation (6.156), when substituted into Equation (6.152), reduces the partial differential equation into a set of N ordinary differential equations with constant coefficients, which is given by:

$$EA \frac{d^2 \hat{u}_n}{dx^2} + \rho A \omega_n^2 \hat{u}_n = 0 \quad (6.157)$$

Here, the summation sign is removed as it is implied. The above equation has a solution of the form $\hat{u}_n = A_n e^{ik_{Ln}x}$. Here, k_{Ln} is called the wavenumber of the wave in question and in the present case it is the longitudinal wavenumber of the elementary rod. Substituting the above solution into Equation (6.157), we get:

$$(-EAk_{Ln}^2 + \rho A \omega_n^2) A_n e^{ik_{Ln}x} = 0$$

Since the system is second order, we will have two roots, one representing the forward moving or incident wave and the other representing the backward moving or reflected wave. From the above equation, we can get the longitudinal wavenumbers for a rod as:

$$k_{Ln} = \pm \omega \sqrt{\frac{\rho A}{EA}} \quad (6.158)$$

The spectrum relation, i.e. the relation between the wavenumber and frequency, is shown in Figure 6.26 below. Hence, the solution for Equation (6.157) is given by:

$$\hat{u}_n = A_n e^{-ik_{Ln}x} + B_n e^{ik_{Ln}x} \quad (6.159)$$

The constants A_n and B_n require to be determined from the boundary conditions of the problem. The first term in the above equation represents the forward-moving wave traveling with a wavenumber of $+k_{Ln}$ and the second term represents the backward-moving or reflected wave traveling with a wavenumber of $-k_{Ln}$. Hence, the total solution is the superposition of both incident and reflected waves. The following are some of the aspects on the behavior of waves in rods:

- The wavenumber is fully 'real' and hence the longitudinal waves in rods are propagating.
- The Spectrum relation (relation between the wavenumber and the frequency) is linear. Hence, the phase and group speeds ($C_p = \omega/k_{Ln} = \sqrt{E/\rho} = d\omega/dk_{Ln} = C_g$) are equal. When such a condition exists, the waves are

termed *Non-dispersive*. The main characteristic of such waves are that they do not change their shape as they propagate. In such a system, the reflections from the boundary can be easily identified and hence have great utility in applications such as identification of ‘damage’.

One can visualize the wave nature in rods by considering an infinite rod. For this system, the second term in Equation (6.159) does not exist as there will be no reflections from an infinite rod. Hence, we can write the displacement field as:

$$\hat{u}_n = A_n e^{-ikL_n x}$$

The constant A_n can be determined from the force boundary condition. That is, if the force, $F(t)$, or its frequency-domain counterpart, $\hat{F}(\omega) = EA \frac{d\hat{u}}{dx}$, are known at some point, say at $x = x_0$, then we can write the displacement field as:

$$\hat{u}_n(x, \omega) = \left(\frac{e^{-ikL_n x}}{e^{-ikL_n x_0}} \right) \hat{F}_n \quad (6.160)$$

We have actually written the response as:

$$\text{Output} = (\text{Transfer function}) \times \text{Input}$$

The term within the bracket in Equation (6.160) represents the *transfer function*. Obtaining the transfer function (also called the *Frequency Response Function* (FRF)) is one of the fundamental advantages of the spectral analysis, which enables this technique to be used in the solution of the inverse problems, such as *Force Identification* (FI) or *System Identification* (SI) problems.

The non-dispersive nature of the waves in rods is displayed in Figure 6.25, wherein the propagation of a triangular impulse in an infinite rod shows that the profile of the incident wave is maintained. The general procedure of using spectral analysis is as follows:

- First, the force is transformed to the Fourier domain by using a forward FFT.
- The frequency, the real and the imaginary parts of the force spectrum are read and stored.
- The transfer function is evaluated at each frequency and at the required spatial point.
- The obtained transfer function is convolved with the load to get the displacement spectrum.
- The velocity and acceleration spectra are obtained by multiplying the displacement spectrum by $i\omega$ and $-\omega^2$, respectively.

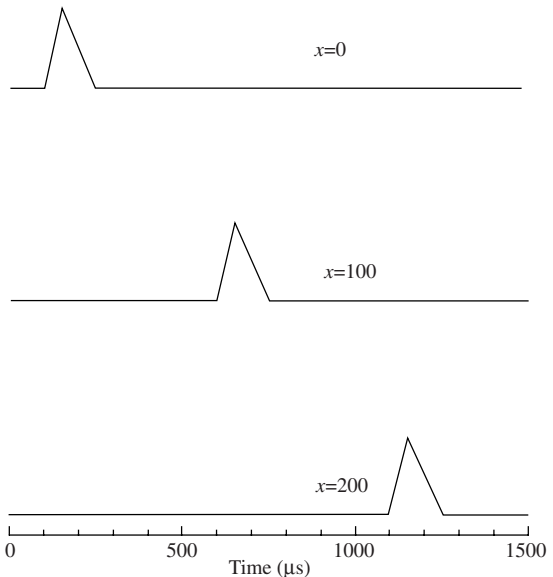


Figure 6.25 Non-dispersive nature of waves in an infinite rod.

- Finally, the time-domain response can be obtained by taking the inverse FFT on the obtained frequency response.

Figure 6.25 is obtained in this way. One of the advantages of the spectral approach is that one can view both the time- and frequency-domain responses in a single analysis and the transfer function is a direct byproduct of the approach.

Using Equation (6.159) and knowing the incident wave, one can construct the reflection responses due to interaction of the incident wave with various boundaries. These are extensively dealt in Doyle [7].

Some of the properties of propagating non-dispersive signals are as follows:

- (a) Waves travel with constant speed and hence do not change their shapes.
- (b) The given time signal requires proper sampling with an appropriate time window. If the time window is small, due to induced periodicity of the wave introduced as a result of using spectral analysis, the waves from the neighboring window will start propagating from the left, distorting the overall response. Hence, the time window is chosen so that (1) there is enough room for propagation of the signal and (2) since there is a connection between the time window and the distance the wave can move, the window size is to be determined by the slowest traveling component

and not the fastest. The time window can be increased by either increasing the number of points N or by decreasing the sampling rate ΔT .

6.3.2.3 Wave propagation in elementary isotropic beams:

Unlike rods, beams represent the fourth-order system in space and hence it can be expected that the wave behavior be much more complex. The beam analysis can be carried out on similar lines to those for rods. That is, we begin with the governing differential equation, which is given by Equation (6.155). We assume that the spectral form of the solution is as follows:

$$w(x, t) = \sum_{n=1}^N \hat{w}_n(x, \omega_n) e^{i\omega_n t} \quad (6.161)$$

Substituting Equation (6.161) into the governing equation (6.155), the governing PDE reduces to a set of ODEs, which is given by:

$$EI \frac{d^4 \hat{w}_n}{dx^4} - \rho A \omega_n^2 \hat{w}_n = 0 \quad (6.162)$$

The above equation is a constant-coefficient ODE and hence we can assume a solution of the type

$\hat{w}_n = A_n e^{-ik_{Bn}x}$. Since the system is fourth order, there will be four wavenumbers. Using this in Equation (6.162), we get all of the four wavenumbers as:

$$\begin{aligned} k_{B1n} &= i\beta_n, & k_{B2n} &= -i\beta_n, & k_{B3n} &= \beta_n, & k_{B4n} &= -\beta_n \\ \beta_n^4 &= \omega_n^2 \frac{\rho A}{EI} \end{aligned} \quad (6.163)$$

Clearly, the wavenumber is a nonlinear function of frequency and hence such waves changes their shapes as they propagate and so they are called a *Dispersive wave system*. From Equation (6.163), it is clear that the first two modes are propagating, while the last two modes are damped or evanescent modes. That is, the waves, in addition to being dispersive, attenuate as they propagate. The spectrum relation is shown in Figure 6.26. The phase and group speeds are given by:

$$\begin{aligned} C_p &= \omega/k_{Bn} = \sqrt{\omega} \left(\frac{EI}{\rho A} \right)^{0.25}, \\ Cg &= d\omega/dk_{Bn} = 2\sqrt{\omega} \left(\frac{EI}{\rho A} \right)^{0.25} \\ C_g &= 2C_p \end{aligned} \quad (6.164)$$

From the above relations, we see that, unlike rods, the phase and group speeds are different and are functions of

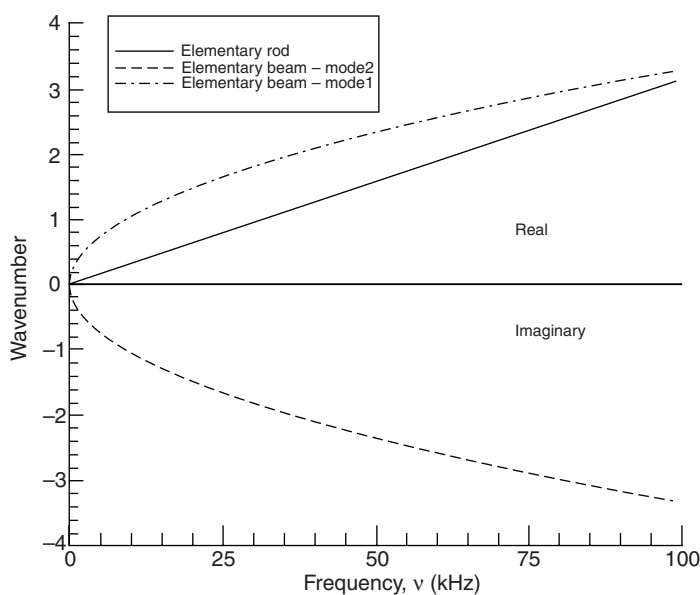


Figure 6.26 Spectrum relationships for an elementary rods and beams.

the frequency. That is, different frequency components of the signal have different speeds. This is one of the characteristics of the dispersive system. The solution of the beam system is given by:

$$\hat{w}_n = A_n e^{-i\beta_n x} + B_n e^{-\beta_n x} + C_n e^{+i\beta_n x} + D_n e^{\beta_n x} \quad (6.165)$$

Here, the first two terms in the above equation represent the forward-moving wave while the last two terms represent the backward-moving wave. As in a rod, the total solution is obtained by superposition of two solutions. If one is dealing with an infinite beam, the last two terms in equation (6.165) need not be considered. Using the above equation, the interaction of the incident wave with various boundaries can be investigated. Further details on these aspects can be found in Doyle [7]. While dealing with dispersive signals such as those occurring in beams, the following are some signal processing aspects that one has to consider:

- The shape of the time signal changes as it propagates and hence it is not possible to identify the original profile.
- The speed of the wave changes with the frequency and hence the low-frequency components take a long time to arrive and hence the signals have long tails.
- When the time window is small, propagation of the signal over long distances causes signal distortion due to the neighboring window ‘coming from the left’. This problem is called a *wraparound problem*. This is due to the low-frequency components occurring first, instead of the high-frequency components. This problem can be avoided by any of the following: (1) by ‘padding’ the time window by zeros; (2) by using what is called *band-pass filtering* – that is, all of the frequency components below a certain frequency would be blocked; (3) by using an N -point moving average, wherein the low-frequency components are averaged by using a suitable least-squares approach; (4) by increasing the time-window size by suitably choosing the sample rate and the number of FFT points.

6.3.2.4 Wave propagation in elementary composite beams

Unlike an elementary isotropic beam, a laminated composite beam exhibits stiffness coupling due to unsymmetrical ply lay up sequences. Due to this, the structure will exhibit bending–axial coupling. Hence, such beams can

undergo three different motions, namely axial, bending (transverse) and rotation. To perform the wave analysis, we need the governing equation, which can be obtained from Equation (6.150) by ‘proper’ reduction. Since the beam is still elementary, the shear deformation, rotational inertia and lateral displacement due to Poisson’s ratio, are not considered. The governing equation can be obtained by setting all of the terms associated with the ψ motion and its derivates to zero in Equation (6.150). In addition, in the third part of this equation the contribution of rotational inertia by the axial degree of freedom is assumed to be zero (that is, the $I_1 \partial^2 u / \partial t^2$ term) and by setting $\phi = \partial w / \partial x$, we get the following two coupled governing partial differential equation, which are given by:

$$\begin{aligned} I_0 \frac{\partial^2 u_0}{\partial t^2} - A_{11} \frac{\partial^2 u_0}{\partial x^2} + B_{11} \frac{\partial^3 w_0}{\partial x^3} &= 0 \\ I_0 \frac{\partial^2 w_0}{\partial t^2} - B_{11} \frac{\partial^3 u_0}{\partial x^3} + D_{11} \frac{\partial^4 w_0}{\partial x^4} &= 0 \end{aligned} \quad (6.166)$$

From the above equations, we can clearly see the stiffness coupling through the term B_{11} . If this term is zero, that is, for a symmetric lay up sequence, the axial and transverse motions will become uncoupled and the behavior would be very similar to that of isotropic rods and beams, respectively. The wave behavior for this coupled system can be determined by representing the two motions in the spectral form, which is given by:

$$\begin{aligned} u_0(x, t) &= \sum_{n=1}^N \hat{u}_n(x, \omega) e^{i\omega_n t}, \\ w_0(x, t) &= \sum_{n=1}^N \hat{w}_n(x, \omega) e^{i\omega_n t} \end{aligned} \quad (6.167)$$

Substituting the above into Equation (6.166) reduces the governing PDE to a set of coupled ODEs with constant coefficients, which is given by:

$$\begin{aligned} -I_0 \omega^2 \hat{u}_n - A_{11} \frac{d^2 \hat{u}_n}{dx^2} + B_{11} \frac{d^3 \hat{w}}{dx^3} &= 0 \\ -I_0 \omega^2 \hat{w} - B_{11} \frac{d^3 \hat{u}}{dx^3} + D_{11} \frac{d^4 \hat{w}}{dx^4} &= 0 \end{aligned} \quad (6.168)$$

The solutions for axial and transverse displacements will be of the types:

$$\hat{u}_n = U_0 e^{-ik_n x}, \quad \hat{w}_n = W_0 e^{-ik_n x}$$

The same wavenumber appears in both the solutions to retain the phase information during propagation. By

using the above solution, Equation (6.168) can be written in matrix form as:

$$\begin{bmatrix} (C_L k_n^2 - \omega_n^2) & i \frac{C_{Cn}^3}{\omega_n} k_n^3 \\ -i \frac{C_C^3}{\omega_n} k_n^3 & \frac{C_{Bn}^4}{\omega_n^2} k_n^4 - \omega_n^2 \end{bmatrix} \begin{Bmatrix} U_0 \\ W_0 \end{Bmatrix} = \begin{Bmatrix} 0 \\ 0 \end{Bmatrix} \quad (6.169)$$

Here, C_L and C_{Bn} are the *longitudinal* and *bending* wave speeds, while C_{Cn} is the wave speed due to stiffness coupling. These are given by:

$$C_L = \sqrt{\frac{A_{11}}{I_0}}, \quad C_{Bn} = \sqrt{\omega_n} \left[\frac{D_{11}}{I_0} \right]^{\frac{1}{4}}, \quad C_{Cn} = \left[\omega_n \frac{B_{11}}{I_0} \right]^{\frac{1}{3}} \quad (6.170)$$

For obtaining the nontrivial solution, it is necessary that the determinant of the above matrix be zero. In doing so, we get a sixth-order characteristic equation to solve for the wavenumber k_n , which is given by:

$$(1 - r)k_n^6 - k_{Ln}^2 k_n^4 - k_{Bn}^4 k_n^2 + k_{Ln}^2 k_{Bn}^4 = 0 \quad (6.171)$$

In the above expression, r is a parameter that represents the stiffness coupling between the axial and flexural motions, while k_{Ln} and k_{Bn} are the longitudinal and flexural wavenumbers in the absence of stiffness coupling. These are given by:

$$r = \frac{B_{11}^2}{A_{11} D_{11}}, \quad k_{Ln} = \frac{\omega_n}{C_L}, \quad k_{Bn} = \frac{\omega_n}{C_{Bn}} \quad (6.172)$$

Equation (6.171) is the sixth-degree polynomial equation corresponding to three motions, namely the axial, bending and rotational displacements. Hence, the solution of Equation (6.168) will have six constants, three of which represent the forward-moving components, while the other three represent the reflected-wave components.

Before attempting to solve the above equation, we can easily see that for a symmetric ply lay up r vanishes and hence there is no stiffness coupling. Equation (6.171) then becomes:

$$(k_n^2 - k_{Ln}^2)(k_n^4 - k_{Bn}^4) = 0$$

That is, the bending and axial motions become uncoupled and the solutions of these are the same as those of the rods and beams described earlier, with EA giving way to A_{11} , EI giving way to D_{11} and ρA making way for I_0 .

The solution of Equation (6.171) is quite complex and requires numerical solution. However, it reduces to solving a cubic equation as the forward- and backward-moving waves always occur in pairs. By looking at the characteristic equation, one cannot say anything about the behavior of any wave mode. Hence, it is quite likely that the axial mode is propagating and hence would be real, while one of the bending modes is likely to be complex, as in the case of an isotropic beam. One of the disadvantages of a numerical solution is to keep track of the mode type. That is, while obtaining the solution, one would not know what mode (bending or axial in this case) that one is solving for. However, there are many numerical methods which will look for only the real roots or complex roots separately. In the present case, we look for the real root, say $\sqrt{\alpha}$, which we will designate as the longitudinal mode. The other roots can be found easily by ‘synthetic division’. Hence, we can now write the wavenumbers as:

$$\begin{aligned} k_{1n} &= \sqrt{\alpha_n}, k_{2n}, k_{3n} \\ &= \frac{1}{\sqrt{2}} \sqrt{(k_{Lrn} - \alpha_n) \pm \sqrt{(k_{Lrn} + \alpha_n)^2 - 4(\alpha_n^2 - k_{Brn})}} \\ k_{Lrn} &= \frac{k_{Ln}^2}{(1 - r)}, \quad k_{Brn} = \frac{k_{Bn}^4}{(1 - r)} \end{aligned} \quad (6.173)$$

It is very difficult to ascertain its behavior by looking at the expression. One thing which is very clear is that the wave behavior will certainly change with the stiffness coupling. In order to investigate this, we plot the spectrum relation and the dispersion relations for an AS/3501 graphite–epoxy laminated composite beam. Ten plies are considered in three different ply stacking sequences to give different degrees of stiffness coupling. The thickness of each ply is assumed to be 1 mm. The three different stacking sequences and their values of stiffness coupling are given as follows:

$$\begin{aligned} [0_{10}] &\longrightarrow r = 0, \quad [0_5/30_2'60_3] \longrightarrow r = 0.312, \\ &[0_5/90_5] \longrightarrow r = 0.574 \end{aligned}$$

The first case is the symmetric one wherein there is no stiffness coupling, while the last represents the case of a crossply laminate, wherein the stiffness coupling is maximum. These plots are shown in Figures 6.27 and 6.28, respectively.

In the spectrum relation (Figure 6.27), the real part of the wavenumber is plotted above the zero and is imaginary below zero to identify the propagating and evanescent

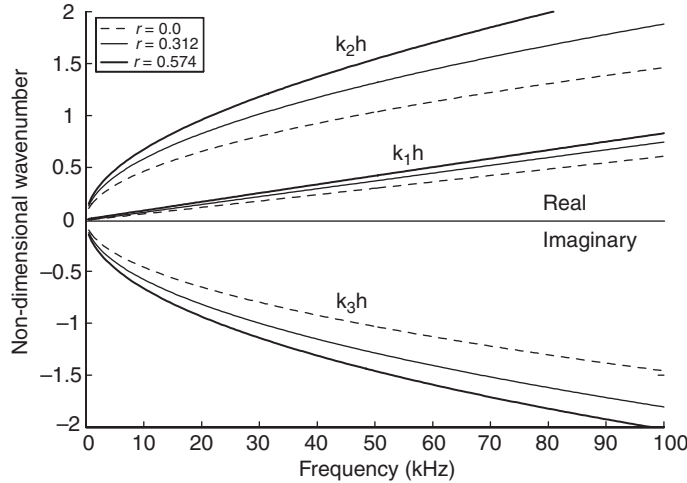


Figure 6.27 Spectrum relationships for elementary composite beam.

components. The axial wavenumber behavior is almost nondispersive for most of the frequency spectrum. However, a mild dispersion is introduced at very high frequencies. This is because the dispersive components from the bending motion, normally introduced through stiffness coupling, are small. This is the reason why the stiffness coupling parameter r has a negligible effect on the longitudinal wavenumber. The flexural-mode behavior is highly dispersive as in the isotropic case; however, the influence of the stiffness coupling parameter r is quite significant and is shown by altering the slope of the

curve. The slope is smaller for a smaller r and hence the speeds will also change with the coupling parameter. This is shown in Figure 6.28. The general tendency is that the stiffness coupling reduces the speeds, both for axial as well as the flexural case. In the axial case, it is seen that a maximum of 26 % reduction in speeds can be achieved, while the reduction in the flexural speed at 50 kHz is about 46 %. More details of this analysis can be found in Roy Mahapatra *et al.* [8]. A similar analysis can be done for higher-order waveguides, where additional constraints are introduced in the

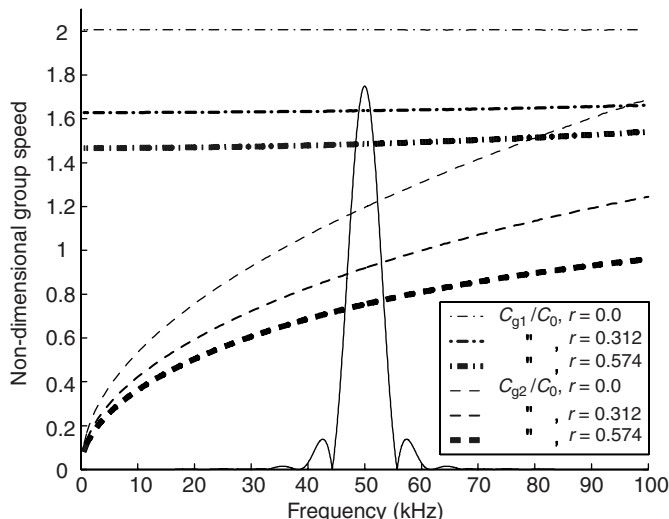


Figure 6.28 Dispersion relationships for an elementary composite beam.

elementary model. For example, when the shear deformation is introduced in the elementary-beam model, the shear strains do not vanish and as a result the beam slope cannot be obtained from the transverse displacement. Hence, the addition of shear constraints will cause an alteration in the behavior of the evanescent wave of the elementary beam. This wave, which starts as a nonpropagating wave at low frequencies, becomes propagating after a certain frequency. This frequency is called the *cut-off frequency*, where the wavenumber traverses from imaginary to real. Details of the wave behavior in a higher-order isotropic beam waveguide can be found in Gopalakrishnan *et al.* [9], while the same for a composite waveguide can be found in Roy Mahapatra and Gopalakrishnan [10]. In the case of a longitudinal waveguide, the higher-order effects are incorporated through the introduction of a *lateral displacement* (also called a

four independent motions for this beam, namely the axial (u), transverse (w), rotational (ϕ) and lateral contraction (ψ) motions.

The displacement field for this case is given in Equation (6.143) and the four-coupled governing equations for this displacement field are given by Equation (6.150). The wave analysis, as before, begins by representing the different motions in their spectral forms and converting the coupled PDEs to a set of coupled ODEs. As in the earlier cases, these ODEs have constant coefficients and hence one can assume exponential solutions. Following the procedure employed for determining the wavenumbers in an elementary composite beam, we can form the eight-order polynomial characteristic equation for the solution of wavenumbers. The eight-order polynomial is obtained from the following equation:

$$\begin{bmatrix} (k_n^2 - k_{Ln}^2) & 0 & \left(\frac{s_1 s_2 k_{Ln}^2}{k_{sn}^2} - \frac{r k_{Ln} k_n^2}{k_{sn}^2} \right) & i \frac{A_{13}}{A_{11}} k_n \\ 0 & (k_n^2 - k_{sn}^2) & -ik_n & \left(\frac{\omega_n^2 I_1}{A_{55}} - \frac{B_{55}}{A_{55}} k_n^2 \right) \\ \left(\frac{r k_{sn}^2 k_n^2}{k_{Ln} k_{Bn}^2} - s_1 s_2 k_{sn} \right) & -ik_n & \left(s_1^2 - 1 - \frac{k_{sn}^2 k_n^2}{k_{Bn}^4} \right) & \left(\frac{-i(B_{55} - B_{13}) k_n^2}{A_{55}} \right) \\ i \frac{A_{13}}{A_{33}} k_n & \left(\frac{\omega_n^2 I_1}{A_{33}} - \frac{B_{55}}{A_{33}} k_n^2 \right) & \left(\frac{-i(B_{55} - B_{13}) k_n^2}{A_{33}} \right) & \left(\frac{\omega_n^2 I_2}{A_{33}} - 1 - \frac{D_{55}}{A_{33}} k_n^2 \right) \end{bmatrix} \begin{Bmatrix} U_0 \\ W_0 \\ \phi_0 \\ \psi_0 \end{Bmatrix} = \begin{Bmatrix} 0 \\ 0 \\ 0 \\ 0 \end{Bmatrix} \quad (6.174)$$

lateral contraction) due to the Poisson's ratio effect in the elementary-rod model. This introduces an additional motion and as a result, increases the order of the governing differential equation. The behavior of waves in an isotropic higher-order rod waveguide can be found in Martin *et al.* [11]. In the next subsection, the behavior of the waves in a higher-order laminated composite beam is discussed, wherein, in addition to the shear deformation, lateral contraction is also introduced. Hence, one can expect a four-way coupling.

6.3.2.5 Wave propagation in higher-order laminated composite beams

Here, we consider the most complicated case of a higher-order laminated composite waveguide wherein the higher-order effects, through shear deformation and lateral contraction via the Poisson's ratio effect, are introduced in the mathematical model. Hence, there are

By setting the determinant of the above matrix to zero, the polynomial of the 8th order is obtained. Clearly, there is a four-way stiffness coupling, namely the axial-transverse-shear-lateral contraction coupling. The behaviors of these modes are difficult to estimate unless one plots these. One can expect cut-off frequencies in the shear and lateral contraction modes, which can be obtained by looking at the frequencies where the wavenumber goes to zero. The cut-off frequencies associated with the contraction and shear modes are given by:

$$\omega_{c-\text{cont}} = \sqrt{\frac{A_{33}}{I_2(1-s_2^2)}}, \quad \omega_{c-\text{shear}} = \sqrt{\frac{A_{55}}{I_2(1-s_2^2)}} \quad (6.175)$$

Since $A_{33} > A_{55}$, the shear cut-off frequency occurs earlier than the contractual cut-off frequency. Figure 6.29 gives the spectrum relation for a higher-order laminated composite beam. Clearly, the longitudinal mode becomes

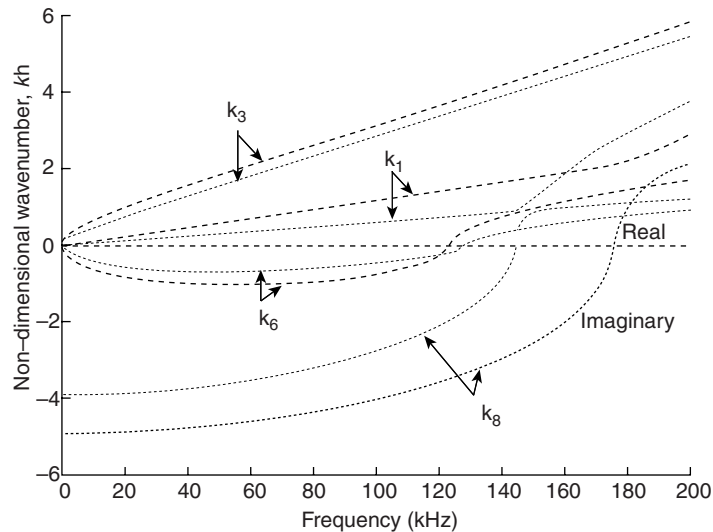


Figure 6.29 Spectrum relationships for a higher-order laminated composite beam.

dispersive at higher frequencies. The first bending mode is always propagating, while the shear mode is evanescent to start with and becomes propagating after the shear cut-off frequency. If the elementary model is used in such cases, the dynamics of the beam motion will be grossly misrepresented. The contractual mode is again evanescent to start with and becomes propagating beyond the contractual cut-off frequency. Hence, it can be concluded that higher-order effects are more pronounced at high frequencies and if these properties are not used at such frequencies, the responses predicted will no longer be reliable.

REFERENCES

1. G. Arfken, *Mathematical Methods for Physicists*, 3rd Edn, Academic Press, San Diego, CA, USA (1985).
2. R.M. Jones, *Mechanics of Composites Materials*, McGraw-Hill, New York, NY, USA (1975).
3. F.K. Chang, 'Built-in structural health monitoring', in *Proceedings of the International Conference on Smart Materials, Structures and Systems: ISSS-SPIE-1999*, A. Selvarajan, A.R. Upadhyay and P.D. Mangalgiri (Eds), Allied Publishers, New Delhi, India, pp. 44–49 (1999).
4. S.W. Tsai, *Introduction to Composite Materials*, Technomic, CT, USA (1980).
5. C. Chatfield, *The Analysis of Time Series: An Introduction*, Chapman Hall, London, UK (1984).
6. I.N. Sneddon, *Fourier Transforms*, McGraw-Hill, New York, NY, USA (1951).
7. J.F. Doyle, *Wave Propagation In Structures*, Springer-Verlag, New York, NY, USA (1997).
8. D. Roy Mahapatra, S. Gopalakrishnan and T.S. Sankar, 'Spectral element based solutions for wave propagation analysis of multiply connected unsymmetric laminated composite beams', *Journal of Sound and Vibration*, **237**, 819–836 (2000).
9. S. Gopalakrishnan, M. Martin and J.F. Doyle, 'A matrix methodology for spectral analysis of wave propagation in multiple connected Timoshenko beams', *Journal of Sound and Vibration*, **158**, 11–24 (1992).
10. D. Roy Mahapatra and S. Gopalakrishnan, 'Axial-shear-bending coupled wave propagation in thick composite beams' *Composite Structures*, **59**, 67–88 (2003).
11. M. Martin, S. Gopalakrishnan and J.F. Doyle, 'Wave propagation in multiply connected deep waveguides', *Journal of Sound and Vibration*, **174**, 521–538 (1994).

Introduction to the Finite Element Method

7.1 INTRODUCTION

The behavior of any smart dynamic system is governed by the equilibrium equation (Equation (6.49)) derived in the last chapter. In addition, the obtained displacements field should satisfy the strain–displacement relationship (Equation (6.27)) and a set of natural and kinematic boundary conditions and initial conditions. Also, if the system happens to be a laminated composite with an embedded smart material patch, there will be electro-mechanical/magnetomechanical coupling introduced through the constitutive model. Obviously, these equations can be solved exactly only for a few typical cases and for most problems one has to resort to approximate numerical techniques to solve the governing equations. Equation (6.49), as such, is not readily amenable for numerical solutions. Hence, one needs alternate statements of equilibrium equations that are more suited for numerical solution. This is normally provided by the variational statement of the problem.

Based on variational methods, there are two different analysis philosophies: one is the displacement-based analysis called the *stiffness method*, where the displacements are treated as primary unknowns and the other is the force-based analysis called the *force method*, where internal forces are treated as primary unknowns. Both these methods split up the given domain into many subdomains (elements). In the stiffness method, a discretized structure is reduced to a kinematically determinate problem and the equilibrium of forces is enforced between the adjacent elements. Since we begin the analysis in terms of displacements, enforcement of compatibility of the displacements (strains) is a non-issue as it will be automatically satisfied. The finite element method falls under this category. In the force method, the problem is reduced to a statically determinate struc-

ture and compatibility of displacements is enforced between adjacent elements. Since the primary unknowns are forces, the enforcement of equilibrium is not necessary as it is ensured. Unlike the stiffness method, where there is only one way to make a structure kinematically determinate (by suppressing all the degrees of freedom), there are many possibilities to reduce the problem into a statically determinate structure in the force method. Hence, the stiffness methods are more popular.

The variational statement is the equilibrium equation in the integral form. This statement is often referred to as the *weak* form of the governing equation. This alternate statement of equilibrium for structural systems is provided by the energy functional governing the system. The objective here is to obtain an approximate solution of the dependent variable (say, the displacements u in the case of structural systems) of the form:

$$u(x, y, z, t) = \sum_{n=1}^N a_n(t) \psi_n(x, y, z) \quad (7.1)$$

where $a_n(t)$ are the unknown time-dependent coefficients to be determined through some minimization procedure and ψ_n are the spatial dependent functions that normally satisfy the kinematic boundary conditions and not necessarily the natural boundary conditions. There are different energy theorems that give rise to different variational statements of the problem and hence different approximate methods can be formulated. The basis for formulation of the different approximate methods is the *Weighted Residual Technique* (WRT), where the residual (or error) obtained by substituting the assumed approximate solution in the governing equation is weighted with a weight function and integrated over the domain. Different types of weighted functions give rise to different approximate

methods. The accuracy of the solution will depend upon the number of terms used in Equation (7.1).

The different approximate methods again are too difficult to use in situations where the structures are complex. To some extent, methods like the Rayleigh–Ritz method [1], which involves minimization of the total energy to determine the unknown constants in Equation (7.1), can be applied to some complex problems. The main difficulty here is to determine the functions ψ_n , which are called *Ritz functions*, and in this case, are too difficult to determine. However, if the domain is divided into number of subdomains, it is relatively easier to apply the Rayleigh–Ritz method over each of these subdomains and solutions of each are pieced together to obtain the total solution. This, in essence, is the *Finite Element Method* (FEM) and each of the subdomains are called the elements of the finite element mesh. Although the FEM is explained here as an assembly of Ritz solutions over each subdomain, in principle all of the approximate methods generated by the WRT, can be applied to each subdomain. Hence, in the first part of this chapter, the complete WRT formulation and various other energy theorems are given in detail. These theorems will then be used to derive the discretized FE governing the equation of motion. This will be followed by formulation of the basic building blocks used in the FEM, namely the stiffness, mass and damping matrices. The main issues relating to their formulation are discussed.

Even though variational methods enable us to get an approximate solution to the problem, the latter is heavily dependent upon the domain discretization. That is, in the finite element technique, the structure under consideration is subdivided into many small elements. In each of these elements, the variation of the field variables (in the case of a structural problem, displacements) is assumed to be polynomials of a certain order. Using this variation in the weak form of the governing equation reduces it into a set of simultaneous equations (in the case of static analysis) or highly coupled second-order ordinary differential equations (in the case of dynamic analysis). If the stress or strain gradients are high (for example, near a crack tip of a cracked structure), then one needs very fine mesh discretization. In the case of wave propagation analysis, many higher-order modes get excited due to the high-frequency content of loading. At these frequencies, the wavelengths are small and the mesh sizes should be of the order of the wavelengths in order that the mesh edges do not act as the fixed boundaries and start reflecting waves from these edges. These increase the problem size enormously. Hence, the size of the mesh is an important parameter that determines the accuracy of the solution.

Another important factor that determines the accuracy of the *Finite Element* (FE) solution is the order of the interpolating polynomial of the field variables. For those systems that is governed by the PDEs of orders higher than two (for example, the Bernoulli–Euler beam and classical plate), the assumed displacement field should not only satisfy displacement compatibility, but also the slope compatibility at the interelement boundaries, since the slopes are derived from displacements. This necessarily requires higher-order interpolating polynomials. Such elements are called C^1 continuous elements. On the other hand, for the same beam and plate systems, if the shear deformation is introduced, then the slopes can no longer be derived from the displacements and as a result one can have the luxury of using lower-order polynomials for displacements and slopes separately. Such shear-deformable elements are called the C^0 continuous elements. When such C^0 elements are used for beams and plates which are thin (where the shear deformation is negligible), these elements cannot degenerate into C^1 elements and as a result the solutions obtained will be many orders smaller than the actual solution. These are commonly referred to as *shear locking* problems. Similarly, there is *incompressible locking* in nearly incompressible materials when the Poisson's ratio tends to 0.5, *membrane locking* in curved members and *Poisson's locking* in higher-order rods. Such problems where one or other forms of locking are present are normally referred to as *constrained media* problems.

There are many different techniques that can be used to alleviate locking [2]. These will be explained in detail in the latter part of this chapter. One of the methods to eliminate locking is to use the exact solution to the governing differential equation as the interpolating polynomial for the displacement field. In many cases, it is not easy to solve a dynamic problem that is governed by a PDE exactly. In such cases, the equations are solved exactly by ignoring the inertial part of the governing equation. The resulting interpolating function will give the exact static stiffness matrix (for point loads) and an approximate mass matrix. These elements can be used both in deep and thin structures and the user need not use his judgment to determine whether locking is predominant or not. Use of these elements will substantially reduce the problem size, especially in wave-propagation analysis as these have super-convergent properties. Hence, a complete section in this chapter is devoted to the formulation of these super-convergent elements.

The super-convergent elements explained above still do not provide accurate inertia distribution, which is extremely important for accurate wave-propagation

analysis. This is because the mass matrix in the super-convergent formulation is formulated using the exact solution to the static part of the governing equation. This approach can be extended to certain PDEs by transforming the variables in the governing wave equation to the frequency domain using the *Discrete Fourier Transform* (DFT). In doing so, the time parameter is replaced by the frequency and the governing PDE reduces to a set of ODEs in the transformed domain, which is easier to solve. The exact solutions to the governing equation in the frequency domain are then used as interpolating functions for element formulation. Such elements formulated in the frequency domain are called the *Spectral Finite Elements* (SFEs). An important aspect of SFEs are that they give the exact dynamic stiffness matrix. Since both the stiffness and the mass are exactly represented in this formulation, the problem sizes are many orders smaller than the conventional FE solution. Hence, the last part of this chapter is exclusively devoted to describing the spectral element formulation.

7.2 VARIATIONAL PRINCIPLES

This section begins with some basic definition of work, complementary work, strain energy, complementary strain energy and kinetic energy. These are necessary to define the energy functional, which is the basis for any finite element formulation. This will be followed by a complete description of the WRT and its use in obtaining many different approximate methods. Next, some basic energy theorems, such as the *Principle of Virtual Work* (PVW), *Principle of Minimum Potential Energy* (PMPE), *Rayleigh–Ritz procedure* and *Hamilton’s theorem* for deriving the governing equations of a system and their associated boundary conditions, are explained. Using Hamilton’s theorem, finite element equations are derived, which is followed by derivation of stiffness and mass matrices for some simple finite elements. Next, the mesh-locking problem in FE formulations and their remedies are explained, followed by the formulation procedures for super-convergent finite elements. Next, the equation solution in static and dynamic analysis is presented. The chapter ends with a full review of *Spectral Finite Element* (SFE) formulation.

7.2.1 Work and complimentary work

Consider a body under the action of a force system described in a vectorial form as $\hat{F} = F_x i + F_y j + F_z k$,

where F_x , F_y and F_z are the components of force in the three coordinate directions. These components can also be time-dependent. Under the action of these forces, the body undergoes infinitesimal deformations, given by $d\hat{u} = du i + dv j + dw k$, where u , v and w are the components of displacements in the three coordinate directions. The work done is then given by the ‘dot’ product of force and displacement vector:

$$dW = \hat{F} \cdot d\hat{u} = F_x du + F_y dv + F_z dw \quad (7.2)$$

The total work done in deforming the body from the initial state to the final state is given by:

$$W = \int_{u_1}^{u_2} \hat{F} \cdot d\hat{u} \quad (7.3)$$

where u_2 is the final deformation and u_1 is the initial deformation of the body. To understand this better, consider a 1-D system under the action of a force F_x and having an initial displacement of zero. Let the force vary as a nonlinear function of displacement (u) given by $F_x = ku^n$, which is shown graphically in Figure 7.1. Here, k and n are some known constants. To determine the work done by the force, a small strip of length du is considered in the lower portion of the curve shown in Figure 7.1. The work done by the force is obtained by substituting the force variation in Equation (7.3) and integrating, which is given by:

$$W = \frac{ku^{n+1}}{n+1} = \frac{F_x u}{n+1} \quad (7.4)$$

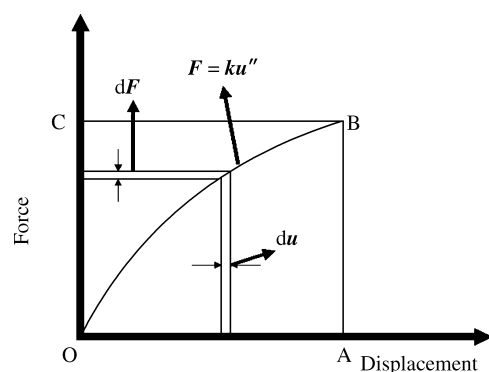


Figure 7.1 Definitions of work ('area OAB') and complimentary work ('area OBC').

Alternatively, work can also be defined as:

$$W^* = \int_{F_1}^{F_2} \hat{u} \cdot d\hat{F} \quad (7.5)$$

where, F_1 and F_2 are the initial and final applied forces. The above definition is normally referred to as *Complementary Work*. Again, by considering a 1-D system with the same nonlinear force-displacement relationship ($F_x = ku^n$), we can write the displacement u as $u = (1/k)F_x^{(1/n)}$. Substituting this into Equation (7.5) and integrating, the complementary work can be written as:

$$W^* = \frac{F_x^{(1/n+1)}}{k(1/n+1)} = \frac{F_x u}{(1/n+1)} \quad (7.6)$$

Obviously, W and W^* are not the same although they were obtained from the same curve. However, for the linear case ($n = 1$), they have the same value, given by $W = W^* = F_x u / 2$, which is nothing but the area under the force-displacement curve. The definition of *Work* is normally used in the stiffness formulation, while the concept of *Complementary Work* is normally used in the force method of analysis.

7.2.2 Strain energy, complimentary strain energy and kinetic energy

Consider an elastic body subjected to a set of forces and moments. The deformation process is governed by the First Law of Thermodynamics, which states that the total change in the energy (ΔE) due to the deformation process is equal to the sum of the total work done by the elastic and inertial forces (W_E) and the work done due to heat absorption (W_H), that is:

$$\Delta E = W_E + W_H$$

If the thermal process is adiabatic, then $W_H = 0$. The energies associated with the elastic and the inertial forces are called the *Strain Energy* (U) and *Kinetic Energy* (T), respectively. If the loads are gradually applied, the time-dependency of the load can be ignored, which essentially means that the kinetic energy T can be assumed to be equal to zero. Hence, the change in the energy $\Delta E = U$. That is, the mechanical work done in deforming the structure is equal to the change in the internal energy (strain energy). When the structure behaves linearly and the load is removed, the strain energy is converted back to mechanical work.

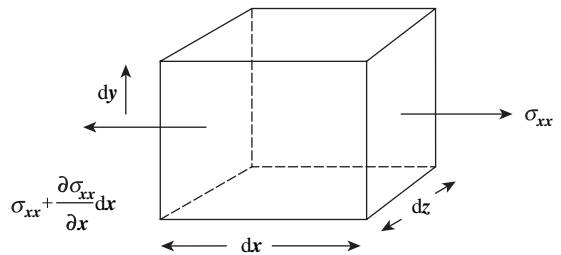


Figure 7.2 Elemental volume for computing the strain energy.

To derive the expression for the strain energy, consider a small element of volume dV of the structure under a 1-D state of stress, as shown in Figure 7.2. Let σ_{xx} be the stress on the left face and $\sigma_{xx} + (\partial\sigma_{xx}/\partial x)dx$ be the stress on the right face. Let B_x be the body force per unit volume along the x -direction. The strain energy increment dU due to the stresses σ_{xx} on face 1 and $\sigma_{xx} + (\partial\sigma_{xx}/\partial x)dx$ on face 2 during infinitesimal deformation du on face 1 and $d(u + (\partial u/\partial x)dx)$ on face 2 is given by:

$$dU = -\sigma_{xx}dydzdu + \left(\sigma_{xx} + \frac{\partial\sigma_{xx}}{\partial x}dx\right)dydzd\left(u + \frac{\partial u}{\partial x}dx\right) + B_x dydz$$

Simplifying and neglecting the higher-order terms, we get:

$$dU = \sigma_{xx}d\left(\frac{\partial u}{\partial x}\right)dydz + du dydz \left(\frac{\partial\sigma_{xx}}{\partial x} + B_x\right)$$

The last term within the brackets is the equilibrium equation, which is equal to zero. Hence, the incremental strain energy now becomes:

$$dU = \sigma_{xx}d\left(\frac{\partial u}{\partial x}\right)dydz = \sigma_{xx}de_{xx}dV \quad (7.7)$$

Now, we introduce the term called incremental *Strain Energy Density*, which we define as:

$$dS_D = \sigma_{xx}de_{xx}$$

Integrating the above expression over a finite strain, we get:

$$S_D = \int_0^{e_{xx}} \sigma_{xx}de_{xx} \quad (7.8)$$

Using the above expression in Equation (7.7) and integrating it over the volume, we get

$$U = \int_V S_D dV \quad (7.9)$$

Similar to the definition of work and complementary work, we can define complimentary strain energy density and complimentary strain energy as:

$$U^* = \int_V S_D^* dV, \quad S_D^* = \int_0^{\sigma_{xx}} \epsilon_{xx} d\sigma_{xx} \quad (7.10)$$

We can represent this graphically in a similar manner as we did for work and complimentary work. This is shown in Figure 7.3.

In this figure, the area of the region below the curve represents the strain energy while the region above the curve represents the complementary strain energy. Since the scope of this chapter is limited to the Finite Element Method, all of the theorems dealing with complimentary strain energy will not be dealt with here.

Kinetic energy should also be considered in evaluating the total energy if the inertial forces are important. Inertial forces are predominant in time-dependent problems, where both loading and deformation have time histories. Kinetic energy is given by the product of mass and the square of velocity. This can be mathematically represented in the integral form as:

$$T = \frac{1}{2} \int_V \rho (\ddot{u}^2 + \dot{v}^2 + \dot{w}^2) dV \quad (7.11)$$

Here, u , v and w are the displacement in the three co-ordinate directions while the dots on the characters

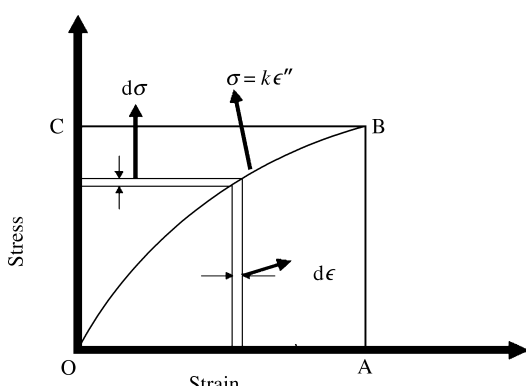


Figure 7.3 Concepts of strain energy ('area OAB') and complimentary strain energy ('area OBC').

represent the first time derivatives and in this case are the three respective velocities.

7.2.3 Weighted residual technique

Any system is governed by a differential equation of the form:

$$Lu = f \quad (7.12)$$

where L is the differential operator of the governing equation, u is the dependent variable of the governing equation and f is the forcing function.

The system may have two different boundaries τ_1 and τ_2 , where the displacements $u = u_0$ and tractions $t = t_0$, respectively, are specified. The WRT is one of the ways to construct many approximate methods of analysis. In most approximate methods, we seek an approximate solution for the dependent variable u by, say \bar{u} (in one dimension), as:

$$\bar{u}(x, t) = \sum_{n=1}^N \alpha_n(t) \phi_n(x) \quad (7.13)$$

Here, α_n are some unknown constants, which are time-dependent in dynamic situations, and ϕ_n are some known functions, which are spatially dependent. When we use discretization in the solution process as in the case of the FEM, α_n will represent the nodal coefficients. In general, these functions satisfy the kinematic boundary conditions of the problem. When Equation (7.13) is substituted into the governing equation, we get $L\bar{u} - f \neq 0$ since the assumed solution is approximate. We can define the error function associated with the solution as:

$$e_1 = L\bar{u} - f, \quad e_2 = \bar{u} - u_0, \quad e_3 = \bar{t} - t_0 \quad (7.14)$$

The objective of any weighted residual technique is to make the error function as small as possible over the domain of interest and also on the boundary. This can be done by distributing the errors in different methods with each method producing a new approximate method of solution.

Let us consider a case where the boundary conditions are exactly satisfied, that is, $e_2 \equiv e_3 \equiv 0$. In this case, we need to distribute the error function e_1 only. This can be done through a weighting function w and integrating over the domain as:

$$\int_V e_1 w dV = \int_V (L\bar{u} - f) w dV = 0 \quad (7.15)$$

Choice of the weighting functions determines the type of WRT. The weighting functions used are normally of the form:

$$w = \sum_{n=1}^N \beta_n \psi_n \quad (7.16)$$

When Equation (7.16) is substituted into Equation (7.15), we get:

$$\sum_{n=1}^N \beta_n \int_V (L\bar{u} - f)\psi_n = 0, \quad n = 1, 2, 3, \dots, N$$

Since β_n are arbitrary, we have:

$$\int_V (L\bar{u} - f)\psi_n = 0, \quad n = 1, 2, \dots, N$$

This process ensures that the number of algebraic equations resulting in using Equation (7.13) for \bar{u} is equal to the number of unknown coefficients chosen.

Now, we can choose different weighting functions to obtain different approximate techniques. For example, if we choose all of ψ_n as the *Dirac delta function*, normally represented by the δ symbol, we get the classical *finite difference technique*. These are the *spike functions* that have a unit value only at the point that they are defined while at all other points they are zero. They have the following properties:

$$\begin{aligned} \int_{-\infty}^{\infty} \delta(x - x_n) dx &= \int_{x-r}^{x+r} \delta(x - x_n) dx = 1 \\ \int_{-\infty}^{\infty} f(x) \delta(x - x_n) dx &= \int_{x-r}^{x+r} f(x) \delta(x - x_n) dx = f(x_n) \end{aligned}$$

Here, r is any positive number and $f(x)$ is any function that is continuous at $x = n$. To demonstrate this method, consider a three-point line element, as shown in Figure 7.4.

The displacement field can be expressed as a three-term series in Equation (7.13) as:

$$\bar{u} = u_{n-1}\phi_1 + u_n\phi_2 + u_{n+1}\phi_3 \quad (7.17)$$

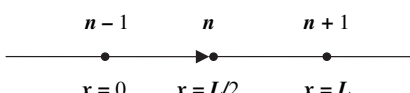


Figure 7.4 Finite differences, according to the weighted residual technique (WRT).

Here, the functions ϕ_1 , ϕ_2 and ϕ_3 satisfy the boundary conditions at the nodes, namely its nodal displacements, and they are given by:

$$\begin{aligned} \phi_1 &= \left(1 - \frac{x}{L}\right) \left(1 - \frac{2x}{L}\right), \quad \phi_2 = \left(\frac{4x}{L} - \frac{4x^2}{L^2}\right), \\ \phi_3 &= \frac{x}{L} \left(\frac{2x}{L} - 1\right) \end{aligned} \quad (7.18)$$

Now the weighting function can be assumed as:

$$\begin{aligned} w &= \beta_1 \delta(x - 0) + \beta_2 \delta(x - L/2) + \beta_3 \delta(x - L) \\ &= \sum_{n=1}^3 \beta_n \delta_n \end{aligned} \quad (7.19)$$

Let us now try to solve the following simple 1-D ordinary differential equation given by:

$$\frac{d^2u}{dx^2} + 4u + 4x = 0, \quad u(0) = u(1) = 0 \quad (7.20)$$

Here, the independent variable x has limits between 0 and 1. Using Equation (7.17) in Equation (7.20), one can find the error function or residue e_1 , say at node n , given by:

$$\begin{aligned} e_1 &= \left(\frac{d^2u}{dx^2} + 4u + 4x \right)_n = \left(\frac{1}{L^2} u_{n-1} - \frac{2}{L^2} u_n + \frac{1}{L^2} u_{n+1} \right) \\ &\quad + 4u_n + 4x_n \end{aligned} \quad (7.21)$$

Here, $L = 1$ is the domain length. If we now substitute the weight function (Equation (7.19)) and integrate, and using the properties of the Dirac delta function, we get:

$$\left[\frac{1}{L^2} (u_{n-1} - 2u_n + u_{n+1}) \right] + 4u_n + 4x_n = 0 \quad (7.22)$$

The above equation is the equation for the *central finite differences*.

The *method of moments* can be derived by assuming the weight functions of the form given by (for the 1-D case):

$$w = \beta_1 + \beta_2 x + \beta_3 x^2 + \beta_4 x^3 + \dots = \sum_{n=0}^N \beta_n x^n \quad (7.23)$$

Consider again the problem given in Equation (7.20). Let us assume only the first two terms in the above series. Let the field variable u be assumed as:

$$\bar{u} = \alpha_1 x(1-x) + \alpha_2 x^2(1-x) \quad (7.24)$$

Each of the functions associated with the unknown coefficients satisfy the boundary conditions specified in Equation (7.20). Substituting the above into the governing equation, the following residue is obtained:

$$e_1 = \alpha_1(-2 + 4x - 4x^2) + \alpha_2(2 - 6x + 4x^2 - 4x^3) + 4x \quad (7.25)$$

If we weight this residual, we get the following equations:

$$\int_0^1 e_1 dx = 2\alpha_1 + \alpha_2 = 3, \int_0^1 xe_1 dx = 5\alpha_1 + 6\alpha_2 = 10$$

Solving the above two equations, we get $\alpha_1 = 8/7$ and $\alpha_2 = 5/7$. Substituting these, we get the approximate solution to the problem as:

$$\bar{u} = \frac{8}{7}x(1-x) + \frac{5}{7}x^2(1-x)$$

The exact solution to Equation (7.20) is given by:

$$u_{\text{exact}} = \frac{\sin(2x)}{\sin(2)} - x$$

To compare the results, say at $x = 0.2$, we get $\bar{u} = 0.205$ and $u_{\text{exact}} = 0.228$. The percentage error involved in the solution is about 10, which is very good considering that only two terms were used in the weight-function series. Next, the procedure of deriving the *Galerkin technique* from the weighted residual method is outlined.

Here, we assume the weight-function variation to be similar to the displacement variation (Equation (7.13)), that is:

$$w = \beta_1 \phi_1 + \beta_2 \phi_2 + \beta_3 \phi_3 + \dots \quad (7.26)$$

Let us now consider the same problem (Equation (7.20)) with the assumed displacement field given by Equation (7.24). Let the weight function variation have only the first two terms in the series, as:

$$w = \beta_1 \phi_1 + \beta_2 \phi_2 = \beta_1 x(1-x) + \beta_2 x^2(1-x) \quad (7.27)$$

The residual e_1 is the same as that given for the previous case (Equation (7.25)). If we weight this residual with the weight function given by Equation (7.27), the following equations are obtained:

$$\int_0^1 \phi_1 e_1 dx = 6\alpha_1 + 3\alpha_2 = 10,$$

$$\int_0^1 \phi_2 e_1 dx = 21\alpha_1 + 20\alpha_2 = 42$$

Solving the above equations, we get $\alpha_1 = 74/57$ and $\alpha_2 = 42/57$. The approximate Galerkin solution then becomes:

$$\bar{u} = \frac{74}{57}x(1-x) + \frac{42}{57}x^2(1-x)$$

The result obtained for $x = 0.2$ is 0.231, which is very close to the exact solution (only a 1.3% error).

In a similar manner, one can design various approximate schemes by assuming different weight functions. The FEM is one such WRT, wherein the displacement variation and the weight functions are the same. The ‘weak form’ of the differential equation becomes the equation involving the energies.

7.3 ENERGY FUNCTIONALS AND VARIATIONAL OPERATOR

The use of the energy functional is an absolute necessity for development of the finite element method. The energy functional is essentially dependent on a number of dependent variables, such as displacements, forces, etc. which themselves are functions of position, time, etc. Hence, a functional is an integral expression, which in essence is the ‘function of many functions’. A formal study in the area of energy functionals requires a deep understanding of functional analysis. Reddy [3] gives an excellent account of the FEM from the functional analysis viewpoint. However, we, for the sake of completeness, merely state those important aspects that are relevant for finite element development. These are mathematically represented between the limits a and b as:

$$I(w) = \int_a^b F \left(x, w, \frac{dw}{dx}, \frac{d^2w}{dx^2} \right) \quad (7.28)$$

Here, a and b are the two boundary points in the domain. For a fixed value of w , $I(w)$ is always a scalar. Hence, a functional can be thought of as a mapping of $I(w)$ from a vector space W to a real number field R , which is mathematically represented as $I : W \rightarrow R$. A functional is said to be *linear* if it satisfies the following condition:

$$F(\alpha w + \beta v) = \alpha F(w) + \beta F(v) \quad (7.29)$$

Here, α and β are some scalars and w and v are the dependent variables.

A functional is called *quadratic functional*, when the following relation exist:

$$I(\alpha w) = \alpha^2 I(w) \quad (7.30)$$

If there are two functions p and q , their inner product over the domain V can be defined as:

$$(p, q) = \int_V p q dV \quad (7.31)$$

Obviously, the inner product can also be thought of as a functional. We can use the above definition to determine the properties of the differential operator of a given differential equation. A given problem is always defined by a differential equation and a set of boundary conditions, which can be mathematically represented by:

$$\begin{aligned} Lu &= f, && \text{over the domain } V \\ u &= u_0, && \text{over } \tau_1 \\ q &= q_0, && \text{over } \tau_2 \end{aligned} \quad (7.32)$$

where L is the differential operator, V is the entire domain, τ_1 is the domain where the displacements are specified (kinematic or essential boundary conditions) and τ_2 is the domain where the forces (natural boundary conditions) are specified. If u_0 is zero, then we call the essential boundary conditions *homogenous*. For non-zero u_0 , the essential boundary condition becomes *non-homogenous*. There is always a functional for a given differential equation provided that the differential operator L satisfies the following conditions:

- The differential operator L requires to be *self-adjoint* or *symmetric*. That is, $(Lu, v) = (u, Lv)$, where u and v are any two functions that satisfy the same appropriate boundary conditions.
- The differential operator L requires to be *positive definite*. That is, $(Lu, u) \geq 0$ for functions u satisfying

the appropriate boundary conditions. The equality will hold only when $u = 0$ everywhere in the domain.

The derivation of these relations is beyond the scope of study here. The interested reader is advised to refer to Shames and Dym [1] and Wazizlu [4] which are classic textbooks on variational principles for elasticity problems.

For a given differential equation, $Lu = f$, that is, subjected to homogenous boundary conditions with the differential operator being self-adjoint and positive definite, one can actually construct the functional. This is given by the following expression:

$$I(w) = (Lw, w) - 2(w, f) \quad (7.33)$$

To see what the above equation means, let us construct the functional for the well-known beam governing equation, which is given by:

$$EI \frac{d^4 w}{dx^4} + q = 0$$

In the above equation, EI is the bending rigidity, w is the dependent variable, which represents the transverse displacements, x is the independent spatial variable and q represents the loading. The domain is represented by the length of the beam l . In the above equation, $L = EI d^4 w / dx^4$ and $f = -q$. Now, the first term in Equation (7.33) becomes:

$$(Lw, w) = \int_0^l EI \frac{d^4 w}{dx^4} w dx$$

Integrating by parts, we get:

$$(Lw, w) = w EI \left[\frac{d^3 w}{dx^3} \right]_{x=0}^{x=l} - \int_0^l EI \frac{d^3 w}{dx^3} \frac{dw}{dx} dx$$

The first term is the boundary term which has two parts – one is the displacement boundary condition while the second part ($EI/d^3 w/dx^3$) is the force boundary condition and in the present case, represents the shear force. For a right-hand coordinate system, this is denoted by $-V$. Hence, the above equation can be written as:

$$(Lw, w) = -w(0)V(0) + w(l)V(l) - \int_0^l EI \frac{d^3 w}{dx^3} \frac{dw}{dx} dx$$

Integrating again the last part of the above equation by parts, we get:

$$\begin{aligned}
 (Lw, w) &= -w(0)V(0) + w(l)V(l) - \frac{dw}{dx} EI \frac{d^2w}{dx^2} \Big|_{x=0}^{x=l} \\
 &\quad + \int_0^l EI \frac{d^2w}{dx^2} \frac{d^2w}{dx^2} dx \\
 &= -w(0)V(0) + w(l)V(l) - \phi(l)M(l) \\
 &\quad + \phi(0)M(0) + \int_0^l EI \left[\frac{d^2w}{dx^2} \right]^2 dx \quad (7.34)
 \end{aligned}$$

Here, ϕ is the rotation of the cross-section (also called the slope) and M is the moment resultant. There are three possible boundary conditions in the beam, namely:

- Fixed end condition, where $w = \frac{dw}{dx} = \phi = 0$.
- Free boundary condition, where $V = -EI \frac{d^3w}{dx^3} = M = EI \frac{d^2w}{dx^2} = 0$.
- Hinged boundary condition, where $w = M = EI \frac{d^2w}{dx^2} = 0$.

For all of these boundary conditions, the boundary terms in Equation (7.34) are zero and hence the equation reduces to:

$$(Lw, w) = 2 \left(\frac{1}{2} \right) \int_0^l EI \left(\frac{d^2w}{dx^2} \right)^2 dx \quad (7.35)$$

Substituting the above into Equation (7.33), we can write the functional as:

$$I(w) = 2 \left[\frac{1}{2} \int_0^l EI \left(\frac{d^2w}{dx^2} \right)^2 dx + \int_0^l qwdx \right] \quad (7.36)$$

The terms inside the bracket are the total potential energy of the beam and the value of the functional is essentially twice the value of the potential energy. Hence, the functionals in structural mechanics are normally called *energy functionals*. We see from the above derivations that the boundary conditions are contained in the energy functional.

7.3.1 Variational symbol

In most approximate methods based on variational theorems, including the finite element technique, it is

necessary to minimize the functional and this minimization process is normally represented by a variational symbol (normally referred to as *delta operator*), mathematically represented as δ . Consider a functional that is a function of the dependent-variable w and its derivatives and is mathematically represented as $F(w, w', w'')$, where the primes ('') and ('') indicate the first and second derivatives, respectively. For a fixed value of the independent variable x , the value of the functional depend on w and its derivatives. During the process of deformation, if the value of w changes to αu , where α is a constant and u is a function, then this change is called the *variation* of w and is denoted by δw . That is, δw represents the admissible change of w for a fixed value of the independent variable x . At the boundary points, where the values of the dependent variables are specified, the variations at these points are zero. In essence, the variational operator acts like a differential operator and hence all of the laws of differentiation are applicable here.

7.4 WEAK FORM OF THE GOVERNING DIFFERENTIAL EQUATION

The variational method gives us an alternate statement of the governing equation, which is normally referred to as the *strong form* of the governing equation. This alternate statement of the equilibrium equation is essentially an integral equation. This is essentially obtained by weighting the residue of the governing equation with a weighting function and integrating the resulting expression. This process not only gives the *weak form* of the governing equation, but also the associated boundary conditions (both essential and natural boundary conditions). We will explain this procedure by again considering the governing equation of an elementary beam. The ‘strong’ form of the beam equation is given by:

$$EI \frac{d^4w}{dx^4} + q = 0$$

Now, we are looking for an approximate solution for \bar{w} in a similar form to that given in Equation (7.13). Now, the residue becomes:

$$EI \frac{d^4\bar{w}}{dx^4} + q = e_1$$

If we weight this with another function v (which also satisfies the boundary conditions of the problem) and integrate over the domain of length l , we get:

$$\int_0^l \left(EI \frac{d^4 \bar{w}}{dx^4} + q \right) v dx$$

Integrating the above expression by parts (twice), we will get the boundary terms, which are a combination of both essential and natural boundary conditions, along with the weak form of the equation. We obtain the following expression:

$$\begin{aligned} v(0)\bar{V}(0) - v(l)\bar{V}(l) - \phi(l)\bar{M}(l) + \phi(0)\bar{M}(0) \\ + \int_0^l \left(EI \frac{d^2 \bar{w}}{dx^2} \frac{d^2 v}{dx^2} + qv \right) dx \end{aligned} \quad (7.37)$$

where $\bar{V} = -EI d^3 \bar{w} / dx^3$, $\bar{M} = EI d^2 \bar{w} / dx^2$ and $\phi = d\bar{w} / dx$. Equation (7.37) is the *weak form* of the differential equation as it requires a reduced continuity requirement when compared to the original differential equation. That is, the original equation is a fourth-order equation and requires functions that are third-order continuous, while the weak order requires solutions that are just second-order continuous. This aspect is exploited fully in the finite element method.

7.5 SOME BASIC ENERGY THEOREMS

In this section, we outline three different theorems, which essentially form the backbone of finite element analysis. Here, the implications of these theorems on the development of finite element techniques are discussed. For a more thorough discussion on these topics, the interested reader is advised to refer to some classic textbooks available in this area, such as Shames and Dym [1], Wazhizu [4] and Tauchert [5]. Here, we discuss the following important energy principles:

- Principle of Virtual Work (PVW).
- Principle of Minimum Potential Energy (PMPE).
- Rayleigh–Ritz method.
- Hamilton’s principle (HP).

While the first two are essential for FE development for static problems, the last theorem is used for deriving the weak form of the equation for time-dependent problems. This section will also describe a few approximate methods which are ‘offshoots’ of these theorems.

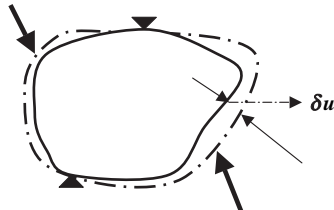


Figure 7.5 Representation of a body under virtual displacements.

7.5.1 Concept of virtual work

Consider a body shown in Figure 7.5, under the action of an arbitrary set of loads P_1, P_2 , etc. In addition, consider any arbitrary point which is subjected to a kinematically admissible infinitesimal deformation. By ‘kinematically admissible’, we mean that it does not violate the boundary constraints. Work done by such small hypothetical infinitesimal displacements, due to applied loads which are kept constant during the deformation process, is called *virtual work*. We denote the virtual displacement by the variational operator δ and in this present case it can be written as δu .

7.5.2 Principle of virtual work (PVW)

This principle states that *a continuous body is in equilibrium, if and only if, the virtual work done by all of the external forces is equal to the virtual work done by internal forces when the body is subjected to a infinitesimal virtual displacement*. If W_E is the work done by the external forces and U is the internal energy (also called the strain energy), then the PVW can be mathematically represented as:

$$\delta W_E = \delta U \quad (7.38)$$

Proof

Let us consider a three-dimensional body of ‘arbitrary material behavior’ which is subjected to surface traction t_i on a portion of the body of area S and a body force per unit volume B_i . The total external work done by the body of volume V on displacements u_i is given by:

$$W_E = \int_S t_i u_i dS + \int_V B_i u_i \quad (7.39)$$

By taking variation of this work, we get:

$$\delta W_E = \int_S t_i \delta u_i dS + \int_V B_i \delta u_i \quad (7.40)$$

Substituting for ‘tractions’ from Equation (6.33) in Chapter 6 in the above equation, we get:

$$\delta W_E = \int_S \sigma_{ij} n_i \delta u_j dS + \int_V B_i \delta u_i \quad (7.41)$$

Here, n_i is the surface normal of the body where the ‘tractions’ are acting. The surface integral on the right-hand side of the above equation is converted to a volume integral by using the *divergence theorem* [1] which states:

$$\int_V \nabla u dV = \int_S u n dS \quad (7.42)$$

where $\nabla = (\partial/\partial x)i + (\partial/\partial y)j + (\partial/\partial z)k$ is the gradient operator, $u = (u_i + v_j + w_z)$ is the displacement vector and $n = (n_x i + n_y j + n_z k)$ is the outward normal vector. Using Equation (7.42) in Equation (7.41) and simplifying, we get:

$$\begin{aligned} \delta W_E &= \int_V \underbrace{\sigma_{ij} \frac{\partial}{\partial x_j} (\delta u_i)}_{\text{Virtual strain}} dV + \int_V \frac{\partial}{\partial x_j} (\sigma_{ij}) \delta u_i dV + \int_V B_i \delta u_i \\ &= \int_V \underbrace{\sigma_{ij} \delta e_{ij} dV}_{\text{Internal virtual work} = \delta U} + \underbrace{\int_V \left[\frac{\partial}{\partial x_j} (\sigma_{ij}) + B_i \right] \delta u_i dV}_{\text{Equation of equilibrium}=0} \end{aligned}$$

Further simplifying, the external virtual work becomes $\delta W_E = \delta U$, which is essentially the virtual work principle.

The direct offshoot of PVE is the *Dummy Displacement method*, which is extensively used for finding the reaction forces in many redundant structures. The details of this method can be found in Tauchert [5] and Reddy [6].

7.5.3 Principle of minimum potential energy (PMPE)

This principle states that *of all the displacement fields which satisfy the prescribed constraint conditions, the correct state is that which makes the total potential energy of the structure a minimum.*

This principle can be directly obtained from the PVW. Here, we define the potential of the external forces V as the negative of the work done by the external forces. That is, $V = -W_E$. Using this in the PVW expression, we have:

$$\delta(U + V) = 0 \quad (7.43)$$

The above principle is the backbone for finite element development. In addition, this principle can be used to derive the governing differential equations of the system, especially for static analysis, and also their associated boundary conditions. This aspect is demonstrated here by deriving the governing equation for a beam, starting from the energy functional.

Consider a beam of bending rigidity EI and subjected to a distributed loading of $q(x)$ per unit length over the entire beam of length L . Let $w(x)$ represent the lateral displacement field of the beam. The strain energy functional and the potential of the external forces can be written as:

$$U = \frac{1}{2} \int_0^L EI \left(\frac{d^2 w}{dx^2} \right)^2 dx, \quad V = - \int_0^L q w dx \quad (7.44)$$

By the PMPE, we have:

$$\delta \left[\frac{1}{2} \int_0^L EI \left(\frac{d^2 w}{dx^2} \right)^2 dx - \int_0^L q w dx \right] = 0$$

Using the operation on the variational operator, we have:

$$\begin{aligned} &\left[\int_0^L EI \left(\frac{d^2 w}{dx^2} \right) \delta \left(\frac{d^2 w}{dx^2} \right) dx - \int_0^L q \delta w dx \right] = 0 \\ &= \left[\int_0^L EI \left(\frac{d^2 w}{dx^2} \right) \left(\frac{d^2 (\delta w)}{dx^2} \right) dx - \int_0^L q \delta w dx \right] = 0 \end{aligned}$$

Integrating the first term by parts (twice) and identifying the boundary terms, as was carried out earlier, we get:

$$\begin{aligned} &\delta w(0)V(0) - \delta w(L)V(L) - \delta \phi(L)M(L) - \delta \phi(0)M(0) \\ &+ \int_0^L \left(EI \frac{d^4 w}{dx^4} + q \right) \delta w dx = 0 \end{aligned}$$

Since the variation of the displacements at the specified locations (boundaries) is always zero and δw is arbitrary, the only non-zero term contained in the large bracket should be the governing differential equation of the beam.

The PMPE can be directly used to derive the well-known *Castigliano's first theorem* used in elementary structural mechanics to determine the reaction forces in a structure discretized by using n generalized degrees of freedom, q_n . Both the strain energy, as well as the potential of external forces, are functions of these

generalized degrees of freedom. Hence, we can write the PMPE statement as:

$$\delta \left[U(q_n) - \sum_{n=1}^N P_n q_n \right] = 0$$

Here, P_n represent the applied load. Taking the first variation of the strain energy and expanding, we can write the above expression as:

$$\begin{aligned} \frac{\partial U}{\partial q_1} \delta q_1 + \frac{\partial U}{\partial q_2} \delta q_2 + \dots + \frac{\partial U}{\partial q_n} \delta q_n - P_1 \delta q_1 - P_2 \delta q_2 \\ - \dots - P_n \delta q_n = 0 \end{aligned}$$

Grouping the terms together, we have:

$$\begin{aligned} \left(\frac{\partial U}{\partial q_1} - P_1 \right) \delta q_1 + \left(\frac{\partial U}{\partial q_2} - P_2 \right) \delta q_2 + \dots \\ + \left(\frac{\partial U}{\partial q_n} - P_n \right) \delta q_n = 0 \end{aligned}$$

Since all of the δq_n are arbitrary, the terms contained in each bracket should be equal to zero. Hence, we have:

$$\left(\frac{\partial U}{\partial q_n} - P_n \right) = 0, \quad \text{or} \quad \frac{\partial U}{\partial q_n} = P_n \quad (7.45)$$

The above statement is essentially the Castiglano's theorem, which states that, if a reaction force at a generalized degree of freedom is required, then differentiating the strain energy with respect to the said degree of freedom will give the required reaction force.

The PMPE can also be used to construct some approximate solutions to the problem. One such method is the Rayleigh–Ritz method [1]. This is one of the most important methods in structural mechanics for determining an approximate solution to a problem. In fact, the Finite Element Method can be considered as a ‘piecewise’ Rayleigh–Ritz method, where this technique is applied at the element level and the total solution is obtained by synthesis of element level solutions. This method is explained next.

7.5.4 Rayleigh–Ritz method

In this method, we are seeking an approximate solution to the governing equation $Lu = f$, where u is the dependent variable normally representing displacements in

structural mechanics. We again assume the approximate solution in the form:

$$\bar{u} = \sum_{n=1}^N a_n \phi_n \quad (7.46)$$

Here, a_n are the unknown generalized degrees of freedom and ϕ_n are the known functions – called the *Ritz functions*. These functions should satisfy the kinematic boundary conditions and need not satisfy the natural boundary conditions. Next, the strain energy and the potential of external forces are written in terms of displacements and the assumed approximate displacement field (Equation (7.46)) and are substituted into the energy expressions and integrated. The PMPE is invoked and the total energy is minimized to get a set of n simultaneous equations, which are solved for determining a_n . Mathematically, we can represent the total energy, which is function of a_n , as:

$$\pi(a_n) = (U + V)$$

By the PMPE, we have that the first variation of the total energy is zero. That is:

$$\begin{aligned} \delta \pi = 0 &= \frac{\partial \pi}{\partial a_1} \delta a_1 + \frac{\partial \pi}{\partial a_2} \delta a_2 + \dots + \frac{\partial \pi}{\partial a_n} \delta a_n \\ &= \sum_{n=1}^N \frac{\partial \pi}{\partial a_n} \delta a_n \end{aligned}$$

Since δa_n is arbitrary, we have:

$$\frac{\partial \pi}{\partial a_1} = \frac{\partial \pi}{\partial a_2} = \dots = \frac{\partial \pi}{\partial a_n} = 0, \quad n = 1, 2, \dots, n$$

This procedure ensures that there are n equations to solve n unknown coefficients. The Ritz functions should be so chosen that they be differentiable up to the order specified by the energy functional. Normally polynomials or trigonometric functions are used as Ritz functions. Since the natural boundary conditions are not satisfied by the assumed field, it is highly likely that the solutions would not yield accurate forces (stresses). Normally, enough terms should be used in Equation (7.46) to get accurate solutions. However, if very few terms are used, then these introduce additional geometric constraints which make the structure stiffer and hence the predicted displacements are always ‘lower-bound’. The application of this method to problems of complex geometry is very difficult.

7.5.5 Hamilton's principle (HP)

This principle is extensively used to derive the governing equation of motion for a structural system under

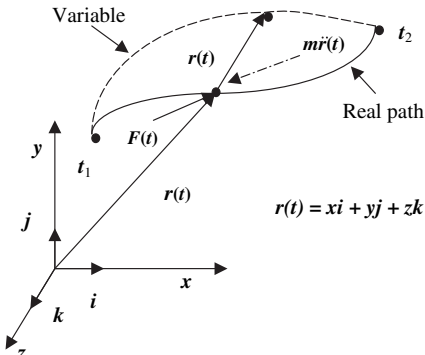


Figure 7.6 Real and variable paths for a particle of mass m .

dynamic loads. In fact, this principle can be thought of as the PMPE for a dynamic system. This principle was first formulated by an Irish mathematician and physicist, Sir William Hamilton. Similar to the PMPE, the HP is an *integral statement of a dynamic system under equilibrium*.

In order to derive this principle, consider a body of mass m and having a position vector with respect to its coordinate system as $r = xi + yj + zk$. Under the action of a force $F(t) = F_x(t)i + F_y(t)j + F_z(t)k$, this mass moves from position 1 at time t_1 to a position 2 at time t_2 , according to Newton's Second Law. Such a path is called the *Newtonian Path*. The motion of this mass is pictorially shown in Figure 7.6.

The total force $F(t)$ comprises conservative forces such as internal forces caused by the strain energies of the structures, the external forces and some non-conservative forces, such as damping forces. Hence the force vector is made up of two parts, which can be written as $F(t) = F_c(t) + F_{nc}(t)$. Each of these will have components in all of the three coordinate directions. This force is balanced by the inertial force generated by the moving mass. If this mass is given a small virtual displacement, $\delta r(t) = \delta u i + \delta v j + \delta w k$, where u , v and w are the displacement components in the three coordinate directions, the path of mass is as shown by the dashed line in Figure 7.6. This path need not be a '*Newtonian path*', however, at time $t = t_1$ and $t = t_2$, the path coincides with the '*Newtonian path*' of the original motion of the mass. That is, we have $\delta r(t_1) = \delta r(t_2) = 0$. The equilibrium of this mass can be written as:

$$F_x(t) - m\ddot{u}(t) = 0,$$

$$F_y(t) - m\ddot{v}(t) = 0,$$

$$F_z(t) - m\ddot{w}(t) = 0$$

Invoking the PVM, which essentially states that the total virtual work done by the infinitesimal virtual displacement should be zero, we have:

$$\begin{aligned} & [F_x(t) - m\ddot{u}(t)]\delta u(t) + [F_y(t) - m\ddot{v}(t)]\delta v(t) \\ & + [F_z(t) - m\ddot{w}(t)]\delta w(t) = 0 \end{aligned} \quad (7.47)$$

Rearranging the terms and integrating the equation between the time t_1 and time t_2 , we have:

$$\begin{aligned} & \int_{t_1}^{t_2} -m[\ddot{u}(t)\delta u(t) + \ddot{v}(t)\delta v(t) + \ddot{w}(t)\delta w(t)] \\ & + \int_{t_1}^{t_2} [F_x(t)\delta u(t) + F_y(t)\delta v(t) + F_z(t)\delta w(t)] \end{aligned} \quad (7.48)$$

Consider the first integral (I_1), which can be written after integrating by parts as:

$$\begin{aligned} I_1 = & -m\dot{u}(t)\delta u(t) - m\dot{v}(t)\delta v(t) - m\dot{w}(t)\delta w(t) \Big|_{t=t_1}^{t=t_2} \\ & + \int_{t_1}^{t_2} m(\dot{u}\delta\dot{u} + \dot{v}\delta\dot{v} + \dot{w}\delta\dot{w})dt \end{aligned}$$

Recognizing that the virtual displacement must vanish at the beginning and end of this varied path, we can write the first integral as:

$$\begin{aligned} I_1 = & \int_{t_1}^{t_2} m(\dot{u}\delta\dot{u} + \dot{v}\delta\dot{v} + \dot{w}\delta\dot{w})dt \\ = & \int_{t_1}^{t_2} \frac{m}{2} \delta(\dot{u}^2 + \dot{v}^2 + \dot{w}^2)dt = \delta \int_{t_1}^{t_2} T dt \end{aligned} \quad (7.49)$$

Here, T represents the total kinetic energy of the system. Now, let us consider the second integral (I_2) in Equation (7.48). The force term in this expression can be written in terms of internal and non-conservative forces. This integral then becomes:

$$\begin{aligned} I_2 = & \int_{t_1}^{t_2} [F_{cx}(t)\delta u(t) + F_{cy}(t)\delta v(t) + F_{cz}(t)\delta w(t)]dt \\ & + \int_{t_1}^{t_2} [F_{ncx}(t)\delta u(t) + F_{ncy}(t)\delta v(t) + F_{ncz}(t)\delta w(t)]dt \end{aligned}$$

The second integral in the above expression is nothing but the variation of the work done by the non-conservative forces and can be written as:

$$\delta \int_{t_1}^{t_2} W_{nc} dt = \delta \int_{t_1}^{t_2} [F_{ncx}(t)u(t) + F_{ncy}(t)v(t) + F_{ncz}(t)w(t)] dt$$

The first integral in I_2 is the work done due to internal forces. From Castiglione's first theorem, which was derived in Section 7.5.3, the internal force is obtained by differentiating the strain energy ($U(u, v, w, t)$) with respect to the corresponding displacement (Equation (7.45)). Accordingly, we can write:

$$F_{cx} = -\frac{\partial U}{\partial u}, \quad F_{cy} = -\frac{\partial U}{\partial v}, \quad F_{cz} = -\frac{\partial U}{\partial w} \quad (7.50)$$

The negative sign is given to indicate that these forces resist the deformation. Using Equation (7.50) in I_2 , we have:

$$\begin{aligned} I_2 &= - \int_{t_1}^{t_2} \left[\frac{\partial U}{\partial u} \delta u(t) + \frac{\partial U}{\partial v} \delta v(t) + \frac{\partial U}{\partial w} \delta w(t) \right] dt \\ &\quad + \delta \int_{t_1}^{t_2} W_{nc} dt \\ &= \delta \int_{t_1}^{t_2} (-U + W_{nc}) dt \end{aligned} \quad (7.51)$$

By using Equations (7.49) and (7.51) in Equation (7.48), Hamilton's principle becomes:

$$\delta \int_{t_1}^{t_2} (T - U + W_{nc}) dt = 0 \quad (7.52)$$

The use of this equation in obtaining the governing equation and its associated boundary conditions was demonstrated in Section 6.3.2 in the last chapter. It is of interest to know that if we omit the inertial energy in Equation (7.52) and assume that all of the quantities are time-independent, then the HP reduces to the PMPE.

One can easily deduce the famous *Lagrange Equation of motion* for a discrete system having the energies

(kinetic, strain energy and non-conservative energy) as a function of the generalized coordinates q_1, q_2, \dots, q_n as:

$$\begin{aligned} T &= T(q_1, q_2, \dots, q_n, \dot{q}_1, \dot{q}_2, \dots, \dot{q}_n) \\ U &= U(q_1, q_2, \dots, q_n) \\ W_{nc} &= P_1 q_1 + P_2 q_2 + \dots + P_n q_n \end{aligned} \quad (7.53)$$

Here, P_1, P_2, \dots, P_n represent the external and damping forces. Taking the first variation of these energies, we have:

$$\begin{aligned} \delta T &= \frac{\partial T}{\partial q_1} \delta q_1 + \frac{\partial T}{\partial q_2} \delta q_2 + \dots + \frac{\partial T}{\partial q_n} \delta q_n + \frac{\partial T}{\partial \dot{q}_1} \delta \dot{q}_1 \\ &\quad + \frac{\partial T}{\partial \dot{q}_2} \delta \dot{q}_2 + \dots + \frac{\partial T}{\partial \dot{q}_n} \delta \dot{q}_n = \sum_{i=1}^n \frac{\partial T}{\partial q_i} \delta q_i + \frac{\partial T}{\partial \dot{q}_i} \delta \dot{q}_i \\ \delta U &= \frac{\partial U}{\partial q_1} \delta q_1 + \frac{\partial U}{\partial q_2} \delta q_2 + \dots + \frac{\partial U}{\partial q_n} \delta q_n = \sum_{i=1}^n \frac{\partial U}{\partial q_i} \delta q_i \\ \delta W_{nc} &= P_1 \delta q_1 + P_2 \delta q_2 + \dots + P_n \delta q_n = \sum_{i=1}^n P_i \delta q_i \end{aligned}$$

Using the above in the HP (Equation (7.52)), we have:

$$\sum_{i=1}^n \int_{t_1}^{t_2} \left(\frac{\partial T}{\partial q_i} \delta q_i + \frac{\partial T}{\partial \dot{q}_i} \delta \dot{q}_i - \frac{\partial U}{\partial q_i} \delta q_i + P_i \delta q_i \right) dt = 0 \quad (7.54)$$

Integrating the second term by parts and recognizing that the virtual displacements vanish at the beginning and end, the above integral becomes:

$$\int_{t_1}^{t_2} \sum_{i=1}^n \left[-\frac{d}{dt} \left(\frac{\partial T}{\partial \dot{q}_i} \right) + \frac{\partial T}{\partial q_i} - \frac{\partial U}{\partial q_i} + P_i \right] \delta q_i dt = 0$$

Since the virtual displacements are arbitrary, the *Lagrange equations* become:

$$\frac{d}{dt} \left(\frac{\partial T}{\partial \dot{q}_i} \right) - \frac{\partial T}{\partial q_i} + \frac{\partial U}{\partial q_i} = P_i \quad (7.55)$$

The above equation is extensively used in the derivation of discretized equations of motion for a dynamic system.

7.6 FINITE ELEMENT METHOD

The FEM uses the 'weak form' of the governing equation to convert a ordinary differential equation to a set of algebraic equations in the case of static analysis and a

coupled set of second-order differential equations in the case of dynamic analysis. In the previous sections of this chapter, different approximate methods were explained, which are very difficult to apply to a problem involving complex geometry and complicated boundary conditions. However, if one takes the approach of subdividing the domain into many subdomains, in each of these sub-domains, one can assume a solution of the type:

$$\bar{u}(x, y, z, t) = \sum_{n=1}^N a_n(t) \phi_n(x, y, z) \quad (7.56)$$

and fit any of the approximate methods described earlier within the subdomains to get an approximate solution to the problem. In the FEM, these subdomains are called *elements*, which normally take the shapes of line elements for 1-D structures, such as rods and beams, rectangles or triangles for 2-D structures and bricks or tetrahedrons for 3-D structures. Each element has a set of nodes, which may vary depending on the order of the functions $\phi_n(x, y, z)$ in Equation (7.56) used to approximate the displacement fields within each element. These nodes have unique IDs, which fix their positions in space of complex structures. In Equation (7.56), $a_n(t)$ normally represents the time-dependent nodal displacements, while $\phi_n(x, y, z)$ are the spatially dependent functions, which are normally referred to as *shape functions*. The entire finite element procedure for obtaining a solution for a complex problem can be summarized as follows:

- The use of the weak form of the governing differential equation and an assumption of the field-variable variation over the element (Equation (7.56)) and its subsequent minimization will yield a *stiffness matrix* and a *mass matrix*. The sizes of these matrices depend on the number of nodes and the number of degrees of freedom each node can support. The mass matrix formulated through the weak form of the equation is called the *consistent mass matrix*. There are other ways of formulating the mass matrix, which are explained in detail in the latter part of this chapter. The *damping matrix* is normally not obtained through weak formulation. For linear systems, this is obtained through a linear combination of stiffness and the mass matrix. Damping through such a procedure is called *proportional damping*.
- The FEM comes under the category of the stiffness method, where satisfaction of the compatibility is automatic as we begin the analysis with a displacement assumption. The issue in the stiffness method is satisfaction of the equilibrium equations. This

condition requires to be enforced. Such an enforcement is made by assembling the stiffness, mass and damping matrices. This is done by adding the stiffness of a particular degree of freedom coming from the contiguous elements. Similarly, the force vectors acting on each node are assembled to obtain the global force vector. If the load is distributed on a segment of the complex domain, then using the equivalent energy concept, it is split into concentrated loads acting on the respective nodes that make up the segment. The size of the assembled stiffness, mass and damping matrices is equal to $n \times n$, where n is the total number degrees of freedom in the discretized domain.

- After assembly of the matrices, the displacement boundary conditions are enforced, which could be homogenous or non-homogenous. If the boundary conditions are homogenous, then the corresponding rows and columns are eliminated to get the reduced stiffness, mass and damping matrices. In the case of static analysis, the obtained matrix equation involving the stiffness matrix is solved to obtain the nodal displacements. In the case of dynamic analysis, we get a coupled set of ordinary differential equations, which are solved by either modal methods or a ‘time-marching’ scheme.

7.6.1 Shape functions

The spatial dependent function in Equation (7.56) is called the *shape function* of the element. These functions are normally assumed as being polynomial, whose order depends on the degrees of freedom that an element can support. These functions relate the nodal displacements with the assumed displacement field. They are normally denoted by the symbol N . We will now give the procedure of finding the shape functions for the elements shown in Figure 7.7.

7.6.1.1 Rod element

Let us now derive the shape functions for a finite rod element having length L and axial rigidity EA . A rod element can support only axial motion and hence this element can have two nodes and each node can support one axial motion, as shown in Figure 7.7(a). That is, we require a function that is only first order continuous (that is C^0 continuous elements). Hence, we can assume the displacement field contains two constants corresponding to two degrees of freedom, that is:

$$u = a_0(t) + a_1(t)x \quad (7.57)$$

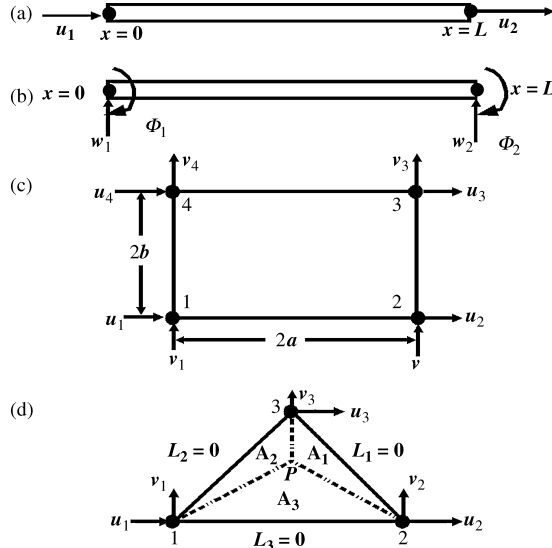


Figure 7.7 Different finite elements: (a) rod element; (b) beam element; (c) rectangular element; (d) triangular element.

The above equation also happens to satisfy the governing static differential equation of a rod, which is given by $EAD^2u/dx^2 = 0$. Equation (7.57) is now converted in terms of nodal coordinates by substituting $u(x=0) = u_1$ and $u(x=L) = u_2$ in the above equation. This will enable us to write constants a_0 and a_1 in terms of the nodal displacements u_1 and u_2 . Eliminating these constants and simplifying, Equation (7.57) can now be written as:

$$u(x) = \left(1 - \frac{x}{L}\right)u_1 + \left(\frac{x}{L}\right)u_2 \quad (7.58)$$

In Equation (7.58), the two functions inside the brackets are the two shape functions of the rod corresponding to two degrees of freedom. Hence, the displacement field can be written in matrix form as:

$$u(x) = [N_1(x) \ N_2(x)] \begin{Bmatrix} u_1 \\ u_2 \end{Bmatrix} = [N]\{u\} \quad (7.59)$$

The shape function N_1 takes the value of 1 at node one while it is zero at node two. Similarly, N_2 is zero at node 1 and one at node 2. In fact, the displacement for any element can be written in the form shown in Equation (7.59).

7.6.1.2 Beam element

One can similarly derive the shape functions for a beam element. The beam element shown in Figure 7.7(b) has two nodes and each node have two degrees of freedom,

namely the transverse displacement w and rotation $\phi = (dw/dx)$. Hence, the nodal degrees of freedom vector is given by $\{u\} = \{w_1 \ \phi_1 \ w_2 \ \phi_2\}^T$, which requires a minimum cubic polynomial for displacement. In addition, since the slope is derived from the transverse displacements, it is required that the polynomial is second-order continuous, that is, it requires a higher continuity when compared to the rod. Such elements are called C^1 continuous elements. We proceed as follows to obtain the shape functions. The interpolating polynomial for the beam is given by:

$$w(x, t) = a_0(t) + a_1(t)x + a_2(t)x^2 + a_3(t)x^3 \quad (7.60)$$

As in the case of rods, the above solution happens to be the exact solution to the governing beam equation. Now, if we substitute $w(0, t) = w_1(t)$, $\phi(0, t) = dw(0, t)/dx = \phi_1(t)$, $w(L, t) = w_2(t)$ and $\phi(L, t) = dw(L, t)/dx = \phi_2(t)$, we get:

$$\begin{Bmatrix} w_1 \\ \phi_1 \\ w_2 \\ \phi_2 \end{Bmatrix} = \begin{bmatrix} 1 & 0 & 0 & 0 \\ 0 & 1 & 0 & 0 \\ 1 & L & L^2 & L^3 \\ 0 & 1 & 2L & 3L^2 \end{bmatrix} \begin{Bmatrix} a_0 \\ a_1 \\ a_2 \\ a_3 \end{Bmatrix} = \{u\} = [G]\{a\}$$

Inverting the above matrix, we can write the unknown coefficients as $\{a\} = [G]^{-1}\{u\}$. Substituting the values of the coefficients in Equation (7.60), we get:

$$\begin{aligned} w(x, t) &= [N_1(x) \ N_2(x) \ N_3(x) \ N_4(x)]\{u(t)\}, \\ N_1(x) &= 1 - 3\left(\frac{x}{L}\right)^2 + 2\left(\frac{x}{L}\right)^3, N_2(x) = x\left(1 - \frac{x}{L}\right)^2 \\ N_3(x) &= 3\left(\frac{x}{L}\right)^2 - 2\left(\frac{x}{L}\right)^3, N_4(x) = x\left[\left(\frac{x}{L}\right)^2 - \left(\frac{x}{L}\right)\right] \end{aligned} \quad (7.61)$$

The above shape function will take a unit value at the nodes and zero everywhere else.

Before we proceed further, we will highlight the necessary requirements an interpolating polynomial of an element has to satisfy, especially from the convergence point of view. These can be summarized as follows:

- The assumed solution should be able to capture the rigid body motion. This can be made sure by retaining a constant part in the assumed solution.
- The assumed solution must be able to attain the constant strain rate as the mesh is refined. This can be assured by retaining the linear part of the assumed function in the interpolating polynomial.

- Most second-order systems require only C^0 continuity, which are easily met in most FE formulations. However, for higher-order systems such as Bernoulli-Euler beams or elementary plates, one requires C^1 continuity, which are extremely difficult to satisfy, especially for plate problems, where interelement slope continuity is very difficult to comply with. In such situations, one can use shear-deformable models, that is, models that also include the effect of shear deformations. In such models, slopes are not derived from the displacements and are independently interpolated. This relaxes the C^1 continuity requirement. However, when such elements are used in thin-beam or plate models, where the effects of shear deformations are negligible, the displacements predicted would be many orders smaller than the correct displacements. Such problems are called *shear-locking* problems, which are addressed in detail in a latter part of this chapter.
- The order of an assumed interpolating polynomial is dictated by the highest order of the derivative appearing in the energy functional. That is, the assumed polynomial should be at least one order higher than that appearing in the energy functional.
- In 2-D formulation, especially for C^1 continuity problems, the polynomials are chosen based on *Pascal's triangle* [7].

7.6.1.3 Rectangular element

We will now determine the shape functions for two-dimensional elements. Let us now consider a rectangular finite element of length $2a$ and width $2b$, as shown in Figure 7.7(c). This element has four nodes and each node can support two degrees of freedom, namely the two displacements, $u(x, y)$ and $v(x, y)$ in the two coordinate directions. Since there are four nodes, we can assume the interpolating polynomial as:

$$\begin{aligned} u(x, y) &= a_0 + a_1x + a_2y + a_3xy \\ v(x, y) &= b_0 + b_1x + b_2y + b_3xy \end{aligned} \quad (7.62)$$

The above function has a linear variation of displacement in both the coordinate directions and hence it is normally referred to as a *bi-linear* element. In the above interpolating polynomial, we substitute $u(-a, -b) = u_1$, $v(-a, -b) = v_1$, $u(-a, b) = u_2$, $v(-a, b) = v_2$, $u(a, b) = u_3$, $v(a, b) = v_3$, $u(a, -b) = u_4$ and $v(a, -b) = v_4$. These help us to relate the nodal displacements to the unknown coefficients as $\{u\} = [G]\{a\}$. Inverting the above relation and substituting for the unknown coefficients in Equation (7.62), we can write the displacement field

and the shape functions as:

$$u(x, y) = [N]\{u\} = [N_1(x, y) \ N_2(x, y) \ N_3(x, y) \ N_4(x, y)]\{u\}$$

$$v(x, y) = [N]\{v\} = [N_1(x, y) \ N_2(x, y) \ N_3(x, y) \ N_4(x, y)]\{v\}$$

$$\{u\} = \{u_1 \ u_2 \ u_3 \ u_4\}^T, \ \{v\} = \{v_1 \ v_2 \ v_3 \ v_4\}^T$$

$$\begin{aligned} N_1(x, y) &= \frac{(x-a)(y-b)}{4ab}, \ N_2(x, y) = \frac{(x-a)(y+b)}{4ab}, \\ N_3(x, y) &= \frac{(x+a)(y+b)}{4ab}, \ N_4(x, y) = \frac{(x+a)(y-b)}{4ab} \end{aligned} \quad (7.63)$$

7.6.1.4 Triangular element

One can similarly write the shape functions for a triangle. However, it is very convenient if one uses the area coordinates for the triangle. Consider the triangle shown in Figure 7.7(d), having coordinates of the three vertices as (x_1, y_1) , (x_2, y_2) and (x_3, y_3) .

Consider an arbitrary point P inside the triangle. This point will split the triangle into three smaller triangles of area A_1 , A_2 and A_3 , respectively. Let A be the total area of the triangle, which can be written in terms of nodal coordinates as

$$A = \frac{1}{2} \begin{vmatrix} 1 & x_1 & y_1 \\ 1 & x_2 & y_2 \\ 1 & x_3 & y_3 \end{vmatrix} \quad (7.64)$$

We will define the area coordinates for the triangle as:

$$L_1 = \frac{A_1}{A}, \quad L_2 = \frac{A_2}{A}, \quad L_3 = \frac{A_3}{A} \quad (7.65)$$

Thus, the position of point P is given by (L_1, L_2, L_3) . These coordinates, which are normally referred to as *area coordinates*, are not independent and satisfy the relation:

$$L_1 + L_2 + L_3 = 1 \quad (7.66)$$

These area coordinates are related to the global x - y coordinate system through:

$$\begin{aligned} x &= L_1x_1 + L_2x_2 + L_3x_3 \\ y &= L_1y_1 + L_2y_2 + L_3y_3 \end{aligned} \quad (7.67)$$

where:

$$L_i = \frac{(a_i + b_ix + c_iy)}{2A} \quad i = 1, 2, 3 \quad (7.68)$$

and:

$$a_1 = x_2y_3 - x_3y_2, \quad b_1 = y_2 - y_3, \quad c_1 = x_3 - x_2$$

The other coefficients are obtained by cyclic permutation. Equation (7.67) requires to be used when the derivative with respect to the coordinate is required.

Now, one can write the shape functions for the triangle as:

$$\begin{aligned} u &= N_1 u_1 + N_2 u_2 + N_3 u_3 \\ v &= N_1 v_1 + N_2 v_2 + N_3 v_3 \\ N_1 &= L_1, N_2 = L_2, N_3 = L_3 \end{aligned} \quad (7.69)$$

These shape functions also follow the normal rules. That is, at point A where the value of $L_1 = 1$, the shape functions take the value of 1. At the same point, $L_2 = L_3 = 0$. Similarly, at the other two vertices, L_2 and L_3 take a unit value, while the other two go to zero.

In summary, for all of the elements, we can express the displacements in terms of shape functions and the nodal displacements as $u = \sum_{n=1}^N N_n u_n$ or $[N] \{u\}$. This spatial discretization will be used in the energy functional to obtain the finite element governing equation. This is shown in the next section.

7.6.2 Derivation of the finite element equation

Consider a body of volume V under the action of surface tractions in the three coordinate directions $\{t_s\} = \{t_x \ t_y \ t_z\}^T$ on the boundary S and the body force vector per unit volume $\{B\} = \{B_x \ B_y \ B_z\}^T$. Let the displacement vector be written as $\{d(x, y, z, t)\} = \{u(x, y, z, t) \ v(x, y, z, t) \ w(x, y, z, t)\}^T$, where u , v and w are the displacement variations in the three coordinate directions. We will now invoke Hamilton's principle, which states that:

$$\delta \int_{t_1}^{t_2} (T - U + W_{nc}) dt = 0 \quad (7.70)$$

where the kinetic energy T is given by:

$$T = \frac{1}{2} \int_V \rho (\ddot{u}^2 + \ddot{v}^2 + \ddot{w}^2) dV$$

Taking the first variation and integrating, we get:

$$\int_{t_1}^{t_2} \delta T dt = \int_{t_1}^{t_2} \int_V \rho \left(\frac{du}{dt} \frac{d(\delta u)}{dt} + \frac{dv}{dt} \frac{d(\delta v)}{dt} + \frac{dw}{dt} \frac{d(\delta w)}{dt} \right) dV dt$$

Integrating by parts, and noting that the first variation vanishes at times t_1 and t_2 :

$$\begin{aligned} \int_{t_1}^{t_2} \delta T dt &= - \int_{t_1}^{t_2} \int_V \rho (\ddot{u} \delta u + \ddot{v} \delta v + \ddot{w} \delta w) dV dt \\ &= - \int_{t_1}^{t_2} \int_V \rho \{\delta d\}^T \{\ddot{d}\} dV dt \end{aligned} \quad (7.71)$$

where $\{\ddot{d}\} = \{\ddot{u} \ \ddot{v} \ \ddot{w}\}^T$ represents the acceleration vector and $\{\delta d\} = \{\delta u \ \delta v \ \delta w\}^T$ represents the vector containing the first variation of the displacements.

The strain energy for a 3-D body in terms of stresses and strains is given by:

$$\begin{aligned} U &= \frac{1}{2} \int_V (\sigma_{xx} \epsilon_{xx} + \sigma_{yy} \epsilon_{yy} + \sigma_{zz} \epsilon_{zz} + \tau_{xy} \gamma_{xy} + \tau_{yz} \gamma_{yz} + \tau_{zx} \gamma_{zx}) dV \\ &= \frac{1}{2} \int_V \{\epsilon\}^T \{\sigma\} dV \end{aligned} \quad (7.72)$$

For the linear elastic case, the constitutive law given by Equation (6.68) in Chapter 6 can be written as $\{\sigma\} = [C]\{\epsilon\}$. Hence, the strain energy becomes:

$$U = \frac{1}{2} \int_V \{\epsilon\}^T [C] \{\epsilon\} dV$$

Taking the first variation and integrating, we have:

$$\int_{t_1}^{t_2} \delta U dt = \int_{t_1}^{t_2} \int_V \{\delta \epsilon\}^T [C] \{\epsilon\} dV dt \quad (7.73)$$

The work done by the body forces, surface forces, damping elements and the concentrated forces are 'clubbed' together under W_{nc} . That is, $W_{nc} = W_B + W_S + W_D$. The work done by the body forces is given by:

$$W_B = \int_V (B_x u + B_y v + B_z w) dV = \int_V \{d\}^T \{B\} dV \quad (7.74)$$

The first variation of the body force work is given by:

$$\begin{aligned} \int_{t_1}^{t_2} \delta W_B dt &= \int_{t_1}^{t_2} \int_V (B_x \delta u + B_y \delta v + B_z \delta w) dV dt \\ &= \int_{t_1}^{t_2} \int_V \{\delta d\}^T \{B\} dV dt \end{aligned} \quad (7.75)$$

The work done by the surface forces is given by:

$$W_S = \int_S \{d\}^T \{t_s\} dS$$

The first variation of this work is given by:

$$\int_{t_1}^{t_2} \delta W_S dt = \int_{t_1}^{t_2} \int_V \{\delta d\}^T \{t_s\} dV dt \quad (7.76)$$

Similarly, the first variation of the work done by the damping force is given by:

$$\int_{t_1}^{t_2} \delta W_D dt = - \int_{t_1}^{t_2} \int_V \{\delta d\}^T \{F_D\} dV dt \quad (7.77)$$

If the damping is of the viscous type, then the damping force is proportional to the velocity and is given by $\{F_D\} = \eta \{d\}$, where η is the damping coefficient and $\{d\} = \{\dot{u} \ \dot{v} \ \dot{w}\}^T$ is the velocity vector in the three coordinate directions. Now, using Equations (7.71) and (7.73)–(7.77), in the Hamilton's principle (Equation (7.70)), we get:

$$\begin{aligned} & - \int_{t_1}^{t_2} \int_V \{\delta d\}^T \rho \{\ddot{d}\} dV dt - \int_{t_1}^{t_2} \int_V \{\delta e\}^T [C] \{e\} dV dt \\ & + \int_{t_1}^{t_2} \int_V \{\delta d\}^T \{B\} dV dt + \int_{t_1}^{t_2} \int_S \{\delta d\}^T \{t_s\} dS dt \\ & - \int_{t_1}^{t_2} \int_V \{\delta d\}^T \{F_D\} dV dt = 0 \end{aligned} \quad (7.78)$$

In the above equation, we substitute the assumed displacement variation in terms of the shape function and nodal displacements, derived earlier. That is, we have:

$$\{d(x, y, z, t)\} = [N(x, y, z)] \{u_e(t)\} \quad (7.79)$$

where $[N(x, y, z)]$ is the shape function matrix and $\{u_e\}$ is the nodal displacement vector of an element. Using the above, we can write velocity, acceleration and its first variation as:

$$\{\dot{d}\} = [N] \{\dot{u}_e\}, \quad \{\ddot{d}\} = [N] \{\ddot{u}_e\} \text{ and } \{\delta d\} = [N] \{\delta u_e\} \quad (7.80)$$

Now the strains can also be written in terms of the strain-displacement relationship (Equation (6.27) in Chapter 6). That is, the six strain components can be written in matrix form as:

$$\left\{ \begin{array}{l} \varepsilon_{xx} \\ \varepsilon_{yy} \\ \varepsilon_{zz} \\ \gamma_{xy} \\ \gamma_{yz} \\ \gamma_{zx} \end{array} \right\} = \begin{bmatrix} \frac{\partial}{\partial x} & 0 & 0 \\ 0 & \frac{\partial}{\partial y} & 0 \\ 0 & 0 & \frac{\partial}{\partial z} \\ \frac{\partial}{\partial y} & \frac{\partial}{\partial x} & 0 \\ 0 & \frac{\partial}{\partial z} & \frac{\partial}{\partial y} \\ \frac{\partial}{\partial z} & 0 & \frac{\partial}{\partial x} \end{bmatrix} \left\{ \begin{array}{l} u \\ v \\ w \end{array} \right\} \quad (7.81)$$

$$\{\varepsilon\} = [B]\{d\} \quad (7.82)$$

$$\{\delta e\} = [B]\{\delta d\} \quad (7.83)$$

Now, we will consider the entries term-by term in Equation (7.78) and further simplify. We have the first term, which is essentially the inertial part of the governing equation. If we substitute Equation (7.79), it becomes:

$$\begin{aligned} \int_V \rho \{\delta d\}^T \{\ddot{d}\} dV &= \int_V \rho \{\delta u_e\}^T [N]^T [N] \{\ddot{u}_e\} dV \\ &= \{\delta u_e\}^T \left[\int_V \rho [N]^T [N] dV \right] \{\ddot{u}_e\} \\ &= \{\delta u_e\}^T [m] \{\ddot{u}_e\} \end{aligned} \quad (7.84)$$

The term inside the brackets is called the *element mass matrix*. The mass matrix obtained from the above form is called the *consistent mass matrix*, although other forms of mass matrix exist. Next, we consider the second term involving strains in Equation (7.78). Using Equation (7.79) and (7.83), the second term can be written as:

$$\begin{aligned} \int_V \{\delta e\}^T [C] \{e\} dV &= \int_V \{\delta u_e\}^T [B]^T [C] [B] \{u_e\} dV \\ &= \{\delta u_e\}^T \left[\int_V [B]^T [C] [B] dV \right] \{u_e\} \\ &= \{\delta u_e\}^T [k] \{u_e\} \end{aligned} \quad (7.85)$$

In the above equation, the term inside the bracket represents the stiffness matrix of the formulated element. The other terms in Equation (7.78) can be written similarly in terms of the nodal displacement vector and its first variation, using Equations (7.79) and (7.80). Now, the term due to body force can be written as:

$$\begin{aligned} \int_V \{\delta d\}^T \{B\} dV &= \int_V \{\delta u_e\}^T [N]^T \{B\} dV = \{\delta u_e\}^T \\ &\times \left[\int_V [N]^T \{B\} dV \right] = \{\delta u_e\}^T \{f_B\} \end{aligned} \quad (7.86)$$

The bracketed term represents the body force vector acting on the element. Similarly, we can write the surface forces as:

$$\int_S \{\delta d\}^T \{t_s\} dS = \{\delta u\}^T \{f_s\}, \quad \{f_s\} = \int_S [N]^T \{t_s\} dS \quad (7.87)$$

Finally, the damping force vector, assuming viscous-type damping, can be written as:

$$\begin{aligned} - \int_V \{\delta d\}^T \eta \{\dot{d}\} dV &= -\{\delta u_e\}^T \left[\int_V \eta [N]^T [N] dV \right] \{\dot{u}_e\} \\ &= -\{\delta u_e\}^T [c] \{\dot{u}_e\} \end{aligned} \quad (7.88)$$

Matrix $[c]$ is the consistent damping matrix. This form is seldom used in actual analysis. There are different ways of treating damping, which is explained in the latter part of this chapter. Now, using Equations (7.84)–(7.88) in Equation (7.78), we have:

$$\int_{t_1}^{t_2} \{\delta u_e\}^T [[m]\{\ddot{u}_e\} + [c]\{\dot{u}_e\} + [k]\{u_e\} - \{f_B\} - \{f_s\}] dt = 0$$

Since the first variation of the displacement vector is arbitrary, we have:

$$[m]\{\ddot{u}_e\} + [c]\{\dot{u}_e\} + [k]\{u_e\} = \{R\} \quad (7.89)$$

Equation (7.89) is the discretized governing equation of motion that we need to solve through the finite element technique. Here, $\{R\}$ is the combined force vector due to body, surface and concentrated forces. Note that the

above equation is a highly coupled second-order linear differential equation. If the inertial and the damping forces are absent, the above equation reduces to a set of simultaneous equations, which are solved to obtain the static behavior. The sizes of the matrices $[m]$, $[k]$ and $[c]$ are equal to the number of degrees of freedom an element can support. All of these matrices are generated for each element and assembled to obtain the global mass matrix $[M]$, stiffness matrix $[K]$ and damping matrix $[C]$, respectively. Before assembling these matrices, displacement boundary conditions are enforced. All of these matrices are symmetric and banded in nature. The bandwidth is dictated by the node numbering of the mesh. This is determined by taking the highest difference in node numbers multiplied by the number of degrees of freedom supported by each node. The present formulation requires modification to handle curved boundaries. Such a formulation is called the *Isoparametric Formulation*.

7.6.3 Isoparametric formulation and numerical integration

Until now we have dealt only with finite elements having straight edges. In practical structures, the edges are always curved and to model such curved edges with straight-edged elements will result in an enormous system size for the problem. In addition, in many practical situations, it is not always required to have a uniform mesh density throughout the problem domain. Meshes are always graded from fine (in the region of a high-stress gradient) to coarse (in the case of a uniform stress field). These curved elements enable us to grade the mesh effectively. With the availability of curved quadrilateral, triangular and wedge elements, it is now possible to model the 3-D geometry of any complex shape.

The elements with curved boundaries are mapped to the straight boundaries through a coordinate transformation which involves mapping functions, which are functions of the mapped coordinates. This mapping is established by expressing the coordinate variation as a polynomial of a certain order with the order of the polynomial decided upon by the number of nodes involved in the mapping. Since we are working with a straight-edged mapped domain, the displacement should also be expressed as a polynomial of a certain order in the mapped coordinates. In this case, the order of the polynomial is dependent upon the number of degrees of freedom that an element can support. Thus, we have two transformations, one involving the coordinates and the other involving the displacements. If the coordinate transformation is of a lower order than the displacement

transformation, then we call such a transformation as *sub-parametric transformation*. That is, if an element has n nodes, while all of the n nodes participate in the displacement transformation, only a few nodes will participate in the coordinate transformation. If the coordinate transformation is of a higher-order compared to the displacement transformation, such a transformation is called a *super-parametric transformation*. In this case, only a small set of nodes will participate in the displacement transformation, while all of the nodes will participate in the coordinate transformation. The most important transformation as regards the FE formulation is when both the displacement and coordinate transformations are of the same order. That is, all of the nodes participate in both transformations. Such a transformation is called an *iso-parametric transformation*. The concept of mapping is shown for 1-D and 2-D elements in Figure 7.8. Next, the concept of isoparametric formulation is demonstrated for 1-D and 2-D elements and the stiffness matrices for some simple elements are derived by using this concept.

7.6.3.1 One-dimensional isoparametric rod element

Figure 7.8(a) shows the 1-D rod element in the original rectangular coordinate system and the mapped coordinate system, with the 1-D mapped coordinate ξ . Note that at the two extreme ends of the rod, where the axial degrees of freedom u_1 and u_2 are defined, the mapped coordinates $\xi = -1$ and $+1$, respectively. We now assume the displacement variation of the rod in the mapped coordinates as:

$$u(\xi) = a_0 + a_1 \xi \quad (7.90)$$

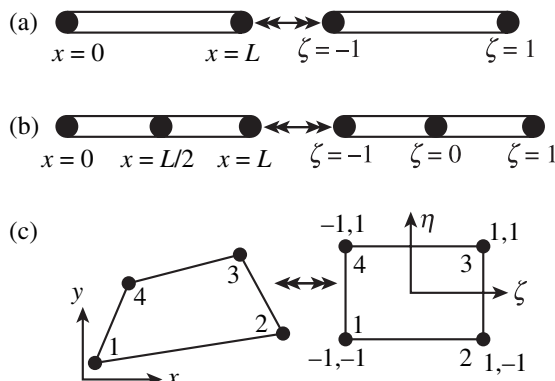


Figure 7.8 Various isoparametric finite elements: (a) linear rod; (b) quadratic rod; (c) quadrilateral.

We now substitute $u(\xi = -1) = u_1$ and $u(\xi = 1) = u_2$ and eliminating the constants, we can write the displacement field in the mapped coordinates as:

$$\begin{aligned} u(\xi) &= \left(\frac{1 - \xi}{2} \right) u_1 + \left(\frac{1 + \xi}{2} \right) u_2 \\ &= \left[\frac{1 - \xi}{2} \quad \frac{1 + \xi}{2} \right] \begin{Bmatrix} u_1 \\ u_2 \end{Bmatrix} = [N(\xi)] \{u_e\} \quad (7.91) \end{aligned}$$

We also assume that the rectangular x -coordinate to vary with respect to the mapped coordinate ξ in the same manner as displacement, that is:

$$x = \left[\frac{1 - \xi}{2} \quad \frac{1 + \xi}{2} \right] \begin{Bmatrix} x_1 \\ x_2 \end{Bmatrix} = [N(\xi)] \{x_e\} \quad (7.92)$$

In the above equation, x_1 and x_2 are the coordinates of the actual element in the rectangular x -coordinate system. We can see that there is a ‘one-to-one correspondence’ of the coordinates in the original and mapped systems. The derivation of the stiffness matrix requires computation of the strain–displacement matrix $[B]$, which requires evaluation of the derivatives of the shape functions with respect to the original x -coordinate system. In the case of a rod, there is only axial strain and hence the $[B]$ matrix becomes:

$$[B] = \left[\frac{dN_1}{dx} \quad \frac{dN_2}{dx} \right] \quad (7.93)$$

However, one coordinate system can be mapped to the different coordinate system by using a *Jacobian*.

That is, by invoking the chain rule of the differentiation, we have:

$$\frac{dN_i}{dx} = \frac{dN_i}{d\xi} \frac{d\xi}{dx} \quad i = 1, 2 \quad (7.94)$$

From Equation (7.92), we have:

$$\begin{aligned} x &= \frac{1 - \xi}{2} x_1 + \frac{1 + \xi}{2} x_2 \\ \frac{dx}{d\xi} &= \frac{(x_2 - x_1)}{2} = \frac{L}{2} = J \quad (7.95) \end{aligned}$$

$$\frac{d\xi}{dx} = \frac{2}{L} = \frac{1}{J}, \quad dx = J d\xi \quad (7.96)$$

Using Equation (7.96) in Equation (7.94), we get:

$$\frac{dN_i}{dx} = \frac{dN_i}{d\xi} \frac{1}{J} = \frac{dN_i}{d\xi} \frac{2}{L} \quad (7.97)$$

Substituting the shape functions in the above equation, the shape function derivatives with respect to the mapped coordinates and hence the $[B]$ matrix become:

$$\frac{dN_1}{d\xi} = \frac{-1}{2}, \quad \frac{dN_2}{d\xi} = \frac{1}{2}, \quad [B] = \begin{bmatrix} -\frac{1}{2} & \frac{1}{2} \end{bmatrix} \quad (7.98)$$

In the case of a rod, there is only axial stress acting and as a result $[C]$, the material matrix in Equation (7.85) for evaluating the stiffness matrix, will have only E , the Young's modulus of the material. The stiffness matrix for a rod is given by:

$$[K] = \int_V [B]^T [C] [B] dV = \int_0^L \int_A [B]^T E [B] dA dx = \int_{-1}^1 [B]^T EA [B] J d\xi \quad (7.99)$$

Substituting Equations (7.95) and (7.98) into the above equation for the Jacobian and $[B]$ matrix, we get the stiffness matrix for a rod as:

$$[K] = \frac{EA}{L} \begin{bmatrix} 1 & -1 \\ -1 & 1 \end{bmatrix} \quad (7.100)$$

The reader can check that one can directly obtain the above result without going through the iso-parametric formulation by directly substituting the shape functions from Equation (7.58) into Equation (7.85) and performing a direct integration. For lower-order and straight-edged elements, the Jacobian is constant and not a function of the mapped coordinate. For complex geometries and higher-order elements, the Jacobian is always a function of the mapped coordinate. In such cases, integration of the expression for computing the stiffness matrix will involve rational polynomials. To demonstrate this, we will consider a higher-order rod having three degrees of freedom, all being axial, as shown in Figure 7.8(b). The displacement variation for this element in the mapped coordinate is given by:

$$u(\xi) = a_0 + a_1 \xi + a_2 \xi^2 \quad (7.101)$$

Following the same procedure as was done for the previous case, we first substitute $u(\xi = -1) = u_1$, $u(\xi = 0) = u_2$ and $u(\xi = 1) = u_3$ into Equation (7.101) to get the following three shape functions corresponding to the three degrees of freedom:

$$N_1 = \frac{\xi(-1+\xi)}{2}, \quad N_2 = (1-\xi^2), \quad N_3 = \frac{\xi(1+\xi)}{2} \quad (7.102)$$

Next, the Jacobian requires to be computed, for which we assume the coordinate transformation as:

$$x = \frac{\xi(-1+\xi)}{2} x_1 + (1-\xi^2) x_2 + \frac{\xi(1+\xi)}{2} x_3 \quad (7.103)$$

In the above expression x_1 , x_2 and x_3 are the coordinates of the three nodes of the element in the original coordinate system. Taking the derivative with respect to the mapped coordinate, we get:

$$\frac{dx}{d\xi} = \frac{(2\xi-1)}{2} x_1 - 2\xi x_2 + \frac{(2\xi+1)}{2} x_3 = J, \quad dx = J d\xi \quad (7.104)$$

Unlike in the two-noded rod case, the Jacobian in the higher-order rod case is a function of the mapped coordinate and its value changes as we move along the bar. If the coordinate x_2 coincides with the mid-point of the rod, the value of the Jacobian becomes $L/2$. The $[B]$ matrix in this case becomes:

$$[B] = \frac{1}{J} \left[\left(\frac{2\xi-1}{2} \right) - 2\xi \left(\frac{2\xi+1}{2} \right) \right] \quad (7.105)$$

The $[B]$ matrix, unlike the two-noded rod, is a function of the mapped coordinate. Hence, the stiffness matrix, given in Equation (7.99) cannot be integrated in the closed form. One can see that it involves integration of rational polynomials. Hence, one has to resort to numerical integration. The most popular numerical integration scheme is through the *Gauss Quadrature*, which is explained a little later in this section.

7.6.3.2 Two-dimensional plane isoparametric element formulation

The original and mapped representations of an isoparametric quadrilateral is shown in Figure 7.8(c). Here, $x-y$ is the original coordinate system and $\xi-\eta$ is the mapped coordinate system. Each of the mapped coordinates range from $+1$ to -1 . This element has four nodes and each node can support two degrees of freedom. In all, the element has eight degrees of freedom and the resulting stiffness matrix would be of size 8×8 . The displacement variation in the two coordinate directions (u along the x -direction and v along the y -direction) is given in terms of the mapped coordinates as:

$$u(\xi, \eta) = a_0 + a_1 \xi + a_2 \eta + a_3 \xi \eta \quad (7.106)$$

$$v(\xi, \eta) = b_0 + b_1 \xi + b_2 \eta + b_3 \xi \eta \quad (7.106)$$

Substituting the mapped coordinates at the four nodes would result in determination of the shape functions. The displacement field, as well as the shape functions, are given by:

$$\begin{Bmatrix} u \\ v \end{Bmatrix} = \begin{bmatrix} N_1 & 0 & N_2 & 0 & N_3 & 0 & N_4 & 0 \\ 0 & N_1 & 0 & N_2 & 0 & N_3 & 0 & N_4 \end{bmatrix} \{u_e\} = [N] \{u_e\}$$

(7.107)

$$\begin{aligned} \{u_e\} &= \{u_1 \quad v_1 \quad u_2 \quad v_2 \quad u_3 \quad v_3 \quad u_4 \quad v_4\}^T \\ N_1 &= \frac{(1-\xi)(1-\eta)}{4}, \quad N_2 = \frac{(1+\xi)(1-\eta)}{4} \\ N_3 &= \frac{(1+\xi)(1+\eta)}{4}, \quad N_4 = \frac{(1-\xi)(1+\eta)}{4} \end{aligned} \quad (7.108)$$

The coordinate transformation between the original and mapped coordinates can be similarly written as:

$$\begin{aligned} \begin{Bmatrix} x \\ y \end{Bmatrix} &= \begin{bmatrix} N_1 & 0 & N_2 & 0 & N_3 & 0 & N_4 & 0 \\ 0 & N_1 & 0 & N_2 & 0 & N_3 & 0 & N_4 \end{bmatrix} \{x_e\} \\ &= [N] \{x_e\} \\ \{x_e\} &= \{x_1 \quad y_1 \quad x_2 \quad y_2 \quad x_3 \quad y_3 \quad x_4 \quad y_4\}^T \end{aligned} \quad (7.109)$$

To compute the derivatives, we will invoke the chain rule. Noting that the original coordinates are functions of both mapped coordinates ξ and η , we have:

$$\frac{\partial}{\partial \xi} = \frac{\partial}{\partial x} \frac{\partial x}{\partial \xi} + \frac{\partial}{\partial y} \frac{\partial y}{\partial \xi}, \quad \frac{\partial}{\partial \eta} = \frac{\partial}{\partial x} \frac{\partial x}{\partial \eta} + \frac{\partial}{\partial y} \frac{\partial y}{\partial \eta}$$

or

$$\begin{Bmatrix} \frac{\partial}{\partial \xi} \\ \frac{\partial}{\partial \eta} \end{Bmatrix} = \begin{bmatrix} \frac{\partial x}{\partial \xi} & \frac{\partial y}{\partial \xi} \\ \frac{\partial x}{\partial \eta} & \frac{\partial y}{\partial \eta} \end{bmatrix} \begin{Bmatrix} \frac{\partial}{\partial x} \\ \frac{\partial}{\partial \eta} \end{Bmatrix} = [J] \begin{Bmatrix} \frac{\partial}{\partial x} \\ \frac{\partial}{\partial \eta} \end{Bmatrix} \quad (7.110)$$

The numerical value of the Jacobian depends on the size, shape and orientation of the element. In addition:

$$\begin{Bmatrix} \frac{\partial}{\partial x} \\ \frac{\partial}{\partial \eta} \end{Bmatrix} = [J]^{-1} \begin{Bmatrix} \frac{\partial}{\partial \xi} \\ \frac{\partial}{\partial \eta} \end{Bmatrix} \quad (7.111)$$

Using Equation (7.111), we can determine the derivatives required for computation of the $[B]$ matrix. Once this

is done, we can derive the stiffness matrix for a plane element as:

$$[K] = t \int_{-1}^1 \int_{-1}^1 [B]^T [C] [B] J d\xi d\eta \quad (7.112)$$

where J is the determinant of the Jacobian matrix and t is the thickness of the element. The stiffness matrix will be 8×8 . $[C]$ is the material matrix, and assuming the plane stress condition, we have:

$$[C] = \frac{E}{1-v^2} \begin{bmatrix} 1 & v & 0 \\ v & 1 & 0 \\ 0 & 0 & \frac{1-v}{2} \end{bmatrix} \quad (7.113)$$

Equation (7.112) cannot be integrated as such in the closed form. It has to be numerically integrated and for this purpose, we use the Gauss Quadrature, which is explained in the next subsection.

7.6.4 Numerical integration and Gauss quadrature

Evaluation of the stiffness and mass matrices, specifically for isoparametric elements, involves an expression such as that given in Equation (7.112), which are necessarily rational polynomials. Evaluation of these integrals in their closed forms is very difficult. One has to use a numerical integration scheme. Although there are several different numerical schemes available, the Gauss Quadrature approach (Cook *et al.* [7] and Bathe [8]) is most ideally suited for isoparametric formulation as it evaluates the value of the integral between -1 and $+1$, which is the typical range of natural coordinates in isoparametric formulation.

Consider an integral of the form:

$$I = \int_{-1}^{+1} F d\xi, \quad F = F(\xi) \quad (7.114)$$

Let $F(\xi) = a_0 + a_1 \xi$. This function requires to be integrated over the domain $-1 < \xi < 1$ with the length of the domain equal to two units. When the above expression is substituted into Equation (7.114), the exact value of the integral is $2a_0$. If the value of the integrand is evaluated at the mid-point (i.e. at $\xi = 0$) and multiplied by the length of the domain (i.e. 2), we obtain the exact value. Hence, an integral of any linear function can be

Table 7.1 Sampling points and weights for the Gauss Quadrature.

Order, <i>n</i>	Location, ξ_i	Weight, W_i
1	0	2
2	$\pm 0.57735\ 02691\ 89626$	1.0
3	$\pm 0.77459\ 66692\ 41483$	0.55555 55555 55556
	0.00000 00000 00000	0.88888 88888 88889
4	$\pm 0.86113\ 63115\ 94053$	0.34785 48451 37454
	$\pm 0.33998\ 20435\ 84856$	0.65214 51548 62546
5	$\pm 0.90617\ 98459\ 38664$	0.23692 68850 56189
	$\pm 0.53846\ 93101\ 05683$	0.47862 86704 99366
	0.00000 00000 00000	0.56888 88888 88889

evaluated in this way. This result can be generalized for a function of any order as:

$$I = \int_{-1}^{+1} F d\xi \approx W_1 F_1 + W_2 F_2 + \dots + W_n F_n \quad (7.115)$$

Hence, to obtain the approximate value of the integral I , we evaluate $F(\xi)$ at several locations ξ_i , multiply the resulting F_i with the appropriate weights W_i and add them together. The points where the integrand is evaluated are called *sampling points*. In the Gauss Quadrature, these are the points of very high accuracy, sometimes referred to as *Barlow Points*. These points are located symmetrically with respect to the center of the interval and symmetrically placed points have the same weight. The number of points required to integrate the integrand depends exactly on the degree of the highest polynomial involved in the expression. If p is the highest degree of the polynomial in the integrand, then the minimum number of points n required to integrate the integrand exactly is equal to $n = (p + 1)/2$. That is, for a polynomial of the second degree, i.e. $p = 2$, the minimum number of points required to integrate is equal to two. Table 7.1 gives the locations and weights for the Gauss Quadrature [7]. In the case of 2-D elements, the stiffness and mass matrix computation involves evaluation of the double integral of the form:

$$\begin{aligned} I &= \int_{-1}^1 \int_{-1}^1 F(\xi, \eta) d\xi d\eta = \int_{-1}^1 \left[\sum_{i=1}^N W_i F(\xi_i, \eta) \right] d\eta \\ &= \sum_{i=1}^N \sum_{j=1}^M W_i W_j F(\xi_i, \eta_j) \end{aligned} \quad (7.116)$$

Here, N and M are the number of sampling points used in the ξ and η directions. Similarly, we can extend this to three dimensions. The sampling points of the Gauss Quadrature are located such that the stresses, which are less accurate than the displacements in the FE method, at the Gauss points are very accurate when compared to other points [9].

Numerical integration for the isoparametric triangle is also possible by using the Gauss Quadrature. However, the Gauss points and the weights are quite different. These are given in Cook *et al.* [7]. The numerical integration of the type given in Equation (7.115) is given by:

$$I = \frac{1}{2} \sum_{i=1}^n W_i F(\alpha_i, \beta_i, \gamma_i)$$

where, α_i , β_i and γ_i are the locations of the Gauss points in area coordinates.

7.6.5 Mass and damping matrix formulation

The expression for the *consistent mass matrix* is represented by Equation (7.84), which is given by:

$$[M] = \int_V \rho [N]^T [N] dV$$

where ρ is the density and $[N]$ is the shape-function matrix. This matrix is a fully populated and banded matrix, whose bandwidth is equal to that of the stiffness matrix. For a rod element of length L , area of cross-section A and density ρ , the shape function is given by Equation (7.58). Using this shape function, the mass matrix becomes:

$$[M] = \int_0^L \int_A \rho \begin{bmatrix} 1-x \\ x \\ \bar{L} \end{bmatrix} \begin{bmatrix} 1-x & x \\ \bar{L} & \bar{L} \end{bmatrix} dx = \frac{\rho AL}{6} \begin{bmatrix} 2 & 1 \\ 1 & 2 \end{bmatrix} \quad (7.117)$$

For the case of a beam of length L and area of cross-section A , the four shape functions are given by Equation (7.61). Substituting these into the mass matrix expression and integrating, we get:

$$[M] = \frac{\rho AL}{420} \begin{bmatrix} 156 & 22L & 54 & -13L \\ & 4L^2 & 13L & -3L \\ \text{SYM} & & 156 & -22L \\ & & & 4L^2 \end{bmatrix} \quad (7.118)$$

In both of these cases, we find that the matrix is symmetric and positive definite.

There are alternate ways to formulate the mass matrix. That is, the masses can be ‘lumped’ corresponding to the main degrees of freedom, which make the mass matrix diagonal. The diagonal mass matrix will result in a very small storage requirement and hence enables faster solution of the dynamic equation of motion. There are certain problems, such as wave propagation, where a lumped mass is preferred to a consistent mass. There are three different methods of lumping of the mass reported in the literature, as follows:

- Adhoc lumping
- HRZ lumping
- Optimal lumping

Adhoc lumping is the simplest way of lumping the mass. The total mass of the structure is computed and is distributed evenly among all of the translational degrees of freedom. If the element has rotational degrees of freedom, then the mass moment of inertia of the element is computed and distributed evenly among the rotational degrees of freedom.

Let us again consider a two-noded rod element of length L , density ρ and area of cross-section A . The total mass of the element is ρAL . If this mass is equally distributed between the two axial degrees of freedom, the lumped mass can be written as:

$$[M]_{\text{lumped}} = \frac{\rho AL}{2} \begin{bmatrix} 1 & 0 \\ 0 & 1 \end{bmatrix}$$

Now consider a three-noded quadratic bar having the same elemental properties as the two-noded bar. The total mass is again equal to ρAL , which can be distributed equally among the three axial degrees of freedom. The lumped mass matrix then becomes:

$$[M]_{\text{lumped}} = \frac{\rho AL}{3} \begin{bmatrix} 1 & 0 & 0 \\ 0 & 1 & 0 \\ 0 & 0 & 1 \end{bmatrix} \quad (7.119)$$

Based on experience, the above matrix is expected to give ‘terrible’ results. On the other hand, if the three-noded bar is split into two halves having mass $\rho AL/2$, then the middle node will get the mass contribution from both halves and the mass matrix becomes:

$$[M]_{\text{lumped}} = \frac{\rho AL}{4} \begin{bmatrix} 1 & 0 & 0 \\ 0 & 2 & 0 \\ 0 & 0 & 1 \end{bmatrix} \quad (7.120)$$

The above mass representation gives much better results as there is a more even distribution of mass. Hence, in adhoc mass lumping, no fixed rules are specified for the lumping procedure. It is purely left to the judgment of the analyst to decide on how the masses should be lumped.

The lumped mass for a beam of length L , density ρ and area of cross-section A , which has four degrees of freedom, including two rotational degrees of freedom, is derived as follows. The total mass m is again equal to ρAL , which can be distributed equally between the two transverse degrees of freedom. The mass corresponding to the rotational degrees of freedom is derived as follows. The mass moment of inertia of a bar is given by $mL^2/3$, where m is the mass of the bar. In our case, for a better approximation, we split the beam into two halves of length $L/2$ and the mass moment of inertia of each half is computed and lumped onto the respective rotational degrees of freedom. That is, the mass moment of inertia is equal to $(1/3)(m/2)(L/2)^2 = \rho AL^3/24$. Hence, the lumped mass for the beam becomes:

$$[M]_{\text{lumped}} = \frac{\rho AL}{420} \begin{bmatrix} \alpha & 0 & 0 & 0 \\ 0 & \beta L^2 & 0 & 0 \\ 0 & 0 & \alpha & 0 \\ 0 & 0 & 0 & \beta L^2 \end{bmatrix},$$

$$\alpha = 210, \quad \beta = 17.5 \quad (7.121)$$

In the above form, one can compare Equation (7.121) with Equation (7.118) and establish the correlation between two different mass matrices.

Hinton *et al.* [10] derived a new lumping scheme that uses the consistent mass matrix. This lumping scheme is called *HRZ lumping*, named after the three authors. The diagonal coefficients are extracted from the consistent mass matrix as follows. The consistent mass matrix is first obtained. If m is the total mass and N_i is the shape function of the i th degree of freedom, then the diagonal coefficients of the mass matrix are given by:

$$M_{ii} = \frac{m}{S} \int_V \rho N_i^2 dV, \quad S = \sum_{n=1}^N (M_{nn})_{\text{consistent}} \quad (7.122)$$

Let us consider the same example of a two-noded bar. The total mass of the bar is $m = \rho AL$. The consistent mass matrix for this linear bar is given by Equation (7.117). We have S in Equation (7.122) as equal to $(2/3)\rho AL$. The shape functions N_1 and N_2 are given in Equation (7.58). Using this and the values of S and m ,

we can write the lumped mass matrix through HRZ lumping as:

$$[M]_{\text{HRZ}} = \frac{\rho AL}{2} \begin{bmatrix} 1 & 0 \\ 0 & 1 \end{bmatrix} \quad (7.123)$$

This matrix is the same as the one derived using adhoc lumping. The same can be established for the beam and 2-D isoparametric elements. In the case of beams, the consistent mass matrix is given by Equation (7.118). For this case, we have two value of S , one for the translational degrees of freedom and one for the rotational degrees of freedom. For the translational degrees of freedom, $S = (\rho AL/420)(156 + 156) = (26/35)\rho AL$ and for the rotational degrees of freedom, $S = (\rho AL/420)(4L^2 + 4L^2) = (2L^2/105)\rho AL$. Using this and the shape functions given in Equation (7.61), we get:

$$[M]_{\text{HRZ}} = \frac{\rho AL}{78} \begin{bmatrix} 39 & 0 & 0 & 0 \\ 0 & L^2 & 0 & 0 \\ 0 & 0 & 39 & 0 \\ 0 & 0 & 0 & L^2 \end{bmatrix} \quad (7.124)$$

Comparing this with the mass matrix obtained by adhoc lumping given in Equation (7.121), the translational degrees of freedom have a similar mass distribution, while the rotational degrees of freedom have smaller values. Similar mass matrices for eight- and nine-noded isoparametric 2-D elements can be obtained. These are shown in Figure 7.9.

HRZ lumping gives very good results for lower-order elements and sometimes this lumping scheme is better than the consistent formulation, although it is less accurate for higher-order elements.

Optimal lumping was first introduced by Malkus and Plesha [11]. This uses a numerical integration scheme to obtain the lumped mass matrix. That is, it uses the property of the shape function which takes the value of unity at the node where it is evaluated. Hence, the scheme

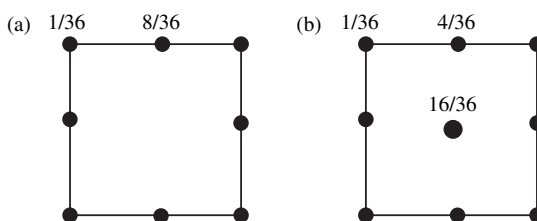


Figure 7.9 HRZ lumping for 2-D elements: (a) eight-noded; (b) nine-noded.

requires an integration scheme that uses the nodes as the sampling points. This process eliminates the off-diagonal terms in the mass matrix. The *Newton–Coates method*, which is the ‘one-third Simpsons’s rule’, provides for integrating numerically with nodal points as the sampling points. The 2-D version of the Newton–Coates method is the *Labatto Integration rule*. The number of sampling points required is determined by the highest order of the polynomial involved in computation of the mass matrix and in general is given by:

$$n = 2(p - m) \quad (7.125)$$

Here, p is the highest order of the polynomial, n is the number of sampling points required for numerical integration and m is the highest order of the derivative appearing in the energy functional. For a plane-stress problem, $m = 1$, while for bending problems, $m = 2$.

Let us consider a three-noded isoparametric quadratic bar element of length L and having three axial degrees of freedom corresponding to the three nodes. The isoparametric shape functions are given in Equation (7.102). In this case, $p = 2$ and $m = 1$ and hence the minimum number of points required according to Equation (7.125) is 2. The Newton–Coates formula for integrating the function $f(x)$ in the interval a to b is given by:

$$\int_a^b f(x)dx = (b - a) \left[\frac{1}{6}f(x = a) + \frac{4}{6}f\left(x = \frac{a+b}{2}\right) + \frac{1}{6}f(x = b) \right] \quad (7.126)$$

Now, the mass matrix of the bar in the indicial notation can be written in terms of the shape functions as:

$$M_{ij} = \int_{-1}^1 \rho AN_i N_j J d\xi \quad (7.127)$$

Here J is the Jacobian and its value is equal to $L/2$ if the middle node is exactly at the center. Now, using the Newton–Coates formula and noting that $b - a = 2$, we get:

$$M_{ij} = \rho AL \left[\begin{aligned} & \frac{1}{6}N_i(\xi = -1)N_j(\xi = -1) + \frac{4}{6}N_i(\xi = 0)N_j(\xi = 0) \\ & + \frac{1}{6}N_i(\xi = 1)N_j(\xi = 1) \end{aligned} \right] \quad (7.128)$$

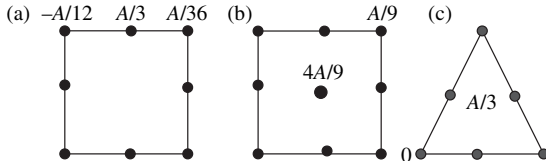


Figure 7.10 Optimal mass lumping for: (a) an eight-noded element; (b) a nine-noded element; (c) a six-noded triangular element (A , area of the element).

Substituting the shape functions and evaluating, we get:

$$[M]_{\text{optimal}} = \frac{\rho AL}{6} \begin{bmatrix} 1 & 0 & 0 \\ 0 & 1 & 0 \\ 0 & 0 & 4 \end{bmatrix} \quad (7.129)$$

One can get the same results if we use HRZ lumping. One can similarly obtain the optimally lumped mass matrix for 2-D triangular and quadrilateral elements, which are shown in Figure 7.10. From this figure, we see that some mass coefficients are zero and can even have negative values. This poses a problem in the solution of dynamic equations. Some special solution schemes are required for the purpose.

Here, we state the general guidelines for the choice of mass matrix. A consistent mass matrix is generally used for flexural problems and in general gives poor results when the mode shape spans more than four elements. This is generally not advised for wave-propagation problems. The computed natural frequencies required for the solution of dynamic equations are always upper bound and these are expensive to store and operate as they are fully populated. However, these are most ideally suited for higher-order elements.

A lumped mass matrix is extensively used for wave propagation and highly transient dynamics problems as it gives very few spurious oscillations. It also gives good results for lower-order elements. However, for higher-order elements, one can use an optimally lumped matrix.

Damping is a very complex phenomenon in structures that is difficult to ascertain exactly. Some of the sources of damping are the material hysteresis and friction in joints. The damping matrix derived from the equation of motion (Equation (7.88)) is seldom used as it is difficult to measure the damping parameter η . The most common method of deriving the damping matrix is known as *Rayleigh's proportional damping*, where the damping matrix is used as a combination of stiffness and mass matrix as:

$$[C] = \alpha[K] + \beta[M] \quad (7.130)$$

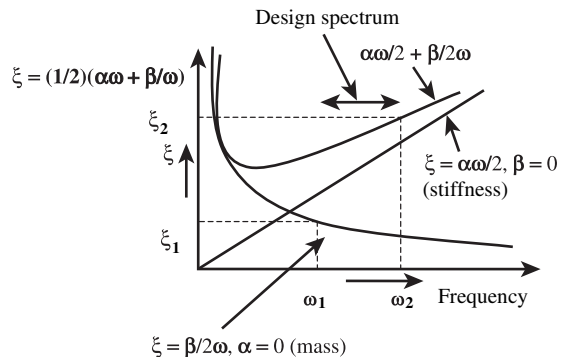


Figure 7.11 Damping behavior as a function of frequency.

where α and β are the stiffness and mass proportional damping coefficients to be determined experimentally. They can be measured by determining the damping ratio ξ from the single-degree-of-freedom model. The damping ratio and the stiffness and mass proportional parameters are related by the equation:

$$\xi = \frac{1}{2} \left(\alpha\omega + \frac{\beta}{\omega} \right) \quad (7.131)$$

A plot of frequency ω with the damping ratio ξ is shown in Figure 7.11. By measuring the damping ratio at two different frequencies, one can find the stiffness and mass proportional damping coefficients. The above damping representation has a great advantage in uncoupling the governing equation for solution of the dynamic equation in the modal domain.

7.7 COMPUTATIONAL ASPECTS IN THE FINITE ELEMENT METHOD

The efficiency of the FE solution scheme is judged by the speed with which the solution can be obtained for a large complex problem. The speed of the FE solution depends on various factors, such as mesh sizes, node and element numbering, type of storage of matrices and the type of 'solvers' used in the solution. This section briefly outlines the various methods available to reduce the system size and the various solutions techniques for static and dynamic problems, without going into much detail. The interested reader is encouraged to refer to various textbooks available on the FE method [7,8], which dwell on this aspect in greater detail.

7.7.1 Factors governing the speed of the FE solution

The FE discretization process requires the solution of a set of simultaneous equations of the form $[K]\{d\} = \{F\}$ in the case of static analysis and a set of coupled second-order ordinary differential equations of the form given in Equation (7.89) in the case of dynamic analysis. For a given mesh, the speed of solution depends upon the following:

- Node and element numbering of the mesh
- Storage of stiffness, mass and damping matrices
- Type of ‘solver’ used
- Type of assignment of arrays in the main FE program

All of the matrices in the FE solution process are symmetric and banded. Hence, it is not necessary to store only the upper half of these matrices. Even in this upper half, there are many zeros, which need not be stored. For example, consider the mesh shown in Figure 7.12(a). Each node here supports two degrees of freedom. Note that the nodes are numbered here along the shorter direction. The stiffness matrix is 12×12 and the bandwidth $B = 8$. The bandwidth is evaluated by using the expression:

$$B = (ND + 1) \times NDOF \quad (7.132)$$

In the above expression, ND is the maximum difference in the node numbers in a given FE mesh and $NDOF$ is the number of degree of freedom that an element can support. That is, for the mesh given in Figure 7.12(a), $ND = 3$, $NDOF = 2$ and hence, $B = 8$.

Now let us consider the mesh shown in Figure 7.12(b), where the nodes are numbered along the longer direction. The stiffness matrix will again be 12×12 and the maximum node number difference $ND = 4$. Hence, the bandwidth B is 10. Therefore, the bandwidth is dependent on the way we number the nodes. If the bandwidth is larger, then we need to store more elements of the stiffness matrix.

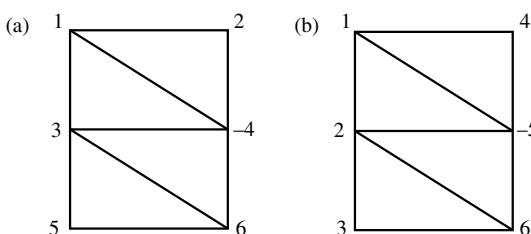


Figure 7.12 A single mesh with two different node numbering(s).

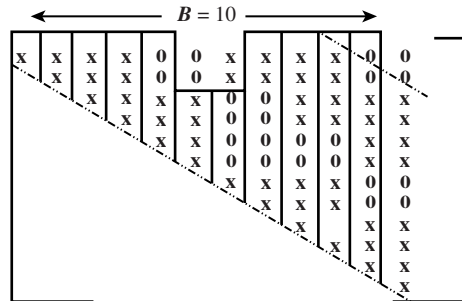


Figure 7.13 Illustration of the skyline storage system.

The following procedure is normally followed while storing the banded matrices. The diagonal entries become the first column of the banded matrix. The next line parallel to the diagonal becomes the second column and so on. In this way, we simplify the storage procedure. Even if the problem is large and the bandwidth is small, the time taken to solve the system of the equation would be of the order NB^2 compared to N^3 of the full system, where N is the size of the matrix and B is the bandwidth.

Alternatively, the matrix can be stored even more efficiently by not storing all of the zeros contained within the bandwidth. Consider the stiffness matrix of the mesh shown in Figure 7.12(b). The stiffness matrix can be stored as shown in Figure 7.13. This storage resembles that of a skyscraper in a city and hence it is called the *skyline storage* scheme. In this storage, the column heights are stored, from which the address of each element in the stiffness matrix can be found. By this approach, many zeros contained within the bandwidth need not be stored.

The type of storage scheme employed is also dependent upon the FE ‘solvers’ used for obtaining the solution. If one uses the Gauss elimination or Cholesky’s decomposition method of solution, it is preferable to use the banded /skyline storage scheme. On the other hand, if one chooses the Frontal method of solution, then the element system matrices need not be assembled and stored to get the global matrices. Instead, the element-wise operation is performed to eliminate those degrees of freedom that do not participate further in the solution process. If one uses the Frontal solution technique, then the way the nodes are numbered is not significant. It is the element numbering that is very important.

The speed of the solution is greatly influenced by the memory allocation of various matrices such as the stiffness, mass and damping matrices in the main program and the way these matrices are accessed by the program.

It is prudent to have single dimension arrays and memory pointers to access the elements of these matrices. More details of the programming part can be obtained from Bathe [12] and Hinton and Owen [13].

7.7.2 Equation solution in static analysis

In the static analysis, we are looking for the solution $\{d\}$ in the equation $[K]\{d\} = \{F\}$, where $[K]$ is the assembled stiffness matrix and $\{F\}$ is the assembled force vector. Although there are many methods of equation solving, there are only a few methods that can be readily adapted under an FE environment. Here, we briefly discuss four such methods.

One of the simplest methods of solving the FE static equation is the *Gauss Elimination Method*. Here, the first equation is considered and the displacement d_1 is then expressed in terms of the others. This involves dividing all of the elements in the first row by its ‘pivot’, that is, K_{11} , which make the diagonal element equal to one. Then, matrix operations are made to make the off-diagonal terms equal to zero. This process is done for all other degrees of freedom. Finally, the original matrix is reduced to the upper diagonal form with all of the diagonal entries equal to one. This process is called *forward reduction*. In this process, the $\{F\}$ vector gets modified. The last equation in this form will be only an algebraic equation containing only the last degree of freedom (n th degree of freedom), which is solved. This is then ‘back-substituted’ in the $(n - 1)$ th equation to get d_{n-1} . This process is continued until all of the degrees of freedom are solved. This process is called *back-substitution*. No search of the pivot is made as it is assumed that it is always large when compared to off-diagonal elements. This is always the case unless the structure is unstable. In this process, each elimination frees a degree of freedom or releases a constraint. The numerical value of the diagonal coefficients continues to decrease but remain positive at all stages of forward reduction.

In the Choleski decomposition method, the stiffness matrix is reduced to the following form:

$$[K] = [U]^T [U] \quad (7.133)$$

where $[U]$ is the upper diagonal matrix. Such decomposition is possible for all square matrices, which are symmetric. That is, we need to solve the equation:

$$[U]^T [U]\{d\} = \{F\} \quad (7.134)$$

Here, we designate $[U]\{d\} = \{y\}$. This is substituted in the above equation and we solve first the equation $[U]^T\{y\} = \{F\}$ for obtaining the vector $\{y\}$ through forward substitution. Once the $\{y\}$ is solved, the actual displacement vector $\{d\}$ is obtained by solving $[U]\{d\} = \{y\}$ through back-substitution. The elements of the matrix U_{ij} are obtained from the stiffness matrix $[K]$ using the following algorithm:

$$U_{ij} = 0, \quad \text{for } i > j \quad (\text{upper triangular form})$$

$$U_{11} = \sqrt{K_{11}}, \quad U_{1j} = \frac{K_{1j}}{U_{11}}$$

$$U_{ii} = \left(K_{ii} - \sum_{k=1}^{i-1} U_{ki}^2 \right)^{0.5} \quad (\text{for } i > 1)$$

$$U_{ij} = \frac{\left(K_{ij} - \sum_{k=1}^{i-1} U_{ki} U_{kj} \right)}{U_{ii}} \quad (\text{for } i > 1 \quad j > 1)$$

The Gauss and Choleski algorithms have same computational efficiency for a full matrix. However, for a ‘sparse’ matrix, their efficiencies are different. Gauss elimination is row-oriented for a banded matrix, while the Choleski method is column-oriented. One of the disadvantages of the Choleski’s method is that it cannot handle indefinite matrices as in the case of mixed finite elements.

The other important solver that is extensively used in the FE solution process is the *wave front or frontal solver*. In this method, assembly of FE equations alternates the FE solution. The details of this method can be found in Hinton and Owen [13] and Irons [14]. As mentioned earlier, this method is driven by element numbering. First, the equations associated with the first element are reduced by using Gauss elimination. Next, the second element number makes its contribution to the stiffness matrix. Those degrees of freedom that are common to elements one and two are reduced. The next reduction awaits further contribution to the partially formed stiffness matrix. The assembly-solution process can be viewed as a “wave” that sweeps over the structure. Proper element numbering will increase the efficiency of the method as the processing of the degrees of freedom proceeds in element-number order. This method requires little main storage but requires extensive bookkeeping of the data.

More recently, *iterative solvers*, such as the *Preconditioned Conjugate Gradient* (PCG) method or *GMRES* method are extensively used. These methods are not sensitive to either node or element numbering. They are based on an initial ‘guess’ and the residue of the governing

equation is obtained and the iteration continued until the solution converges. These methods are dealt with in great detail in Kane [15].

7.7.3 Equation solution in dynamic analysis

The governing partial differential equation of a dynamic structural system reduces to a coupled set of second-order ordinary differential equations on the application of FE discretization, which is given by $[M]\{\ddot{d}\} + [D]\{\dot{d}\} + [K]\{d\} = \{R\}$. This equation requires to be solved to obtain the dynamic response to the time-dependent input. The following are two different and distinct methods of obtaining the response:

- Modal method
- Direct time integration

As before, only a short introduction to these methods is given here. Readers can obtain further details from many classic FE textbooks and journal papers available in the literature.

7.7.3.1 Modal method

In this method, first the undamped free-vibration problem is solved, which is an eigenvalue problem given by:

$$[K]\{d\} = \omega^2[M]\{d\} \quad (7.135)$$

Here, ω_i^2 is the i th eigenvalue, which happens to be the natural frequency of the i th degree of freedom of the system and $\{d\}_i$ is the eigenvector or mode shape of the i th degree of freedom. There are different eigenvalue extraction schemes and all of these are necessarily iterative. The most commonly used methods of eigenvalue extraction are as follows:

- Jacobi's method
- Subspace iteration method
- Lanchoz's method
- Determinant search method
- Inverse iteration method
- Forward iteration method

These methods are explained very briefly here.

Jacobi's method uses a set of transformations to reduce both the stiffness and mass matrix into a diagonal form. In this form, the eigenvalues are given by $\omega^2 = K_{ii}^r/M_{ii}^r$, where the r superscript is used to denote the reduced or transformed stiffness or mass matrices. This method

computes all of the eigenvalues at a time and hence is a very costly and time-consuming process. In conventional dynamic analysis, all of the eigenmodes are seldom computed. Hence, this method is limited to problems of small system size.

Subspace iteration is the most famous eigenvalue/vector extraction technique which is extensively used in many general-purpose FE software. Here, the property of orthogonality of the modes is used to reduce the size of matrices from $n \times n$ to $m \times m$, where $m \ll n$. On this reduced set of matrices, Jacobi's method is used to compute the eigenvalues/vectors.

Lanchoz's method is also a powerful technique, which uses a set of transformations to reduce the stiffness and consistent matrices into tridiagonal form using suitable transformations. The extraction of eigenvalue for tridiagonal matrices is very fast and well-established. This method has some in-built parallelism and is hence extensively used along with many parallel FE codes.

A determinant of the matrix $[[K] - \omega^2[M]]$ will give a polynomial of order n , whose solution will give the eigenvalues of the problem. Since the general structural problem will have a large number of degrees of freedom, explicit determination of the coefficients of the characteristic polynomial is extremely difficult. In the *Determinant search method*, these coefficients are computed without actually solving the characteristic polynomial. This is done through use of the *Strum sequence check*, which states that if we assume the magnitude of an eigenvalue, one can then split the effective dynamic stiffness matrix into a Choleski's decomposition, that is:

$$[[K] - \mu[M]] = [U][D][U]^T \quad (7.136)$$

where μ is the assumed value of the eigenvalue and $[U]$ is the upper diagonal matrix. The number of negative elements in the diagonal matrix $[D]$ indicates the number of eigenvalues less than μ . Using this property, one can converge on the actual eigenvalue. However, this method is not recommended for large-scale dynamic analysis.

Inverse and forward iteration techniques are normally used to find the lowest and highest natural frequencies of the problem having n degrees of freedom. They are normally used to determine the frequency bounds of the problem in hand, which is very useful in choosing the method of analysis for computing the dynamic response. It uses Rayleigh's principle in determining the eigenvalues, which states that:

$$\omega^2 = \frac{\{d\}^T[K]\{d\}}{\{d\}^T[M]\{d\}} \quad (7.137)$$

Here, $\{d\}$ is the ‘best-guess’ displacement profile of the structure. In principle, the static solution can form the best initial guess, and this solution can be iterated to get the correct eigenvalue.

It is apparent that the extraction of eigenvalues/vectors is the most computationally costly activity in the entire analysis process. The computational time and the memory cost involved in the various schemes are dealt with in great detail in Bathe [12]. For a system with n degrees of freedom, only the first m natural frequencies and mode shapes are computed, where $m \ll n$.

After obtaining the first m eigenvalues/vectors, these are put in the matrix form as $[\Phi]$ and $[\Lambda]$. The former is called the *modal matrix*, which is of size $n \times m$. In this matrix, the modes are stored column-wise. The latter is a diagonal matrix of size $m \times m$ containing the natural frequencies of the computed m modes. This matrix is also called the *spectral matrix*. The modal matrix is orthogonal with respect to both the stiffness and mass matrix. These two matrices along with the orthogonality conditions are used to estimate the dynamic response. There are two orthogonality conditions, which can be stated as:

$$[\Phi]^T [K] [\Phi] = [\Lambda], \quad [\Phi]^T [M] [\Phi] = [I] \quad (7.138)$$

In general, modal methods use similarity transformation to convert the actual degrees of freedom $\{d\}$ of size $n \times 1$ to generalized degree of freedom $\{Z\}$ of size $m \times 1$. This similarity transformation is given by:

$$\{d(t)\}_{n \times 1} = [\Phi]_{n \times m} \{Z(t)\}_{m \times 1} \quad (7.139)$$

There are two different modal methods by which the response can be computed. These are:

- Normal Mode method or Mode Displacement method
- Mode Acceleration method

In the *Normal Mode method*, the orthogonality relations are used to uncouple the governing differential equation. This is done in the following manner. The FE differential equation is given by:

$$[M]\{\ddot{d}\} + [C]\{\dot{d}\} + [K]\{d\} = \{F\}$$

In this equation, let us use Rayleigh’s proportional damping of the form $[C] = \alpha[K] + \beta[M]$. The reason for using such a damping scheme will become clear in the next

few steps. Now, we substitute Equation (7.139) into the above equation, which becomes:

$$[M][\Phi]\{\ddot{Z}\} + (\alpha[K] + \beta[M])[\Phi]\{\dot{Z}\} + [K][\Phi]\{Z\} = \{F\}$$

Premultiplying $[\Phi]^T$ and using the orthogonality conditions (Equation (7.138)) uncouples the differential equation and can be explicitly written, say for the r th mode as:

$$\ddot{Z}_r + 2\xi_r \omega_r \dot{Z}_r + \omega_r^2 Z_r = \{\phi_r\}^T \{F\} = \bar{F}_r \quad (7.140)$$

Note that, by using a smaller set of modes, we have reduced n coupled differential equation to m uncoupled differential equations. In the above equation, $\xi_r = (C_r/2M_r\omega_r)$ is the damping ratio of the r th mode and $\{\phi_r\}$ is the eigenvector of the r th mode. Equation (7.140) is nothing but the governing equation for a single degree of freedom vibratory system, which can be easily solved in terms of generalized degrees of freedom. Using these, the actual degrees of freedom is evaluated using the similarity transformation (Equation (7.139)).

One of the fundamental limitations of the normal mode method is that it cannot recover the static displacements in the limit as the frequency tends to zero. As a result, this method requires more modes to represent the dynamic response. This limitation is circumvented in the *Mode Acceleration method*. This method is described below.

The similarity transformation (Equation (7.139)) is first expressed in terms of summation as, say for the k th degree of freedom, as:

$$d_k(t) = \sum_{r=1}^m \phi_{kr} Z_r \quad (7.141)$$

From Equation (7.140), we can write Z_r as:

$$Z_r = \frac{\bar{F}_r}{\omega_r^2} - \frac{2\xi_r}{\omega_r} \dot{Z}_r - \frac{1}{\omega_r^2} \ddot{Z}_r$$

Using this in Equation (7.141), we get:

$$d_k(t) = \sum_{r=1}^m \phi_{kr} \left(\frac{\bar{F}_r}{\omega_r^2} - \frac{2\xi_r}{\omega_r} \dot{Z}_r - \frac{1}{\omega_r^2} \ddot{Z}_r \right) \quad (7.142)$$

Now, we can write the inverse of the stiffness matrix, that is, $[K]^{-1}$, by using the first orthogonality condition. The inverse can be written as:

$$[K]^{-1} = \frac{\{\phi_r\}^T \{\phi_r\}}{\omega_r^2} \quad (7.143)$$

Using the above in Equation (7.138) and noting that $\bar{F}_r = \{\phi_r\}^T \{F\}$, we can write this equation as:

$$d_k(t) = [K]^{-1} \{F\} - \sum_{r=1}^m \phi_{kr} \left(\frac{2\xi_r}{\omega_r} \dot{Z}_r + \frac{1}{\omega_r^2} \ddot{Z}_r \right) \quad (7.144)$$

The first term is the static response. This representation gives a quite accurate response using a smaller set of modes.

Modal methods are not suitable for wave-propagation problems, which are necessarily high-frequency-content problems. Such problems require evaluation of higher-order modes and natural frequencies, which are computationally prohibitive. For such problems, one normally uses *Direct Time Integration*, which is described next.

7.7.3.2 Direct time integration

Here, we write the differential equation at a particular time instant, say n , where the time derivatives are written in terms of the finite difference coefficients. This method can be universally applied to both low- and high-frequency-content problems as well as both linear and nonlinear problems. The modal methods cannot be applied to nonlinear problems. Hence, this method is extensively used in highly transient dynamics and wave-propagation problems. There two different time integration schemes. These are:

- Explicit Time Integration
- Implicit Time Integration

7.7.3.3 Explicit time integration

In this type of integration, the displacement, velocity and acceleration histories before the current time instant are known. This method is very easy to implement and gives very good results for wave-propagation problem. However, one of the main disadvantages of this method is that the method is conditionally stable, that is, there is a constraint placed on the time step.

Consider the variation of a function that requires to be integrated with respect to time, shown in Figure 7.14. The governing equation at time step n can be written as:

$$\begin{aligned} [M]\{\ddot{d}\}_n + [C]\{\dot{d}\}_n + \{R^{in}\}_n &= \{F\}_n, \{\mathbf{R}^{in}\}_n \\ &= \left[\int_V [\mathbf{B}]^T \{\sigma\}_n dV \right] \{d\} \end{aligned} \quad (7.145)$$

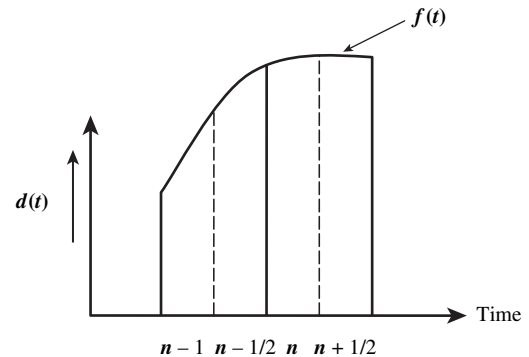


Figure 7.14 Displacement variation at different times for the finite difference approximation.

The above form is generally used for nonlinear problems, where $\{R^{in}\}$ represents the internal force vector. In linear problems, $\{R^{in}\} = [K]\{d\} = [\int_V [\mathbf{B}]^T [\mathbf{D}] [\mathbf{B}] dV] \{d\}$. Using the forward and backward difference at times $n+1/2$ and $n-1/2$, the velocities can be written as:

$$\begin{aligned} \{\dot{d}\}_{n+1/2} &= \frac{\{d\}_{n+1} - \{d\}_n}{\Delta t}, \\ \{\dot{d}\}_{n-1/2} &= \frac{\{d\}_n - \{d\}_{n-1}}{\Delta t} \end{aligned} \quad (7.146)$$

Here, Δt is the time step adopted for the time-marching scheme. Combining these, we can write the velocities and accelerations at time step n as:

$$\begin{aligned} \{\dot{d}\}_n &= \frac{\{d\}_{n+1} - \{d\}_{n-1}}{2\Delta t}, \\ \{\ddot{d}\}_n &= \frac{\{d\}_{n+1} - 2\{d\}_n + \{d\}_{n-1}}{\Delta t^2} \end{aligned} \quad (7.147)$$

The above representation of the second derivative is ‘second-order accurate’. The above scheme is called the *central difference* scheme. Substituting the above into Equation (7.145), we get:

$$\begin{aligned} \left[\frac{[M]}{\Delta t^2} + \frac{[C]}{2\Delta t} \right] \{d\}_{n+1} &= \{F\}_n - [K]\{d\}_n + \frac{1}{\Delta t^2} [M](2\{d\}_n \\ &\quad - \{d\}_{n-1}) + \frac{1}{2\Delta t} [C]\{d\}_{n-1} \end{aligned} \quad (7.148)$$

In the above expression, the right-hand side contains expressions that depend on time instants previous to the current time step. After the displacements are obtained, the velocities and accelerations can be obtained from

Equation (7.147). If matrices $[M]$ and $[C]$ are diagonal, then the equations are uncoupled and one can obtain displacements without solving the simultaneous equations. Equation (7.148) requires the value of $\{d\}_{-1}$ and $\{\ddot{d}\}_0$ at time $t = 0$; $\{d\}_{-1}$ is obtained by expanding the $\{d\}_n$ by a Taylor series and substituting $t = 0$ in the expression. $\{\ddot{d}\}_0$ is obtained by the governing differential equation written at $t = 0$. These are given by:

$$\begin{aligned} \{d\}_{-1} &= \{d\}_0 - \Delta t \{\dot{d}\}_0 + \frac{\Delta t^2}{2} \{\ddot{d}\}_0 \\ \{\ddot{d}\}_0 &= [M]^{-1} \{F\}_0 - [K] \{d\}_0 - [C] \{\dot{d}\}_0 \end{aligned} \quad (7.149)$$

This method is conditionally stable. That is, a large time step would result in divergence of the displacements. Hence, a constraint is placed on the time step. This constraint is derived based on a rigorous error analysis based on Z-transforms [7]. This constraint is given by:

$$\Delta t = \frac{2}{\omega_{\max}} \quad (7.150)$$

The ω_{\max} can be evaluated in the following ways:

- (1) The frequency content of the input signal can be obtained through the FFT and the maximum frequency can be determined from the FFT plot. This will normally be used in wave-propagation problems.
- (2) The ω_{\max} can also be evaluated from the global stiffness and mass matrix as:

$$\omega_{\max}^2 = \text{Max} \left(K_{ii} + \sum_{j=1}^N |K_{ij}| \right) / M_{ii}$$

- (3) For each element, the eigenvalue problem is solved. Then, the critical time step can be obtained by $\Delta t = \text{Min}(2/\omega_e^2)$, where ω_e is the maximum natural frequency of each element.

7.7.3.4 Implicit time integration

Implicit time integration requires information of quantities beyond the current time step. That is, for computing the displacements at time step n , information of displacements, velocities and accelerations at time steps $n+1$ and $n+2$ are required. This integration method uses the well-known *Trapezoidal rule* and *Simpson's rule* to come up with different time-marching schemes. Here, we describe a simple integration scheme based on the *Trapezoidal rule*. This is called the *average acceleration*

method and when applied to a parabolic PDE is sometimes referred to as the *Crank–Nicholson Method*. The implicit schemes are hard to implement; however, these methods are unconditionally stable.

In this scheme, we write the governing equation at time step $n+1$, which is given by:

$$[M] \{\ddot{d}\}_{n+1} + [C] \{\dot{d}\}_{n+1} + [K] \{d\}_{n+1} = \{F\}_{n+1} \quad (7.151)$$

Using the Trapezoidal rule, the displacements and velocities at time $n+1$, can be written in terms of velocities and accelerations as:

$$\begin{aligned} \{d\}_{n+1} &= \{d\}_n + \frac{\Delta t}{2} (\{\dot{d}\}_n + \{\dot{d}\}_{n+1}), \\ \{\dot{d}\}_{n+1} &= \{\dot{d}\}_n + \frac{\Delta t}{2} (\{\ddot{d}\}_n + \{\ddot{d}\}_{n+1}) \end{aligned} \quad (7.152)$$

The velocities and accelerations at time $n+1$ can now be written as:

$$\begin{aligned} \{\dot{d}\}_{n+1} &= \frac{2}{\Delta t} (\{d\}_{n+1} - \{d\}_n) - \{\dot{d}\}_n \\ \{\ddot{d}\}_{n+1} &= \frac{4}{\Delta t^2} (\{d\}_{n+1} - \{d\}_n) - \frac{4}{\Delta t} \{\dot{d}\}_n - \{\ddot{d}\}_n \end{aligned} \quad (7.153)$$

Substituting these into Equation (7.151), we get:

$$[K^{\text{eff}}] \{d\}_{n+1} = \{F^{\text{eff}}\}_{n+1} \quad (7.154)$$

where:

$$\begin{aligned} [K^{\text{eff}}] &= \frac{4}{\Delta t^2} [M] + \frac{2}{\Delta t} [C] + [K] \\ \{F^{\text{eff}}\}_{n+1} &= \{F\}_{n+1} + [M] \left(\frac{4}{\Delta t^2} \{d\}_n + \frac{4}{\Delta t} \{\dot{d}\}_n + \{\ddot{d}\}_n \right) \\ &\quad + [C] \left(\frac{2}{\Delta t} \{d\}_n + \{\dot{d}\}_n \right) \end{aligned} \quad (7.155)$$

Equation (7.154) is solved for finding out the displacements at time step $n+1$ using the information available at time step n . Velocities and accelerations are computed using Equation (7.153). At each step, Equation (7.154) is a highly coupled set of simultaneous equations even when $[M]$ and $[C]$ are diagonal. This is unlike the explicit method. Hence, there is no merit in using lumped approximations for the mass. It is similar to solving a static problem at each time step. When implementing this

scheme, one can perform Choleski decomposition on $[K^{\text{eff}}]$ only once for forward reduction as it is a function of only the time step, which is decided *a priori* before the analysis. If $[M]$ is positive definite, $[K^{\text{eff}}]$ is nonsingular even for singular $[K]$. This scheme is said to give poor convergence for nonlinear problems. This scheme gives better results with the use of a consistent mass matrix. The most important advantage of this method is that it is unconditionally stable. That is, even for a large time step, the solution will not diverge. This does not, however, mean unconditional accuracy. For nonlinear problems, the time step should be small for better accuracy.

In general, both of the integration schemes, namely the implicit and explicit, do not provide for automatic dissipation of high-frequency noise, which normally exists. Hence, there are many integration schemes that are designed to incorporate additional parameters that would take care of dissipating this high-frequency noise. One such method, which is extensively used in many general purpose packages, is the Newmark- β method. This method has two parameters that dictate the amount of dissipation and the type of integration scheme, namely explicit or implicit. That is, by appropriately tuning these parameters, we can make the integration scheme purely explicit or implicit. More details of this method can be found in Bathe [12].

7.8 SUPERCONVERGENT FINITE ELEMENT FORMULATION

The FEM is an approximate technique and the accuracy of the solution is heavily dependent upon the element size and the order of the interpolating polynomial. To improve the accuracy in the case of elements formulated with lower-order polynomials, it is necessary to increase the mesh density, especially for transient dynamic problems and also for problems with high stress gradients. Such an approach for increasing the mesh density is called the *h-FEM* approach. Alternatively, one can increase the order of the polynomial, thereby increasing the number of nodes in each element. Such an approach is called the *p-FEM* approach. In the case of transient dynamic problems, what is required for accurate solution is accurate mass distribution. This necessarily requires a fine mesh density, no matter what type of approach one adopts. The problems in smart structures, especially structural health monitoring problems, are necessarily high-frequency-content problems. In most cases, it requires interrogation of a high-frequency tone-burst-type signal to infer the state of the structure. The

frequency content of such signals is of the order of 50 kHz–2 MHz. In such problems, all higher-order modes not only get excited but also have high-energy contents. To capture these higher modes, the mesh sizes should be so fine that they should match the wavelength of the stress wave that is set up due to the given excitation. Hence, such problems are beyond the reach of the FEM.

The problem of obtaining an accurate mass distribution ‘boils down’ to how close the assumed displacement field satisfies the governing equation. In the FEM, time-dependency does not enter explicitly in the solution. Hence, if we choose our interpolating functions to satisfy the spatial part (static part) of the governing equation, one would exactly characterize the stiffness of the structure, while the mass distribution of the structure will still be approximate. However, it is the accurate prediction of resonances or natural frequencies that is key to obtaining an accurate solution to the dynamic problem. If one carries out an error analysis of an assumed solution, it can be shown that the order of error magnitude in stiffness characterization is quite a lot higher as opposed to mass. This aspect is proved in Strang and Fix [16]. Hence, one can expect a better prediction of higher-order modes using smaller finite element meshes by employing the above approach. We call this formulation the *Super Convergent Finite Element Formulation* (SCFEM). In fact, the elementary rod and beam elements described earlier in this chapter are super-convergent elements as they satisfy the static part of the governing equation exactly. As a result, one element, no matter how long the element is, is sufficient to capture the static response exactly. This is true as long as the structure is subjected to point loads, which is normally the case in most wave-propagation problems.

Another situation where the SCFEM is very useful is in constraint media problems. These problems occur when finite elements based on higher-order theory are used to predict responses in the models based on elementary theory. For example, let us consider the Timoshenko beam and Euler–Bernoulli beam models. The basic difference between the two models is that, in the former shear deformation is introduced. Introduction of shear deformation violates the condition that “plane sections remain plane before and after bending”. Hence, the beam slopes cannot be obtained by differentiating the transverse displacement and therefore, in finite element formulations, it requires to be separately interpolated. This reduces the continuity requirement from C^1 in the elementary beam to C^0 in the Timoshenko beam. When this Timoshenko beam model is used to predict responses

in very thin beams (where the shear strains are zero), one obtains solutions that are many orders smaller than the correct solution. This problem is called the *shear locking* problem. The reason for this locking is that the formulation introduces two stiffness matrices, one due to bending and the other due to shear. It is this shear stiffness matrix that introduces the shear constraints, which makes the structure excessively stiff. That is, the shear stiffness matrix is non-singular. If one needs to eliminate shear locking, the shear matrix should be made ‘rank-deficient’, which makes this matrix singular. This is accomplished by ‘under-integrating’ the shear stiffness using the Gauss Quadrature. These schemes are explained in greater detail in Prathap and Bhashyam [17], Hughes *et al.* [18] and Prathap [19].

In such constrained media problems, the SCFEM can be employed. In this formulation, the user need not know if the higher-order effects are predominant or not. In addition, it is extremely useful in solution of the transient dynamics problems using smaller problem sizes. In the next subsection, we introduce the SCFEM formulation for a deep rod, where the higher-order effects due to lateral contraction introduce an additional degree of freedom.

7.8.1 Superconvergent deep rod finite element

An elementary rod can support only axial motion. Hence, a linear polynomial is sufficient to capture the static response exactly under point loads. In the deep rod, the lateral displacements are significant due to Poisson’s ratio. This is accounted for through an additional degree of freedom ψ . This lateral motion is shown in Figure 6.24 in Chapter 6. This was earlier introduced in Chapter 6 to study the wave-propagation behavior in composites (Section 6.3.2). Here, we consider an isotropic rod of length L , axial rigidity EA , density ρ , Poisson’s ratio ν and shear rigidity GK . A and I are the area and moment of inertia of the cross-section. The assumed displacement field can be taken as:

$$u(x, t) = u(x, t), \quad w(x, t) = z\psi(x, t) \quad (7.156)$$

In the above expression, $u(x, t)$ and $w(x, t)$ are the axial and lateral displacement fields and z the depth coordinate. Using this, we write the strains by using the strain-displacement relations (Equation (6.27)) and stresses, using Equation (6.68) (Chapter 6). These are then used to write the strain and kinetic energies in terms of displacements, which is used in Hamilton’s principle (Equation (7.52)) to obtain the following governing

equations for a deep rod:

$$\begin{aligned} \frac{EA}{1-\nu^2} \left[\frac{\partial^2 u}{\partial x^2} + \nu \frac{\partial \psi}{\partial x} \right] &= \rho A \frac{\partial^2 u}{\partial t^2} \\ GIK \frac{\partial^2 \psi}{\partial x^2} - \frac{EA}{1-\nu^2} \left[\psi + \nu \frac{\partial u}{\partial x} \right] &= \rho IK_1 \frac{\partial^2 \psi}{\partial t^2} \end{aligned} \quad (7.157)$$

In the above equations, the two constants K and K_1 are introduced to compensate for the approximations enforced in the analysis. When this equation is uncoupled in terms of the axial displacement $u(x, t)$, it becomes a fourth-order partial differential equation, as opposed to the second order of the elementary rod. The elementary rod theory can be recovered by setting $\psi = -\nu(\partial u / \partial x)$, $GIK = 0$ and $\rho IK_1 = 0$. In regular finite element analysis, a linear polynomial in u and ψ would have been sufficient to formulate the basic element. Such an element would behave very well in a deep-rod situation. However, in the limit as $\psi = -\nu(\partial u / \partial x)$, this rod element would lock, giving responses much smaller than the true solution. In order to circumvent this problem, we ignore the dynamic part in Equation (7.157) (the right-hand side of the equation) and solve the coupled ordinary differential equation exactly. This exact solution can be used in interpolating functions for FE formulation. In doing so, we get the following solution:

$$\begin{aligned} u(x) &= a_0 + a_1 x + a_2 e^{-\beta(L-x)} + a_3 e^{-\beta x} \\ \psi(x) &= b_0 + b_1 e^{-\beta(L-x)} + b_2 e^{-\beta x} \end{aligned} \quad (7.158)$$

Here, $\beta^2 = EA/GIK$ and L is the length of the finite element. In reality, the above function is a polynomial of infinite order. If $GIK = 0$, then we would recover our elementary rod solution. In the above equation, we have seven constants and only four boundary conditions at both ends. Hence, there are three dependent constants which can be expressed in terms of independence by substituting the solution (Equation (7.158)) in the governing differential equation (Equation (7.157)). In doing so, we get the following relations among the constants:

$$b_0 = -\nu a_1, \quad b_1 = -a_2 \frac{\beta}{\nu}, \quad b_2 = a_3 \frac{\beta}{\nu} \quad (7.159)$$

Now, the interpolating polynomial can be written only in terms of four constants as:

$$\begin{aligned} u(x) &= a_0 + a_1 x + a_2 e^{-\beta(L-x)} + a_3 e^{-\beta x} \\ \psi(x) &= -\nu a_1 - a_2 \frac{\beta}{\nu} e^{-\beta(L-x)} + a_3 \frac{\beta}{\nu} e^{-\beta x} \end{aligned} \quad (7.160)$$

Here, we see that some of the coefficients associated with lateral contraction are material-dependent. This is one of the features of the SCFEM. First, the shape functions are established. This is done by enforcing $u(0) = u_1$, $u(L) = u_2$, $\psi(0) = \psi_1$ and $\psi(L) = \psi_2$. This will give a relation between the unknown coefficients $\{a\} = \{a_0 \ a_1 \ a_2 \ a_3\}^T$ and the nodal degrees of freedom $\{u\} = \{u_1 \ \psi_1 \ u_2 \ \psi_2\}^T$, which can be written as $\{a\} = [G]\{u\}$. These coefficients are substituted back into Equation (7.158), and hence we can write the displacement field as:

$$\begin{aligned} u(x) &= [N_u]\{u\}, \\ [N_u] &= [1 \ x \ e^{-\beta(L-x)} \ e^{-\beta x}] \\ [G] &= [N_{u1} \ N_{u2} \ N_{u3} \ N_{u4}] \\ \psi(x) &= [N_\psi]\{u\}, \\ [N_\psi] &= [0 \ -v \ e^{-\beta(L-x)} \ e^{-\beta x}] \\ [G] &= [N_{\psi1} \ N_{\psi2} \ N_{\psi3} \ N_{\psi4}] \end{aligned} \quad (7.161)$$

Here, $[N_u]$ and $[N_\psi]$ are the 1×4 shape function matrices corresponding to u and ψ degrees of freedom at the two ends of the rod. The above shape functions are exact shape functions for performing static analysis. The formulation from here is the same as was carried out for a regular finite element. First, the strain displacement matrix $[B]$ is established. The strains are as follows:

$$\begin{aligned} \epsilon_{xx} &= \frac{du}{dx}, \quad \epsilon_{yy} = \frac{dv}{dy} = \psi, \quad \gamma_{xy} = \frac{du}{dy} + \frac{dv}{dx} = z \frac{d\psi}{dx} \end{aligned} \quad (7.162)$$

This can be written in matrix form as:

$$\left\{ \begin{array}{c} \epsilon_{xx} \\ \epsilon_{yy} \\ \gamma_{xy} \end{array} \right\} = \left[\begin{array}{cccc} \frac{dN_{u1}}{dx} & \frac{dN_{u2}}{dx} & \frac{dN_{u3}}{dx} & \frac{dN_{u4}}{dx} \\ N_{\psi1} & N_{\psi2} & N_{\psi3} & N_{\psi4} \\ z \frac{dN_{\psi1}}{dx} & z \frac{dN_{\psi2}}{dx} & z \frac{dN_{\psi3}}{dx} & z \frac{dN_{\psi4}}{dx} \end{array} \right] \left\{ \begin{array}{c} u_1 \\ u_2 \\ \psi_1 \\ \psi_2 \end{array} \right\} = [B]\{u\} \quad (7.163)$$

The constitutive matrix assuming the plane stress condition is given by Equation (7.113). Using the formulated $[B]$ matrix and the material matrix $[C]$, the expression for the stiffness matrix is given by:

$$[K] = \int_0^L \int_A [B]^T [C] [B] dA dx \quad (7.164)$$

The explicit expressions for the elements of the stiffness matrix is given by:

$$\begin{aligned} k_{11} &= \frac{R}{\Delta}, \quad k_{12} = \frac{-\alpha LS}{\Delta}, \quad k_{13} = -k_{11}, \quad k_{14} = k_{12} \\ k_{22} &= \frac{L^2 \alpha (R^2 + S^2 - 2v\alpha RS)}{2vS\Delta}, \quad k_{23} = -k_{12}, \\ k_{24} &= \frac{L^2 \alpha (R^2 - S^2 - 2v\alpha RS)}{2vS\Delta} \\ k_{33} &= k_{11}, \quad k_{34} = -k_{12}, \quad k_{44} = k_{22} \\ R &= 1 + e^{-\beta L}, \quad S = 1 - e^{-\beta L}, \\ \alpha &= \frac{v}{\beta L}, \quad \Delta = R - 2v\alpha S, \quad \beta = \sqrt{\frac{EA}{GIK}} \end{aligned} \quad (7.165)$$

Using the shape functions given in Equation (7.161), we can also formulate the consistent mass matrix. It has two components, one due to axial motion and the other due to lateral contraction. Hence, we can write the mass matrix as:

$$\begin{aligned} [M] &= [M_u] + [M_\psi] \\ [M_u] &= \rho A \int_0^L [N_u]^T [N_u] dx, \quad [M_\psi] = \rho I K_1 \int_0^L [N_\psi]^T [N_\psi] dx \end{aligned} \quad (7.166)$$

Substituting for the shape functions from Equation (7.161), we can write the mass matrix as:

$$[M] = \rho A L [G]^T [m^u] [G] + \rho I K_1 L [G]^T [m^\psi] [G] \quad (7.167)$$

The elements of $[m^u]$ and $[m^\psi]$ are given by:

$$\begin{aligned} m_{11}^u &= 1, \quad m_{12}^u = \frac{L}{2}, \quad m_{13}^u = \frac{S\alpha}{v}, \quad m_{14}^u = m_{13}^u \\ m_{22}^u &= \frac{L^2}{3}, \quad m_{23}^u = \frac{L\alpha}{v} \left(1 - \frac{S\alpha}{v} \right), \quad m_{24}^u = \frac{L\alpha}{2v} \left(S - R + \frac{2S\alpha}{v} \right) \\ m_{33}^u &= \frac{RS\alpha}{2v}, \quad m_{34}^u = \frac{R-S}{2}, \quad m_{44}^u = m_{33}^u \end{aligned} \quad (7.168)$$

$$m_{11}^\psi = m_{12}^\psi = m_{13}^\psi = m_{14}^\psi = 0$$

$$m_{22}^\psi = v^2 L, \quad m_{23}^\psi = S, \quad m_{24}^\psi = -S$$

$$m_{33}^\psi = \frac{RS}{2v\alpha L}, \quad m_{34}^\psi = \frac{R-S}{2L\alpha^2}, \quad m_{44}^\psi = m_{33}^\psi \quad (7.169)$$

Before we use this element, we should determine the values of the parameters K and K_1 . This is normally done

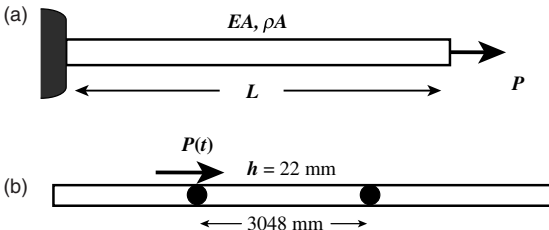


Figure 7.15 Examples used in deep-rod formulation: (a) cantilevered rod with a tip axial load; (b) infinite deep rod.

by looking at the limiting behavior of the rod at very high frequencies. Since the present theory is an approximation of the 2-D behavior, a practical approach would be to consider a better representation of this model with a 2-D FE model and choose the values of K and K_1 to get the best results in the frequency of interest. This was carried out by Martin *et al.* [20] and values of $K = 1.2$ and $K_1 = 1.75$ were suggested.

To demonstrate the utility of this element, two examples are considered – one is a static-analysis example while the other is a wave-propagation example. For static analysis, we consider a cantilever rod of axial rigidity EA and length L under a tip axial load, as shown in Figure 7.15(a). One single element will give an exact static response. If the rod is elementary, then the tip axial displacement will be equal to PL/AE . A single deep rod element will give the tip axial displacement as:

$$u_{\text{tip}} = \frac{PL}{AE} \left[1 - \frac{2v\alpha RS}{R^2 + S^2} \right] \quad (7.170)$$

Here, the parameters R , S , etc. are defined in Equation (7.165). The second term in the brackets is the error in using the elementary theory. A plot of the error with the L/h ratio, where h is the depth of the rod, would show that even for a very thick rod (very small L/h ratio), the error is only about 8 %. This was reported by Gopalakrishnan [21]. Hence, the errors are not large enough to justify the use of a higher-order model for static analysis. An elementary rod model is sufficient.

It has been shown by Gopalakrishnan [21], Doyle [22], Chakraborty and Gopalakrishnan [23] and Roy Mahapatra and Gopalakrishnan [24] that a very high-frequency behavior gets affected by introduction of the lateral contraction mode. That is, an additional propagating mode is introduced at very high frequencies, which was shown in Chapter 6 for an unsymmetric laminate (Section 6.3.2). To demonstrate the presence of an additional propagating mode, an infinite isotropic rod is considered, as shown in Figure 7.15(b).

This rod is subjected to a tone-burst narrow-banded signal sampled at 125 kHz. This frequency is chosen so that the tone-burst frequency is beyond the cut-off frequency for this rod to ensure that the second propagating contraction mode is excited. The cut-off frequency for a deep rod with aluminum properties has been given by Gopalakrishnan [21].

$$\omega_0 = \sqrt{\frac{EA}{(1 - v^2)\rho K_1}} = 88 \text{ kHz} \quad (7.171)$$

The pulse is allowed to propagate a distance of 3048 mm for the contraction mode to appear. The infinite rod was modeled using 9000 formulated finite elements to make sure that the element size matches the wavelength at this high frequency. Figure 7.16 shows a comparison of the solutions between the present model and the spectral model [20]. At about 2000 μs , one can see the contraction mode appearing in both of the models. The finite element model over estimates the speed due to an approximate mass distribution. This narrow-banded tone-burst pulse is very useful for performing structural health monitoring studies.

The SCFEM models are now available for practically all 1-D models such as deep composite beams [23], first-order shear-deformable composite beams [25], functionally graded beams [26] and thin-walled composite box beams with and without smart ‘patches’ [27,28]. One practical difficulty in the SCFEM is that it is extremely difficult to formulate 2-D and 3-D elements as exact solutions of the governing equations, as these are very difficult to obtain.

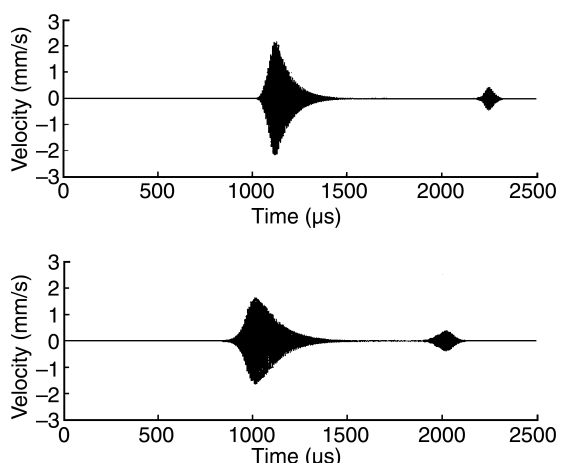


Figure 7.16 Two propagating modes in a deep rod: (a) finite element solution; (b) spectral element solution.

7.9 SPECTRAL FINITE ELEMENT FORMULATION

Application of the FEM for wave propagation requires a very fine mesh to capture the mass distribution accurately. The mesh size should be comparable to the wavelengths, which are very small at high frequencies. Hence, the problem size increases enormously. Many applications in smart structure applications, such as structural health monitoring or active wave control in composite structures, require wave-based modeling since one has to use high-frequency interrogating signals. If one needs online diagnostic tools in structures, wave-based modeling is an absolute must. For such problems, the FEM by itself cannot be used as a modeling tool as it is very expensive from the computational viewpoint. Hence, one needs an alternate formulation wherein the frequency content of the exciting signal is not an issue. That is, we need a modeling tool that can give a smaller problem size for high-frequency loading, at the same time retaining the matrix structure of the FEM. Such a technique is feasible through the *spectral finite element* (SFEM) technique.

The SFEM is the FEM formulated in the frequency domain and wavenumber space. That is, these elements will have interpolating functions that are complex exponentials or Bessel functions. These interpolating functions are also functions of the wavenumbers. In Chapter 6 (Section 6.3.2), we have seen that a governing partial 1-D wave equation, when transformed into the frequency domain using DFT, removes the time derivative and reduces the PDE to a set of ODEs, which have complex exponentials as solutions. In the SFEM, we use these exact solutions as the interpolating functions. As a result, the mass is distributed exactly and hence, one single element is sufficient between any two discontinuities to get an exact response, irrespective of the frequency content of the exciting pulse. That is, one SFEM can replace hundreds of FEMs normally required for wave-propagation analysis. Hence, the SFEM is an ideal candidate for developing online health monitoring software. In addition to smaller system sizes, other major advantages of the SFEM include the following:

- Since the formulation is based on the frequency domain, system transfer functions are the direct byproduct of the approach. As a result, one can perform inverse problems such as force identification/system identification in a straightforward manner.
- The approach gives the dynamic stiffness matrix as a function of frequency, directly from the formulation.

Hence, we have to deal with only one element of dynamic stiffness as opposed to two matrices in the FEM (stiffness and mass matrices).

- Since different normal modes have different amounts of damping at various frequencies, by formulating the elements in the frequency domain one can treat the complex damping mechanisms more realistically.
- The SFEM lets you formulate two sets of elements – one is the finite length element and the other is the infinite element or ‘throw-off element’. This ‘throw-off element’ acts as a conduit of energy out of the system. There are various uses of this infinite ‘throw-off element’, such as adding maximum damping, obtaining good resolution of the responses in the time and frequency domains and also in modeling large lengths, which are computationally very expensive to model in the FEM.
- The SFEM is probably the only technique that gives you responses in both the time and frequency domains in a single analysis.

The SFEM can be formulated in a similar manner to the FEM by writing the ‘weak form’ of the governing differential equation and substituting the assumed functions for displacements and integrating the resulting expression. Since the functions involved are much more complex, integration of these functions in the ‘closed form’ takes a longer time. In addition, by this approach we cannot obtain the dynamic stiffness matrix of the ‘throw-off element’, as the latter is normally complex. Hence, we adopt an equilibrium approach of element formulation, which eliminates integration of the complex functions. In this chapter, we show this formulation for a simple isotropic rod element, while the procedure remains the same for other elements.

Formulation of the spectral elements requires determination of the spectrum (the variation of wavenumber with frequency) relations and the dispersion relations (speed with frequency). The procedure to determine these were given in Chapter 6 (Section 6.3.2). The SFEM begins with transformation of the governing equation into the frequency domain by using a discrete Fourier transform. The solution of this transformed equation becomes the interpolating function for the spectral element formulation. The procedure of formulating the SFEM for a simple 1-D rod is illustrated below.

The governing differential equation for a uniform rod with associated boundary conditions are given by:

$$EA \frac{\partial^2 u}{\partial x^2} = \rho A \frac{\partial^2 u}{\partial t^2}, \quad F = EA \frac{\partial u}{\partial x} \quad (7.172)$$

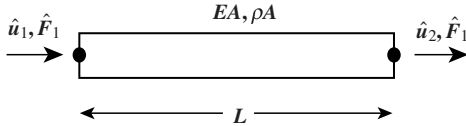


Figure 7.17 Degrees of freedom for a spectral rod element.

where EA is the axial rigidity and ρ is the density of the material. Assuming the spectral form of solution (or Fourier transform) given by:

$$u(x, t) = \sum_{n=1}^N \hat{u}_n(x, \omega) e^{i\omega_n t}$$

Substituting the above spectral form of the solution into Equation (7.172) converts the PDE to a set of ODEs, which is given by:

$$\sum_{n=1}^N \left(EA \frac{d^2 \hat{u}_n}{dx^2} + \rho A \omega^2 \hat{u}_n \right) = 0 \quad (7.173)$$

The longitudinal wavenumber for the rod is given by $k = \omega \sqrt{\rho A / EA}$, where ω is the frequency.

Consider a rod of length L . The force and displacement degrees of freedom are shown in Figure 7.17. Note here that all of the variables with a “hat” indicate frequency-dependent quantities. The interpolating function for element formulation, which is the exact solution of Equation (7.173), is given by:

$$\hat{u}(x, \omega) = Ae^{-ikx} + Be^{-ik(L-x)} \quad (7.174)$$

We now substitute the boundary conditions, that is, at $\hat{u}(0) = \hat{u}_1, \hat{u}(L) = \hat{u}_2$, we get:

$$\begin{Bmatrix} \hat{u}_1 \\ \hat{u}_2 \end{Bmatrix} = \begin{bmatrix} 1 & e^{-ikL} \\ e^{-ikL} & 1 \end{bmatrix} \begin{Bmatrix} A \\ B \end{Bmatrix}, \quad \{\hat{u}\}_e = [\hat{G}] \{a\} \quad (7.175)$$

Inverting the above relation, we get:

$$\begin{Bmatrix} A \\ B \end{Bmatrix} = \frac{1}{(1 - e^{-2ikL})} \begin{bmatrix} 1 & -e^{-ikL} \\ -e^{-ikL} & 1 \end{bmatrix} \begin{Bmatrix} \hat{u}_1 \\ \hat{u}_2 \end{Bmatrix},$$

$$\{a\} = [G]^{-1} \{\hat{u}\}_e \quad (7.176)$$

Substituting Equation (7.176) into Equation (7.174), we get the spectral shape functions, which are given by:

$$\begin{aligned} \hat{u}(x, \omega) &= [e^{-ikx} \ e^{-k(L-x)}] \{a\} = [e^{-ikx} \ e^{-k(L-x)}] [G]^{-1} \{\hat{u}\}_e \\ &= [\hat{N}] \{\hat{u}\}_e, \quad [\hat{N}] = [\hat{N}_1 \ \hat{N}_2] = [e^{-ikx} \ e^{-k(L-x)}] [G]^{-1} \end{aligned} \quad (7.177)$$

Now, we consider the force results at the two ends, which are given in Equation (7.172) and can write the resultants in terms of the boundary resultants as:

$$\hat{F}_1 = -EA \frac{d\hat{u}}{dx} \Big|_{x=0}, \quad \hat{F}_2 = EA \frac{d\hat{u}}{dx} \Big|_{x=L}$$

The above relation can be put in the matrix form as:

$$\begin{Bmatrix} \hat{F}_1 \\ \hat{F}_2 \end{Bmatrix} = \frac{EA}{L} ikL \begin{bmatrix} 1 & -e^{-ikL} \\ e^{-ikL} & -1 \end{bmatrix} \begin{Bmatrix} A \\ B \end{Bmatrix}$$

Substituting Equation (7.175) into the above equation and carrying out the required matrix multiplication will give the required force-displacement relation in the frequency domain through a dynamic stiffness matrix, which is given by:

$$\begin{Bmatrix} \hat{F}_1 \\ \hat{F}_2 \end{Bmatrix} = \frac{EA}{L} \frac{ikL}{(1 - e^{-2ikL})} \begin{bmatrix} 1 + e^{-2ikL} & -2e^{-ikL} \\ -2e^{-ikL} & 1 + e^{-2ikL} \end{bmatrix} \begin{Bmatrix} \hat{u}_1 \\ \hat{u}_2 \end{Bmatrix}$$

$$\{\hat{F}\}_e = \frac{EA}{L} [\hat{K}] \{\hat{u}\}_e \quad (7.178)$$

Here, $[\hat{K}]$ is the element dynamic stiffness matrix, which is symmetric and real, as in the case of a conventional finite element dynamic stiffness matrix, which is given by:

$$\begin{aligned} [\hat{K}]_{\text{FEM}} &= [K] - \omega^2 [M] = \frac{EA}{L} \begin{bmatrix} 1 & -1 \\ -1 & 1 \end{bmatrix} \\ &\quad - \omega^2 \frac{\rho AL}{6} \begin{bmatrix} 2 & 1 \\ 1 & 2 \end{bmatrix} \end{aligned} \quad (7.179)$$

Figure 7.18 gives a comparison of some stiffness coefficients of the SFEM and FEM at low and medium frequencies.

We see that at low frequencies they practically match each other. At medium frequencies, we see that the stiffness coefficients differ substantially. We can make the FEM stiffness match the spectral stiffness if we use many elements to model the rod. This is one of the reasons why the model sizes of the SFEM are very small. The formulation of various spectral elements for 1-D isotropic waveguides is given in Doyle [22]. Spectral elements for 1-D elementary and first-order shear deformable composite waveguides are given in Roy Mahapatra and Gopalakrishnan [24] and Roy Mahapatra *et al.* [29]. Spectral elements are also available for composite tubes [30] and functionally graded beams [31]. Spectrally formulated elements are also available for 2-D isotropic

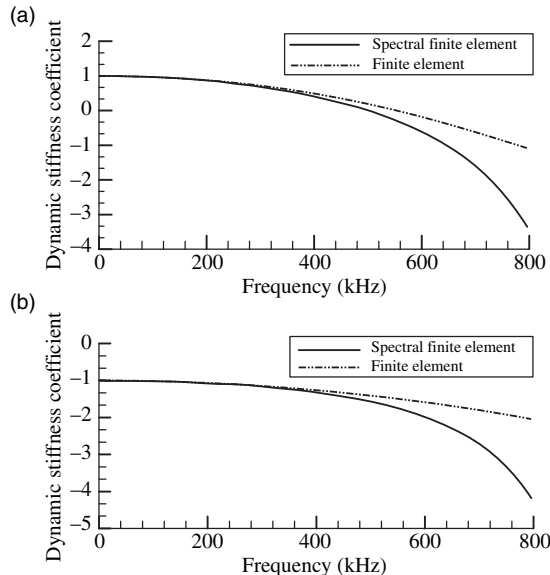


Figure 7.18 Dynamic stiffness comparison between SFEM and FEM: (a) stiffness coefficient, k_{11} ; (b) stiffness coefficient, k_{12} .

membrane waveguides [32] and composite waveguides [33]. In all of these works, exact solutions to the interpolating functions were used for element formulation. There are a few approximate spectral elements, where an approximate solution, along with the frequency-domain variational principle, was used to formulate the spectral element. These are available for a shear-deformable tapered beam [34] and an inhomogeneous rod [35].

The SFEM computer code has many resemblances to the FEM code. That is, as in the FEM the element dynamic stiffness matrix is generated, assembled and solved. However, all of these operations have to be performed for each frequency. Since the system sizes are small, these do not pose a major computational ‘roadblock’.

The analysis procedure using the SFEM can be summarized as follows:

- (1) The given forcing signal is fed into the FFT program and the output is stored in a file, which contains three columns containing the frequency and real and the imaginary parts of the forcing function. The sampling rate of the signal and the number of FFT points is decided by various factors, such as the nature of the wave (dispersive or nondispersive), length of propagation and level of damping.
- (2) These frequencies, along with the real and imaginary components, are read and stored.

- (3) The analysis begins over a big ‘do-loop’ over the frequency. The analysis is performed over all of the frequency components, but only up to the Nyquist frequency. For each frequency, the element dynamic stiffness matrix is generated, assembled and stored for further use. This is unlike the FEM, where the matrices (stiffness and mass) are generated and assembled before the analysis is performed over a ‘loop’ of time steps.
- (4) The equations are solved in the frequency domain by using the conventional Gauss elimination with Choleski decomposition. However, the ‘solver’ should be able to handle complex variables. The equations are first solved for a unit impulse – this will give the *system transfer function* (FRF) directly, which has a varied use in addition to computing responses. If the number of different time histories is used in the analysis, computing the FRF needs to be done only once. By multiplying this FRF with the input, we get the displacement response in the frequency domain. If we are performing inverse problems such as force identification, the input is divided by the FRF to get the force response in the frequency domain.
- (5) If quantities such as stresses, strains or energies are needed, the displacement response is ‘post-processed’ as is done in the conventional time-domain FEM. However, the computed responses will be frequency-dependent.
- (6) The frequency-domain responses are converted into time-domain responses by using the inverse FFT.

One of the major disadvantages of the spectral approach is that the exact solutions are limited to only a few waveguides. It is not possible to develop spectral elements for geometries of arbitrary shape or for structural waveguides with discontinuities such as cracks or holes. These can be modeled in several ways within the SFEM environment. In Gopalakrishnan and Doyle [36], waveguides with cracks and holes were modeled with the FEM over a small region and reduced as ‘super-spectral elements’, which are then coupled with regular spectral elements and the analysis is performed.

REFERENCES

1. I.H. Shames and C.L. Dym, *Energy and Finite Element Methods in Structural Mechanics*, John Wiley & Sons, Ltd, London, UK (1991).
2. S. Gopalakrishnan, ‘Behavior of isoparametric quadrilateral family of lagrangian fluid finite elements’, *International Journal for Numerical Methods in Engineering*, **54**, 731–761 (2002).

3. J.N. Reddy, *Applied Functional Analysis and Variational Methods in Engineering*, McGraw-Hill, Singapore (1986).
4. K. Wazizlu, *Variational Methods in Elasticity and Plasticity*, 2nd Edn, Pergamon Press, New York, NY, USA (1974).
5. T.R. Tauchert, *Energy Principles in Structural Mechanics*, McGraw-Hill, Tokyo, Japan (1974).
6. J.N. Reddy, *Energy Principles and Variational Methods in Applied Mechanics*, 2nd Edn, John Wiley & Sons, Inc., Hoboken, NJ, USA (2002).
7. R.D. Cook, R.D. Malkus and M.E. Plesha, *Concepts and Applications of Finite Element Analysis*, John Wiley & Sons, Inc., New York, NY, USA (1989).
8. K.J. Bathe, *Finite Element Procedures*, 3rd Edn, Prentice Hall, Englewood Cliffs, NJ, USA (1996).
9. G. Prathap, 'Barlow points and Gauss points and the aliasing and best fit paradigms', *Computers and Structures*, **58**, 321–325 (1996).
10. E. Hinton, T. Rock and O.C. Zienkiewicz, 'A note on mass lumping and related processes in the finite element method', *Earthquake Engineering and Structural Dynamics*, **4**, 245–249 (1976).
11. D.S. Malkus and M.E. Plesha, 'Zero and negative masses in finite element vibration and transient analysis', *Computer Methods in Applied Mechanics and Engineering*, **59**, 281–306 (1986).
12. K.J. Bathe, *Finite Element Procedures in Engineering Analysis*, Prentice Hall, Englewood Cliffs, NJ, USA (1982).
13. E. Hinton and D.R.J. Owen, *Finite Element Programming*, Academic Press, New York, NY, USA (1977).
14. B.M. Irons, 'A frontal solution program', *International Journal for Numerical Methods in Engineering*, **2**, 5–32 (1970).
15. J.H. Kane, *Boundary Element Analysis in Engineering Continuum Mechanics*, Prentice Hall, Englewood Cliffs, NJ, USA (1992).
16. G. Strang and G.J. Fix, *An Analysis of Finite Element Method*, Prentice Hall Series in Automatic Computation, Prentice Hall, Englewood Cliffs, NJ, USA (1973).
17. G. Prathap and G.R. Bhashyam, 'Reduced integration and shear flexible beam element', *International Journal for Numerical Methods in Engineering*, **18**, 211–243 (1982).
18. T.G.R. Hughes, R.L. Taylor and W. Kanoknukulchai, 'A simple and efficient finite element for plate bending', *International Journal for Numerical Methods in Engineering*, **11**, 1529–1543 (1977).
19. G. Prathap, *The Finite Element in Structural Mechanics*, Kluwer Academic Publishers, Dordrecht, The Netherlands (1993).
20. M. Martin, S. Gopalakrishnan and J.F. Doyle, 'Wave propagation in multiply connected deep waveguides', *Journal of Sound and Vibration*, **174**, 521–538 (1994).
21. S. Gopalakrishnan, 'A deep rod finite element for structural dynamics and wave propagation problems', *International Journal for Numerical Methods in Engineering*, **48**, 731–744 (2000).
22. J.F. Doyle, *Wave Propagation in Structures*, Springer-Verlag, New York, NY, USA (1997).
23. A. Chakraborty and S. Gopalakrishnan, 'Study of Poisson's contraction effects in a deep laminated composite beam through a new finite element formulation', *Mechanics of Advanced Structures and Materials*, **10**, 1–21 (2003).
24. D. Roy Mahapatra and S. Gopalakrishnan, 'Axial-shear-bending coupled wave propagation in thick composite beams', *Composite Structures*, **59**, 67–88 (2003).
25. A. Chakraborty, D. Roy Mahapatra and S. Gopalakrishnan, 'Finite element analysis of free vibration and wave propagation in asymmetric composite beams with structural discontinuities', *Composite Structures*, **55**, 23–36 (2002).
26. A. Chakraborty, S. Gopalakrishnan and J.N. Reddy, 'A new beam finite element for the analysis of functionally graded materials', *International Journal for Mechanical Sciences*, **45**, 519–539 (2003).
27. Mira Mitra, S. Gopalakrishnan and M. Seetharama Bhat, 'Vibration control in a composite box beam with piezoelectric actuators', *Smart Structures and Materials*, **13**, 676–690 (2004).
28. Mira Mitra, S. Gopalakrishnan and M. Seetharama Bhat, 'A new super convergent thin walled composite beam element for analysis of box beam structures', *International Journal of Solids and Structures*, **41**, 1491–1518 (2004).
29. D. Roy Mahapatra, S. Gopalakrishnan and T.S. Sankar, 'Spectral element based solutions for wave propagation analysis of multiply connected unsymmetric laminated composite beams', *Journal of Sound and Vibration*, **237**, 819–836 (2000).
30. D. Roy Mahapatra and S. Gopalakrishnan, 'A spectral finite element for analysis of wave propagation in uniform composite tubes', *Journal of Sound and Vibration*, **268**, 429–463 (2003).
31. A. Chakraborty and S. Gopalakrishnan, 'A spectrally formulated finite element for wave propagation in functionally graded beams', *International Journal of Solids and Structures*, **40**, 2421–2448 (2003).
32. S.A. Rizzi and J.F. Doyle, 'A spectral element approach to wave motion in layered solids', *ASME Journal of Vibration and Acoustics*, **114**, 569–577 (1992).
33. A. Chakraborty and S. Gopalakrishnan, 'A spectrally formulated finite element for wave propagation analysis in layered composite media', *International Journal for Solids and Structures*, **41**, 5155–5183 (2004).
34. S. Gopalakrishnan and J.F. Doyle, 'Wave propagation in connected waveguides of varying cross-section', *Journal of Sound and Vibration*, **175**, 347–363 (1994).
35. A. Chakraborty and S. Gopalakrishnan, 'Various numerical techniques for analysis of longitudinal wave propagation in inhomogeneous one dimensional waveguides', *Acta Mechanica*, **162**, 1–27 (2003).
36. S. Gopalakrishnan and J.F. Doyle, 'Spectral super-elements for wave propagation in structures with local non-uniformities', *Computer Methods in Applied Mechanics and Engineering*, **121**, 77–90 (1995).

Modeling of Smart Sensors and Actuators

8.1 INTRODUCTION

Modeling of systems with structures having smart sensors and actuators are very similar to conventional structures wherein numerical techniques, such as the FEM or spectral techniques, as outlined in Chapter 7, can be used. However, the modeling has to take care of additional complexities arising due to the material properties of smart materials that make up the smart sensors and actuators. These are reflected in the constitutive laws in the form of electromechanical coupling, as in the case of piezoceramic or PVDF sensors or magneto-mechanical coupling, as in the case of magnetostrictive sensors/actuators, such as Terfenol-D. From the modeling point of view, these complexities would lead to additional matrices in FEM/SFEM approaches.

Piezoelectric or magnetostrictive materials have two constitutive laws, one of which is used for sensing and the other for actuation purposes. For 2-D problems, the constitutive model for a piezoelectric material is of the form:

$$\{\sigma\}_{3 \times 1} = [C]_{3 \times 3}^{(E)} \{\varepsilon\}_{3 \times 1} - [e]_{3 \times 2} \{E\}_{2 \times 1} \quad (8.1)$$

$$\{D\}_{2 \times 1} = [e]_{2 \times 3}^T \{\varepsilon\}_{3 \times 1} + [\mu]_{2 \times 2}^{(\sigma)} \{E\}_{2 \times 1} \quad (8.2)$$

The first of this constitutive law is called the *actuation law*, while the second is called the *sensing law*. Here, $\{\sigma\}^T = \{\sigma_{xx} \ \sigma_{yy} \ \tau_{xy}\}$ is the stress vector, $\{\varepsilon\}^T = \{\varepsilon_{xx} \ \varepsilon_{yy} \ \gamma_{xy}\}$ is the strain vector, $[e]$ is the matrix of piezoelectric coefficients of size 3×2 , which has units of $N/(V \text{ mm})$, $\{E\}^T = \{E_x \ E_y\} = \{V_x/t \ V_y/t\}$ is the applied field in two coordinate directions, where V_x and V_y are the applied voltages in the two coordinate directions, and t is the thickness parameter. The latter has units of V/mm ; $[\mu]$ is the permittivity matrix of size 2×2 , measured at constant

stress and has units of N/V/V and $\{D\}^T = \{D_x \ D_y\}$ is the vector of electric displacement in two coordinate directions. This has units of $N(V \text{ mm})$. $[C]$ is the mechanical constitutive matrix measure at constant electric field. Equation (8.1) can also be written in the form:

$$\{\varepsilon\} = [S]\{\sigma\} + [d]\{E\} \quad (8.3)$$

In the above expression, $[S]$ is the compliance matrix, which is the inverse of the mechanical material matrix $[C]$, and $[d] = [C]^{-1}[e]$ is the electromechanical coupling matrix, where the elements of this matrix have units of mm/V and the elements of this matrix are ‘direction-dependent’. In most analyses, it will be assumed that the mechanical properties will change very little with the change in electric field and as a result, the actuation law (Equation (8.1)) can be assumed to behave linearly with the electric field, while the sensing law (Equation (8.2)) can be assumed to behave linearly with stress. This assumption will considerably simplify the analysis process.

The first part of Equation (8.1) represents the stresses developed due to mechanical load, while the second part of the same equation gives the stresses due to voltage input. From Equations (8.1) and (8.2), it is clear that the structure will be stressed due to the application of electric field, even in the absence of a mechanical load. Alternatively, when the mechanical structure is loaded, it generates an electric field. In other words, the above constitutive law demonstrates electromechanical coupling, which is exploited for a variety of structural applications, such as vibration control, noise control, shape control and structural health monitoring. Actuation using piezoelectric materials can be demonstrated by using a plate of dimensions $L \times W \times t$, where L and W are the length and width of the plate and t is its thickness. Thin piezoelectric electrodes are placed on the top and

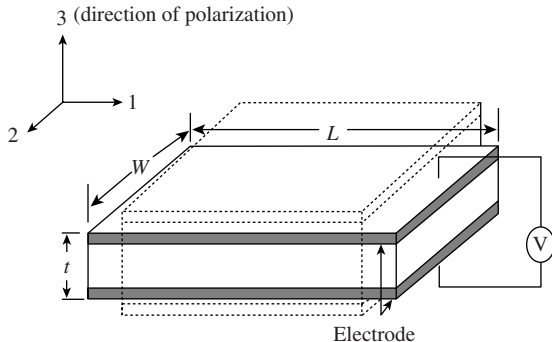


Figure 8.1 Illustration of the actuation effect in a piezoelectric plate.

bottom surfaces of the plate, as shown in Figure 8.1. Such a plate is called a *Bimorph* plate. When a voltage is passed between the electrodes, as shown in the figure (which is normally referred as the poling direction), the deformations in the length, width and thickness directions are given by:

$$\begin{aligned}\delta L &= d_{31}E_1L = \frac{d_{31}VL}{t}, \\ \delta W &= d_{31}E_2W = \frac{d_{31}VW}{t}, \quad \delta t = d_{33}V\end{aligned}\quad (8.4)$$

Here, d_{31} and d_{33} are the electromechanical coupling coefficients in the directions 1 and 3, respectively. Conversely, if a force F is applied in any of the length, width or thickness directions, the voltage V developed across the electrodes in the thickness direction is given by:

$$V = \frac{d_{31}F}{\mu L} \quad \text{or} \quad \frac{d_{31}F}{\mu W} \quad \text{or} \quad \frac{d_{33}F}{\mu LW} \quad (8.5)$$

Here, μ is the dielectric permittivity of the material. The reversibility between the strain and voltages makes piezoelectric materials ideal for both sensing and actuation. Finite element modeling of the mechanical part is very similar to what was discussed in Chapter 7, except that the coupling terms introduce additional energy terms in the variational statements, which results in additional coupling matrices in the FE formulation.

There are different types of piezoelectric materials that are used for many structural applications. The most commonly used material is PZT (Lead Zirconate Titanate) which is extensively used as a bulk actuator material as it has a high electromechanical coupling factor. Due to this low electromechanical coupling factor, ‘Piezo polymers’ (PVDF) are extensively used as sensor materials. With the advent of smart composite structures, a new brand of material, called *Piezo Fiber Composites* (PFCs) have

been found to be very effective actuator materials for use in vibration/noise control applications.

The constitutive laws (both actuation and sensing) for magnetostrictive materials, such as Terfenol-D, are much more complex than those of piezoelectric materials. These are highly nonlinear and have a similar form to those of piezoelectric materials, which are given by:

$$\{\varepsilon\} = [S]^{(H)}\{\sigma\} + [d]^T\{H\} \quad (8.6)$$

$$\{B\} = \{d\}\{\sigma\} + [\mu]^{(\sigma)}\{H\} \quad (8.7)$$

Here, $[S]$ is the compliance matrix measured at a constant magnetic field H , $[d]$ is the magneto-mechanical coupling matrix, the elements of which have units of m/A and $\{B\}$ is the vector of magnetic flux density in the two coordinate directions. It has units called teslas, equal to weber/metre³. $\{H\}$ is the magnetic field intensity vector in the two coordinate directions and has units called oersted, equal to ampere/meter. It is related to the AC current ($I(t)$) through the relation $H = nI$, where n is the number of turns in the actuator; $[\mu]$ is the matrix of magnetic permeability measured at constant stress and has units of weber/(Ampere meter). As in the case of piezoelectric materials, the first equation (Equation (8.6)) is the actuation constitutive law, while the second equation (Equation (8.7)) is the sensing law. The stress-strain relations are different for different magnetic field intensities. The strain is linear with stress only for small magnetic field intensities. For higher magnetic field intensities, both sensing and actuator equations require to be simultaneously solved to arrive at the correct stress-strain relation. This is because a change in the magnetic field changes the stress, which changes the magnetic permeability. Hence, characterization of the material properties of Terfenol-D is more difficult when compared to the piezoelectric material.

In this book we will assume only linear behavior of these materials and proceed with modeling of these smart sensors and actuators based on this assumption. This chapter gives the FE modeling of both 1-D and 2-D structures with both piezo and magnetostrictive material patches and 1-D Spectral element modeling of beam structures with smart material patches.

More recently, micro electromechanical systems (MEMS) have found extensive applications in almost all fields of science and engineering. These structures are of micron-level thickness and millimeter-level dimensions. Most MEMS devices are micro sensors. A typical MEMS device has a substrate usually made of silicon or a polymer. Over this substrate the electrodes are placed to obtain the necessary electromechanical coupling. Hence,

the design of these sensors involves mechanical design as well as the design of the electrical circuit. As in the case of smart materials, these sensors exhibit strong electro-mechanical coupling. When these are bonded to the main structure (of macro dimensions), they contribute negligibly to the stiffness and as such do not alter the mechanics of the macro structure. If one needs to assess the device performance, a local analysis of the device on the host structure is required. In other words, we need to resort to multi-scale modeling techniques to analyze the bulk structures with MEMS-type devices. In addition, if one needs to design these sensors, it is necessary to perform local FE analysis of the MEMS device since the device itself could be of any arbitrary shape. However, if one needs to design a distributed sensor of micron-level thickness and long dimensions, it is necessary to model the host structure as well as the sensor itself. The long dimension of the sensor may result in incomplete transfer of the response to the sensor from the host for effective sensing. That is, there may be some response loss. In such cases, it is necessary to perform the analysis taking into consideration the mechanics of the host structure and also accounting for this loss. One such analysis for the design of capacitive sensors is given in this chapter.

Presently, research is being focused to further miniaturize sensors from the micro scale to the nano scale. This was made possible by the discovery of new forms of stable carbon atoms, namely the C_{60} fullerenes and carbon nanotubes (CNTs), in the late 1980s and early 1990s, respectively. These have opened up new area of researchs in material science to harness their immense potential in various fields. More importantly, when these materials are dispersed in a matrix, due to their enormous strength and low density they have immense potential to become ‘next-generation’ structural materials. They are currently a fertile area of research the world over. The properties of CNTs were discussed in detail in Chapter 2. One of the key properties of CNTs is that they can propagate waves at the terra-frequency levels. This aspect is investigated in this chapter.

In the next section, FE modeling of piezoelectric sensors and actuators is given. In this section, a general 3-D formulation is outlined from which 2-D plane stress/ plane strain finite elements will be deduced. Next, a superconvergent thin-walled box beam FE element with an embedded piezoelectric actuator is formulated. This is followed by a section on the modeling of magnetostrictive sensors/actuators where first the numerical characterization of the nonlinear constitutive law is described, followed by the formulation of a general 3-D FE formulation of magnetostrictive sensors and actuators. Following this, there is a subsection that will deal with the

modeling of 1-D structures with piezoelectric/magnetostrictive sensors/actuators using spectral finite element methods. This is followed by a subsection that will address the modeling of MEMS devices and in particular will address the analysis of distributed thin-film-type capacitive sensors. The last part of this chapter will address the modeling issues and the continuum spectral element modeling of single-walled and multi-walled carbon nanotubes. All these sections will also carry some numerical examples, which highlight the capabilities and utilities of these analytical/numerical tools.

8.2 FINITE ELEMENT MODELING OF A 3-D COMPOSITE LAMINATE WITH EMBEDDED PIEZOELECTRIC SENSORS AND ACTUATORS

8.2.1 Constitutive model

Fundamental to any FE modeling is to first establish the constitutive model and this is also true for a 3-D laminate with embedded piezoelectric sensors/actuators. Here, we take the same approach as we had taken for conventional composite structures described in Chapter 6 (Section 6.2). That is, we first establish the constitutive model at the lamina level in the fiber coordinate system, which is transformed to the global coordinate system. These relations are then synthesized for all the laminas to establish the constitutive model of the laminate. However, additional matrices will arise in this case due to the presence of electromechanical coupling. Consider a lamina with a piezoelectric layer, as shown in Figure 8.2. The constitutive model in directions 1, 2, and 3 for such a lamina is given by Equations (8.1) and (8.2), respectively. In matrix form, it is given by:

$$\begin{Bmatrix} \{\sigma\} \\ \{D\} \end{Bmatrix} = \begin{bmatrix} [C] & -[e] \\ [e]^T & [\mu] \end{bmatrix} \begin{Bmatrix} \{\varepsilon\} \\ \{E\} \end{Bmatrix} \quad \text{or} \quad \{\bar{\sigma}\} = [\bar{C}] \{\bar{\varepsilon}\} \quad (8.8)$$

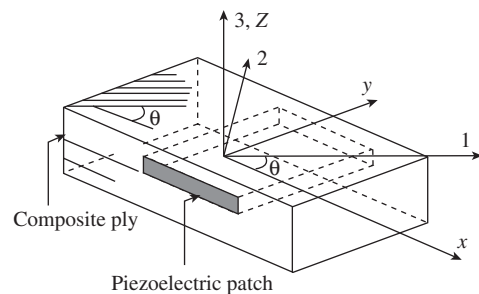


Figure 8.2 Local and global coordinate systems for a lamina with an embedded piezoelectric patch.

Expanding the above equation, we get:

$$\left\{ \begin{array}{l} \sigma_{11} \\ \sigma_{22} \\ \sigma_{33} \\ \sigma_{23} \\ \sigma_{31} \\ \sigma_{12} \\ D_1 \\ D_2 \\ D_3 \end{array} \right\} = \left[\begin{array}{ccccccc} C_{11} & C_{12} & C_{13} & 0 & 0 & 0 & 0 & -e_{31} \\ C_{12} & C_{22} & C_{23} & 0 & 0 & 0 & 0 & -e_{32} \\ C_{13} & C_{23} & C_{33} & 0 & 0 & 0 & 0 & -e_{33} \\ 0 & 0 & 0 & C_{44} & 0 & 0 & 0 & -e_{24} \\ 0 & 0 & 0 & 0 & C_{55} & 0 & -e_{15} & 0 \\ 0 & 0 & 0 & 0 & 0 & C_{66} & 0 & 0 \\ 0 & 0 & 0 & 0 & e_{15} & 0 & \mu_{11} & 0 \\ 0 & 0 & 0 & e_{24} & 0 & 0 & 0 & \mu_{22} \\ e_{31} & e_{32} & e_{33} & 0 & 0 & 0 & 0 & \mu_{33} \end{array} \right] \times \left\{ \begin{array}{l} \varepsilon_{11} \\ \varepsilon_{22} \\ \varepsilon_{33} \\ \varepsilon_{23} \\ \varepsilon_{31} \\ \varepsilon_{12} \\ E_1 \\ E_2 \\ E_3 \end{array} \right\} = \left\{ \begin{array}{l} \sigma_{xx} \\ \sigma_{yy} \\ \sigma_{zz} \\ \sigma_{yz} \\ \sigma_{zx} \\ \sigma_{xy} \\ D_x \\ D_y \\ D_z \end{array} \right\} = \left[\begin{array}{cccccccc} \bar{C}_{11} & \bar{C}_{12} & \bar{C}_{13} & 0 & 0 & 0 & 0 & -\bar{e}_{31} \\ \bar{C}_{12} & \bar{C}_{22} & \bar{C}_{23} & 0 & 0 & 0 & 0 & -\bar{e}_{32} \\ \bar{C}_{13} & \bar{C}_{23} & \bar{C}_{33} & 0 & 0 & 0 & 0 & -\bar{e}_{33} \\ 0 & 0 & 0 & \bar{C}_{44} & 0 & 0 & 0 & -\bar{e}_{24} \\ 0 & 0 & 0 & 0 & \bar{C}_{55} & 0 & -\bar{e}_{15} & 0 \\ 0 & 0 & 0 & 0 & 0 & \bar{C}_{66} & 0 & 0 \\ 0 & 0 & 0 & 0 & \bar{e}_{15} & 0 & \bar{\mu}_{11} & 0 \\ 0 & 0 & 0 & \bar{e}_{24} & 0 & 0 & 0 & \bar{\mu}_{22} \\ \bar{e}_{31} & \bar{e}_{32} & \bar{e}_{33} & 0 & 0 & 0 & 0 & \bar{\mu}_{33} \end{array} \right] \left\{ \begin{array}{l} \varepsilon_{xx} \\ \varepsilon_{yy} \\ \varepsilon_{zz} \\ 2\varepsilon_{yz} \\ 2\varepsilon_{zx} \\ 2\varepsilon_{xy} \\ E_x \\ E_y \\ E_z \end{array} \right\} \quad (8.10)$$

In expanded form, the above equation becomes:

Here, $E_i = -\nabla\Phi$, where Φ is the electric potential vector. The above constitutive model is then transformed to the global x - y - z coordinate system using the transformation matrix, which is given by:

$$[T] = \begin{bmatrix} [T_{11}] & [0] \\ [0] & [T_{22}] \end{bmatrix} \quad (8.9)$$

where:

$$[T_{11}] = \begin{bmatrix} C^2 & S^2 & 0 & 0 & 0 & -2CS \\ S^2 & C^2 & 0 & 0 & 0 & 2CS \\ 0 & 0 & 1 & 0 & 0 & 0 \\ 0 & 0 & 0 & C & S & 0 \\ 0 & 0 & 0 & S & C & 0 \\ CS & -CS & 0 & 0 & 0 & C^2 - S^2 \end{bmatrix},$$

$$[T_{22}] = \begin{bmatrix} C^2 & S^2 & 0 \\ S^2 & C^2 & 0 \\ 0 & 0 & 1 \end{bmatrix}, \quad C = \cos(\theta), \quad S = \sin(\theta)$$

Here, θ is the fiber orientation of the lamina. The constitutive model in the global x - y - z direction is then given by:

$$\{\sigma\} = [T]^T \begin{bmatrix} [C] & -[e] \\ [e]^T & [\mu] \end{bmatrix} [T] \{\varepsilon\} = \begin{bmatrix} [\bar{C}] & -[\bar{e}] \\ [\bar{e}] & [\mu] \end{bmatrix} \{\varepsilon\}$$

The elements of $[\bar{C}]$ and $[\bar{e}]$ are given by:

$$\begin{aligned} \bar{C}_{11} &= 4C_{66}C^2S^2 + C^2(C_{11}C^2 + C_{12}S^2) \\ &\quad + S^2(C_{12}C^2 + C_{22}S^2) \\ \bar{C}_{12} &= -4C_{66}C^2S^2 + S^2(C_{11}C^2 + C_{12}S^2) \\ &\quad + C^2(C_{12}C^2 + C_{22}S^2), \quad \bar{C}_{13} = C_{13}C^2 - C_{23}S^2 \\ \bar{C}_{16} &= -2C_{66}CS(C^2 - S^2) + CS(C_{11}C^2 + C_{12}S^2) \\ &\quad - CS(C_{12}C^2 + C_{22}S^2), \quad \bar{C}_{21} = \bar{C}_{12} \\ \bar{C}_{22} &= 4C_{66}C^2S^2 + S^2(C_{11}S^2 + C_{12}C^2) \\ &\quad + C^2(C_{12}S^2 + C_{22}C^2), \quad \bar{C}_{23} = C_{23}C^2 + C_{13}S^2 \\ \bar{C}_{26} &= 2C_{66}CS(C^2 - S^2) + CS(C_{11}S^2 + C_{12}C^2) \\ &\quad - CS(C_{12}S^2 + C_{22}C^2), \quad \bar{C}_{31} = \bar{C}_{13}, \quad \bar{C}_{32} = \bar{C}_{23} \\ \bar{C}_{33} &= C_{33}, \quad \bar{C}_{36} = CS(C_{13} - C_{23}), \\ \bar{C}_{44} &= C_{44}C^2 + C_{55}S^2, \quad \bar{C}_{45} = CS(C_{55} - C_{44}) \\ \bar{C}_{54} &= \bar{C}_{45}, \quad \bar{C}_{55} = C_{44}S^2 + C_{55}C^2, \quad \bar{C}_{61} = \bar{C}_{16}, \\ \bar{C}_{62} &= \bar{C}_{26}, \quad \bar{C}_{63} = \bar{C}_{36} \\ \bar{C}_{66} &= C_{66}(C^2 - S^2)^2 + C^2S^2(C_{11} - C_{12}) \\ &\quad - C^2S^2(C_{12} - C_{22}) \\ \bar{e}_{31} &= (e_{31}C^2 + e_{32}S^2), \quad \bar{e}_{32} = (e_{31}S^2 + e_{32}C^2), \\ \bar{e}_{33} &= e_{33}, \quad \bar{e}_{14} = (e_{15}C^2S + e_{24}CS^2) \\ \bar{e}_{24} &= (e_{24}C^3 + e_{15}S^3), \quad \bar{e}_{15} = (e_{15}C^3 - e_{24}S^3), \\ \bar{e}_{25} &= (e_{24}C^2S - e_{15}CS^2) \\ \bar{e}_{36} &= CS(e_{31} - e_{32}), \quad \bar{\mu}_{11} = \mu_{11}C^4 + \mu_{22}S^4, \\ \bar{\mu}_{12} &= C^2S^2(\mu_{11} + \mu_{22}) \\ \bar{\mu}_{22} &= \mu_{22}C^4 + \mu_{11}S^4, \quad \bar{\mu}_{33} = \mu_{33} \end{aligned} \quad (8.11)$$

For 2-D analysis, we normally employ either plane stress or plane strain assumptions. For the plane stress assumption in the x - y plane, we substitute $\sigma_{yy} = \sigma_{xz} = \sigma_{yz} =$

$D_x = D_y = 0$ in Equation (8.10). Simplifying this, we can write the constitutive model for a 2-D piezoelectric composite as:

$$\begin{aligned} \left\{ \begin{array}{l} \{\sigma\} \\ D_z \end{array} \right\} &= \begin{bmatrix} [\hat{C}] & -[\hat{e}] \\ [\hat{e}]^T & \hat{\mu} \end{bmatrix} \left\{ \begin{array}{l} \{\varepsilon\} \\ E_z \end{array} \right\} = \begin{Bmatrix} \sigma_{xx} \\ \sigma_{zz} \\ \sigma_{xz} \\ D_z \end{Bmatrix} \\ &= \begin{bmatrix} \hat{C}_{11} & \hat{C}_{12} & 0 & -\hat{e}_{31} \\ \hat{C}_{13} & \hat{C}_{33} & 0 & -\hat{e}_{32} \\ 0 & 0 & \hat{C}_{55} & 0 \\ \hat{e}_{31} & \hat{e}_{32} & 0 & \hat{\mu}_{33} \end{bmatrix} \begin{Bmatrix} \varepsilon_{xx} \\ \varepsilon_{zz} \\ 2\varepsilon_{xz} \\ E_z \end{Bmatrix} \end{aligned} \quad (8.12)$$

where:

$$\begin{aligned} \hat{C}_{11} &= \bar{\bar{C}}_{11} + \frac{1}{A} \left[\bar{\bar{C}}_{12} (\bar{\bar{C}}_{26} \bar{\bar{C}}_{16} - \bar{\bar{C}}_{66} \bar{\bar{C}}_{12}) \right. \\ &\quad \left. + \bar{\bar{C}}_{16} (\bar{\bar{C}}_{26} \bar{\bar{C}}_{16} - \bar{\bar{C}}_{22} \bar{\bar{C}}_{16}) \right] \\ \hat{C}_{13} &= \bar{\bar{C}}_{13} + \frac{1}{A} \left[\bar{\bar{C}}_{12} (\bar{\bar{C}}_{26} \bar{\bar{C}}_{36} - \bar{\bar{C}}_{66} \bar{\bar{C}}_{23}) \right. \\ &\quad \left. + \bar{\bar{C}}_{16} (\bar{\bar{C}}_{26} \bar{\bar{C}}_{23} - \bar{\bar{C}}_{22} \bar{\bar{C}}_{36}) \right] \\ \hat{C}_{33} &= \bar{\bar{C}}_{33} + \frac{1}{A} \left[\bar{\bar{C}}_{23} (\bar{\bar{C}}_{26} \bar{\bar{C}}_{36} - \bar{\bar{C}}_{66} \bar{\bar{C}}_{23}) \right. \\ &\quad \left. + \bar{\bar{C}}_{36} (\bar{\bar{C}}_{26} \bar{\bar{C}}_{23} - \bar{\bar{C}}_{22} \bar{\bar{C}}_{36}) \right] \\ \hat{C}_{55} &= \bar{\bar{C}}_{55} - \frac{\bar{\bar{C}}_{44}^2}{\bar{\bar{C}}_{44}} \quad (8.13) \\ \hat{e}_{31} &= \bar{\bar{e}}_{31} + \frac{1}{A} \left[\bar{\bar{e}}_{32} (\bar{\bar{C}}_{12} \bar{\bar{C}}_{66} - \bar{\bar{C}}_{16} \bar{\bar{C}}_{26}) \right. \\ &\quad \left. + \bar{\bar{e}}_{36} (\bar{\bar{C}}_{16} \bar{\bar{C}}_{22} - \bar{\bar{C}}_{12} \bar{\bar{C}}_{26}) \right] \\ \hat{e}_{32} &= \bar{\bar{e}}_{32} + \frac{1}{A} \left[\bar{\bar{e}}_{32} (\bar{\bar{C}}_{23} \bar{\bar{C}}_{66} - \bar{\bar{C}}_{26} \bar{\bar{C}}_{36}) \right. \\ &\quad \left. + \bar{\bar{e}}_{36} (\bar{\bar{C}}_{36} \bar{\bar{C}}_{22} - \bar{\bar{C}}_{23} \bar{\bar{C}}_{26}) \right] \\ \hat{\mu}_{33} &= \bar{\bar{\mu}}_{33} + \frac{1}{A} \left[\bar{\bar{e}}_{36} (\bar{\bar{C}}_{22} \bar{\bar{C}}_{69} + \bar{\bar{C}}_{66} \bar{\bar{C}}_{29}) \right. \\ &\quad \left. + \bar{\bar{e}}_{32} (\bar{\bar{C}}_{29} \bar{\bar{C}}_{66} - \bar{\bar{C}}_{26} \bar{\bar{C}}_{69}) \right] \end{aligned}$$

8.2.2 Finite element modeling

Let us consider a 2-D composite laminate under plane stress in the x - z plane. Let $u(x, y, t)$ and $w(x, y, t)$ be its displacement components. First, the weak form of the

governing differential equation is written. This requires that the energy associated with the problem be written in terms of displacements. The kinetic, strain and electrical energy for the smart laminate having a volume V are given by:

$$\begin{aligned} T &= \frac{1}{2} \int_V \rho \{ \dot{u} \}^T \{ \dot{u} \} dV, \quad U = \frac{1}{2} \int_V \{ \sigma \}^T \{ \varepsilon \} dV, \\ U_e &= \frac{1}{2} \int_V E_z \mu_z dV \end{aligned} \quad (8.14)$$

where:

$$\{u\}^T = \{u \ v\}, \quad \{\sigma\}^T = \{\sigma_{xx} \ \sigma_{zz} \ \sigma_{xz}\}$$

Here, ρ is the density of the smart composite. The stresses are related to the strain using Equation (8.12), which can be expressed in terms of displacement using the strain-displacement relationship (Equation (6.27) in Chapter 6). Using these energies in Hamilton's principle, we get the following strong form of the governing equation and its associated boundary conditions:

$$\begin{aligned} \rho \frac{\partial^2 u}{\partial t^2} - \hat{C}_{11} \frac{\partial^2 u}{\partial x^2} - \hat{C}_{13} \frac{\partial^2 w}{\partial x \partial z} - \hat{C}_{55} \left(\frac{\partial^2 u}{\partial z^2} + \frac{\partial^2 w}{\partial x \partial z} \right) \\ + \hat{e}_{31} \frac{\partial E_z}{\partial x} = F_{sx} + \hat{e}_{31} \frac{\partial E_s}{\partial x} \\ \rho \frac{\partial^2 w}{\partial t^2} - \hat{C}_{33} \frac{\partial^2 w}{\partial z^2} - \hat{C}_{13} \frac{\partial^2 u}{\partial x \partial z} - \hat{C}_{55} \left(\frac{\partial^2 w}{\partial x^2} + \frac{\partial^2 u}{\partial x \partial z} \right) \\ + \hat{e}_{33} \frac{\partial E_z}{\partial z} = F_{sz} - \hat{e}_{33} \frac{\partial E_s}{\partial z} \\ \hat{e}_{31} \frac{\partial u}{\partial x} + \hat{e}_{33} \frac{\partial w}{\partial z} + \bar{\bar{\mu}}_{33} E_z = -D_s - \bar{\bar{\mu}}_{33} E_s \end{aligned} \quad (8.15)$$

where $\{F_s\}^T = \{F_{sx} \ F_{sz}\}$ is the surface force vector in the two directions and E_s and D_s are the residual electrical field and the electrical displacement in the smart composite. In the above equation, the first two represent the force equilibrium in the x - and z -directions, while the third equation represents the equation for electrical field equilibrium. The associated force boundary conditions on the edge parallel to the z -axis are:

$$\begin{aligned} \hat{C}_{11} \frac{\partial u}{\partial x} + \hat{C}_{13} \frac{\partial w}{\partial z} - \hat{e}_{31} E_z &= F_{cx} + \hat{e}_{31} E_s \quad \text{or } u \text{ prescribed} \\ \hat{C}_{55} \left(\frac{\partial u}{\partial z} + \frac{\partial w}{\partial x} \right) &= F_{cz} \quad \text{or } w \text{ prescribed} \end{aligned} \quad (8.16)$$

Similarly, the force boundary conditions on the edge parallel to the x -axis are:

$$\begin{aligned} \hat{C}_{13} \frac{\partial u}{\partial x} + \hat{C}_{33} \frac{\partial w}{\partial z} - \hat{e}_{33} E_z &= F_{cz} + \hat{e}_{33} E_s \quad \text{or } w \text{ prescribed} \\ \hat{C}_{55} \left(\frac{\partial u}{\partial z} + \frac{\partial w}{\partial x} \right) &= F_{cx} \quad \text{or } u \text{ prescribed} \end{aligned} \quad (8.17)$$

where F_{cx} and F_{cz} are the sum of all point loads in the x - and z -directions, respectively. The main goal here is to solve Equation (8.15). These are very difficult to solve exactly. Hence, it is necessary to recast the above equilibrium equation in its weak form and best-fit an approximate solution using the FE procedure.

The weak form of the governing differential equation is obtained by adopting the procedure outlined in Chapter 7 (Section 7.4). This is obtained by performing a variational minimization (Hamilton's Principle) of the total energy, which can be written as:

$$\delta \left(\begin{array}{l} \frac{1}{2} \int_{t_1 V}^{t_2} \{\dot{u}\}^T \rho \{\dot{u}\} dV dt + \frac{1}{2} \int_{t_1 V}^{t_2} \{\sigma\}^T \{\varepsilon\} dV dt \\ + \frac{1}{2} \int_{t_1 V}^{t_2} E_z D_z dV dt + \int_{t_1}^{t_2} \{u\}^T \{F_c\} dt \\ + \int_{t_1 S_1}^{t_2} \{u\}^T \{F_s\} dS_1 dt + \int_{t_1 S_2}^{t_2} E_z D_s dS_2 dt \end{array} \right) = 0 \quad (8.18)$$

where S_1 and S_2 are the surfaces in the structure where the surface forces and residual displacements act. Substituting for stresses and electrical displacements from

Equation (8.12), the weak form of the differential equation becomes:

$$\begin{aligned} & \int_{t_1 V}^{t_2} \int \{\delta \dot{u}\}^T \rho \{\dot{u}\} dV dt \\ &+ \int_{t_1 V}^{t_2} \int \{\delta \varepsilon\}^T [\bar{C}] \{\varepsilon\} dV dt - \int_{t_1 V}^{t_2} \int \delta E_z [\bar{e}]^T \{\varepsilon\} dV dt \\ &+ \int_{t_1 V}^{t_2} \int \delta E_z [\bar{e}]^T \{\varepsilon\} dV dt + \int_{t_1 V}^{t_2} \int \delta E_z \mu E_z dV dt \\ &+ \int_{t_1}^{t_2} \{\delta u\}^T \{F_c\} dt + \int_{t_1 S_1}^{t_2} \int \{\delta u\}^T \{F_s\} dS_1 dt \\ &+ \int_{t_1 S_2}^{t_2} \int \delta E_z D_s dS_2 dt = 0 \end{aligned} \quad (8.19)$$

The above equation is the weak form of the governing equation (Equation (8.15)) for a composite laminate with piezoelectric smart patches. This is the starting point for the FE formulation.

8.2.3 2-D Isoparametric plane stress smart composite finite element

Here, we outline the procedure for formulating a four-node isoparametric plane stress smart composite finite element. The element configuration is shown in Figure 8.3. This element will have two mechanical degrees of freedom, namely the two displacement components $u(x, y, t)$ and $w(x, y, t)$, respectively, and a single electrical degree of freedom $E_z(x, y, t)$ in the z -direction. The electric field in this direction will induce stresses in

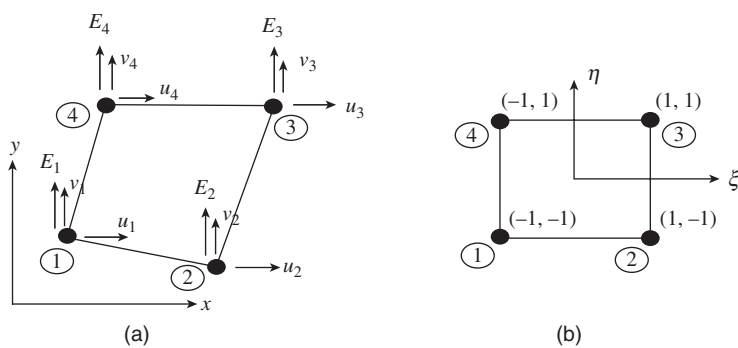


Figure 8.3 (a) Element degrees of freedom and (b) the isoparametric coordinate system.

the x -direction. Thus, this element will have a total of twelve degrees of freedom. Here, we will use the isoparametric formulation outlined in Chapter 7 (Section 7.6.3). Since the proposed element is four-noded, we will use the bilinear shape functions for the mechanical displacements required, which can be written as:

$$\begin{aligned} u(x, y, t) &= \sum_{i=1}^4 N_i(\xi, \eta) u_i(t), \quad w(x, y, t) \\ &= \sum_{i=1}^4 N_i(\xi, \eta) w_i(t) \end{aligned} \quad (8.20)$$

where ξ and η are the isoparametric coordinates and $u_i(t)$ and $w_i(t)$ are the nodal mechanical degrees of freedom. The four bilinear shape functions are given by:

$$\begin{aligned} N_1 &= \frac{1}{4}(1-\xi)(1-\eta), \quad N_2 = \frac{1}{4}(1+\xi)(1-\eta), \\ N_3 &= \frac{1}{4}(1+\xi)(1+\eta), \quad N_4 = \frac{1}{4}(1-\xi)(1+\eta) \end{aligned} \quad (8.21)$$

Now, in order to choose the interpolating polynomial for the electrical degrees of freedom, we look at the strong form of the governing equation (Equation (8.15)). By substituting the linear variation for the mechanical degrees of freedom, we find that for consistency of the displacement field we also require a bilinear variation of the electrical field. Hence, we assume the electric field to vary as:

$$E_z(x, y, t) = \sum_{i=1}^4 N_i(\xi, \eta) E_{zi}(t) \quad (8.22)$$

where the same shape function given in Equation (8.21) is also used here, and E_{zi} are the nodal electrical degrees of freedom at the four nodes.

In isoparametric formulation, we map the actual geometry of the element to a square of size two defined in the generalized coordinate system (ξ, η) through a Jacobian transformation. This requires the variation of the coordinate system in the generalized coordinates in terms of the nodal coordinates of the actual element geometry. Hence, one can use the same displacement shape functions to describe this variation and which can be written as:

$$x(x, y) = \sum_{i=1}^4 N_i(\xi, \eta) x_i, \quad z(x, y) = \sum_{i=1}^4 N_i(\xi, \eta) z_i \quad (8.23)$$

The Jacobian can be computed using the procedure given in Chapter 7 (Section 7.6.3). The strains are evaluated by

using the strain–displacement relationship, that is:

$$\begin{Bmatrix} \varepsilon_{xx} \\ \varepsilon_{zz} \\ 2\varepsilon_{xz} \\ E_z \end{Bmatrix} = \begin{bmatrix} \partial/\partial x & 0 & 0 \\ 0 & \partial/\partial z & 0 \\ \partial/\partial z & \partial/\partial x & 0 \\ 0 & 0 & 1 \end{bmatrix} \begin{Bmatrix} u \\ w \\ D_z \end{Bmatrix}$$

Using Equations (8.20) and (8.22) in the above equation enables us to express the strains in terms of the nodal displacement vector $\{u\}_e = \{u_1 \quad w_1 \quad u_2 \quad w_2 \quad u_3 \quad w_3 \quad u_4 \quad w_4\}^T$ and the electric field vector $\{E_z\}_e = \{E_{z1} \quad E_{z2} \quad E_{z3} \quad E_{z4}\}^T$. That is, the strain can be written as

$$\{\varepsilon\} = [B]\{u\} = \begin{bmatrix} [B]_{u(3 \times 8)} & 0 \\ 0 & [B]_{E(1 \times 4)} \end{bmatrix} \quad (8.24)$$

where the $[B]$ matrix, is given by:

$$[B] = \begin{bmatrix} \frac{\partial N_1}{\partial x} & 0 & \frac{\partial N_2}{\partial x} & 0 & \frac{\partial N_3}{\partial x} & 0 & \frac{\partial N_4}{\partial x} & 0 & 0 & 0 & 0 & 0 \\ 0 & \frac{\partial N_1}{\partial z} & 0 & \frac{\partial N_2}{\partial z} & 0 & \frac{\partial N_3}{\partial z} & 0 & \frac{\partial N_4}{\partial z} & 0 & 0 & 0 & 0 \\ \frac{\partial N_1}{\partial z} & \frac{\partial N_1}{\partial x} & \frac{\partial N_2}{\partial z} & \frac{\partial N_2}{\partial x} & \frac{\partial N_3}{\partial z} & \frac{\partial N_3}{\partial x} & \frac{\partial N_4}{\partial z} & \frac{\partial N_4}{\partial x} & 0 & 0 & 0 & 0 \\ 0 & 0 & 0 & 0 & 0 & 0 & 0 & 0 & N_1 & N_2 & N_3 & N_4 \end{bmatrix} \quad (8.25)$$

Using Equations (8.24) and (8.25) in the weak form of the equation (Equation (8.19)), and performing variational minimization, we get:

$$\begin{aligned} \{\delta u\}_e^T &\left(\int_V [N]^T \rho [N] dV \right) \{\ddot{u}\}_e \\ &+ \{\delta u\}_e^T \left(\int_V [B_u]^T [\hat{C}] [B_u] dV \right) \{u\}_e \\ &- \{\delta u\}_e^T \left(\int_V [B_u]^T \hat{e} [B_E] dV \right) \{E_z\}_e \\ &- \{\delta E_z\}_e^T \left(\int_V [B_E]^T [\hat{e}]^T [B_u] dV \right) \{u\}_e \\ &- \{\delta E_z\}_e^T \left(\int_V [B_E]^T \hat{\mu}_{33} [B_E] dV \right) \{E_z\}_e \\ &- \{\delta u\}_e^T \{F_c\} - \{\delta u\}_e^T \int_{S_1} [N]^T \{F_s\} dS_1 \\ &- \{\delta E_z\}_e^T \int_{S_2} [B_E]^T D_s dS_2 = 0 \end{aligned} \quad (8.26)$$

Since $\{\delta u\}_e$ and $\{\delta E_z\}_e$ are arbitrary, the above expression can be written in a concise matrix form as:

$$\begin{bmatrix} [M_{uu}] & [0] \\ [0] & [0] \end{bmatrix} \begin{Bmatrix} \{\ddot{u}\}_e \\ \{\dot{E}_z\}_e \end{Bmatrix} + \begin{bmatrix} [K_{uu}] & [K_{uE}] \\ [K_{uE}]^T & [K_{EE}] \end{bmatrix} \begin{Bmatrix} \{u\}_e \\ \{E_z\}_e \end{Bmatrix} = \begin{Bmatrix} \{F\}_e \\ \{q\}_e \end{Bmatrix} \quad (8.27)$$

The above equation is the elemental equilibrium in the discretized form, where $[M_{uu}]$ is the mass matrix, $[K_{uu}]$ is the stiffness matrix corresponding to the mechanical degrees of freedom, $[K_{uE}]$ is the stiffness matrix due to electromechanical coupling and $[K_{EE}]$ is the stiffness matrix due to the electrical degrees of freedom alone. Note that all of these matrices require the volume integral to be evaluated. Since the exact integration of these is most difficult to achieve, we resort to numerical integration (see Chapter 7, Section 7.6.3). Here, $\{F\}_e$ is the elemental nodal vector and $\{q\}_e$ is the elemental charge vector. These matrices are given by:

$$\begin{aligned} [M_{uu}] &= t \int_{-1}^1 \int_{-1}^1 [N]^T \rho [N] |J| d\xi d\eta \\ [K_{uu}] &= t \int_{-1}^1 \int_{-1}^1 [B_u]^T [\hat{C}] [B_u] |J| d\xi d\eta \\ [K_{uE}] &= -t \int_{-1}^1 \int_{-1}^1 [B_u]^T [\hat{e}] [B_E] |J| d\xi d\eta \\ [K_{EE}] &= t \int_{-1}^1 \int_{-1}^1 [B_E]^T \hat{\mu}_{33} [B_E] |J| d\xi d\eta \end{aligned} \quad (8.28)$$

The elemental load and charge vectors are given by:

$$\{F\}_e = \{F\}_c + \int_{S_1} [N]^T \{F\}_s dS_1, \quad \{q\}_e = - \int_{S_2} [N]^T D_s dS_2 \quad (8.29)$$

The matrices in Equation (8.27) are then assembled to obtain their global counterparts and solved for obtaining solutions for displacements and electric field. Note that this has a zero diagonal block in the mass matrix. The methods of solution for the sensing and actuation problems are quite different. For the sensing problem, for a given mechanical loading, we need to determine the voltage developed across the smart patch. This is done

by first obtaining the mechanical displacement due to the given mechanical load, which is then used to obtain the electric field and hence the voltage developed in the sensor patch. In order to solve this, the global matrix equation can be expanded and written as:

$$\begin{aligned} [M_{uu}] \{\ddot{u}\} + [K_{uu}] \{u\} + [K_{uE}] \{E_z\} &= \{F\} \\ [K_{uE}]^T \{u\} + [K_{EE}] \{E_z\} &= \{q\} \end{aligned} \quad (8.30)$$

We can write the second part of the above equation as:

$$\{E_z\} = [K_{EE}]^{-1} \{q\} - [K_{EE}]^{-1} [K_{uE}]^T \{u\} \quad (8.31)$$

Using the above equation in the first part of Equation (8.30) and simplifying, we get

$$[M_{uu}] \{\ddot{u}\} + [\bar{K}_{uu}] = \{\bar{F}\} \quad (8.32)$$

where:

$$\begin{aligned} [\bar{K}_{uu}] &= [K_{uu}] - [K_{uE}] [K_{EE}]^{-1} [K_{uE}]^T \\ \{\bar{F}\} &= \{F\} - [K_{EE}]^{-1} \{q\} \end{aligned} \quad (8.33)$$

Note that Equation (8.32) is only in terms of mechanical displacements, which can be solved by using the conventional solution techniques given in Chapter 7 (Section 7.7). Using this solution, electrical fields are obtained using Equation (8.31), from which the voltages can be obtained. For the actuation problem, the voltages and hence the electric fields go as input. That is, the second part of Equation (8.27) is not required. Hence, the equation that requires solution becomes:

$$[M_{uu}] \{\ddot{u}\} + [K_{uu}] \{u\} = \{F\} - [K_{uE}] \{E_z\} = \{F^*\} \quad (8.34)$$

If an arbitrary value of E_z is specified, the problem comes under the category of *open-loop control*. If the value of E_z comes from the sensor output that is fed back to the controller, then the control scheme is referred to as *closed-loop control*. These aspects are discussed in more detail in the next chapter.

8.2.4 Numerical example

In order to discuss the validity of the formulated four-noded quadrilateral element and to check its performance and behavior, a numerical example is presented. The results obtained from the formulated element are then compared with standard published results.

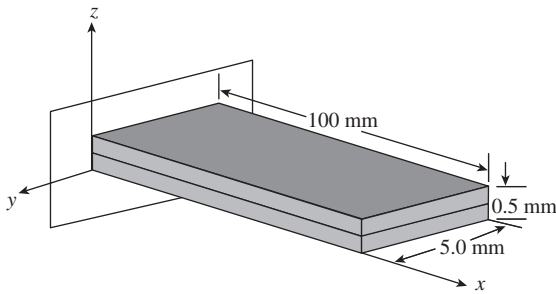


Figure 8.4 Schematic of the piezoelectric PVDF bimorph cantilever beam.

In this study, the modeling and static analysis of a piezoelectric bimorph composite beam is done using the formulated smart composite element. Chen *et al.* [1] presented a comparative study of the bending of a bimorph beam due to an external applied voltage as part of verifying the accuracy of the piezoelectric FE solution, with this bimorph beam configuration being adopted from Hwang and Park [2]. In this study, the same configuration of the bimorph beam is considered to verify the accuracy of the formulated FE. The bimorph beam consists of two identical PVDF beams laminated together with opposite polarities. A schematic diagram of the bimorph beam is shown in Figure 8.4. The dimensions of the beam are taken as 100 mm \times 5.0 mm \times 0.5 mm. The material properties of the PVDF bimorph beam are taken as being the same as that of Chen *et al.* [1] and are given in Table 8.1. The theoretical solution for transverse displacement for the above problem is presented in Chen *et al.* [1], and given by:

$$w(x) = 0.375 \frac{e_{31}V}{E} \left(\frac{x}{t}\right)^2 \quad (8.35)$$

Table 8.1 Material properties used in the numerical example.

Property	Value
Young's modulus, E_{11}	$0.2 \times 10^{10} \text{ N/m}^2$
Shear modulus, G_{12}	$0.775 \times 10^{10} \text{ N/m}^2$
Poisson's ratio, v_{12}	0.29
Poisson's ratio, v_{21}	0.28
Piezoelectric constant, e_{31}	0.046 C/m^2
Piezoelectric constant, e_{32}	0.046 C/m^2
Piezoelectric constant, e_{33}	0.0

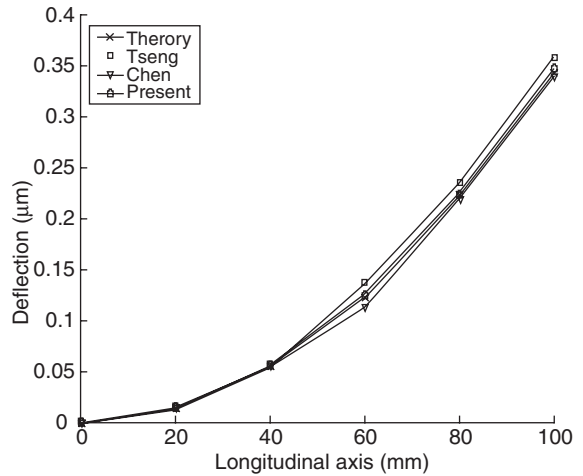


Figure 8.5 Centerline deflections for a PVDF bimorph beam under a unit voltage.

where V is the applied voltage and t is the thickness of the beam. This beam is modeled using 200 formulated elements along the $x-z$ plane. When an external active voltage is applied across the thickness, the induced strain generates control forces that bend the bimorph beam. A unit voltage is applied across the thickness and the deflections at the nodes are computed. The deflection of the beam along the central longitudinal axis obtained from the present formulation is compared with the theoretical value given by Equation (8.35) and the works of Chen *et al.* [1] and Tzou and Tseng [3], respectively. Figure 8.5 shows the comparison of deflection along the length of the beam for a unit voltage applied across the thickness.

Next, the deflection of the beam is calculated for different applied voltages over the range 0–200 V. The calculated deflections from the present study are compared with those of Chen *et al.* [1] and Tzou and Tseng [3] and Equation (8.35). Chen *et al.* [1] used a first-order shear-deformable plate finite element, while Tzou and Tseng [3] used hexahedral solid elements to model the same problem. These are plotted in Figure 8.6. Figure 8.7 shows the variation of the deflection along the central longitudinal axis for various values of applied voltages.

This problem solved here is associated with actuation with open-loop control. That is, for an electrical load caused by the voltage, strains are generated, which in turn cause deformations. In Figure 8.7, we can clearly see that greater voltages produce larger deformations. The results presented here show close agreement between the

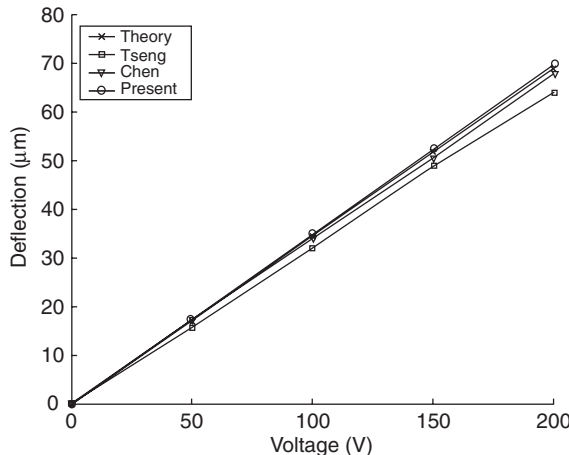


Figure 8.6 Tip deflection for a PVDF bimorph beam as a function of voltage.

theoretical and the formulated element and also with the established works. This present study has demonstrated the accuracy of the formulated element to handle problems involving electromechanical coupling.

8.3 SUPERCONVERGENT SMART THIN-WALLED BOX BEAM ELEMENT

The procedure for formulating a superconvergent FE was given in Chapter 7 (Section 7.8). In this section, a generic smart composite thin-walled beam element having an

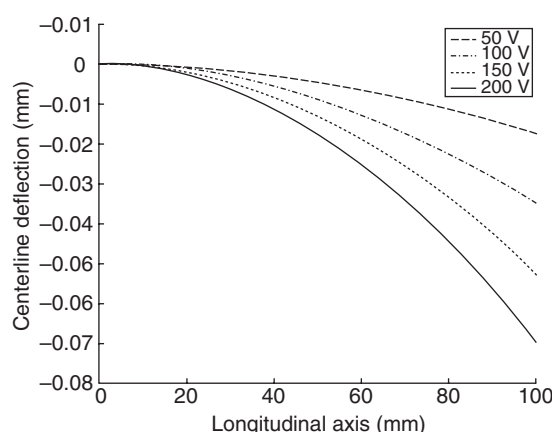


Figure 8.7 Deflection profile for a PVDF bimorph beam for various voltages.

arbitrary cross-section with open and closed contours is developed. This element will find its use in the modeling of aircraft structures, which are essentially thin-walled. The element uses higher-order interpolating polynomials that are derived by solving the static homogeneous coupled governing differential equation and hence predicts the exact elemental stiffness matrix and a electro-mechanically coupling matrix. Each node has seven degrees of freedom (dof) including extension, two in the bending dof in the span-wise and chord-wise directions, corresponding shears and twist and a single electrical dof.

First-order shear deformation theory is used for transverse shear deformation and out-of-plane torsional warping is modeled by using Vlasov theory. A higher-order interpolating polynomial for twist eliminates the need of a separate dof for the resulting restrained torsional warping. The element is then validated by comparing the electrically actuated response of different smart beam configurations to those available in the literature. The fundamental aspect of the superconvergent finite element formulation is the interpolating polynomials that satisfy the static part of the governing equation exactly. Hence, deriving the governing differential equation is the first step in the formulation of this element. This is taken up in the next subsection.

8.3.1 Governing equation for a thin-walled smart composite beam

The general coordinate system for deriving the governing equation is shown in Figure 8.8. The proposed element is assumed to undergo three translations and three rotations. From geometrical considerations and assuming the

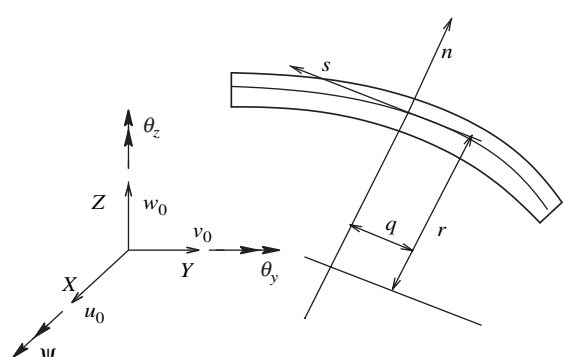


Figure 8.8 General coordinate system adopted for the box-beam element formulation.

in-plane deformation to be very small, the beam displacement field considering *First-Order Shear Deformation Theory* (FSDT) and Vlasov theory for torsion can be written as:

$$\begin{aligned} w(s) &= v_0 \frac{\partial z}{\partial s} - w_0 \frac{\partial y}{\partial s} - q\psi \\ v(s) &= v_0 \frac{\partial y}{\partial s} + w_0 \frac{\partial z}{\partial s} + r\psi \\ u(s) &= u_0 + z\theta_y + y\theta_z + \varphi \frac{\partial \psi}{\partial x} \end{aligned} \quad (8.36)$$

where u_0 , v_0 and w_0 are the displacements in the x , y and z directions; ψ , θ_y and θ_z are the rotations about the x , y and z directions (see Figure 8.8). The torsional warping function φ for a closed cross-section of wall thickness t is expressed as in Megson [4].

$$\varphi = - \int_0^s r ds + 2A_e \frac{\delta_{os}}{\delta}, \quad \delta_{os} = \int_0^s \frac{ds}{Gt}, \quad \delta = \oint \frac{ds}{Gt} \quad (8.37)$$

where A_e is the cross-sectional area enclosed by the mid-line contour, G is the shear modulus, r is the radius, s is the tangential coordinate and n is the normal coordinate. For open contours, neglecting secondary warping, φ is given by:

$$\varphi = - \int_0^s r ds \quad (8.38)$$

The relevant strains are the axial strain ε_{xx} and the two shear strains, which are given by:

$$\varepsilon_{xx} = \frac{\partial u}{\partial x} = \frac{\partial u_0}{\partial x} + z \frac{\partial \theta_y}{\partial x} + y \frac{\partial \theta_z}{\partial x} + \varphi \frac{\partial^2 \psi}{\partial x^2} \quad (8.39)$$

$$\begin{aligned} \gamma_{xs} &= \frac{\partial u}{\partial s} + \frac{\partial v}{\partial x} = \left[\left(\frac{\partial w_0}{\partial x} + \theta_y \right) \frac{\partial z}{\partial s} + \left(\frac{\partial v_0}{\partial x} + \theta_z \right) \frac{\partial y}{\partial s} \right] \\ &\quad + \left[\left(r - \frac{\partial \varphi}{\partial s} \right) \frac{\partial \psi}{\partial x} \right] \end{aligned} \quad (8.40)$$

$$\begin{aligned} \gamma_{xn} &= \frac{\partial u}{\partial n} + \frac{\partial w}{\partial x} = \left[\left(\theta_z \frac{\partial y}{\partial n} - \frac{\partial w_0}{\partial x} \frac{\partial y}{\partial s} \right) \right. \\ &\quad \left. + \left(\theta_y \frac{\partial z}{\partial n} + \frac{\partial v_0}{\partial x} \frac{\partial z}{\partial s} \right) \right] - \left[\left(q + \frac{\partial \varphi}{\partial n} \right) \frac{\partial \psi}{\partial x} \right] \end{aligned} \quad (8.41)$$

The last square brackets in Equations (8.40) and (8.41) are due to torsional displacement, which are normally quite small and hence neglected in the present formulation. A state of plane stress is assumed and a reduction procedure as adopted in Chapter 7 (Section 7.2.1) is again done here starting from the 3-D constitutive model given in Equation (8.8) to arrive at the required constitutive relations, which can be written for smart laminated thin-walled structures as:

$$\begin{Bmatrix} \sigma_{xx} \\ \tau_{xs} \\ \tau_{xn} \end{Bmatrix} = \begin{bmatrix} \hat{C}_{11} & \hat{C}_{16} & 0 \\ \hat{C}_{16} & \hat{C}_{66} & 0 \\ 0 & 0 & \hat{C}_{55} \end{bmatrix} \begin{Bmatrix} \varepsilon_{xx} \\ \gamma_{xs} \\ \gamma_{xn} \end{Bmatrix} - \begin{bmatrix} \hat{e}_{31} \\ \hat{e}_{36} \\ 0 \end{bmatrix} E \quad (8.42)$$

where:

$$\begin{aligned} \hat{C}_{11} &= \bar{C}_{11} - \frac{\bar{C}_{12}^2}{\bar{C}_{22}}, & \hat{C}_{16} &= \bar{C}_{16} - \frac{\bar{C}_{12}\bar{C}_{26}}{\bar{C}_{22}}, \\ \hat{C}_{66} &= \bar{C}_{66} - \frac{\bar{C}_{26}^2}{\bar{C}_{22}}, & \hat{C}_{55} &= \bar{C}_{55} - \frac{\bar{C}_{45}^2}{\bar{C}_{44}} \\ \hat{e}_{31} &= \bar{e}_{31} - \frac{\bar{C}_{12}\bar{e}_{32}}{\bar{C}_{22}}, & \hat{e}_{36} &= \bar{e}_{36} - \frac{\bar{C}_{26}\bar{e}_{32}}{\bar{C}_{22}} \end{aligned} \quad (8.43)$$

The equations of motion are derived using Hamilton's Principle for which it is necessary to write down all of the energies associated with the problem, expressed in terms of deformations. That is, there are three energies associated with the problem, namely the strain energy, kinetic energy and the energy due to electrical degrees of freedom, which can be written as:

$$\begin{aligned} U &= \frac{1}{2} \int_0^L \int_A \left(\sigma_{xx} \varepsilon_{xx} + \tau_{xs} \gamma_{xs} + \tau_{xn} \gamma_{xn} \right) dA dx, \\ T &= \frac{1}{2} \int_0^L \int_A \left(\dot{u}^2 + \dot{v}^2 + \dot{w}^2 \right) dA dx \\ U_E &= \frac{1}{2} \int_0^L \int_A E D dA dx \end{aligned} \quad (8.44)$$

where E is the electrical field, D is the electrical displacement and L is the length of the beam. Applying Hamilton's principle, we get seven highly coupled partial differential equations corresponding to seven degrees of freedom.

freedom, which are given by:

$$\begin{aligned} I_0 \frac{\partial^2 u_0}{\partial t^2} + I_1 \frac{\partial^2 \theta_y}{\partial t^2} + \bar{I}_1 \frac{\partial^2 \theta_z}{\partial t^2} + I_\varphi \frac{\partial^3 \psi}{\partial x \partial t^2} - A_{11} \frac{\partial^2 u_0}{\partial x^2} \\ - A_{ys16} \frac{\partial^2 v_0}{\partial x^2} - A_{zs16} \frac{\partial^2 w_0}{\partial x^2} - A_{\psi11} \frac{\partial^3 \psi}{\partial x^3} \\ - A_{z16} \frac{\partial^2 \psi}{\partial x^2} - B_{11} \frac{\partial^2 \theta_y}{\partial x^2} - A_{zs16} \frac{\partial \theta_y}{\partial x} - B_{11} \frac{\partial^2 \theta_z}{\partial x^2} \\ - A_{ys16} \frac{\partial \theta_z}{\partial x} + A_{e31} \frac{\partial E}{\partial x} = 0 \end{aligned} \quad (8.45)$$

$$\begin{aligned} (I_{zs}^2 + I_{ys}^2) \frac{\partial^2 v_0}{\partial t^2} - (I_{zsq}^2 - I_{ysr}^2) \frac{\partial^2 \psi}{\partial t^2} - A_{ys16} \frac{\partial^2 u_0}{\partial x^2} \\ - (A_{ys66}^2 + A_{zs66}^2) \frac{\partial^2 v_0}{\partial x^2} \\ - (A_{zsys66} - A_{zsyz55}) \frac{\partial^2 w_0}{\partial x^2} + A_{ys\varphi16} \frac{\partial^3 \psi}{\partial x^3} - A_{ysz16} \frac{\partial^2 \psi}{\partial x^2} \\ - B_{ys16} \frac{\partial^2 \theta_y}{\partial x^2} - (A_{zsys66} - A_{zsyz55}) \frac{\partial \theta_y}{\partial x} - \bar{B}_{ys16} \frac{\partial^2 \theta_z}{\partial x^2} \\ - (A_{ys66}^2 + A_{yng55}) \frac{\partial \theta_z}{\partial x} + A_{e36ys} \frac{\partial E}{\partial x} = 0 \end{aligned} \quad (8.46)$$

$$\begin{aligned} (I_{zs}^2 + I_{ys}^2) \frac{\partial^2 w_0}{\partial t^2} + (I_{ysq} + I_{zsq}) \frac{\partial^2 \psi}{\partial t^2} - A_{zs16} \frac{\partial^2 u_0}{\partial x^2} \\ - (A_{yszs66} - A_{yszs55}) \frac{\partial^2 v_0}{\partial x^2} - (A_{zs66}^2 + A_{ys66}^2) \frac{\partial^2 w_0}{\partial x^2} \\ + A_{zs\varphi16} \frac{\partial^3 \psi}{\partial x^3} - A_{zs266} \frac{\partial^2 \psi}{\partial x^2} - B_{zs16} \frac{\partial^2 \theta_y}{\partial x^2} \\ - (A_{zs66}^2 - A_{yszn55}) \frac{\partial \theta_y}{\partial x} - \bar{B}_{zs16} \frac{\partial^2 \theta_z}{\partial x^2} \\ - (A_{yszs66} - A_{yng55}) \frac{\partial \theta_z}{\partial x} + A_{e36zs} \frac{\partial E}{\partial x} = 0 \end{aligned} \quad (8.47)$$

$$\begin{aligned} - I_\varphi \frac{\partial^3 u_0}{\partial x \partial t^2} - (I_{zsq} - I_{ysr}) \frac{\partial^2 v_0}{\partial t^2} + (I_{ysq} + I_{zsq}) \frac{\partial^2 w_0}{\partial t^2} \\ + (I_{q^2} + I_{r^2}) \frac{\partial^2 \psi}{\partial t^2} - I_{\varphi^2} \frac{\partial^4 \psi}{\partial t^2 \partial x^2} + I_{z\varphi} \frac{\partial^3 \theta_y}{\partial x \partial t^2} \\ + I_{y\varphi} \frac{\partial^3 \theta_z}{\partial x \partial t^2} - A_{\varphi11} \frac{\partial^3 u_0}{\partial x^3} - A_{z16} \frac{\partial^2 u_0}{\partial x^2} - A_{ys\varphi16} \frac{\partial^3 v_0}{\partial x^3} \\ - A_{ys266} \frac{\partial^2 v_0}{\partial x^2} - A_{zs\varphi16} \frac{\partial^3 w_0}{\partial x^3} - A_{zs266} \frac{\partial^2 w_0}{\partial x^2} + A_{\varphi211} \frac{\partial^4 \psi}{\partial x^4} \\ - A_{x^266} \frac{\partial^2 \psi}{\partial x^2} - B_{\varphi11} \frac{\partial^3 \theta_y}{\partial x^3} - (B_{z16} + A_{zs\varphi16}) \frac{\partial^2 \theta_y}{\partial x^2} \\ - A_{zs266} \frac{\partial \theta_y}{\partial x} - \bar{B}_{\varphi11} \frac{\partial^3 \theta_z}{\partial x^3} - (\bar{B}_{z16} + A_{zs\varphi16}) \frac{\partial^2 \theta_z}{\partial x^2} \\ - A_{ys266} \frac{\partial \theta_z}{\partial x} + A_{e31\varphi} \frac{\partial^2 E}{\partial x^2} + A_{e36\lambda} \frac{\partial E}{\partial x} = 0 \end{aligned} \quad (8.48)$$

$$\begin{aligned} I_1 \frac{\partial^2 u_0}{\partial t^2} + I_2 \frac{\partial^2 \theta_y}{\partial t^2} + \bar{I}_2 \frac{\partial^2 \theta_z}{\partial t^2} - I_{2\varphi} \frac{\partial^3 \psi}{\partial t^2 \partial x} \\ - B_{11} \frac{\partial^2 u_0}{\partial x^2} + A_{zs16} \frac{\partial u_0}{\partial x} - B_{ys16} \frac{\partial^2 v_0}{\partial x^2} \\ + (A_{yszs66} + A_{zsyz55}) \frac{\partial v_0}{\partial x} - B_{zs16} \frac{\partial^2 w_0}{\partial x^2} \\ + (A_{zs66}^2 + A_{ysyz55}) \frac{\partial w_0}{\partial x} + B_{\varphi11} \frac{\partial^3 \psi}{\partial x^3} \\ - (A_{ys\varphi16} + B_{z16}) \frac{\partial^2 \psi}{\partial x^2} + A_{zs266} \frac{\partial \psi}{\partial x} - D_{11} \frac{\partial^2 \theta_y}{\partial x^2} \\ + (A_{zs66}^2 + A_{zn55}) \theta_y - \bar{D}_{11} \frac{\partial^2 \theta_z}{\partial x^2} \\ - (B_{ys16} - \bar{B}_{zs16}) \frac{\partial \theta_z}{\partial x} + (A_{yszs66} + A_{yng55}) \theta_z \\ + B_{e31} \frac{\partial E}{\partial x} - A_{e36zs} E = 0 \end{aligned} \quad (8.49)$$

$$\begin{aligned} \bar{I}_1 \frac{\partial^2 u_0}{\partial t^2} + \bar{I}_2 \frac{\partial^2 \theta_y}{\partial t^2} + \bar{I}_2 \frac{\partial^2 \theta_z}{\partial t^2} - I_{y\varphi} \frac{\partial^3 \psi}{\partial t^2 \partial x} \\ - \bar{B}_{11} \frac{\partial^2 u_0}{\partial x^2} + A_{ys16} \frac{\partial u_0}{\partial x} - \bar{B}_{ys16} \frac{\partial^2 v_0}{\partial x^2} \\ + (A_{ys66}^2 + A_{zsyn55}) \frac{\partial v_0}{\partial x} - \bar{B}_{zs16} \frac{\partial^2 w_0}{\partial x^2} \\ + (A_{zs66}^2 - A_{ysyn55}) \frac{\partial w_0}{\partial x} + \bar{B}_{\varphi11} \frac{\partial^3 \psi}{\partial x^3} \\ - (A_{ys\varphi16} + \bar{B}_{z16}) \frac{\partial^2 \psi}{\partial x^2} + A_{ys266} \frac{\partial \psi}{\partial x} - \bar{D}_{11} \frac{\partial^2 \theta_y}{\partial x^2} \\ + (A_{zsys66} + A_{yng55}) \theta_y - \bar{D}_{11} \frac{\partial^2 \theta_z}{\partial x^2} \\ + (B_{ys16} - \bar{B}_{zs16}) \frac{\partial \theta_y}{\partial x} + (A_{ysys66} + A_{zny55}) \theta_y \\ + \bar{B}_{e31} \frac{\partial E}{\partial x} - A_{e36ys} E = 0 \end{aligned} \quad (8.50)$$

$$\begin{aligned} A_{e31} \frac{\partial u_0}{\partial x} + A_{e36ys} \frac{\partial v_0}{\partial x} + A_{e36zs} \frac{\partial w_0}{\partial x} \\ - A_{e36\varphi} \frac{\partial^2 \psi}{\partial x^2} + A_{e36\lambda} \frac{\partial \psi}{\partial x} + B_{e31} \frac{\partial \theta_y}{\partial x} \\ + A_{e36zs} \theta_y + \bar{B}_{e31} \frac{\partial \theta_z}{\partial x} + A_{e36ys} \theta_z + A_{\mu33} E = 0 \end{aligned} \quad (8.51)$$

where the stiffness constants are given by:

$$\begin{aligned} & \left[A_{f(s,n)ij}, B_{f(s,n)ij}, \bar{B}_{f(s,n)ij}, D_{f(s,n)ij}, \bar{D}_{f(s,n)ij}, \bar{\bar{D}}_{f(s,n)ij} \right] \\ &= \int_s \int_n \hat{C}_{ijf}(s, n) [1, z, y, z^2, y^2, yz] ds dn \end{aligned}$$

and:

$$f(s, n) \in \left[1, z_s, y_s, z_n, y_n, r, q, \varphi, \left(r - \frac{\partial \varphi}{\partial s} \right) \right]$$

Here, $(r - \partial \varphi / \partial s)$ is taken equal to α . The stiffness coefficients associated with smart or electrical degrees of freedom are given by:

$$\begin{aligned} [A_{eijf(s,n)}, B_{eijf(s,n)}, \bar{B}_{eijf(s,n)}] &= \int_s^n \hat{e}_{ijf}(s, n) [1, z, y] ds dn, \\ A_{\mu 33} &= \int_s^n \hat{\mu}_{33} ds dn \end{aligned}$$

Hamilton's principle will also give the six essential (force) boundary conditions, which are necessary for the element formulations. These essential boundary conditions are given by:

$$\begin{aligned} A_{11} \frac{\partial u_0}{\partial x} + A_{ys16} \frac{\partial v_0}{\partial x} + A_{zs16} \frac{\partial w_0}{\partial x} \\ - A_{\varphi 11} \frac{\partial^2 \psi}{\partial x^2} + A_{z16} \frac{\partial \psi}{\partial x} + B_{11} \frac{\partial \theta_y}{\partial x} + A_{zs16} \theta_y \\ + \bar{B}_{11} \frac{\partial \theta_z}{\partial x} + A_{ys16} \theta_z - A_{e31} E = P \end{aligned} \quad (8.52)$$

$$\begin{aligned} A_{ys16} \frac{\partial u_0}{\partial x} + (A_{ys^266} + A_{zs^255}) \frac{\partial v_0}{\partial x} \\ + (A_{zsyz66} + A_{zsyz55}) \frac{\partial w_0}{\partial x} - A_{ys\varphi 16} \frac{\partial^2 \psi}{\partial x^2} \\ + A_{ysz66} \frac{\partial \psi}{\partial x} + B_{ys16} \frac{\partial \theta_y}{\partial x} + (A_{zsyz66} + A_{zsxn55}) \theta_y \\ + \bar{B}_{ys16} \frac{\partial \theta_z}{\partial x} + (A_{ys^266} + A_{ynz55}) \theta_z \\ - A_{e36ys} E = V_y \end{aligned} \quad (8.53)$$

$$\begin{aligned} A_{zs16} \frac{\partial u_0}{\partial x} + (A_{yzsz66} - A_{yzsz55}) \frac{\partial v_0}{\partial x} \\ + (A_{zs^266} + A_{ys^255}) \frac{\partial w_0}{\partial x} - A_{zs\varphi 16} \frac{\partial^2 \psi}{\partial x^2} \\ + A_{zsyz66} \frac{\partial \psi}{\partial x} + B_{zs16} \frac{\partial \theta_y}{\partial x} + (A_{zs^266} - A_{yszn55}) \theta_y \\ + \bar{B}_{zs16} \frac{\partial \theta_z}{\partial x} + (A_{yzsz66} - A_{ynys55}) \theta_z \\ - A_{e36zs} E = V_z \end{aligned} \quad (8.54)$$

$$\begin{aligned} A_{\varphi 11} \frac{\partial^2 u_0}{\partial x^2} + A_{z16} \frac{\partial u_0}{\partial x} + A_{ys\varphi 16} \frac{\partial^2 v_0}{\partial x^2} + A_{ysz66} \frac{\partial v_0}{\partial x} \\ + A_{zs\varphi 16} \frac{\partial^2 w_0}{\partial x^2} + A_{zsyz66} \frac{\partial w_0}{\partial x} \\ - A_{\varphi^2 11} \frac{\partial^3 \psi}{\partial x^3} + A_{z^2 66} \frac{\partial \psi}{\partial x} + B_{\varphi 11} \frac{\partial^2 \theta_y}{\partial x^2} \\ + (B_{z16} + A_{zs\varphi 16}) \frac{\partial \theta_y}{\partial x} + A_{zsyz66} \theta_y \\ + \bar{B}_{\varphi 11} \frac{\partial^2 \theta_z}{\partial x^2} + (\bar{B}_{z16} + A_{ysz66}) \theta_z - A_{e31\varphi} \frac{\partial E}{\partial x} \\ - A_{e36z} E = T \end{aligned} \quad (8.55)$$

$$\begin{aligned} B_{11} \frac{\partial u_0}{\partial x} + B_{ys16} \frac{\partial v_0}{\partial x} + B_{zs16} \frac{\partial w_0}{\partial x} - B_{\varphi 11} \frac{\partial^2 \psi}{\partial x^2} \\ + B_{z16} \frac{\partial \psi}{\partial x} + D_{11} \frac{\partial \theta_y}{\partial x} + B_{zs16} \theta_y \\ + \bar{D}_{11} \frac{\partial \theta_z}{\partial x} + B_{ys16} \theta_z - B_{e31} E = M_y \end{aligned} \quad (8.56)$$

$$\begin{aligned} \bar{B}_{11} \frac{\partial u_0}{\partial x} + \bar{B}_{ys16} \frac{\partial v_0}{\partial x} + \bar{B}_{zs16} \frac{\partial w_0}{\partial x} - \bar{B}_{\varphi 11} \frac{\partial^2 \psi}{\partial x^2} \\ + \bar{B}_{z16} \frac{\partial \psi}{\partial x} + \bar{D}_{11} \frac{\partial \theta_y}{\partial x} + \bar{B}_{zs16} \theta_y \\ + \bar{D}_{11} \frac{\partial \theta_z}{\partial x} + \bar{B}_{ys16} \theta_z - \bar{B}_{e31} E = M_z \end{aligned} \quad (8.57)$$

These governing equations and the associated boundary conditions will be used for finite element formulation.

8.3.2 Finite element formulation

The proposed element is a two-noded box beam element and each node has three translational degrees of freedom, namely the u , v and w displacement components, three rotational degrees of freedom, namely θ_y , θ_z and ψ , and one electrical degree of freedom, E . These are shown in Figure 8.9.

The first task here is to solve the static part of the governing equation exactly and use this solution as interpolating functions for FE formulation. However, the static part of the governing equations (Equations (8.45)–(8.51)) is highly coupled and complex and needs careful analysis before one assumes a solution that could be nearly exact. Looking at the governing differential equations, we see that the axial displacement (u_0) and slopes about the y - and z -axis (θ_y and θ_z) require a quadratic polynomial while the lateral and transverse displacements (v_0 and w_0) and the rotation

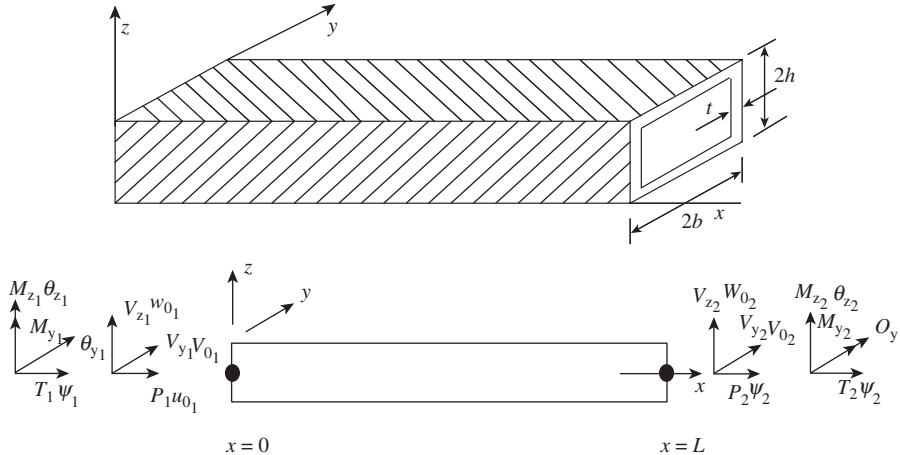


Figure 8.9 Schematic of a thin-walled box beam with nodal degrees of freedom.

about the longitudinal axis (twist ψ) require cubic polynomials.

Assuming a polynomial variation for the electrical degree of freedom is very involved. Here, we assume that the electrical degree of freedom will be prevalent only in those regions where the structures have these smart PZT patches, which are normally of small length over a small area and hence variation of the electrical field over this small length can be assumed constant. This amounts to assuming that all of the gradients of the electric field are equal to zero. Hence, we can assume the solution to the governing equation as:

$$\begin{aligned} u_0(x) &= a_1 + a_2x + a_3x^2, \\ v_0(x) &= a_4 + a_5x + a_6x^2 + a_7x^3 \\ w_0(x) &= a_8 + a_9x + a_{10}x^2 + a_{11}x^3, \\ \psi(x) &= a_{12} + a_{13}x + a_{14}x^2 + a_{15}x^3 \\ \theta_y(x) &= a_{16} + a_{17}x + a_{18}x^2, \\ \theta_z(x) &= a_{19} + a_{20}x + a_{21}x^2, \quad E(x) = a_e \end{aligned} \quad (8.58)$$

There are a total of twenty two constants in the assumed solutions. However, there are only twelve mechanical degrees of freedom. All of the other nine constants in the mechanical displacement field are dependent constants. The dependent constants and the constant associated with the electric field can be obtained in terms of the independent constants by substituting the assumed displacement field (Equation 8.58) into the electromechanically

coupled governing equations (Equations (8.45)–(8.51)). Here, two vectors are introduced, $\{a\}$ and $\{\bar{a}\}$, where the former contains all the unknown constants, while the latter contains all the dependent constants. These can be written as:

$$\{a\} = \{a_1 \ a_2 \ a_4 \ a_5 \ a_8 \ a_9 \ a_{12} \ a_{13} \ a_{16} \ a_{17} \ a_{19} \ a_{20}\}^T \quad (8.59)$$

$$\{\bar{a}\} = \{\{a_u\} \ a_e\}^T = \{a_3 \ a_6 \ a_7 \ a_{10} \ a_{11} \ a_{14} \ a_{15} \ a_{18} \ a_{21} \ a_e\}^T \quad (8.60)$$

We first establish the relationship between the dependent and independent coefficients by substituting the assumed field in the governing equations. This can be written as:

$$[A_1]\{\bar{a}\} = [A_2]\{a\} \quad (8.61)$$

where $[A_1]$ and $[A_2]$ are matrices dependent on the material properties. These are of sizes 10×10 and 10×12 , respectively. Inverting the above relation and rewriting the above relation:

$$\begin{aligned} \{\bar{a}\} &= \left\{ \begin{array}{c} \{a_u\} \\ a_e \end{array} \right\} = [A_1]^{-1}[A_2]\{a\} = \left[\begin{array}{c} [A] \\ [A_E] \end{array} \right]\{a\} \\ \{a_u\} &= [A]\{a\}, \quad a_e = [A_E]\{a\} \end{aligned} \quad (8.62)$$

The matrices $[A_1]$ and $[A_2]$ can be found in Mira Mitra [5]. Matrices $[A]$ and $[A_E]$ are evaluated by inverting

matrix $[A_1]$ numerically. Evaluation of these matrices will help in writing the displacement field only in terms of the unknown independent coefficients $\{a\}$.

The next step is to evaluate the exact shape functions. For this, we need to define the nodal mechanical degrees of freedom vector, which is given by:

$$\{u\}_e = \begin{bmatrix} u_{01} & v_{01} & w_{01} & \psi_1 & \theta_{y1} & \theta_{z1} & u_{02} \\ v_{02} & w_{02} & \psi_2 & \theta_{y2} & \theta_{z2} \end{bmatrix}^T \quad (8.63)$$

The displacement field is evaluated at the two nodes of the box beam element located at $x = 0$ and at $x = L$. This enables us to write the nodal degrees of freedom in terms of the unknown coefficients as:

$$\{u\}_e = [R]\{a\} \quad (8.64)$$

Inverting the above equation, we get:

$$\{a\} = [R]^{-1}\{u\}_e = [B]\{u\}_e \quad (8.65)$$

Similarly, we can express the electric field in terms of mechanical nodal displacements. For this, we use Equation (8.62) and (8.65), from which we can write:

$$a_e = [A_E]\{a\} = [A_E][B]\{u\}_e = [K_s]\{u_e\} \quad (8.66)$$

Next, we use the six force boundary conditions given in Equations (8.52)–(8.57) and express them in terms of nodal forces, that is:

$$\begin{aligned} P(0) &= -P_1, & V_y(0) &= -V_{y1}, & V_z(0) &= -V_{z1}, \\ T(0) &= -T_1, & M_y(0) &= -M_{y1}, & M_z(0) &= -M_{z1} \\ P(L) &= P_2, & V_y(L) &= V_{y2}, & V_z(L) &= V_{z2}, \\ T(L) &= T_2, & M_y(L) &= M_{y2}, & M_z(L) &= M_{z2} \end{aligned}$$

Substituting these in the six force boundary conditions (Equations (8.52)–(8.57)), we can write the nodal force vector as:

$$\{F\} = [C]\{a\} - [K_A]E \quad (8.67)$$

where the matrix $[K_A]$ is of the form:

$$[K_A] = \begin{bmatrix} -A_{e31} & -A_{e36ys} & -A_{e36zs} & -A_{e36x} & -A_{e31} & -\bar{B}_{e31} \\ A_{e31} & A_{e36ys} & A_{e36zs} & A_{e36x} & A_{e31} & -\bar{B}_{e31} \end{bmatrix} \quad (8.68)$$

$[K_A]$ is the electromechanical coupling matrix which gives the expression for the actuating force due to the

electric field E applied to the PZT patch. Substituting for $\{a\}$ from Equation (8.65) into Equation (8.67), we get:

$$\begin{aligned} \{F\} &= [C]\{B\}\{u\}_e - [K_A]E \Rightarrow [K]\{u\}_e - [K_A]E \\ \text{or } \{F\} + [K_A]E &= [K]\{u\}_e \end{aligned} \quad (8.69)$$

Here, $[K]$ is the exact static stiffness matrix, which is derived from the interpolating polynomials that exactly satisfy the governing differential equations.

8.3.3 Formulation of consistent mass matrix

The consistent mass matrix for this element is obtained by using the material-dependent shape functions $[N]$ and is given by:

$$[M] = \int_0^L \int_A \rho [N]^T [N] dnds \quad (8.70)$$

Hence, it is necessary to first establish the shape functions. For this, we use Equation (8.65) in the interpolating polynomials given by Equation (8.58) and these can be written as:

$$\begin{aligned} u_0(x) &= [1 \quad x \quad 0 \quad 0] \{a\} \\ &\quad + [x^2 \quad 0 \quad 0] [A]\{a\} \\ v_0(x) &= [0 \quad 0 \quad 1 \quad x \quad 0 \quad 0] \{a\} \\ &\quad + [0 \quad x^2 \quad x^3 \quad 0 \quad 0 \quad 0 \quad 0 \quad 0 \quad 0] [A]\{a\} \\ w_0(x) &= [0 \quad 0 \quad 0 \quad 0 \quad 1 \quad x \quad 0 \quad 0 \quad 0 \quad 0 \quad 0 \quad 0] \{a\} \\ &\quad + [0 \quad 0 \quad 0 \quad x^2 \quad x^3 \quad 0 \quad 0 \quad 0 \quad 0] [A]\{a\} \\ \psi(x) &= [0 \quad 0 \quad 0 \quad 0 \quad 0 \quad 0 \quad 1 \quad x \quad 0 \quad 0 \quad 0 \quad 0] \{a\} \\ &\quad + [0 \quad 0 \quad 0 \quad 0 \quad 0 \quad x^2 \quad x^3 \quad 0 \quad 0] [A]\{a\} \\ \theta_y(x) &= [0 \quad 0 \quad 1 \quad x \quad 0 \quad 0] \{a\} \\ &\quad + [0 \quad 0 \quad 0 \quad 0 \quad 0 \quad 0 \quad 0 \quad x^2 \quad 0] [A]\{a\} \\ \theta_z(x) &= [0 \quad 0 \quad 1 \quad x \quad 0] \{a\} \\ &\quad + [0 \quad 0 \quad x^2] [A]\{a\} \end{aligned} \quad (8.71)$$

Using $\{a\}$ from Equation (8.65) in the above equation, we can write the displacement vector as:

$$\{u\} = [N]\{u\}, \quad [N] = [N_u \quad N_v \quad N_w \quad N_\psi \quad N_{\theta_y} \quad N_{\theta_z}] \quad (8.72)$$

where $[N_u \quad N_v \quad N_w \quad N_\psi \quad N_{\theta_y} \quad N_{\theta_z}]$ are the shape functions corresponding to the six displacement fields.

Equation (8.72) is then substituted into Equation (8.70) to get the mass matrix, which becomes:

$$\begin{aligned}
 [M] = & I_0 \int_0^L [N_u]^T [N_u] dx \\
 & + \left(I_{zs^2} + I_{ys^2} \right) \int_0^L \left([N_v]^T [N_v] + [N_w]^T [N_w] \right) dx \\
 & - (I_{zsq} - I_{ysr}) \int_0^L \left([N_v]^T [N_\psi] + [N_\psi]^T [N_v] \right) dx \\
 & + (I_{zsr} + I_{ysq}) \int_0^L \left([N_w]^T [N_\psi] + [N_\psi]^T [N_w] \right) dx \\
 & + (I_{r^2} + I_{q^2}) \int_0^L \left([N_\psi]^T [N_\psi] \right) dx + I_2 \int_0^L [N_{\theta_y}]^T [N_{\theta_y}] dx \\
 & + \bar{I}_2 \int_0^L [N_{\theta_z}]^T [N_{\theta_z}] dx + \bar{I}_1 \int_0^L \left([N_{\theta_z}]^T [N_u] + [N_u]^T [N_{\theta_z}] \right) dx \\
 & + I_1 \int_0^L \left([N_{\theta_y}]^T [N_u] + [N_u]^T [N_{\theta_y}] \right) dx \\
 & + \bar{I}_2 \int_0^L \left([N_{\theta_y}]^T [N_{\theta_z}] + [N_{\theta_z}]^T [N_{\theta_y}] \right) dx \\
 & + I_{1\varphi} \int_0^L \left([N_{\theta_y}]^T [N_{\psi,x}] - [N_{\theta_y,x}]^T [N_\psi] \right) dx
 \end{aligned}$$

$$\begin{aligned}
 & \bar{I}_{1\varphi} \int_0^L \left([N_{\theta_z}]^T [N_{\psi,x}] - [N_{\theta_z,x}]^T [N_\psi] \right) dx \\
 & - I_\varphi \int_0^L \left([N_u]^T [N_{\psi,x}] - [N_\psi]^T [N_{u,x}] \right) dx \\
 & - I_{\varphi^2} \int_0^L [N_\psi]^T [N_{\psi,xx}] dx
 \end{aligned} \quad (8.73)$$

where the inertial constants are given by:

$$\begin{aligned}
 & [I_0, I_1, \bar{I}_1, I_2, \bar{I}_2, I_{f(s,n)}] \\
 & = \int_s \int_n \rho [1, z, y, z^2, y^2, ys, f(s, n)] ds dn
 \end{aligned}$$

8.3.4 Numerical experiments

The performance of the formulated element is first examined for an open-loop response due to electrical actuation. The static and dynamic responses are then compared with the experimental and numerical results available in the literature.

The static analysis is performed on a bimorph PVDF (piezoelectric poly(vinylidene fluoride)) cantilever beam due to an applied voltage of 1 V using the formulated element. The beam has two layers of PVDF with opposite polarities for bending actuation. The dimensions of the beam are shown in Figure 8.10. The PVDF material has a Young's modulus of 2 GPa, a Poisson's ratio of 0.29 and a density of 1800 kg/m³. It also has piezoelectric coefficients $d_{31} = d_{32} = 2.2 \times 10^{-11}$ m/V. The

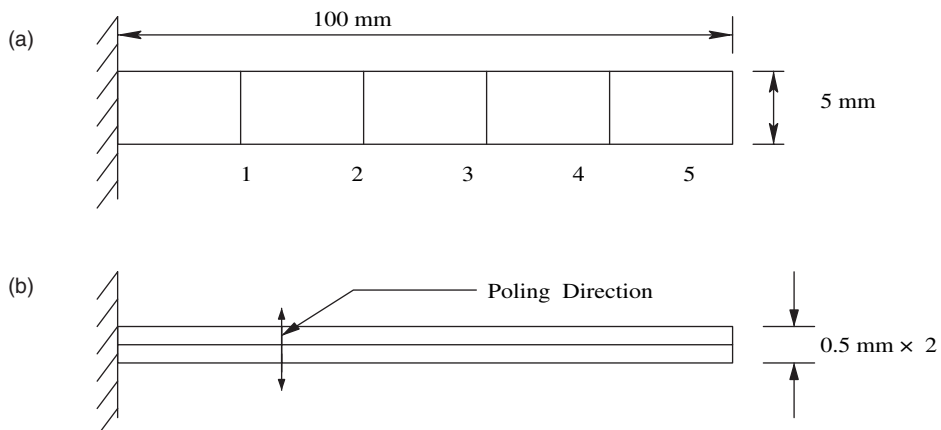


Figure 8.10 Schematic of a PVDF bimorph beam for static analysis: (a) top view; (b) side view.

Table 8.2 Comparison of the results obtained for a PVDF bimorph beam with literature values (all entries $\times 10^{-7}$ m).

Nodes	1	2	3	4	5
Experiment [6]	—	—	—	—	3.15
Solid FE [3]	0.124	0.508	1.16	2.10	3.30
Shell FE [7]	0.132	0.528	1.19	2.11	3.30
Present formulation	0.132	0.528	1.19	2.11	3.30

tip displacements of the beam were obtained experimentally by Tzou [6]. In Table 8.2, the displacements at the five nodes (see Figure 8.9) are presented and compared with experimental and 3-D and shell FE results available in the literature.

A good correlation is observed with the FE results. The tip displacement obtained with the formulated element converges with just one element, confirming the exactness of the solution. The 3-D FE results were obtained by Tzou and Tseng [3] using 5, 11-noded hexahedron elements. The shell FE results were obtained by Tzou and Ye [7] using a 12-noded piezoelectric triangular shell elements with four dof per node.

An experimental dynamic analysis of a cantilever aluminum beam with PZT actuators was done by Reaves and Horta [8]. This beam had one PZT actuator mounted on the top surface and near the root. A schematic of this beam is shown in Figure 8.11. A PZT actuator (type PZT-5A) was used, the material properties of which are the following: Young's modulus, $E = 1.0 \times 10^7$ lb/in 2 ;

Table 8.3 Natural frequencies (Hz) for the aluminum beam shown in Figure 8.10.

Mode	MSC/NASTRAN [12]	Present formulation
1 (bending)	5.68	5.76
2 (bending)	33.59	33.77
3 (torsion)	60.24	59.06
4 (bending)	91.21	90.48

Poisson's ratio = 0.3; Shear modulus $G = 3.82 \times 10^6$ lb/in 2 ; density = 7.16×10^{-4} (lb s 2)/in 4 ; piezoelectric constant, $d_{31} = 6.73 \times 10^{-9}$ in/V. For this problem, the first four natural frequencies were obtained in Reaves and Horta [8] using a general-purpose software package (MSC/NASTRAN). Here, the same model is modeled with ten formulated elements. The results of these two analyses are compared and shown in Table 8.3. These results show excellent agreement between the two models.

Next, a composite T300/976 graphite–epoxy box beam, shown in Figure 8.12, having two bimorph surface-mounted PZT actuators, is considered. This problem was again studied in Reaves and Horta [8] using MSC/NASTRAN. The material properties of the PZT actuators are the same as in the previous example. The properties of the T300/976 graphite–epoxy beam are as follows:

$$\begin{aligned} E_{11} &= 2.17 \times 10^7 \text{ lb/in}^2, \quad E_{22} = 1.305 \times 10^6 \text{ lb/in}^2, \\ G_{12} &= 1.03 \times 10^6 \text{ lb/in}^2 = G_{13}, \quad G_{23} = 1.305 \times 10^6 \text{ lb/in}^2, \\ \rho &= 1.49 \times 10^{-4} (\text{lb/s}^2)/\text{in}^4 \end{aligned}$$

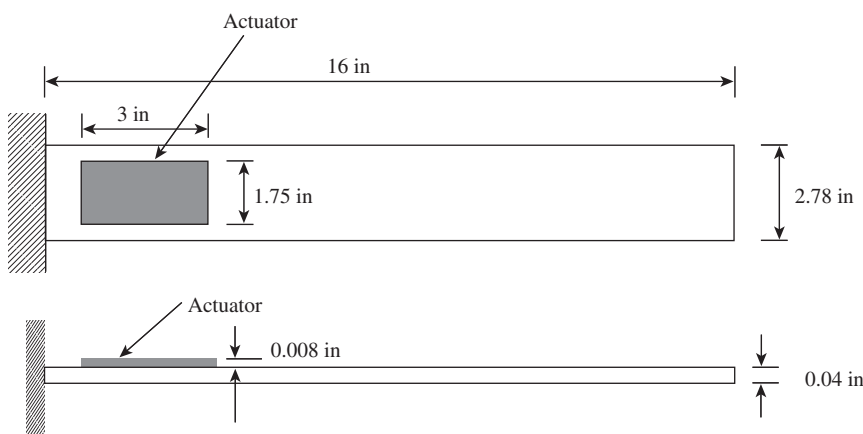


Figure 8.11 Schematic of the PZT-mounted aluminum beam for dynamic analysis.

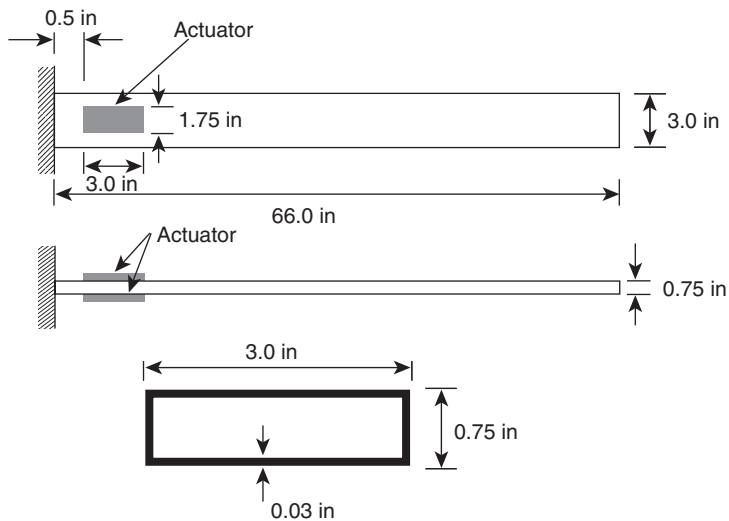


Figure 8.12 Schematic of the PZT actuator mounted on a T300/976 graphite–epoxy box beam.

As before, the above beam was modeled with ten superconvergent FEs and Table 8.4 shows comparison of the results between the present element and the MSC/NASTRAN results, which again shows excellent correlation.

8.4 MODELING OF MAGNETOSTRICTIVE SENSORS AND ACTUATORS

8.4.1 Constitutive model for a magnetostrictive material (Terfenol-D)

Some magnetic materials (magnetostrictive) show elongation and contraction in the magnetization direction due to an induced magnetic field. This is called *magnetostriction*, which is due to the switching of a large amount of magnetic domains caused by spontaneous magnetization, below the Curie temperature point. Thus, magnetostrictive materials have the ability to convert magnetic

energy into mechanical energy, and vice versa. This coupling between magnetic and mechanical energies represents what is called the *transductor capability*, which allows a magnetostrictive material to be used in both actuation and sensing applications.

One of the main issues in the design of these magnetostrictive sensors/actuators is to predict their behaviors under various mechanical and/or magnetic excitation conditions through the constitutive relationships of the materials. The constitutive relationship of magnetostrictive materials consists of two equations, i.e. a sensing and an actuation equation. In the sensing equation, the magnetic flux density is a function of the applied magnetic field and stress whereas in the actuation equation, the strain is a function of the applied magnetic field and stress. Both sensing and actuation equations are coupled through the applied magnetic field and mechanical stress level. As a result, the constitutive relations for a magnetostrictive material, such as Terfenol-D, are highly nonlinear.

The analysis of structures with magnetostrictive sensors/actuators is generally performed by using uncoupled models. Uncoupled models are based on the assumption that the magnetic field within the magnetostrictive material is proportional to the electric coil current multiplied by the number of coil turns per unit length. Due to this assumption, the actuation and sensing equations become uncoupled. For the actuator, the strain due to the magnetic field (which is proportional to the coil current) is incorporated as the equivalent nodal load in the finite element model for calculating the ‘block’ force. Thus,

Table 8.4 Natural frequencies (Hz) for the composite beam shown in Figure 8.11.

Mode	MSC/NASTRAN [8.12]	Present formulation
1 (bending)	11.1	10.9
2 (bending)	68.9	67.7
3 (torsion)	186.7	187.7
4 (bending)	279.6	239.1

with this procedure the analysis is carried out without taking smart (magnetic) degrees of freedom in the finite element model. Similarly for the sensor, where generally the coil current is assumed to be zero, the magnetic flux density is proportional to the mechanical stress, which can be calculated from the finite element results through ‘post-processing’. This assumption for the magnetic field leads to ‘violation’ of the flux line continuity, which is one of the four Maxwell’s equations in electromagnetism. On the other hand, in the coupled model it is considered that the magnetic flux density and/or strain of the material are functions of the stress and magnetic field, without any additional assumptions for the magnetic field, as in the uncoupled model.

The 3-D constitutive law for a magnetostrictive material is given by:

$$\begin{aligned}\{\varepsilon\} &= [S^{(H)}]\{\sigma\} + [d]^T\{H\} \Rightarrow \{\sigma\} = [Q]\{\varepsilon\} - [e]^T\{H\} \\ \{B\} &= [d]\{\sigma\} + [\mu^{(\sigma)}]\{H\} \Rightarrow \{B\} = [e]\{\varepsilon\} + [\mu^e]\{H\}\end{aligned}\quad (8.74)$$

where $\{\varepsilon\}$ and $\{\sigma\}$ are the strain and stress, respectively; $[S^{(H)}]$ represents the elastic compliance matrix measured at a constant magnetic field $\{H\}$ and $[\mu^{(\sigma)}]$ represents the permeability measured at a constant stress $\{\sigma\}$. Here, $[d]$ is the magneto-mechanical coupling coefficient matrix, which provides a measure of the coupling between the mechanical strain and magnetic field. In general, $[S]$, $[d]$ and $[\mu]$ are nonlinear as they depend upon $\{\sigma\}$ and $\{H\}$. The first part of Equation (8.74) is often referred to as the *direct effect* and is called the *actuation equation*, while the second part of Equation (8.74) is known as the *converse effect*. It should be noted that the elastic constants which are used correspond to the fixed magnetic field values while the permeabilities correspond to the fixed stress values. Alternatively, we can write the constitutive relations as given on the right-hand side of Equation (8.74). Here, $[Q]$ is the elasticity matrix, which is the inverse of the compliance matrix, $[\mu^e]$ is the permeability matrix measured at constant strain and $[e]$ is the magneto-mechanical stress coefficient matrix. $[\mu^e]$ and $[e]$ are related to $[Q]$ through the relation:

$$[e] = [d][Q], \quad [\mu^e] = [\mu^\sigma] - [d][Q][d]^T$$

Let us consider a simple 1-D model. A look at Equation (8.74) reveals that for each value of the magnetic field H , there is a different stress-strain curve. Similarly, for each stress level, there is a separate magnetostriction-magnetic field curve. In other words, unlike piezoelectric

materials, one has to solve the sensing and actuation equations simultaneously to get all of the required quantities. Hence, the equations require to be solved iteratively. This is done in Ghosh and Gopalakrishnan [9] through two approaches. In the first approach, an *Artificial Neural Network* is created by ‘training’ the network with the data supplied by ETREMA Inc., USA, which is one of the few companies in the world which market the products derived from Terfenol-D. If the stress level and the magnetic field intensity are fed into this network, then the required stress-strain and magnetostriction-magnetic field relations can be obtained. In the second approach, the data supplied by ETREMA Inc., USA are used to fit a fifth-degree polynomial for magnetostriction as a function of the magnetic field H . This curve is later used to get the required curve for stress-strain. These curves are shown in Figures 8.13 and 8.14. These two plots were obtained through an iterative solution of Equation (8.74) and match exactly with the plots given in the ETREMA manual [10] on Terfenol-D. In addition, the stress-strain and magnetostriction-magnetic field curves are given for different levels of magnetic field/stress not covered in the ETREMA manual.

8.4.2 Finite element modeling of composite structures with embedded magnetostrictive patches

The finite element formulation of structures with embedded magnetostrictive patches differs depending upon whether the constitutive model is coupled or uncoupled. For the uncoupled model, the magnetic field is assumed to be proportional to the coil current and as a result, the sensing and actuation constitutive relations are solved independently.

That is, there is no need to have the magnetic field as the independent degree of freedom. However, in a coupled model, both the sensing and actuation constitutive laws need to be solved simultaneously, since no explicit variation of the magnetic field with respect to the magnetostrictive patch parameters are available. This requires that the magnetic field be taken as an independent degree of freedom. Here, we outline the procedure of modeling magnetostrictive sensors/actuators for both uncoupled and coupled constitutive laws.

Finite element formulation begins by writing the associated energy in terms of the nodal degrees of freedom by assuming displacement and magnetic field variations in three coordinate directions over each element. That is, the displacement field can be written as:

$$\{U\} = \{u \ v \ w\} = [N_u]\{U\}_e \quad (8.75)$$

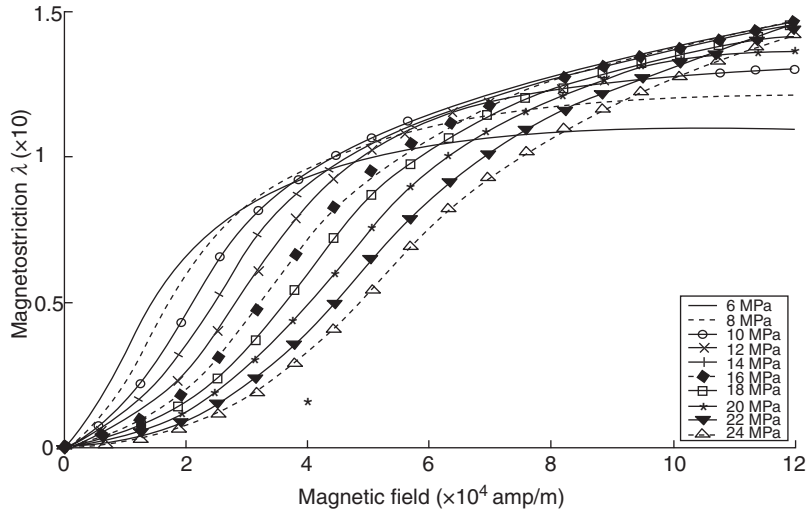


Figure 8.13 Magnetostriction–magnetic field curves for different stress levels in Terfenol-D.

Here, $u(x, y, t)$, $v(x, y, z, t)$ and $w(x, y, z, t)$ are the displacement components in the three coordinate directions, $[N_u]$ is the shape functions associated with mechanical degrees of freedom and $\{U\}_e$ is the nodal displacement vector. If an isoparametric formulation is used, then the conventional isoparametric shape functions in natural

coordinate could be adopted. The strains can be expressed in terms of displacement through a strain–displacement relationship, that is:

$$\{\varepsilon\} = \{\varepsilon_{xx} \quad \varepsilon_{yy} \quad \varepsilon_{zz} \quad \gamma_{yz} \quad \gamma_{xz} \quad \gamma_{xy}\}^T = [\bar{B}]\{U\}_e \quad (8.76)$$

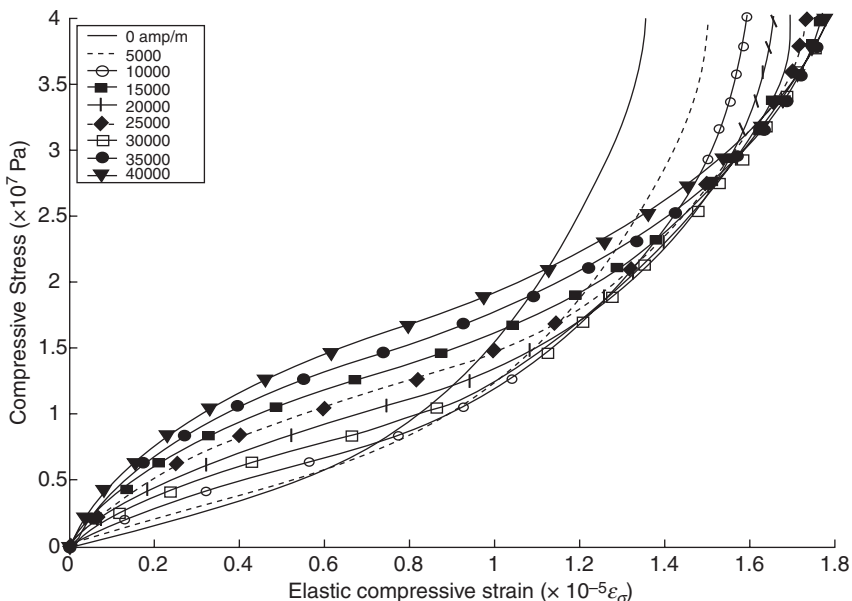


Figure 8.14 Stress–strain curves for different magnetic field intensities in Terfenol-D.

where $[\bar{B}]$ is the strain-displacement matrix and its evaluation is given in Chapter 7. For coupled analysis, we need to take the magnetic field as the independent degree of freedom. In such cases, we can write the magnetic field in the three coordinate directions as:

$$\{H\} = \{H_x \ H_y \ H_z\} = [N_H]\{H\}_e \quad (8.77)$$

where $\{H\}_e$ is the nodal magnetic field vector and $[N_H]$ is the shape function associated with the magnetic field degree of freedom.

The strain energy in a structure with magnetostrictive patches over a volume V is given by:

$$V_e = \frac{1}{2} \int_V \{\varepsilon\}^T \{\sigma\} dV$$

Substituting for $\{\sigma\}$ from Equation (8.74) converts the above equation into terms of strains and magnetic field vectors. In this equation, the strains are expressed in terms of displacement using Equation (8.76) and the magnetic field in terms of the nodal magnetic field vector using Equation (8.77).

The resulting expression for the strain energy will become:

$$V_e = \frac{1}{2} \{U\}_e^T [K_{uu}] \{U\}_e - \frac{1}{2} \{U\}_e^T [K_{uH}] \{H\}_e \quad (8.78)$$

where:

$$[K_{uu}] = \int_V [\bar{B}]^T [Q] [\bar{B}] dV, \quad [K_{uH}] = \int_V [\bar{B}]^T [e]^T [N_H] dV \quad (8.79)$$

and $[K_{uu}]$ is the stiffness matrix associated with the mechanical degrees of freedom and $[K_{uH}]$ is the coupling stiffness matrix, which couples the mechanical and magnetic degrees of freedoms. The kinetic energy is given by:

$$T_e = \frac{1}{2} \int_V \{\dot{U}\}^T \rho \{\dot{U}\} dV \quad (8.80)$$

Here, $\{\dot{U}\}$ is the velocity vector and ρ is the average density of the host material. Using Equation (8.75) in the above equation, we can write the kinetic energy as:

$$T_e = \frac{1}{2} \{\dot{U}\}^T [M_{uu}] \{\dot{U}\} \quad (8.81)$$

where $[M_{uu}]$ is the mass matrix associated only with mechanical degrees of freedom and is given by:

$$[M_{uu}] = \int_V [N_u]^T \rho [N_u] dV \quad (8.82)$$

The magnetic potential energy for the system can be written as:

$$V_m = \frac{1}{2} \int_V [B]^T \{H\} dV \quad (8.83)$$

Substituting for $[B]$ from Equation (8.74) and for $\{H\}$ from Equation (8.77), we can write the magnetic potential energy as:

$$V_m = \frac{1}{2} \int_V \left\{ [e] \{\varepsilon\} + [\mu^e] \{H\} \right\}^T \{H\} dV \quad (8.84)$$

Substituting for strains from Equation (8.76), we get:

$$V_m = \frac{1}{2} \{U\}_e^T [K_{uH}]^T \{H\}_e + \frac{1}{2} \{H\}_e^T [K_{HH}] \{H\}_e \quad (8.85)$$

where:

$$[K_{HH}] = \int_V [N_H]^T [\mu^e] [N_H] dV \quad (8.86)$$

When an applied current I (amp) (AC or DC) is fed to the patch having N number of coils, it creates a magnetic field, which in turn introduces an external force in the patch. The external work done over a magnetostrictive patch of area A due to this field is given by:

$$W_m = IN \int_A [\mu^\sigma] \{H\} dA \quad (8.87)$$

Here, $[\mu^\sigma]$ is the permeability matrix measured at constant stress. It is necessary to convert this area integral into a volume integral. If n is the number of coil turns per unit length and $\{l_c\}$ is the direction cosine vector of the coil axis, the above area integral can be converted into the volume integral by replacing N by $n\{l_c\}^T$. Substituting for the magnetic field from Equation (8.77), Equation (8.87) becomes:

$$W_m = \{F_H\}^T \{H\}_e, \quad \{F_H\} = In\{l_c\}^T \int_V [\mu^\sigma] [N_H] dV \quad (8.88)$$

The external mechanical work done due to the body force or surface traction vector can be written in the form:

$$W_e = \{R\}^T \{U\}_e \quad (8.89)$$

Using Hamilton's principle, $\delta \int_{t_1}^{t_2} (T_e - V_e + V_m + W_m + W_e) dt = 0$, gives the necessary FE governing equation. This takes a varied form for uncoupled and coupled models, which are given below.

In the uncoupled model, the magnetic field is assumed to be proportional to the coil current and hence a variation with respect to the magnetic field is not performed. That is, the magnetic field is normally equal to $H = nI$, where n is normally the coil turns per unit length of the magnetostrictive material patch. With this assumption, Hamilton's principle will give the equation of motion as:

$$[M_{uu}] \{\ddot{U}\}_e + [K_{uu}] \{U\}_e = [K_{uH}] \{H\}_e - \{R\} \quad (8.90)$$

where $\{\ddot{U}\}_e$ is the elemental acceleration vector and the magnetic field in the above equation is obtained by $\{H\}_e = n_e I$, with n_e being the elemental coil turns per unit length.

In the case of the coupled model, one has to also take a variation on the magnetic field as there is no explicit relation of this with respect to any of the parameters. Hence, both mechanical and magnetic degrees of freedom are considered as unknowns. Hamilton's principle will give the following coupled set of equations:

$$\begin{bmatrix} [M_{uu}] & [0] \\ [0] & [0] \end{bmatrix} \begin{Bmatrix} \{\ddot{U}\}_e \\ \{\dot{H}\}_e \end{Bmatrix} + \begin{bmatrix} [K_{uu}] & -[K_{uH}] \\ [K_{uH}]^T & [K_{HH}] \end{bmatrix} \begin{Bmatrix} \{U\}_e \\ \{H\}_e \end{Bmatrix} = \begin{Bmatrix} -\{R\} \\ \{F_H\} \end{Bmatrix} \quad (8.91)$$

Note that the stiffness matrix is not symmetric and we have a block zero diagonal matrix in the mass matrix as the magnetic field does not contribute to the inertia of the composite. For an effective solution, the above equation is expanded and the magnetic degrees of freedom are condensed out. The reduced equation of motion can be written as:

$$[M_{uu}] \{\ddot{U}\}_e + [K_{uu}^*] \{U\}_e = \{R^*\} \quad (8.92)$$

where:

$$\begin{aligned} [K_{uu}^*] &= \left[[K_{uu}] + [K_{uH}] [K_{HH}]^{-1} [K_{uH}]^T \right], \\ \{R^*\} &= [K_{uH}] [K_{HH}]^{-1} \{F_H\} - \{R\} \end{aligned} \quad (8.93)$$

The assembly of matrices and solution procedures are similar to those detailed in Chapter 7.

After computation of the nodal displacements and velocities, we can compute the sensor open-circuit voltage. This is particularly of great interest in structural health monitoring studies. The processes of computing this for coupled and uncoupled models are quite different. Using Faraday's law, the open-circuit voltage V_v in the sensing coil can be calculated from the magnetic flux passing through the sensing patch.

In the uncoupled model, the nodal magnetic field is assumed constant over the element and with zero sensor coil current. To get the open-circuit voltage, the magnetic flux density can be expressed in terms of strain from the sensing equation (second part of Equation (8.74)), which is given by:

$$\{B\} = [d]\{\sigma\} = [d][Q]\{\varepsilon\} = [e]\{\varepsilon\} = [e][\bar{B}]\{U\}_e$$

Now using Faraday's Law, the open-circuit voltage of the sensor having N_s turns and area A , can be calculated from the expression:

$$V_v = -N_s \int_A \frac{\partial}{\partial t} \{[e]\{\varepsilon\}\} dA \quad (8.94)$$

The above integral can be converted into the volume integral as before by multiplying it with the direction cosine vector and the open-circuit voltage can now be written as:

$$V_v = \{F_v\}^T \{U_e\}, \quad F_v = -n_s \{l_c\}^T \int_V [e][\bar{B}] dV \quad (8.95)$$

Here, n_s is the coil turns per unit length of the sensor.

In the case of the coupled model, the magnetic flux density is computed from the nodal magnetic field, which is obtained from finite element analysis. Thus, the open-circuit voltage in the sensor takes a different expression and can be calculated from the expression:

$$V_v = -N_s \int_A \frac{\partial}{\partial t} [\mu^\sigma] \{H\} dA \quad (8.96)$$

This can again be converted into the volume integral as before. Substituting for $\{H\}$ from Equation (8.77) in terms of the nodal magnetic degrees of freedom, for which the second part of Equation (8.91) is used, and

finally after simplification, the open-circuit voltage can be written as:

$$\begin{aligned} V_v &= \{F_v\}^T \{U_e\}, \\ \{F_v\}^T &= -n_s \{l_c\}^T \left[\int_V [\mu^\sigma] [N_H] dV \right] [K_{HH}]^{-1} [K_{uH}]^T \end{aligned} \quad (8.97)$$

relevant stiffness matrices and the load vector due to the magnetic field. These are given by:

$$\begin{aligned} [M_{uu}] &= \frac{\rho AL}{6} \begin{bmatrix} 2 & 1 \\ 1 & 2 \end{bmatrix}, \quad [K_{uu}] = \frac{EA}{L} \begin{bmatrix} 1 & -1 \\ -1 & 1 \end{bmatrix}, \\ [K_{uH}] &= \frac{EAd}{2} \begin{bmatrix} -1 & -1 \\ 1 & 1 \end{bmatrix}, \\ [K_{HH}] &= \frac{AL\mu^\sigma}{6} \begin{bmatrix} 2 & 1 \\ 1 & 2 \end{bmatrix}, \quad \{F_H\} = \frac{nIAL\mu^\sigma}{2} \begin{Bmatrix} 1 \\ 1 \end{Bmatrix} \end{aligned} \quad (8.99)$$

8.4.3 Numerical examples

In this section, the effect of coupling on the overall response of a 1-D composite structure is brought out. Hence, for all analysis the results are compared with the uncoupled model to see the effect of coupling. Here, we consider two examples of a one-dimensional structure – the first is a 1-D magnetostrictive rod model, while the second is a composite beam model based on first-order shear deformation theory. For the last example, static, frequency response and time history analyses are performed to bring out the essential differences between the coupled and uncoupled models.

8.4.3.1 Effect of coupling in a Terfenol-D rod

The displacement field in a rod is given by:

$$u(x, y, z, t) = u(x, t), \quad v(x, y, z, t) = 0, \quad w(x, y, z, t) = 0$$

and the magnetic field is present only in the axial direction and is given by $H(x, t)$. Consider a Terfenol-D rod of length L , cross-sectional area A , Young's modulus E , magneto-mechanical coefficient d and constant stress permeability μ^σ . For finite element formulation, we use conventional rod shape functions for both displacement and magnetic degrees of freedom, which are given by:

$$\begin{aligned} u(x, t) &= [N_u] \{U\}_e = N_1(x)u_1(t) + N_2(x)u_2(t) \\ H(x, t) &= [N_H] \{H\}_e = N_1(x)H_1(t) + N_2(x)H_2(t) \\ N_1 &= \left(1 - \frac{x}{L}\right), \quad N_2 = \left(\frac{x}{L}\right) \end{aligned} \quad (8.98)$$

where u_1 and u_2 are the two axial degrees of freedom at the two ends of the rod. Using the above equations, strains can be evaluated as a function of nodal displacement. Substituting Equation (8.98) into Equations (8.79), (8.82), (8.86), (8.88), we can get the mass matrix, all the

Uncoupled analysis For uncoupled static analysis, the corresponding equations become:

$$\frac{EA}{L} \begin{bmatrix} 1 & -1 \\ -1 & 1 \end{bmatrix} \begin{Bmatrix} u_1 \\ u_2 \end{Bmatrix} - \frac{EAd}{2} \begin{bmatrix} -1 & -1 \\ 1 & 1 \end{bmatrix} \begin{Bmatrix} H_1 \\ H_2 \end{Bmatrix} = \begin{Bmatrix} R_1 \\ R_2 \end{Bmatrix} \quad (8.100)$$

where u_1 and u_2 are the two nodal axial displacements in a magnetostrictive rod. For uncoupled analysis, $H_1 = H_2 = nI$. Here, we consider the following three cases:

- Keeping the boundaries fixed, that is, $u_1 = u_2 = 0$, by solving Equation (8.100) for the block force, we get $R_1 = -R_2 = AdEH_1 = AdEIn$ and the stress $\sigma = R_1/A = R_2/A = dEIn$.
- Next, if we consider the completely fixed-free boundary conditions, where $R_1 = R_2 = u_1 = \sigma = 0$, we get the tip displacement and strain as $u_2 = LdnI$, $\varepsilon = dnI$.
- If the coil current is zero and the rod is subjected to a ‘pure’ tension F , then a purely mechanical state exists and for the fixed-free boundary condition, we have $u_2 = FL/AE$, which is the conventional strength-of-material solution.

Now, the same set of analyses is performed using the coupled model to see the essential differences in responses.

Coupled analysis Coupled analysis requires solution of the following equation:

$$\begin{aligned} \frac{EA}{L} \begin{bmatrix} 1 & -1 \\ -1 & 1 \end{bmatrix} \begin{Bmatrix} u_1 \\ u_2 \end{Bmatrix} - \frac{EAd}{2} \begin{bmatrix} -1 & -1 \\ 1 & 1 \end{bmatrix} \begin{Bmatrix} H_1 \\ H_2 \end{Bmatrix} &= \begin{Bmatrix} R_1 \\ R_2 \end{Bmatrix} \\ \frac{EAd}{2} \begin{bmatrix} -1 & 1 \\ -1 & 1 \end{bmatrix} \begin{Bmatrix} u_1 \\ u_2 \end{Bmatrix} + \frac{AL\mu^\sigma}{2} \begin{bmatrix} 2 & 1 \\ 1 & 2 \end{bmatrix} \begin{Bmatrix} H_1 \\ H_2 \end{Bmatrix} &= \frac{AL\mu^\sigma In}{2} \begin{Bmatrix} 1 \\ 1 \end{Bmatrix} \end{aligned} \quad (8.101)$$

The same three analyses are again performed here:

- For fixed–fixed boundary conditions, the second part of the above equation gives:

$$H_1 = H_2 = In \frac{\mu^\sigma}{\mu^e} \quad (8.102)$$

The value of the magnetic field is less than the generally considered value (In) for the uncoupled model. The value of the magnetic field will increase (decrease) with the increase (decrease) in the ratio of constant stress and constant strain permeability. Similarly, the blocked force in the support is obtained from the first part of Equation (8.101) and is given by:

$$R_1 = -R_2 = AdEH_1 = AdEIn \frac{\mu^\sigma}{\mu^e} \quad (8.103)$$

which is less than the value generally considered ($AdEIn$). These also depend on the ratio of the permeabilities.

- For fixed–free boundary conditions, the solution of Equation (8.101) gives:

$$H_1 = H_2 = H = In, \quad u_2 = LdnI, \quad \varepsilon = dnI \quad (8.104)$$

That is, $H = In$ is only true for fixed–free boundary conditions. For the other boundary condition (fixed–fixed), the magnitude of the magnetic field depends on the ratio of permeabilities.

- For fixed–free boundary conditions and a tensile force F acting at the tip with zero coil current ($I = 0$), the solution of Equation (8.101) gives:

$$H_1 = H_2 = \frac{Fd}{A\mu^\sigma}, \quad u_2 = \frac{FL\mu^e}{AE\mu^\sigma} \quad (8.105)$$

Here again, the dependence on the ratio of permeabilities is noticeable. If this ratio of permeabilities is equal to 1, the effect of coupling vanishes. However, for Terfenol-D, the ratio of permeabilities (μ^σ/μ^e) is in the range of 0.4 to 0.5. Hence, the effect of coupling is quite significant.

8.4.3.2 Modeling of a laminated composite beam with embedded Terfenol-D patch

The displacement field for the beam based on the first-order Shear Deformation Theory (FSDT) is given by:

$$\begin{aligned} u(x, y, x, t) &= u_0(x, t) - z\phi(x, t), & v(x, y, z, t) &= 0, \\ w(x, y, x, t) &= w(x, t) \end{aligned} \quad (8.106)$$

As before, the magnetic field (H) is only in the axial direction. Next, we need to assume the necessary polynomials for the mid-plane axial displacement u_0 , lateral displacement w_0 and slope ϕ . Since the slopes are independent and not derivable from the lateral displacement, a C^0 continuous formulation is sufficient and hence of the use linear polynomials given in Equation (8.98) is sufficient. All of the formulated matrices are numerically integrated. However, this formulation is prone to exhibit what is called the *shear-locking* problem, which was explained in Chapter 7. One of the simplest ways to eliminate locking is to ‘reduce-integrate’ the part of the mechanical stiffness matrix contributed by the shear stress. This is undertaken in this formulation.

The approach to formulation is very similar to rod formulation, and hence all of the details are skipped here. We will write down only the final forms of the elemental matrices involved. The mechanical stiffness matrix [K_{uu}] is 6×6 and is given by:

$$[K_{uu}] = \begin{bmatrix} \frac{A_{11}}{L} & \frac{A_{15}}{L} & \left(\frac{A_{15}}{2} - \frac{B_{11}}{L}\right) & -\frac{A_{11}}{L} & -\frac{A_{15}}{L} & \left(\frac{A_{15}}{2} + \frac{B_{11}}{L}\right) \\ \frac{A_{55}}{L} & \left(\frac{A_{55}}{2} - \frac{B_{15}}{L}\right) & -\frac{A_{15}}{L} & -\frac{A_{55}}{L} & \left(\frac{A_{55}}{2} + \frac{B_{15}}{L}\right) & \\ \left(\frac{A_{55}L}{4} - B_{15}\right) & \left(-\frac{A_{15}}{2} + \frac{B_{11}}{L}\right) & \left(-\frac{A_{55}}{2} + \frac{B_{15}}{L}\right) & \left(\frac{A_{55}L}{4} + B_{11}\right) & \left(\frac{A_{55}L}{4} - D_{11}\right) & \\ & A_{11} & A_{15} & \left(\frac{A_{15}}{2} - \frac{B_{11}}{L}\right) & A_{55} & \left(\frac{A_{55}}{2} - \frac{B_{15}}{L}\right) \\ & & & & & \left(\frac{A_{55}L}{4} + B_{15} + D_{11}\right) \end{bmatrix}_{\text{SYM}}$$

where:

$$[A_{ij}, B_{ij}, D_{ij}] = \int_A Q_{ij}[1, z, z^2] dA$$

The magneto–mechanical coupling matrix is given by:

$$[K_{uH}]^T = \frac{1}{2} \begin{bmatrix} -e^0_{11} & 0 & e^1_{11} & e^0_{11} & 0 & -e^1_{11} \\ -e^0_{11} & 0 & e^1_{11} & e^0_{11} & 0 & -e^1_{11} \end{bmatrix}$$

where:

$$[e^0_{11} \quad e^1_{11}] = \int_A e_{11}[1 \quad z] dA$$

The matrix [K_{HH}] is given by:

$$[K_{HH}] = \frac{L\mu^0}{6} \begin{bmatrix} 2 & 1 \\ 1 & 2 \end{bmatrix}, \quad \mu^0 = \int_A \mu^e dA$$

In the case of the coupled model, we require the force vector $\{F_H\}$, which is given in Equation (8.88). This vector becomes:

$$\{F_H\} = \frac{In\mu^0 L}{2} \begin{Bmatrix} 1 \\ 1 \end{Bmatrix}$$

The mass matrix is given by:

$$[M_{uu}] = \begin{bmatrix} 2I_0 & 0 & -2I_1 & I_0 & 0 & -I_1 \\ 2I_0 & 0 & 0 & I_0 & 0 & 0 \\ & 2I_2 & -I_1 & 0 & I_2 & \\ & & 2I_0 & 0 & -2I_1 & \\ \text{SYM} & & & 2I_0 & 0 & 2I_2 \end{bmatrix}$$

where:

$$[I_0, I_1, I_2] = \int_A \rho [1, z, z^2] dA$$

The composite magnetostrictive bimorph beam shown in Figure 8.15 is analyzed to verify the effectiveness of the formulated element. Static and frequency response analyses are performed on this beam to bring out the effects of coupling. The length and width of the beam are 500 mm and 50 mm, respectively. The beam is made of 12 layers with the thickness of each layer being 0.15 mm. Surface-mounted magnetostrictive patches on the top and bottom layers are considered as sensor and actuator, respectively. The elastic moduli of the composite are assumed as 181 and 10.3 GPa in the parallel (E_1) and perpendicular (E_2) directions of the fiber, respectively. The density (ρ) and shear modulus (G_{12}) of the composite are 1.6 g/ml and 28 GPa, respectively. The elastic modulus (E_m), shear modulus (G_m) and density (ρ_m) of

the magnetostrictive material are taken as 30 GPa, 23 GPa and 9.25 g/ml, respectively.

The magneto-mechanical coupling coefficient is taken as 15×10^{-9} m/amp, and the permeability in vacuum or air is assumed to be 400π nH/m. The constant-stress relative permeability of the magnetostrictive material is assumed to be equal to 10, while the number of coil turns per meter (n) in the sensor and actuator is assumed to be 20 000.

Static analysis The effect of coupling of a magnetostrictive material in a laminated composite beam for static actuation is analyzed for a 1 amp DC actuation coil current. It is observed that the tip deflection for coupled analysis is 2.17 mm, whereas for uncoupled analysis it is 2.44 mm. The ratio between these two is 1:12. As the thickness of the actuator is smaller when compared to the thickness of the composite beam, the effective increase of stiffness in the global stiffness matrix due to coupling is very much smaller. The increases in thickness of the sensor and actuator patches will increase the effective thickness and hence decrease the effective deflection, especially in the coupled analysis. In addition, an increase in the ply angle will also increase the stiffness in the transverse direction. These observations are quite evident from Table 8.5 for different ply angles of 0° and 90° . It is very clear from this table that for 90° ply angle, the effect of coupling is considerable. This reinforces the need for coupled analysis for structures with magnetostrictive patches.

Frequency response analysis To observe the effects of the coupling terms on the behavior of a cantilever beam with a magnetostrictive material in the frequency domain, the frequency response function (FRF) is computed with both coupled and uncoupled models for the same cantilever composite beam up to a 500Hz frequency. The FRFs for 0 and 90° ply angles are shown in Figures 8.16

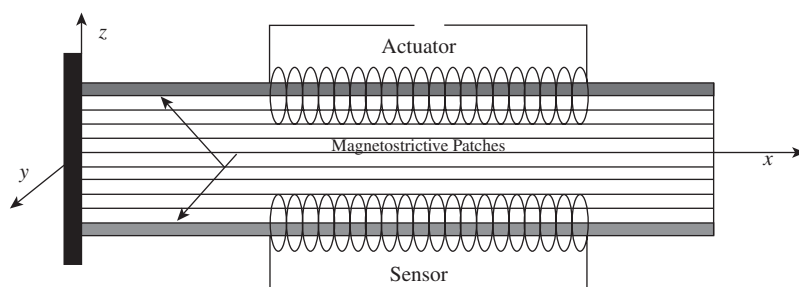


Figure 8.15 Schematic of a magnetostrictive cantilever bimorph beam.

Table 8.5 Ratios of uncoupled and coupled analysis tip displacement of a cantilever beam with magnetostrictive patches.

Ply sequence	Coupled analysis w_c (mm)	Uncoupled analysis w_u (mm)	Ratio, $\frac{w_u}{w_c}$
$m/[0]_{10}/m$	2.17	2.44	1.12
$m/[30]_{10}/m$	2.83	3.30	1.17
$m/[45]_{10}/m$	3.84	4.78	1.24
$m/[60]_{10}/m$	5.52	7.69	1.39
$m/[90]_{10}/m$	8.62	15.40	1.78
$m/[0/90]_5/m$	3.44	4.80	1.40
$m/[90/0]_5/m$	7.62	10.73	1.48
$[m]_2/[0]_8/[m]_2$	5.25	6.97	1.33
$[m]_2/[30]_8/[m]_2$	6.03	8.41	1.39
$[m]_2/[45]_8/[m]_2$	7.07	10.58	1.5
$[m]_2/[90]_8/[m]_2$	10.72	21.56	2.01
$[m]_2/[90]_4/[0]_4/[m]_2$	10.77	19.57	1.82
$[m]_3/[90]_6/[m]_3$	12.15	25.53	2.10
$[m]_3/[90]_3/[0]_3/[m]_3$	12.88	26.31	2.04
$[m]_4/[90]_2/[0]_2/[m]_4$	14.06	30.44	2.17

and 8.17, respectively. For a 0° ply angle, we see that the first three modes are least affected due to the effects of coupling. However, we can see a significant shift in the resonant frequencies of the higher modes. For the 90° ply angle, we see shifts in the natural frequencies, even for the lower modes. This further reinforces our belief that uncoupled analysis underestimates the stiffness of the structure with a magnetostrictive material.

8.4.4 Modeling of piezo fibre composite (PFC) sensors/actuators

The concept of broadband distributed active control in flexible structures has evolved in recent times. Tremendous technological success in the field of micro electro-mechanical systems (MEMS) has laid the path toward implementation of such concepts. Especially, structures made of multifunctional multiphase composites [11–14] have provided a wide range of platforms for structural sensing, actuation and control-related applications [15,16]. Currently, a number of designs are available which use different forms of PZT ceramic fibers and conventional matrices. Experimental observations have shown sustained electromechanical properties of these composites that match well with the microscopic models

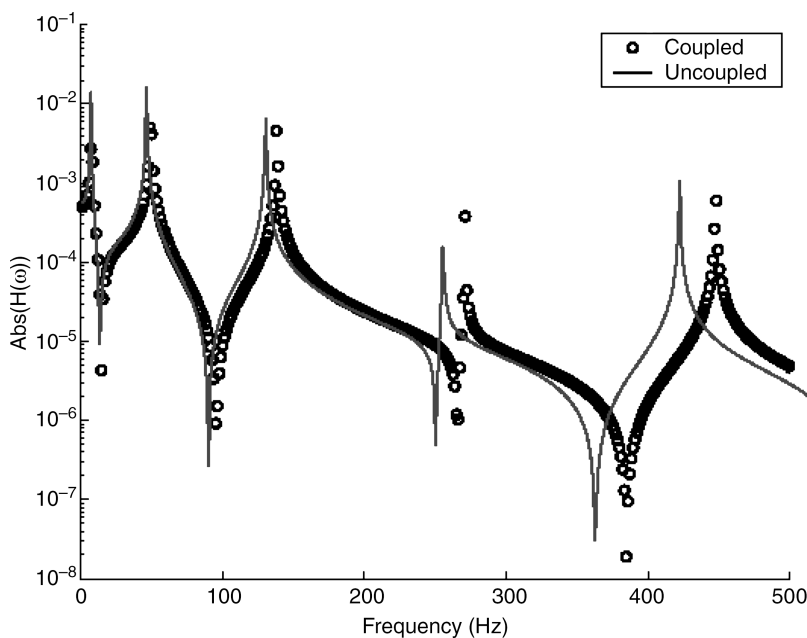


Figure 8.16 Frequency response function for a laminated composite magnetostrictive bimorph beam with 0° ply angles.

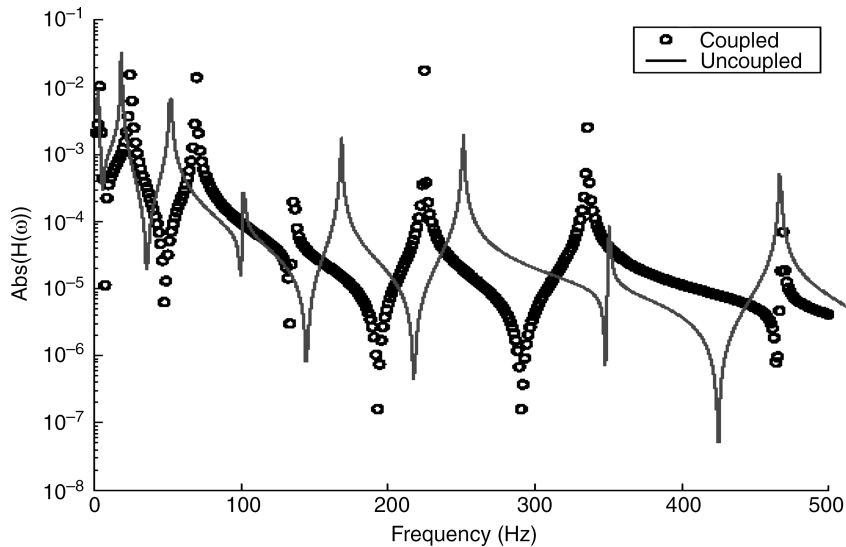


Figure 8.17 Frequency response function for a laminated composite magnetostrictive bimorph beam with 90° ply angles.

mathematically derived from their bulk forms in the linear and high-frequency regimes. Following the performance standardization of these active composites as distributed actuators, the main task remains as to how better control performances can be achieved, particularly in transverse actuation. Before real-scale implementation, various complexities due to embedded electronics, limitations in the electro-magnetic properties and interactions with the host structures need detailed analysis. Some physical insight into the macroscopic behavior of these PFC actuators has been reported [17,18].

Here, we consider a PFC with an interdigitated surface electrode as the distributed actuator element and a broadband vibration sensor capable of measuring far-field as well as near-field. The computational model accounts for the axial–flexural coupling due to the out-of-plane actuation effort and unsymmetric mechanical stiffness and inertia across the beam thickness. As the frequency content of the external disturbance increases, wavelengths of the traveling waves decrease. Therefore, scattering of the waves at minute discontinuities in the structural interfaces becomes significant at these high-frequency ranges. Here, the spectral finite element model is used to characterize the waves at the high-frequency ranges. This model is used in tandem with the *Active Spectral Finite Element Model* (ASFEM) (to be dealt with in detail in the next chapter) for active wave control. Here, we will describe the constitutive model for a PFC actuator. We will use this SFEM along with the

ASFEM for controlling broadband applications in the next chapter.

To illustrate the derivation of the constitutive model for piezoelectric fiber composite (PFC) actuation, we consider rectangular-packing square PZT fibers with a matrix as shown in Figure 8.18. The rectangular cross-section of the fibers can provide a maximum volume fraction of ceramic, which is preferable for actuation. The configuration can be obtained using fibers that have been tape-cast and diced, extruded or cast into a mold.

Figure 8.18 shows an actuator element (say, the *q*th) with its host composite structure and having a local coordinate system (X_a^q, Y_a^q, Z_a^q). The representative volume element (RVE), of the two-phase ceramic–matrix composite system is described by one quadrant axisymmetric model about the x_3 axis. Here, h is the total depth of a single PFC layer, p is the uniform spacing of the interdigitated electrodes spanning along x_i and b is the width of each electrode. The constitutive relations for an orthotropic active ceramic bulk form [19] can be represented as:

$$\begin{Bmatrix} \sigma_{xx} \\ \sigma_{zz} \\ \tau_{xz} \\ D_z \end{Bmatrix} = \begin{bmatrix} C^E_{11} & C^E_{12} & C^E_{13} & -e_{31} \\ C^E_{12} & C^E_{22} & C^E_{23} & -e_{32} \\ C^E_{13} & C^E_{23} & C^E_{33} & -e_{33} \\ e_{31} & e_{32} & e_{33} & \mu_{33}^s \end{bmatrix} \begin{Bmatrix} \varepsilon_{xx} \\ \varepsilon_{zz} \\ \gamma_{xz} \\ E_z \end{Bmatrix}$$

This is of a very similar form to that of a PZT actuator. For 1-D waveguide analysis, this requires reduction into a single equivalent constitutive law by considering the

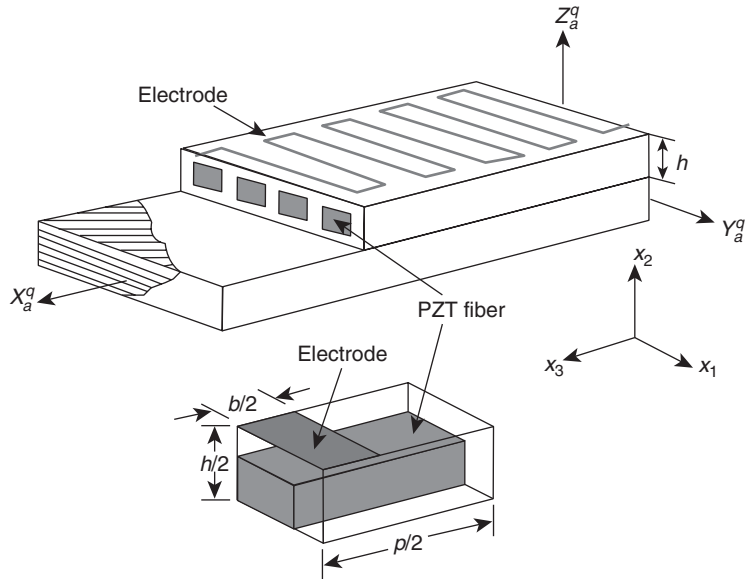


Figure 8.18 Configuration of a piezoelectric fiber composite (PFC) for composite beam actuation.

volume fraction of the piezo fiber (PZT) to the total volume of the laminate. For a pure piezoceramic, $C_{11}^E = C_{22}^E$, $C_{23}^E = C_{13}^E$ and $e_{32} = e_{31}$. For the matrix phase, all e_{ij} are zero and their mechanical and dielectric properties are represented without superscripts. Assuming negligible distortion of the equipotential lines and electric fields beneath the electrodes, and imposing a proper field continuity between the ceramic and matrix phases, the effective unidirectional constitutive law for a PFC beam structure can be expressed as:

$$\sigma_{zz} = C_{33}^{eff} \varepsilon_{zz} - e_{33}^{eff} E_z \quad (8.107)$$

where:

$$C_{33}^{eff} = (\bar{C}_{33} V_1^p + C_{22} V_1^m) - \frac{V_1^p V_1^m (C_{12} - \bar{C}_{13})^2}{C_{22} V_1^p + \bar{C}_{11} V_1^m} \quad (8.108)$$

$$e_{33}^{eff} = \bar{e}_{33} V_1^p + \frac{\bar{e}_{31} V_1^p V_1^m (C_{12} - \bar{C}_{13})}{C_{22} V_1^p + \bar{C}_{11} V_1^m} \quad (8.109)$$

$$\bar{C}_{11} = (\bar{C}_{11} V_2^p + C_{22} V_2^m) - \frac{V_2^p V_2^m (C_{12} - \bar{C}_{13})^2}{C_{11} V_2^p + \bar{C}_{12} V_2^m}$$

$$\bar{C}_{13} = (\bar{C}_{13} V_2^p + C_{12} V_2^m) - \frac{V_2^p V_2^m (C_{12} - \bar{C}_{13}) C_{12} - \bar{C}_{23}}{C_{11} V_2^p + \bar{C}_{22} V_2^m}$$

$$\bar{C}_{11} = (\bar{C}_{33} V_2^p + C_{11} V_2^m) - \frac{V_2^p V_2^m (C_{12} - \bar{C}_{23})^2}{C_{11} V_2^p + \bar{C}_{22} V_2^m} \quad (8.110)$$

$$\begin{aligned} \bar{e}_{31} &= \bar{e}_{31} V_2^p + \frac{\bar{e}_{32} V_2^p V_2^m (C_{12} - \bar{C}_{13})}{C_{11} V_2^p + \bar{C}_{22} V_2^m} \\ \bar{e}_{33} &= \bar{e}_{33} V_2^p + \frac{\bar{e}_{32} V_2^p V_2^m (C_{12} - \bar{C}_{23})}{C_{11} V_2^p + \bar{C}_{22} V_2^m} \end{aligned} \quad (8.111)$$

$$\begin{aligned} \bar{C}_{jk} &= C_{jk}^E + \frac{V_3^m e_{3j} e_{3k}}{V_3^m \mu_{33} + V_3^m \mu_{33}^s}, \\ \bar{e}_{3j} &= \frac{\mu_{33} e_{3j}}{V_3^p \mu_{33} V_3^m \mu_{33}^s} \end{aligned} \quad (8.112)$$

Here, v_i^p and v_i^m , for $i = 1$ and 2 represent, respectively, the length fractions of the ceramic and matrix phases along direction i and:

$$V_3^p = \frac{\frac{p}{h}}{\frac{p}{h} + (1 - V_2^p)} b \ll p \quad (8.113)$$

represents the volume fraction of the ceramic phase in the RVE. The details of the above derivation can be found in Roy Mahapatra [20]. Similar models for uniform-packing circular fibers can be found in Bent [13]. Essentially, these models provide dominant electromechanical coupling in direction '3', which can be aligned along the local host beam axis during bonding or embedding. This is unlikely in a uniformly electroded PZT plate structure.

8.4.4.1 Spectral element modeling of beams with PFC sensors/actuators

Assuming a Euler–Bernoulli-type displacement field for the PFC actuator or sensor system integrated with the host composite beams and considering cross-sectional unsymmetry and neglecting rotational inertia, the governing wave equations can be written as:

$$\begin{aligned} \rho A \frac{\partial^2 u_0}{\partial t^2} - A_{33} \frac{\partial^2 u_0}{\partial x^2} + B_{33} \frac{\partial^3 w}{\partial x^3} + A_{33}^{PFC} \frac{\partial E_z}{\partial x} &= 0 \\ \rho A \frac{\partial^2 w}{\partial t^2} - B_{33} \frac{\partial^3 u_0}{\partial x^3} + D_{33} \frac{\partial^4 w}{\partial x^4} + B_{33}^{PFC} \frac{\partial^2 E_z}{\partial x^2} &= 0 \end{aligned} \quad (8.114)$$

where u_0 , w and E_z are the mid-plane axial displacement, transverse displacement and electric field intensity in the z -direction and ρ is the density of the composite having an area of cross-section A . The three associated force boundary conditions, which are required for the spectral and active spectral finite element models, are given by:

$$\begin{aligned} A_{33} \frac{\partial u_0}{\partial x} - B_{33} \frac{\partial^2 w}{\partial x^2} - A_{33}^{PFC} E_z &= N_x, \\ B_{33} \frac{\partial^2 u_0}{\partial x^2} - D_{33} \frac{\partial^3 w}{\partial x^3} - B_{33}^{PFC} \frac{\partial E_z}{\partial x} &= V_x \\ -B_{33} \frac{\partial u_0}{\partial x} + D_{33} \frac{\partial^2 w}{\partial x^2} + B_{33}^{PFC} E_z &= M_x \end{aligned} \quad (8.115)$$

where:

$$\begin{aligned} [A_{33}, B_{33}, D_{33}] &= \int_A C_{33}^{eff} [1, z, z^2] dA, \quad [A_{33}^{PFC}, B_{33}^{PFC}] \\ &= \int_A e_{33}^{eff} [1, z] dA \end{aligned} \quad (8.116)$$

N_x is the axial force, V_x is the shear force and M_x is the bending moment. Once the constitutive model, the governing differential equation and its associated boundary conditions are known, then one can proceed to formulate the required spectral finite element, as outlined in Chapter 7. For this, first the wavenumbers are characterized, followed by the solution of the differential equation in the transformed domain, which is used as the interpolating function for spectral element formulation.

8.4.4.2 Spectral element modeling of beams with magnetostrictive sensors/actuators

The spectral element formulation for modeling composite beams with embedded/surface-mounted magneto-

trictive sensors/actuators is very similar. The constitutive law for the magnetostrictive material is of the form:

$$\varepsilon_z = S_{33}^H \sigma_z + d_{33}^m H_z, \quad B_z = d_{33}^m \sigma_z + \mu_{33}^a H_z \quad (8.117)$$

The governing equation for a beam with a magnetostrictive actuator using the Euler–Bernoulli beam model is given by:

$$\begin{aligned} \rho A \frac{\partial^2 u_0}{\partial t^2} - A_{33} \frac{\partial^2 u_0}{\partial x^2} + B_{33} \frac{\partial^3 w}{\partial x^3} + A_{33}^m \frac{\partial H_z}{\partial x} &= 0 \\ \rho A \frac{\partial^2 w}{\partial t^2} - B_{33} \frac{\partial^3 u_0}{\partial x^3} + D_{33} \frac{\partial^4 w}{\partial x^4} + B_{33}^m \frac{\partial^2 H_z}{\partial x^2} &= 0 \end{aligned} \quad (8.118)$$

and the associated force boundary conditions are:

$$\begin{aligned} A_{33} \frac{\partial u_0}{\partial x} - B_{33} \frac{\partial^2 w}{\partial x^2} - A_{33}^m H_z &= N_x, \\ B_{33} \frac{\partial^2 u_0}{\partial x^2} - D_{33} \frac{\partial^3 w}{\partial x^3} - B_{33}^m \frac{\partial H_z}{\partial x} &= V_x \\ -B_{33} \frac{\partial u_0}{\partial x} + D_{33} \frac{\partial^2 w}{\partial x^2} + B_{33}^m H_z &= M_x \end{aligned} \quad (8.119)$$

where:

$$\begin{aligned} [A_{33}, B_{33}, D_{33}] &= \int_A S_{33} [1, z, z^2] dA, \\ [A_{33}^m, B_{33}^m] &= \int_A d_{33} [1, z] dA \end{aligned} \quad (8.120)$$

The rest of the procedure of spectral finite element formulation is similar to that outlined in Chapter 7

8.5 MODELING OF MICRO ELECTROMECHANICAL SYSTEMS

Modeling and analysis of an MEMS device is absolutely essential for validating the design and performance. These devices are of a few millimeters in dimensions and a few microns in thickness. The most important question one has to answer here is that ‘can we employ the analysis tool developed for macro structures’?. ‘Can we idealize the constitutive model for these structures in the same manner as the macro structures, since it is a question of scale?’ . Most MEMS analyses are performed using the conventional finite element technique and the experience reported in many papers in the literature is that the techniques for macro models give acceptable

results. When an MEMS device is used in structural applications, they are surface bonded and as such, they contribute to negligible stiffness to the complete structure. Since the area of application of the device is small, it can be considered as a point-sensing case. In such cases, the performance of the MEMS device can be assessed based on the component analysis. However, in certain applications, such as crack sensing in a structure, the stresses at the crack tip are theoretically infinite and hence small devices mounted at a number of location may not perform to the desired level. In such cases, one has to go onto distributed sensing, where the sensor could be a few centimeters in dimensions and will still retain the micron-level thickness. In such a case, due to longer dimensions, the modeling of the MEMS device should also take care of the host structure to account for the losses during response transfer. The mechanics here is more complex compared to the point-sensing case.

There are different types of MEMS device available with the most common type being the capacitive device, where the performance (sensitivity) and design of the device is essentially assessed based on the capacitance of the electrical circuit of the device. Typically, an MEMS device will have a wafer of a few microns thickness and in most cases are made of silicon or a polymer and in many cases, they are also made of PZT material. Over these wafers, IDTs (interdigitated transducers) or electrodes are placed to get the required actuation due to the electric field. Hence, the constitutive models for these devices are very similar to those of bulk piezoelectric (PZT) materials. The general procedure for design of MEMS capacitive sensors is that first the minimum capacitance required by the electrical circuit of the device for sustaining the general mechanical loading is obtained through electromechanical analysis. The electrical circuit is then designed to get the required capacitance.

There are many papers on the analysis of MEMS devices, such as pressure sensors, accelerometers, rate gyroscopes etc., available in the literature. Most of these use the FE technique to model the device and assess its performance without considering on what structure it is going to be mounted. This is because of the assumption of point-sensing. Hence, the aspects of modeling point-sensors are not addressed here since a knowledge of the FEM addressed earlier in this book (Chapter 7) will be sufficient enough for this. Here, we address the analysis and design aspects of distributed MEMS sensors, wherein the modeling will take care of the host structure material properties and the properties of sensors such as the thickness of wafers, thickness of the IDT, material properties of the sensor and the loss factor due to leakage

of response from the structure and sensor. Modeling of one such sensor, namely the capacitive thin film sensor, is addressed in the next subsection.

8.5.1 Analytical model for capacitive thin-film sensors

Here, a novel analytical technique towards the design and development of thin-film distributed and deformable capacitive sensors in a composite structure is presented. The approach is a ‘one-step’ improvement over the already prevailing analysis and design methodology for conventional micro electromechanical transducers. In engineering structural health monitoring (SHM) applications, the identification of hidden structural defects and any damage process taking place at the sub surface and/or in deep interlaminar regions in composites are of great importance. Conventional strain gauges and MEMS sensor arrays are being used for performing the damage detection task. Similarly, in electroactive flexible adaptive structures for shape and vibration-control applications, understanding the effects of various material and geometric parameters on the electromechanical coupling is essential.

One of the major concerns for MEMS is the relatively poor reliability caused by delamination, brittle fracture and fatigue degradation of multilayer thin-film structures. However, identification of the damage configuration, which is non-local and spatio-temporal, can be performed best if a continuous distributed film sensor with segmented electrode arrays (like a synthetic skin with active pixels/grids for imaging) can be modeled, designed and fabricated. While validating such a design concept, it is essential to incorporate several effects, such as electromechanical coupling in the sensor structure, dissipation factor in the sensor materials, bulk electrical resistivity of the sensor material and AC frequency and loss factor of the matrix, as against the conventional design, where all of these factors are not taken into consideration. For certain materials, where the dipoles do not get oriented instantly and hence show significant reaction times, there is a phase delay in the polarization that results from the sinusoidal electric field. A detail analytical model incorporating all of these effects appears necessary.

Most of the analytical and finite element analysis techniques for coupled electromechanical simulations reported in the literature are based on iterations over the mechanical and electrical equivalents of the stress field to achieve optimum capacitances and voltages (Schrag *et al.* [21]). In recent times, there has been

increasing effort in developing analytical techniques to study the constrained effect on thin films [22,23]. Similar problems in deformable capacitive devices for distributed transducer applications are also expected to play an important role and a systematic analytical model of the coupled electromechanical field appears advantageous. Here, we develop an electromechanical continuum field model to analyze the constrained boundary effects on the transduction performance of thin films based on the method of stress transfer and strain continuity.

Here, we shall consider a simple model of the sensor film bonded to the surface of the host structure. A constant in-plane tensile stress profile in the host layer is considered to be directly transferred to the film, along with the condition of strain continuity at the interface. A plane-stress case of a surface-mounted sensor on the host structure is considered here. The free-body diagram of the sensor is shown in Figure 8.19. The stress transfer mechanism is based on the shear-lag model [24].

In the following derivation, we use the superscript *s* to indicate the variables in the host structural domain and a superscript *a* to indicate the variables in the film domain. As shown in Figure 8.19, t_s , t_m and $t_{a/2}$ are, respectively, the thickness of the host structure (an equivalent thickness for effective stress transfer), the thickness of the bonding layer and the thickness of the film. Considering a ‘span-wise’ segment of infinitesimal length dx of the film along with the bonding layer, the equilibrium equations can be written as:

$$d\sigma_{xx}t_a b + 2bdx\tau_{xz} = 0, \quad d\sigma_{xx}^s t_s b - bd\sigma_{xx}^s = 0 \quad (8.121)$$

where τ_{xz} is the shear stress transferred from the host structure to the film through the bonding layer. From the shear-lag model, we have:

$$\tau_{xz} = G^* \frac{u^s - u^a}{t_m} \quad (8.122)$$

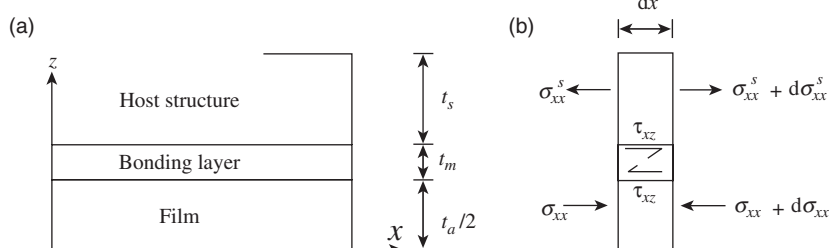


Figure 8.19 Schematic of a surface-mounted sensor based on stress transfer and strain continuity at the bonding layer.

Differentiating Equation (8.121) three times and substituting $\sigma_{xx} = C_{11}\epsilon_{xx}$ and $\sigma_{xx}^s = C_{11}^s\epsilon_{xx}^s$, after some simplification, we get:

$$\frac{d^4\epsilon_{xx}^s}{dx^4} - \Gamma_0^2 \frac{d^2\epsilon_{xx}^s}{dx^2} = 0, \quad \frac{d^4\epsilon_{xx}}{dx^4} - \Gamma_0^2 \frac{d^2\epsilon_{xx}}{dx^2} = 0 \quad (8.123)$$

where:

$$\Gamma_0^2 = \frac{G^*}{C_{11}^s t_s t_m} \left(\frac{2C_{11}^s t_s + C_{11} t_a}{C_{11} t_a} \right) \quad (8.124)$$

Here, G^* is the complex shear modulus of the bonding layer taking into account its viscoelastic properties as a generalization of the analytical model and C_{11}^s and C_{11} are the 1-D material constants of the sensor and host, respectively; u^s and u^a are the interface displacements of sensor and host structure, respectively. The general solution for Equation (8.123) is given by:

$$\begin{aligned} \epsilon_{xx}^s &= a_1 + a_2 x - \frac{C_{11} t_a}{2C_{11}^s t_s} (a_3 \sinh(\Gamma_0 x) + a_4 \cosh(\Gamma_0 x)) \\ \epsilon_{xx} &= a_1 + a_2 x + (a_3 \sinh(\Gamma_0 x) + a_4 \cosh(\Gamma_0 x)) \end{aligned} \quad (8.125)$$

Boundary conditions are now applied separately on the host structure and on the film, which are:

$$\epsilon_{xx}^s(x) = \frac{\sigma_{xx}^s}{C_{11}^s}, \quad \sigma_{xx}(\pm L/2) = 0 \quad (8.126)$$

The above boundary conditions enable determination of all constants in Equation (8.125), which are given by:

$$\begin{aligned} a_1 &= \frac{\sigma_{xx}^s}{C_{11}^s \left(1 + \frac{C_{11} t_a}{2C_{11}^s t_s} \right)}, \quad a_2 = 0, \quad a_3 = 0, \\ a_4 &= -\frac{a_1}{\cosh\left(\Gamma_0 \frac{L}{2}\right)} \end{aligned} \quad (8.127)$$

For pure sensory transduction, that is, assuming all the stresses are transformed into electric potential and dissipated through the circuit:

$$\sigma_{xx} = C_{11}\varepsilon_{xx} - e_{31}\frac{\Delta\Phi}{t_a}, \quad D_z = e_{31}\varepsilon_{xx} + \mu_{33}\frac{\Delta\Phi}{t_a} \quad (8.128)$$

where $\Delta\Phi$ is the change in the electric potential. Note that the electric potential is related to the electric field by the relation $E_z = d\Phi/dz$. The surface charge accumulated over the film segment of width b and span x ($= -L/2, +L/2$) is given by:

$$Q = \int_{-L/2}^{+L/2} D_z b dx = \left(\frac{e^2_{31}}{C_{11}} + \mu_{33} \right) \frac{b C_{11} \sigma_{xx}}{e_{31} C_{11}^s \left(1 + \frac{C_{11} t_a}{2 C_{11}^s t_s} \right)} \int_{-L/2}^{L/2} \left[1 - \frac{\cosh(\Gamma_0 x)}{\cosh(\Gamma_0 \frac{L}{2})} \right] dx \quad (8.129)$$

Equating the deformation-induced electric power generated, the equivalent capacitance $\Re = (\int_0^L (D_z b dx / \Delta\Phi))$ of the film segment L is obtained as:

$$\Re = \left(\frac{e^2_{31}}{C_{11}} + \mu_{33} \right) \frac{b}{t_a} \left[L - \frac{4 \sinh(\Gamma_0 \frac{L}{2})}{\cosh(\Gamma_0 \frac{L}{2}) \Gamma_0} + \frac{1}{4 \cosh^2(\Gamma_0 \frac{L}{2})} \left(\frac{2 \sinh(\Gamma_0 L)}{\Gamma_0} + 2L \right) \right] \quad (8.130)$$

Clearly, the capacitance value depends on both the host material as well as on the sensor properties. In addition, in the absence of any piezoelectric effect, the conventional form of electrostatic capacitance given by $b \mu_{33} (L_2 - L_1) / t_a$ can be clearly seen from Equation (8.130).

8.5.2 Numerical example

In this section we show the variation in the capacitance and output voltage based on the proposed model and compared with the results from the conventional expression of electrostatics. Note that in this simple one-dimensional model, only a constant in-plane tensile stress profile in the host structure is assumed to be directly

Table 8.6 Material properties of the films used in numerical studies.

Property	PVDF	PZT
C_{11} (GPa)	2.00	69.00
C_{13} (GPa)	0.768	23.664
C_{33} (GPa)	2.00	55.00
C_{55} (GPa)	0.746	26.336
Poisson's ratio, ν	0.34	0.31
d_{31} (pC/N)	8	-175
d_{33} (pC/N)	15	350
e_{31} (N(V m))	0.02753	-3.79256
e_{33} (N/(V m))	0.03615	15.1088
Relative permittivity, $\epsilon_{33}^s/\epsilon_0$, at $\omega = 1$ MHz	11	1800
Dissipation factor, η_k	0.018	0.018
Volume Resistivity, ρ (ohm m)	5×10^{12}	2×10^{10}

transferred to the sensor film. In addition, further assumption is that the effective thickness t_s of the host structure over which the stress transfer takes place is known.

The material properties of the PVDF and PZT films used in the numerical simulations are shown in Table 8.6. Carbon–epoxy composite (55 % fiber volume fraction) is used as the host structural material with $C_{11} = 55.1$ GPa. The shear modulus of the bonding layer is assumed as $G = 1$ GPa. The viscoelastic property of this bonding layer is modeled as $G^* = G(1 - i\eta)$ where the loss factor $\eta = 0.007$ is assumed. The frequency-dependent dielectric including the effect of AC loss [24] is assumed as:

$$\mu_{33} = \mu_{33}^s (1 - i\eta_\mu) - \frac{i}{\rho_r \omega}$$

where μ_{33}^s is the DC component of the dielectric, η_μ is the AC component of the dielectric loss, ρ_r is the volume resistivity and ω is the AC frequency. In numerical simulations, the thickness of the bonding layer t_m ($= 10 \mu\text{m}$), the film width b ($= 1 \text{ mm}$), the film lengths L ($= 2 \text{ mm}$ and 3 mm), respectively, for PVDF and PZT, and the film thicknesses t_a ($= 10 \mu\text{m}$ and $100 \mu\text{m}$), respectively, are assumed.

Figures 8.20 and 8.21, respectively, show the dependences of the capacitances of the surface-mounted PVDF sensor and PZT sensor on their geometric properties, that is, the film thickness and length.

It can be seen that for both of the PVDF and PZT sensors, the results predicted by the present model differ

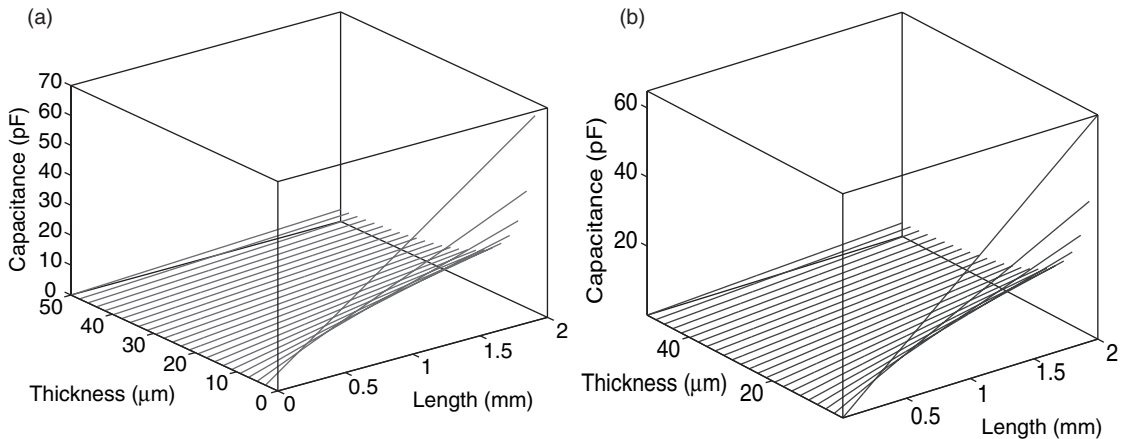


Figure 8.20 Capacitance of a PVDF sensor: (a) present formulation; (b) conventional electrostatics formulation.

from the results predicted by the conventional electrostatics model. This can be attributed to the higher stiffness and higher thickness range that significantly affect the constrained electro mechanical behavior.

Figures 8.22 and 8.23, respectively, shows the variations in the output voltages of the surface-mounted PVDF and PZT sensors on carbon–epoxy composite. It is clear that the low stiffness of the PVDF film produces a smaller voltage amplitude compared to PZT sensor, which has a high stiffness. Normally it is assumed that the admissible in-plane tensile stress is constant throughout the film span, which is not the exact case because of a certain amount of horizontal shear deformation across the sensor film thickness, as the film stiffness increases. This additional contribution of shear energy should be

included in the model to get a better prediction of the voltage.

From the design point of view, it is necessary that for maximum sensitivity of the sensor the capacitance of the electrical circuit is maximized. This will result in minimum impedance and hence a maximum voltage output. Hence, the above model can help in a better design of the capacitive sensors.

8.6 MODELING OF CARBON NANOTUBES (CNTs)

The basic properties of CNTs, their construction, forms and properties were described in Chapter 2. In most

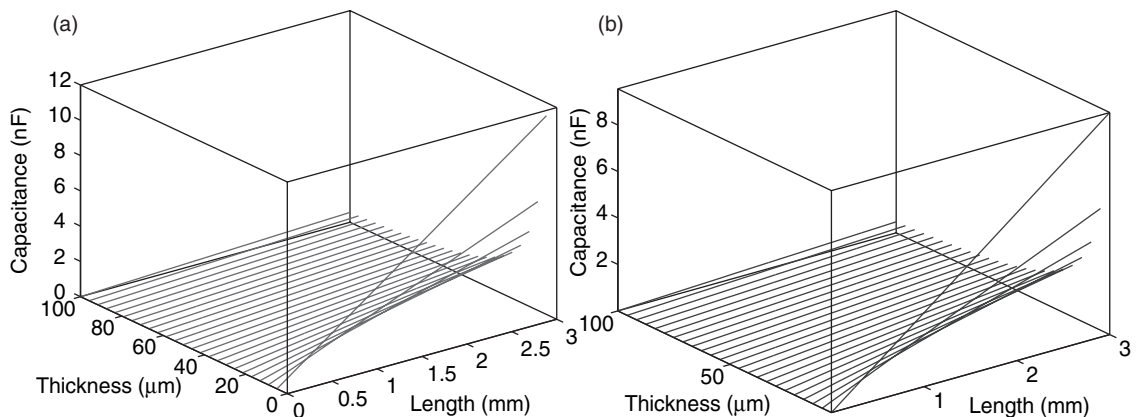


Figure 8.21 Capacitance of a PZT sensor: (a) present formulation; (b) conventional electrostatics formulation.

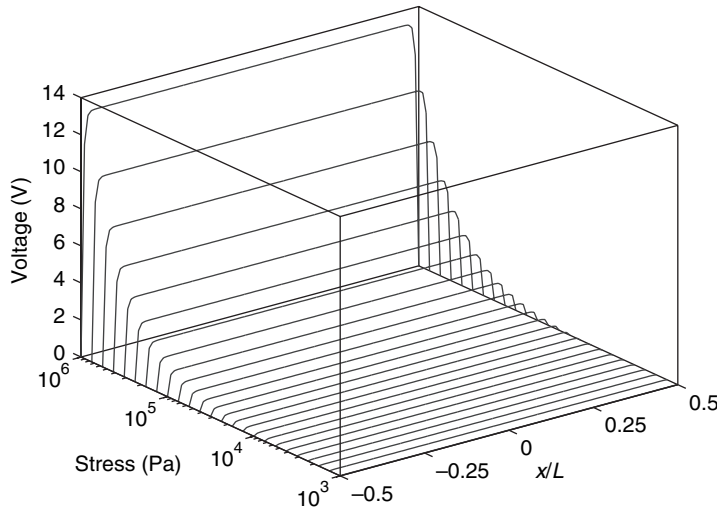


Figure 8.22 Output voltage of a PVDF sensor surface-mounted on carbon–epoxy composite.

structural application, a CNT is normally used as a reinforcing material for the development of new classes of highly strong and lightweight nanocomposites. It has been shown that 1 % by weight of a CNT mixed with a matrix material can yield an increase in stiffness in the range of 36–42 % and an increase in tensile strength of 25 %. The mechanical load-carrying capacity of these nanocomposites are also increased by many orders of magnitude. Hence, when these CNTs are used in conjunction with other materials, the length scales and the

time scales of the host materials and the CNTs are different. Conventional modeling and simulation methods are not well suited for these problems since they are typically formulated at a single time or length scale. It is a great challenge to break the boundaries between scales and develop a robust method that is capable of integrating the different length and time scales involved in a general class of applications. There are essentially three different modeling techniques that have unique time and length scales. These are summarized in Table 8.7.

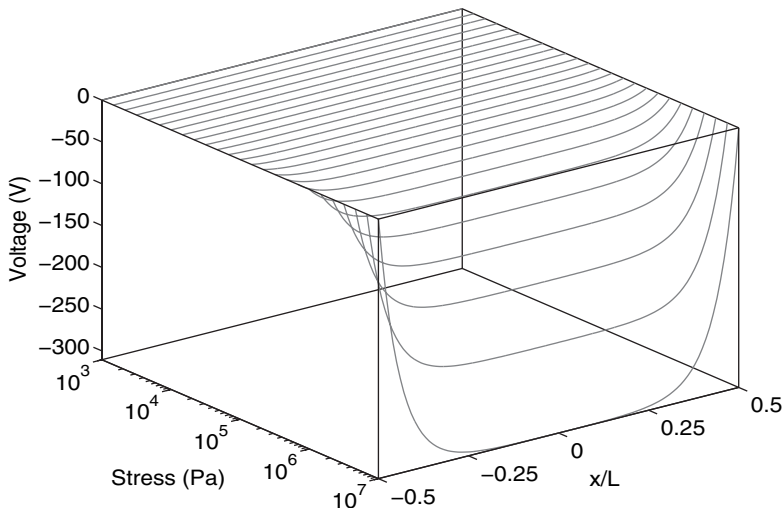


Figure 8.23 Output voltage of a PZT sensor surface-mounted on carbon–epoxy composite.

Table 8.7 Modeling and simulation approaches with their length and time scales.

Modeling approach	Length scale (m)	Time scale (s)
Continuum mechanics	$>10^{-3}$	$>10^{-3}$
Micromechanics	$10^{-6}\text{--}10^{-4}$	$10^{-9}\text{--}10^{-3}$
Molecular dynamics	$10^{-10}\text{--}10^{-6}$	$10^{-12}\text{--}10^{-9}$

The modeling of a CNT alone should be typically performed using *Molecular Dynamics* (MD) simulation. Since the length scales and time scales are very small, the computational cost of modeling is enormous. However, it is the most accurate method of modeling a CNT. The MD approach has provided abundant simulation results for understanding the behaviors of individual and bundled CNTs [24–32]. However, MD simulations cannot deal with the larger length scales in studying nanocomposites. Nanocomposites for engineering applications must expand from nano to micro, and eventually to macro-length scales.

The next alternative is *Micromechanics* (MM) modeling, where a *Representative Volume Element* (RVE) with a built-in CNT is considered, as shown in Figure 8.24. This is classified as a ‘middle-level’ analysis inbetween the molecular dynamics method and *Continuum Mechanics* (CM) modeling.

Many micromechanical models have been developed to predict the macroscopic behavior of composite materials reinforced with fibers, such as laminated compo-

sites, that are much larger than the CNT. These models assume that the fiber, matrix and sometimes the interface, are *continuous* materials and the constitutive equations for the bulk composite material are formulated based on assumptions of continuum mechanics. That is, an RVE is isolated and the continuum theory (*Theory of Elasticity*) is applied to this isolated RVE. The RVE can be of any shape. Many researchers have studied the behavior of CNTs embedded in a matrix using both cylindrical and square RVEs [33]. If the properties of the CNT and its volume fraction are known, then the effective properties of this nanocomposite can be computed using the law of mixtures given in Chapter 6 (Section 6.2). The MM analysis is based on the assumption that quantities such as mass, momentum and energy exist in a mathematical sense, irrespective of the length or time scales. In most cases reported in the literature, RVE analysis has been used for estimation of the material properties. Due to the computational limitation of the MD approach, researchers have adopted continuum mechanics to model a CNT, that is, by using an idealization of an SWCNT, as shown in Figure 8.25. In most models, elastic, isotropic and small deformations are assumed. Yakobson *et al.* [34] gave the analytical energy expressions for shells in terms of the local stresses and deformations. The parameters entering this expression were derived from atomistic simulations. The various deformation modes and critical strains were calculated analytically and found to be in good agreement with the results from microscopic studies. Govindjee and Sackman [35] used the Bernoulli–Euler beam bending theory to investigate the applicability of continuum theory to study the behavior of a CNTs. They emphasized that the tube should be broken down

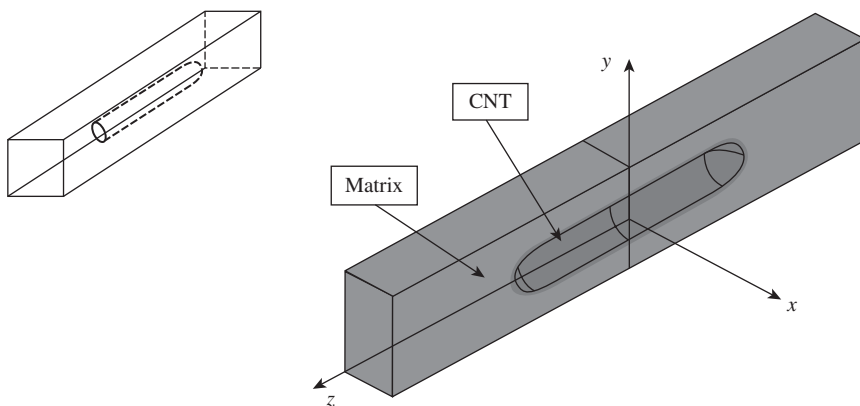


Figure 8.24 Representative volume element (RVE) of a carbon nanotube embedded in a matrix. Reprinted from Computational Materials Science, 29, pp. 1–11, Copyright 2004, with permission from Elsevier

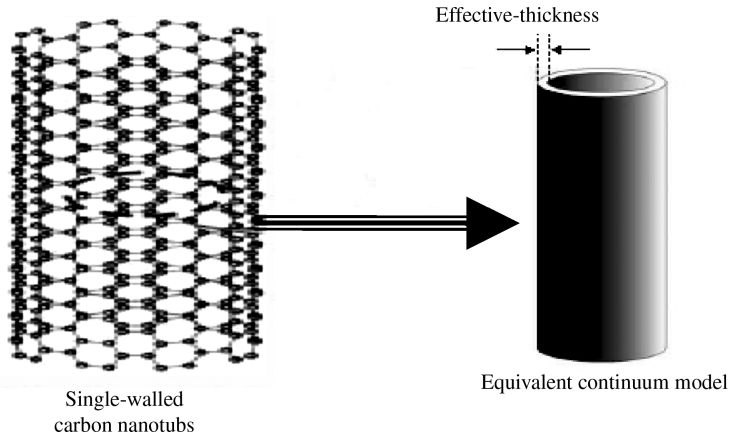


Figure 8.25 Equivalent continuum model of a single-wall carbon nanotube.

into a number of parallel cross-sections, rather than described as a single rod/beam. A similar point was made by Ru [36] who emphasized that the continuum shell theory breaks down once atomic dimensions are reached. Thus, attempts to reconcile the continuum theory with atomistic simulations had to use parameters, such as the effective thickness of the shell, whose physical origins are doubtful at best. Finally, a clear breakdown of the continuum theory occurs when the tubes undergo plastic deformation, since the continuum model is insensitive to the chirality of the wrapping index, while tight-binding MD simulations are believed to show a dependence of the elastic limit on chirality. Clearly, the continuum approximation can be very valuable and may be the only feasible approach for large and complex systems, but its applicability deserves further investigation.

Some of the common models in continuum mechanics, such as finite element techniques, are normally employed to study the behaviors of SWCNTs and MWCNTs. These are straightforward approaches, which were dealt with extensively in the last chapter. The only difference is that the modeling is done on the nano scale. Hence, FE modeling of a CNT is not dealt with here. However, recently CNTs have been used for a variety of applications which require propagation of signals at very high frequencies [37,38]. These frequencies are in THz range and at these frequencies it is almost unthinkable to use conventional FE modeling due to the very small wavelengths and hence very small element sizes (of the order of nm–μm). In such situations spectral FE modeling is the only option. Hence, we outline the spectral finite

element modeling of single- and multi-walled nano tubes and show how one can propagate the THz frequencies in such tubes.

8.6.1 Spectral finite element modeling of an MWCNT

The spectral FE formulation begins by computing the wavenumbers to determine the types of waves propagating in the CNT. For this, we need to first establish the governing PDE of the multi-walled CNT. The multiple-elastic beam model for an N -walled CNT, based on the Euler-Bernoulli beam theory, is governed by the following set of N -coupled equations:

$$\begin{aligned}
 c_1(w_2 - w_1) &= EI_1 \frac{\partial^4 w_1}{\partial x^4} + \rho A_1 \frac{\partial^2 w_1}{\partial x^2} \\
 &\dots \\
 &\dots \quad p = 2, 3, \dots, N-1 \\
 c_p(w_{p+1} - w_p) - c_{p-1}(w_p - w_{p-1}) &= EI_p \frac{\partial^4 w_p}{\partial x^4} + \rho A_p \frac{\partial^2 w_p}{\partial x^2} \\
 &- c_{N-1}(w_N - w_{N-1}) = EI_N \frac{\partial^4 w_N}{\partial x^4} + \rho A_p \frac{\partial^2 w_N}{\partial x^2}
 \end{aligned} \tag{8.131}$$

where x is the axial coordinate of the beam, t is the time, $w_p(x, t)$ ($p = 2, \dots, N$) is the deflection of p th CNT, I_p and A_p are, respectively, the moment of inertia and the area of the cross-section of the p th tube. The Young's modulus $E = 1$ TPa (with an effective thickness 0.35 nm) and the mass density $\rho = 1300$ kg/cm³. The interaction

coefficients c_p ($p = 1, 2, \dots, N$), arising due to van der Waals interactions between any two adjacent layers, can be estimated approximately as given in Yoon *et al.* [39]:

$$c_p = \frac{400R}{16d^2} \text{ erg/cm}^2, \quad d = 0.142 \text{ nm}, \quad p = 1, 2, \dots, N-1 \quad (8.132)$$

where R_p is the inner radius of the p th wall. The coefficients c_p are estimated as the second derivative of the energy-interlayer spacing relations of two flat monolayers. Hence, they do not take the curvature effects of the CNTs into account. The spectral formulation begins by assuming the displacement field as a synthesis of plane waves of the form:

$$w_p(x, t) = \sum_{n=1}^{N_q} \tilde{w} e^{j k x} e^{j \omega_n t} \quad (8.133)$$

where k is the wavenumber, ω_n is the circular frequency at the n th sampling point and $j^2 = -1$; N_q is the frequency index corresponding to the Nyquist frequency in the Fast Fourier Transform (FFT). When Equation (8.133) is substituted into Equation (8.131), we get:

$$\begin{aligned} c_1(\tilde{w}_2 - \tilde{w}_1) - (EI_1 k^4 - \rho A_1 \omega^2) \tilde{w}_1 &= 0 \\ \dots & \\ \dots & \\ c_p(\tilde{w}_{p+1} - \tilde{w}_p) - c_{p-1}(\tilde{w}_p - \tilde{w}_{p-1}) - (EI_p k^4 - \rho A_p \omega^2) \tilde{w}_p &= 0 \\ - c_{N-1}(\tilde{w}_N - \tilde{w}_{N-1}) - (EI_N k^4 - \rho A_N \omega^2) \tilde{w}_N &= 0 \end{aligned} \quad (8.134)$$

The above equation is a complicated polynomial that requires special schemes for the solution of the wavenumbers. The order of the polynomial increases with an increase in the value of N , the number of walls. Instead of using some adhoc schemes, we need a generalized and robust scheme of polynomial equation solving. In addition, after the solution of the wavenumbers, spectral formulation requires computation of wave amplitudes for all propagating modes. In numerical solution schemes for the roots of the above polynomial equation, it is practically impossible to keep track of individual modes. There are two different methods of equation solving that can remove most of the above problems, namely the *Companion Matrix* (CM) approach and the *Polynomial Eigenvalue Problem* (PEP) approach. These methods can be employed with the *Singular Value Decomposition* (SVD) technique to obtain the wave amplitudes. These

methods, in relation to the wave propagation, are explained in great detail in Chakraborty [40].

In the present case, the PEP approach is used to solve for the wavenumbers. We can write Equation (8.134) as:

$$\left(k^4[A_4] + [A_0] \right) \{v\} = [W]\{v\} = 0, \quad \{v\} = \{w_1 \dots w_N\}^T \quad (8.135)$$

where $[A_4]$ and $[A_0]$ are $N \times N$ matrices given by:

$$[A_4] = \text{Diag}(EI_p, \quad p = 1, 2, \dots, N), \quad [A_0] = [C] - \omega^2[M] \quad (8.136)$$

Furthermore, the matrices $[M]$ and $[C]$ are defined as:

$$[M] = \text{Diag}(\rho I_p, \quad p = 1, 2, \dots, N), \quad [C] = \Re^N_{n=1}(c_n) \quad (8.137)$$

where \Re is an assembly operator (like the stiffness matrix assembler of a rod element) and the matrix c_n is defined as:

$$[c_n] = \begin{bmatrix} c_n & -c_n \\ -c_n & c_n \end{bmatrix}$$

On solving Equation (8.135), the eigenvalues k and the eigenvectors $\{v\}$ can be obtained, which will be used in subsequent element formulation. Since, in the PEP the coefficient matrices of k , k^2 and k^3 are zero, we can minimize the cost of computation by substituting λ for k^4 in Equation (8.135) and solving the PEP as a generalized eigenvalue problem:

$$[A_0]\{v\} = \lambda[-A_4]\{v\}$$

and the desired wavenumbers can be expressed as ± 1 and $\pm j$ times $\lambda^{1/4}$. However, the eigenvectors obtained in this method will be of no consequence and the real eigenvectors need to be computed in a different way.

For an N -walled nanotube, there are $4N$ wavenumbers and corresponding N phase speeds (c_p) and group speeds (c_g). The definition of these speeds is defined in Chapter 6 (Section 6.3). Although the phase speeds can be computed directly from the wavenumbers, it is not straightforward to compute the group speeds. Here, they are computed using the characteristic equation, which is given by:

$$\phi(k) = \det(k^4[A_4] + [A_0]) = 0 \quad (8.138)$$

These equations are polynomials in k , whose general form is:

$$\phi(k) = \sum_{p=0}^N a_p k^{4p}$$

where the coefficients a_p are dependent on material properties and other than a_0 , all are functions of ω . Differentiating $\phi(k)$ with respect to k , and using the definition of the expression for (c_g) the latter becomes:

$$c_g = \frac{d\omega}{dk} = \frac{\sum_{p=1}^N (4pa_p k^{4p-1})}{\sum_{p=1}^N a'_p k^{4p}} \quad (8.139)$$

where a'_p indicates the derivative of a_p with respect to ω . While computing the group speeds using the above expression, for $Re(k) < 0$, the group speeds will be zero. One characteristic of this multi-walled beam-based model is that there are $N - 1$ frequencies where the wavenumber becomes zero, thus rendering the group speed equals to zero and the phase speed escapes to infinity. These frequencies are called the ‘cut-off frequencies’, whose expression can be obtained by substituting $k = 0$ in the dispersion relation and solving for k . However, for large N , the problem of root finding of a polynomial becomes a cumbersome task (even if we use the companion-matrix-based technique, we have to form the related matrices). The problem becomes simple if $k = 0$ is substituted into Equation (8.135) and the task of finding ω is identified as another PEP:

$$([C] - \omega^2[M])\{x\} = 0 \quad (8.140)$$

where $\{x\}$ is a hypothetical eigenvector of no consequence in our subsequent formulation. For $N = 2$, there is one cut-off frequency given by:

$$\omega_c = \left[\frac{c_1(A_1 + A_2)}{\rho A_1 A_2} \right] \quad (8.141)$$

which for equal cross-sectional properties reduces to $2c_1/\rho A$.

For the spectral element formulation, it is essential to know the eigenvectors $\{v\}$ of the PEP given in Equation (8.135), which are also known as the wave vectors. This PEP can be solved directly by the method of linearization

for obtaining $\{v\}$ or the method of singular value decomposition (SVD) can be adopted. In the first method, the PEP is converted into a generalized eigenvalue problem in terms of the matrices $[A_4]$ and $[A_0]$. These matrices are constructed in the following way. If the PEP is posed as:

$$\Psi(\lambda)x = (\lambda^l A_l + \lambda^{l-1} A_{l-1} + \dots + \lambda A_1 + A_0)\{x\} = 0, \\ A_l \in C^{m \times m}$$

then the problem is linearized to:

$$[A]\{z\} = \lambda[B]\{z\} \quad (8.142)$$

where:

$$[A] = \begin{bmatrix} [0] & [I] & [0] & \dots & [0] \\ [0] & [0] & [I] & \dots & [0] \\ \vdots & \ddots & \ddots & \ddots & \vdots \\ \vdots & \ddots & \ddots & \ddots & \vdots \\ [-A_0] & [-A_1] & [-A_2] & \dots & [-A_{l-1}] \end{bmatrix},$$

$$[B] = \begin{bmatrix} [I] & & & & \\ & [I] & & & \\ & & \ddots & & \\ & & & [I] & \\ & & & & -[A_l] \end{bmatrix}$$

and the relation between $\{x\}$ and $\{z\}$ is given by:

$$\{z\} = \left\{ \{x\}^T \quad \lambda\{x\}^T \quad \dots \quad \lambda^{l-1}\{x\}^T \right\}^T$$

Here, $[B]^{-1}[A]$ is a block companion matrix of the PEP. The generalized eigenvalue problem of Equation (8.142) can be solved by the QZ algorithm, iterative method, Jacobi–Davidson method or the rational Krylov method. Each one of these has its own advantages and disadvantages; however, the QZ algorithm is the most powerful method for small-to-moderate-sized problems and hence for this present problem, as the order of the matrices $[A]$ and $[B]$ is not large ($l = 4$, $m = N$) and hence the computation can be performed by the economic and efficient subroutines available in many mathematical software packages, such as LAPACK.

In the second method, it is noted that $\{v\}$ are the elements of the null space of the matrix $[W]$ (which has non-trivial elements as the matrix is singular). In the

SVD technique, $[W]$ is factorized as $[W] = [U][S][V]^H$ where $[S]$ is a diagonal matrix containing the singular values. Since, $[W]$ is singular, there will be zero diagonal elements in $[S]$ and the columns of $\{v\}$ corresponding to the zero singular values are the elements of the null space of $[W]$ (actually they form a basis for the null space). The SVD can be also be performed by the LAPACK subroutines.

After the wavenumbers and wave amplitudes are computed, the spectral element formulation procedure is same as that given in Chapter 7 (Section 7.9). Hence, the formulation is not repeated here. Now, we will take a closer look at the behavior of waves in an MWCNT.

The wavenumber and group speed variations for $N = 3$ are plotted in Figures 8.26 and 8.27, respectively. These plots were obtained using the following properties; Young's modulus E equal to 1.0 TPa, shear modulus G equal to 0.4 TPa, density ρ equal to 1300 kg/m^3 , inner wall radius equal to 5 nm, wall thickness equal to 0.35 nm and the van der Waals interaction force equal to 0.62 TPa. The plot above the zero value represents the real (propagating components) wavenumber while the plot below the zero value is the imaginary value of the wavenumber (evanescent components). As previously

mentioned, there are two cut-off frequencies, one at 1.014 and another at 1.757 THz. At these frequencies, the wavenumber becomes zero, while the corresponding phase speed becomes infinite and the group speed zero. However, before the cut-off frequencies, the wavenumbers (k_2 and k_3) have real as well as imaginary parts, which indicate that there are propagating components of these modes. Due to the presence of the imaginary part, these waves will, however, attenuate while propagating. Thus, these waves are the so-called *inhomogeneous waves*. Thus, there are non-zero phase and group speeds before the cut-off frequencies.

For $N = 10$, the spectrum relations and phase speed variations are given in Figures 8.28 and 8.29, respectively. The characteristic remains the same as before, where there are nine cut-off frequencies. The minimum of these is at 0.2886 THz and the maximum at 1.891 THz. Thus, it becomes apparent, even for this many number of tubes that there is no great variation in the maximum cut-off frequency. This suggests that there exists an upper bound to the range of cut-off frequencies and similarly a lower bound. To study this aspect, the number of walls N was varied from 2 to 100 and for these values the

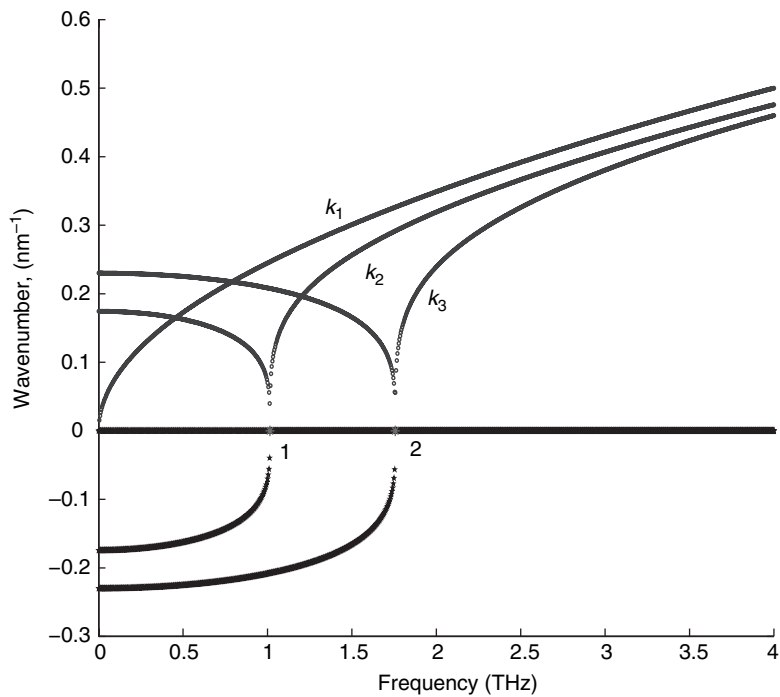


Figure 8.26 Wavenumbers in multi-wall carbon nanotubes for $N = 3$.

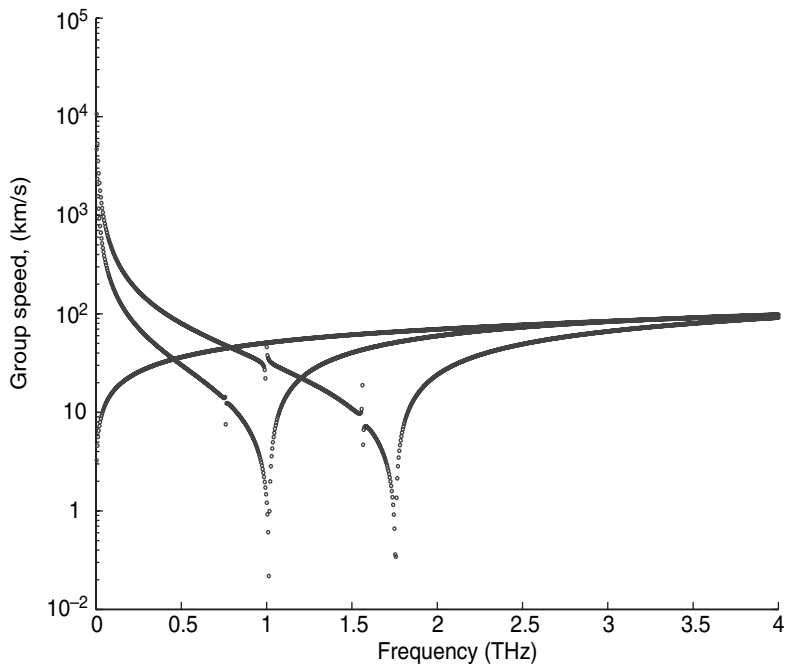


Figure 8.27 Group speeds in multi-wall carbon nanotubes for $N = 3$.

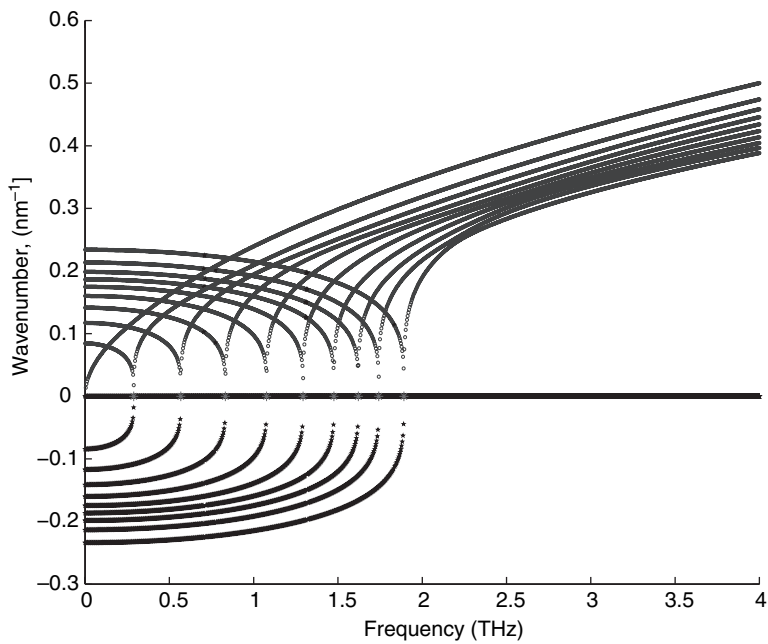


Figure 8.28 Wavenumbers in multi-wall carbon nanotubes for $N = 10$.

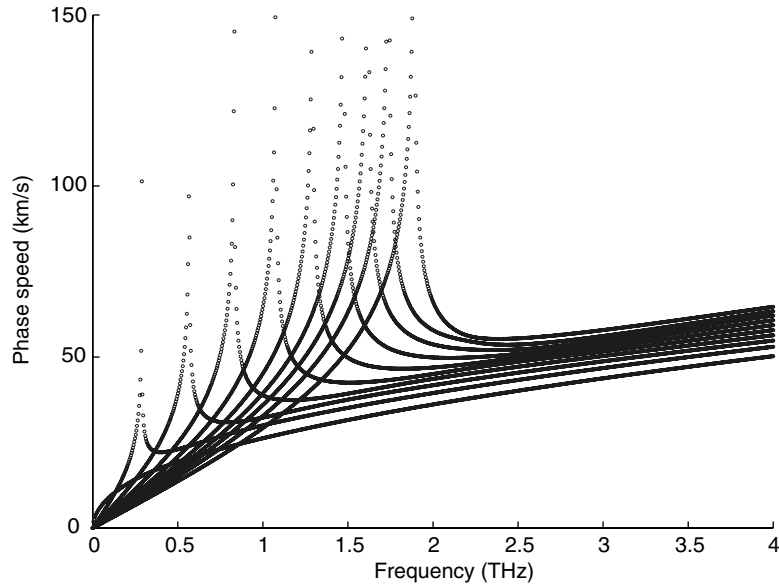


Figure 8.29 Phase speeds in multi-wall carbon nanotubes for $N = 10$.

maximum and minimum cut-off frequencies are plotted in Figure 8.30. This figure suggests that indeed there is both an upper and lower bound of the cut-off frequencies, which, for this particular material and geometric para-

meters, are at 1.891 THz and 0.0169 THz. Since there is no appreciable difference in cut-off frequency with wall numbers, an MWCNT can be approximated by a *Double-Walled Carbon Nanotube* (DWCNT), where the

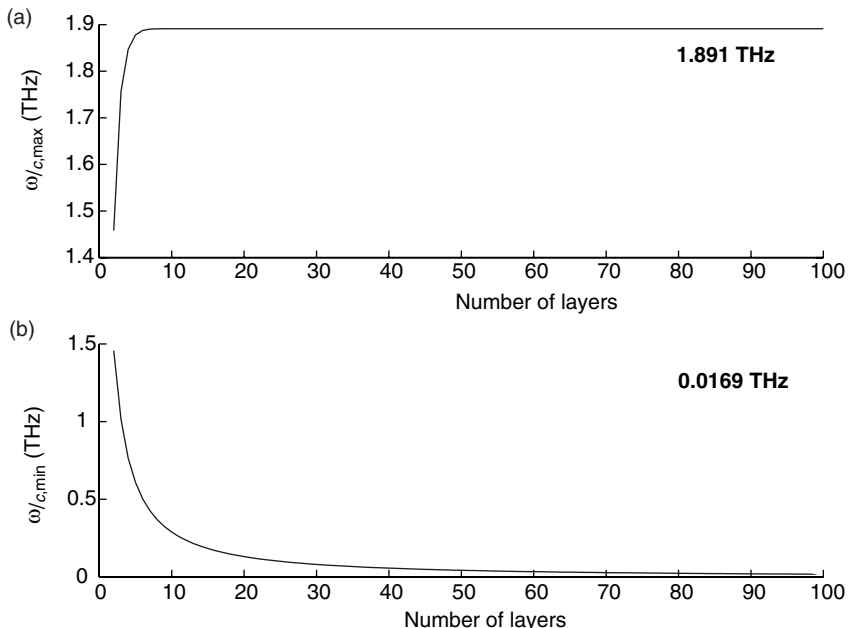


Figure 8.30 Variation of (a) maximum and (b) minimum cut-off frequencies as a function of N .

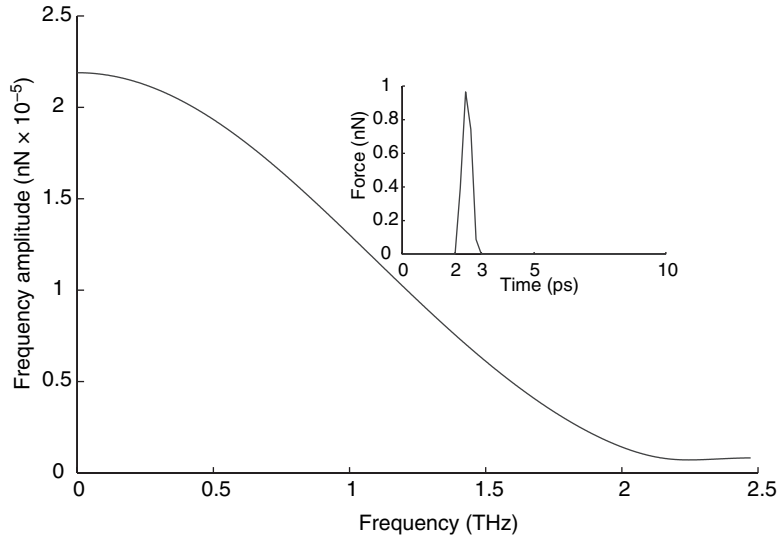


Figure 8.31 Broad-band pulse loading and its frequency amplitude.

effective inner radius of the DWCNT can be obtained from the magnitudes of the maximum and minimum cut-off frequencies. For example, in this present case, for an identical DWCNT, the inner radius will be 1.737 nm, which is obtained by using the maximum cut-off frequency and Equation (8.141).

Once the characteristics of the waves are known, real-time data can be obtained by using the formulated spectral element with a small-duration loading of suitable frequency content. A broad-band pulse is considered with a frequency content of around 2.1 THz, shown in Figure 8.31, which is above the highest cut-off frequency for any N .

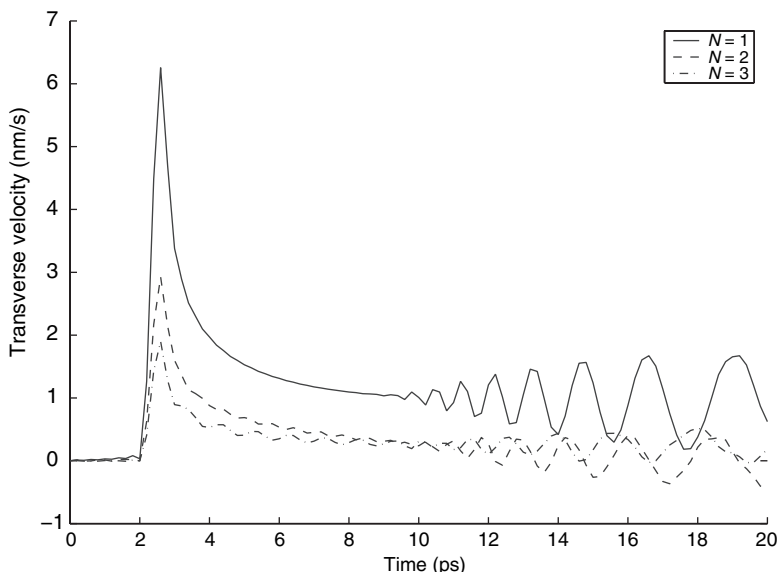


Figure 8.32 Transverse velocity at the free end of a cantilevered multi-wall carbon nanotube for different values of N .

The time-domain data of the loading is shown in the inset in Figure 8.31. As this figure suggests, the load starts at 2 ps and is completed by 3 ps, within which it attains a maximum magnitude of unity. This load is applied at the free end of a cantilever MWCNT and the responses are measured at the tip. The load is equally distributed at all of the tubes so that the total load is always 1 nN.

The transverse velocity history at the tip of the beam is shown in Figure 8.32 for different numbers of walls. The initial peak is the instantaneous effect of the loading, whereas the oscillations at the latter part are reflections from the fixed end of MWCNT. As this figure suggests, with increasing N the overall stiffness increases considerably and the group speed decreases, as is evident from the decreasing magnitude and arrival time of the boundary reflections.

REFERENCES

1. S.H. Chen, Z.D. Wang and X.H. Liu, 'Active vibration control and suppression for intelligent structures, *Journal of Sound and Vibration*, **200**, 167–177 (1997).
2. W.-S. Hwang and H.-C. Park, 'Finite element modeling of piezoelectric sensors and actuators', *AIAA Journal*, **31**, 930–937 (1993).
3. H.S. Tzou and C.I. Tseng, 'Distributed piezoelectric sensor/actuator design for dynamic measurement/control of distributed parameter systems: a piezoelectric finite element approach', *Journal of Sound and Vibration*, **138**, 17–34 (1990).
4. T.H.G. Megson, *Linear Analysis of Thin-Walled Elastic Structures*, Surrey University Press, Guildford, UK (1974).
5. Mira Mitra, *Active Vibration Suppression of Composite Thin Walled Structures*, M.Sc. Thesis, Indian Institute of Science, Bangalore, India (2003).
6. H.S. Tzou, *Piezoelectric Shells (Distributed Sensing and Control of Continua)*, Kluwer Academic Press, Dordrecht, The Netherlands (1993).
7. H.S. Tzou and R. Ye, 'Analysis of piezoelectric structures with laminated piezoelectric triangle shell elements', *AIAA Journal*, **34**, 110–115 (1996).
8. M.C. Reaves and L.G. Horta, 'Test cases for modeling and validation of structures with piezoelectric actuators', in *Proceedings of the 42nd AIAA/ASME/ASCE/AHS/ASC Structures, Structural Dynamics and Materials Conference*, American Institute of Aeronautics and Astronautics (AIAA), Reston, VA, USA (2001) [on CD-Rom].
9. D.P. Ghosh and S. Gopalakrishnan, 'Role of coupling terms in constitutive relationships of magnetostrictive materials, *Computers, Materials and Continua*, **1**, 213–227 (2004).
10. J.L. Butler, *Application manual for the design of Terfenol-D magnetostrictive transducers*, Technical Report TS 2003, Edge Technologies, Inc., Ames, IA, USA (1988).
11. U.K. Vaidya, 'Integrated and multi-functional thick section and sandwich composite materials and structures', in *Proceedings of the ISSS–SPIE International Conference on Smart Materials Structures and Systems*, A. Selvarajan, A.R. Upadhyay and P.D. Mangalgiri (Eds), Allied Publisher, New Delhi, India, pp. 311–318 (1999).
12. J. French, J. Weitz, R. Luke, R. Cass, P. Jadidian, P. Bhargava and A. Safari, 'Production of continuous piezoelectric ceramic fibers for smart materials and active control devices', *SPIE*, **3044**, 406–412 (1997).
13. A.A. Bent, *Active Fiber Composites for Structural Actuation*, Ph.D. Thesis, Massachusetts Institute of Technology, Cambridge, MA, USA (1997).
14. Y. Wu, *Magnetostrictive Particulate Actuator and its Characterization for Smart Structure Applications*, Ph.D. Thesis, University of Maryland, Baltimore Country, MD, USA (1997).
15. J.P. Rodgers and N.W. Hagood, 'Design, manufacture and testing of an integral twist-actuated rotor blade', in *Proceedings of the 8th International Conference on Adaptive Structures and Technology*, pp. 63–72 (1993).
16. S. Yoshikawa and T. Shrout, 'Multilayer piezoelectric actuators – structures and reliability', AIAA Paper, **93-1711-CP**, 3581–3586 (1993).
17. N.W. Hagood, R. Kindel, K. Ghandi and P. Gudenz, 'Improving transverse actuation of piezoceramics using integrated surface electrodes', *SPIE*, **1917**, 1917–1925 (1993).
18. A. Bent, N.W. Hagood and J.P. Rodgers, 'Anisotropic actuation with piezoelectric composites', *Journal of Intelligent Material Systems and Structures*, **6**, 338–49 (1995).
19. Institute of Electrical and Electronics Engineers, *IEEE Standard on Piezoelectricity*, IEEE Standard 176-1978, The Institute of Electrical and Electronics Engineers, Piscataway, NJ, USA (1978).
20. D.R. Roy Mahapatra, *Spectral Element Models for Wave Propagation Analysis, Structural Health Monitoring and Active Control of Waves in Composite Structures*, Ph.D. Thesis, Indian Institute of Science, Bangalore, India (2004).
21. G. Schrag, G. Zelder, H. Kapels and G. Wachutka, 'Numerical and experimental analysis of distributed electromechanical parasitics in the calibration of a fully BiCMOS-integrated capacitive pressure sensor', *Sensors and Actuators: Physical*, **76A**, 19–25 (1999).
22. T.C. Chen, H.C. Wu and C.-L. Lin, 'Longitudinal anisotropic stress and deformation in multilayered film heterostructures due to lattice misfit', *Journal of Crystal Growth*, **249**, 44–58 (2003).
23. N. Mokni, F. Sidoroff and A. Danescu, 'A one-dimensional viscoelastic model for lateral relaxation in thin films', *Computational Materials Science*, **26**, 56–60 (2003).
24. A. Pizzochero, *Residual Actuation and Stiffness Properties of Piezoelectric Composites: Theory and Experiment*, M.Sc. Thesis, Massachusetts Institute of Technology, Cambridge, MA, USA (1998).
25. M. Macucci, G. Iannaccone, J. Greer, J. Martorell, D.W.L. Sprung, A. Schenk, I.I. Yakimenko, K.F. Berggren, K.

- Stokbro and N. Gippius, 'Status and perspectives of nanoscale device modeling' *Nanotechnology*, **12**, 136–142 (2001).
26. J. Han, A. Globus, R. Jae and G. Deardor, 'Molecular dynamics simulations of carbon nanotube-based gears', *Nanotechnology*, **8**, 95–102 (1997).
 27. C.F. Cornwell and L.T. Wille, 'Elastic properties of single walled carbon nanotubes in compression', *Solid State Communications*, **101**, 555–558 (1997).
 28. S.B. Sinnott, O.A. Shenderova, C.T. White and D.W. Brenner, 'Mechanical properties of nanotubule fibers and composites determined from theoretical calculations and simulations', *Carbon*, **36**, 1–9 (1998).
 29. T. Halicioglu, 'Stress calculations for carbon nanotubes', *Thin Solid Films*, **312**, 11–14 (1998).
 30. G.H. Gao, T. Cagin and W.A. Goddard, 'Energetics, structure, mechanical and vibrational properties of single-walled carbon nanotubes', *Nanotechnology*, **9**, 184–191 (1998).
 31. M. Buongiorno Nardelli, J.L. Fattebert, D. Orlikowski, C. Roland, Q. Zhao and J. Bernholc, 'Mechanical properties, defects and electronic behavior of carbon nanotubes', *Carbon*, **38**, 1703–1711 (2000).
 32. J.W. Kang and H.J. Hwang, 'Mechanical deformation study of copper nanowire using atomistic simulation', *Nanotechnology*, **12**, 295–300 (2001).
 33. Y.J. Liu and X.L. Chen, 'Evaluations of the effective materials properties of carbon nanotube-based composites using a nanoscale representative volume element', *Mechanics of Materials*, **35**, 69–81 (2003).
 34. B.I. Yakobson, C.J. Brabec and J. Bernholc, 'Nanomechanics of carbon tubes: instabilities beyond linear range', *Physical Review Letters*, **76**, 2511–2514 (1996).
 35. S. Govindjee and J.L. Sackman, 'On the use of continuum mechanics to estimate the properties of nanotubes', *Solid State Communications*, **110**, 227–230 (1999).
 36. C.Q. Ru, 'Effect of van der Waals forces on axial buckling of a double-walled carbon nanotube', *Journal of Applied Physics*, **87**, 7227–7231 (2000).
 37. J. Yoon, C.Q. Ru and A. Mioduchowski, 'Timoshenko-beam effects on transverse wave propagation in carbon nanotubes', *Composites: Engineering*, **B35**, 87–93 (2004).
 38. J. Yoon, C.Q. Ru and A. Mioduchowski, 'Vibration of an embedded multiwall carbon nanotube', *Composites Science and Technology*, **63**, 1533–1542 (2003).
 39. J. Yoon, C. Ru and A. Mioduchowski, 'Non-coaxial resonance of an isolated multiwall carbon nanotube', *Physical Review*, **B66**, 233–402 (2002).
 40. A. Chakraborty, *Wave Propagation in Anisotropic and Inhomogeneous Structures*, Ph.D. Thesis, Indian Institute of Science, Bangalore, India (2004).

9

Active Control Techniques

9.1 INTRODUCTION

The concept of control, which originated in early 1900, has advanced tremendously to the level that every designed system has a control component in its various functions. One cannot visualize a robot performing without built-in control systems. Today, control plays a major role in almost all branches of engineering. In many space vehicles, missile guidance and robotic systems, control has become an integral part of the manufacturing process. In structural applications, which are mainly addressed in this book, we require control techniques for controlling displacements (velocities or accelerations), pressure (force or stress), temperature, humidity, viscosity, etc. Controlling these quantities translates into many applications such as:

- Vibration control, where control techniques are used to reduce the dynamic displacements.
- Noise control, where acoustical disturbances (dynamical responses) are regulated by using control techniques. In helicopters, we can induce the twist of the rotor blades to control exterior noise (air borne) or treat the path of disturbance to radiate it so as to control the interior noise (structure-borne).
- Shape control, wherein the shape of the structure is modified for a particular application. For example, the shape of the aerofoil of wing or tail surfaces of an aircraft can be altered to change the flow conditions.
- More recently, there have been efforts to control or delay the growth of cracks. The severity of a crack is measured by a quantity called the *Stress Intensity Factor* (SIF) and not the stress. This is because the stress at the crack tip is infinite. Hence, for delaying the growth of cracks, control systems are designed. Here, the quantity that is controlled is the SIF.

The principle behind all control techniques for structural applications is to generate additional forces for enforcing control of the required variable. For example, in vibration-control problems, the control system generates damping forces that reduce the dynamic displacement amplitudes, which are one of the control variables. Hence, for generating such additional forces, an additional input is needed in conventional structures, which in many cases is difficult to generate. However, this is not the case in structures with built-in smart sensors and actuators. Smart sensors/actuators, made of piezoelectric or Terfenol-D materials, exhibit strong electromechanical coupling. As explained in Chapter 8, this results in additional terms in both the actuator and sensor constitutive laws. Here, we are only concerned with the actuator law, wherein this additional term helps in generating the additional input required for the control of the desired variable. This is one of the main reasons why a smart actuator is much more popular as opposed to conventional hydraulic or other types of actuators.

In this chapter, we will not go into greater depth on the control theory. The interested reader is advised to go through some classic control textbooks, such as Ogata [1], for greater detail on automatic modern control theory. Here, we will deal only with those topics that are directly relevant for smart actuation in structural applications. Before going into greater detail on smart actuation, we will define some common definitions that we will encounter while dealing with control theory:

- (1) **Control.** This means a sustained release of energy for limiting or controlling the response of a desired control variable by inducing an additional input in the form of a manipulated variable to the system.
- (2) **Control variable.** This is a quantity such as displacement, force, stress or strain (in structural

applications) that requires to be measured and/or controlled. These are necessarily the output variables. ‘Control of the control variable’ is normally performed through an additional input to the system called the *manipulated variable*.

- (3) **Plant.** This is defined as the physical object that requires control, such as a mechanical device (helicopter rotor blade, mechanical gear, cantilever beam etc.), aircraft, spacecraft, etc.
- (4) **Disturbance.** A signal that propagates through a system carrying a considerable amount of energy is called a disturbance. For enforcing control of a system, one may require many such disturbances, which can be internally generated (by using smart materials) or externally given as an input.
- (5) **Feedback Control.** If due to a disturbance, the difference between the output of the system to some reference input is reduced, and if this reduction was obtained based on this difference, then we term the operation as feedback control.
- (6) **Error Signal.** The difference between the output signal and the feedback signal is called the error signal. In many cases, the feedback signal may be a function of the output signal or its derivatives. In structural applications, the output signals are normally displacements or strain and its derivatives, namely the velocities and accelerations.
- (7) **Closed-loop control.** When the output of the system is brought to the desired value by feeding an error signal to the controller under feedback control, such an action is called closed-loop control.
- (8) **Open-loop control.** A system, in which the outputs do not play any role in the control action of bringing down the response is termed as an open-loop response. That is, the error signal is not needed in the control action and therefore the output is not compared with any reference signal. Hence, a fixed operating condition exists for all inputs and so the accuracy is always not assured and depends on the calibration.
- (9) **Linear System.** A system is said to be linear if the principle of superposition holds for such a system. That is, the response to several inputs can be obtained by treating one input at a time and adding the result. If the governing equation describing the system is of a constant coefficient type, such a system is called a *linear time invariant system*.

As mentioned earlier, we, in this chapter, will give only a ‘bird’s eye view’ of control theory. The material given will address only the smart actuation normally encountered in smart structures applications.

This chapter is organized as follows. First, the mathematical concept of control theory is described, wherein the state-space modeling of a second-order system along with determination of the transfer function and frequency response function are discussed. This is followed by a section on the stability of control systems. This is followed by a section on design concepts and methodology for control systems. Different FE model-order reduction schemes are given next. Finally, the concept of the *Active Spectral Finite Element* (ASFEM) and its use in controller design is addressed.

9.2 MATHEMATICAL MODELS FOR CONTROL THEORY

For the analysis and design of control systems, a proper mathematical model is necessary. A number of different methods are available for the design of control systems. Each method requires a different mathematical model. Central to all of these methods is the second-order differential equation. This differential equation can be characterized in many different forms, depending upon the type of controller that requires to be designed. For example, in a *Single-Input-Single-Output* (SISO) system, the transfer-function-based approach is mostly suitable. This is generally performed either in the Laplace or Fourier (frequency) domain. More recently, the frequency-domain-based *Active Spectral Finite Element* has been used for *Multiple-Input-Multiple-Output* (MIMO) systems. This is discussed in the latter part of this chapter. The most common method adopted for MIMO systems is the approach based on state-space modeling. This chapter gives some important aspects of these modeling techniques.

9.2.1 Transfer function

The output and input of the system are algebraically related through what is called the *transfer function*. Such a relation is possible only in the frequency (or Laplace) domain and is not valid in the time domain. If the output of the system in the transformed frequency domain is $\hat{u}(x, y, z, \omega)$ (where x, y, z are the spatial dimensions and ω is the circular frequency at which the output is sampled) and $\hat{F}(x, y, z, \omega)$ is the input, then the transfer function $\hat{G}(x, y, z, \omega)$ is obtained by the equation $\hat{u} = \hat{G}\hat{F}$. In structural dynamic applications, the transfer functions are normally called *Frequency Response Functions* (FRF), which essentially gives all of the resonant frequencies and their corresponding energies associated

with each of the modes. In the design of controllers, it is necessary to obtain transfer functions, which are normally characterized using Laplace transforms. The use of Laplace transform is, however, limited to smaller SISO systems. If we use an FE for solving a dynamic problem, then we need to reduce the order of the system for the design of the controller. There are many model order reduction schemes available. Some of these important schemes are given in the latter part of this chapter.

9.2.1.1 Transfer function in Laplace and Fourier domains

Here, Laplace transformation is used to transform the variable from the time domain to the Laplace domain. Laplace transformation for a function $f(x, y, t)$ is defined as:

$$L(f(x, y, t)) = \hat{f}(x, y, s) = \int_0^{\infty} f(x, y, t) e^{-st} dt \quad (9.1)$$

The Laplace transformation for the derivative of the function $f(x, y, t)$ is given by:

$$\begin{aligned} L\left[\frac{df(x, y, t)}{dt}\right] &= s\hat{f}(x, y, s) - f(x, y, 0) \\ L\left[\frac{d^2f(x, y, t)}{dt^2}\right] &= s^2\hat{f}(x, y, s) - sf(x, y, 0) - \dot{f}(x, y, 0) \end{aligned} \quad (9.2)$$

Here, $f(x, y, 0)$ and $\dot{f}(x, y, 0)$ are the value of the function and its derivative at time $t = 0$. The use of Laplace transformation on a differential equation reduces the same to an algebraic equation. Let y be the output variable and x the input variable. The linear differential equation that has an n th-order temporal derivative and an m th-order temporal input derivative, where $n > m$, can be written as:

$$\begin{aligned} A_0 \frac{d^n y}{dt^n} + A_1 \frac{d^{n-1} y}{dt^{n-1}} + \dots + A_{n-1} \frac{dy}{dt} + A_n y \\ = B_0 \frac{d^m x}{dt^m} + B_1 \frac{d^{m-1} x}{dt^{m-1}} + \dots + B_{m-1} \frac{dx}{dt} + B_m x \end{aligned} \quad (9.3)$$

Applying the Laplace transformation reduces the above equation to an algebraic equation. The transfer function that relates the output to the input under a ‘zero initial condition’ is then given by:

$$\frac{\hat{y}(s)}{\hat{x}(s)} = \frac{B_0 s^m + B_1 s^{m-1} + \dots + B_{m-1} s + B_m}{A_0 s^n + A_1 s^{n-1} + \dots + A_{n-1} s + A_n} \quad (9.4)$$

If the highest power of s is n , then the system is called an n th-order system. Both the numerator and the denominator can be factorized and written as:

$$\frac{\hat{y}(s)}{\hat{x}(s)} = \frac{(s + \alpha_1)(s + \alpha_2) \dots (s + \alpha_m)}{(s + \beta_1)(s + \beta_2) \dots (s + \beta_m)} \quad (9.5)$$

Here, $-\alpha_1, -\alpha_2, \dots, -\alpha_m$ are the points in the s -plane, where the value of the transfer function is zero and are called the *zeros of the transfer function*, while $-\beta_1, -\beta_2, \dots, -\beta_n$ are the points where the value of the transfer function goes to infinity. These points are called the *poles of the transfer function*. Poles and zeros are very important parameters in the design of controllers. In vibrational analysis, poles represent the resonant condition, where at this frequency (normally referred to as the resonant frequency) the response increases steeply.

Let us now consider a second-order single-degree-of-freedom mechanical system that governs the vibrational motion of a spring–mass–damper system, which is given by:

$$m\ddot{x} + c\dot{x} + kx = f(t) \quad (9.6)$$

In the above equation, m denotes the mass of the system, c is the viscous damping coefficient and k represents the effective stiffness of the system. Here, x, \dot{x}, \ddot{x} represent the displacement, velocity and acceleration of the system and $f(t)$ is the force and is considered as the point-input. When a Laplace transformation is applied to both sides of Equation (9.6) and assuming that the initial conditions are zero, we get:

$$\begin{aligned} (ms^2 + cs + k)\hat{x}(s) &= \hat{f}(s) \\ \frac{\hat{x}(s)}{\hat{f}(s)} &= \frac{1}{ms^2 + cs + k} \end{aligned} \quad (9.7)$$

The second part of the above equation gives the transfer function and can be factorized and written as:

$$\begin{aligned} \frac{\hat{x}(s)}{\hat{f}(s)} &= \frac{1}{(s + \alpha_1)(s + \alpha_2)} \\ \alpha_1 &= -\frac{c}{2m} + \sqrt{\left(\frac{c}{2m}\right)^2 - \frac{k}{m}}, \\ \alpha_2 &= -\frac{c}{2m} - \sqrt{\left(\frac{c}{2m}\right)^2 - \frac{k}{m}} \end{aligned} \quad (9.8)$$

From the above equation, we have no zeros and the two poles at α_1 and α_2 . Here, α_1 and α_2 can be real or

complex, depending on the radical under the square root. For the design of a controller, it is necessary that the values of the real parts of α_1 and α_2 should be negative. This aspect is dealt within more detail in the next section on the stability of control systems.

From Equation (9.7), when we substitute $s = i\omega$, we can transform the problem from the Laplace domain to the Fourier domain. That is, the transfer function becomes:

$$\frac{\hat{x}(\omega)}{\hat{f}(\omega)} = \frac{1}{-m\omega^2 + i\omega + k} \quad (9.9)$$

The right-hand side of the above equation is called the *Frequency Response Function* (FRF), which is normally obtained in conventional vibration analysis.

9.2.1.2 Transfer function from the finite element method

The discretized form of the governing equation in the Finite Element method is of the form:

$$[M]\{\ddot{x}\} + [C]\{\dot{x}\} + [K]\{x\} = \{F\} \quad (9.10)$$

Here, $[M]$, $[C]$, and $[K]$ are the mass, damping and stiffness matrices of size $n \times n$ and $\{x\}$, $\{\dot{x}\}$, $\{\ddot{x}\}$ are the displacement, velocity and acceleration vector of size $n \times 1$ and $\{F\}$ is the applied force vector. Applying a Fourier (or Laplace) transformation to the above equation and assuming the initial conditions to be zero, we get:

$$[\hat{K}]\{\hat{x}\} = \{\hat{F}\}, [\hat{K}] = [-\omega^2[M] + i\omega[C] + [K]] \quad (9.11)$$

where $[\hat{K}]$ is the frequency-dependent dynamic stiffness matrix. To obtain the transfer function, we apply a unit impulse at the desired degree of freedom and Equation (9.11) is solved for this unit impulse. Such an n degree of freedom will have n poles (resonant frequency). If n is very large, control design becomes extremely difficult and one has to reduce the FE system. This can be accomplished by *Modal Order Reduction*.

9.2.2 State-space modeling

A system is said to be in *state* if for a given input, the response can be completely determined for all future

times with a minimum amount of information. Mathematically, a dynamic system is defined by a differential equation of the form given by:

$$\frac{d^n y}{dt^n} + A_{n-1} \frac{d^{n-1}y}{dt^{n-1}} + \dots + A_1 \frac{dy}{dt} + A_0 y = R(t) \quad (9.12)$$

The above differential equation is of the n th order and hence all of the n derivatives are defined and it requires n initial conditions for its solution. We may choose to call each of the variables y and each of the first $(n - 1)$ derivatives as *state variables*. The number of state variables required to model a differential equation is equal to the order of the differential equation. The fundamental to the state-space modeling is to provide a systematic mathematical approach to analysis of the characteristics of the system by reducing a single differential equation into a coupled set of first-order differential equations with each equation defining one state. This set of equations is called the *state equations*.

In Equation (9.12), $R(t)$ represents the forcing term. Let us first assume that $R(t)$ does not involve any derivative terms and is equal to $f(t)$. We can now assume that $y(t)$, $dy/dt, \dots, d^{n-1}y/dt^{n-1}$ as a set of n state variables. Let us now define:

$$\begin{aligned} x_1 &= y, & x_2 &= \frac{dy}{dt} = \frac{dx_1}{dt} \\ x_3 &= \frac{d^2y}{dt^2} = \frac{dx_2}{dt}, & x_4 &= \frac{d^3y}{dt^3} = \frac{dx_3}{dt} \\ &\vdots & &\vdots \\ x_{n-1} &= \frac{d^{n-2}y}{dt^{n-2}} = \frac{dx_{n-2}}{dt}, & x_n &= \frac{d^{n-1}y}{dt^{n-1}} = \frac{dx_{n-1}}{dt} \end{aligned} \quad (9.13)$$

The n th-state equation is obtained by using the above definition in Equation (9.12) that is:

$$\frac{dx_n}{dt} = f(t) - A_0 x_1 - A_1 x_2 - \dots - A_{n-2} x_{n-1} - A_n x_n \quad (9.14)$$

Equations (9.13) and (9.14) can be put in matrix forms as:

$$\{\dot{x}\} = [A]\{x\} + [B]\{f\} \quad (9.15)$$

where:

$$\{x\} = \begin{Bmatrix} x_1 \\ x_2 \\ \vdots \\ x_n \end{Bmatrix},$$

$$[A] = \begin{bmatrix} 0 & 1 & 0 & \dots & \dots & 0 \\ 0 & 0 & 1 & \dots & \dots & 0 \\ \vdots & & & & & \\ -A_0 & -A_1 & -A_2 & \dots & \dots & -A_{n-1} \end{bmatrix},$$

$$[B] = \begin{Bmatrix} 0 \\ 0 \\ \vdots \\ 1 \end{Bmatrix}$$

The output can be written in the form given by:

$$y = [1 \ 0 \ \dots \ 0] \begin{Bmatrix} x_1 \\ x_2 \\ \vdots \\ x_n \end{Bmatrix} \quad \text{or } y = [C]\{x\} \quad (9.16)$$

Here, $[A]$ is called the *state matrix*, $[B]$ is called the *input matrix* and $[C]$ is called the *output matrix*.

Now, let us consider a case where the right-hand side of Equation (9.12) has, in addition to the forcing function $f(t)$, its time derivatives, that is:

$$R(t) = B_0 f(t) + B_1 \frac{df}{dt} + \dots + B_{n-1} \frac{d^{n-1}f}{dt^{n-1}} + B_n \frac{d^n f}{dt^n} \quad (9.17)$$

In this case, defining the state variables are not straightforward. The earlier definitions of state variables, given in Equation (9.13), will not yield unique solutions. In this case, the state variables must be chosen such that they will eliminate the derivatives of the input $f(t)$. This can be accomplished if we define the n state variables as:

$$x_1 = y - c_0 f, \quad x_2 = \frac{dy}{dt} - c_0 \frac{df}{dt} - c_1 f = \frac{dx_1}{dt} - c_1 f$$

$$x_3 = \frac{d^2y}{dt^2} - c_0 \frac{d^2f}{dt^2} - c_1 \frac{df}{dt} - c_2 f = \frac{dx_2}{dt} - c_2 f$$

$$\vdots$$

$$x_n = \frac{d^{n-1}y}{dt^{n-1}} - c_0 \frac{d^{n-1}f}{dt^{n-1}} - c_1 \frac{d^{n-1}f}{dt^{n-2}} - \dots - c_{n-1} f$$

$$f = \frac{dx_{n-1}}{dt} - c_{n-1} f \quad (9.18)$$

where:

$$c_0 = b_0, \quad c_1 = b_1 - a_1 c_0, \quad c_2 = b_2 - a_1 c_1 - a_2 c_0,$$

$$\vdots$$

$$c_n = b_n - a_1 c_{n-1} - \dots - a_{n-1} c_1 - a_n c_0 \quad (9.19)$$

The choice of the above state variables ensures the uniqueness of the solution of the state equation. Now, the reduced first order state equation can be written as:

$$\frac{dx_1}{dt} = x_2 + c_1 f$$

$$\frac{dx_2}{dt} = x_3 + c_2 f$$

$$\vdots$$

$$\frac{dx_{n-1}}{dt} = x_n + c_{n-1} f$$

$$\frac{dx_n}{dt} = -a_n x_1 - a_{n-1} x_2 - \dots - a_1 x_n + c_n f$$

The above set of equations can be written in the matrix form as:

$$\begin{Bmatrix} \dot{x}_1 \\ \dot{x}_2 \\ \vdots \\ \dot{x}_{n-1} \\ \dot{x}_n \end{Bmatrix} = \begin{bmatrix} 0 & 1 & 0 & \dots & 0 \\ 0 & 0 & 1 & \dots & 0 \\ \vdots & \vdots & \vdots & \ddots & \vdots \\ 0 & 0 & 0 & \dots & 1 \\ -a_n & -a_{n-1} & -a_{n-2} & \dots & -a_1 \end{bmatrix} \times \begin{Bmatrix} x_1 \\ x_2 \\ \vdots \\ x_{n-1} \\ x_n \end{Bmatrix} + \begin{bmatrix} c_1 \\ c_2 \\ \vdots \\ c_{n-1} \\ c_n \end{bmatrix} f$$

$$y = [1 \ 0 \ \dots \ 0] \begin{Bmatrix} x_1 \\ x_2 \\ \vdots \\ x_{n-1} \\ x_n \end{Bmatrix} + c_0 f$$

That is, in the shortened form, these equations can be written as:

$$\begin{aligned}\{\dot{x}\} &= [A]\{x\} + [B]f \\ y &= [C]\{x\} + Df\end{aligned}\quad (9.21)$$

Equation (9.21) is the state-space representation of Equation (9.12), wherein the right-hand side has derivatives of the forcing function.

One can now obtain the transfer function of the system from the state equation (Equation (9.21)). This can be done if one takes the Laplace transform of Equation (9.21), that is:

$$\begin{aligned}s\{\hat{x}(s)\} - \{x(0)\} &= [A]\{\hat{x}(s)\} + [B]\hat{f}(s) \\ \hat{y}(s) &= [C]\{\hat{x}(s)\} + D\hat{f}(s)\end{aligned}\quad (9.22)$$

Here, $\{\hat{x}(s)\}$ and $\hat{f}(s)$ are the Laplace transform of the state vector $\{x(t)\}$ and the forcing function $f(t)$. Transfer functions are normally derived by assuming a zero initial condition. From the first part of Equation (9.22), we have:

$$\{\hat{x}(s)\} = [s[I] - [A]]^{-1}[B]\hat{f}(s) \quad (9.23)$$

Using the above in the second part of Equation (9.22), we can relate the output to the input, that is, the transfer function is given by:

$$\frac{\hat{y}(s)}{\hat{f}(s)} = G(s) = [C][s[I] - [A]]^{-1}[B] + D \quad (9.24)$$

That is, the transfer function computation involves computation of $[s[I] - [A]]^{-1}$. Hence, the determinant of matrix $[s[I] - [A]]$ will give the characteristic polynomial of the transfer function and the eigenvalue of matrix $[A]$ will give the poles of the system.

Let us now consider a simple single degree of freedom of the spring–mass vibratory system, the governing differential equation of which is given by:

$$m\ddot{x} + c\dot{x} + kx = f(t) \quad (9.25)$$

where m is the mass of the system, c is the viscously damped damper coefficient and k is the stiffness of the system. For state-space representation of the system, we define the state variables $x_1(t) = x(t)$ and $x_2(t) = \dot{x}(t)$. Using these state variables, Equation (9.25) reduces to

the following two first-order equations (state equations), written in the matrix form as:

$$\begin{aligned}\begin{Bmatrix} \dot{x}_1 \\ \dot{x}_2 \end{Bmatrix} &= \begin{bmatrix} 0 & 1 \\ -\frac{k}{m} & -\frac{c}{m} \end{bmatrix} \begin{Bmatrix} x_1 \\ x_2 \end{Bmatrix} + \begin{Bmatrix} 0 \\ \frac{1}{m} \end{Bmatrix} f, \\ y &= [1 \quad 0] \begin{Bmatrix} x_1 \\ x_2 \end{Bmatrix}\end{aligned}\quad (9.26)$$

The above equation is in the conventional form of state equations given by Equation (9.21). Substituting the matrices $[A]$, $[B]$, $[C]$ and $[D]$ derived from the above equation in Equation (9.24), we can write the transfer function as:

$$G(s) = \frac{1}{ms^2 + cs + k} \quad (9.27)$$

This is the same as what was derived in Equation (9.7), obtained by taking a Laplace transformation on the governing equation.

In designing controllers for multi-input multi-output systems, especially for structural applications, one will have to depend extensively on the discretized mathematical model as that derived from FE techniques. The discretized Finite Element governing equation of any structure is of the form:

$$[M]\{\ddot{x}\} + [C]\{\dot{x}\} + [K]\{x\} = \{f\} \quad (9.28)$$

Here, $[M]$, $[C]$, and $[K]$ are the mass, damping and stiffness matrices, respectively.

These matrices are of size $n \times n$. $\{x\}$ is the degree of freedom vector and $\{f\}$ is the force vector, both of which are of size $n \times 1$. The above equation is similar to the single-degree-of-freedom equation (Equation (9.25)) and the state space equation will be of the form of Equation (9.26). Hence, the state vectors for the FE equation are $\{x_1\} = \{x\}$ and $\{x_2\} = \{\dot{x}\}$. The reduced-state-space-form of Equation (9.28) and its corresponding output vector $\{y\}$ is given by:

$$\begin{aligned}\begin{Bmatrix} \dot{x}_1 \\ \dot{x}_2 \end{Bmatrix} &= \begin{bmatrix} [0] & [I] \\ -[M]^{-1}[K] & -[M]^{-1}[C] \end{bmatrix} \begin{Bmatrix} x_1 \\ x_2 \end{Bmatrix} \\ &\quad + \begin{Bmatrix} 0 \\ [M]^{-1} \end{Bmatrix} \{f\} \\ \{y\} &= \begin{bmatrix} [I] & [0] \end{bmatrix} \begin{Bmatrix} x_1 \\ x_2 \end{Bmatrix}\end{aligned}\quad (9.29)$$

The above is in the standard form given in Equation (9.21), wherein we can clearly identify matrices $[A]$, $[B]$

and $[C]$, respectively. Equation (9.29) represents a $2n \times 2n$ system. That is, an $n \times n$ second-order system (Equation (9.28)), when reduced to state-space form, becomes $2n \times 2n$ of the first-order system. In addition, the input and the output are related, especially for the feedback, by:

$$\{f\} = [G]\{y\} \quad (9.30)$$

In the above equation, $[G]$ is the gain matrix of size $n \times r$, when r states are chosen for input feedback to reduce the response, especially for vibration control applications. Using the second part of Equation (9.29) in the above equation, we can write the output–input relation in terms of the state vector as:

$$\{f\} = [G][C]\{x\} \quad (9.31)$$

Once we reduce the governing equation in the state-space form, and using Equation (9.26), one can determine the transfer function. However, normally, the system size of the FE system is quite high, especially for dynamic systems. In order to design the control system, it is practically impossible to consider the entire FE system due to its large system size. In most control applications to structural problems, such as vibration or noise control, only the first few modes are targeted for reduction based on their energy content. In such a situation, one has to reduce the order of the system using suitable reduction techniques. The concepts of dynamic reduction are addressed in the latter part of this chapter.

9.3 STABILITY OF CONTROL SYSTEM

A control system design should adhere to some basic concepts that ensure the stability of the system. In this section, some of the commonly used methods in determining the stability of the system are highlighted.

An engineer's definition of stability is that a system should have enough damping to damp out all of the transients and resumes a steady-state condition. That is, a system is said to be *stable* if a finite duration input causes a finite duration response. On the other hand, a system is said to be *unstable* if a finite duration input causes the response to diverge from its initial value. That is, when the output changes 'unidirectionally' and 'shoots up' with ever increasing amplitude, the system is said to be unstable.

Here, let us consider a linear system. Most systems we come across are differential equations, second-order in

time, and in most cases are equations with constant coefficients. One of the fundamental features of constant coefficient equations is that they have exponential solutions of the form:

$$y(t) = Ae^{r_1 t} + Be^{r_2 t} + Ce^{r_3 t} + De^{r_4 t} + \dots \quad (9.32)$$

In the above equation, the constants A , B , C , etc. are determined by using the initial conditions and the forcing functions; r_1, r_2 , etc. are the roots or eigenvalues of the characteristic polynomial. The stability of Equation (9.32) depends on the values of r . If these are negative and real, then the output tends to zero value as $t \Rightarrow \infty$. Such a system, where all of the r 's are negative and real, is said to be a *stable* system. If the roots of the characteristic polynomial are positive and real, then the output of Equation (9.32) grows without a bound as $t \Rightarrow \infty$. Such a system is said to be an *unstable* system. If all of the r 's are purely imaginary, then the system exhibits continuous oscillations due to the presence of sine and cosine terms in the output equation. Finally, if all of the r 's are complex, having both real and imaginary parts, it amounts to attenuation of the response due to a growth in time. Hence, the determination of the stability of the system amounts to determination of the roots of the characteristic polynomial. In terms of the complex variable s , a system is said to be stable if all of the roots are in the left half of the s -plane and unstable if any roots are on the imaginary axis or in the right half of the s -plane.

If the system is linear, then testing of the stability of the system amounts to determining whether any root is in the right half of the s -plane or on the imaginary axis. The following are the different methods of testing the stability of a control system:

- (1) Numerically determining the roots of the characteristic polynomial.
- (2) Routh–Hurwitz criterion.
- (3) Nyquist criterion.
- (4) Root Locus method.
- (5) Using the state-space or transfer-function approach.

The choice of using the above tests is 'problem-dependent'. We will now briefly describe the above methods in a few sentences. The reader is advised to refer to Kuo[2] for a detailed account of these methods.

In the first test, a characteristic polynomial of order n is first obtained and its roots are determined numerically. There are many elementary root-finding algorithms, such as the Newton–Raphson technique, bisection method,

secant method, etc. For complex differential equations, some of the more recent techniques, such as the companion matrix method or polynomial eigenvalue method, can be used. These are discussed in Chakraborty [3]. In Finite Element terminology, an n degree of freedom model will yield a characteristic polynomial of order n . If n is very large, as in the case of the transient dynamic problem, then solving for all poles from the characteristic polynomial is an ‘horrendous’ task. Hence, the system size of the FE equations is reduced using proper model order reduction.

The Routh–Hurwitz criterion test gives us the number of roots if any of these exist to the right of the s -plane. It does not give the location of these roots on the s -plane and hence does not give any guidance for design procedures. It can be conveniently used for lower-order systems and is relatively simple to implement.

The Nyquist criterion [4] helps in identifying the poles that are located on the right half of the s -plane. This is a frequency-domain technique that is based on conformal mapping and complex variable theory. The method involves plotting the open-loop Frequency Response Function (FRF) and looking at the frequency amplitude at the resonant frequencies. From this, one can infer on the stability of the system. The main advantage of this criterion is that one can modify the control design by reshaping the frequency-response plots.

The root locus is again a graphical method, wherein the curves are constructed in the s -plane that show the response of each root of the characteristic polynomial as a specified system parameter is varied. Using this method, it is possible to evaluate the root location for a given value of the system parameter and also establish the conditions for stability. Again, due to the graphical nature of the method, design procedures can be developed based on reshaping of the curves.

In the state-space approach, the eigenvalues of the state matrix $[A]$ (see Equation 9.21) will give the poles in the s -plane from which the stability of the system can be assessed. From the FE point of view, this method is ideal. As a part of the FE code, there are many eigenvalue/vector extraction routines, which are used in free/forced vibration analysis. These routines can be used to extract the pole information from the state matrix $[A]$.

There are two other terms that are normally used in the control theory as regards the stability of the system. These are *Controllability* and *Observability*. These terms are commonly used in the control theory as they play an important role in the design of controllers, particularly when using the state-space approach. These were introduced by Kalman. A system is said to be ‘not

controllable’ if it does not satisfy the controllability and observability conditions. Hence, some conditions are specified in terms of the control parameters, which a system is made to satisfy for if it is to become controllable and observable. These conditions can be derived by using the following definitions. A system is said to be controllable at some time t_0 if it is possible to transfer the system from an initial state $x(t_0)$ to any other state in a finite interval of time by using an unconstrained control vector. A system, which is in the state $x(t_0)$, is said to be observable at some time t_0 , if it is possible to determine this state from observation of the output over a finite interval of time.

Using the above definition, we can derive the conditions for both input and output controllability. Here, a ‘mere’ condition is stated without going into much detail. Let us consider the governing differential equation of order n in the state-space form given in Equation (9.21). The condition of controllability of the input is that the vectors $[B], [A][B], \dots, [A]^{n-1}[B]$ are linearly independent and the matrix is given by:

$$[[B] \quad [A][B] \quad \dots \quad [A]^{n-1}[B]] \quad (9.33)$$

which is of rank n or is not singular. Similarly, we can state the condition of output controllability of the state equation given by Equation (9.21) in a similar manner. That is, we can write the output controllable matrix as:

$$[[C][B] \quad [C][A][B] \quad [C][A]^2[B] \quad \dots \quad [C][A]^{n-1}[B] \quad [D]] \quad (9.34)$$

The above matrix is of the order $m \times (n+1)r$, where matrix $[A]$ is $n \times n$, vector $[B]$ is $n \times r$, $[C]$ is $m \times r$ and $[D]$ is $m \times r$. The condition for output controllability is that the matrix given in Equation (9.34) is of the rank m .

On similar lines, we can write the observability condition by using the definition. That is, the state equation given by Equation (9.21) is observable, if and only if, the matrix given by:

$$[[C^T] \quad [A^T][C^T] \quad \dots \quad [A^T]^{n-1}[C^T]] \quad (9.35)$$

is of the rank n . We can also state the conditions for complete controllability and observability in the s -plane. That is, the system is not completely controllable or observable if there exists common factors in the transfer functions in the numerator and denominator. For example, a transfer function given by:

$$G(s) = \frac{(s+1)(s+4)}{(s+1)(s+2)(s+3)}$$

is not completely controllable or observable due to the common factor $(s + 1)$ in both numerator or denominator of the above equation.

9.4 DESIGN CONCEPTS AND METHODOLOGY

The fundamental to the design of the control system is to place the poles at the appropriate positions so that the stability of the system is ensured. The plant is a part of the control system that has unchangeable parts and is described by the transfer functions or state variables. The poles can be shifted to the appropriate positions by closing a loop around the plant with a feedback signal with appropriate gain. The gain matrix is the one that relates the output vector to the input vector. The gains can be constant or variable, depending upon the control system design. The basic or minimum system is determined by having a closed-loop unit feedback. Normally, sensors are assumed ideal (unit gain) and only an amplifier is added between the error signal and the plant. The gain is then set accordingly to meet the steady-state and bandwidth requirements, which are followed by a stability analysis. For a smart system, we have a sensor(s) and an actuator(s) to receive the sensor input and a controller. The stability of such a smart system is governed by the placement of the sensor, the placement of actuator, the error signal, the gain variation and the type and method of control design.

Design of a control system involves a design of compensation. Compensation can be designed in two different ways. The main objective of the first way is to modify the basic system in order that the stability of the system is ensured. Stability analysis is a very important preliminary step that determines how unstable (or stable) the system is and hence tells the designer how much compensation is necessary to ensure stability. The second step in the design process is to mathematically determine the parameters for the chosen value.

It has been mentioned earlier that the unstable system will have roots in the right half of the s -plane. To stabilize an unstable system, we need to move these roots to the left half of the s -plane. In addition, for a stable transient response, these moved poles need to be reallocated in a suitable area in the s -plane. The roots are generally complex and the real part of the root determines the duration of the transient and the imaginary part determines the oscillating characteristics. In general, one can move the roots by (a) changing gain, (b) changing

plant, (c) placing a dynamic element (filter) at the forward transmission path, (d) placing a dynamic element (filter) at the feedback path and (e) feedback all or some of the states. Of the above, the first two ((a) & (b)) are seldom permissible. All of the other four are possible options a designer can use. Selection of these is a matter of engineering judgment and also depends on the nature of the problem. Although one can design the control system using frequency-response or root-locus techniques, in this chapter the state-variable approach is used, keeping in mind that the designed control system can handle the multiple-input-multiple-output problem. Under this approach, two different design schemes are outlined, namely the PID controller and the controller based on eigenstructure assignment. These are discussed in the following subsections.

9.4.1 PD, PI and PID controllers

From the previous discussion, it is clear that gain is an important parameter governing the design of a controller. An increase in the gain increases the bandwidth and makes the response faster and accurate. However, an increase in gain decreases the damping. The damping is improved by introducing a derivative signal and if there is a need to increase the accuracy substantially, then an integrator is used. Several commercially available controllers combine several of these concepts. The most common among them are the following:

- *PD Controller* = Proportional + Derivative
 $\Rightarrow G(s) = K_p + K_d s$
- *PI Controller* = Proportional + Integral
 $\Rightarrow G(s) = K_p + \frac{K_I}{s}$
- *PID Controller* = Proportional + Integral + Derivative
 $\Rightarrow G(s) = K_p + \frac{K_I}{s} + K_d s$

In the above equations, K_p , K_d and K_I are the gain parameters, which are adjustable. Among the above, PID controllers are extremely popular and successful and have been used in many applications, such as autopilots in ships and aircraft. Ziegler and Nichols [5] have developed adjustment procedures, which is one of the reasons why such controllers are so popular.

Let us now consider the transfer function of a PD controller. This is given by:

$$G(s) = K_p + K_d s = K_d \left(s + \frac{K_p}{K_d} \right) \quad (9.36)$$

This controller simply introduces a free zero and the design requires a zero to be placed at the appropriate location and adjust the gain accordingly.

The *Proportional–Integral* (PI) is a type of feedback controller whose output is $u(t)$, with a control variable (CV) which is generally based on the error signal $e(t)$ between some user-defined set point (SP) and some measured process variable (PV). The control action of a proportional plus integral controller with $u(t)$ as the output of the controller and an $e(t)$ actuating error signal input is defined by:

$$u(t) = K_p e(t) + K_I \int_0^t e(t) dt$$

plus where the transfer function of the controller is given by:

$$G(s) = K_p + \frac{K_I}{s} = \frac{K_p(s + K_I/K_p)}{s} \quad (9.37)$$

The proportional gain K_p is multiplied by the error – this is an adjustable amplifier. In many systems, K_p is responsible for process stability. If it is too low, the PV can drift away; if it is too high, the PV can oscillate. The integral gain K_I is multiplied by the integral of error. In many systems, K_I is responsible for driving the error to zero; however, if K_I is set too high, there will be oscillation, instability, integrator windup or actuator saturation. The integral adds zeros at $s = -K_I/K_p$ and a pole at $s = 0$ to the open-loop transfer function. The effects of K_p and K_I on a closed-loop system are summarized in Table 9.1. These correlations may not be exactly accurate, because K_p and K_I are dependent on each other and changing one can bring about a change in the other.

The PI controller involves adjustment of K_p and K_I or tuning to achieve some user-defined optimal character of system response. The industrially accepted procedure is the Ziegler–Nichols technique [5], which is as follows.

Table 9.1 Effect of gains K_p and K_I on close-loop response.

Closed-loop response	Rise time	Overshoot	Settling time	S-S error
K_p	Decrease	Increase	Small change	Decrease
K_I	Decrease	Increase	Increase	Eliminate

First, $K_I = 0$ is set and using proportional action only, K_p is increased from 0 to a critical value K_{cr} where the output first exhibits sustained oscillations. Thus, the critical gain and corresponding period P_{cr} are experimentally determined.

To get the error signal, sensors are required. The sensing is normally done through accelerometers. The acceleration sensed varies with the location of the accelerometers. The corresponding $[C]$ matrix entries are then estimated. The feedback is given as a proportional gain matrix $[G_p]$ times the acceleration vector $\{\ddot{q}\}$ and an integral gain matrix $[G_I]$ times the velocity vector $\{\dot{q}\}$. For acceleration and velocity feedback, the output vector $\{y\}$ can be written as:

$$\{y\} = [C_p]\{\dot{x}\} + [C_I]\{x\}$$

where $[C_p]$ and $[C_I]$ are measurement matrices.

Let us now consider the PID controller. The transfer function in this case is given by:

$$G(s) = K_p + \frac{K_I}{s} + K_d s = \frac{K_d s^2 + K_p s + K_I}{s} \quad (9.38)$$

This requires a pole to be placed at the origin and two zeros at the desired locations for adjustment of the dynamic response. The two zeros may be real or complex, depending on the gains used and it will always be on the left-half plane. PID controllers can be digitally implemented with microprocessors.

9.4.2 Eigenstructure assignment technique

The eigenstructure assignment technique for feedback control system design allows the closed-loop system to have specified eigenvalues and eigenvectors. The forced response of a multi-variable system depends on both these eigen parameters; thus, this technique is an efficient tool for effective controller design, where the number of closed-loop eigen parameters can be specified *a priori* depending on the number of measurable outputs and inputs.

For a linear time-invariant system, the governing equations written using the standard notations are given by Equation (9.29). It was mentioned previously that the eigenvalues of matrix $[A]$ give the poles of the system. Each of these eigenvalues/vectors satisfy the identity:

$$[A]\{v_i\} = \lambda_i\{v_i\} \quad (9.39)$$

where λ_i is the i th eigenvalue and $\{v_i\}$ is the corresponding eigenvector. The free transient response of the system

to a non-zero initial condition $\{x_0\}$ is given by the equation:

$$\{x(t)\} = e^{[A]t}\{x_0\} \quad (9.40)$$

Assuming the eigenvalues of $[A]$ to be distinct, a non-singular modal matrix $[\Phi]$ consisting of eigenvectors can be found, where:

$$[\Phi] = [v_1 \ v_2 \ v_3 \ \dots \ v_n] \quad (9.41)$$

and:

$$[A] = [\Phi][\Lambda][\Phi]^{-1} \quad (9.42)$$

where $[\Lambda]$ is the diagonal matrix of eigenvalues. Now, the response in Equation (9.40) can be written as:

$$\{x(t)\} = [\Phi]e^{[\Lambda]t}[\Phi]^{-1}x_0 \quad (9.43)$$

By defining:

$$[\Phi]^{-1} = [w_1 \ w_2 \ w_3 \ \dots \ w_n]^T, \theta_k = \sum_{j=1}^n w_{kj}x_{0j} \quad (9.44)$$

Substituting the above equation in Equation (9.43), we get:

$$x_i(t) = v_{1i}\theta_1 e^{\lambda_1 t} + v_{2i}\theta_2 e^{\lambda_2 t} + \dots + v_{ni}\theta_n e^{\lambda_n t} \quad (9.45)$$

From the above equation it can be interpreted that:

- The state-variable response consists of a combination of all existing modes.
- Each eigenvalue determines the growth/decay rate of the corresponding mode.
- The amplitude of contribution from a particular mode depends on the eigenvectors.

9.4.2.1 Design methodology

A linear time-invariant, multi-variable, controllable and observable system is given by:

$$\{\dot{x}\} = [A]\{x\} + [B]\{u\}, \quad \{y\} = [C]\{x\} \quad (9.46)$$

where there are n state vector ($\{x\}$), m input vectors ($\{u\}$) and r output vectors ($\{y\}$). The objective here is to find a control law of the form:

$$\{u\} = [K]\{y\} \quad (9.47)$$

such that the closed-loop system matrix is $([A] + [B][K][C])$ (after applying feedback) satisfies:

$$([A] + [B][K][C])v_i = \lambda_i v_i, \quad i = 1, 2, \dots, n \quad (9.48)$$

where λ_i is the i th desired eigenvalue and v_i is the corresponding desired eigenvector. The general methodology to achieve this eigenstructure involves three numerical steps, as follows:

- Computation of the allowable subspace of the eigenvectors.
- Choice of eigenvectors.
- Computation of the gain value for assignment of the above eigenstructure.

In the eigenstructure assignment technique, the number of assignable eigenvalues is determined by the number of outputs and inputs. Full-state feedback requires that all of the state variables are measurable, which is often not possible and in such cases the output feedback is used. Here, eigenstructure assignment using output feedback is implemented to get a desirable closed-loop eigenstructure. With accelerometers used as sensors, the measurable quantities are the acceleration and velocity as integral of the acceleration.

9.5 MODAL ORDER REDUCTION

We have seen that design of a control system involves placement of the poles at the appropriate positions so as to ensure stability of the system. If one uses FE methods for mathematical modeling of the dynamic system, the system size of the problem is determined by the FE mesh density, which is usually very high for transient dynamics problems. That is, if the FE model of the system has n degrees of freedom, there will be n different poles in the system and the characteristic polynomial of the system is of the order n . If n is very large, then handling the design of the control system becomes ‘horrendous’ since most of the control system design techniques are mostly to shift the first few poles of the system. Even in real-world problems, such as vibration control in structures, it is sufficient that the first few modal amplitudes are reduced through a control system. In essence, the large system size of the FE model of the problem requires to be reduced for design of the control system. This can be achieved through what is called *modal order reduction*. In this section, all of the available model order reductions are reviewed and the behavior of

these techniques are compared for a transient dynamics problem through numerical examples.

9.5.1 Review of available modal order reduction techniques

The general procedure for modal order reduction is as follows:

- First, a few important degrees of freedom (dof) of the full order system are selected as the ‘master’ dof and these are retained in the reduction process and the rest of the dof are designated as the ‘slave’ dof that is to be condensed out. The selected configuration of the ‘master–slave’ dof depends on the nature of the problem sought for solution and also upon the algorithm adopted for reduction.
- A linear coordinate transformation (also called a similarity transformation) that transforms the original full-order system to a reduced-order system is defined.
- All of the system matrices (mass, stiffness and damping matrices) are then transformed to this new transformed coordinate system to obtain the reduced-order matrices.

With the usual FEM notations, the second-order governing differential equation of motion for a dynamical system of order n is expressed as:

$$[M]\{\ddot{u}(t)\} + [C]\{\dot{u}(t)\} + [K]\{u(t)\} = \{f(t)\} \quad (9.49)$$

where $[M]$, $[C]$ and $[K]$ are the system mass matrix, damping matrix and stiffness matrix, respectively, of order $n \times n$. Here, $\{u\}$, $\{\dot{u}\}$ and $\{\ddot{u}\}$ are the displacement, velocity and acceleration vectors, respectively, of size $n \times 1$ while $\{f(t)\}$ is the nodal force vector of size $n \times 1$. After selection of the master and slave dofs of orders m and s , respectively, the objective of *reduced-order modeling* (ROM) is to establish an equivalent model for the above equation of order m instead of n , where $m \ll n$. This reduced model can be expressed as:

$$[\tilde{M}]\{\ddot{u}_m(t)\} + [\tilde{C}]\{\dot{u}_m(t)\} + [\tilde{K}]\{u_m(t)\} = \{\tilde{f}(t)\} \quad (9.50)$$

The overhead ‘tilde’ indicates the system matrices of the equivalent ROM. The transformation matrix $[T]$ relates the full-scale model to the reduced scale and is expressed in terms of the displacement vectors of the full and reduced models, respectively, as shown below:

$$\{u(t)\} = \begin{Bmatrix} \{u_m(t)\} \\ \{u_s(t)\} \end{Bmatrix} = [T]\{u_m(t)\} \quad (9.51)$$

wherein the subscripts m refers to the retained (master) dof and s to the condensed (slave) dof. Substituting Equation (9.51) into Equation (9.49) and ‘pre-multiplying’ $[T]^T$, the expression in Equation (9.49) reduces to:

$$\begin{aligned} & [T]^T[M][T]\{\ddot{u}_m(t)\} + [T]^T[C][T]\{\dot{u}_m(t)\} \\ & + [T]^T[K][T]\{u_m(t)\} = [T]^T\{f(t)\} \end{aligned} \quad (9.52)$$

which can be written in form given in Equation (9.50). Hence, we have:

$$\begin{aligned} & [\tilde{M}] = [T]^T[M][T], \quad [\tilde{C}] = [T]^T[C][T] \\ & [\tilde{K}] = [T]^T[K][T], \quad \{\tilde{f}\} = [T]^T\{f\} \end{aligned} \quad (9.53)$$

Different model-order reduction methods prescribe steps for computation of the transformation matrix $[T]$. The review of theoretical formulations of different ROMs and derivation of the corresponding transformation matrices are discussed in this section. A similar transformation applies for the ROM of the system in the state-space framework. The state-space equation for the full system is given by:

$$\{\dot{x}\} = [A]\{x\} + [B]\{f\} \quad (9.54)$$

with the output vector given by:

$$\{y\} = [C]\{x\}$$

The state-space equation of the ROM and the corresponding reduced output state vector are given by:

$$\{\dot{x}_m\} = [\tilde{A}]\{x_m\} + [\tilde{B}]\{\tilde{f}_m\}, \quad \{y_m\} = [\tilde{C}]\{x_m\} \quad (9.55)$$

In this section, three important model-order reduction techniques are reviewed in detail.

9.5.1.1 Guyan reduction technique

Time-domain model-order reduction methods that are applicable to steady-state structural problems date back to the 1960s, due to the work of Guyan [6]. These methods are based on the assumption that the effects of inertial forces on the eliminated physical coordinates are negligible, that is, the condensed dof does not experience any force and the effect of associated inertia and damping are not included in the transformation. Upon partitioning the mass and stiffness matrices into submatrices and the displacement and force vectors as subvectors

based on the master and slave configurations, the equation of motion can be expressed as:

$$\begin{bmatrix} [M_{mm}] & [M_{ms}] \\ [M_{ms}]^T & [M_{ss}] \end{bmatrix} \begin{Bmatrix} \{\ddot{u}_m\} \\ \{\ddot{u}_s\} \end{Bmatrix} + \begin{bmatrix} [K_{mm}] & [K_{ms}] \\ [K_{ms}]^T & [K_{ss}] \end{bmatrix} \begin{Bmatrix} \{u_m\} \\ \{u_s\} \end{Bmatrix} = \begin{Bmatrix} \{f_m\} \\ 0 \end{Bmatrix} \quad (9.56)$$

Expanding the second equation and neglecting the masses associated with the ‘slave’ degrees of freedom, we get:

$$[K_{ms}]^T \{u_m\} + [K_{ss}] \{u_s\} = 0 \quad (9.57)$$

The above equation helps us to relate the ‘slave’ dof in terms of the ‘master’ dof, which can be written as:

$$\{u_s\} = -[K_{ss}]^{-1} [K_{ms}]^T \{u_m\} \quad (9.58)$$

The transformation matrix required for order reduction is given by:

$$\{u\} = \begin{Bmatrix} \{u_m\} \\ \{u_s\} \end{Bmatrix} = [T] \{u_m\}, \quad [T] = \begin{bmatrix} I \\ -[K_{ss}]^{-1} [K_{ms}]^T \end{bmatrix} \quad (9.59)$$

This method is simple and has been used in various engineering applications. In dynamic analysis, Guyan’s method is adopted by usually considering the dof with small inertia as the ‘slave’ dof. A computational algorithm was proposed by Shah and Reymand [7] for analytical selection of ‘master’ and ‘slave’ configurations in Guyan’s reduction.

9.5.1.2 Dynamic condensation method

This method is an improvement over Guyan’s reduction method in the sense that the transformation is based on the dynamic stiffness matrix $[D]$ rather than the static stiffness matrix $[K]$. This method is a ‘frequency-selective’ approach. At a given frequency ω , the equilibrium equation in the frequency domain is expressed as:

$$\begin{aligned} [K] - \omega^2 [M] \{\hat{u}(\omega)\} &= \{\hat{f}(\omega)\}, \\ [D(\omega)] \{\hat{u}(\omega)\} &= \{\hat{f}(\omega)\} \end{aligned} \quad (9.60)$$

The above equation is obtained by taking a Fourier transform on the displacement and acceleration parameters in the original governing equation (Equation (9.49)) and $\{\hat{u}\}$ and $\{\hat{f}\}$ are the frequency-domain

amplitudes’ displacement and force vectors, respectively. Again, partitioning the above in terms of matrices associated with the ‘master’ and ‘slave’ dofs, we get:

$$\begin{bmatrix} [D_{mm}] & [D_{ms}] \\ [D_{ms}]^T & [D_{ss}] \end{bmatrix} \begin{Bmatrix} \{\hat{u}_m(\omega)\} \\ \{\hat{u}_s(\omega)\} \end{Bmatrix} = \begin{Bmatrix} \{\hat{f}_m\} \\ 0 \end{Bmatrix} \quad (9.61)$$

Following the same procedure used in Guyan’s reduction, we first express the ‘slave’ dof in terms of the ‘master’ dof through the second equation. Then, the transformation matrix becomes:

$$\{\hat{u}\} = \begin{Bmatrix} \{\hat{u}_m\} \\ \{\hat{u}_s\} \end{Bmatrix} = [T] \{\hat{u}_m\}, \quad [T] = \begin{bmatrix} I \\ -[D_{ss}]^{-1} [D_{ms}]^T \end{bmatrix} \quad (9.62)$$

Based on this approach, a central frequency ω for condensation was proposed by Paz [8]. For dynamic problems, where multiple modes participate, as in the case of wave problems, the use of the geometric mean as the central frequency over the frequency band under interest has been employed by Paz [8].

9.5.1.3 System equivalent reduction and expansion process (SEREP)

SEREP was proposed by O’Collahan [9], primarily as a technique for a cross-orthogonality check between analytical and experimental modal vectors, linear and non-linear forced response studies and analytical model improvement. This method uses a modal matrix instead of a stiffness matrix to derive the required transformation matrix. That is, this method proposes transformation of the dynamic characteristics through the collection of desired eigenmodes. The modal matrix $[\psi]$ of the system computed for p numbers of modes is partitioned as $[\psi_m]$ and $[\psi_s]$ for m numbers of the ‘master’ dof and s numbers of the ‘slave’ dof and is expressed as:

$$[\psi] = \begin{bmatrix} [\psi_m] \\ [\psi_s] \end{bmatrix} \quad (9.63)$$

The modal matrix relates the generalized displacements to the modal displacements through the expression given as:

$$\begin{Bmatrix} \{u_m\} \\ \{u_s\} \end{Bmatrix} = \begin{bmatrix} [\psi_m] \\ [\psi_s] \end{bmatrix} \{Z\} \quad (9.64)$$

where $\{Z\}$ is the generalized degree of freedom vector. From the above equation, we can write:

$$\{Z\} = [\psi_m]^+ \{u_m\} \quad (9.65)$$

where $[\psi_m]^+$ is the generalized inverse of $[\psi_m]$, which is a rectangular matrix of size $m \times p$, where m is the number of ‘master’ dofs and p is the number of modes retained in the transformation. To and Ewins [10] discussed the computation of a generalized inverse for a rectangular matrix, which is given by:

$$\begin{aligned} [\psi_m]^+ &= [[\psi_m]^T [\psi_m]]^{-1} [\psi_m]^T && \text{when } m > p \\ [\psi_m]^+ &= [\psi_m]^T [[\psi_m][\psi_m]^T]^{-1} && \text{when } m < p \end{aligned} \quad (9.66)$$

Substituting for $\{Z\}$ from Equation (9.65) into Equation (9.64), we get:

$$\left\{ \begin{array}{l} \{u_m\} \\ \{u_s\} \end{array} \right\} = \left[\begin{bmatrix} [\psi_m] \\ [\psi_s] \end{bmatrix} \right] [\psi_m]^+ \{u_m\} \quad (9.67)$$

The transformation matrix in this case is given by:

$$[T] = \left[\begin{bmatrix} [\psi_m] \\ [\psi_s] \end{bmatrix} \right] [\psi_m]^+ \quad (9.68)$$

As discussed by O’Callahan [9], this method allows an arbitrary selection of the modes that are to be selected in the ROM and the quality of the ROM does not depend upon the location of the ‘master’ dof. However, the number of modes included in the transformation should be more than or equal to the number of ‘master’ dofs. In addition, the frequencies and modes shapes of the ROM are exactly the same as those of the selected frequencies and mode shapes of the full-system model. This is one of the great advantages in the design of control systems, wherein one has to design the same by using a limited number-of-degrees-of-freedom model. Since the reduced mathematical model based on the SEREP can exactly represent the dynamic characteristics of the full model, the control theory tolerances are greatly enhanced.

In addition to the above three ROM techniques, there are three other techniques reported in the literature. These are the *Condensation Modal Order Reduction Technique*, based on the *Projection Operator*, proposed by Dyka *et al.* [11] and referred to as the CMR method, the *Improved Reduced System* of O’Callahan [12], referred to as the IRS method and the *Dynamic Improved Reduced System* of Friswell *et al.* [13], referred to as the DIRS method. The above three methods are not discussed here, although some of the results from these methods are used in the next subsection for comparison purposes.

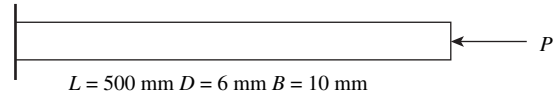


Figure 9.1 Schematic of a cantilever beam used for the comparative study.

9.5.1.4 Reduced order modeling in transient dynamics: a comparative study

The main objective of this section is to identify the reduction technique that results in the most accurate response for the given master–slave dof configuration. It was explained previously that the characteristics of the transient dynamic problem is that the frequency content of the forcing function is quite high. In other words, the time duration is very short, normally of the order of microseconds. Hence, it excites all higher-order modes. This results in very fine FE discretization and hence a very large system size. Thus, when using an ROM, one has to be very careful in choosing the master–slave dof combination.

For comparative study of different ROMs, a 2-D cantilever beam under plane-stress conditions and subjected to axial impact, shown in Figure 9.1 is considered. The dimensions of the beam are $500 \text{ mm} \times 6.0 \text{ mm} \times 9.0 \text{ mm}$ and the isotropic material properties are $E = 72.0 \text{ GPa}$, $v = 0.3$, and $\rho = 2700 \text{ kg/m}^3$. The time history and the frequency spectrum of the applied load is shown in Figure 9.2 and the load is acting axially at the free end of the cantilever beam. The full system model is

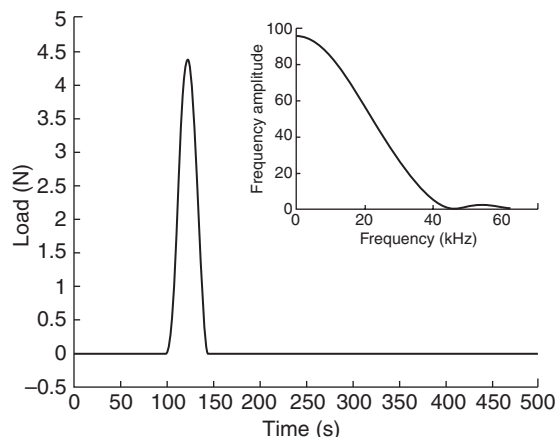


Figure 9.2 Input load history and its frequency spectrum used in the comparative study.

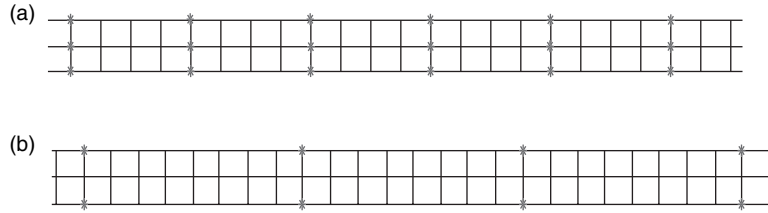


Figure 9.3 Configurations showing the spatial distributions of the master-slave dofs: (a) pattern 1 – master dof of 150; (b) pattern – master dof of 50.

descretized based on the wavelength consideration. The full system matrix is of the order 624×624 . For comparison of the response, three reduced-order models, namely, the *Dynamic Condensation* (DC), *Dynamic IRS* (DIRS) and *SEREP* are considered and the response is computed for the same ‘master–slave’ dof configuration for all of the methods. Two different patterns of ‘master–slave’ dof configurations are used in the investigation, which form the reduced-order system matrices of order 150×150 and 50×50 , respectively. The configurations indicating the spatial distribution of the ‘master–slave’ dof for the two patterns are shown in Figure 9.3. The locations of the ‘master’ dofs at the nodes are shown by * marks.

The axial velocities are plotted at the middle node of the free end of the beam. For pattern 1 with 150 dof, the axial velocity plot is given in Figure 9.4. In this case, the location and amplitude of the incident and first reflection of the wave are accurately captured for all of the reduction methods; however, the response through SEREP is observed to be able to capture even a small dispersion exhibited by the longitudinal wave and the

results match exactly with the full-system response. The number of modes included in the transformation in the case of SEREP is equal to the number of ‘master’ dofs, that is, 150. The condensing frequency used in the DC method is the fundamental frequency of the system (185.09 Hz). Figure 9.5 gives a comparison of the same for the pattern-2 (dof 50) configuration of the ‘master–slave’ dof. In this case, the response by SEREP matches accurately with that of the full-system response, but the response histories by DC and DIRS have shown some time lag in the occurrences of the reflected pulses, while there is no such time lag observed for the incident pulse. That is, the other two ROMs under-predict the axial wave velocity. In addition, a slight under-prediction of response and perturbation is observed in the cases of DC and DIRS. The accurate matching of the response in this case for the ROM through SEREP can be explained by the fact that the first few eigenmodes carry maximum spectral energy, which can be observed by the FFT diagram of the load history, as shown in Figure 9.2 and SEREP can be said to work excellently with inclusion of the eigenmodes that carry maximum energy.

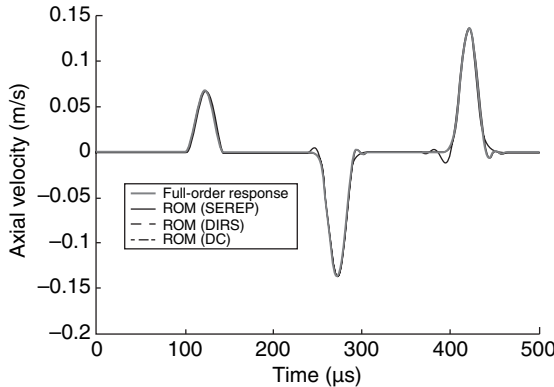


Figure 9.4 Comparison of axial velocity for pattern 1 (150 dof) for different ROMs.

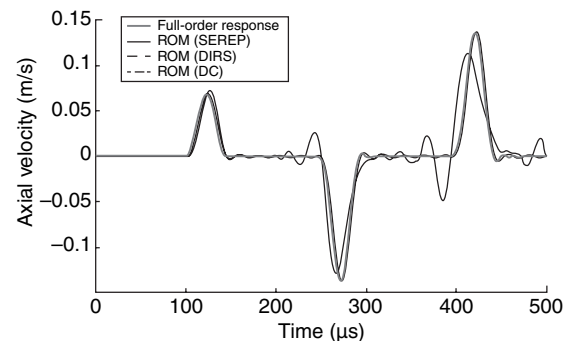


Figure 9.5 Comparison of axial velocity for pattern 2 (50 dof) for different ROMs.

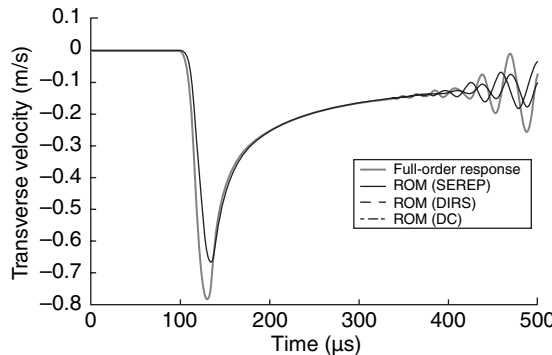


Figure 9.6 Comparison of transverse velocity for pattern 1 (150 dof) for different ROMs.

Next, the transverse loading is considered. For the same cantilever beam and for two different ‘master–slave’ configurations, the free-end transverse responses are plotted in Figures 9.6 and 9.7, respectively. The ROM simulation of wave propagation for the transverse excitation is observed to be more sensitive to the order of reduction and the ‘master–slave’ dof configuration. For the case of the ROM of order 150 (pattern 1), all of the methods are observed to give a slight decay in the amplitude of the transverse velocity corresponding to the occurrence of the incident pulse.

For the case of the ROM of order 50 (pattern 2), SEREP gives the most accurate solution, which matches exactly with the full-system response after the occurrence of the incident pulse peak. DC and DIRS result in an oscillatory response and a slight perturbation from the original system response at a longer time range. In all of

the simulations discussed above, for SEREP the number of modes is always taken equal to the number of ‘master’ dofs, while for DIRS and DC the condensing frequency is taken as the fundamental frequency of the system. From the above example, it is quite clear that the SEREP method is perhaps the best ROM from the computational viewpoint. That is, whatever the modes that are retained in the transformation, those modes are accurately represented in the ROM. This is particularly useful in multi-modal control, wherein the modes that require suppression are *a priori* assigned while designing the control law.

9.6 ACTIVE CONTROL OF VIBRATION AND WAVES DUE TO BROADBAND EXCITATION

The FE model of a system is usually very ‘high’, especially for transient dynamics and wave-propagation problems. Designing a control system for such problems is very difficult due to the very ‘high’ system size. For example, in vibration-control problems, it is customary to reduce the vibration amplitudes of the first few modes using suitable control algorithms. This can be easily accomplished by using a reduced-order model of the complete system that has all of the necessary information about the first few relevant modes. This ROM can be used in conjunction with state-space modeling or the transfer function approach that was outlined earlier, for designing the control law. However, transient dynamics or wave-propagation problems are multi-modal problems. That is, if we use the FE approach, then one cannot design the controller based on the first few modes, since many higher-order modes carry significant portion of kinetic energy. Obtaining all of the higher-order eigenvalues/vectors is computationally very prohibitive. That leaves one with no other option but to look for an alternate mathematical tool that has a smaller system size and yet contains all of the model information. A tool that fits into the above description is the *Spectral Finite Element Model* (SFEM) which was dealt within Chapters 7 and 8. In this present chapter, a new design philosophy based on Fourier transforms is developed, wherein the existing SFEM is modified to model the control elements, namely the sensor and the actuator, and also the controller. Since the system size of the SFEM model is very small and also contains all modal information, no model-order reduction is required. In addition, the controller can be designed for the entire eigenspectrum and hence in cases of vibration- or noise-control problems,

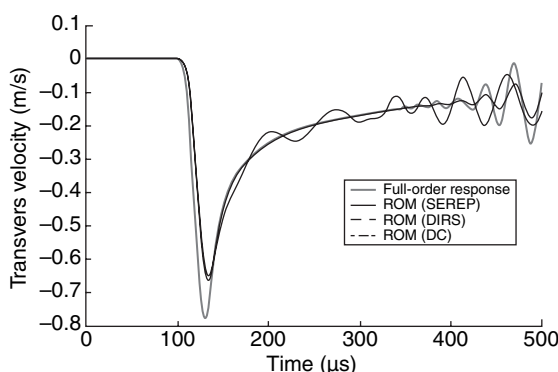


Figure 9.7 Comparison of transverse velocity for pattern 2 (50 dof) for different ROMs.

one can obtain the Frequency Response Function of the structure after the feedback signal is enforced. This will quantitatively give the amount of vibration amplitude reduction over the entire eigenspectrum. This will give a great reduction in the computational effort as opposed to the traditional approaches. One other major advantage of the model is that one can handle arrays of sensors/actuators and any sensor(s) can be fed to any actuator(s) or set of actuators. That is, it is quite simple to handle both collocated and non-collocated sensor–actuator configurations. This aspect is extremely difficult to handle in the traditional approaches.

9.6.1 Available strategies for vibration and wave control

Design of smart structural systems based on control of the first few resonant modes, individually, is the most common in practice. For many vibration-control applications, this serves the control objective, since the modal energy is distributed over the first few resonant modes only. The basic steps behind development of such active control system models can be described as follows:

- First, an appropriate kinematics and constitutive model is assumed. For actuators or load cells mounted on the host structure, appropriate ‘lumping’ of the control force and actuator inertia can be considered. For surface-bonded or embedded layered sensors/actuators, the same kinematics as the host structure with additional constraints (for example, shear-lag to model active/pассив constrained layers, discontinuous functions to represent interfacial slip while handling inclusions, air-gap, etc.) can be used.
- Next, one has to adopt an application-specific control scheme. For a known harmonic disturbance, a control force can be applied in the open-loop having an optimal phase difference with the mechanical disturbance. An actuator force can directly be specified to add onto the equivalent mechanical force vector. For unknown dynamic loading, and as required in most stable controller designs, closed-loop control schemes are to be adopted. The initial configuration of the error sensors, whose placements and numbers are to be fixed based on optimal control performance (observability and controllability), can be used for feedback or feed-forward control. These error measurements are considered as inputs to the controller under design. The controller output vector is to be used as the input electrical signal to the actuators. For an off-line

optimal control design based on a conventional optimization technique, the above steps are to be repeated at every iteration while extremizing the cost function(s). For an off-line optimal control design based on soft-computing tools (e.g. genetic algorithms), these solution spaces can be explored directly.

- Once all of the system parameters (stiffness, mass, damping, electromechanical properties of sensors and actuators, sensor locations, actuator locations, actuator input, etc.) for a particular configurations are available, one has to develop a global model for the passive structure and sensor/actuator segment using analytical or finite techniques. Under certain cases of electromechanical coupling, the system matrices can be decoupled into passive and active components. For the fully coupled electromechanical case, an analytical solution can be obtained for only a few electromechanical boundary conditions and for this, one can use a detailed finite element model. For mounted actuator or load cells, the effect of actuator stiffness, inertia and force can be ‘lumped’.
- Next, one has to adopt suitable methods of system solution in temporal or modal space. When the discretized system size is large, an appropriate reduced-order modeling technique can be used. *Dynamic Condensation*, *Proper Orthogonal Decomposition* (POD) or the *System Equivalent Reduction Expansion Process* (SEREP), among many reduced-order modeling techniques, are found useful. Based on the formalism of the control cost function construction, a state-space model (first-order representation) is often used instead of a direct second-order representation. This is particularly suitable for conventional designs based on the quadratic regulator approach, where the state-space plant matrix, the input/output matrix, along with the required weighting matrices, are introduced. Peak-response specifications are generally found to be linear matrix functions of the design variables, which allow them to be incorporated within the design framework without increasing the complexity of the optimization [14]. In time-marching schemes (for example, Newmark time integration) while designing optimal control system, the control cost function is minimized, including special control system features (e.g. gain scheduling, feedback delay, etc.). When modal analysis is adopted, the modified dynamic stiffness matrix (including the contributions of sensor, controller and actuator parameters) is to be optimized so that the prescribed modes are controlled. In this approach, the control efficiency is quantified in terms of reduction in the modal amplitude level in the frequency response.

- Once the range of control system parameters and the sensor/actuator collocation pattern is obtained, sensitivity and stability studies are carried out. Sensitivity studies are important to identify the most effective solution-space of the design parameters. This also helps in visualizing the deviation in the desired response due to control uncertainty and measurement of noise. With the narrowed-down solution-space of the design parameters thus obtained above, the locus of the roots of the characteristic system, that is, poles (resonances) and zeros (anti-resonances) of the system transfer function for varying design parameters are studied. The range of design parameters that produces the root locus on the right-half phase-plane are unstable and are avoided in the final design. A secondary objective is often placed for control of transient disturbances, which is to minimize the transient response time of the controller.
- For real-time automatic control systems, the off-line design discussed above is augmented by an adaptive filter that tunes the control gains in the presence of measurement errors and uncertainty [15]. In addition, there are certain drawbacks of the finite dimensional design to control a distributed parameter system, such as control spillover. This is the result of insufficient modes considered in the MIMO state-space model. Although adaptive filters can augment the performance of an off-line design based on a finite number of states, better modeling techniques for distributed parameter systems are often advantageous. This is where techniques such as SFEM score over other methods available for the solution. A modified SFEM that includes the modeling of control elements such as sensors, actuators and control elements is what is called the *Active Spectral Finite Element Model* (ASEM). This formulation is built on the same lines as the FEM and removes most of the limitations of the other off-line techniques. This method is explained in the next subsection.

9.6.2 Active spectral finite element model (ASEM) for broadband wave control

In this subsection, a generalized active spectral finite element model (ASEM) capable of handling arbitrary distributed sensor-actuator configurations with a PID feedback scheme is presented. The main objective is to develop an efficient and faster computational technique for the analysis and design of multiple sensor-actuator configurations for active control of broadband waves in connected composite beams. The ASEM can be used to

study structure-control interactions produced by various types of mounted or embedded active actuators and sensors, along with classical transducers modeled as ‘lumped’ devices. Among the specific advantages are the accurate sensors and actuators dynamics based on a uniform micro electromechanical field model, consideration of multiple scattering of waves through structural joints and boundaries and near-field effects on the sensors. Numerical experiments on a slender laminated composite cantilever beam with a bonded piezoelectric fiber composite (PFC) (explained in Section 8.4.4, chapter 8) are performed. Various aspects of low-authority control against parametric variations are explained. Some physical insight into the macroscopic behavior of these PFC actuators has been reported in Bent [16] and Hagood *et al.* [17].

In this ASEM model, the beam network is discretized and classified into three different classes of elements, as follows: (1) a spectral element for finite beams with mechanical and passive properties; (2) distributed or point sensors; (3) distributed or point actuators. A schematic diagram of a sensor-actuator element configuration is shown in Figure 9.8. Here, it is assumed that that the controller output for a single actuator can be designed based on a feedback signal constructed from a group of sensors. Furthermore, in Figure 9.8, the connectivity between the p th sensor and the q th actuator is also shown, where the sensor response is measured at the local coordinate system (X_s^p, Y_s^p) and the actuation force is provided at the local coordinate system (X_a^q, Y_a^q) .

9.6.2.1 Spectral element for finite beams

The SFEM outlined in Chapter 7 is again used here to represent the dynamics of the beam structure. For the

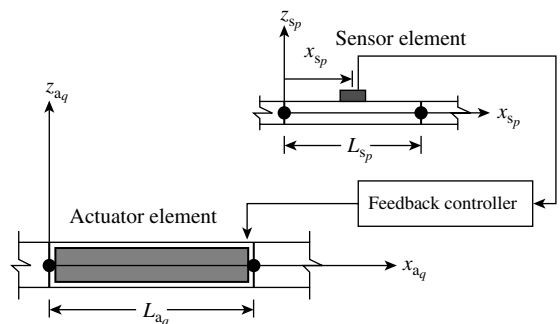


Figure 9.8 Sensor-actuator configuration for the active spectral finite element model.

sake of completeness, the element-level equations involving the nodal displacement vector are repeated here. Assuming the beam to have three degrees of freedom (two translational dofs and one rotational dof) per node and having two nodes, the elemental displacement vector in the frequency domain is given by:

$$\{\hat{u}_e\} = \begin{Bmatrix} \hat{u}_1^0 & \hat{w}_1 & \hat{\theta}_1 & \hat{u}_2^0 & \hat{w}_2 & \hat{\theta}_2 \end{Bmatrix} \quad (9.69)$$

and the corresponding nodal force vector is given by:

$$\{\hat{F}\}_e = \begin{Bmatrix} \hat{N}_1 & \hat{V}_1 & \hat{M}_1 & \hat{N}_2 & \hat{V}_2 & \hat{M}_2 \end{Bmatrix} \quad (9.70)$$

The use of the spectral form of solution for the governing equation and its eventual solution in the frequency domain results in the dynamic shape functions for the spectral element formulation, which can be written as:

$$\begin{Bmatrix} \hat{u}(x, \omega) \\ \hat{w}(x, \omega) \\ \hat{\theta}(x, \omega) \end{Bmatrix} = \begin{Bmatrix} [\aleph_1] & [0] & [0] \\ [0] & [\aleph_2] & [0] \\ [0] & [0] & [\aleph_3] \end{Bmatrix} \begin{Bmatrix} \{\hat{u}_e\}_e \\ \{\hat{w}_e\}_e \\ \{\hat{\theta}_e\}_e \end{Bmatrix}, \{\hat{F}\}_e = [\hat{K}]_e \{\hat{u}_e\}_e \quad (9.71)$$

where $[\aleph_1], [\aleph_2], [\aleph_3]$ are the exact spectral element shape-function matrices corresponding to the axial, transverse and rotational degrees of freedom, and $[\hat{K}]_e$ is the exact element dynamic stiffness matrix. As in the case of the FE, the stiffness matrix in the elemental coordinate system is transformed to the global coordinate system by using a suitable transformation matrix.

9.6.2.2 Sensor element

For illustrative purposes, a point sensor has been considered in the modeling. However, it should be noted that the formulation does allow for distributed sensors such as piezoelectric film sensors. The force-balance equations for the sensor element are identical in form to Equation (9.71). Based on the response measured by a displacement sensor (s), which is located at (x_{s_p}, z_{s_p}) in the p th sensor element (denoted by subscript s_p), the actuator input spectrum can be expressed with the help of Equation (9.71) as:

$$\hat{\eta}_u(x_{s_p}, w_{s_p}, \omega_n) = (i\omega_n)^m \alpha \left[\sum_{j=1}^6 (\aleph_{1j} - z_{s_p} \aleph_{3j}) \hat{u}_{je} \right] \quad (9.72)$$

when longitudinal displacement is measured, and:

$$\hat{\eta}_u(x_{s_p}, w_{s_p}, \omega_n) = (i\omega_n)^m \alpha \left[\sum_{j=1}^6 \aleph_{2j} \hat{u}_{je} \right] \quad (9.73)$$

when transverse displacement is measured. In Equations (9.72) and (9.73), $i = \sqrt{-1}$, α is the sensor sensitivity parameter and $m = 0, 1$ and 2 , for displacement, velocity, and acceleration spectra, respectively. Similarly, if a strain sensor is used, one can write the actuator input spectrum:

$$\hat{\eta}_u(x_{s_p}, w_{s_p}, \omega_n) = (i\omega_n)^m \alpha \left[\sum_{j=1}^6 \left(\frac{\partial \aleph_{1j}}{\partial x} - z_{s_p} \frac{\partial \aleph_{3j}}{\partial x} \right) \hat{u}_{je} \right] \quad (9.74)$$

9.6.2.3 Actuator element

In the formulation of the ASFEM presented here, we consider the PID (Proportional–Integral–Derivative) feedback control scheme [18]. Other types of frequency domain control schemes, such as feed-forward control can also be implemented. The controller output in the form of current spectrum \hat{I} (or voltage spectrum $\hat{\phi}$) for the q th actuator, and the resulting field (magnetic field \hat{H} for a magnetostrictive material or electric field \hat{E} for a piezoelectric material) can be written as:

$$\hat{I} = \sum_p \gamma \hat{\eta}, \quad \hat{H} = \beta \hat{I}, \quad \hat{\eta} = (\hat{\eta}_u, \hat{\eta}_w, \hat{\eta}_e) \quad (9.75)$$

where $\hat{\eta}$ is given by Equations (9.72)–(9.74). The constant γ is a scalar gain and β is the actuator sensitivity parameter introduced to account for the actuator assembly and packaging properties (e.g. the solenoid configuration for a packaged Terfenol-D rod actuator [19], voltage-to-electric field conversion factor for plane-polarized PZT wafers, etc.). Next, after substituting for \hat{H} from the magnetomechanical (or electromechanical) force-boundary condition (Equation (8.119) in chapter 8) into Equation (9.75) and following the same procedure as used for discretizing the purely mechanical domain using the SFEM, the force-balance equation for the q th actuator element (denoted by subscript a_q) in the actuator local coordinate system can be obtained as:

$$\begin{aligned} \{\hat{F}\}_{aq} &= [\hat{K}]_{aq} \{\hat{u}_e\}_{aq} + \\ &[A_{33}^{eff} \quad 0 \quad -B_{33}^{eff} \quad -A_{33}^{eff} \quad 0 \quad B_{33}^{eff}]_{aq}^T \beta \gamma \hat{\eta} \end{aligned} \quad (9.76)$$

where:

$$[A_{33}^{eff}, B_{33}^{eff}] = \int e_{33}^{eff}[1, z]dz \quad (9.77)$$

defines the equivalent mechanical stiffness due to the effective magnetomechanical (or electromechanical) coupling coefficient e_{33}^{eff} (see Equation (8.109) in chapter 8 for the PFC) for actuation in the longitudinal mode. A similar vector with non-zero second and fifth elements in Equation (9.76) be used. After substituting \hat{u} in terms of the sensor element shape function matrix $[N]$ and the corresponding nodal displacement vector $\{\hat{u}_e\}$ from Equations (9.72)–(9.74), Equation (9.76) can be rewritten as:

$$\{F_e\}_{a_q} = [\hat{K}_e]_{a_q} \{\hat{u}_e\}_{a_q} + [\hat{K}_e]_{a_q \leftarrow s_p} \{\hat{u}_e\}_{s_p} \quad (9.78)$$

where the notation $[\hat{K}_e]_{a_q \leftarrow s_p}$ is introduced to represent the *Sensor–Actuator Stiffness Influence Matrix* (SASIM). This equation is transformed to the global coordinates as in a regular FE solution. This procedure leads to the final expression for the q th actuator element with the p th feedback sensor. If $[\Gamma]_{s_p}$ is the transformation matrix that transforms the stiffness matrix of a sensor element from local coordinates to global coordinates, and $[\Gamma]_{a_p}$ is the transformation matrix for the actuator element, then the assembled closed-loop MIMO system with a general sensor–actuator configuration in the ASEM is obtained in the form:

$$\begin{aligned} & \left\{ \begin{array}{c} \{\hat{F}\}_{s_p} \\ \vdots \\ \{\hat{F}\}_{a_p} \end{array} \right\} \\ &= \begin{bmatrix} [\Gamma_{s_p}]^T [\hat{K}_e]_{s_q} [\Gamma_{s_p}] & \dots & [0] \\ \vdots & \ddots & \vdots \\ [\Gamma_{a_p}]^T [\hat{K}_e]_{a_q \leftarrow s_p} [\Gamma_{s_p}] & \dots & [\Gamma_{a_p}]^T [\hat{K}_e]_{a_q} [\Gamma_{a_p}] \end{bmatrix} \\ & \times \left\{ \begin{array}{c} \{\hat{u}\}_{s_p} \\ \vdots \\ \{\hat{u}\}_{a_p} \end{array} \right\} \end{aligned} \quad (9.79)$$

As evident from the above derivation, restrictions are not placed on the sensor and actuator locations. In addition, in terms of computational cost and broadband analysis capabilities, the proposed ASEM is a better option compared to the conventional state-space models which are of very high order and several accuracy-related problems due to errors in model-order reduction, modal truncation etc. need to be addressed before they can be applied for broadband *Low Authority Control* (LAC). So far as LAC is concerned, after combining the displacement (or strain) field generated by the primary disturbance (external mechanical load) and the secondary sources (actuators), one can obtain the wave coefficient vector $\{\hat{u}\}$ for a subdomain Ω of interest as:

$$\{\hat{u}\}_\Omega = [\hat{T}_\Omega]^{-1} [[\hat{K}] + [\hat{K}(x_s)_{a \leftarrow s}]]^{-1} \{\hat{F}\}_\Omega \quad (9.80)$$

In the above equation, $[\hat{T}_\Omega]$ is the matrix that relates the displacement field to the wave vector. At this stage, if a transfer-function-based concept of wave cancellation is chosen for designing the controller, Equation (9.80) provides a direct way to carry out identification of appropriate control gains for known sensor and actuator locations that will reduce certain elements of $\{\hat{u}\}_\Omega$ to zero, and hence the corresponding wave components can be controlled. However, the analytical approach to achieve this is limited by the fact that one cannot obtain an explicit expression for the dependence of local wave components on sensor and actuator locations and other control parameters for a complex problem, which may have more than one discretized subdomain. Hence, a semiautomated scheme integrated with an ASEM is chosen to analyze the spatially rediscretized system by changing sensor locations or actuator locations on an iterative basis. This is feasible because of the fast computation and small system size permitted by the ASEM.

9.6.2.4 Numerical implementation

As the initial step, input time-dependent forces or disturbances are decomposed into Fourier components by using the forward FFT. Note that all of the element-level operations as well as the global system-level operations are carried out at each discrete frequency ω_n . Except for this basic difference, the proposed program architecture is almost identical (for an open-loop configuration) to a finite element program in terms of features such as input, assemblage, solving of the system and output. For a closed-loop system, we use Equation (9.79) to implement the explicit form of the global dynamic stiffness matrix at a particular frequency, which is in most of the cases,

neither banded nor symmetric. Here, a non-symmetric sparse complex matrix inversion routine needs to be used as part of the global system solver. After solving the closed-loop system at each frequency, the time history of displacements, strains, stresses, etc. are then post-processed using an inverse FFT.

9.6.2.5 Effect of broadband distributed actuator dynamics

Here, we consider a composite cantilever beam with surface-bonded PFC to study the effect of distributed actuator dynamics towards broadband control of transverse response of the cantilever tip under transverse-impact-type loading. Essentially, the control point of interest for LAC in this case is the cantilever tip. This requires a feedback sensor to be placed at the cantilever tip. It is well known that optimal placement of an actuator is dictated by the location of high average strain [20]. Hence, while controlling the static or first mode shape under tip loading on a cantilever beam, it is essential that the actuator be placed at the root of the cantilever beam. For velocity feedback with a collocated sensor, Crowley and Luis [20] has shown that the damping of a particular vibration mode, while using a surface-bonded PZT wafer, can be expressed as:

$$\xi = \frac{e_{31}\gamma_w}{2M\omega_0 L_B} \frac{\psi h_B b}{(6 + \psi)} \left[\frac{d\hat{\phi}(x_2)}{dx} - \frac{d\hat{\phi}(x_1)}{dx} \right] \quad (9.81)$$

where γ_w is the velocity feedback gain, ω_0 is the natural frequency associated with the mode, M is the modal mass, L_B is the length of the beam, b is the width of the beam, h_B is the thickness of the beam, $\psi = (C_B h_B)/(C_{PZT} h_B)$ is the effective stiffness ratio for a PZT wafer thickness of h_B , and $d\hat{\phi}(x_2)/dx - d\hat{\phi}(x_1)/dx$ is the difference between the gradients of the strain mode shape at the two ends (x_1, x_2) of the PZT actuator. With the specified actuator-to-beam length scale, the maximum modal damping of a single mode is obtained for maximum feedback gain as:

$$(\gamma_w) = \frac{E_{\max} h_{PZT}}{\omega_0 \hat{w}_{\max}} \quad (9.82)$$

where E_{\max} is the saturation electric field. Note that when the feedback sensor is placed non-collocated with the actuator, the sensor output signal will have a phase difference with the modal strain at the actuator ends and the effect can be destabilizing for a phase difference

of more than 180° . A similar consequence will also be evident while controlling more than one mode using the same configuration. For example, while controlling the second mode along with the first mode, one has to overcome the difficulty of almost zero average modal strain around the strain node (point of zero modal strain) at $x = 0.216L_B$. Two options are available to overcome this difficulty. One is to use segmented actuators, where one of the actuator located at $x < 0.216L_B$ must be driven 180° out of phase with a second actuator located at $x > 0.216L_B$. Obviously, control over further numbers of modes means more strain nodes and hence further numbers of segmented actuators. In addition, the possibility of interaction between the controlled modes and modal spillover for multiple-segmented actuators becomes evident. This necessitates the requirement of appropriate optimal control strategy. The second option for multi-modal control is to use a single actuator at the root of the cantilever beam with an optimal length of the actuator and a frequency-weighted optimal gain while using a non-collocated sensor. Direct feedback from the control point of interest is found to be more suitable when a large number of modes over a broad frequency band are to be controlled. The fundamental behavior of this non-collocated sensor–actuator configuration for LAC resembles that of the disturbance propagation in a structural network [21].

In the following numerical simulation, the sensitivity of the PFC actuator length (actuator located at the cantilever root) while using velocity feedback from the sensor (located at the cantilever tip) is studied. The configuration is shown in Figure 9.9. The beam is of length $L = 1$ m and thickness = 2 cm. An AS/3501-6 graphite–epoxy material with a play-stacking sequence of $[0_5^0]/[90_5^0]$ is considered. Assuming Euler–Bernoulli

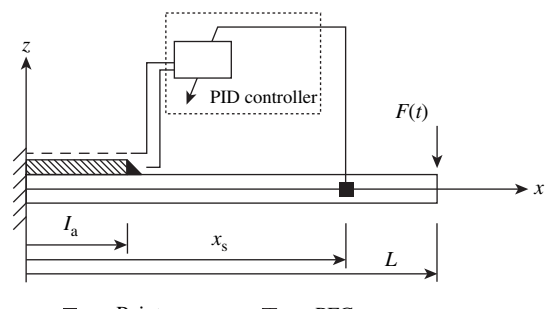


Figure 9.9 Schematic of composite cantilever beam with a surface-bonded PFC actuator and a non-collocated velocity feedback sensor for broadband local control at the tip.

beam kinematics, the coupled electromechanical wave equation can be expressed as:

$$\begin{aligned} \rho A \frac{\partial^2 u_0}{\partial t^2} - A_{33} \frac{\partial^2 u_0}{\partial x^2} + B_{33} \frac{\partial^3 w}{\partial x^3} + A_{33}^{eff} \frac{\partial E_3}{\partial x} &= 0 \\ \rho A \frac{\partial^2 w}{\partial t^2} - B_{33} \frac{\partial^3 u_0}{\partial x^3} + D_{33} \frac{\partial^4 w}{\partial x^4} + B_{33}^{eff} \frac{\partial^2 E_3}{\partial x^2} &= 0 \end{aligned} \quad (9.83)$$

The associated force-boundary conditions are:

$$\begin{aligned} A_{33} \frac{\partial u_0}{\partial x} - B_{33} \frac{\partial^2 w}{\partial x^2} - A_{33}^{eff} E_3 &= N_x \\ B_{33} \frac{\partial^2 u_0}{\partial x^2} - D_{33} \frac{\partial^3 w}{\partial x^3} - A_{33}^{eff} \frac{\partial E_3}{\partial x} &= V_x \\ -B_{33} \frac{\partial u_0}{\partial x} + D_{33} \frac{\partial^2 w}{\partial x^2} + B_{33}^{eff} E_3 &= M_x \end{aligned} \quad (9.84)$$

In Equations (9.83) and (9.84), the mechanical stiffness coefficients A_{ij} , B_{ij} and D_{ij} are defined in Equation (8.120) of Chapter 8 and the electromechanical stiffness coefficients A_{33}^{eff} and B_{33}^{eff} are described in Equation (9.77). One actuator element and one composite beam element (with a point sensor in it) is used in the ASFEM.

The beam is subjected to an impact loading (Figure 9.2) in the transverse direction at the cantilever tip. Note that under such loading, which is likely to excite many higher-order modes, the control analysis becomes challenging because of additional axial–flexural coupling due to the unsymmetric ply-stacking sequence. Control of multiple spectral peaks in the frequency response of the transverse tip displacement is considered as the local control objective. If satisfied, this requirement will also ensure the stability of the close-loop system. That is, all of the resonant modes will be damped and hence the poles will be moved to the left-half of the complex phase plane. In addition, the possibility of modal truncation over a sufficiently large frequency band can be eliminated. It is important to note that the waves that will travel from the tip to the fixed-end of the beam will be of the same order of magnitude as the incident impact. It is also necessary that the scattered axial and flexural waves from the fixed end be suppressed. This is also one of the reasons, apart from those discussed in the context of Equations (9.81) and (9.82), why the PFC actuator is placed adjacent to the fixed end. The sensor is assumed at $x = x_s$, which is considered near the tip for direct velocity feedback to the actuator in advance. A non-dimensional scalar feedback gain g is derived from the feedback gain γ (Equation (9.75) to perform parametric study. These two quantities are related as $g = (c_0 \alpha \beta) \gamma / E_0$,

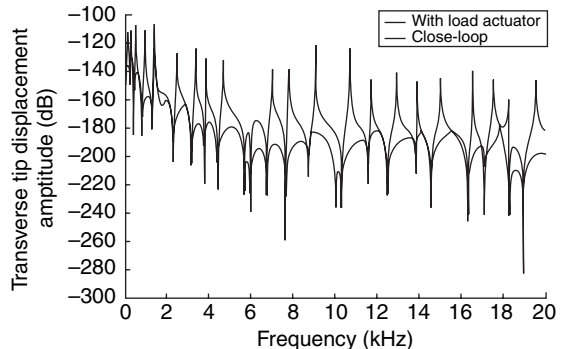


Figure 9.10 Closed-loop transverse displacement at the cantilever tip under impulse excitation.

where E_0 is a reference AC voltage and c_0 is the speed of sound in air. An optimal closed-loop performance which corresponds to $L_a = 0.25$ m, $x_s = 1.0$ m (at the tip) and $g = 3.4 \times 10^6$ is shown in Figure 9.10.

From Figure 9.10, which shows the locations of the forced resonances and anti-resonances along the frequency axis and the corresponding spectral amplitudes of transverse displacement at the tip, it can be seen that the configuration is able to suppress most of the resonant modes. Furthermore, we study the effects of parametric variation on the amplitude level over the frequency range of 20 kHz under consideration. First, it is assumed that the feedback gain g chosen above is optimal and is not sensitive to small variations in other parameters, such as L_a and x_s . L_a is slowly varied from 0.15 m to 0.35 m, corresponding to velocity feedback from various sensor locations x_s moving away from the cantilever tip (Figure 9.9). The integral effect of the change in

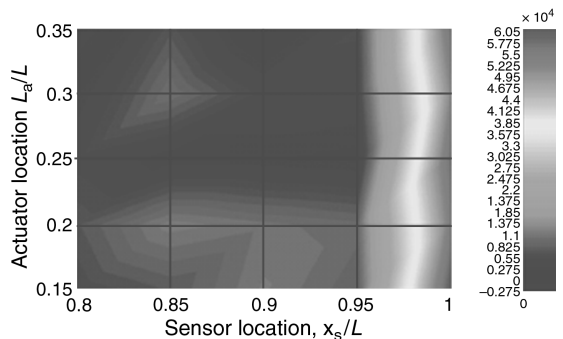


Figure 9.11 Performance of actuator and control point interaction by variation in total amplitude level of the transverse tip response.

amplitude level of the closed-loop response (transverse displacement at the tip) over the whole frequency range is evaluated by using the control cost function:

$$\prod = \sum_{n=1}^{N/2} (20.0) \left[\log_{10} |\hat{w}(\omega_n)^2_{\text{open}}| - \log_{10} |\hat{w}(\omega_n)^2_{\text{close}}| \right] \quad (9.85)$$

In Figure 9.11, the sensitivity of \prod is shown by a two-dimensional solution space involving the actuator length L_a and sensor location x_s .

This plot confirms the result of Figure 9.11 that one optimum solution exists at $(x_s/L = 1.0, L_a/L = 0.25)$ and yields a total reduction of 6.025 dB in \prod . Figure 9.11 also predicts that another solution exists at $(x_s/L = 1.0, L_a/L = 0.15)$.

REFERENCES

1. K. Ogata, *Mordern Control Engineering*, 3rd Edn, Prentice-Hall, Englewood Cliffs, NJ, USA (1999).
2. B.C. Kuo, *Automatic Control Systems*, 4th Edn, Prentice-Hall, Englewood Cliffs, NJ, USA (1999).
3. A. Chakraborty, *Wave Propagation in Anisotropic and Inhomogeneous Structures*, Ph.D. Thesis, Indian Institute of Science, Bangalore, India (2004).
4. H. Nyquist, "Regeneration theory", *Bell Systems Technical Journal*, **11**, 126–147 (1932).
5. J.G. Ziegler and N.B. Nichols, "Optimum settings for automatic controllers", *ASME Transactions*, **64**, 959–768 (1942).
6. R.J. Guyan, "Reduction of mass and stiffness matrices", *AIAA Journal*, **3**, 380 (1965).
7. V.N. Shah and M. Raymund, "Analytical selection of masters for the reduced eigenvalue problem", *International Journal of Numerical Methods in Engineering*, **18**, 89–98 (1982).
8. M. Paz, "Dynamic condensation", *AIAA Journal*, **22**, 724–727 (1984).
9. J. O'Callahan, "System equivalent reduction and expansion process", in *Proceedings of 7th International Modal analysis conference*, Society of Experimental Mechanics, Bethel, CT, USA, 29–37 (1989).
10. W.M. To and D.J. Ewins, "The role of generalized inverse in structural dynamics", *Journal of Sound and Vibration*, **186**, 185–195 (1995).
11. C.T. Dyka, R.P. Ingel and L.D. Flippin, "A new approach to dynamic condensation for FEM", *Computers and Structures*, **6**, 763–773 (1996).
12. J. O'Callahan, "A procedure for an Improved Reduced System (IRS)", in *Proceedings of 7th International Modal analysis conference*, Society of Experimental Mechanics, Bethel, CT, USA, 17–21 (1989).
13. M.I. Friswell, S.D. Garvey and J.E.T. Penny, "Model reduction using dynamic and iterated IRS techniques", *Journal of Sound and Vibration*, **186**, 311–323 (1995).
14. D.J. Leo and C.A. Smith, "Performance tradeoffs in active-passive vibration isolation", in *Proceedings of 11th Symposium on Structural Dynamics and Control*, 25–31 (1997).
15. E.H. Anderson and J.P. How, "Active vibration isolation using adaptive feed forward control", in *3, American Control Conference*, Albuquerque, New Mexico, USA, Paper I-97115B, 1783–1788 (1997).
16. A.A. Bent, *Active Fiber Composites for Structural Actuation*, Ph.D. Thesis, Massachusetts Institute of Technology, (Cambridge, MA, USA) (1997).
17. N.W. Hagood, R. Kindel, K. Ghandi and P. Gudenz, "Improving transverse actuation of piezoceramics using integrated surface electrodes", *SPIE*, 1917, 1917–1925 (1993).
18. B.D.O. Anderson and J.B. Moore, *Optimal Control*, Prentice-Hall, Englewood Cliffs, NJ, USA (1990).
19. J.L. Butler, *Application manual for the design of Terfenol-D magnetostrictive transducers*. Technical Report TS 2003, Edge Technologies, Inc., Ames Iowa, IA, USA (1988).
20. E.F. Crawley and J. Luis, "Use of piezoelectric actuators as elements of intelligent structures", *AIAA Journal*, **25**, 1373–1385 (1987).
21. D.W. Miller, S.R. Hall and A. von Flotow, "Optimal control of power flow in structural junctions", *Journal of Sound and Vibration*, **140**, 475–497 (1990).

Part 4

Fabrication Methods and Applications

Silicon Fabrication Techniques for MEMS

10.1 INTRODUCTION

The technology of micro electromechanical systems (MEMS) spun off from developments in the integrated circuit (IC) fabrication processes, enabling co-fabrication of sensors, actuators and control functions on silicon chips. Since then, remarkable research progress has been achieved in MEMS areas under strong capital promotions from both government and industry. In addition to several applications already commercialized, the feasibility of more complex MEMS devices have been proposed in microfluidics, aerospace, biomedical fields, chemical analysis, wireless communications, data storage, display, optics, etc. [1,2]. These sensors and actuators could also form the building blocks of several smart systems.

Micromachining is the fundamental technology for the fabrication of micro electromechanical system (MEMS) devices, in particular, miniaturized sensors and actuators having dimensions in the sub-millimeter range. Silicon micromachining is the most mature of the micromachining technologies and has been a key factor for the tremendous progress of MEMS within a short time. Micromachining refers to the fashioning of microscopic mechanical parts out of a silicon substrate or on a silicon substrate, making the structures three-dimensional, thus bringing new avenues to designers.

Silicon micromachining comprises two technologies: bulk micromachining, in which structures are etched into a silicon substrate, and surface micromachining in which the micromechanical layers are formed from layers and films deposited on the surface. Yet another but less common method, LIGA 3-D microfabrication, has been used for the fabrication of high-aspect ratio and three-dimensional microstructures for MEMS [3–5]. However,

three-dimensional microfabrication processes incorporating more material layers have been recently reported for MEMS in some specific application areas (e.g. biomedical devices) and micro-actuators with higher output powers [6–11]. Employing materials such as crystalline silicon, polycrystalline silicon and silicon nitride, a variety of mechanical microstructures including beams, diaphragms, grooves, orifices, springs, gears, suspensions and numerous other complex mechanical structures have been fabricated [12–16]. These processes are reviewed briefly in the subsequent sections of this chapter.

10.2 FABRICATION PROCESSES FOR SILICON MEMS

Important steps in the fabrication of silicon-based MEMS are as follows:

- Lithography
- Resists and mask formation
- Lift-off technique
- Etching techniques
- Wafer bonding

Hardly any MEMS device is fabricated without going through all of these steps. Hence, a brief description of these is provided in the following paragraphs.

10.2.1 Lithography

The patterning of geometries is an essential process step in the fabrication of devices for microelectronics and MEMS. The process of transferring a geometrical

pattern from a mask to the radiation-sensitive resist is called *lithography*. Both additive and subtractive processes are employed in the industry to define features after transferring the pattern. In both cases, suitable resists are first spin-coated onto the wafer surface. The wafer surface is then irradiated with the mask placed above it. Depending on the choice of resist material and mask (c.f. Section 10.2.2), part of the resists gets cured, thereby affecting its solubility. Thus, the resist may be used either to protect areas that need not be etched (subtractive) or to protect areas that should not be deposited on (additive). After etching or depositing, the resist itself is removed by dissolving it in suitable chemicals.

The mask is often made on glass or quartz with a chrome pattern on areas where we intend the radiation to be blocked from reaching the resist. Often, the mask itself is made by (higher-precision) lithography. UV light (e.g. from a high-pressure mercury lamp) is the most common source of radiation.

Several types of lithographic tools are in use in the industry. For example, *contact aligners* can be used to interlock the mask and the wafer before the latter is being exposed. Resolution of the order of $0.5\text{ }\mu\text{m}$ can be obtained with this approach. Resolution is defined as the minimum feature size with good fidelity that can be transferred onto the resist film coated on the wafer. The radiation schemes employed depend on the desired resolution; electromagnetic (UV or X-rays) or particulate (electrons or ions) beams may be used for the irradiation.

Contact aligners with optical lithography use UV radiation ($0.2\text{--}0.4\text{ }\mu\text{m}$ wavelengths). The minimum line width with this approach is $\approx\sqrt{\lambda g}$, where λ is the optical wavelength used and g is the spacing between the mask and the wafer. Since the mask covers the entire wafer, the process involves single exposure. This technique results in a feature size the same as that on the mask. An alternate approach uses *stepper technology* to improve the resolution ($\approx 0.25\text{ }\mu\text{m}$) of features. In this case, the radiation is passed through a focusing lens arrangement, after it encounters the mask. Although the mask is simpler and cleaner, the equipment cost far exceeds that with the contact aligner.

Fresnel diffraction of the radiation beam at the edges of the features on the mask is the limiting factor in the resolution of the features obtained with lithography. Significant reduction in minimum feature size is therefore possible with *electron beam lithography*. The beam from an electron source, typically of a 20 nm diameter spot, is passed through electrostatic plates to direct onto the wafer in vacuum. This technique, however, does not

use a mask, but instead relies on a ‘direct-write’ technique. The steering and blanking (switching) of the beam is controlled by a computer with the geometry loaded in a computer-aided design (CAD) package. However, the writing process is time-consuming (several hours per wafer) and the equipment used is far more expensive than other approaches.

Several new techniques are emerging for better resolution, with a potential for mass production, especially in the context of the increased thrust for nanotechnology. *Embossing lithography*, also known as *nano-imprinting lithography*, uses a mold made by the electron beam lithography to imprint the pattern onto a substrate coated with a resist (e.g. PMMA). Metal lines of 10 nm width have been reported based on this approach [17]. By repeatedly using the mold, a higher throughput is obtained at the cost of reduced resolution. *Scanning probe lithography* is another high-resolution method in which electrostatic discharge from the probe tip is used as the stimulant to modify (e.g. by oxidizing) the wafer surface, thereby creating a pattern on it [18].

10.2.2 Resists and mask formation

As mentioned previously, accurate fabrication of the mask and selection of the proper resist material are vital to the success of lithography. The mask-making process is quite similar to lithography itself. The equipment consists of a UV light source, an automated $x\text{-}y$ positioning stage and optical control and reduction units. The positioning stage and the optical aperture are controlled by a computer with a CAD package in which the required mask geometry is loaded. For better resolution, low-expansion glass or quartz is used as the substrate. An optical blocking material, such as chromium or iron oxide, is used to define the mask features.

Geometrical patterns are transferred to *resists* prior to deposition or etching of substrates. Since optical radiation is most often used, these materials are generally called *photoresists*. These may be either positive or negative resists – depending on how these respond to the radiation. The processes of developing positive and negative resists are compared in Figure 10.1. The positive resists becomes soluble in a developer after being exposed to radiation, leaving patterns on the substrate the same as that on the mask. In contrast, when a negative resist is exposed to radiation, it becomes less soluble to the developer, thus leaving a pattern the reverse of that on the mask. Some of the commercially positive and negative resists for various lithography approaches are listed in Table 10.1.

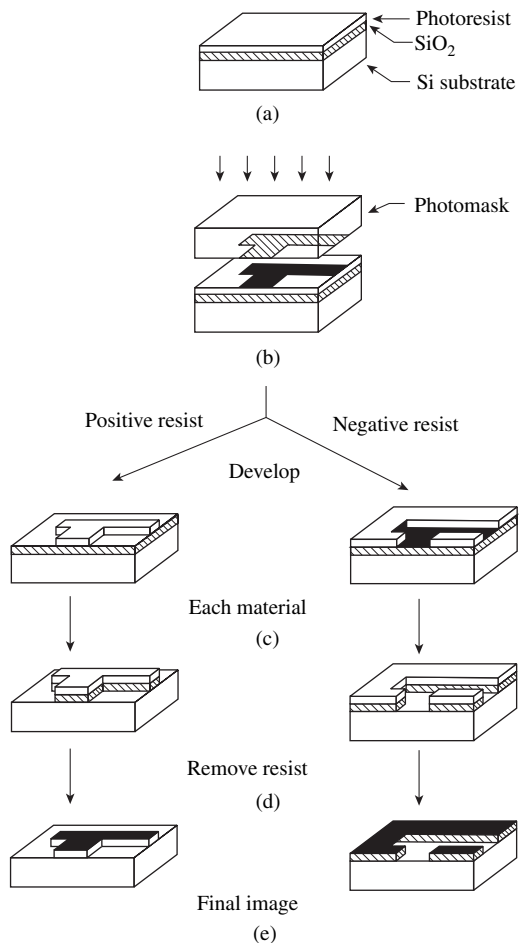


Figure 10.1 Images formed using positive and negative resists [19]. Reproduced by permission of John Wiley & Sons, Ltd

Table 10.1 Types of some commercially available resists.

Resist type	Commercial name	Lithography
Positive	AZ-1350J	Optical
Positive	PR 102	Optical
Positive	Poly(methyl methacrylate)	E-beam and X-ray
Negative	Kodak 747	Optical
Negative	Dichloropropyl acrylate and glycidyl methacrylate- <i>co</i> -ethyl acrylate	X-ray
Negative	Poly[(glycidyl methacrylate)- <i>co</i> -ethylacrylate]	E-beam and X-ray

The resist is formed on the substrate by spin-coating. By this process, a thin uniform film is deposited on the substrate. The clean wafer is placed on the wafer holder of a spinner and is held tight by using vacuum. The resist in the liquid form is dropped on the surface of the wafer. The spinner motor is then operated at a specified speed for good-quality films. The wafer is dried and then baked at the desired temperature after spin-coating the solution. The baking step is required to strengthen the adhesion of the resist to the wafer before further processing.

10.2.3 Lift-off technique

The lift-off technique is used to define a structural geometry on a substrate. The process steps involved in this are schematically shown in Figure 10.2. The resist is spin-coated and then exposed to the radiation through a mask. A thin film of the desired material (e.g. a metal) is then deposited on the top of this structure by any of the processes described in Chapter 2. The resist can be dissolved in an appropriate solution, which detaches the film on top of the resist as well. The primary criterion for this lift-off process to be effective is that the thickness of the deposited thin film should be less than that of the resist. Some of the features of the lift-off process of patterning are:

- The film thickness should be smaller than that of the resist.
- High-resolution geometries can be produced.
- Discrete devices can be patterned.

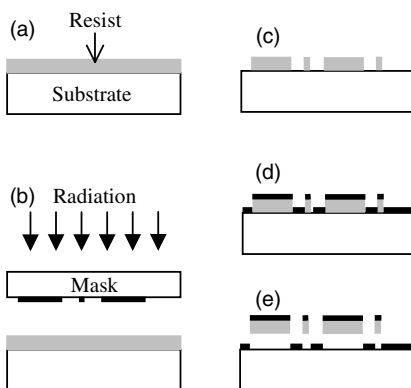


Figure 10.2 Steps involved in the lift-off process of patterning.

10.2.4 Etching techniques

Etching is the key technological step for bulk micromachining. The etch process employed in the micromachining of silicon comprises one or several of the following techniques:

- Wet etching – isotropic/anisotropic
- Dry etching – plasma/reactive ion

These etch processes are standard technologies widely employed in the microelectronics industries. Process parameters that characterize etching are etch rate, etch selectivity and etch uniformity. *Etch rate* is the thickness of the material removed per unit time. *Etch selectivity* is a measure of the effectiveness of the removal of unwanted material without affecting other materials or films present on the wafer. This is often represented as the ratio between the etch rate of the material to be etched and other materials (such as an etch mask) on the wafer. The performance of etchants used to remove some of the common materials used in the microelectronics and MEMS industries are listed in Table 10.2. Wet etching is done by dipping the substrate into an etchant bath or spraying it with etchants. Wet etching can be either isotropic or anisotropic, depending on the structure of the materials or the etchants used. If the material is amorphous or polycrystalline, isotropic wet etching is employed. During isotropic etching (Figure 10.3(a)), the resist is always undercut, meaning that the deep etching is not practical for MEMS. In this process, the etchant used is an acid solution. Single-crystal silicon can be

anisotropically etched. The etching features are determined by the etching speed which is dependent on the crystal's orientation. The etching slows down significantly at the (111) planes of silicon, relative to other planes. With the chosen wafers with different crystal orientation, different features can be achieved (Figure 10.3 (b,c)). The most common etchants used for the anisotropic etching of silicon include alkali hydroxide etchants (KOH, NaOH, etc.), ammonium-based solutions (NH_4OH , TMAH ($(\text{CH}_3)_4\text{NOH}$), etc.) and EDP (ethylene diamine, pyrocatechol and water). These etchants have different etch rates in different crystal orientations of silicon [13,20].

The etch process can be made selective by the use of dopants (heavily doped regions etch slowly), or may even be halted electrochemically (e.g. etching stops upon encountering a region of different polarity in a biased p–n junction). A region at which wet etching tends to slow down or diminish is called an ‘etch-stop’. Methods that make use of an etch-stop region include doping-selective etching (DSE) and bias-dependent DSE [13,20,21].

Wet etching in many cases is done from the back side of the wafer while plasma etching preferred for the front side. Dry etching is done by chemical or physical interaction between the ions in the gas and the atoms of the substrate. The non-plasma, isotropic dry etching is possible by using xenon difluoride or mixture of interhalogen gases and provides very high selectivity for aluminum, silicon dioxide, silicon nitride, photoresists, etc. Common methods for dry etching of bulk silicon are plasma etching and reactive ion etching, where the external energy in the form of radio frequency (RF) drives chemical reactions in low-pressure reaction chambers. A wide variety of chlorofluorocarbon gases, sulfur hexafluoride, bromine compounds and oxygen are commonly used as reactants. The anisotropic dry etching processes are widely used in MEMS because of the geometry flexibility and sometimes less chemical contamination than in wet etching. Arbitrarily oriented features etched deep into silicon by using anisotropic dry etching are shown in Figure 10.3 (f). Very deep silicon microstructures can be obtained by the deep RIE (DRIE) dry etching process [14]. During plasma etching, radicals react chemically with the wafer and selectively remove the material. Diluents such as inert gases are introduced into the chamber to maintain the reaction rate. Increasing RF power helps increase ionization, but may affect wafer uniformity and selectivity at very high levels of power. Corrosion, reproducibility, sidewall profile and loss of critical dimensions are issues to be addressed while evaluating and optimizing etching.

Table 10.2 Wet etchants used in etching selected electronic materials.

Material	Composition of the etchant	Etch rate ($\mu\text{m}/\text{min}$)
Si	HF (3 ml) + HNO_3 (5 ml)	35
GaAs	H_2SO_4 (8 ml) + H_2O_2 (1 ml) + H_2O (1 ml)	8
SiO_2	HF (28 ml) + H_2O (170 ml) + NH_4F (113 g)	0.1
	HF (15 ml) + HNO_3 (10 ml) + H_2O (300 ml)	0.012
Si_3N_4	Buffered HF	0.005
	H_3PO_4	0.01
Al	HNO_3 (1 ml) + CH_3COOH (4 ml) + H_3PO_4 + H_2O (1 ml)	0.035
Au	KI (4 g) + I_2 (1 g) + H_2O (40 ml)	10

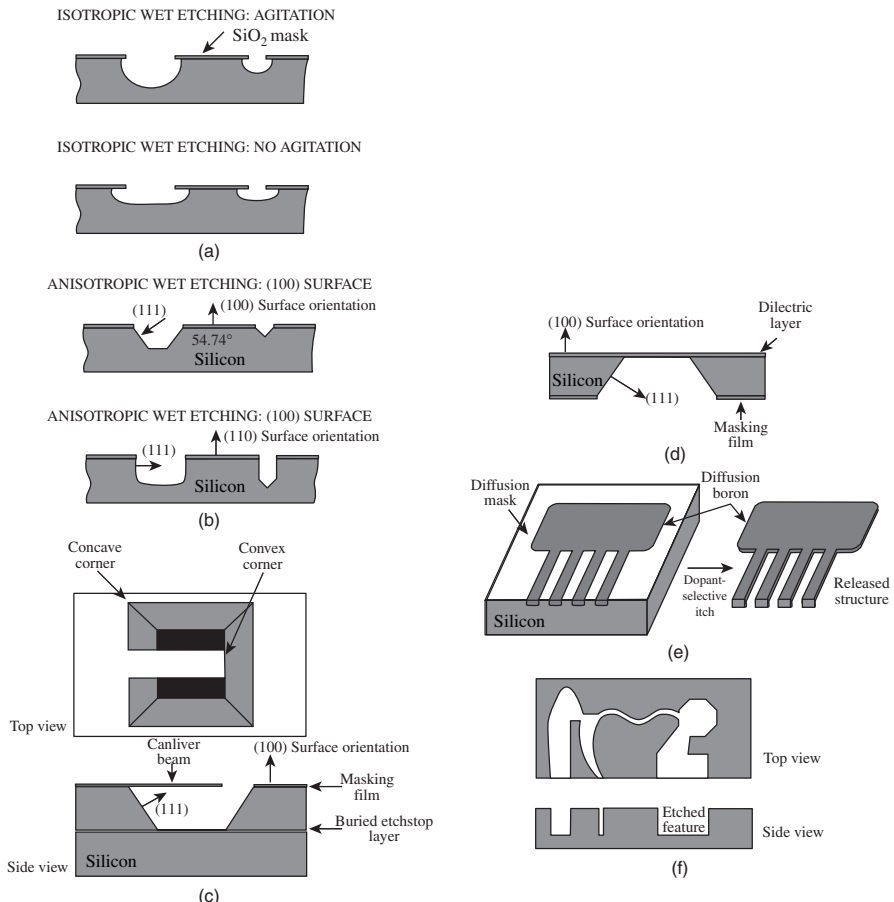


Figure 10.3 Silicon etching by various methods: (a) isotropic etching; (b) anisotropic etching; (c) anisotropic etching with buried ‘etch-stop’ layer; (d) dielectric membrane released by ‘back side’ bulk etching; (e) dopant-dependant wet etching; (f) anisotropic dry etching [22]. G.T.A. Kovacs, N.I. Maluf, K.E. Petersen, Bulk micromachining of silicon, Proc. IEEE, vol. 86, No. 8, © 1998 IEEE

10.2.5 Wafer bonding for MEMS

As silicon micromachining has limitations in forming complex three-dimensional microstructures in a monolithic format, multi-chip structures have been proposed for advanced MEMS, where wafer-to-wafer bonding is critical in the formation [23]. Wafer bonding of silicon for MEMS can be categorized into three major types: anodic bonding, intermediate-layer assisted bonding and direct bonding.

10.2.5.1 Anodic bonding

Anodic bonding is typically done between a sodium glass and silicon for MEMS. For anodic bonding, a cathode

and an anode are attached to the glass (or silicon with a thin coating glass) and silicon wafer (Figure 10.4), respectively – the voltages applied range from 200 to 1000 V. At the same time, the anode is put on a heater to provide the bonding temperature of 180–500 °C. During the bonding, oxygen ions from the glass migrate into the

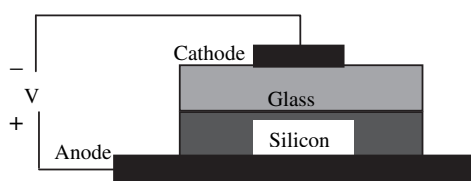


Figure 10.4 Schematic of the process of anodic bonding.

silicon, resulting in the formation of a silicon dioxide layer between the silicon wafer and glass wafer to form a strong and hermetic chemical bond. The advantage of anodic bonding for MEMS is that the low temperatures used can ensure the metallization layers (e.g. aluminum) could withstand this temperature without degradation. This technique is also called *field-assisted thermal bonding* or *electrostatic bonding*. Anodic bonding is also used to seal two silicon wafers together by using a thin sputter-deposited glass layer. The equipment used in this case is basically a heat chuck element with an electrode capable of supplying a high voltage across the structure to be bonded. The system automatically controls the temperature and power supply during the bonding process. In this process, after surface cleaning and polishing, one of the wafers (referred to here as the *top wafer*) is coated with a few-microns-thick glass film (usually by sputtering). The top wafer is placed on top of a second silicon wafer (referred to as the *support wafer*) for these two wafers to be bonded. The support wafer rests on an aluminum chuck. The two wafers are usually sealed together at temperatures less than 400 °C with an electrostatic DC voltage of 50 to 200 V. The negative electrode is connected to the top wafer. The voltage should be applied over a sufficiently long time (10 to 20 min) to allow the current to reach a minimum steady-state level. This bond process usually takes place in air at atmospheric pressure.

10.2.5.2 Direct bonding

Direct bonding is based on a chemical reaction between the OH groups present at the surface of native silicon or grown oxides covering the wafers [24]. Direct bonding is also called *silicon fusion bonding*, since it is used for silicon–silicon fusion bonding. This process is usually done in three steps: surface preparation, contacting and thermal annealing.

The surface-preparation step involves cleaning the surfaces of the two wafers to form a hydrate surface. The wafer surface should be ‘mirror-smooth’, the roughness should be no greater than 10 Å, and the bow of a 4" wafer should be less than 5 µm to achieve the necessary flatness [23]. Following this preparation, the wafers are aligned and contacted in a clean-room environment by gently pressing the two wafers at the surface central point. The surface attraction of the two hydrated surfaces creates an intimate contact over the entire wafer surfaces. At room temperature, these wafers adhere via hydrogen bridge bonds of chemisorbed water molecules that subsequently react during the annealing process to form

Si–O–Si bonds. Consequently, wafer pre-treatment procedures such as hydrophilization steps (wet-cleaning processes, plasma hydrophilization) assist the bonding process. The final step in direct bonding is to anneal the bonding from room temperature to 1200 °C. This anneal process increases the bond strength by more than one order of magnitude at a temperature as high as 800–1200 °C. However, high-temperature annealing is not allowed for the metallized wafers. The direct bonding prevails in the high-strength bonding and the devices’ dimensions design could be scaled down if direct bonding approaches other than anodic bonding are used.

In the last decade, several groups [25–27] have demonstrated that the fusion of hydrophilic silicon wafers is possible for obtaining silicon-on-insulator (SOI) materials. Since then, wafer-bonding techniques have found various applications in the field of microelectronics such as in static random access memories (SRAMs), CMOS and power devices. For micromechanical applications, fusion bonding has rendered possible the fabrication of complex structures by combining two or more patterned wafers.

According to the reaction mechanism, annealing at temperatures above 1000 °C for several hours should result in an almost complete reaction of the interface. Annealing at 1000 °C for about 2 h would give a sufficiently high bond strength for all subsequent treatments [28]. It is not possible to separate the two bonded Si wafers without breaking the silicon. Although high-temperature annealing increases the strength of the bond, this step (usually if the temperature is above 800 °C) may introduce problems, such as doping profile broadening, thermal stresses, defect generation and contamination. Annealing also prevents the use of bonding technology for compound semiconductor materials since their dissociation temperatures are often low. In addition, post-metallization bonding also requires bonding temperatures that are less than ≈450 °C since most of the common metals used in device fabrication melt below this temperature. Therefore, in order to make full use of the potential provided by wafer bonding for microstructures, low-temperature bonding methods have to be developed. To summarize, three ranges of annealing temperature are of interest in wafer bonding:

- < 450 °C – for post-metallization wafers.
- > 800 °C – for wafers with diffusion dopant layers (e.g. p^+ etch-stop layers).
- > 1000 °C – for wafer bonding before processing.

A major concern of all bonding processes is the presence of non-contacting areas which are generally called *voids*.

Voids are mainly caused by particles, organic residues, surface defects and inadequate ‘mating’. Therefore, both the surfaces being fusion-bonded have to be perfectly smooth and clean since the smallest of particles could cause large voids. Optimized processing includes wafer surface inspection, surface pre-treatment (hydrophilization, cleaning), and mechanically controlled, aligned mating in a particle-free environment.

10.2.5.3 Intermediate layer assisted bonding

This type of bonding for MEMS requires an intermediate layer, which can be metal, polymer, solders, glasses, etc., to fulfill the bonding between wafers [23]. One of the earliest wafer bonding – eutectic bonding – utilized Au as the intermediate layer for Si–Si bonding in a pressure sensor [29]. The Au–Si eutectic bonding takes place at 363 °C, well below the critical temperature of the metallized Al layer. However, the stress generated during bonding was found significant and introduced ‘sensor drift’ [29].

The use of polymers as intermediate layers for bonding requires very low temperatures and results in reasonably high strength and low stress due to the low-elasticity polymers. Usually, UV photoresists such as polyimide, AZ-4000, SU-8, PMMA and other UV-curable cross-linked polymers can be used for this purpose [24]. The major disadvantage of this approach is that the device bonded with polymer may not have the performance of hermetic sealing.

Glasses with low melting temperatures as intermediate layers for the bonding has also been demonstrated, where a layer of glass frit is usually deposited onto the silicon wafer. The flatness of the deposited frit layer is critical to obtaining uniform, strong, low-stress bonding. A screen-printed glass frit has been used to bond a pressure sensor [29].

10.2.5.4 Bonding of silicon-based materials

Fusion bonding of polysilicon, silicon dioxide or silicon nitride to silicon proceeds in a manner similar to silicon-to-silicon bonding. For examples, to bond polysilicon to silicon, a polishing step for the two surfaces to be bonded is necessary to produce two smooth defect-free surfaces. The bonding mechanism is mostly identical to silicon-to-silicon fusion bonding in that in both cases Si–OH groups are present at the surface. Thus, the pre-treatment (hydrophilization) and annealing conditions are also similar. Because of the dissimilar mechanical characteristics of the different bonded materials, the yield of void-

free wafers can be significantly reduced by ‘wafer bow’ or defects caused by stress during thermal treatment. Bonding of wafers covered with a thin thermal oxide or a thin silicon nitride results in homogenous-bonded wafers, while wafers with thicker oxide or nitride films generally developed voids [30].

10.3 DEPOSITION TECHNIQUES FOR THIN FILMS IN MEMS

Deposition and etching of thin films facilitates ‘quasi-3D’ structures based on planar processing techniques commonly used in the semiconductor industry. Solid thin films can be deposited from liquid, plasma, gas or the solid state. The deposition process is usually followed by thermal processing for achieving desired material properties and substrate adhesion. Some of the materials used in MEMS and microelectronics are Si, Al, Au, Ti, W, Cu, Cr, O, N and Ni–Fe alloys. Some materials are used in MEMS and not in microelectronics applications, i.e. Zr, Ta, Ir, C, Pt, Pd, Ag, Zn and Nb. A large number of distinct material systems are usually required in sensors and biomedical devices. The quality of the deposited film is evaluated by ascertaining the grain size, film composition, thickness, uniformity, step-coverage, adhesion and corrosion resistance.

Many different kinds of thin films are used in the fabrication of MEMS:

- (1) Metallization of thin films.
- (2) Thermal deposition of silicon dioxide.
- (3) Chemical vapor deposition (CVD) for dielectric layers.
- (4) CVD of polycrystalline silicon (poly-Si).
- (5) Deposition of ceramic thin films.

Metal films are used to form low-resistance ohmic connections both to heavily doped n^+ / p^+ regions and poly-Si layers and rectifying (non-ohmic) contacts in metal–semiconductor barriers. The dielectric layers include silicon dioxide (referred to as ‘oxide’) and silicon nitride. These dielectrics are used for insulation between conducting layers, for diffusion and ion-implantation masks and for passivation to protect devices from impurities, moisture and scratches. Poly-Si is used as a gate electrode in metal–oxide–semiconductor (MOS) devices, as a conductive material for multilevel metallization and as a contact material for devices with shallow junctions. In addition, several smart system applications require deposition of ceramic thin film materials.

10.3.1 Metallization techniques

Metallization is a process whereby metal films are formed on the surface of a substrate. These metallic films are used for interconnections and ohmic contacts, apart from structures. Hence their continuity, uniformity and surface properties are critical in the device performance. Metal films can be formed by using various methods, the most important being physical vapor deposition (PVD). PVD is performed under vacuum using evaporation or sputtering techniques. In these, physical mechanisms such as evaporation or impact are used as the means of deposition. In contrast, in chemical vapor deposition (CVD) methods, a chemical reaction is taking place under favorable conditions.

10.3.1.1 Evaporation

An evaporation system consists of a vacuum chamber, pump, wafer holder, crucible and a shutter, as shown in Figure 10.5. The source metal to be deposited is placed in an inert crucible, and the chamber is evacuated to a pressure of 10^{-6} – 10^{-7} torr. The crucible is heated using a tungsten filament or an electron beam to ‘flash-evaporate’ the metal from the crucible and condense onto the cold substrate. The

film thickness is determined by the length of time that the shutter is opened and can be measured using a QMB-based film thickness monitor. The evaporation rate is a function of the vapor pressure of the metal. Hence, metals that have a low melting point (e.g. 660 °C for aluminum) are easily evaporated, whereas refractory metals require much higher temperatures (e.g. 3422 °C for tungsten) and can cause damage to polymeric or plastic samples. In general, evaporated films are highly disordered and have large residual stresses; thus, only thin layers of the metal can be evaporated. The chemical purity of the evaporated films depends on the level of impurities in the source, contamination of the source from the heater, crucible or support materials, or due to residual gases within the chamber [31]. In addition, this deposition process is relatively slow.

For depositing metal alloys, the constituents are evaporated independently of one another. The deposited film has atoms that are less tightly bound than inorganic compounds [31]. Sources of individual metals are often kept at different temperatures.

10.3.1.2 Sputtering

Sputtering is a physical phenomenon involving the acceleration of ions via a potential gradient and the bombardment of a ‘target’ or cathode. Through momentum transfer, atoms near the surface of the target metal become volatile and are transported as a vapor to a substrate. A film grows at the surface of the substrate via deposition. Figure 10.6 shows a typical sputtering system comprising a vacuum chamber, a sputtering target

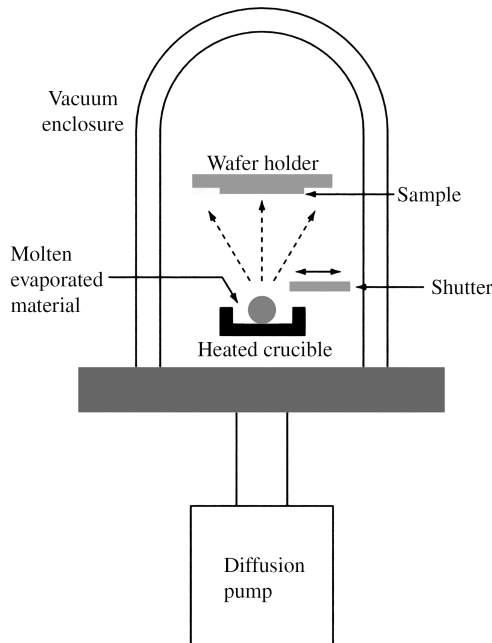


Figure 10.5 Schematic of a thermal expansion unit for depositing metals and other materials.

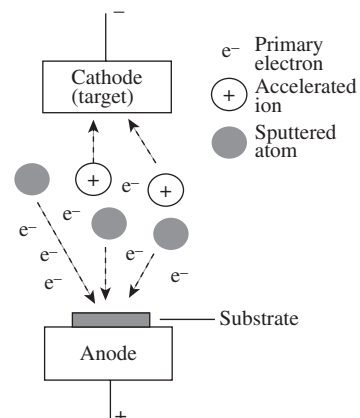


Figure 10.6 Schematic of sputtering unit for depositing materials.

of the desired film, a substrate holder and a high-voltage DC or RF power supply. After evacuating the chamber down to a pressure of 10^{-6} – 10^{-8} torr, an inert gas such as helium is introduced into the chamber at a few mtorr of pressure. Plasma of the inert gas is then formed. The energetic ions of the plasma bombard the surface of the target. The energy of the bombarding ions (\approx keV) is sufficient to make some of the target atoms escape from the surface. Some of these atoms land on the sample surface and form a thin film. Sputtered films tend to have better uniformity than evaporated ones, and the high-energy plasma overcomes the temperature limitations of evaporation.

Most elements from the Periodic Table can be sputtered, as well as inorganic and organic compounds. Refractory materials can be sputtered with ease. In addition, materials from more than one target can be sputtered at the same time. This process is referred to as ‘co-sputtering’ and can be used to form compound thin films on the substrate. The sputtering process can, however, be used to deposit films with the same stoichiometric composition as the source, and hence allows the utilization of alloys as targets [31]. Sputtered thin films have better adhesion to the substrate and many more grain orientations than evaporated films.

The structure of sputtered films is mainly amorphous, and their stress and mechanical properties are sensitive to specific sputtering conditions. Some atoms of an inert gas can be trapped in the film, causing anomalies in its mechanical and structural characteristics. Therefore, the exact properties of a thin film vary according to the precise conditions under which it was made. The deposition rate is proportional to the square of current density and inversely proportional to the spacing between the electrodes.

10.3.1.3 Metallo-organic chemical vapor deposition (MOCVD)

Metallo-organic chemical vapor deposition (MOCVD) is a relatively low temperature (200–800 °C) process for the epitaxial growth of metals on semiconductor substrates. Metallo-organics are compounds where each atom of the element is bound to one or many carbon atoms of hydrocarbon groups. For precise control of the deposition, high-purity materials and most accurate controls are necessary [32]. However, due to the high cost, this approach is used only where high-quality metal films are required. A summary of the MOCVD reaction parameters for depositing various metals are given in Table 10.3.

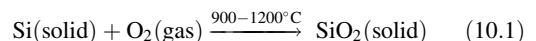
Table 10.3 Reactants and reaction conditions for MOCVD of various metals (adapted from Pierson [32]).

Metal	Reactant	Conditions
<i>Al</i>	Trimethyl aluminum	200–300 °C,
	Triethyl aluminum	1 atm
	Tri-isobutyl aluminum	
	Demethyl aluminum hydride	
<i>Au</i>	Dimethyl-1,2,4-pentadionate gold	—
	Dimethyl-(1,1,1-trifluoro-2,4-pentadionate) gold	
	Dimethyl-(1,1,1,5,5 hexafluoro-2,4-pentadionate) gold	
<i>Cd</i>	Dimethyl cadmium	10 Torr
<i>Cr</i>	Dicumene chromium	320–545 °C
<i>Cu</i>	Copper acetylacetone	260–340 °C
	Copper hexafluoroacetylacetone	200 °C
<i>Ni</i>	Nickel alkyl	200 °C in H ₂
	Nickel chelate	250 °C
<i>Pt</i>	Platinum hexafluoro-2,4-pentadio nate	200–300 °C in H ₂
	Tetrakistrifluorophosphine	
<i>Rh</i>	Rhodium acetylacetone	250 °C, 1 atm
	Rhodium trifluoroacetylacetone	400 °C, 1 atm
<i>Sn</i>	Tetramethyl tin	500–600 °C
	Triethyl tin	
<i>Ti</i>	Tris(2,2'bipyridene) titanium	< 600 °C

10.3.2 Thermal oxidation for silicon dioxide

Thermal oxidation is the method by which a thin film of SiO₂ is grown on a silicon wafer. This is a key method in modern IC technology. The basic thermal oxidation apparatus is shown in Figure 10.7. This comprises a resistance-heated furnace, a cylindrical fused-quartz tube containing the silicon wafers held vertically in a slotted-quartz boat and a source of either pure, dry oxygen or pure water vapor. The loading end of the furnace tube protrudes into a vertical flow hood where a filtered flow of air is maintained. The hood reduces dust in the air surrounding the wafers and minimizes contamination during wafer loading.

The thermal oxidation of silicon in oxygen or water vapor can be described by the following two chemical reactions:



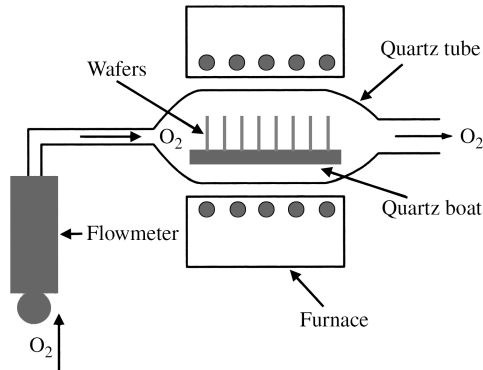
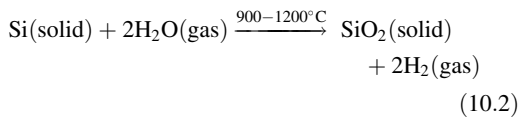


Figure 10.7 Schematic of the furnace used for thermal oxidation of silicon wafers.

and:



Using the densities and molecular weights of silicon and silicon dioxide, it can be shown that by consuming an ‘ x -thick’ layer of silicon, a ‘ $2.27x$ ’ thick oxide layer can be grown.

10.3.3 CVD of dielectrics

Three methods based on chemical vapor deposition (CVD) are commonly used to form a dielectric thin film, such as silicon dioxide or silicon nitride, on a substrate. These are:

- (1) Atmospheric-pressure chemical vapor deposition (APCVD).
- (2) Low-pressure chemical vapor deposition (LPCVD).
- (3) Plasma-enhanced chemical vapor deposition (PECVD).

The appropriate method from among these three deposition methods is based on the substrate temperature, the deposition rate and film uniformity, the morphology, the electrical and mechanical properties and the chemical composition of the dielectric films.

Schematics of two CVD systems (LPCVD and PECVD) are shown in Figure 10.8. In Figure 10.8(a), the quartz tube is heated by a three-zone furnace and gas is introduced at one end of the reactor and pumped out at the opposite end. The substrate wafers are held vertically in a slotted quartz boat. The type of LPCVD reactor

shown in Figure 10.8(a) is a ‘hot-wall’ LPCVD reactor where the quartz tube wall is heated by the furnace, in contrast to a ‘cold-wall’ LPCVD, such as the horizontal epitaxial reactor that uses radio frequency (RF) heating. Usually, the reaction-chamber LPCVD process parameters are in the following ranges:

- Pressure – 0.2–2.0 torr
- Gas flow – 1–10 cm³/s
- Temperature – 300–900 °C

Figure 10.8(b) shows two views of a parallel-plate, radial-flow PECVD reactor that comprises a vacuum-sealed cylindrical glass chamber. Two parallel aluminum plates are mounted in the chamber with an RF voltage applied to the upper plate while the lower plate is grounded. The RF voltage causes a plasma discharge between the plates (electrodes). Wafers are placed in the lower electrode, which is heated between 100 and 400 °C by resistance heaters. Process gas flows through the discharge from outlets located along the circumference of the lower electrode.

CVD is used extensively in depositing SiO₂, silicon nitride (Si₃N₄) and polysilicon. The CVD of SiO₂ does not replace thermally grown SiO₂ which has superior electrical and mechanical properties to CVD oxide. However, CVD oxides are used, instead, to complement thermal oxides and in many cases to form oxide layers that grow much thicker in relatively very short times than thermal oxides. SiO₂ can be deposited by CVD by several methods. It can be deposited from reacting silane and oxygen in an LPCVD reactor at 300 to 500 °C where:



SiO₂ can also be deposited by LPCVD by decomposing tetraethyl orthosilicate (TEOS) (Si(OC₂H₅)₄). TEOS is vaporized from a liquid source. Alternatively, dichlorosilane can be used as follows:



Likewise, Si₃N₄ can be deposited by LPCVD by an intermediate-temperature process or a low-temperature PECVD process. In the LPCVD process, which is the more common process, dichlorosilane and ammonia react according to the reaction:



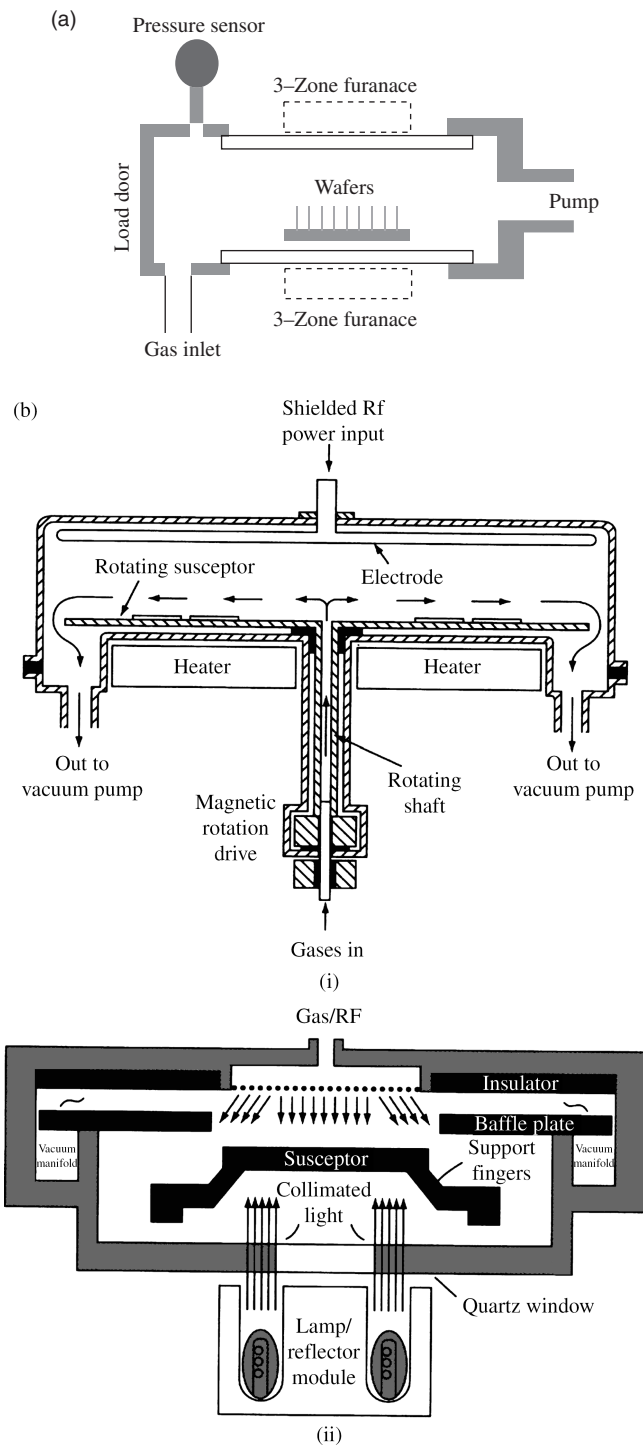


Figure 10.8 (a) Typical layout of (a) an LPCVD reactor; (b) two views of a PECVD reactor.

10.3.4 Polysilicon film deposition

Polysilicon comprises small crystallites of single-crystal silicon, separated by grain boundaries. Polysilicon is often used as a structural material in MEMS. It is also used in MEMS and microelectronics for electrode formation and as a conductor or high-value resistor, depending on its doping level (must be highly doped to increase conductivity). Polysilicon is commonly used for MOSFET gate electrodes since it can form an ohmic contact with Si, its resistivity can be made up to 500–525 $\mu\Omega\text{ cm}$ by doping, and it is easy to pattern.

A low-pressure reactor, such as the one shown in Figure 10.8(a), operated at a temperature of between 600 and 650 $^{\circ}\text{C}$, is used to deposit polysilicon by pyrolyzing silane according to the following reaction:



Most common low-pressure processes used for polysilicon deposition operate at pressures between 0.2 and 1.0 torr using 100% silane.

10.3.5 Deposition of ceramic thin films

Ceramics are another major class of materials widely used for silicon-based MEMS. These materials generally have better hardness and high-temperature strength. Both crystalline as well as non-crystalline materials are used in the context of MEMS. Examples of ceramic-based MEMS include ceramic pressure microsensors for high-temperature pressure measurement [33] and silicon carbide MEMS for harsh environments [34]. In addition to these structural ceramics, functional ceramics such as ZnO, BST and PZT have also been incorporated into MEMS.

Ceramic thin films have been fabricated by conventional methods, such as RF sputtering [35], laser ablation [36], MOCVD [37] and hydrothermal processes [37]. Even though sputtering is widely used for the deposition of thin films, it has the potential for film degradation by neutral and negative-ion bombardment during its growth. This ‘re-sputtering’ can lead to ‘off-stoichiometric’ films and degradation of electrical properties.

Figure 10.9 illustrates the inverted cylindrical magnetron (ICM) RF sputtering gun set-up [38]. This consists of a water-cooled copper cathode which houses a cylindrical target material surrounded by a ring magnet concentric with the target. A stainless steel thermal shield is mounted to shield the magnet from the thermal radiation coming from the heated table. The anode is recessed in the hollow-cathode space. It aids in collecting electrons and negative ions minimizing ‘re-sputtering’ the growing

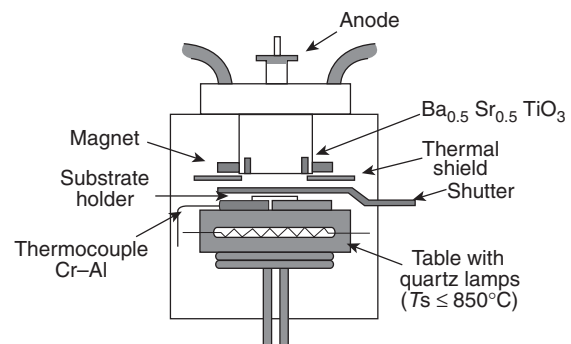


Figure 10.9 Schematic of an ICM sputter gun [38].

film. Outside the deposition chamber, a copper ground wire is attached between the anode and the stainless steel chamber. A DC bias voltage could be applied to the anode to alter the plasma characteristics in the cathode/anode space. The sputter gas enters the cathode region through the space surrounding the table.

Using the above set-up, Cukauskas *et al.* [38] were able to deposit BST films at temperatures ranging from 550 to 800 $^{\circ}\text{C}$. The substrate temperature was maintained by two quartz lamps, a type-K thermocouple and a temperature controller. The films were deposited at 135 W to a film thickness of 7000 Å. The films were cooled to room temperature in 1 atm of oxygen before removing them from the deposition unit. This was then followed by annealing the films in 1 atm of flowing oxygen at a temperature of 780 $^{\circ}\text{C}$ for 8 h in a tube furnace.

10.4 BULK MICROMACHINING FOR SILICON-BASED MEMS

Starting in the early 1960s, bulk micromachining has since matured as the principal silicon micromachining technology. Bulk micromachining is employed to fabricate the majority of commercial devices available today. The term ‘bulk micromachining’ arises from the fact that this type of micromachining is used to realize micro-mechanical structures within the bulk of a single-crystal silicon wafer by selectively removing the wafer material. The microstructures fabricated using bulk micromachining may have thicknesses ranging from sub-microns to the full thickness of a wafer (usually 200 to 500 μm), and lateral dimensions ranging from microns to the full diameter of a wafer (usually 75 to 200 mm).

For bulk-micromachined silicon microstructures, a wafer-bonding technique is necessary for the assembled

MEMS devices. The bulk micromachining technique allows us to selectively remove significant amounts of silicon from a substrate to form membranes on one side of a wafer, a variety of trenches, holes or other structures (Figure 10.3). In recent years, a vertical-walled bulk micromachining techniques known as *single crystal reactive etching and metallization* (SCREAM) which is a combination of anisotropic and isotropic plasma etching, is used [29].

The construction of any complicated mechanical device requires not only the machining of individual components but also the assembly of the components to form a complete set. In micromachining, bonding techniques are used to assemble individually micromachined parts to form a complete structure. For example, wafer bonding, when used in conjunction with micromachining techniques, allows the fabrication of 3-dimensional structures that are thicker than a single wafer. Several processes have been developed for bonding silicon wafers. The most common bonding process is *fusion bonding*. These techniques are described in Section 10.2.5. In the following sections, we will describe the commonly used bulk micromachining processes.

10.4.1 Wet etching for bulk micromachining

Wet chemical etching is widely used in semiconductor processing. It is used for lapping and polishing to give an optically flat and damage-free surface and to remove contamination that results from wafer handling and storing. Most importantly, it is used in the fabrication of discrete devices and integrated circuits of relatively large dimensions to delineate patterns and to open windows in insulating materials. It is to be noted that most of the wet etching processes are isotropic. That is, etch rate is unaffected by crystallographic orientation.

However, some wet etchants are orientation dependent, i.e. have the property of dissolving a given crystal plane of a semiconductor much faster than other planes (see Table 10.4). In diamond and zinc blende lattices, the (111) plane is more closely packed than the (100) plane and, hence, for any given etchant the etch rate is expected to be slower.

A commonly chemical used orientation-dependent etchant for silicon consists of a mixture of KOH in water and isopropyl alcohol. The etch rate is about $2.1 \mu\text{m}/\text{min}$ for the (110) plane, $1.4 \mu\text{m}/\text{min}$ for the (100) plane and only $0.003 \mu\text{m}/\text{min}$ for the (111) plane at 80°C ; therefore, the ratio of the etch rates for the (100) and (110) planes to the (111) plane are very high, at 400:1 and 600:1, respectively.

Table 10.4 Anisotropic etching characteristics of different wet etchants for single-crystalline silicon. Reprinted from Applied Surface Science, vol. 164, R.K. Kupka, F. Bouamrane, C. Cremers, and S. Megert, Microfabrication: LIGA-X and applications, pp. 97–110, Copyright 2000, with permission from Elsevier

Etchant	Temperature ($^\circ\text{C}$)	Etch rate ($\mu\text{m}/\text{h}$)		
		Si (100)	Si (110)	Si (111)
KOH:H ₂ O	80	84	126	0.21
KOH	75	25–42	39–66	0.5
EDP	110	51	57	1.25
N ₂ H ₄ H ₂ O	118	176	99	11
NH ₄ OH	75	24	8	1

10.4.2 Etch-stop techniques

Properties that make etchants indispensable to the micromachining of three-dimensional structures are their selectivity and directionality. As etching processes in polar solvents are fundamentally charge-transport phenomena, the etch rate will depend on the type of dopant and its concentration, and an external bias. Etch processes can therefore be made selective by the use of dopants – heavily doped regions etch slower or are halted electrochemically when observing the sudden rise in current through an etched *n–p* junction.

A region at which wet (or dry) etching tends to slow down (or halt) is called an ‘etch stop’. There are several ways in which an etch-stop region can be created. In the following paragraphs, we discuss such methods by which etch selectivity is achieved.

In the *electrochemical etching* of silicon, a voltage is applied between the silicon wafer (anode) and a counter-electrode (cathode) in the etching solution. The fundamental steps of the etching mechanism are:

- (1) Injection of holes into the semiconductor to raise it to a higher oxidation state, Si⁺.
- (2) Attachment of negatively charged hydroxyl groups (OH⁻) to positively charged Si.
- (3) Reaction of the hydrated silicon with the complexing agent in the solution.
- (4) Dissolution of the reaction products into the etchant solution.

The conventional electrochemical etch-stop technique is an attractive method for fabricating microsensors and

micro-actuators since it has the potential for allowing reproducible fabrication of moderately doped *n*-type silicon microstructures with good thickness control. However, a major limiting factor in the use of this process is the effect of a reverse-bias leakage current in the junction. Since the selectivity between *n*-type and *p*-type silicons in this process is achieved through the current-blocking action of the diode, any leakage in this diode will affect the selectivity. In particular, if the leakage current is very large, it is possible for etching to terminate well before the junction is reached. In some situations, the etching process may fail completely because of this leakage. This effect is well known, and alternative biasing schemes employing three (or four) electrodes have been proposed to minimize this problem. Alternately, dopant-selective techniques that use pulsed anodizing voltages applied to silicon samples immersed in etching solutions can be used [39].

In *bias-dependent etching*, oxidation is promoted by a positive voltage applied to the silicon wafer, which causes an accumulation of holes at the Si–solution interface. Under these conditions, oxidation at the surface proceeds rapidly while the oxide is readily dissolved by the solution. Holes, such as H^+ ions, are transported to the cathode and are released as hydrogen (gas). Excess hole-electron pairs can, in addition, be created at the silicon surface, e.g. by optical excitation, to increase the etch rate.

Silicon membranes are generally fabricated using the etch-stop phenomenon of a thin, heavily boron-doped layer, which can be epitaxially grown or formed by the diffusion or implantation of boron into a lightly doped substrate. This stopping effect is a general property of basic etching solutions such as KOH, NaOH, ethylene diamine pyrocatechol (EDP) and hydrazine (see Table 10.5). Due to the heavy boron-doping, the lattice constant of silicon decreases slightly. This leads to highly strained membranes that often show *slip planes*. They are, however, taut and fairly rugged, even at a few micron thickness and ~ 1 cm diameter. The technique, however, is not suited to stress-sensitive microstructures as this could lead to the movement of structures without an external load.

The main benefits of the high-boron etch stop are the independence of crystal orientation, the smooth surface finish and the possibilities it offers for fabricating released structures with an arbitrary lateral geometry in a single etch step. On the other hand, the high levels of boron required are known to introduce considerable mechanical stress into the material, which may cause buckling or even fracture in a diaphragm or other ‘double-clamped’ structures. Moreover, the introduction of electrical components for sensing purposes into these microstructures, such as the implantation of piezoresistors, is inhibited by the excessive background doping. The latter consideration constitutes an important limitation to the applicability of the high-boron-dose etch stop.

The *pulsed potential anodization* technique is used to selectively etch *n*-type silicon [39]. The difference in the dissolution time of anodic oxide formed on *n*-type and *p*-type silicon samples under identical conditions is used for etch selectivity. However, the difference in dissolution time is believed to be due to a difference in oxidation rates caused by the limited supply of holes in *n*-type samples [39]. This technique is applicable in a wide range of anodizing voltages, etchant compositions and temperatures. It differs from the conventional *p–n* junction etch stop in that the performance of the etch stop does not depend on the rectifying characteristics or quality of a diode. Using this technique, *p*-type microstructures of both low and moderate doping can be fabricated. Hence, the pulsed potential anodization technique opens up the possibility for the creation of fragile microstructures in *p*-type silicon.

The main problems with the conventional electrochemical etch stop and the pulsed potential anodization techniques are related to the etch holders required for contacting the epitaxial layer (and the substrate with several electrodes) and for protecting the ‘epitaxial-side’ of the wafer from the etchant. Any leakage in these holders interferes with proper operation of the etch stop. Moreover, mechanical stress introduced by the holder reduces production yield substantially. The development

Table 10.5 Dopant-dependent etch rates of selected silicon wet etchants. W.C. Tang, “Micromechanical devices at JPL for space exploration,” IEEE Aerospace Applications Conference Proceedings, vol. 1, © 1998 IEEE

Etchant (diluent)	Temperature (°C)	(100) Etch rate ($\mu\text{m}/\text{min}$) for boron doping $\ll 10^{19} \text{ cm}^{-3}$	(100) Etch rate ($\mu\text{m}/\text{min}$) for boron doping $\sim 10^{20} \text{ cm}^{-3}$
EDP (H_2O)	115	0.75	0.015
KOH (H_2O)	85	1.4	0.07
NaOH (H_2O)	65	0.25–1.0	0.025–0.1

of a reliable wafer holder for anisotropic etching with an electrochemical etch stop is not straightforward. The process of making contact to the wafer itself can also be critical and difficult to implement. Therefore a single-step fabrication of released structures with either a conventional electrochemical etch stop or pulsed potential anodization techniques may be troublesome.

An alternative etch-stop technique which does not require any external electrodes (or connections to be made to the wafer) has been recently developed. This new technique is referred to as the *photovoltaic electrochemical etch-stop technique* (PHET) [40]. The PHET approach can be used to produce the majority of structures that can be formed by either the high-boron or the electrochemical etch-stop process [40]. PHET does not require the high impurity concentrations of the boron etch stop and does not require external electrodes or an etch holder as in the conventional electrochemical etch-stop or pulsed anodization techniques. Free-standing *p*-type structures with an arbitrary lateral geometry can be formed in a single etch step. In principle, PHET is to be seen as a two-electrode electrochemical etch stop where the potential and current required for anodic growth of a passivating oxide is not applied externally, but is generated within the silicon itself. The potential essentially consists of two components, being the photovoltage across an illuminated *p–n* junction and the ‘Nernst’ potential of an *n*-Si/metal/etchant solution electrochemical cell.

The *buried oxide process* generates microstructures by means of exploiting the etching characteristics of a buried layer of silicon dioxide. After implanting oxygen into a silicon substrate using suitable ion-implantation techniques, high-temperature annealing causes the oxygen ions to interact with the silicon to form a *buried* layer of silicon dioxide. The remaining thin layer of single-crystal silicon can still support the growth of an epitaxial layer from a few microns to many tens of microns thick. In micromachining, the buried silicon dioxide layer is used as an etch stop. For example, the etch rate of an etchant such as KOH slows down markedly as the etchant reaches the silicon dioxide layer. However, this process has the potential for generating patterned silicon-dioxide-buried layers by appropriately implanting oxygen.

10.4.3 Dry etching for micromachining

As discussed above, bulk micromachining processes using wet chemical etchants, such as EDP, KOH and hydrazine, can yield microstructures on single-crystal silicon (SCS) by ‘undercutting’ the silicon wafer. The

etch stop in these cases can be either crystal-orientation-dependent or dopant-concentration-dependent. However, the type, shape and size of the SCS structures that can be fabricated with the wet chemical etch techniques are severely limited. On the other hand, a dry-etch-based process sequence has been developed to produce suspended, SCS mechanical structures and actuators [41]. This process is known as the SCREAM (single crystal reactive etching and metallization) process. SCREAM uses RIE processes to fabricate released SCS structures with lateral feature sizes down to 250 nm and with arbitrary structure orientations on a silicon wafer. SCREAM includes process options to make integrated, ‘side-drive’ capacitor actuators. A compatible high step-coverage metallization process using metal sputter deposition and isotropic metal dry etch is used to form ‘side-drive’ electrodes. The metallization process complements the silicon RIE processes used to form the ‘movable’ SCS structures.

The SCREAM process can be used to fabricate complex circular, triangular structures in SCS, often with a single mask. These structures can include integrated, high-aspect-ratio and conformable capacitor actuators. The capacitor actuators are used to generate electrostatic forces and so produce micromechanical motion.

10.5 SILICON SURFACE MICROMACHINING

Since the beginning of the 1980s, much interest has been directed towards micromechanical structures fabricated by a technique called *surface micromachining*. The resulting ‘2½-dimensional’ structures are mainly located on the surface of a silicon wafer and exist as a thin film – hence, the ‘half-dimension’. The dimensions of these surface-micromachined structures can be an order of magnitude smaller than bulk-micromachined structures. The main advantage of surface-micromachined structures is their easy integration with IC components, since the same wafer surface can also be processed for the IC elements.

Surface micromachining does not shape the bulk silicon, but instead builds structures on the surface of the silicon by depositing thin films of ‘sacrificial layers’ and ‘structural layers’ and by removing eventually the sacrificial layers to release the mechanical structures (Figure 10.10). The dimensions of these surface-micromachined structures can be several orders of magnitude smaller than bulk-micromachined structures. The prime advantage of surface-micromachined structures is their easy integration with IC components, since the

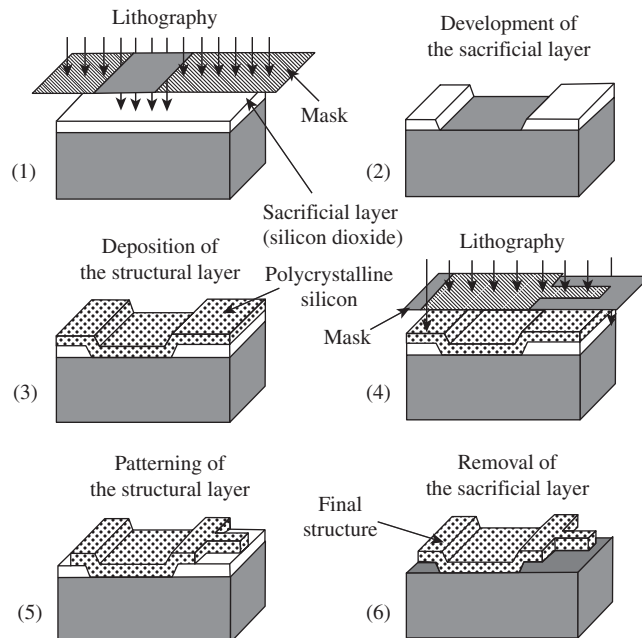


Figure 10.10 Processing steps for a typical micromachining process [23]. Reproduced by permission of Gabor Kiss

wafer is also the ‘working’ one for the IC elements. Surface micromachining can therefore be used to build monolithic MEMS devices.

Surface micromachining could also be performed using dry-etching methods. Plasma etching of the silicon substrate with SF₆/O₂-based and CF₄/H₂-based gas mixtures is advantageous since high selectivities for the photoresist, silicon dioxide and aluminum masks can be achieved. However, when using plasma etching, a large ‘undercut’ of the mask is observed. This is due to the isotropic fluorine-atom-etching of silicon which is known to be high compared with the vertical etch induced by ion bombardment. In contrast, reactive-ion etching of poly-Si using a chlorine/fluorine gas combination produces virtually no ‘undercut’ and almost vertical etch profiles when using a photoresist as a masking material. Thus, rectangular silicon patterns which are up to 30 µm deep can be formed by using chlorine/fluorine plasmas out of poly-Si films and silicon wafer surfaces.

Silicon microstructures fabricated by surface micromachining are usually planar (or two dimensional) structures. Other techniques involving the use of thin-film structural materials released by the removal of an underlying sacrificial layer have helped to extend conventional

surface micromachining into the ‘third dimension’. By connecting polysilicon plates to the substrate and to each other with hinges, 3-D micromechanical structures can be assembled after release. Another approach to 3-D structures have used the conformal deposition of polysilicon and sacrificial oxide films to fill deep trenches previously etched in the silicon substrate.

Sacrificial-layer technology generally uses polycrystalline rather than single-crystal silicon (SCS) as the structural material for the fabrication of microstructures. Low-pressure chemical vapor deposition (LPCVD) of polysilicon is well known in standard IC technologies and has excellent mechanical properties similar to those of SCS. When polycrystalline silicon is used as the structural layer, sacrificial-layer technology normally employs silicon dioxide as the sacrificial material. This sacrificial layer is required during the fabrication process to realize some microstructures but does not constitute any part of the final device.

The key processing steps in sacrificial-layer technology are:

- (1) Deposition and patterning of a sacrificial silicon dioxide layer on the substrate.
- (2) Deposition and definition of a polysilicon film.

- (3) Removal of the sacrificial oxide by lateral etching in hydrofluoric acid (HF), i.e. etching away of the oxide underneath the polysilicon structure.

Here, we refer to polysilicon and silicon dioxide as the structural and sacrificial materials, respectively. Several other material combinations are also used in surface micromachining.

10.5.1 Material systems in sacrificial layer technology

An important consideration in the fabrication of an ideal mechanical microstructure is that it is without any residual mechanical stress, so that the films deposited have no significant residual strain. In particular, doubly supported free-standing structures will buckle in the presence of a relatively modest residual compressive strain in the structural material. By choosing the appropriate deposition conditions and by optimizing the annealing step, an almost strain-free structural material layer can be obtained.

Surface micromachining requires a compatible set of structural materials, sacrificial materials and chemical etchants. The structural materials must possess the physical and chemical properties that are suitable for the desired application. In addition, the structural materials must have appropriate mechanical properties, such as high yield and fracture strengths, minimal creep and fatigue and good wear resistance. The sacrificial materials should also be able to avoid device failure during the fabrication process. Furthermore, they should have good adhesion and a low residual stress in order to eliminate device failure by delamination and/or cracking. The etchants must have excellent etch selectivity and they must be able to etch-off the sacrificial materials without affecting the structural ones. In addition, the etchants must also have appropriate viscosity and surface tension characteristics.

The common IC-compatible materials used in surface micromachining are as follows. (1) Poly-Si/silicon dioxide – LPCVD-deposited poly-Si as the structural material and LPCVD-deposited oxide as the sacrificial material. The oxide is readily dissolved in HF solution without the poly-Si being affected. Together with this material system, silicon nitride is often used for electrical insulation. (2) Polyimide/aluminum – in this case, polyimide is the structural material and aluminum is the sacrificial material. Acid-based etchants are used to dissolve the aluminum sacrificial layer. (3) Silicon nitride/poly-Si – silicon nitride is used as the structural material, whereas poly-Si is the sacrificial material. For this material system,

silicon anisotropic etchants, such as KOH and EDP, are used to dissolve the poly-Si. (4) Tungsten/silicon dioxide – CVD-deposited tungsten is used as the structural material with oxide as the sacrificial material. HF solution is used to remove the sacrificial oxide. Other IC-compatible materials, such as silicon carbide, ‘diamond-like’ carbon, zinc oxide and gold, are also used.

10.5.1.1 Polycrystalline silicon/silicon dioxide

The poly-silicon/silicon dioxide material system is the most common one used in the silicon-surface micromachining of MEMS. This uses poly-silicon deposited by LPCVD as the structural material and a thermally grown (or LPCVD) oxide as the sacrificial material. The oxide is readily dissolved in HF solution, without affecting the poly-silicon. Silicon nitride is often used, together with this material system for electrical insulation. The advantages of this material system include the following:

- (1) Both poly-silicon and silicon dioxide are used in IC processing and, therefore, their deposition technologies are readily available.
- (2) Poly-silicon has excellent mechanical properties and can be doped for various electrical applications. Doping not only modifies the electrical properties but can also modify the mechanical properties of poly-silicon. For example, the maximum ‘mechanically-sound’ length of a free-standing beam is significantly larger for a phosphorous-doped compared with undoped poly-silicon. However, in most cases the maximum length attainable is limited by the tendency of the beam to stick to the substrate.
- (3) The oxide can be thermally grown and deposited by CVD over a wide range of temperatures (from about 200 to 1200 °C) which is very useful for various processing requirements. However, the quality of oxide will vary with the deposition temperature.
- (4) The material system is compatible with IC processing. Both poly-silicon and silicon dioxide are standard materials for IC devices. This commonality makes them highly desirable in sacrificial-layer-technology applications which demand integrated electronics.

10.5.1.2 Polyimide/aluminum

In this second material system, the polymer ‘polyimide’ is used for the structural material while aluminum is used for the sacrificial material. Acid-based aluminum etchants are used to dissolve the aluminum sacrificial layer.

Table 10.6 Comparison of bulk-and surface-micromachining processes for MEMS fabrication.

Aspect	Bulk micromachining	Surface micromachining
Maturity	Well established	Relatively new
Ruggedness	Yes – structures can withstand vibration and shock	Less rugged
Die area	Large mass/area (suitable for accelerometers, increases cost)	Small mass/area (reduced sensitivity, reduces cost)
IC compatibility	Not fully integrated	IC compatible
Structural geometry	Limited	Wide range possible
Materials	Well characterized	Relatively new

The three main advantages of this material system are:

- (1) Polyimide has a small elastic modulus which is ~ 50 times smaller than that of polycrystalline silicon.
- (2) Polyimide can take large strains before fracture.
- (3) Both polyimide and aluminum can be prepared at relatively low temperatures ($< 400^\circ\text{C}$).
- (4) However, the main disadvantage of this material system lies with polyimide in that it has unfavorable viscoelastic characteristics (i.e. it tends to creep) and so such devices may exhibit considerable parametric drift.

10.5.1.3 Other material systems

In the third material system of silicon nitride/poly-Si, silicon nitride is used as the structural material and poly-Si as the sacrificial material. For this material system, silicon anisotropic etchants such as KOH and EDP are used to dissolve the poly-Si.

In the fourth material system of tungsten/oxide, tungsten deposited by CVD is used as the structural material with the oxide as the sacrificial material. Here again, an HF solution is used to remove the sacrificial oxide.

Similarly, silicon nitride is employed as the structural material with aluminum as the sacrificial layer instead of poly-Si.

10.6 PROCESSING BY BOTH BULK AND SURFACE MICROMACHINING

Many MEMS devices are fabricated by either bulk micromachining or surface micromachining, as described in the previous sections. Their relative merits and demerits are compared in Table 10.6. It is possible to combine

advantages of both of these approaches by following a ‘mixed route’ for fabricating MEMS. The process flow for a ‘microgripper’ fabricated with this mixed approach is shown in Figure 10.11. In the first step, with thermally grown silicon dioxide as a mask, boron is diffused into the wafer at 1125°C . The masking SiO_2 and borosilicate glass (BSG) grown during this diffusion are removed. Then, a $2\ \mu\text{m}$ thick layer of phosphosilicate glass (PSG) and a $2.5\ \mu\text{m}$ thick polysilicon layer are deposited by LPCVD. This polysilicon layer is patterned by RIE in a CCl_4 plasma. Polysilicon at the back side of the wafer is later removed. Then, the PSG film is deposited in three steps to reach a thickness of $6\ \mu\text{m}$. This is used for diffusing phosphorous into the polysilicon layer (by annealing at 1000°C) and to protect it while bulk micromachining. The alignment window in Figure 10.11(c) is used for ‘front-to-back’ reference. Break lines are patterned on the PSG around the polysilicon gripper area to prevent cracks. The PSG film on the back side is also patterned. Unwanted silicon from the back side is removed by etching in EDP (bulk micromachining). On the front side, the EDP causes undercut etching of channels beneath the PSG break line, eventually connecting to the open space caused from the back side etch. The PSG film (sacrificial layer) is then removed from both the top and bottom. Thus, the structure on the top side of the wafer is thought of as being fabricated by surface micromachining.

10.7 LIGA PROCESS

Even though miniaturization is immensely increased by silicon surface micromachining, the small sizes/masses created are often insufficient for viable sensors and, particularly, actuators. The problem is most acute in

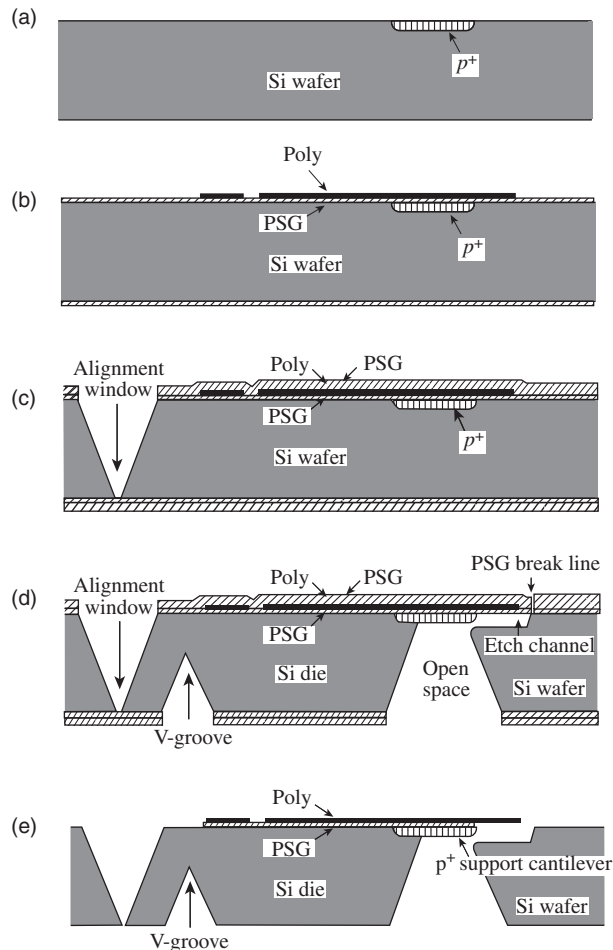


Figure 10.11 Process flow for MEMS ‘microgripper’ fabricated with bulk and surface micromachining. C.-J. Kim, A.P. Pisano, and R.S. Muller, Silicon-Processed overhanging microgripper, J. Microelectromechanical Systems, Vol. 1, © 1992 IEEE

capacitive mechanical microsensors and especially capacitively driven micro-actuators because of the low coupling capacitances. Deep etching techniques, such as LIGA, have been developed in order to address this problem but are difficult to realize for silicon.

‘LIGA’ is a German acronym for Lithographie, Galvanoformung, Abformung (lithography, galvanoforming, molding). This versatile technique was developed by the Research Center in Karlsruhe in Germany in the early 1980s using X-ray lithography for mask exposure, galvanoforming to form the metallic parts and molding to produce micro-parts with plastics, metals, ceramics, or their combinations [42,43]. A schematic diagram of the LIGA process flow is shown in Figure 10.12. The X-ray

LIGA relies on synchrotron radiation to obtain necessary X-ray fluxes and uses X-ray proximity printing. Inherent advantages are its extreme precision, depth of field and very low intrinsic surface roughness [44]. With the LIGA process, the microstructure heights can be up to hundreds of microns to several millimeters, while the lateral resolution is kept at the submicron level due to the advanced X-ray lithography. Various materials can be incorporated into the LIGA process, allowing electrical, magnetic, piezoelectric, optical and insulating properties of sensors and actuators with a high-aspect ratio, which are not possible to make with the silicon-based processes. In addition, by combining the sacrificial layer technique and the LIGA process, advanced MEMS with moveable microstructures

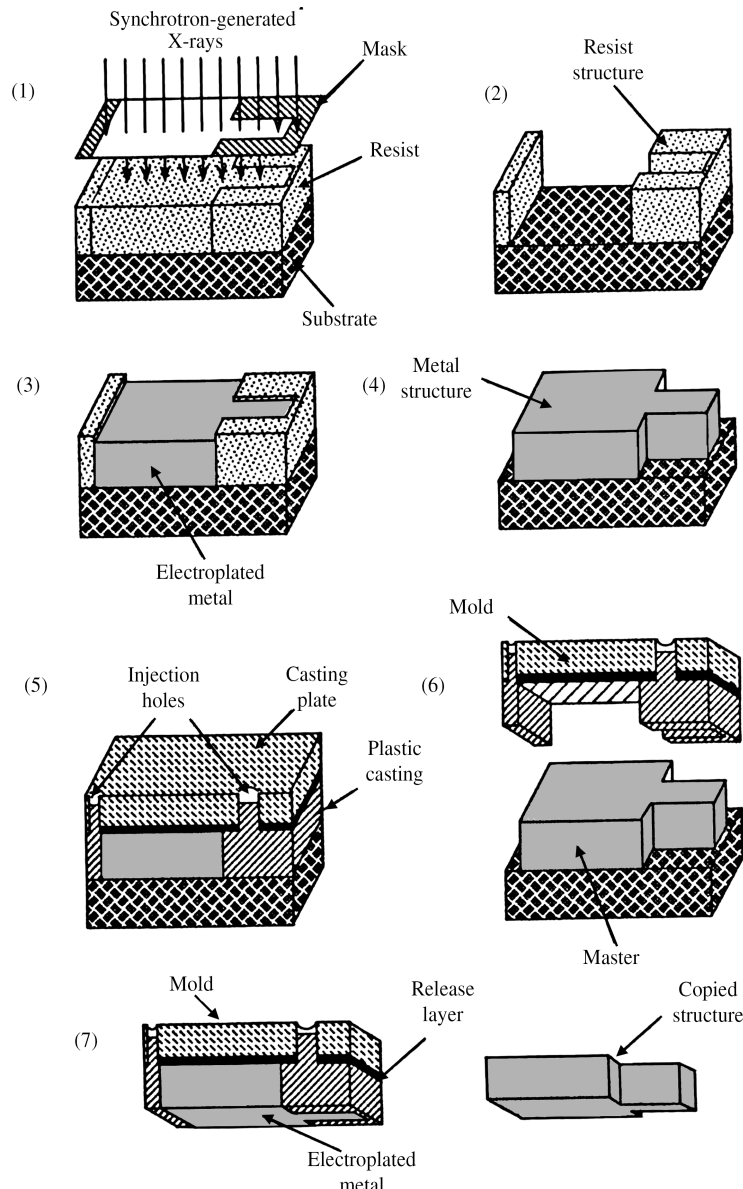


Figure 10.12 Schematic of the LIGA process [23]. Reproduced by permission of Gabor Kiss

can be built (Figure 10.13). However, the high production cost of the LIGA process, due to the fact that it is not easy to access the X-ray source, limits the application of LIGA. Another disadvantage of the LIGA process relies on the fact that structures fabricated using LIGA are not truly three-dimensional, because the third dimension is always in a ‘straight’ feature. The quality of fabricated structures

often depends on secondary effects during exposure and effects like resist adhesion. A similar technique, UV-LIGA, relying on thick UV resists, is a useful fabrication process, but with less precision. Modulating the spectral properties of synchrotron radiation, 3-D components with different size regimes can be fabricated using X-ray lithography [44]. Considerations for these cases are shown in Table 10.7.

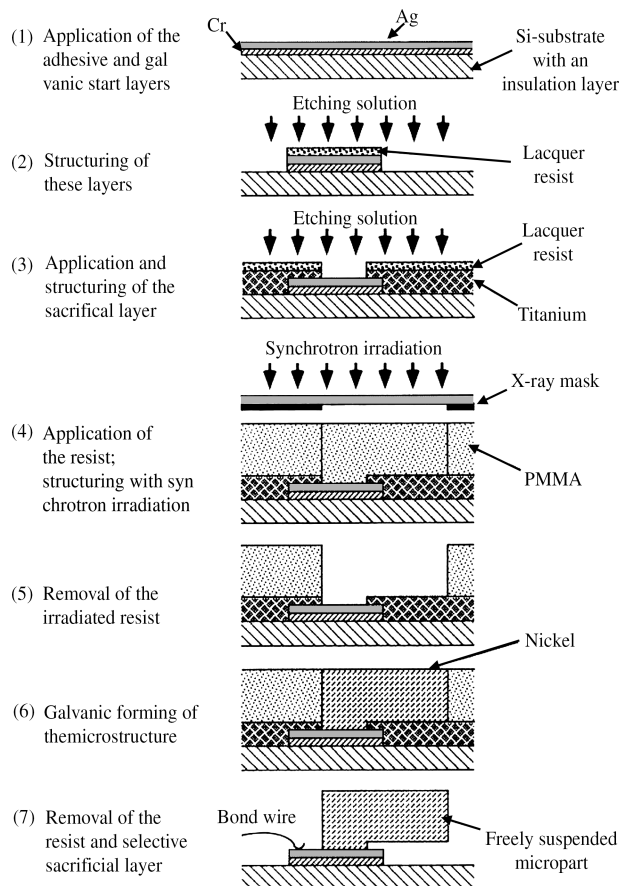


Figure 10.13 Combination of LIGA process and sacrificial layer process [45]. A. Rogner, et al., “LIGA based flexible microstructures for fiber chip coupling,” J. Micromech. Microeng., vol. 1, 1991, © IOP

Table 10.7 X-ray lithography for various feature sizes [44]. Reprinted from Applied Surface Science, vol. 164, R.K. Kupta, F. Bouamrane, C. Cremers, and S. Megtert, Microfabrication: LIGA-X and applications, pp. 97–110, Copyright 2000, with permission from Elsevier

Feature	Low-aspect-ratio nanostructures	High-aspect-ratio nanostructures	High-aspect-ratio microstructures	High-aspect-ratio ‘cm structures’
Photon energy range	500 eV–2 keV	2–5 keV	4–15 keV	> 15 keV
Exposeable resist (PMMA) thickness	< 5 μm	< 50 μm	< 1 mm	< 2 cm
Membrane thickness	SiC, 2 μm; diamond, 5 μm Be, 20 μm	Be, 50 μm; D263, 5 μm	Be, 300 μm; D263, 15 μm	Be, 500 μm; D263, 50 μm
Absorber (Au, W) thickness	100–500 nm	500 nm to 10 μm	10–20 μm	20–50 μm
Proximity contrast	<10 dB	10–15 dB	15–20 dB	>20 dB
Development time	s–min	min–h	h–days	days
Application	Rapid mass production of nanostructures	2-D photonic crystals	Micromechanics, micro-optics	—

Table 10.8 Various technologies used in MEMS fabrication [46]. W.C. Tang, ‘Micromechanical devices at JPL for space exploration,’ IEEE Aerospace Applications Conference Proceedings, vol. 1, © 1998 IEEE

Feature	Bulk (100) wafer	Surface	LIGA
Maximum structure thickness	Wafer thickness	< 50 µm	< 500 µm
Planar geometry	Rectangular	Unrestricted	Unrestricted
Minimum planar feature size	1.4 × depth	1 µm	3 µm
Side-wall features	54.74° slope	Limited by dry etch	0.2 µm runout over 400 µm
Surface and edge definitions	Excellent	Mostly adequate	Very good
Material properties	Very well controlled	Mostly adequate	Well controlled
Integration with electronics	Demonstrated	Demonstrated	Difficult
Capital investments and cost	Low	Medium	High

LIGA-based fabrication procedures of various systems for micromechanics (such as micromotors, microsensors, spinnerets, etc.) and micro-optics, micro-hydrodynamics, microbiology, medicine, biology and chemistry (microchemical reactors) are under various stages of development. A comparison of LIGA with the bulk and surface micromachining technologies used in MEMS is given in Table 10.8 [46].

REFERENCES

- H. Fujita, ‘Future of actuators and microsystems’, *Sensors and Actuators*, **A56**, 105–111 (1996).
- H. Fujita, ‘Microactuators and micromachines’, *Proceedings of the IEEE*, **86**, 1721–1732 (1998).
- G.T.A. Kovacs, N.I. Maluf and K.E. Petersen, ‘Bulk micromachining of silicon’, *Proceedings of the IEEE*, **86**, 1536–1551 (1998).
- J.M. Bustillo, R.T. Howe and R.S. Muller, ‘Surface micromachining for microelectromechanical systems’, *Proceedings of the IEEE*, **86**, 1552–1574 (1998).
- H. Guckel, ‘High-aspect-ratio micromachining via deep X-ray lithography’, *Proceedings of the IEEE*, **86**, 1586–1593 (1998).
- Y. Xia and G.M. Whitesides, ‘Soft lithography’, *Angewandte Chemie, International Edition*, **37**, 550–575 (1998).
- V.K. Varadan and V.V. Varadan, ‘Three dimensional polymeric and ceramic MEMS and their applications’, *Proceedings of SPIE*, **2722**, 156–164 (1996).
- K. Ikuta and K. Hirowatari, ‘Real three dimensional micro-fabrication using stereo lithography and metal molding’, in *Proceedings of IEEE MEMS’93*, IEEE, Piscataway, NJ, USA, pp. 42–47, (1993).
- T. Katagi and N. Nakajima, ‘Photoforming applied to fine machining’, in *Proceedings of IEEE MEMS’93*, IEEE, Piscataway, NJ, USA, pp. 173–178, (1993).
- C.S. Taylor, P. Cherkas, H. Hampton, J.J. Frantzen, B.O. Shah, W.B. Tiffany, L. Nanis, P. Booker, A. Salahieh and R. Hansen, ‘A spatial forming – a three dimensional printing process’, in *Proceedings of IEEE MEMS’94*, IEEE, Piscataway, NJ, USA, pp. 203–208 (1994).
- G. Thornell and S. Johansson, ‘Microprocessing at the fingertips’, *Journal of Micromechanical and Microengineering*, **8**, 251–262 (1998).
- S. Middelhoek and S.A. Audet, *Silicon Sensors*, Academic Press, London, UK (1989).
- K.E. Peterson, ‘Silicon as a mechanical material’, *Proceedings of the IEEE*, **70**, 420–457 (1982).
- J. Bryzek, K. Peterson and W. McCulley, ‘Micromachines on the march’, *IEEE Spectrum*, **31**(5), 20–31 (May 1994).
- L.-S. Fan, Y.-C Tai and R.S. Muller, ‘Integrated movable micromechanical structures for sensors and actuators’, *IEEE Transactions: Electron Devices*, **35**, 724–730 (1988).
- V.K. Varadan, X. Jiang and V.V. Varadan, *Microstereolithography and other Fabrication Techniques for 3D MEMS*, John Wiley & Sons, Ltd, London, UK (2001).
- C. Vieu, F. Carcenac, A. Pépin, Y. Chen, M. Mejias, A. Lebib, L. Manin-Ferlazzo, L. Couraud and H. Launois, ‘Electron beam lithography: resolution limits and applications’, *Applied Surface Science*, **164**, 111–117 (2000).
- S. Gwo, ‘Scanning probe oxidation of Si₃N₄ masks for nanoscale lithography, micromachining and selective epitaxial growth on silicon’, *Journal of Physics and Chemistry of Solids*, **62**, 1673–1687 (2001).
- S.M. Sze, *Physics of Semiconductor Devices*, John Wiley & Sons, Inc., New York, NJ, USA (1981).
- H. Seidel, ‘The mechanism of anisotropic silicon etching and its relevance for micromachining’, in *Proceedings of the International Conference on Solid-State Sensors and Actuators*, Institute of Electrical Engineers of Japan Tokyo, Japan, pp. 120–125 (1987).
- K.W. Shaw, Z.L. Zhang and N.C. MacDonald, ‘SCREAM: a single mask, single-crystal silicon, reactive ion etching

- process for microelectromechanical structures', *Sensors and Actuators*, **A40**, 63–70 (1994).
22. G.T.A. Kovacs, N.I. Maluf and K.E. Petersen, 'Bulk micromachining of silicon', *Proceedings of the IEEE*, **86**, 1536–1551 (1998).
 23. G. Stix, 'Trends in micromechanics: micron machinations', *Scientific American*, 72–80 (November 1992).
 24. M. Madou, *Fundamentals of Microfabrication*, CRC Press, Boca Raton, FL, USA (1997).
 25. J.B. Lasky, 'Wafer bonding for silicon-on-insulator technologies', *Applied Physics Letters*, **48**, 78–80, (1986).
 26. H. Ohashi, J. Ohura, T. Tsukakoshi and M. Simbo, 'Improved dielectrically isolated device integration by silicon-wafer direct bonding (SDB) technique', in *International Electron Devices Meeting Technical Digest IEEE*, New York, NY, USA, pp. 210–213 (1986).
 27. U. Apel, H.G. Graf, C. Harendt, B. Hofflinger and T. Ifstrom, 'A 100-V lateral DMOS transistor with a 0.3 micron channel in a 1 micron silicon-film-on-insulator-on silicon', *IEEE Transactions: Electron Devices*, **38**, 1655–1659 (1991).
 28. C. Harendt, H.G. Graf, B. Hollinger and E. Penteker, 'Silicon direct bonding for sensor applications – characterization of the bond quality', *Sensors and Actuators*, **A25**, 87–92 (1991).
 29. W.H. Ko, J.T. Suminto and G.J. Yeh, 'Bonding techniques for microsensors', *Studies in Electrical and Electronic Engineering* **20**, 41–61 (1985).
 30. J.W. Gardner, V.K. Varadan and O. Awadelkarim, *Micro-sensors, MEMS and Smart Devices*, John Wiley & Sons, Ltd, London, UK (2001).
 31. M. Ohring, *The Materials Science of Thin Films*, Academic Press, San Diego, CA, USA (1991).
 32. H.O. Pierson, *Handbook of Chemical Vapor Deposition (CVD): Principles, Technology and Applications*, 2nd Edn, Noyles Publications, New York, NY, USA (1999).
 33. M. Jennifer and M.G. Allen, 'Wireless micromachined ceramic pressure sensors', in *Proceedings of the IEEE MEMS' 99*, IEEE, Piscataway, NJ, USA, pp. 511–516 (1999).
 34. L.C. Chin, V.V. Varadan and V.K. Varadan, 'Hybrid finite element formulation for periodic piezoelectric arrays subjected to fluid loading', *International Journal of Numerical Methods in Engineering*, **37**, 2987–3003 (1994).
 35. J.H. Won, H. Paek, Y.S. Huang, K.K. Kim and Y.S. Cho, 'Phase formation and characteristics of RF sputtering of barium strontium titanate thin films on various bottom layers', *Journal of Materials Science Materials in Electronics*, **6**, 161–164 (1995).
 36. X.X. Xi, H.-C. Li, W.Si, A.A. Sirenko, I.A. Akimou, J.R. Fox, A.M. Clark and J. Hao, 'Oxide thin films for Tunable microwave devices', *Journal of Electroceramics*, **4**, 393–405 (2000).
 37. I. Levin, R.D. Leapman and D.L. Kaiser, 'Microstructure and chemistry of nonstoichiometric $(\text{Ba},\text{Sr})\text{TiO}_3$ thin films deposited by metalorganic chemical vapor deposition', *Journal of Materials Research*, **15**, 1433–1436 (2000).
 38. E.J. Cukauskas, S.W. Kirchofer and J.M. Pond, 'Low-loss $\text{Ba}_{0.5}\text{Sr}_{0.5}\text{TiO}_3$ thin films by inverted magnetron sputtering', *Journal of Applied Physics*, **88**, 2830–2835 (2000).
 39. S.S. Wang, V.M. McNeil and M.A. Schmidt, 'An etch-stop utilizing selective etching of *n*-type silicon by pulsed potential anodization', *Journal of Microelectromechanical Systems*, **1**, 187–192, (1992).
 40. E. Peeters, D. Lapadatu, R. Puers and W. Sansen, 'PHET, an electrodeless photovoltaic electrochemical etch-stop technique', *Journal of Microelectromechanical Systems*, **3**, 113–123 (1994).
 41. Z.L. Zhang and N.C. McDonald, 'An RIE process for submicron, silicon electromechanical structures', *Journal Micromechanical and Microengineering*, **2**, 31–38 (1992).
 42. H. Guckel, 'High-aspect-ratio micromachining via deep X-ray lithography', *Proceedings of the IEEE*, **86**, 1586–1593 (1998).
 43. J. Mohr, P. Bley, C. Burabaum, W. Menz and U. Wallarabe, 'Fabrication of microsensor and microactuator elements by the LIGA process', in *Transducers'91, Proceedings of the International Conference in Solid-State Sensors and Actuators*, IEEE Electron Devices Society, IEEE, New York, NY, USA, pp. 607–609 (1991).
 44. R.K. Kupka, F. Bouamrane, C. Cremers and S. Megert, 'Microfabrication: LIGA-X and applications', *Applied Surface Science*, **164**, 97–110 (2000).
 45. A. Rogner, W. Ehrfeld, D. Manchmeyer, P. Bley, C. Burabaum and J. Mohr, 'LIGA based flexible microstructures for fiber chip coupling', *Journal of Micromechanical and Microengineering*, **1**, 167–170, (1991).
 46. W.C. Tang, 'Micromechanical devices at JPL for space exploration', in *IEEE Aerospace Applications Conference Proceedings*, Vol. 1, IEEE, Piscataway, NJ, USA, pp. 461–470 (1998).

11

Polymeric MEMS Fabrication Techniques

11.1 INTRODUCTION

The advancement of silicon-based micro electromechanical systems (MEMS) closely follows developments in silicon semiconductor processing technology. Various processing approaches have already been established for the integration of silicon-based MEMS with standard CMOS processing. For precision devices, and for devices requiring integrated electronics, silicon is presently unrivaled. However, it is not necessarily the best material for all applications. For example, silicon is brittle, it is only available in specific shapes (wafers), it is limited to 2-D or very limited 3-D structures, it is incompatible with many chemical and biological substances and fabrication requires sophisticated, expensive equipment operated in a clean-room environment. These often limit the low-cost potential of silicon-based MEMS. Polymer-based MEMS are gaining momentum rapidly due to their potential for conformability and other special characteristics not available with silicon. In general, polymer-based devices may not be as small or as complex as those with silicon. However, polymers are flexible, chemically and biologically compatible, available in many varieties and can be fabricated in truly 3-D shapes. Most of these materials and their fabrication methods are inexpensive.

Polymer MEMS are particularly advantageous in moderate-performance devices which are low cost or disposable. Many silicon devices are packaged inside polymers. On the other hand, polymer MEMS can be ‘self-packaged’. Active polymer components can take advantage of several functional polymers to increase their functionality. MEMS can definitely benefit from the fairly large polymer industry. While conventional integrated circuits cannot be made in polymers, electronic circuits based on organic thin-film transistors (TFTs)

are feasible. The technology of organic TFTs is nearing its maturity, and is finding several applications in systems requiring large coverage area, structural flexibility and low cost. These noticeable advantages are also common for polymer MEMS. Although the existing technology of organic TFTs cannot rival the well-established silicon semiconductor technology, especially in terms of speed, they are still useful in displays, several high-volume, low-performance, disposable devices and sensors.

Polymers are very large molecules (macromolecules) made up of a number of small molecules. The small molecules that connect with each other to build up the polymer are referred to as monomers, and the reaction by which they connect together is called polymerization. Two types of polymers are employed for micromachining polymeric MEMS devices – structural polymers and sacrificial polymers. The structural polymer is usually a UV-curable polymer with urethane acrylate, epoxy acrylate or acryloxy silane as the main ingredient. Its low viscosity allows easy processing through automatic equipment or manual methods without the addition of solvents or heat to reduce the viscosity. It also complies with all VOC regulations. It has excellent flexibility and resistance to fungus, solvents, water and other chemicals. Other physical, chemical, mechanical and thermal properties are given in Table 11.1 [1]. This structural polymer may be used as a backbone structure for building the multifunctional polymer described below.

For 3-D MEMS devices, the polymers need to have conductive and possibly piezoelectric or ferroelectric properties. In addition, for these polymers to be used for polymeric MEMS, they should have strong interfacial adhesion between the functional polymer and conducting polymer layers, elastic moduli to support the deformation initiated by MEMS devices, excellent overall dimensional stability (allowing local mobility) and long-term

Table 11.1 General properties of polymers used in MEMS.

<i>Physical properties</i>	
Adhesion (#600 ‘Cellotape’)	Excellent
Clarity	Transparent
Flammability, ASTM D635	Self-extinguishing
Flexibility	Good
Weather resistance	Excellent
<i>Chemical properties</i>	
Fungus resistance, ASTM G21	Excellent
Resistance to chemicals	Excellent
Resistance to solvents	Excellent
Resistance to water	Excellent
<i>Thermal properties</i>	
Continuous operating range (°C)	65–125
Decomposition temperature (°C)	242
<i>Mechanical properties</i>	
Tensile strength (psi), ASTM D 683	3454
Percentage elongation, ASTM D 683	5.2
<i>Dielectric properties</i>	
Dielectric permittivity (200–1000 MHz)	1.9–2.0
Loss tangent (200–1000 MHz)	0.023–0.05

environmental stability. In addition, their processes should help attachment of nanoceramics and/or conductive phases and formation of a uniform coating layer. Furthermore, many of these polymers provide a large strain under an electric field and thus can be used as actuators for MEMS-based devices such as micro pumps.

The polymer processing techniques include photopolymerization, electrochemical polymerization and vacuum polymerization, either stimulated by electron bombardment or initiated by ultraviolet irradiation or microwave-assisted polymerization. These methods are also widely used for processing and curing thin and thick polymer films on silicon-based electronic components.

Several polymeric materials useful in MEMS have already been discussed in Chapter 2. It has been mentioned that UV-radiation curing has significant advantages in the context of fabricating MEMS devices. In this

chapter, we discuss the technologies involved in such fabrication.

Stereolithography has evolved as a viable technique for rapid prototyping used in several industries. Micro-stereolithography is a natural extension of this for fabricating objects at a smaller scale. Another common technique for fabricating three-dimensional polymer structures is by molding. Microstereolithography and micromolding can be extended to fabricate ceramic and metallic structures by starting with a mixture of their powders in a suitable polymer matrix. Special techniques such as electroplating can also be used to fabricate 3-D metallic structures. Fabrication techniques for 3-D structures with both polymers and metals are discussed next. The last section in this chapter addresses combined architectures where silicon-based and polymer-based techniques are combined for increased flexibility.

11.2 MICROSEREOEOLITHOGRAPHY

Several new manufacturing technologies that build devices ‘layer-by-layer’ have emerged recently. Using these technologies, the time for fabricating these devices of virtually any complexity has become short, measurable in hours rather than in days, weeks or months. These rapid prototyping (RP) technologies consist of various manufacturing processes by which a solid physical model of a device is fabricated directly from its 3-D CAD model, without the need for any special tooling. This CAD model is generated by 3-D CAD software programs, scan or model data created by 3-D digitizing systems. An important difference between RP and traditional micromachining techniques is that here devices are built by adding a material (e.g. ‘layer-by-layer’) instead of removing it.

11.2.1 Overview of stereolithography

Stereolithography (SL) is the best known rapid prototyping system. SL was introduced in the early 1980s by teams around the world [2–4], as a three-dimensional manufacturing process based on photopolymerization, where a laser beam is directed onto the surface of a optically curable liquid plastic (resin) to produce solid objects. The stereolithography process begins with the generation of a three-dimensional CAD model of the desired object, followed by slicing this model into a series of closely spaced horizontal planes representing the two-dimensional cross-sections of the 3-D object, each at a slightly different z -coordinate. All of these 2-D models are next translated into numerical

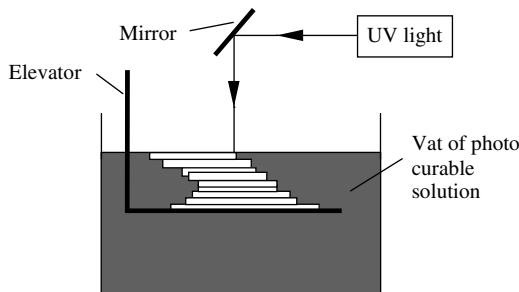


Figure 11.1 Principle of Stereolithography.

control codes and merged together into a final ‘build file’ to control the laser beam scanning and z -axis movement. The desired object is then built from a UV-curable resin in a layer-by-layer additive fashion (Figure 11.1).

SL is a photopolymerization process, linking small molecules (monomers) into larger molecules (polymer). Most SL systems utilize the principle of UV-radiation curing of polymers. Different photopolymers based on free-radical photopolymerization and cationic photopolymerization are normally used in SL prototyping. In general, photopolymerization is a process initiated by the photons generated by UV light leading to either breaking of the monomer double bonds or ring opening (so-called ‘reactive species’), resulting in chain propagation and the cross-linked polymer chain is finally formed when the chain propagation is terminated.

The generalized molecular structures of three major photopolymer systems, namely monofunctional acrylate, epoxy and vinyl ether, are shown in Figure 11.2. The selection of the photopolymer for a particular SL fabrication process depends on the requirements for dimensional accuracy and mechanical properties of each individual photopolymer formulation.

Three-dimensional modeling for the prototypes is done with CAD software on a PC or workstation. The design model and the support data are converted to a STL format through a specific interface [5]. STL files comprise a mesh of connected triangles, representing the 3-D object. These triangle categories determine how the vectors are generated to represent the surfaces to build the part. Vectors are very small lines which are traced by the laser to fabricate polymer objects [6].

After necessary corrections to the model, the designed object is then sliced into a number of layers consisting of cross-sections of a 3-D object (slice files or SLI files). The slicing layer thickness may be selected from consideration of the ‘stair-casing’ effect. When these triangles are sliced, three types of vectors are created to define

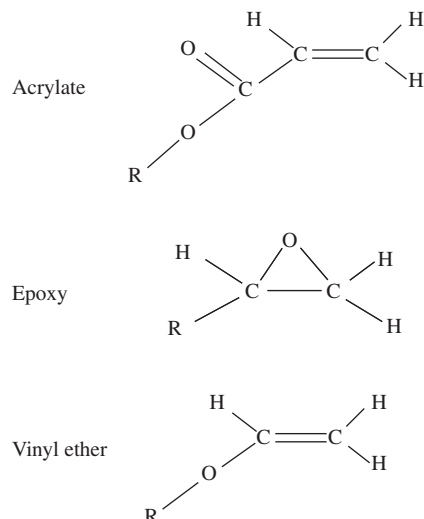


Figure 11.2 General structures of monofunctional acrylate, epoxy, and vinyl ether monomers [5].

the surface boundaries and internal structure on a layer-by-layer basis – layer borders, cross-hatches and skin fill. The cross-hatch vectors in the internal grid structures are created to strengthen the walls and maintain structure integrity. The skin-filling vectors, usually a series of closely located parallel vectors, define the horizontal surfaces.

All slice files (support and object files) are then merged to generate SLA format data in the form of four files (layer, vector, range and parameter files). The layer file defines the types of vector blocks in each layer. The vector file contains vector data used to build each layer and the range file contains user-specified ranges and parameters for fabrication. The parameter file has the control for global part building. The numerical control (NC) codes for controlling the light scanning and elevator movement are included in these files. Parameters, such as laser intensity and scanning speed, should also be selected before executing these NC codes.

SL systems have components with CAD design and layer preparation functions and a laser scanning or imaging system. A typical SL system is shown schematically in Figure 11.3. The imaging system for SL includes a light source (laser or lamp) and beam delivery and focusing elements (Figure 11.3). The laser or lamps must be appropriate for the resin used. Wavelength, output beam shape and available power are important characteristics. Helium–cadmium (He–Cd) and argon lasers are preferred in most SL systems due to the availability of appropriate wavelengths. The key advantages of He–Cd lasers are

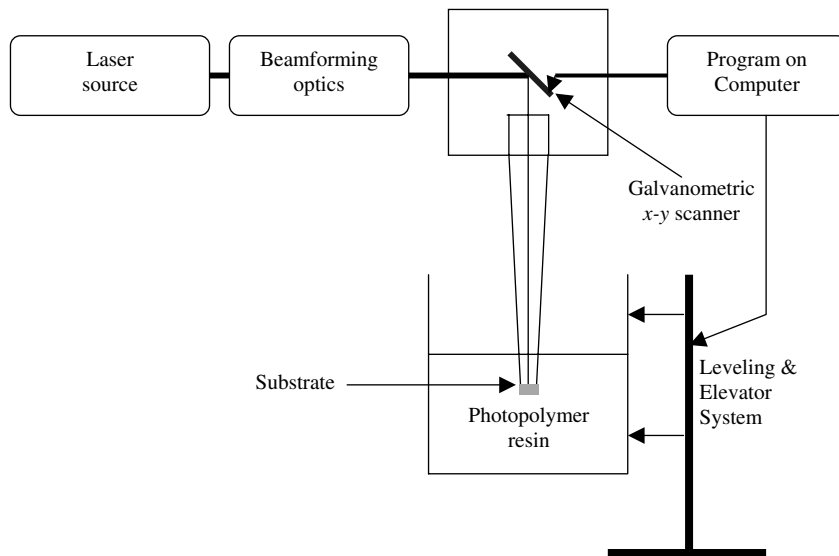


Figure 11.3 Block schematic of a typical stereolithography system [5].

low power consumption, long lifetime and low installation and operation costs. One disadvantage of this is the low output power. At present, He–Cd lasers with output powers of 50 to 100 mW are available at 325 nm. In contrast, argon lasers with high UV output powers (over 1 W) at 351 and 364 nm are available. However, disadvantages of argon-laser-based SL systems include higher power consumption, shorter lifetimes and higher installation and operating costs.

Beam-delivery elements are used to limit the laser beam path, to keep the overall size compact and to provide an appropriately sized laser spot on the surface of the resin. A typical SL system may employ two orthogonally mounted, servo-controlled, galvanometer-driven mirrors to direct the laser beams onto the surface of the vat. A focused beam with a small-beam-spot size is obtained when the beam passes through a focusing objective and shoots onto the resin surface. An optical shutter is usually used to control the beam ‘on/off’ which functions according to the build files. Mechanical shutters requiring about 1 ms to change the state have been replaced with an acoustic optical modulator with a typical response time of 1 μ s, allowing faster and more precise fabrication.

11.2.2 Introduction to microstereolithography

Microstereolithography (MSL) is a method derived from conventional stereolithography and works on similar principles, but in much smaller dimensions. MSL (also

called ‘micro-photoforming’) was introduced in 1993 to fabricate high-aspect-ratio and complex 3-D microstructures [7,8]. In contrast to conventional subtractive micromachining, microstereolithography is an additive process, which enables fabrication of high-aspect-ratio microstructures with novel smart materials. MSL is compatible in principle with silicon processes and batch fabrication [9,10].

In MSL, a UV laser beam is focused to a spot size of about 1 to 2 μ m to solidify a thin layer of about 1 to 10 μ m thickness. Submicron resolution of the x - y - z translation stages and a very fine UV beam spot enable precise fabrication of complex 3-D microstructures using MSL. Unlike SL, MSL usually does not need supports during the fabrication because the solidified polymer is strong enough to support its own weight and the floatation force can support free-standing polymer microstructures [7]. Monomers used in MSL and SL are both UV-curable systems, but their viscosity requirements are different. In MSL, the viscosity of the monomers should be kept low to ensure a good layer recoating since surface tension may prevent efficient filling of the liquid and the formation of a flat surface on the micro-scale. The viscosity of the monomer systems used in SL [11] varies from 170 cps to 3800 cps, while in MSL the viscosity of the monomer is two orders of magnitude lower (e.g. 6 cps for HDDA) [7]. Another difference is that some of the monomer systems used for most projection-type MSL are visible-light curable.

An MSL system operates with the same working procedure as an SL system. A 3-D solid model designed with CAD software is sliced into a series of 2-D layers with uniform thickness. The NC codes generated for each sliced 2-D file is then executed to control the UV beam scanning. The focused scanning UV beam is absorbed by an UV-curable solution consisting of monomer and photoinitiators, leading to the polymerization. As a result, a polymer layer is formed according to each sliced 2-D layer. After one layer is solidified, the elevator moves downward and a new layer of liquid resin can be solidified. With the synchronized beam scanning and the z-axis motion, complicated 3-D micro-parts are built in a layer-by-layer fashion.

Various MSL systems aimed at improving the precision and speed of fabrication have been developed. Scanning MSL [7–9,11,12] and projection MSL [10,13–15] are the two major approaches. Scanning MSL builds the solid micro-objects in a spot-by-spot and line-by line fashion, while projection MSL builds one layer with one exposure, significantly saving the time of fabrication.

11.2.3 MSL by scanning methods

Most of the MSL systems developed thus far are based on a scanning method which is similar to the widely used conventional stereolithography. A 3-D microstructure can be fabricated with the scanning method in which a well-focused laser beam (with spot size of $\sim 1 \mu\text{m}$) is directed onto the resin surface to initiate the polymerization, scanning either the light beam or the work piece and by repeating the layer preparation. This scanning method is also called *vector-by-vector MSL* [16].

Although the classical MSL system has a focusing problem which prevents high-resolution fabrications, its fast fabrication speed is a definite advantage due to its implication in industrial mass production. One of the limitations of conventional MSL is that commercially available galvanometric mirrors are not suitable for high-resolution MSL because of de-focusing and the resulting poor scanning resolution (hundreds of microns). A series of integrated hardened (IH) polymer stereolithography processes have been developed to overcome this limitation [7,17]. These IH processes are based on the scanning method.

The schematic for an MSL system with the IH process is shown in Figure 11.4, where the light source used is UV lamp (xenon lamp) and the beam is focused on the resin surface through a glass window. The focus point of the apparatus remains fixed during the fabrication and the workpiece in a container attached to an x-y stage is

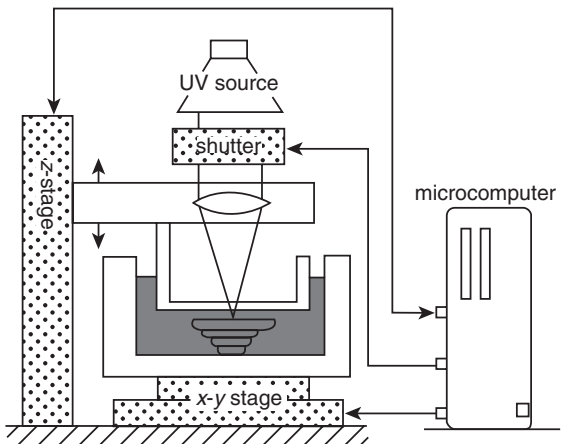


Figure 11.4 Schematic of a system for the IH process [7]. K. Ikuta, and K. Hirowatari, Real three dimensional microfabrication using stereo lithography and metal molding, Proc. IEEE MEMS' 93, © 1993 IEEE

moved, in order to emulate the scanning done by the galvanometric mirrors in the conventional system. Using an x-y stage to move the workpiece leads to a smaller focus spot, indicating a higher fabrication resolution. In addition, there is no need of a dynamic focus lens as the focal point is fixed. The glass window was attached to the z-stage for precise control of the layer thickness.

Typical specifications of the IH process are listed below:

- Spot size of UV beam, $5 \mu\text{m}$.
- Position accuracy, $0.25 \mu\text{m}$ (in the x-y direction) and $1.0 \mu\text{m}$ in the z-direction.
- Minimum unit size of hardened polymer, $5 \mu\text{m} \times 5 \mu\text{m} \times 3 \mu\text{m}$ (in the x, y, and z directions).
- Maximum size of fabricated structure, $10 \text{ mm} \times 10 \text{ mm} \times 10 \text{ mm}$.

Features of the IH process include a capability for building real 3-D and high-aspect-ratio microstructures, processibility of various materials, a ‘mask-less’ and cost-effective process, a medium range of accuracy ($3\text{--}5 \mu\text{m}$) and the possibility of ‘desktop’ micro-fabrication. It should be pointed out that the fabrication speed is relatively lower than that of classical MSL, because the scanning speed of the x-y stage with the container is lower than that of galvanometric scanning.

To overcome the limitation of fabrication speed of the basic IH process, a mass-producible IH process, called the *Mass-IH process*, was proposed by Ikuta et al. in

1996 to demonstrate the possibility of mass production of 3-D microstructures by MSL [10]. The Mass-IH process uses optical fibers for multi-beam scanning. An array composed of numerous single-mode optical fibers is used here to enable high-speed production of multiple structures. Other specifications of the system remain the same as those of the original IH process. Although the fabrication speed can be improved significantly, this Mass-IH process needs further improvements in its resolution and capability for integration of more fibers.

Both the IH and Mass-IH processes are based on a scanning method with layer-by-layer fabrication, sharing the same principles of conventional SL. Problems caused by this fabrication approach include limitation of the depth resolution by thickness of the stacked-up layer and the micro-scale deformation and destruction of the solidified microstructures due to the viscous nature of the liquid monomer. The surface tension of the liquid monomer decreases the precision of the 3-D fabrication [18].

The *Super IH process* can be used to solidify the monomer at a specific point in the 3-D space by focusing a laser beam *into* the liquid monomer. Thus, 3-D structures are fabricated by scanning the focused spot in three dimensions inside the liquid, enabling 3-D fabrication without any supports or sacrificial layers. Since there is no layer preparation step in the super IH process, the influence of viscosity and surface tension is minimal. A schematic diagram of the super IH process is shown in Figure 11.5, which consists of an He-Cd laser (442 nm), optical shutter, galvano-scanner set, *x-y-z* stages, objective lens, etc. The laser beam was focused inside the monomer volume and by co-ordinating the beam scanning and *z*-stage movement, any 3-D structures can be formed inside the liquid. The properties of a UV-curable monomer system must be precisely tuned to ensure that the polymerization happens only in the focus point, similar to two-photon MSL [11]. A typical UV monomer system used in this case is a mixture of urethane acrylate oligomer, monomer and photoinitiator [18].

Although the resolution of the super IH process is less than 1 μm and the fabrication speed can be increased by combining the galvano-scanning mirror and *x-y* stage, the optics system used in this case is more expensive than the other two types of IH processes. This process also requires the development of specific monomer systems.

A limitation of most scanning MSL processes is the minimum thickness of the resin layer during the layer preparation due to the viscosity and surface tension of the liquid monomer. The two-photon MSL process overcomes this problem since the resin does not have to be layered. Usually, only one photon is absorbed during the

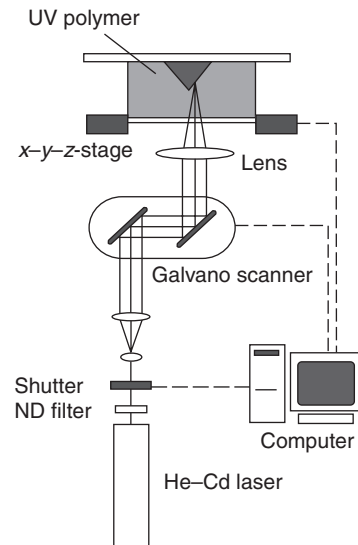


Figure 11.5 Schematic of the super IH process [18]. K. Ikuta, S. Maruo, and S. Kojima, New micro stereo lithography for freely moved 3D micro structure- super IH process with sub-micron resolution, Proc. IEEE MEMS' 98, © 1998 IEEE

photochemical change. However, recently a large number of experiments in which multiple photons are absorbed for the photochemical change in a single particle have been observed. Multi-photon excitation is a non-linear process, observed only at high intensities [19].

Two-photon absorption is one of the most popular methods of multiple-photon excitation for photochemical change. There are two kinds of mechanisms for two-photon excitation. The first is called *sequential* excitation, which involves a *real* intermediate state of the absorbing species. This intermediate state becomes very populated by the first photon, and can act as the starting point for the absorption of the second one. The real intermediate state A^* has a well-defined lifetime, typically 10^{-4} to 10^{-9}s . This means that the second photon must be absorbed by the same particle within the lifetime of A^* to cause the photochemical change. Since in sequential excitation the particle is best excited by a resonantly absorbed photon, the overall sequential process is also referred to as *resonant two-photon excitation*.

A set-up for the two-photon MSL is shown in Figure 11.6. The beam from a mode-locked titanium sapphire laser is directed to the galvanic-scanning mirrors and is focused with an objective lens into the resin. The monitoring system including a camera is used to ensure focusing and to monitor fabrication. A *z*-stage moves along the optical axis for multilayer fabrication. The longest total

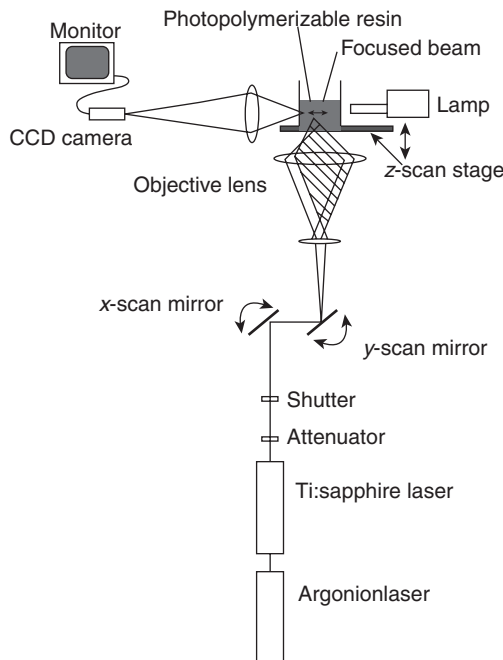


Figure 11.6 Schematic of 3-D micro-fabrication with two-photon absorption [20]. S. Maruo, and S. Kawata, Two-photon-absorbed near-infrared photopolymerization for three-dimensional microfabrication, J. of Microelectromechanical Systems, Vol. 7, No. 4, © 1998 IEEE

length of a structure in the direction of the optical axis is a limitation of two-photon MSL although this has a very good depth resolution. In addition, the system is more expensive than most of the other MSL systems.

Another widely used MSL apparatus for 3-D micro-fabrications is based on a *free-surface method* that utilizes *x-y* stage scanning (Figure 11.7) [9,12]. In this

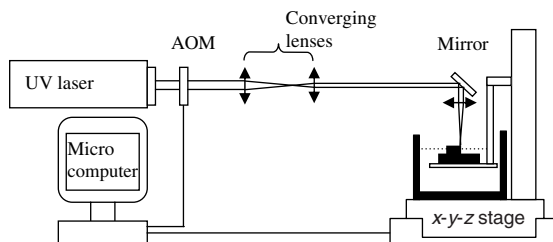


Figure 11.7 Schematic of free-surface microstereolithography [12]. Microsystem Technologies, 2-2, 1996, pp. 97–102, Stereolithography and microtechnologies, S. Zissi, A. Bertsch, J.Y. Jezequel, S. Corbel, J.C. Andre, and D.J. Lougnot, with kind permission of Springer Science and Business Media

method, all of the optics for the beam delivery remain fixed, but an *x-y* stage moves simultaneously the resin tank and the vertical axis onto which the plate supporting the fabrications was attached. The scanning method is similar to the one used in the IH process, but the galvo-scanning is replaced with an *x-y* stage scanning so that system is simplified and the focus precision is enhanced. In this MSL process, a free-surface method was adopted for layer preparation, rather than the constrained surface (with a window) method used in the IH process. This overcomes the disadvantage of the latter, where microstructures may be destroyed because of the parts sticking to the window, by utilizing free-surface layer preparation. With the free-surface method, the time needed to obtain a fresh layer of resin on top of a cured layer depends on the rheological properties of the resin, and so a resin with a low viscosity is preferred. Free-surface MSL is a single-photon-based photopolymerization process, and hence the curing volume is relatively large. However, by adding a light-absorbing medium into the resin, the line width and depth can be decreased as required [9,12]. If the beam delivery system is optimized to obtain the finest beam spot size, the line width of 1–2 μm and a depth of 10 μm can be obtained with free-surface MSL [12].

The advantages of free-surface MSL include a simple set-up, good focusing and high resolution. However, the workpiece scanning has a limitation in the scanning speed due to the fact that relative movement between the workpiece and the liquid resin may cause a waved surface on the fabricated micro-objects. In addition, precision stages are required for this MSL because any stage motion errors will be reflected directly in the fabricated parts.

11.2.4 Projection-type methods of MSL

As seen from the previous section, although the scanning MSL can be used for the fabrication of very fine, high-aspect-ratio, 3-D microstructures, the fabrication speed for mass production of components is low. The scanning MSL builds objects in a layer-by-layer fashion, but each layer is built in a line-by-line way. The projection MSL is proposed for building 3-D microstructures more rapidly, although still in a layer-by-layer way. However, in this case each layer is built by just one exposure through a mask, thus significantly saving time. Two types of projection MSL are introduced here: one is with real mask to generate pattern projection for exposure curing [14] and the other is with dynamic-mask projection (LCD projection method) [13].

In *real-mask-projection lithography*, similar to photolithography, an image is transferred to the liquid

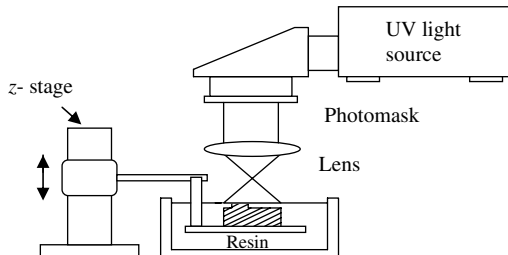


Figure 11.8 Microstereolithography using real-mask projection [14].

photopolymer by irradiating a UV beam through a patterned mask (as shown in Figure 11.8) and another fresh layer of liquid photopolymer is then prepared on top of the patterned solid polymer. By repeating the above mask-based exposure and layer preparation, multilayer 3-D microstructures will be finally built by the described mask-projection MSL [14,17,21].

Similar to scanning MSL, the fabrication precision in this case can be related to the exposure. The curing depth strongly depends on the laser exposure and the distance between the mask and the resin surface. The lateral dimension is marginally influenced by the exposure but is determined mainly by the mask pattern if the distance between mask and resin surface is fixed. A large distance between the mask and resin surface results in relatively large lateral dimensions due to diffraction of the beam [14]. Therefore, in high-precision mask-projection MSL, the mask should be located close to the resin surface to reduce light diffraction. This real-mask-projection MSL can produce high-aspect-ratio micro-fabrications with a few different cross-sections at a high fabrication precision. However, for truly 3-D micro-fabrications, a number of masks are needed, making it not only time-consuming but also expensive.

Dynamic-mask-projection MSL utilizes a dynamic-mask generator instead of the real mask and allows the fabrication of a complete layer by just one exposure. This leads to quick fabrication of complex 3-D micro objects. A schematic of a dynamic-mask-projection MSL is shown in Figure 11.9 [13]. For the exposure of a complete layer, the irradiation beam is shaped with a computer-controlled liquid crystal display (LCD) used as a dynamic-mask generator.

In general, an addressed LCD light valve array (or panel) acting as a projector is used to control light ‘on/off’. The liquid crystal effect is adopted to modulate the light transparency of the panel. By the liquid crystal effect the electrical and optical characteristics of the liquid crystal materials are changed upon application of an electric field. The nematic phase is one of the most

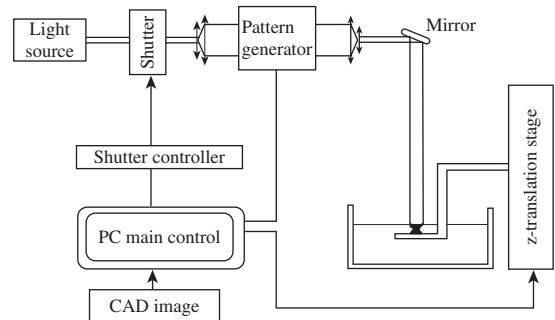


Figure 11.9 Schematic of dynamic-mask-projection microstereolithography [13]. Microsystem Technologies, 1997, pp. 42–47, Microstereolithography using a liquid crystal display as dynamic mask-generator, A. Bertsch, S. Zissi, J.Y. Jezequel, S. Corbel, and J.C. Andre, Fig 4, with kind permission of Springer Science and Business Media

important materials for light valves applications. It consists of rod-like molecules, more or less parallel to each other. The vector that defines the orientation of the long axes of these molecules is called the ‘director’. The optical properties of nematic liquid crystals can be varied by manipulation of the orientation of the director in a device by an electric field. The LCD panel is made of pixels physically separated by a thread of electrical connections being used for control. Every pixel is a small cell which contains matter in its liquid crystal state, and can be set either to its transparent or to its opaque state by changing the orientation of the molecules it is made of. The pixels in their opaque state stop the light, in contrast to those in their transparent state. Usually, the LCD panel is addressed by a thin-film-transistor (TFT) array.

For using an LCD in projection MSL, a CAD file with white and black coloring is translated into a numerical control code which is sent to the LCD device via a computer; the LCD can then function as a dynamic mask with controlled imaging. When a beam passes through this LCD, it carries the pattern of the layer. The light beam is focused on the resin surface, allowing selective polymerization of the exposed areas corresponding to the transparent pixels on the LCD. The remaining principles of operation, such as layer preparation, beam on/off control, etc., are similar to the standard MSL. It may be noticed that the z-stage is the only movable element in the system.

The dynamic-projection MSL fabrication process has a reasonably good accuracy. Even though dynamic-projection MSL has disadvantages, such as low lateral resolution and small scope of fabrication (currently only several millimeters), this MSL process has great

potential due to its capability for batch fabrication of 3-D microstructures.

11.3 MICROMOLDING OF POLYMERIC 3-D STRUCTURES

Although a number of micro-fabrication techniques, including silicon micromachining, LIGA and microsterolithography, have been developed for MEMS, many of them are faced with problems of low speed of fabrication and/or high cost of production [22]. In this context, micromolding technology assumes significance in MEMS fabrication because of its capability of large volume capacity. The micromolding techniques useful for MEMS include injection molding [23], hot embossing [24], jet molding [25], replica molding [26], micro-transfer molding [27], micromolding in capillaries [28] and solvent-assisted micromolding [29] (Table 11.2). In principle, the first three processes can be used for fabrication of micro-parts with high-aspect-ratios and even 3-D features and the last four are especially useful for thin microstructures.

The key aspects in micromolding include degassing prior to molding, thermal or photochemical curing and ‘demolding’ [23]. Vacuum molding and hot isostatic pressing have been demonstrated as helpful to exempt

gas [30]. In order to remove the polymer mold, selective plasma etching is preferred to using the burnout process, to prevent ‘topple’ in fine structures with high-aspect-ratios [30,31]. The micromolding techniques are fairly well established for plastics and ceramics.

‘Master molds’ are often built using polymers, metals or silicon. ‘Polymer masters’ can be built using photolithography, stereolithography, etc. ‘Metal masters’ are formed mostly by micro-electroplating, LIGA and the DEEMO process utilizing metallic molds [32,33]. ‘Silicon masters’ are fabricated using wet or dry etching [24,33].

The polymer mold inserts should withstand a certain level of mechanical strength and thermal resistance since pressure and heating are necessary during molding. Materials used for such mold inserts range from common photoresists to UV-curable resins used in microstereolithography. To fabricate elastomer mold inserts, the photoresist is first patterned using photolithography, the elastomer solution (PDMS and solvent) is then poured into the pattern followed by solvent evaporation and curing. The PDMS mold insert is then obtained by dissolving the photoresist pattern (Figure 11.10).

Most micromold inserts used for micromolding are made of metals. These are widely used for plastic, metal and ceramic micro-moldings. The fabrication approaches include precision mechanical machining (e.g. micro electro-discharge machining (EDM)) and lithography

Table 11.2 A brief comparison of micromolding techniques.

Molding type	Molding material	Feature size	Mold insert material	Notes	Reference
Injection molding	Plastic	Hundreds of microns high	Nickel	LIGA	[32]
Embossing	Polymer	~ 100 µm	Nickel	DEEMO	[33]
Photoreaction; injection molding	Polymer (photocuring)	~ mm	Brass	Faster curing than thermal reaction molding	[23]
Jet molding	PZT	~ 40 µm thick	—	Slow process.	[25]
Embossing	Plastic	~ 21 µm thick, 30 µm wide	Silicon	Limited 3-D	[24]
Pyrolysis molding	Ceramic	Aspect ratio of 5	Polymer	Good filling, degassing, but too high shrinkage (~ 60 %)	[34]
Microtransfer molding	Polymer	Several µm	Polymer	Small thin structure, limited 3-D	[27]
Injection molding	Plastics, ceramics, metals	Aspect ratio of 20	Polymer	A broad variety of materials can be molded	[35]

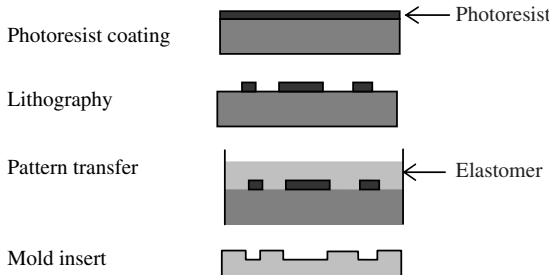


Figure 11.10 Elastomer mold inserts fabrication.

(e.g. E-beam, UV, X-ray) or excimer laser ablation or microstereolithography followed by electroplating [22].

Through-mask electroplating has been used extensively in the fabrication of metal mold inserts. Nickel is the most commonly used material for the fabrication of such inserts because of its well-known electroplating potential, the high replication accuracy and low internal stresses. However, the hardness of nickel is relatively low compared with iron or stainless steel, resulting in a limited lifetime for nickel mold inserts. Other materials such as nickel–iron or tungsten–cobalt alloys with enhanced hardness are also considered [22].

Laser micromachining is also used for the fabrication of metal mold inserts [36]. As shown in Figure 11.11, a polymer (e.g. PMMA) is machined by an excimer laser beam. The polymer structure is then coated with a thin evaporated metal layer which serves as the ‘seed’ layer for the following electroplating. After electroplating, the polymer is removed and the metal mold insert is ready for molding. Features of mold inserts fabricated by laser micromachining include the possibility of a large variety of 3-D shapes, a lateral resolution of the order of microns

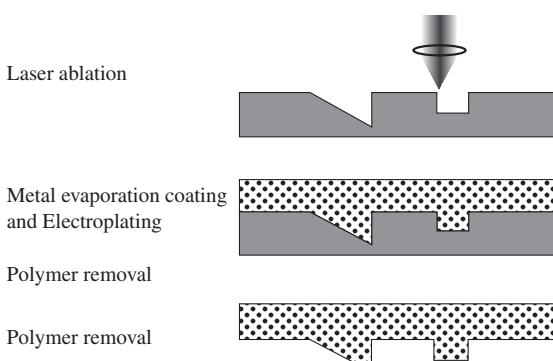


Figure 11.11 Metal mold insert fabrication using laser ablation and electroplating [36].

and the feasibility for ‘hundreds-of-micron-high’ structures. This is a *mask-less* process.

Mechanical machining processes such as micromilling, sawing, grinding and micro-EDM are suitable for the fabrication of metal micromold inserts. Several materials are available for such precision machining processes. Since the fabrication of metal mold inserts by precision mechanical machining results in large structures, lithography can be used for micro-scale mold insert fabrication [22]. However, lithography-based mold insert fabrications have limited applications due to abrasion and wear of nickel, slow speed of electroplating and the possibility of voids in the electroplated mold insert structures.

Silicon micromold inserts are useful for micromolding with flat and even surfaces [37]. Both silicon wet and dry etching can be used for their fabrication. For example, a silicon mold insert with a lateral dimension of 5 µm and an aspect ratio of 2 has been fabricated by RIE etching [37]. Although silicon mold inserts have limited shaping variations, a high resolution of mold insert is possible by the approach. Silicon mold inserts are useful for hot embossing of polymer structures and isotropic pressing casting of ceramic microstructures [24,31].

11.3.1 Micro-injection molding

Injection molding is a widely used technique for shaping plastics, metals, metal alloys and ceramics. However, several modifications should be made in the conventional injection molding technique to facilitate micro-scale injection molding. There are many air-vent slots in conventional injection molding to facilitate the escape of air during molding. Since the dimensions of these vents are generally close to the size of the microstructures, similarly sized unwanted structures will be formed if they are used in micro-injection molding. To avoid this, the air inside the mold is removed before molding, and hence air-vent slots are not necessary in micro-injection molding. In addition, a temperature-variation program must be included in micro-injection molding because of the high aspect ratio of the microstructures. The temperatures of the mold inserts should be kept higher and for longer durations, to ensure good mold filling. Furthermore, since the microstructures are relatively weak at high temperatures, it is necessary to cool the mold down to a stable temperature at which the molded part has sufficient mechanical strength and stable chemical properties. Therefore, in addition to the heating used in conventional injection molding, an inside heating and cooling technique (called the *variotherm* process) should be used in micro-injection molding [35].

A typical micro-injection molding process has the following steps:

- Placing mold insert into the molding chamber.
- Evacuation of the chamber.
- Heating the plastic pellets to above the melting point.
- Injection of polymer at controlled pressure and temperature.
- Cooling.
- De-molding.

The molding temperature is set above the melting point of the polymer being used. The pressure applied ranges from 500 to 2000 bars. Typically, injection-molded micro-parts have a minimum wall thickness of $20\text{ }\mu\text{m}$ and an aspect ratio of more than 20. However, structural details below $0.2\text{ }\mu\text{m}$ have been achieved. The thermoplastics used in micro-injection molding include polysulfone (PSU), polycarbonate (PC), polyoxymethylene (POM), polyamide (PA) and poly(ether ether ketone) (PEEK) [35,39].

11.3.2 Micro-photomolding

Micro-photomolding is a process based on micro-injection molding that uses a photocuring technique to solidify the feedstock system instead of the heating/cooling-based phase change in micro-injection molding. The feedstock system is a reactive polymer resin with a low viscosity (e.g. methyl methacrylates, unsaturated polyesters). The steps involved in the micro-photomolding process are [23]:

- Sealing the molding chamber and its evacuation.
- Injection of the liquid resin (injection pressure < 20 bar).
- Curing using intense UV/visible radiation under constant holding pressure to compensate curing shrinkage.
- Removal of the molded micro-component from the molding tool.

The curing time of the micro-photomolding process depends on the photochemical properties of the resin, mold thickness and radiation intensity. Usually, a few minutes are needed to complete photomolding. The photomolding of powders is made possible by the addition of ceramic or metal powders into the resin [23].

11.3.3 Micro hot-embossing

Hot embossing is a process for the replication of plastics by heating and pressing the polymer thick films to fit into the mold insert, as shown in Figure 11.12. Hot embossing

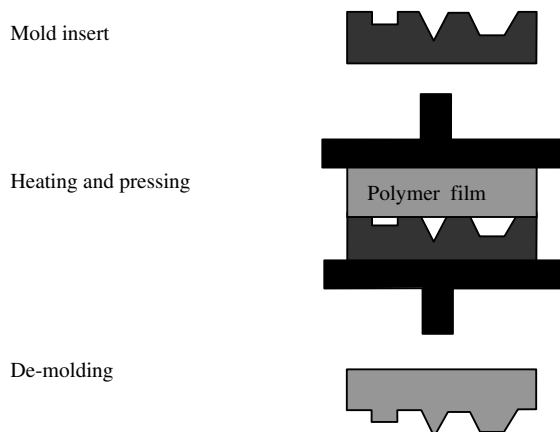


Figure 11.12 Hot embossing for polymer micro-component fabrication.

differs from injection molding in the fact that the heating temperature is just above the glass transition temperature in hot embossing, while the temperature should be above the melting point used in injection molding. Another difference is that polymer films are used as the starting materials in this case, compared to the pellets of polymers used in injection molding.

The embossing tool and the polymer film substrate are mounted in the hot embossing machine and are heated separately to a temperature just above the glass transition temperature of the polymer material. For most thermoplastic materials, the glass transition temperature is in the range $120\text{--}180^\circ\text{C}$. The tool is then driven into the substrate under a controlled force, which is kept up for several seconds. The tool–substrate–sandwich is then cooled below the glass transition temperature of the polymer material. After the polymer material solidifies, the tool is taken out of the structure. Advantages of this method are its flexibility and the low internal stresses and high structural replication accuracy due to the small thermal cycle (ca. 40°C), which facilitate structural replications in the nm-range [37].

11.3.4 Micro transfer-molding

Micro transfer-molding (μTM) was developed to fabricate 3-D polymer and ceramic microstructures with sub-micron-and nanometer-scale features. A schematic diagram of micro transfer-molding is shown in Figure 11.13. As a mold insert, an elastomeric tool must be fabricated first. Unlike injection molding and hot embossing where the hardness of the mold inserts should be high, a soft

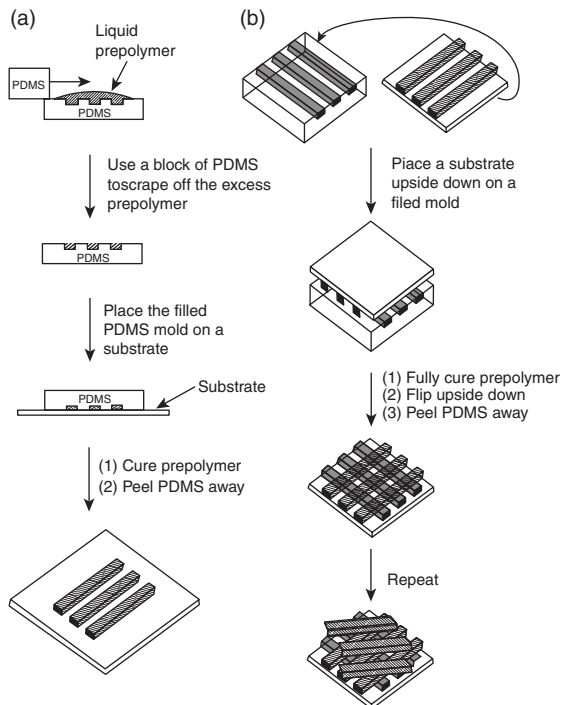


Figure 11.13 Schematic diagram of micro-transfer molding: (a) Process flow for a single layer; (b) multiple layer structure fabrication [27]. Reproduced with permission of John Wiley & Sons, Ltd.

elastomeric material should be used to fabricate the mold inserts for μ TM. Usually, polydimethylsiloxane (PDMS) is used for elastomeric tool fabrication. The Micro contact-printing process or RIE etching may be used for fabricating the PDMS molding tool [27]. The thickness of this tool is controlled to be less than 2 mm to ensure its flexibility.

A drop of liquid precursor is placed on the patterned surface of the PDMS tool and the excess liquid is removed by a piece of flat PDMS, followed by blowing away any drops of liquid left on the raised areas of the mold. The filled PDMS tool is then placed onto a substrate where the polymer structure will be built. The prepolymer is next fully cured thermally or photochemically and the PDMS tool is finally peeled away and the polymer microstructure is left on the substrate.

Multilayer microstructures can be fabricated with this technique. Another characteristic of μ TM is that polymer microstructures can be formed on non-planar surfaces [27]. One of the limitations of using μ TM is that there is a thin ($< 0.1 \mu\text{m}$) film formed between the polymeric

features due to the polymer transfer of prepolymer from the raised surfaces of the mold and capillary ‘wicking’ of prepolymer from the PDMS relief tool.

11.3.5 Micromolding in Capillaries (MIMIC)

The micromolding in capillaries process is used to fabricate polymeric microstructures by generating a network of capillaries formed by contacting an elastomeric master with a surface embossed with an appropriate relief structure, and by allowing the liquid precursor to fill the channels by capillary action [26,28]. Figure 11.14 shows the procedure of an MIMIC process. Similar to micro transfer-molding, an elastomer (PDMS) tool is fabricated first and is patterned with a relief structure on its surface. It is then placed on the surface of a substrate to form a network of channels between them. When a drop of precursor solution is then placed at one end of these channels, it fills the channels by capillary action. After the solvent is evaporated and the PDMS tool is carefully removed, the polymer microstructures are left on the surface of the substrate. Although the capillary action takes a long time (hours) to fill the channels with solution, especially for small-diameter channels (microns) and highly viscous precursor

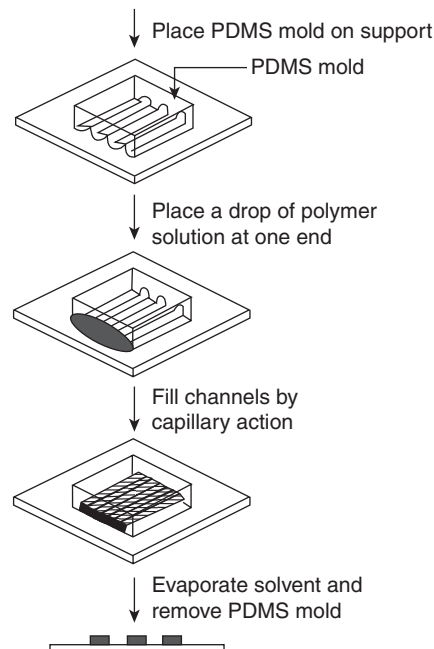


Figure 11.14 Schematic of micromolding in capillaries [40]. Reproduced with permission of John Wiley & Sons, Ltd.

solutions, the MIMIC process has advantages such as high fabrication resolution and processibility of a variety of precursor materials.

Care should be taken in choosing the solvent, as this should not swell the PDMS mold. MIMIC is usually used for micro-fabrications of structures ranging from 350 nm to 50 μm size, with low processing temperatures and no pressure applied. This method is compatible with the semiconductor micromachining process.

11.4 INCORPORATION OF METALS AND CERAMICS BY POLYMERIC PROCESSES

The fabrication of several advanced MEMS for special applications often requires the integration of polymers, ceramics, metals and metal alloys to utilize their unique properties. These functional and structural ceramic materials possess unique properties, such as high temperature/chemical resistance, low thermal conductivity, ferroelectricity and piezoelectricity. The use of ceramic materials in MEMS has attracted a great deal of attention recently [41–45]. The three-dimensional (3-D) ceramic microstructures are of special interest in applications such as microengines [42] and microfluidics [43]. Various novel approaches for ceramic micro-fabrication have been developed. In this section, some fundamental processes are introduced to show how these can be incorporated into the fabrication cycle, starting with some of the processes described thus far for polymeric materials.

11.4.1 Burnout and sintering

In 3-D ceramic and metallic micro-fabrications, polymers are usually used as binders to bond solid particles to form the desired shape. Since in most of the cases, pure metal or ceramic structures are required, the binder is removed (*debinding*) and the structures are sintered for densification. Since binders are used in most ceramic and metallic 3-D micro-fabrications, an understanding of the burnout and sintering process is necessary for obtaining highly dense ceramic and metal parts. In addition, electrochemical deposition is one of the most frequently used processes for 3-D micro-fabrications. Some of the recently developed 3-D micro-fabrication processes for ceramics, metals and polymer/metals will also be introduced.

Debinding techniques can be done by either a solvent or a thermal process. Since in most of the photoforming processes the polymer is cross-linked, solvent cannot be used to dissolve the binders and hence thermal degradation is preferred. Therefore, the debinding process is often

called the *burnout process*. Thermal degradation involves several basic steps [46]. During the early stages of heating, thermal expansion of the liquid binder induces an hydraulic pressure in the fully saturated part. As the temperature rises, binder removal, due to evaporation from the surface, increases. When the saturation level of the binder is sufficiently reduced, the liquid remaining in the mix is driven to the surface by capillary pressure, where it evaporates. As binder removal by liquid transfer continues, gas pockets begin to coalesce, forming a network of interconnected pores. Finally, this internal structure creates passages for gas to flow through, allowing diffusion to play an important role in debinding.

Once the overall debinding time is determined, the heating rate and peak temperature must be carefully selected. The heating rate is directly related to the retaining shape. Since rapid heating often leads to cracks and distortion, slow heating is necessary at the beginning of the degradation. In some cases, the debinding, however, cannot be processed in air, to avoid oxidation, e.g. debinding of metallic structures. A controlled atmosphere should be provided for the debinding. Hydrogen, argon or nitrogen is often used in these cases.

Sintering is the term used to describe the consolidation of the product by firing. Consolidation requires that within the components, particles have to be joined together into an aggregate for better strength. Geometric shrinkage and densification usually occurs during sintering. Sintering densification occurs close to the melting temperature of the material. The bonds between particles grow by the motion of individual atoms, which is related to the temperature. This relationship between atomic motion and temperature varies for different materials with different melting temperatures. For example, steel is often sintered near 1250 °C, alumina near 1600 °C, copper near 1045 °C and PZT near 1200 °C. Measures of sintering include shrinkage and final sintering density. Successful sintering leads to a density ρ_g close to the material density. Theoretically, a final sintering density level can be 95–100 %. [47].

Recently, microwave sintering has been used for bulk ceramics [48,49]. The obvious advantage of microwave sintering is the possibility of quick heating, but its non-uniformity is a concern. However, for micro-scale sintering, microwave sintering may be a good choice since the heating uniformity will be fairly good.

11.4.2 Jet molding

Jet molding is a process developed for microfabrication of metal and ceramic microstructures. Mixture of gas and

ultra-fine particles ($< 0.1 \mu\text{m}$) is heated and ejected to the substrate and form microstructures. There are three major forming methods: free forming, insert molding and mask deposition. The fabrication is controlled by the substrate movement in the case of free forming, while the fabricated object is defined by the mold insert or mask in the cases of insert molding and mask deposition, respectively.

Figure 11.15 shows schematically a jet-molding system [25]. There are two chambers and nozzles for different materials supply: one for metal materials and the other for ceramics. A heating system is used to heat the powders in a crucible so that the powders have good bonding after being ejected. An excimer laser is used for mold-insert fabrication and mask generation to facilitate a rapid fabrication. As an example, the typical experimental conditions required for jet molding of silver and PZT are listed in Table 11.3.

Table 11.3 Typical experimental conditions for jet molding of Ag and PZT.

Experimental parameters	Jet molding with Ag	Jet molding with PZT
Pressure in molding chamber	3 torr	0.55 torr
Distance between mask and substrate	100 mm	400 mm
Distance between mask and nozzle	3 mm	5 mm
Orifice of the nozzle	5 mm × 150 mm	5 mm × 350 mm
Deposition time	20 min	120 min
Substrate temperature	Room	Room
Crucible temperature	1250 °C	—

11.4.3 Fabrication of ceramic structures with MSL

Unlike these molding or printing-based micro-fabrication processes, microstereolithography can be used to build complex ceramic 3-D microstructures in a rapid ‘free-form’ fashion without high pressure or a heat-curing process [50]. Ceramic MSL differs from polymeric MSL in several aspects. First, the resin system for ceramic MSL is composed of ceramic powders, dispersant and diluents in addition to monomers and photo-

initiators that are used in polymer MSL [50–52]. Dispersant and diluent are used to obtain a homogeneous ceramic suspension with relatively low viscosity. After UV polymerization, the ceramic particles are bonded by the polymer and the ceramic ‘green body’ is thus formed. Generally, the viscosities of ceramic suspensions used for MSL are higher than the viscosities of most liquid polymers, leading to a slow layer preparation. A

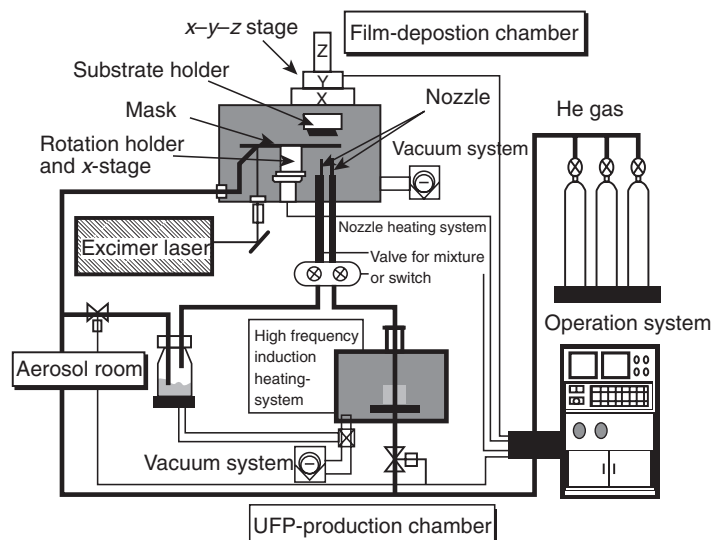


Figure 11.15 Schematic of a jet-molding system [25]. J. Akedo, et al., Fabrication of three dimensional micro structure composed of different materials using excimer laser ablation and jet molding, Proc. MEMS' 97, © 1997 IEEE

precision blade may be used for layer preparation to solve this problem [50]. Secondly, light transmission during MSL processing is complicated in the two-phase medium (solid and liquid). Light scattering by solid ceramic particles affects both the curing depth and the line width.

In general, UV curing of ceramic suspensions for MSL can be considered to be similar to UV curing with pigmentation. Two effects may occur as the UV radiation travels into a highly concentrated suspension. Particles scatter the radiation and the UV-curable solution absorbs part of the radiation, thereby reducing its intensity. The radiation which is not absorbed travels further into the suspension. The energy of the radiation reaches a critical level, E_c , at which the radiation energy is absorbed by the monomer system. This critical level of energy is required for the gellation of the monomer.

The fabrication of ceramic microstructures using MSL follows the steps shown in Figure 11.16. A homogeneous ceramic suspension is first prepared. Submicron ceramic powders are mixed with monomer, photoinitiator, dispersant, diluents, etc. by ball-milling for several hours. The prepared ceramic suspension is then put into the vat for MSL based on the CAD design. After MSL, the ‘green bodies’ of ceramic micro-parts are obtained. To get dense micro-ceramic parts, the ‘green body’ is first kept inside a furnace to burn out the polymer binders and is then sintered in a high-temperature furnace. The binder burnout and sintering temperature vary for different polymers and ceramics.

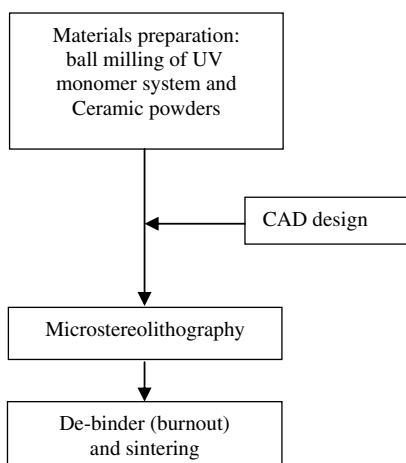


Figure 11.16 Schematic of the flow for ceramic microstereolithography and post-processing.

Table 11.4 Micro-photomolding with powders in an unsaturated polyester- or PMMA-based resins.

Powder materia	Particle size (μm)	Maximum solid loading (vol%)	Curing time (min/mm)
SiO_2	10	64	10
Al_2O_3	0.4–0.6	54	20
ZrO_2	0.2–0.4	24	17
SiC	0.5	42	20
TiO_2	0.021	23	17
Carbonyl-Fe	4.5	53	5
Ag/Al	44	52	14

The photomolding of powders is made possible by the addition of ceramic or metal powders into the resin [23]. The addition of solid powders inside resins will introduce problems of radiation scattering and absorption, hence resulting in a longer curing time. However, the addition of a thermal initiator will help to decrease the curing time [23]. Table 11.4 shows the particle sizes, volume solid loadings to and curing times of some resin systems.

11.4.4 Powder injection molding

Powder injection molding (PIM) extends the shaping advantages of injection molding to metals and ceramics. The PIM process starts with the feedstock preparation by mixing a small quantity of a polymer with an inorganic powder. During injection molding, the metal or ceramic parts are shaped by the bonding of the polymer binder containing these inorganic powders. The polymeric binder is later removed by the burnout process and the object is sintered, to yield pieces that are as dense as the bulk material.

Micro powder injection molding (MPIM) has been used for fabricating MEMS with metallic and ceramic micro-components [53]. Materials, such as carbonyl iron powder, aluminum oxide and zirconium oxide, have been used for MPIM. The powder with mean particle sizes ranging from 0.6 to 5 μm is mixed with polyclefin/wax to make the feedstock. The nickel mold inserts used for MPIM is fabricated via the LIGA process. The debinding process is critical to obtain crack-free metal and ceramic micro-parts. Thermal elimination of the organic components or catalytical de-binding can be used for a polyacetal-based polymer system. The sintering procedure is done inside a tube furnace. A reducing N_2/H_2 atmosphere is necessary to sinter metal microstructures, although ceramic micro-parts can be sintered in air. The

fabrication resolution and the final density of the fabricated micro-parts obtained by MPIM vary with the different powders used and the solid loading in the feedstock system. Although the fabrication resolution is not comparable with silicon micromachining, it is good enough for many metal and ceramic micro-component applications. A high density of the feed stock will ensure high strength, stiffness and other mechanical properties of the metal and ceramics micro-parts.

11.4.5 Fabrication of metallic 3-D microstructures

Metallic microstructures have been fabricated extensively for MEMS. Three-dimensional metallic microstructures have been built by spatial forming, electrochemical fabrication (EFAB), localized electrodeposition, selective laser sintering and laser cladding [54–57]. Some of these processes are introduced in this section due to their relatively higher fabrication resolution and prospects.

11.4.5.1 Electroplating

Electroplating is a process of electrodeposition in which an electric current is carried across an electrolyte in an effort to deposit material onto a substrate at one of the electrodes. A simple electrodeposition system may contain an electrolyte, an anode, a cathode and an electric power supply, as shown in Figure 11.17.

The electrolyte is a conducting medium which allows the flow of electric current as a means of movement of the matter. Any liquid or solution containing ions can be used as the electrolyte. A large majority of commercial electrolytes, however, use water as the solvent and are therefore called *aqueous electrolytes*. Deposition occurs at the cathode. This deposition reaction is related

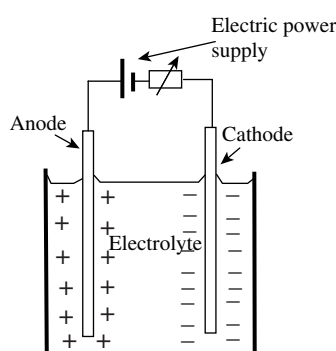


Figure 11.17 Schematic of electrodeposition.

to the quantity of current that reaches the cathode. The current flow into the cathode is usually expressed as current density or quantity of current per unit surface area of the electrode. Hence, current density is more frequently used as the ‘control parameter’ in electroplating. The anode is the electrode which acts as the source for deposition at the cathode. The position of the anode has much to do with the distribution of current at the cathode and further influences the plating rate and quality.

Electrodeposition follows Faraday’s laws:

- The quantities of different elements liberated at the anode or cathode during electrolysis are proportional to the quantity of electricity that passes through the electrolyte.
- The quantities of different elements or radicals liberated by the same quantity of electricity are proportional to their equivalent weights.

One gram equivalent weight of ions is discharged at the cathode by 1 faraday (F) ($= 965\,000$ coulombs (c)) charge flow. One gram equivalent weight of a metal is its atomic weight divided by its valency (equal to the number of charges available in the ion). Based on these definitions, one can calculate the metal deposited (in grams) on the cathode per faraday (Table 11.5).

The total deposition thickness d is an important factor in electroplating [58]:

$$d = \frac{MI}{ZF\rho A} \quad (11.1)$$

where M is the molar mass (atomic weight (g/mol)), I is the current, t is the time, Z is the valency, F is the Faraday

Table 11.5 Calculation of the metals deposited at the cathode.

Metal	Ion	Atomic weight	Valency	Metal deposited per faraday (g)
Silver	Ag^+	107.88	1	107.88
Copper	Cu^+	63.57	1	63.57
Copper	Cu^{2+}	63.57	2	31.78
Gold	Au^+	197.20	1	197.20
Tin	Sn^{4+}	118.70	4	29.67
Chromium	Cr^{3+}	52.02	3	17.34
Nickel	Ni^{2+}	58.7	2	29.35
Zinc	Zn^{2+}	65.38	2	32.69

constant ($F = 965\,000\text{ C}$), ρ is the mass density and A is the area of the substrate.

The above calculation is useful for estimating an approximate value of the plating thickness and plating rate, assuming a cathode efficiency of 100 %. In practice, the cathode efficiency is not as high because some fraction of the current is consumed in producing hydrogen. In addition, the distribution of deposition may vary over the surface of an object. To achieve a desired deposition with expected properties, such as hardness, strength and functional properties, there are two parameters that can be modified. These include altering the bath composition and changing the operating conditions of plating. Among the operating conditions for plating, three principal changes that may be made for a given bath are (i) current density, (ii) method or degree of agitation and (iii) temperature.

In general, it is desirable to use high current densities to increase the plating rate in accordance with the above. It is noticed that within certain limits, an increase in current density decreases the crystal size [59]. However, once the current density exceeds such a limit, there is a tendency to produce ‘rough’ or ‘treed’ depositions. The current density far beyond this limit may yield ‘spongy’ or ‘burnt’ depositions. Agitation of the solution brings up a fresh supply of metal salts or ions to the cathode and thus replenishes the metal ions or compounds at the cathode surface. Another advantage of agitation is that it removes gas bubbles. The increase in the temperature causes an increase in the crystal size and increases the mobilities of the metal ions and decreases the viscosity of the solution, so that the cathode film is replenished more rapidly. Another advantage of relatively high temperatures is that there is usually less absorption of hydrogen in the deposits, less stress and tendency toward cracking.

11.4.5.2 Micro-electroplating

Micro-electroplating works on the same principles as electrodeposition discussed in the previous section. Micro-electroplating has advantages in forming thick metallic films, metallic microstructures with high-aspect-ratios and even 3-D features [60]. Micro-electroplating can be divided into two major categories: through-mask-plating (or through-mold-plating) and mask-less plating. The electroplated micro-parts can be either directly used for functional devices or act as molds for subsequent micromolding. Most of the micro-electroplating processes used for MEMS belong to through-mask-plating (Figure 11.18), which has been used for electronics fabrication since the 1960s [60]. Electro-

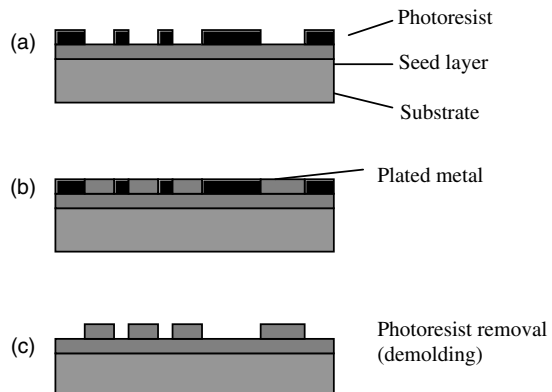


Figure 11.18 Schematic of the through-mask-plating process.

plating used for MEMS differ from that used for conventional electronics in several aspects. First, thick photoresist molds (several microns to hundreds of microns thick) are used for MEMS while several-microns-thick molds are sufficient for conventional electronics. Secondly, multilayer electroplating may be necessary for MEMS to form micro-metallic structures with 3-D and high-aspect-ratio features. In contrast, only single-layer electroplating is often required for electronics. Materials electroplated for MEMS include gold, copper, aluminum, nickel and their alloys, for micro systems with different applications (Table 11.6).

Mask less electroplating is done by either localized electroplating or laser-enhanced electroplating [53,61]. Although rapid fabrication of 3-D structures is a unique property of mask-less electroplating, its limitation for mass production restricts its usefulness.

11.4.5.3 Spatial forming

The spatial forming process combines several technologies to generate solid metallic microstructures from fine powders, as shown in Figure 11.19 [56]. As in projection MSL, data for cross-sections of objects from their solid CAD models are used for patterning a chrome mask with images. A custom-built offset printing press prints negative materials (space around the solid parts) on a ceramic substrate with multiple registered layers of pigmented organic ink ($\sim 0.5\,\mu\text{m}$ thick) and are cured with UV light. After forming a certain number of layers (~ 30) of negative materials, the positive ink heavily loaded with metal powders (e.g. 50 vol%) is ‘knifed’ onto the assembly, filling the voids (Figure 11.19). This step is followed by curing of the filled material

Table 11.6 Micro-electroplating: materials and features.

Type ^a	Material plated	Material of plating mold	Formation of plating mold	Feature size	Functional device	Reference
TMP	Ni	PMMA	X-ray	~ 1000 µm thick	—	[62]
TMP	Ni, Cu	Polyimide	UV lithography	~ 150 µm thick	—	[63]
TMP	Ni	Si	UV, plasma etching	~ 140 µm	—	[50]
TMP	Al	Polyimide	UV	Aspect ratio of 21	—	[63]
TMP	NiFe	AZ4562 (positive photoresist)	UV	~ 20 µm thick	Used for data storage	[64]
TMP	Au, Cu, NiFe	AZ 4000	UV	Aspect ratio > 10	Micro-coil	[65]
TMP	Ni, NiFe	PMMA	X-ray	~ hundreds of µm	Electrostatic actuator	—
TMP	Ni	Polyimide	UV	—	Micro-accelerometer	[66]
TMP	Cu, Ni	Polymer, metal	UV	—	RF inductor	[67]
TMP	Cu, NiFe	Polyimide	UV	—	Magnetic device	[68]
MLP	Cu, Ni	—	—	Ar ⁺ laser	—	[69]
MLP	Ni	—	—	Tool tip	Helical spring	[53]

^aTMP, through-mask plating ; MLP, mask-less plating.

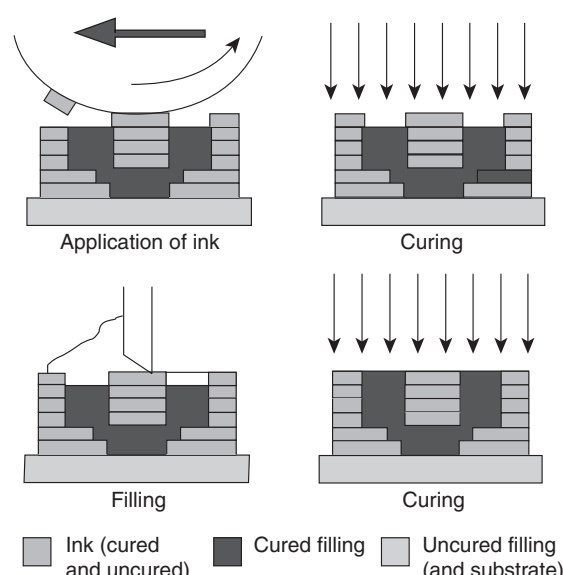


Figure 11.19 Schematic of the spatial-forming process [56]. C. S. Taylor, P. Cherkas, H. Hampton, J.J. Frantzen, B.O. Shah, W. B. Tiffany, L. Nanis, P. Booker, A. Salahieh, R. Hansen, A spatial forming—three dimensional printing process, Proc. IEEE MEMS' 94, © 1994 IEEE

with UV light. The above steps are repeated until the desired thickness (typically 500 µm) of the ‘green-body’ metallic micro-parts is reached. The ‘green-body’ parts are then ‘de-binderized’ to remove organic binders and are sintered in controlled atmosphere furnaces to obtain the finished pure metallic micro-parts. In principle, mass production is feasible with the spatial forming process [56].

11.4.5.4 Electrochemical fabrication process

Electrochemical fabrication (EFAB) is a micromachining process, based on solid freeform fabrication principles, for high-aspect-ratio and 3-D metallic microsystems [55]. The major fabrication steps in EFAB include instant masking and selective electroplating, blanket deposition and planarization (Figure 11.20).

Instant masking makes use of photolithographically patterned masks on the anode for the following selective electroplating. The instant mask consists of a conformable insulator since the pattern may be topologically complex. Instant masking patterns a substrate by simply pressing the insulator mask against it and depositing electroplating materials onto the substrate through apertures in the insulator mask. The mask consists of a layer

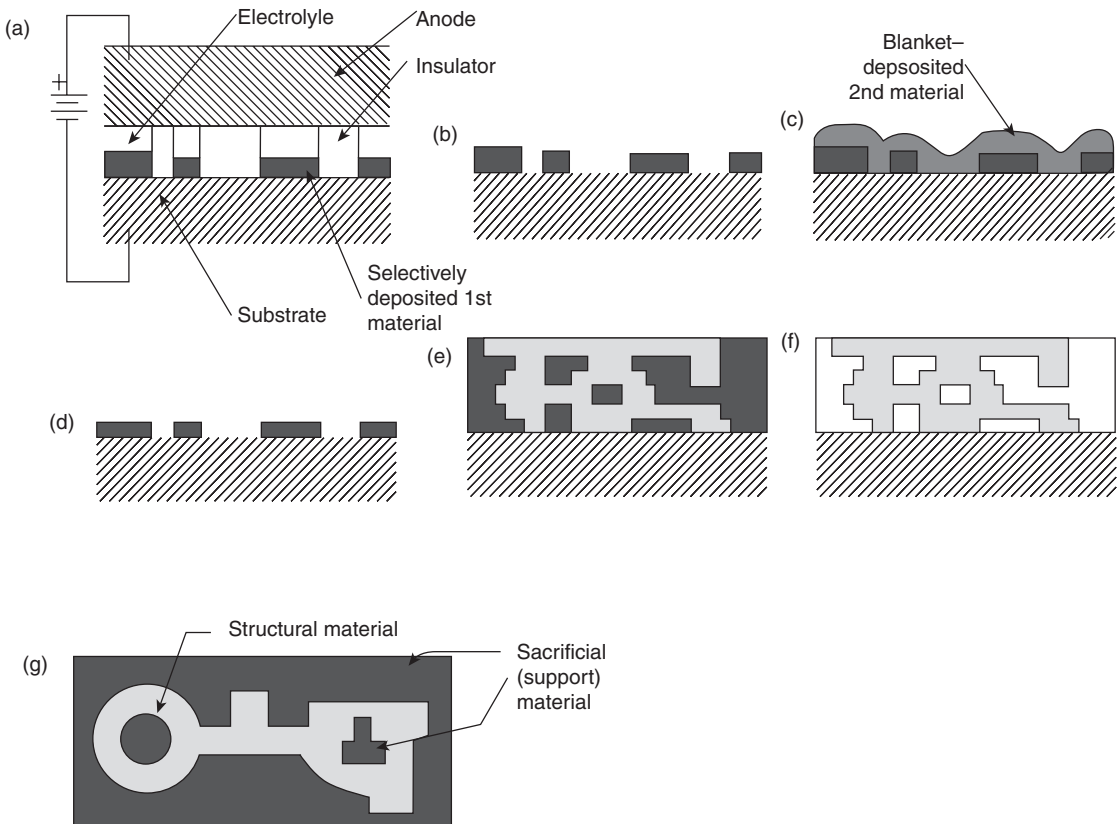


Figure 11.20 The EFAB process: (a) electroplating through an instant mask; (b) instant-mask removal; (c) blanket deposition of the structural material; (d) planarization by polishing; (e) repetition of electroplating, blanket deposition and planarization until the final structure is formed; (f) remove of the sacrificial materials; (g) cross-sectional view of one layer consisting of structural material and sacrificial materials [55]. A. Cohen, G. Zhang, F. Tseng, U. Frodis, F. Mansfeld, P. Will, EFAB: rapid, low-cost desktop micromachining of high aspect ratio true 3-D MEMS, Proc. IEEE MEMS' 99, © 1999 IEEE

of insulator patterned on a flat Cu disk. In selective electroplating, pressure is applied between the Cu anode with the mask and the Ni substrate (cathode).

Blanket deposition is also based on the electroplating technique, but without a mask. Basically, the blanket-deposited material (e.g. Ni) is different from the selective plated one (Cu), so that one of them acts as the sacrificial material and could be removed later. The planarization is done by lapping the surplus materials to achieve a precise layer thickness and flatness before deposition of the subsequent layer. By repeating the above steps, a metallic 3-D microstructure can be formed (Figure 11.20).

The EFAB process is in its development stage. The resolution obtained is around $25\text{ }\mu\text{m}$ and the smearing caused by lapping and ‘misregistration’ also affects the

fabrication precision. Moreover, the fabrication speed is a concern since too many time-consuming electroplating steps are involved, although a throughput of two planarized 5 mm layers per hour or about 50 layers per day was anticipated [55].

11.4.5.5 Localized electrochemical deposition

A localized electrochemical deposition apparatus is schematically shown in Figure 11.21 [53]. The tip of a sharply pointed electrode is placed in a plating solution and brought near the surface where deposition is to occur. A potential is applied between the tip and the substrate. The electric field generated for electrodeposition is then confined to the area beneath the tip, as shown in Figure 11.21(a).

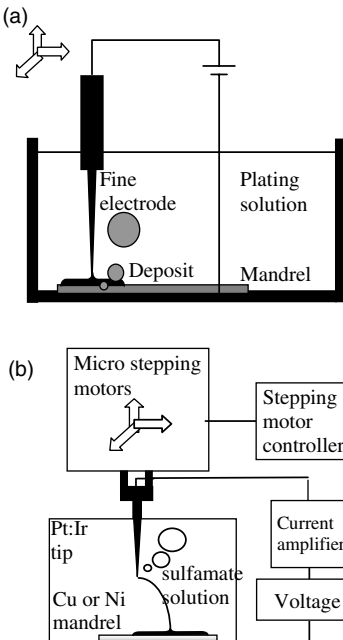


Figure 11.21 Localized electrochemical deposition for 3-D micro-fabrication: (a) concept; (b) apparatus [53]. Madden, J.D.; Hunter, I.W., “Three-dimensional microfabrication by localized electrochemical deposition,” Journal of Microelectromechanical Systems, Volume 5, Issue 1, © 1996 IEEE

In principle, truly 3-D microstructures can be formed by using localized electrochemical deposition, provided it is ‘electrically continuous’ with the substrate. The spatial resolution of this process is determined by the size of the microelectrode. Another important parameter that needs to be considered in this process is the electrodeposition rate. The deposition rate in this case can be $6 \mu\text{m/s}$ – two orders of magnitude greater than those of conventional electroplating [53]. The shape and geometry of the microelectrode used for localized electrochemical deposition is critical for the deposition profile.

11.4.6 Metal–polymer microstructures

Composite metal/polymer microstructures are becoming very popular for MEMS. A process developed in Cabrera *et al.* [70] allows build layer-by-layer the 3-D object so as to obtain conductive and non-conductive parts together, instead of manufacturing them separately and assembling afterwards, for example, to build the cylindrical object described in Figure 11.22, which consists of a metallic element ('Part 1') freely rotating inside a polymer housing ('Part 2'). The major steps involved in the fabrication include the following:

- Electroplating of copper to make Part 1.
- ‘Local’ laser silver plating on the polymer to get the conductive base for the following.
- Electroplating of copper.
- Microstereolithography (MSL) with an insoluble resin to make Part 2.
- MSL with a soluble resin to make a sacrificial structure between Parts 1 and 2.

11.5 COMBINED SILICON AND POLYMER STRUCTURES

The MSL process can be used for fabrication of polymer 3-D microstructures, while the silicon micromachining processes have their own advantages in circuit and sensing and actuating element fabrication. Hence, a combined silicon and polymeric microstructure will be attractive for MEMS applications. Some of the research efforts in this direction are introduced in this section.

11.5.1 Architecture combination by MSL

Architecture combination is a technology for building complicated structures by mechanically connecting two or more architectures made by different micromachining processes. This approach can enable fabrication of a system consisting of LIGA linkages driven by a Si micromotor

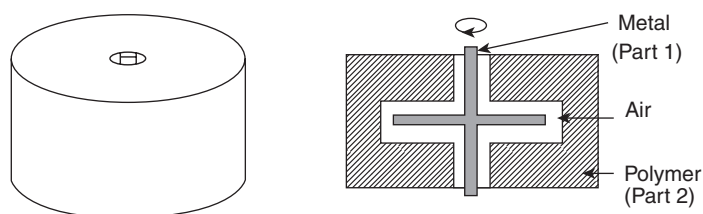


Figure 11.22 Complex 3-D metal–polymer part [70].

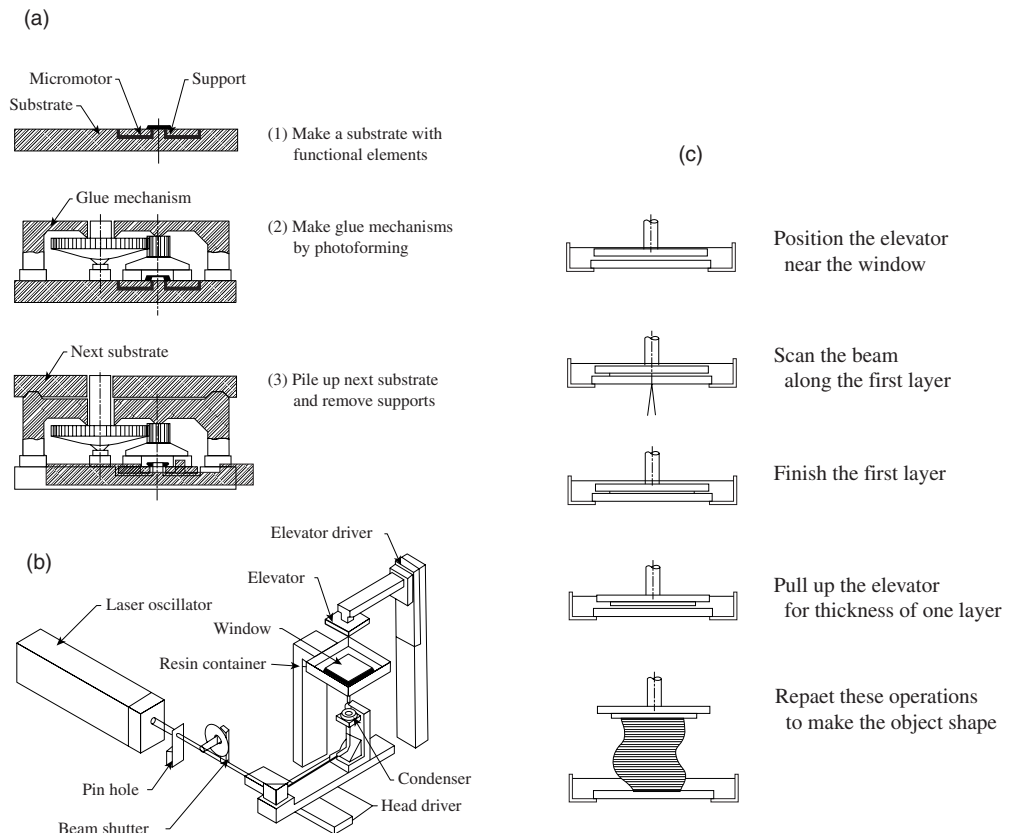


Figure 11.23 (a) 3-D micro-fabrication by the combined process; (b) schematic of a photoforming system; (b) process flow for photoforming [71]. T. Takagi, and N. Nakajima, Architecture combination by micro photoforming process, Proc. IEEE MEMS 94, © 1994 IEEE

and housed in a polymer structure (Figure 11.2). Photo-forming (its use here is the same as in MSL) is developed for this because of its relatively high resolution and 3-D fabrication capability (Figure 11.23(c)) [71].

Since in this approach the components fabricated with different processes are joined together during the photo-forming process, their proper alignment is critical to achieve a successful architecture combination.

11.5.2 MSL integrated with thick-film lithography

Many micromechanical components have been fabricated using planar processes, such as thin-film and bulk-silicon micromachining and high-aspect-ratio micromachining (e.g. LIGA, deep RIE and thick-resist lithography), which have high fabrication resolutions, but do not allow true 3-D fabrications. On the other hand, MSL allows the building of 3-D complex micro-

structures, but with limited resolution and the problems associated with the manipulation and assembling of the obtained polymer structures. An approach of combining MSL and thick-resist lithography may provide a unique technique to build 3-D microstructures with more functions [72].

11.5.3 AMANDA process

AMANDA is a process which combines surface micromachining, micromolding and diaphragm transfer to fabricate micro-parts from polymers. A flexible diaphragm with other functional or structural materials is deposited and patterned on a silicon substrate using a surface micromachining process. The molding process is then used to build the housing for the fabricated diaphragm and is then transferred from the silicon substrate to the polymeric housing. Hence, the AMANDA process

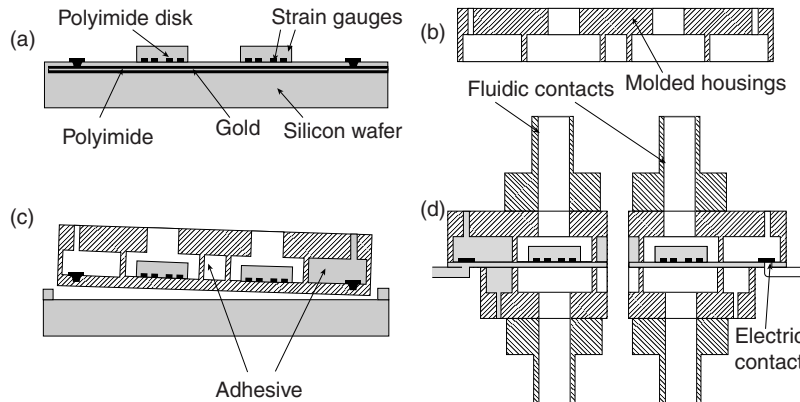


Figure 11.24 Major flow of AMANDA process; (a) a diaphragm is fabricated by silicon surface micromachining; (b) housings are fabricated by molding or mechanical machining; (c) a diaphragm is transferred from the silicon substrate to the housing; (d) diced chips with electric and fluidic contacts [73]. Reprinted from Sensors and Actuators A, 70, W.K.Schomburg, R. Ahrens, W. Bacher, C. Goll, S. Meinzer, A. Quinte, AMANDA—low-cost production of microfluidic devices, pp. 153–158, Copyright 1998, with permission from Elsevier

allows low-cost production of reliable micro devices by batch fabrication.

As an example for the AMANDA process, the fabrication process for a pressure transducer is shown in Figure 11.24. A silicon wafer is covered with 60 nm of gold by PVD and then with 1.5 mm of polyimide by spin-coating. The polyimide is patterned by photolithography and an additional 100 nm gold is evaporated on top of the polyimide layer. The second layer of gold is patterned to form strain gauges. A second polyimide disk with a thickness of 30 μm is built on these strain gauges by spin-coating and photolithography.

The housing of AMANDA devices are produced by molding. Typically, several housings can be fabricated in a batch. Injection molding is generally used for the molding in AMANDA in order to save time [73]. The housing can be molded from thermoplastic materials such as polysulfone, PMMA, PA, PC, PVDF or PEEK. [73]. Mold inserts are fabricated by milling and drilling with an CNC machine, LIGA, deep RIE, etc.

The diaphragm is then transferred into the housing. An adhesive is injected into the cavities inside the housings. In the example shown in Figure 11.24, the housings are ‘adhesively’ bonded to the polyimide on the wafer. The polyimide outside the housing is cut and the housing, together with the polyimide diaphragm, is then separated from the wafer. The polyimide can be peeled off from the wafer because adhesion of the first gold layer to silicon is low. Usually, the diaphragm is encapsulated by a second shell, which is molded and bonded similarly to the first shell.

The dimensional accuracy of the microstructures fabricated by the AMANDA process depends on the lithography, precision of the mold insert and molding process and alignment and temperature control during bonding of the molded part and diaphragm. The lateral accuracy of the pattern on the diaphragm can be very high because it is fabricated by photolithography. Transfer of the diaphragm to the polymer housing causes an overall shrinkage due to thermal expansion of the housing and the heating for bonding. The precision of the mold insert for housing fabrication can be very high if the LIGA process is used. The precision of molding can be of several microns but can be improved with injection molding or hot-embossing molding. Disadvantages of this process are in the alignment and control of shrinkage which affects the dimensional accuracy of the AMANDA process [73].

REFERENCES

1. B. Zhu and V.K. Varadan, ‘Integrated MOSFET based hydrophone device for underwater applications’, *Proceedings of SPIE*, **4700**, 101–110 (2002).
2. C.W. Hull, ‘Apparatus for production of three-dimensional objects by stereolithography’, *US Patent 4 575 330* (1984).
3. J.C. André, A. Le Méhauté and O. de Witte, ‘Dispositif pour réaliser un modèle de pièce industrielle’, *French Patent*, 8 411 241 (1984).
4. H. Kodama, ‘Automatic method for fabricating a three-dimensional plastic model with photo-hardening polymer’, *Review of Scientific Instruments*, **52**, 1770–1773 (1981).

5. P.F. Jacobs, *Rapid Prototyping and Manufacturing: Fundamentals of Stereolithography*, Society of Manufacturing Engineers, Dearborn, MI, USA (1992).
6. D. Kochan, *Solid Freeform Manufacturing*, Elsevier, Amsterdam, The Netherlands (1993).
7. K. Ikuta, and K. Hirowatari, 'Real three dimensional microfabrication using stereo lithography and metal molding', in *Proceedings of IEEE: MEMS'93*, IEEE, Piscataway, NJ, USA, pp. 42–47 (1993).
8. T. Katagi and N. Nakajima, 'Photoforming applied to fine machining', in *Proceedings of IEEE:MEMS'93* IEEE, Piscataway, NJ, USA, pp. 173–178 (1993).
9. X. Zhang, X.N. Jiang and C. Sun, 'Micro-stereolithography of polymeric and ceramic microstructures', *Sensors and Actuators: Physical*, **A77**, 149–156 (1999).
10. K. Ikuta, T. Ogata, M. Tsubio and S. Kojima, 'Development of mass productive micro stereo lithography (Mass-IH process)', in *Proceedings of IEEE: MEMS'96*, IEEE, Piscataway, NJ, USA, pp. 301–305 (1996).
11. P.F. Jacobs, *Stereolithography and Other RP&M Technologies: From Rapid Prototyping to Rapid Tooling*, American Society of Mechanical Engineers, New York, NY, USA (1996).
12. S. Zissi, A. Bertsch, J.Y. Jezequel, S. Corbel, J.C. Andre and D.J. Lougnot, 'Stereolithography and microtechnologies', *Microsystem Technologies*, **2**, 97–102 (1996).
13. A. Bertsch, S. Zissi, J.Y. Jezequel, S. Corbel and J.C. Andre, 'Microstereolithography using a liquid crystal display as dynamic mask-generator', *Microsystem Technologies*, **3**, 42–47 (1997).
14. T. Nakamoto and K. Yamaguchi, 'Consideration on the producing of high aspect ratio micro parts using UV sensitive photopolymer', in *Proceedings of the Seventh International Symposium on Micro Machine and Human Science*, IEEE, New York, USA, pp. 53–58 (1996).
15. S. Monneret, V. Loubere and S. Corbel, 'Microstereolithography using a dynamic mask generator and a non-coherent visible light source', *Proceedings of SPIE*, **3680**, 553–561 (1999).
16. L. Beluze, A. Bertsch and P. Renaud, 'Microstereolithography: a new process to build complex 3D objects', *Proceedings of SPIE*, **3680**, 808–817 (1999).
17. T. Katagi and N. Nakajima, 'Photoforming applied to fine machining', in *Proceedings of IEEE: MEMS'93*, IEEE, Piscataway, NJ, USA, pp. 173–178 (1993).
18. K. Ikuta, S. Maruo and S. Kojima, 'New micro stereo lithography for freely moved 3D micro structure – super IH process with submicron resolution', in *Proceedings of IEEE: MEMS'98*, IEEE, Piscataway, NJ, USA, pp. 290–295 (1998).
19. B.P. Wayne, *Principles and Applications of Photochemistry*, Oxford University Press, Oxford, UK (1988).
20. S. Maruo and S. Kawata, 'Two-photon-absorbed near-infrared photopolymerization for three-dimensional micro-fabrication', *Journal of Microelectromechanical Systems*, **7**, 411–415 (1998).
21. K. Suzumori, A. Koga and R. Haneda, 'Microfabrication of integrated FMs using stereo lithography', in *Proceedings of IEEE: MEMS'94*, IEEE, Piscataway, NJ, USA, pp. 136–141 (1994).
22. L. Weber, W. Ehrfeld, H. Freimuth, M. Lacher, H. Lehr and B. Pech, 'Micro molding – a powerful tool for the large scale production of precise microstructures', *Proceedings of SPIE*, **2879**, 156–167 (1996).
23. T. Hanemann, R. Ruprecht and J.H. HanBelt, 'Micromolding and photopolymerization', *Advanced Materials*, **9**, 927–929 (1997).
24. L. Lin, C.-J. Chiu, W. Bache and M. Heckele, 'Microfabrication using silicon mold insert and hot embossing', in *MHS'96, Proceedings of the Seventh International Symposium Micro Machine and Human Science*, IEEE, Piscataway, NJ, USA, pp. 67–71 (1996).
25. J. Akedo, M. Ichiki, K. Kikuchi and R. Maeda, 'Fabrication of three-dimensional micro structure composed of different materials using excimer laser ablation and jet molding', in *Proceedings of the IEEE: The Tenth Annual International Workshop on Micro electro Mechanical Systems*, IEEE, Piscataway, USA, pp. 135–140 (1997).
26. Y. Xia and G.M. Whitesides, 'Soft lithography', *Angewandte Chemie: International Edition*, **37**, 350–375, (1998).
27. X.-M. Zhao, Y. Xia and G.M. Whitesides, 'Fabrication of three-dimensional micro-structures: microtransfer molding', *Advanced Materials*, **8**, 837–840 (1996).
28. E. Kim, Y. Xia and G.M. Whitesides, 'Polymer microstructure formed by moulding in capillaries', *Nature (London)*, **376**, 581–584 (1995).
29. E. Kim, Y. Xia, X.-M. Zhao and G.M. Whitesides, 'Solvent-assisted microcontact molding: a convenient method for fabricating three-dimensional structures on surfaces of polymers', *Advanced Materials*, **9**, 651–654 (1997).
30. Y. Hirata, H. Okuyama, S. Ogino, T. Numazawa and H. Takada, 'Piezoelectric composites for micro-ultrasonic transducers realized with deep-etch X-ray lithography', in *Proceedings of IEEE: MEMS'95*, IEEE, Piscataway, NJ, USA, pp. 191–196 (1995).
31. S.N. Wang, J.-F. Li, R. Toda, R. Watanabe, K. Minami and M. Esashi, 'Novel processing of high aspect ratio 1–3 structures of high density PZT', in *Proceedings of IEEE: MEMS'98*, IEEE, Piscataway, NJ, USA, pp. 223–228 (1998).
32. W. Bacher, W. Menz and J. Mohr, 'The LIGA technique and its potential for microsystems — a survey', *IEEE Transactions: Industrial Electronics*, **42**, 431–441 (1995).
33. J. Elders, H.V. Jansen, M. Elwenspoek and W. Ehrfeld, 'DEEMO: a new technology for the fabrication of micro-structures', in *Proceedings of IEEE: MEMS'95*, IEEE, Piscataway, NJ, USA, pp. 238–243 (1995).
34. H. Freimuth, V. Hessel, H. Koelle, M. Lacher, W. Ehrfeld, T. Vaahs and M. Brueck, 'Formation of complex ceramic miniaturized structures by pyrolysis of poly(vinylsilazane)', *Journal of the American Ceramics Society*, **79**, 1457–1465 (1996).
35. V. Piotter, T. Benzler, T. Hanemann, H. Wollmer, R. Ruprecht and J. Hausselt, 'Innovative molding technologies

- for the fabrication of components for microsystems, *Proceedings of SPIE*, **3680**, 456–463 (1999).
36. Website: [http://potomac-laser.com/applications_micromold.htm].
 37. H. Becker and U. Heim, ‘Silicon as tool material for polymer hot embossing’, in *Proceedings of IEEE: MEMS’99*, IEEE, Piscataway, NJ, USA, pp. 228–231 (1999).
 38. O. Kemmann, C. Schaumburg and L. Webber, ‘Micro moulding behavior of engineering plastics’, *Proceedings of SPIE*, **3680**, 464–471, (1999).
 39. L. Weber, W. Ehrfeld, M. Begemann, U. Berg and F. Michel, ‘Fabrication of plastic microparts on wafer level’, *Proceedings of SPIE*, **3874**, 44–52 (1999).
 40. W.S. Beh, I.T. Kim, D. Qin, Y. Xia and G.M. Whitesides, ‘Formation of patterned microstructures of conducting polymers by soft lithography and applications in microelectronic device fabrication’, *Advanced Materials*, **11**, 1038–1041 (1999).
 41. J.M. English and M.G. Allen, ‘Wireless micromachined ceramic pressure sensors’, in *Proceedings of IEEE: MEMS’99*, IEEE, Piscataway, NJ, USA, pp. 511–516 (1999).
 42. A.H. Epstein, S.D. Senturia, G. Ananthasuresh, A. Ayon, K. Breuer, K.-S. Chen, F. Ehrich, G. Gauba, R. Ghodssi, C. Groshenry, S. Jacobson, J. Lang, C.-C. Mehra, J. Mur Miranda, S. Nagle, D. Orr, E. Piekos, M. Schmidt, G. Shirley, S. Spearing, C. Tan, Y.-S. Tseng and I. Waitz, ‘Power MEMS and ‘Power MEMS and microengines’, in *Proceedings of Transducers’97: International Conference on Solid State Sensors and Actuators*, Vol. 2(2), IEEE, Piscataway, NJ, USA, pp. 753–756 (1997).
 43. H.H. Bau, S.G.K. Ananthasuresh, J. J. Santiago-Aviles, J. Zhong, M. Kim, M. Yi, P. Espinoza-Vallejos and L. Sola-Laguna, ‘Ceramic tape-based meso systems technology’, in *Proceedings of the ASME International Mechanical Engineering Congress and Exposition on Micro-Electro-Mechanical Systems (MEMS)*, ASME, New York, NY, USA, pp. 491–498 (1998).
 44. D.L. Polla and L.F. Francis, ‘Ferroelectric thin films in microelectromechanical systems applications’, *MRS Bulletin*, **59**–65 (July 1996).
 45. V.K. Varadan, V.V. Varadan and S. Motojima, ‘Three-dimensional polymeric and ceramic MEMS and their applications’, *Proceedings of SPIE*, **2722**, 156–164 (1996).
 46. B.C. Mutusuddy and R.G. Ford, *Ceramic Injection Molding*, Chapman & Hall, London, UK (1995).
 47. R.M. German, and A. Bose, *Injection Molding of Metals and Ceramics*, Metal Powder Industries Federation, Princeton, NJ, USA (1997).
 48. R. Roy, D. Agrawal, J. Cheng and S. Gedevanishvili, ‘Full sintering of powdered-metal bodies in a microwave field’, *Nature (London)*, **399**, 668–670 (1999).
 49. W. Bartusch, P. Mehringer and G.A. Muller, ‘Microwave sintering – from the laboratory to industrial scale’, *Keramische Zeitschrift*, **50**, 810–817 (1998).
 50. X.N. Jiang, C. Sun, X. Zhang, B. Xu and T.H. Ye, ‘Micro-stereolithography of lead zirconate titanate thick film on silicon substrate’, *Sensors and Actuators: Physical*, **87A**, 72–77 (2000).
 51. X. Zhang, X.N. Jiang and C. Sun, ‘Micro-stereolithography for MEMS’, in *Proceedings of the ASME International Mechanical Engineering Congress and Exposition on Micro-Electro-Mechanical Systems (MEMS)*, ASME New York, NY USA, pp. 3–9 (1998).
 52. M.L. Griffith, and J.W. Halloran, ‘Stereolithography of ceramics’, in *Proceedings of the 27th International SAMPE Technical Conference*, SAMPE, Covina, CA, USA, pp. 970–979 (1995).
 53. T. Benzler, V. Piotter, T. Hanemann, K. Mueller, P. Norajitra, R. Ruprecht and J. Hausselt, ‘Innovations in molding technologies for microfabrication’, *Proceedings of SPIE*, **3874**, 53–60 (1999).
 54. J.D. Madden and I.W. Hunter, ‘Three-dimensional micro-fabrication by localized electrochemical deposition’, *Journal of Microelectromechanical Systems*, **5**, 24–32 (1996).
 55. A. Cohen, G. Zhang, F. Tseng, U. Frodis, F. Mansfeld and P. Will, ‘EFAB: rapid, low-cost desktop micromachining of high aspect ratio true 3-D MEMS’, in *Proceedings of IEEE: MEMS’99*, IEEE, Piscataway, NJ, USA, pp. 244–251 (1999).
 56. C.S. Taylor, P. Cherkas, H. Hampton, J.J. Frantzen, B.O. Shah, W.B. Tiffany, L. Nanis, P. Booker, A. Salahieh and R. Hansen, ‘A spatial forming – a three dimensional printing process’, in *Proceedings of IEEE: MEMS’94*, IEEE, Piscataway, NJ, USA, pp. 203–208 (1994).
 57. Y.P. Kathuria, ‘Rapid prototyping: an innovative technique for microfabrication of metallic parts’, in *Proceedings of the Seventh International Symposium on Micro Machine and Human Science*, IEEE, Piscataway, NJ, USA, pp. 59–65 (1996).
 58. J.B. Mohler and H.J. Sedusky, *Electroplating for the Metallurgist, Engineer and Chemist*, Chemical Publishing Co., Inc., New York (1951).
 59. W. Blum and G.B. Hogboom, *Principles of Electroplating and Electroforming*, McGraw-Hill, New York, NY, USA (1949).
 60. L.T. Romankiw, ‘A path from electroplating through lithographic masks in electronics to LIGA in MEMS’, *Electrochimica Acta*, **42**, 2985–3005 (1997).
 61. R.J. von Gutfeld and K.G. Sheppard, ‘Electrochemical microfabrication by laser-enhanced photothermal processes’, *IBM Journal of Research and Development*, **42**, 639–653 (1998).
 62. E.W. Becker, W. Ehrfeld, P. Hagmann, A. Maner and D. Muenschmeyer, ‘Fabrication of microstructures with high aspect ratios and great structural heights by synchrotron radiation lithography, galvoforming and plastic moulding (LIGA process)’, *Microelectronic Engineering*, **4**, 35–56 (1986).
 63. A.B. Frazier and M.G. Allen, ‘Metallic microstructures fabricated using photosensitive polyimide electroplating molds’, *Journal of Microelectromechanical Systems*, **2**, 87–94 (1993).
 64. J.-M. Quemper, S. Nicolas, J.P. Gilles, J.P. Grandchamp, A. Bosseboeuf, T. Bourouina and E. Dufour-Gergam, ‘Permal-

- loy electroplating through photoresist molds', *Sensors and Actuators: Physical*, **A74**, 1–4, (1999).
65. B. Loechel, A. Maciossek, H.J. Quenzer and B. Wagner, 'Ultraviolet depth lithography and galvoforming for micromachining', *Journal of Electrochemical Society*, **143**, 237–244 (1996).
66. Y. Konaka and M.G. Allen, 'Single- and multi-layer electroplated microaccelerometers', in *Proceedings of IEEE: MEMS'96*, IEEE, Piscataway, NJ, USA, pp. 168–173 (1996).
67. J.-B. Yoon, B.K. Kim, C.H. Han, E. Yoon and C.K. Kim, 'Surface micromachined solenoid on-Si and on-glass inductors for RF applications', *IEEE Electron Device Letters*, **20**, 487–489 (1999).
68. C.H. Ahn and M.G. Allen, 'Micromachined planar inductors on silicon wafers for MEMS applications', *IEEE Transactions : Industrial Electronics*, **45**, 866–876 (1998).
69. Q. Lin, K.G. Sheppard, K.G. M. Datta and L.T. Romankiw, 'Laser-enhanced electrodeposition of lead–tin solder', *Journal of the Electrochemical Society*, **139**, L62–L63 (1992).
70. M. Cabrera, A. Bertsch, J. Chassaing, J.Y. von Jezequel and J. C. Andre, 'Microphotofabrication of very small objects: pushing the limits of stereolithography', *Molecular Crystals and Liquid Crystals*, **315**, 223–234 (1998).
71. T. Takagi and N. Nakajima, 'Architecture combination by micro photoforming process', in *Proceedings of IEEE: MEMS'94*, IEEE, Piscataway, NJ, USA, pp. 211–216 (1994).
72. A. Bertsch, H. Lorenz and P. Renaud, 'Combining micro-stereolithography and thick resist UV lithography for 3D microfabrication', in *Proceedings of IEEE: MEMS'98*, IEEE, Piscataway, NJ, USA, pp. 18–23 (1998).
73. W.K. Schomburg, R. Ahrens, W. Bacher, C. Goll, S. Meinzer and A. Quinte, 'AMANDA – low-cost production of microfluidic devices', *Sensors and Actuators*, **A70**, 153–158 (1998).

Integration and Packaging of Smart Microsystems

12.1 INTEGRATION OF MEMS AND MICROELECTRONICS

The integration of an MEMS sensor with electronics has several advantages when dealing with small signals. The function of electronics is to make sure that the MEMS components operate correctly. The state-of-the-art in MEMS is combination with ICs, utilizing advanced packaging techniques to create a system-on-a-package (SOP) or a system-on-a-chip (SIP) [1]. However, in such cases it is important that the process used for MEMS fabrication does not adversely affect the electronics. MEMS devices can be fabricated as pre- or post-processing modules, which are integrated by standard processing steps. The choice of integration depends on the application and different aspects of its implementation technology. Various approaches for their integration with microelectronics are considered in this section.

In general, three possibilities exist for monolithic integration of CMOS and MEMS: (a) CMOS first, (b) MEMS in the middle, and (c) MEMS first [2,3]. In addition, a hybrid approach, known as a *multichip module* is also used often for such integration. Each of these methods has its own advantages and disadvantages. A comparison is listed in Table 12.1. It may be recalled that a number of materials, such as ceramics, are used in the fabrication of various MEMS, unlike in CMOS. Annealing of polysilicon or sintering of most ceramics generally require higher processing temperatures, often exceeding that allowed in CMOS. For example, at temperatures in excess of about 800 °C, aluminum metallizations may diffuse and cause performance degradation. Hence, if ceramic processing at a higher temperature is involved, it may be preferable to fabricate

the MEMS first. In contrast, if the MEMS involves delicate structures, several common CMOS processes, such as ‘lift off’, may degrade the MEMS performance. Hence, the choice of process sequence is highly dependent on the particular MEMS structure at hand.

12.1.1 CMOS first process

In this approach, first developed at UC Berkeley, the temperature limitation due to aluminum is eliminated by using tungsten as the conducting layer [4]. In this process, known as ‘modular integration of CMOS with microstructures’ (MICSs), CMOS circuits are first fabricated using conventional processes, and polysilicon microstructures are then fabricated on the top after passivating with SiN and using a phosphosilicate glass (PSG) sacrificial layer. Rapid thermal annealing (RTA) of polysilicon in nitrogen at 1000 °C for ‘stress relief’ does not affect the CMOS performance. A cross-sectional view of the device is shown in Figure 12.1. In an alternate approach, MEMS fabrication is limited to below 400 °C so that these steps do not adversely affect the CMOS fabricated first. Some examples of successful microsystems fabricated by this approach as listed in Table 12.2.

12.1.2 MEMS first process

In the method, MEMS structures are first fabricated on the silicon wafer [12,13]. The primary advantage is that higher processing temperature can be used to achieve better process optimization. In this process, developed at the Sandia National Laboratories, shallow trenches are first anisotropically etched on the wafer and the MEMS is

Publisher's Note:

Permission to reproduce this image online was not granted by the copyright holder. Readers are kindly requested to refer to the printed version of this chapter.

built within these trenches [14]. Silicon nitride and sacrificial oxide may be deposited within these trenches for the MEMS structures. A polysilicon layer on top of these layers helps establish contacts with the subsequent CMOS processing. Chemical-mechanical planarization (CMP) and high-temperature annealing are done to optimize this polysilicon layer. The sacrificial oxide covering the MEMS structure is removed after fabrication of the CMOS device. A photoresist is used as a protective layer during the release process. A cross-sectional view of a typical device fabricated with this process is shown in Figure 12.2. Some examples of successful microsystems fabricated by this approach are listed in Table 12.3.

12.1.3 Intermediate process

The simplest form of an integrated MEMS device is where the existing layers for fabricating the IC are used for the mechanical components in MEMS [17–19]. Standard microelectronics processes require a number of layers on top of the wafer, such as oxide, polysilicon, metal and nitride. Utilizing these layers in an MEMS requires only a few additional steps of masking and etching, as explained in Figure 12.3. Some examples of successful microsystems fabricated by this approach are listed in Table 12.4.

12.1.4 Multichip module

The incompatibilities in the fabrication processes of MEMS and ICs have made their monolithic integration difficult. Multichip module (MCM) packaging provides an efficient solution to integrate MEMS with microelectronic circuits as it supports a variety of die types in a common substrate without the need for resorting to significant changes in the fabrication process of either component. Several sensors, actuators or a combination can be combined in a single chip using the MCM technique [22]. Using this approach, both surface- and bulk-micromachined components may be integrated with the electronics. When using this approach, separate procedures are required for releasing and assembling the MEMS structures without degrading the package or other dies in the module.

Several variants of this approach exist: high-density interconnect (HDI), chip-on-flex (COF) and micro-module system (MMSs) MCM-D. These are compared in

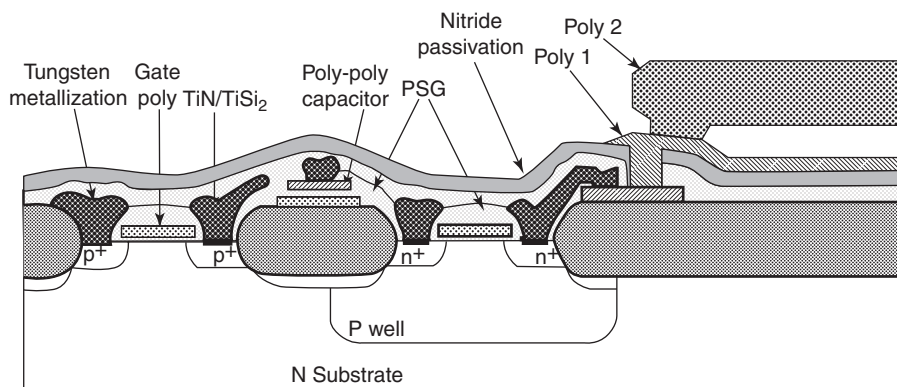


Figure 12.1 Cross-sectional view of a device fabricated with the MICS process [4]. W. Yun; Howe, R.T.; Gray, P.R., “Surface micromachined, digitally force-balanced accelerometer with integrated CMOS detection circuitry,” 5th Solid-State Sensor and Actuator Workshop, 1992. Technical Digest, © 1992 IEEE

Table 12.2 Examples of the *CMOS first* approach for the fabrication of microsystems [5].

Organization	Microsystem	Remarks	Reference
UC Berkeley	Micro-accelerometer	Tungsten metallization to increase temperature limit of CMOS; by MICS process	[4]
Texas Instruments	Digital micro-mirror	An array of aluminum micro-mirrors integrated over a static random access memory	[6]
University of Michigan/ Delphi Automotive Systems	Gyroscope	—	[7]
University of Bremen/Infineon	Acceleration switch	MEMS parts built by additive electroplating technology	[8]
Honeywell	Infrared thermal imager	SiN encapsulation of emitter for electrical isolation and mechanical support	[9]
Stanford University	Biosensor with disposable cartridges	A hybrid glass/PDMS/silicon chamber in a cell cartridge that includes fluidic interchanges, physiological sensors and environmental regulation	[10]
Austrian Micro Systems	Capacitive acceleration sensor	Wafer bonding of a polysilicon sensor wafer with a CMOS substrate	[11]

Table 12.5. In standard HDI process the dies are embedded in cavities milled on the base substrate and then a thin-film interconnecting layer is deposited on top of the components. Holes for the interconnecting vias are made by laser

ablation using a 350 nm argon ion laser. Physical access to the MEMS die is provided by an additional laser ablation step. Figure 12.4(a) shows a typical HDI process flow, compared with an augmented HDI process for MEMS

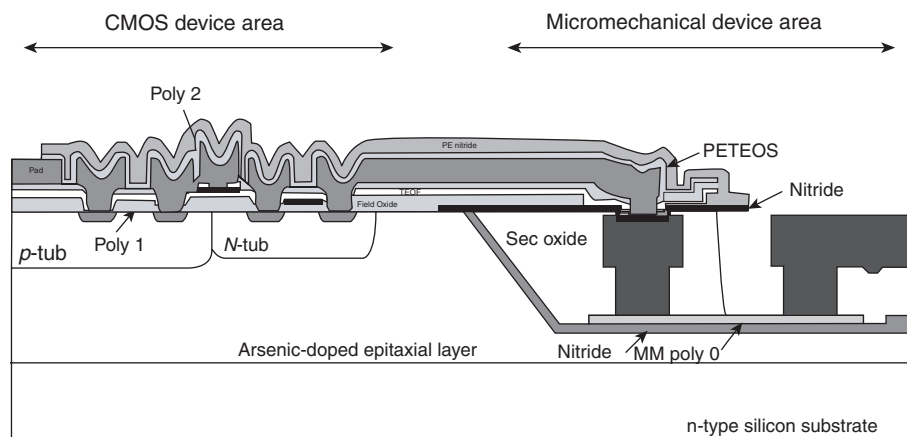


Figure 12.2 Cross-sectional view of a typical device fabricated with an MEMS – first fabrication process developed at the Sandia National Laboratories [14]. J.H. Smith, S. Montague, J.J. Snieowski, J.R. Murray, and P.J. McWhorter, “Embedded micromechanical devices for monolithic integration of MEMS with CMOS,” IEDM’95 Tech. Digest, © 1995 IEEE

Table 12.3 Examples of the *MEMS first* approach for the fabrication of microsystems [5].

Organization	Microsystem	Remarks	Reference
Sandia National Laboratories	—	Microstructures embedded below the CMOS by an integrated MEMS (iMEMS) process	[14]
Physical Electronics Laboratory, Zurich/Infineon	Trench-Hall device	Hard mask, consisting of SiO ₂ /SiN/SiO ₂ , is first deposited for etching trenches and a polysilicon layer for electrical shielding	[15]
Microsystems Technology Laboratory, MIT	Pressure sensor and angular rate sensor	Micromachined parts are added to the CMOS fabricated parts by wafer fusion bonding	[16]

packaging (Figure 12.4(b)) by an additional laser-ablation step to allow physical access to the MEMS die. The windows in the dielectric overlay above the MEMS device are selectively etched used laser ablation. COF is a lower-cost variant of HDI in which a molded plastic substrate replaces the ceramic.

In the MCM-D approach, the interconnected layers are deposited on the substrate and the dies are mounted above these. Interconnection between the dies and the packaging is done by wire bonding. Most of the common wet-etching techniques are not suitable for bulk micromachining of structures while following this approach. Hence, isotropic dry etching using XeF₂ can be used for selectively etching silicon. Wet etching using HF can, however, be used for releasing the surface-micromachined structure parts of this chip after shielding the bulk micromachined parts by a positive photoresist.

The main disadvantage of the MCM approach is the possibility for signal degradation due to parasitic effects between the components and the apparent added packaging expenses.

12.2 MEMS PACKAGING

Packaging is the science of establishing interconnections between the various subsystems and providing an appropriate operating environment for the electromechanical circuits to process the gathered information. The discipline of microelectromechanical systems (MEMS) was developed so closely with silicon processing that most of the early packaging technologies for MEMS were directly adapted from microelectronics. However, in contrast to the case of microelectronics, most MEMS devices need a physical access to the outside world,

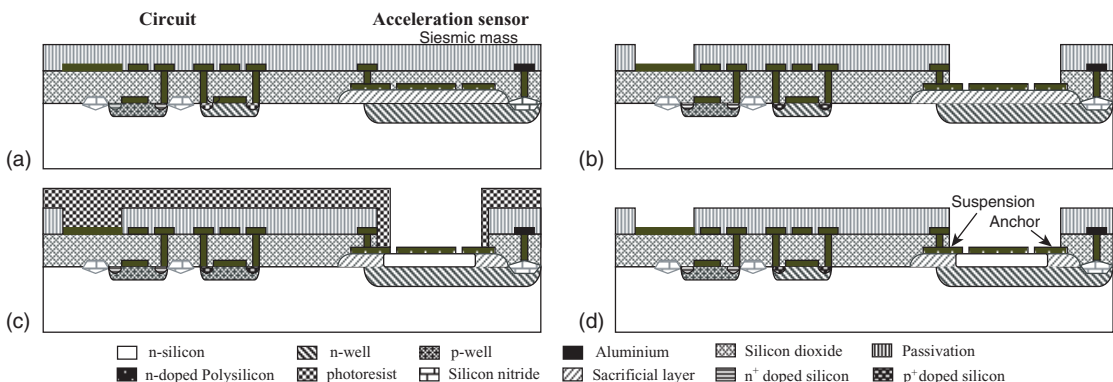


Figure 12.3 Integration of surface micromachining with CMOS [17]. Hierold, C., Hildebrandt, A., Naher, U., Scheiter, T., Mensching, B., Steger, M., Tielert, R. “A pure CMOS surface micromachined integrated accelerometer,” The 9th Annual Int'l Workshop on Micro Electro Mechanical Systems, 1996, MEMS '96, Proceedings. IEEE, 11–15 Feb, © 1996 IEEE

Table 12.4 Examples of the *intermediate* approach for the fabrication of microsystems [5].

Organization	Microsystem	Reference
Analog Devices	Accelerometer	[20]
Infineon	Pressure sensor	[21]

either to mechanically react with an external parameter or to sense a physical variable. In state-of-the art microelectronics, the device normally accesses the outside world via electrical connections alone and the systems are totally sealed and isolated. Therefore, unlike electronic packaging, where a standard package can be used for a variety of applications, MEMS packages tend to be customized.

Challenges in the design of packaging depend on the overall complexity of the ultimate application of the device. However, there are no sharp boundaries between these classes. The size of the package, choice of its shape and material, alignment of the device, mounting for the isolation of shock and vibration and sealing are some of the many concerns in MEMS packaging. Considerations in packaging may be different, depending on whether the device is used as an MOEMS, RF MEMS or simpler sensors or actuators. Furthermore, special considerations, such as biocompatibility, may have to be examined when designing the packaging of a system. Many important lessons that have been learned throughout years of

Table 12.5 A comparison of various MCM technologies [22]. Butler J.T., Bright V.M., Chu P.B. and Saia R.J., Adapting Multichip module foundries for MEMS packaging, Proc of IEEE International Conf on Multichip modules and High density Packaging, © 1998 IEEE

Property	MCM-D	HDI
Substrate	Aluminum	Alumina
Dielectric material	Polyimide	Kapton
Conductor metallization	Copper	Ti/Cu/Ti
Die-interconnection method	Wire bond	Direct metallization
Maximum operating frequency	100–400 MHz	>1 GHz
Requirement for process modifications	None	Additional laser ablation required for open access to MEMS dies.

experience in the microelectronics industry could be adapted to the packaging of MEMS devices.

In MEMS, mechanical structures and electrical components are combined to form a functional system. While packaging, these electrical and mechanical components are interconnected and the electrical inputs are interfaced with external circuits. MEMS components can be extremely fragile and must be protected from mechanical damage and hostile environments. This section presents the fundamentals of microelectronic packaging adapted for MEMS technology.

12.2.1 Objectives in packaging

The objective of packaging is to integrate all components of a system such that cost, mass and complexity are minimized. The MEMS package should protect the device, while at the same time letting it perform its intended functions with less attenuation of signal in a given environment [23,24]. Packaging is an expensive process since it seeks to protect relatively fragile structures integrated into the device. For a standard integrated circuit, the packaging process may take up to 95 % of the total manufacturing cost. Issues in MEMS packaging are more difficult to solve due to stringent requirements in processing and handling and the diversity and fragile nature of the microstructures.

MEMS packages provide a mechanical support, an electrical interface to the other system components and protection from the environment. In addition, packages should also provide an interface between the system and the physical world. Many of the MEMS sensors often require an interface between the sensing media and the sensing area. For example, a pressure-sensor packaging requires incorporation of a pressure port to transmit fluid pressure to the sensor. This makes the major difference between the standard semiconductor device packages and the MEMS packages.

12.2.1.1 Mechanical support

Once the MEMS devices are wire-bonded and other electrical connections are made, the assembly must be protected by covering the base or by encapsulating the assembly in plastic or ceramic materials and the electrical connections are usually made through its walls. If the packaging creates excessive stress in the sensing structure, it can cause a change in device performance. Managing package-induced stress in the device becomes important for MEMS package design. With most MEMS being mechanical systems, protection and isolation of such

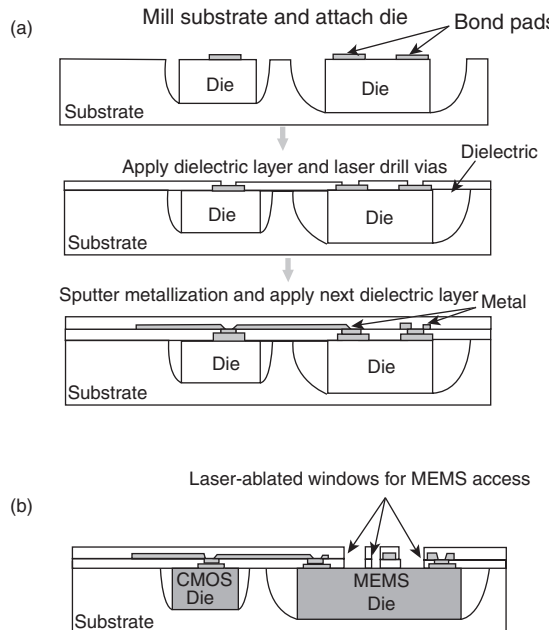


Figure 12.4 (a) HDI process; (b) MEMS access in the HDI process [22]. Butler J.T., Bright V.M., Chu P.B. and Saia R.J., Adapting Multichip module foundries for MEMS packaging, Proc of IEEE International Conf on Multichip modules and High density Packaging, © 1998 IEEE

devices from thermal and mechanical shock, vibration, acceleration and other physical damages during their operation is critical to their performance. The mechanical stress affecting a system depends on the application. For example, the device package for a military aircraft is different from those used in communication satellites. The coefficient of thermal expansion of the package material should be equal to that of silicon for reliability because the thermal cycle may cause cracking or delamination if they are unmatched.

12.2.1.2 Electrical interface

The connection between the MEMS and the signal lines is usually made with wire bonds or flip-chip die attachments and multilayer interconnections. Wire bonds and other electrical connections to the device should be made with care taken to protect the device from scratches and other physical damages. DC and RF signals to the MEMS systems are given through these connections and interfaces. In addition, these packages should be able to distribute signals to all components within the package. Examples of the external interfaces required

when packaging various types of devices are shown in Table 12.6.

12.2.1.3 Protection from environment

Many of the MEMS devices and sensors are designed to measure variables from the surrounding environment. MEMS packages must protect the micromachined parts from the environment and at the same time it must provide interconnections to electrical signals, as well as access to and interaction with the external environment. The hermetic packaging generally useful in microelectronic devices is not suitable in such MEMS devices. These devices might be integrated with the circuits or mounted on a circuit board. Special attention in packaging can protect a micromachined device from aggressive surroundings and mechanical damage. Elements that cause corrosion or physical damage to the metal lines as well as other components, such as moisture, remain a concern for many MEMS devices. Moisture may be introduced into the package during fabrication and before sealing can damage the materials. For example, aluminum lines can corrode quickly in the presence of moisture. Junctions of dissimilar metals can also corrode in the presence of moisture.

Hermetic MEMS packages provide good barriers to liquids and gases. In hermetic packages, the electrical interconnections through a package must confirm hermetic sealing. Wire bonding is the popular technique to electrically connect the die to the package. Bonding of gold wires is easier than bonding aluminum wires. The use of wire bonding has serious limitations in MEMS packaging due to the application of ultrasonic energy at

Table 12.6 External interfaces required when packaging various types of devices.

Device	Electrical interface	Non-electrical interface
Microelectronics	Input/ Output	—
MEMS sensors	Output	Fluid channels (gas/liquid) Physical contact (pressure/temperature) None (navigational)
MEMS actuators	Control	Fluid channels (micro pump)
RF-MEMS	Control	RF cables/connectors
MOEMS	Control	Optical fibers/couplers

a frequency between 50 to 100 kHz as these frequencies may stimulate oscillations by the microstructures. Since most microstructures have resonant frequencies in the same range, the chance of structural failure during the wire bonding is high [25].

In most spaceborne applications, parts are hermetically sealed due to the perceived increase in reliability and to minimize the outgassing. When epoxies or cyanate esters are used to attach the die, they outgas while curing. Outgassing is a concern for many devices since these particles could be deposited on the components, hence degrading their performance. This leads to ‘stiction’ and corrosion of the device. Die-attachment materials with a low Young’s modulus allow the chip to move during the ultrasonic wire bonding, so resulting in low bond strength.

12.2.1.4 Thermal considerations

MEMS devices used for present-day applications do not have a high-power-dissipation requirement. The thermal dissipation from MEMS devices is not a serious problem since the temperature of the MEMS devices usually does not increase substantially during operation. However, as the integration of MEMS with other high-power devices, such as amplifiers, in a single package increases, the need for heat dissipation arises to ensure proper operations of these devices. Thus, thermal management is an important consideration in package design.

Heat-transfer analysis and thermal management become more complex by packaging different functional components into a tight space. This miniaturization also raises issues such as coupling between the system configurations and the overall heat dissipation to the environment. The configuration of the system shell becomes important for heat dissipation from the system to the environment [26,27]. Heat spreading in the thin space is one of the most important modes of heat transfer in compact electronic equipment and microsystems. As the system shrinks, the space available for installation of a fan or pump inside the system shell disappears and the generated heat has to be dissipated through the shell to the surrounding environment. In general, the primary motives in heat-transfer design are to diffuse heat as rapidly as possible and to maximize the heat dissipation from the system shell to the environment.

12.2.2 Special issues in MEMS packaging

Although it follows a similar path as microelectronics packaging, the design of MEMS packages does need to

address several unique challenges. Some of these, as well as their typical solutions, are described in the following paragraphs.

12.2.2.1 Release of structures

During the fabrication of MEMS polysilicon structures by surface micromachining techniques, these are protected against damage or contamination by silicon dioxide layers. In order to release these polysilicon structures, the oxide layers should be etched out, often by HF solution. The issue here is the timing of this release etch, vis-à-vis the packaging. If this is done before the start of packaging, it may weaken the structure, but if done during or after packaging, there is scope for contamination and incompatibility issues. Another associated risk is stiction – a phenomenon by which microstructures tend to stick to one another after release. This is caused by capillary action of the droplets of the rinse solutions used after etching and may be reduced by incorporating ‘dimples’ into the structures. Other solutions, such as freeze drying and critical CO₂ drying, are also useful to reduce stiction after release. To further reduce the possibilities of stiction during the lifetime of the device, non-stick dielectric films may be inserted during the fabrication process.

12.2.2.2 Die separation

‘Dicing’ is a common process used in microelectronics fabrication for separating mass-produced devices. The current standard die-separation method adopted for silicon is to cut the wafer by using a diamond-impregnated blade. The blade and the wafer are ‘flooded’ with high-purity water while the blade spins at 45 000 rpm. This creates no problem for standard ICs because the surface is essentially sealed to the effects of water and silicon dust. However, if a released MEMS device is exposed to water and debris, the structures may break off or get clogged and the moisture may adversely affect their performance. Efforts to protect these surfaces with photoresist and other coatings have provided only limited success. Another possibility is to delay the release of the structures to until after the dicing. An alternate process called wafer cleaving, used in III–IV semiconductor lasers, may also be useful in MEMS die separation [3].

12.2.2.3 Die handling

During automated processes, vacuum pick-up heads are commonly used in handling the die in microelectronics.

As these may not be used for MEMS devices, due to the presence of delicate structures, additional clamp attachments are required to handle the MEMS die, possibly by their edges. However, the requirement for this special equipment may be eliminated by wafer level encapsulation. In this approach, a capping wafer is used during dicing, such that each MEMS chip has a protective chip attached to it. These wafers are bonded by using direct binding or anodic bonding. However, the additional process steps required may cause an increase in the cost of the device.

12.2.2.4 Interfacial stress

Thermal annealing is required for MEMS structures fabricated with polysilicon. There are several other processes during packaging of the device (such as the use of hard solders for die attachments, package lid sealing, etc.) that may introduce additional thermal stress. The application of high temperatures for these purposes on a complex structure, such as MEMS involving several materials with varying coefficients of thermal expansion (CTEs) may result in device deformation, misalignment of parts, change in the resonant frequencies of the structures and ‘buckle’ in long beam elements. Lower-moduli die-attach materials may solve these problems to a limited extent but may introduce additional complications, such as ‘creep over time’ [3]. They may also allow the chip to move during wire bonding, so resulting in low bond strength.

12.2.2.5 Control of outgassing

Many die-attachment materials outgas during their curing. These vapors and moisture may deposit on structures and cause stiction or corrosion and may result in degradation of performance. The solution may include using low-outgassing materials and/or the removal of outgassing vapors during the die-attachment curing process.

12.2.3 Types of MEMS packages

Although MEMS represent a relatively new topic, the methods of packaging of very small mechanical devices are not new. For example, the aerospace and watch industries have been performing this task for a very long time. However, MEMS applications usually require specialized package designs, depending on the application and optimization procedures. In general, the possible group of packages for MEMS can be categorized into metal, ceramic, plastic and multilayer packages.

12.2.3.1 Metal packages

Metal packages are often used in MMIC and hybrid circuits due to their thermal dissipation and electromagnetic shielding effectiveness. In addition, these packages are sufficiently rugged, especially for larger devices. Hence, these are also often preferred for MEMS applications. Materials like CuW (10/90), SilverTM (Ni–Fe alloy), CuMo (15/85) and CuW (15/85) are good thermal conductors and have higher coefficients of thermal expansion (CTEs) than silicon.

A ‘baking’ step is performed before the final assembly in order to remove trapped gas and moisture, thus reducing the possibility of corrosion. Au–Sn solders are preferred since these are especially suited when joining dissimilar materials. An alternate method is to use welding by localized heating methods, such as by the use of lasers. The primary limitation of these packages is the presence of the glass or ceramic ‘feedthroughs’, as these may be brittle if not handled properly.

12.2.3.2 Ceramic packages

Ceramic packaging is one of the most common types used in the microelectronics industry, due to its features such as low mass, low cost and easy mass production. The ceramic packages can be made hermetic, adapted to multilayer designs and be easily integrated for the signal ‘feedthrough’ lines. Multilayer packages reduce the size and cost of integration of multiple MEMS into a single package. The electrical performances of the packages can be tailored by incorporating multilayer ceramics and ‘interconnect’ lines.

Co-fired multilayered ceramic packages are constructed from individual ‘green’ pieces of thin films. Metal lines are deposited in each film by thick-film processing, such as screen printing, and via holes for the interconnections to be drilled. The unfired layers are then stacked and aligned and laminated together by firing at high temperatures. MEMS and the necessary components are then attached using epoxy or solders and wire bonds are made.

There are several problems associated with the ceramic packaging. The ‘green state’ shrinks during the firing process and the amount of shrinkage depends on the number of via holes (and hence may be different in each layer.) The ceramic-to-metal adhesion is not as strong as the ceramic-to-ceramic adhesion. The processing temperatures of ceramics limit the choice of metal lines as the metal may react with ceramics at high temperatures. In such cases, metals used are W and Mo are employed but if low-temperature ‘co-fired’ ceramics (LTCCs) are

used, the most frequently used metal lines are Ag, Au and Au-Pt.

12.2.3.3 Thin-film multilayer packages

This method of packaging uses layers of thin films of polyimide instead of the ceramics described above. These, having lower dielectric constants result in lower line capacitances (faster circuits) and less line-to-line couplings (miniaturization). These packages may be put together by individually processing thick (25 μm) polyimide sheets or by spin-coating polyimide thin films on a substrate and processing the interconnecting metal layers.

12.2.3.4 Plastic packages

Plastic packages are common in the electronic industry because of their low manufacturing cost. However, the hermetic seals, generally required for high reliability, are not possible when using plastic packages. Plastic packages are also susceptible to cracking during temperature cycling.

12.3 PACKAGING TECHNIQUES

Each MEMS device may have its own packaging methods, which may be absolutely suitable for its functioning. The type of packaging should be decided at the very beginning of the device development.

12.3.1 Flip-chip assembly

'Flip-chip' is the most favored assembly technology for high-frequency applications because the short-bump interconnections can reduce parasitics. In flip chips, the IC die is placed on a circuit board with the bond pads facing down and directly joining the bare die with the substrate. The bumps form electrical contacts as well as mechanical joints to the die. This reduces the electrical pathlength and the associated capacitance and inductance, which is particularly suited for high-density RF applications. The minimization of the parasitic capacitance and inductance can reduce the signal delay in high-speed circuits. The technology was developed by IBM during the 1960s and was termed as 'controlled collapse chip connection' (C4).

Flip-chip bonding involves the bonding of die, top-face down on a package substrate. Electrical connections are made by means of plated solder bumps between the

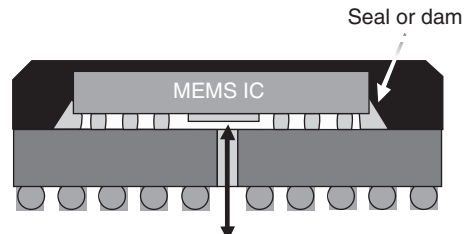


Figure 12.5 Flip-chip MEMS package [29]. S.J. Kim, Kwon Y.S., and Lee H.Y., "Silicon MEMS packages for coplanar MMICs," Proc of 2000 Asia-Pacific Microwave Conf., Australia, © 2000 IEEE

bond pads on the die and metal pads on the substrate [28]. The attachment is intimately associated with relatively small spacing ($\sim 100 \mu\text{m}$) between the die and the substrate. In flip-chip assemblies, the bumps serve as electrical contacts to the substrate, as well as to the mechanical joints.

Figure 12.5 shows the flip-chip design of a MEMS package. Since the active surface of the MEMS is placed towards the substrate, the cavity will protect the movable elements of the MEMS. The stand-off distance can be accurately controlled by the bump height. Flip-chip technology is therefore a very flexible assembly method suitable for several applications. Figure 12.6(a) presents the flip-chip bonding process on a ceramic substrate, such as alumina. The bump with an acute tail makes it easy to deform, so making the bonding area more stable under thermal conditions. However, another consideration in deciding the bump height is that taller bumps

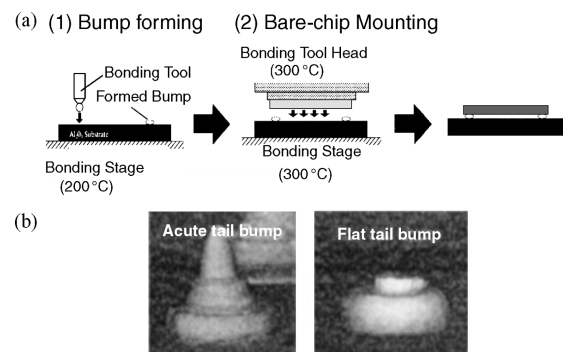


Figure 12.6 (a) Flip-chip bonding procedure; (b) photographs of acute and flat-tail bumps used for flip-chip bonding [30]. H. Kusamitsu, Morishita Y., Marushashi K., Ito M. and Ohata K., "The flip-chip bump interconnection for millimeter wave GaAs MMIC," IEEE Trans on Electronics Packaging and Manuf., vol. 22, © 1999 IEEE

introduce additional series inductances which degrade high-frequency performance.

Flip-chip bonding is attractive to the MEMS industry because of its ability to closely package a number of dies on a single package with multiple levels of electrical traces. A similar system can be built with wire bonding, but it may require a larger area and raise the reliability issues due to the number of gold wires within the package. The process is self-aligning, since the wetting action of the solder align the chip's bump to the substrate pads and compensates for slight misalignment between them. Another feature of this process is that it allows removal or replacement without scrapping the components. However flip-chip packaging may not be compatible for MEMS with microstructures that should be exposed to the open environment.

Figure 12.7 shows the cross-sectional view of the three dimensional multilayered packaging for MEMS structures on a silicon substrate. Passive elements, such as filters and matching circuits, are formed in each layer (on GaAs) and active devices (on Si) are assembled on the top layer using flip-chip technology. The structure is a three-dimensional hybrid IC using silicon, which is more cost effective than GaAs.

The primary advantages of this process are [31]:

- Size and weight reduction.
- Applicability for existing chip designs.
- Performance enhancement and increased production.
- Feasibility for chip replacement.

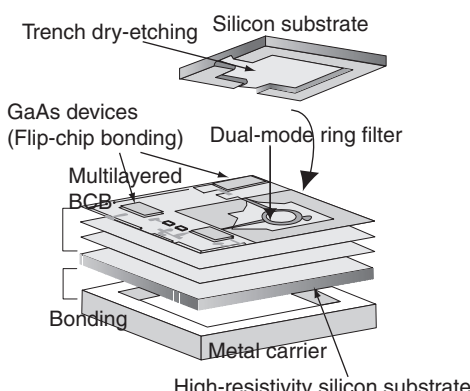


Figure 12.7 Three-dimensional millimeter wave MEMS IC [32]. K. Takahashi, Sangawa U., Fujita S., Matsuo M., Urabe T., Ogura H. and Y. ubuki H., "Packaging using Microelectromechanical technologies and planar components," IEEE Trans on Microwave Theory and Tech., vol. 49, © 2001 IEEE

- Increased I/O capability, extendable for RF and optical interfaces.

The reliability of this scheme depends on the difference in the coefficients of thermal expansion of the substrate and the chip which may introduce thermal and mechanical stresses on the bumps.

12.3.2 Ball-grid array

The ball-grid array (BGA) is a surface-mounted chip package containing a grid of solder balls for interconnections. This approach leads to small size, high 'lead count' (due to this being surface mounted) and low 'parasitic' inductance. Both ceramic and plastic variants are available. A miniaturized version, known as the *micro-ball-grid array* (μ BGA) results in package sizes very close to the die size. In this scheme, a flexible circuit tape is used as the substrate and a low-stress elastomer for the die attachment. The die is mounted face-down and the electrical connections are made by bonding. The leads are encapsulated with epoxy for protection.

12.3.3 Embedded overlay

An embedded overlay [33] concept for MEMS packaging is derived from the chip-on-flex (COF) process widely used for microelectronics packaging. COF is a high-performance multichip packaging technology in which the dies are encased in a molded plastic substrate and interconnections are made by using a thin-film structure formed over these components. The electrical interconnections are made through a patterned overlay with the die embedded in a plastic substrate, as shown in Figure 12.8. The chips are attached face-down on the COF overlay using polyimide or thermoplastic adhesives. The substrate is formed after bonding the chips around the components by using a plastic mold-forming process, such as transfer, compression or injection molding. The electrical connections are made by drilling via

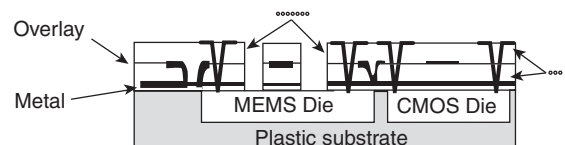


Figure 12.8 COF MEMS packaging concept [33]. J.T. Butler and V.M. Bright, "An embedded overlay concept for Microsystems Packaging," IEEE Trans on advanced Packaging, vol. 23, © 2000 IEEE

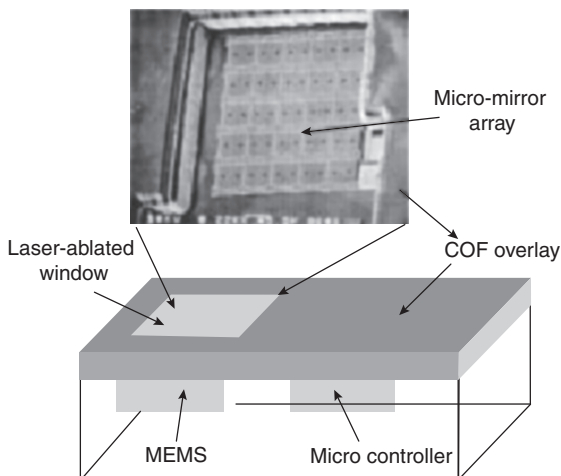


Figure 12.9 COF MEMS package of a 5×5 array of micro-mirrors [33]. J.T. Butler and V.M. Bright, “An embedded overlay concept for Microsystems Packaging,” IEEE Trans on advanced Packaging, vol. 23, © 2000 IEEE

holes, using a continuous argon ion laser at 350 nm. Ti/Cu metallization is sputtered and patterned to form the electrical interconnections. The use of varying laser ablation power levels, with plasma cleaning and high-pressure water scrubs, provides an effective means of removing the COF overlay without damaging the embedded MEMS device. Figure 12.9 shows a 5×5 array of micro-mirrors packaged in COF/MEMS modules with integrated control circuitry.

12.3.4 Wafer-level packaging

A cost-efficient method for MEMS packaging is by wafer-level packaging [34,35]. Designing the packaging schemes and incorporating these into the device-manufacturing process itself can reduce the overall cost. Versatile packaging may be needed for many devices in which MEMS and microelectronics are on a single chip. Since MEMS devices have movable structures built on the surface of the wafer, the addition of a ‘cap’ wafer on the silicon substrate enables their use in many applications. The cap provides protection against handling damage, as well as avoiding atmospheric damping. This is done by bonding the substrate with an active device to a second wafer, which need not be of the same material as the substrate. The bonding is done by using a glass frit or by an anodic bond created by an electrical potential. Precision-aligned wafer bonding is the key

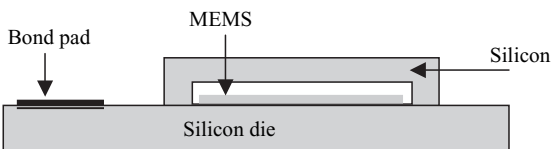


Figure 12.10 Silicon wafer-level packaging of an MEMS. K. Gelleo, “MEMS Packaging issues and materials,” Proc of IEEE Int Symp on Advanced Packaging: Process, Properties and Interfaces, © 2001 IEEE

technology for high-volume, low cost packaging of MEMS devices [36,37]. State-of-the art silicon wafer bonding can provide assembly level packaging solutions for many MEMS devices.

The wafer-level package, which protects the device at the wafer stage itself, is a clear choice to make in the product-design stage. This involves an extra fabrication process, where a micromachined wafer has to be bonded to a second wafer with appropriate cavities etched on it. Figure 12.10 shows a schematic diagram of a device after wafer-level packaging. This approach enables the MEMS device to move freely in vacuum or an inert atmosphere with hermetic bonding which prevents any contamination of the structure. Etching cavities in a blank silicon wafer and bonding it with the substrate by placing over the device can make a hermetic seal.

Cavities are formed by any of the etching methods. Anisotropic wet etching of bulk silicon along certain crystal planes by using strong alkaline solutions such as KOH can create thin diaphragms, through-wafers via holes and V-grooves with typical masking layers like silicon dioxide or LPCVD silicon nitride. The fastest etch rates for the silicon are for the (100) and (110) crystal planes while the slowest is for the (111) plane. Examples of successful development and packaging using silicon micromachining are ink-jet heads and silicon piezoresistive pressure sensors for automotive and industrial control applications. Many of these devices require silicon wafer bonding to another substrate as a ‘first-level’ packaging solution. Anodic (electrostatic) bonding of silicon to glass, low-temperature glass-frit bonding of silicon to silicon, silicon direct-wafer bonding and, eutectic bonding epoxy bonding are examples of the few methods available to bond a silicon wafer to another silicon entity.

Another concept in wafer-level packaging is to apply a *microcap* to the device and then package with a standard procedure. However, conventional wafer bondings like line-fusion or anodic bonding cannot be employed because the micromechanical circuits can be damaged due to high temperatures or high electric fields. Low-temperature

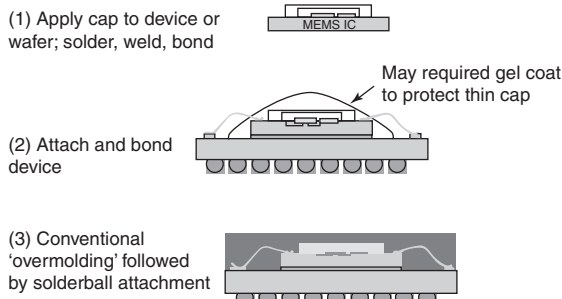


Figure 12.11 Cap-on-chip packaging [38].

bonding techniques may increase the cost of packaging. If MEMS devices can be packaged at the device level first, then the remaining packaging can be done the same as IC packaging by using common procedures. Figure 12.11 shows the concept of cap-on-chip packaging for MEMS.

Microscale riveting [39,40] or *eutectic bonding* [41] can be performed by directional etching of silicon for the rivet molds and directional electroplating in an electric field for rivet formation. The wafer joining can be done at room temperature and with low voltages. The protected devices after micro riveting can be treated the same as for IC wafers during the dicing process. Once the joining is complete, the resulting chips can be handled in the same way as IC chips during the remaining packaging steps, such as wire-bonding and molding for plastic packages.

Figure 12.12 shows the concept of a protected chip with an MEMS device. Rivets are formed all around the

cap wafer, thereby holding the cap-base pair together. Figure 12.13 shows the prepared cap and base wafers and the electroplating set-up. Nickel can be easily electroplated as a rivet material. A 'seed' layer of 125 Å Cr and 750 Å of Ni is deposited on the surface of the base wafer by thermal evaporation. The cap and the base wafers are held together during the plating process so that the plating can start at the exposed area of the seed layer, grow through the rivet hole in the cap wafer and form the rivet. Simple mechanical clamping of the wafer together in the electrolyte is sufficient to rivet them together since electroplating does not occur in the microscopic wafer gap.

In *fusion bonding*, polysilicon is deposited and patterned as the heating and bonding material. Fusion bonding is mostly used in silicon-on-insulator (SOI) technology, such as Si-SiO₂ [42–44] and silicon bonding [45]. Aluminum-to-glass [46] bonding using localized heating can be applied for hermetic packaging. In eutectic bonding, gold resistive heaters are sputtered and used as the heating and bonding materials. The temperature of the micro-heater rises upon the flow of current, which activates the bonding process. The principle of the localized bonding is shown in Figure 12.14. The effectiveness of the micro-heater depends on the selection of materials and design of the geometrical shape of the structure. For example, a high temperature of 1000 °C can be created by using micro-heaters, while the temperature less than 2 µm away can drop to 100 °C [26]. Figure 12.14(b) shows the experimental set-up for the localized eutectic bonding. This set-up can be used for silicon–gold as well as for silicon–glass eutectic bonding. The conventional bonding takes 1 h to reach the temperature while localized eutectic heating will take only less than 5 min. A summary of the various bonding process conditions is provided in Table 12.7.

Phosphorous-doped polysilicon and gold resistive heaters are used in silicon-to-glass fusion and silicon-to-gold eutectic bonding process, respectively. Both processes can be completed in less than 5 min.

The aligned wafer-bonding process typically consists of two separate steps. The wafers are aligned initially to each other in a bond aligner. This system can align a mask to a wafer for conventional photolithography, as well as it can align two wafers to each other. The aligned wafers are clamped with an appropriate separation gap between them in a bond fixture. The next step is to load the bond fixture into a vacuum-bond chamber where the wafers are contacted together. Some of the common methods of wafer bonding are compared in Table 12.8.

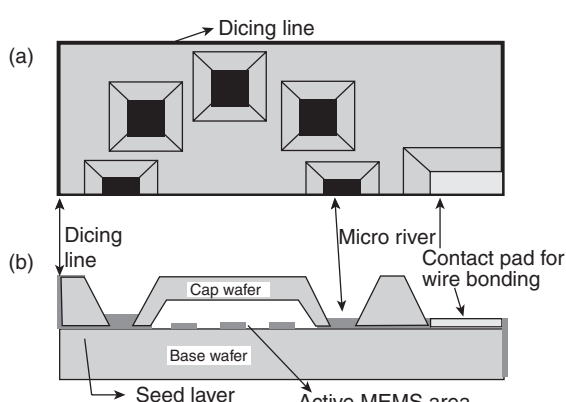


Figure 12.12 Views of a packaged chip using micro rivets: (a) top (showing half the die); (b) cross-section [39]. B. Shivkumar and C.J. Kim, "Microrivets for MEMS packaging: Concept, fabrication and strength testing," J. Microelectromechanical Systems, vol. 6, © 1997 IEEE

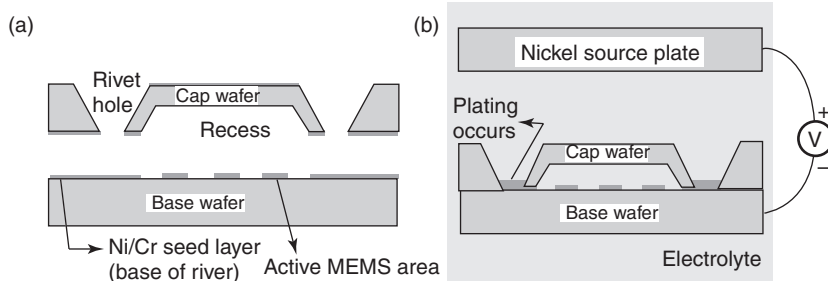


Figure 12.13 Schematics of (a) the prepared cap and (b) the electroplating set-up [39]. B. Shivkumar and C.J. Kim, “Microrivets for MEMS packaging: Concept, fabrication and strength testing,” J. Microelectromechanical Systems, vol. 6, © 1997 IEEE

Micromachining technology has proved to be a flexible approach for the development of small-sized components as well as micropackages that provide self-packaging [12] of individual components. The upper wafer has an air-filled cavity that is mounted over the metallic conductors. Integration of both of the upper and lower shielded circuits results in a *self-packaged device*.

12.4 RELIABILITY AND KEY FAILURE MECHANISMS

As with any other commercial system, extensive studies have been done on the reliability and mechanisms of failure of various MEMS components. Reliability requirements for MEMS are significantly different for various applications, especially in systems with unique MEMS devices. Hence, standard reliability testing is not

possible until a common set of reliability requirements are developed. The chain of events that establishes the reliability of an MEMS package is described in Table 12.9

An understanding of the reliability of the systems comes from a knowledge of their failure behaviors and failure mechanisms. The common failure mechanisms of MEMS devices are summarized as follows.

Stiction and wear. These cause most of the failures of MEMS devices. Stiction occurs due to microscopic adhesion when two surfaces come into contact. This adhesion is caused by van der Waals forces, resulting from the interaction of instantaneous dipole moments of the atom. To reduce stiction, various dielectric thin-film materials are often inserted between these surfaces.

Wear occurs due to the movement of one surface over another, and is defined as the removal of material from a solid surface by some kind of mechanical action. The primary mechanisms of wear in MEMS devices are

completed in less than 5 minutes.

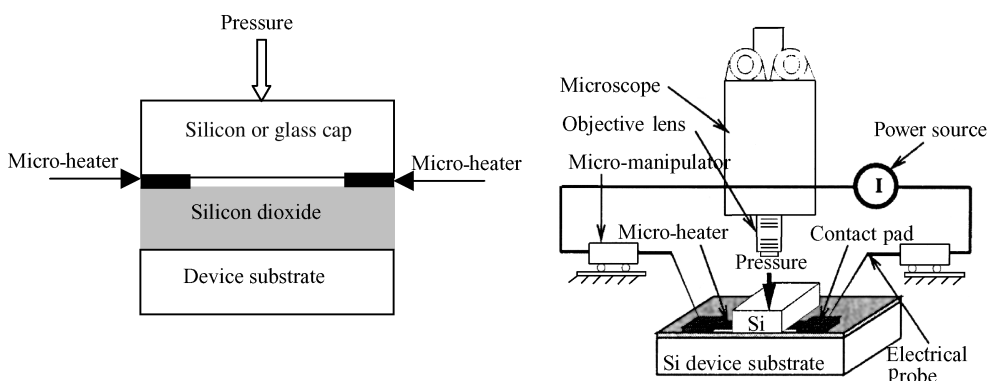


Figure 12.14 Schematics of (a) the micro-heater locations and (b) the experimental set-up for the localized heating and bonding test [26]. L. Lin, “MEMS post-packaging by localized heating and bonding,” IEEE Trans Advanced Packaging, vol. 23, © 2000 IEEE

Table 12.7 Typical process conditions for anodic, glass frit and silicon direct-wafer-bonding (DWB) (adapted from Mirza and Ayon [47]).^a

Parameter	Anodic	Glass frit	DWB
Temperature	300–500	400–500	1000
Pressure (bar)	N/A	1	N/A
Voltage (V)	0.1–1 kV	N/A	N/A
Surface roughness (nm)	20	N/A	0.5
Precise gap	Yes	No	Yes
Hermetic seal	Yes	Yes	Yes
Vacuum level during bonding (torr)	10^{-5}	10	10^{-3}

^aN/A, not available.

adhesion (one surface pulling sections of another, due to surface bonding), abrasion, corrosion and surface fatigue. Corrosion is caused by one or more of the following:

- Moisture ingress
- Loss of hermeticity
- Galvanic corrosion
- Crevice corrosion
- Pitting corrosion
- Surface oxidation
- Stress corrosion
- Corrosion resulting from contaminants or micro-organisms

Table 12.8 Comparison of wafer-bonding schemes [26]. L. Lin, “MEMS post-packaging by localized heating and bonding,” IEEE Trans Advanced Packaging, vol. 23, 4, © 2000 IEEE

Type	Bonding temperature	Sensitivity to roughness	Hermeticity
Fusion bonding	Very high	High	Yes
Anodic bonding	Medium	High	Yes
Epoxy bonding	Low	Low	No
Integrated process	High	Medium	Yes
Low-temperature bonding	Low	High	—
Eutectic bonding	Medium	Low	Yes
Brazing	Very high	Low	Yes

Table 12.9 Typical flow of events to establish the reliability of MEMS device packaging.^a

Testing	Objective
Historic data research	Investigation of all previous failure mechanisms of MEMS
External visual	Use of lower-power optical microscopy in examination of all aspects of MEMS packaging
Electrical test	Identification of failure modes by verification of non-functionality
Bake and electrical testing	Use of unbiased baking, followed by assessment of functionality
Use of X-radiography	Analyses of internal connections and alignments, especially where decapsulation might have an effect on the integrity of the MEMS
Hermeticity and internal Testing atmosphere	Assessment of hermeticity MEMS cavity packages and internal atmosphere by residual gas analysis (RGA) to identify the sealing environment
Decapsulation testing	Exposure of internal aspects of the component by a variety of mechanical or chemical methods or the preparation of plastic encapsulated samples for infrared microscopy examination by ‘back-polishing’
Electrical ‘re-testing’	Examination to ensure that decapsulation has not altered the failure mode
Non-destructive analysis	Thermal analysis or material analysis by energy- or wavelength-dispersive spectroscopy (EDS or WDS)
Destructive analysis	‘Bond pull’ and ‘die shear,’ circuit -node probing and circuit element isolation, section and stain, selective etching, etc.

^aSource – corrosion effects on micro electromechanical systems (MEMS) by Ivars Gutmanis, Hobe Corporation.

Delamination. MEMS devices may fail due to delamination of bonded thin-film materials. Failure of bonds between dissimilar materials or wafer-to-wafer bonding can also cause delamination in MEMS [48].

Dampening. This arises as being critical for MEMS devices because of the mechanical nature of the parts and their resonant frequency. Dampening can be caused by

many variables, including atmospheric gases. Good sealing is critical for MEMS devices. Since MEMS devices have mechanical moving parts, they are more susceptible to environmental failure than packaging systems.

Fatigue. Failure of structures caused by continuous variation of loading characteristics below their thresholds is known as fatigue. Such cyclic loading causes formation of micro-cracks which weaken the material over time and create localized deformations. The duration it takes for a structure to ultimately fail depends on various factors, including material properties, geometry and variation in load characteristics. It is believed that in MEMS devices, for example, structures made of polysilicon, formed by deposition techniques such as chemical vapor deposition, have rough surfaces that result from the plasma etching used in the final stages of MEMS processing. Under compressive loading, these surfaces come into contact, and their wedging action produces micro-cracks that grow during subsequent tension and compression cycles. This fatigue strength is strongly influenced by the ratio of compression to tension stresses experienced during each cycle [49].

Mechanical failure. Changes in elastic properties affect the resonant and damping characteristics of the beam and will cause a change in the sensor performance.

12.5 ISSUES IN PACKAGING OF MICROSYSTEMS

The three levels of packaging strategy may be adaptable for MEMS packaging. This includes (i) die level, (ii)

device level, and (iii) system level. Die-level packaging involves the passivation and isolation of the delicate and fragile devices. These devices have to be dieced and wire-bonded. The device level packaging involves connection of the power supply, signal and interconnection lines. The system-level packaging integrates MEMS devices with signal conditioning circuitry or ASICs for custom applications.

The major barriers in MEMS packaging technology can be attributed to lack of information and standards in materials, shortage of cross-disciplinary knowledge and experience in the fields of electrical/mechanical/RF/optics/materials/processing/analysis/software. Microsystem packaging is more a combination of engineering and science, which has to share and exchange the experience and information in a dedicated fashion. Table 12.10 presents different challenges and solutions facing microsystem packaging.

Packaging design standards have yet to be made. Apart from certain types of pressure and inertial sensors used by the automotive industry, most MEMS devices are custom-built. Standardized design and packaging methodology are virtually impossible at this present time due to the lack of data available in these areas. However, the joint efforts of industry and academies/research institutions can develop sets of standard for the design of microsystems. In addition, the thin-film mechanics which includes constitutive relations of thin-film materials used in FEM and other numerical analysis systems need to be thoroughly investigated.

Table 12.10 Issues in packaging: challenges and some solutions (adapted from Ma Ishe *et al.* [1].

Packaging parameters	Challenges	Possible solutions
Release etch and dry	Stiction of devices	Freeze drying, supercritical CO ₂ drying, roughening of contact surfaces such as dimples, non-stick coatings
Dicing/Cleaving	Contamination risks, elimination of particles generated	Release die after dicing, cleaving of wafers, laser swing, wafer-level encapsulation
Die handling	Device failure, top die face is very sensitive to contact	Fixtures that hold the MEMS die by sides rather than the top face
Stress	Performance degradation and resonant frequency shifts	Low-modulus die attachment, annealing, compatible CTE match-ups
Out-gassing	Stiction, corrosion	Low out-gassing epoxies, cyanate esters, low-moduli solders, new die attachment materials, removal of out-gassing vapors
Testing	Applying non-electric stimuli to devices	Test all that is possible using wafer-scale probing, and finish with cost-effective specially modified test systems

REFERENCES

1. A.P. Malshe, C. O'Neal, S. Singh and W.D. Brown, 'Packaging and integration of MEMS and related microsystems for system-on-a-package (SOP)', in *Proceedings of the SPIE Symposium on Smart Structures and Devices*, Vol. 4235, D.K. Sood, R.A. Lawes and V.V. Varadan (Eds), SPIE, Bellingham, WA, USA, pp. 198–208 (2001).
2. H.Xie and G.K. Fedder 'Integrated microelectromechanical gyroscopes', *Journal of Aerospace Engineering*, **16**, 65–75 (2003).
3. C.B. O'Neal, A.P. Malshe, S.B. Singh and W.D. Brown, 'Challenges in packaging of MEMS', in *proceedings of the IEEE International Symposium on Advanced Packaging Materials*, IEEE, Piscataway, NJ, USA, 41–47 (1999).
4. W. Yun, R. Howe and P. Gray, 'Surface micromachined digitally force-balanced accelerometer with integrated CMOS detection circuitry' in *Proceedings of the IEEE Solid State Sensor and Actuator Workshop*, IEEE, Piscataway, NJ, USA, pp. 126–131 (1992).
5. H. Baltes, O. Brand, A. Hierlemann, D. Lange and C. Hagleitner, "CMOS MEMS – present and future", in *Proceedings of the IEEE Micro Electro Mechanical Systems (MEMS) Conference*, IEEE, Piscataway, NJ, USA, pp. 459–466 (2002).
6. P.F. van Kessel, L.J. Hornbeck, R.E. Meier and M.R. Douglass, "A MEMS-based projection display", *Proceedings of the IEEE*, **86**, 1687–1704 (1998).
7. D.R. Sparks, X. Huang, W. Higdon and J.D. Johnson, "Angular rate sensor and accelerometer combined on the same micromachined CMOS chip", *Microsystem Technologies*, **4**, 139–142 (1998).
8. S. Michaelis, H.J. Timme, M. Wucisk and J. Binder, 'Acceleration threshold switches from an additive electroplating MEMS process', *Sensors and Actuators: Physical* **A85**, 418–423 (2000).
9. B.E. Cole, R.E. Higaki and R.A. Wood, 'Monolithic two-dimensional arrays of micromachined microstructures for infrared applications', *Proceedings of the IEEE*, **86**, 1679–1686 (1998).
10. B.D. DeBusschere and G.T.A. Kovacs, "Portable cell-based biosensor system using integrated CMOS cell-cartridges", *Biosensors and Bioelectronics*, **16**, 543–556 (2001).
11. M. Brandl and V. Kempe, 'High performance accelerometer based on CMOS technologies with low cost add-ons', in *Proceedings of the IEEE Micro Electro Mechanical Systems (MEMS) Conference*, IEEE, Piscataway, NJ, USA, pp. 6–9 (2001).
12. Y.B. Gianchandani, H. Kim, M. Shinn, B. Ha, B. Lee, K. Najafi and C. Song, 'MEMS – first fabrication process for integrating CMOS circuits with polysilicon microstructures' in *Proceedings of the IEEE Micro Electro Mechanical Systems (MEMS) Conference*, IEEE, Piscataway, NJ, USA, pp. 257–262 (1998).
13. Y.B. Gianchandani, H. Kim, M. Shinn, B. Ha, B. Lee, K. Najafi and C. Song, 'Fabrication process for integrating polysilicon microstructures with post-processed CMOS circuits', *Journal of Micromechanics and Microengineering*, **10**, 380–386 (2000).
14. J.H. Smith, S. Montague, J.J. Snieowski, J.R. Murray and P.J. McWhorter, 'Embedded micromechanical devices for monolithic integration of MEMS with CMOS', *IEDM'95 Technical Digest*, 609–612 (1995).
15. R. Steiner Vanha, F. Kroener, T. Olbrich, R. Baresch and H. Baltes, 'Trench–Hall devices', *Journal of microelectromechanical Systems*, **9**, 86–87 (2000).
16. L.P. Parameswaran, C.H. Hsu and M.A. Schmidt, 'A merged MEMS–CMOS process using silicon wafer bonding', *IEDM'95 Technical Digest*, 613–616 (1995).
17. P.J. French, 'Integration of MEMS devices', in *Proceedings of SPIE Device and Process Technologies for MEMS and Microelectronics*, Vol. 3892, N.W. Bergamann, O. Reinhold and N.C. Tien (Eds), SPIE, Bellingham, WA, USA, pp. 39–48 (1999).
18. T.-R. Hsu, 'Packaging design of microsystems and meso-scale devices', *IEEE Transactions: Advanced Packaging*, **23**, 596–601 (2000).
19. R. Ramesham and R., Ghaffarian, 'Challenges in interconnection and packaging of microelectromechanical systems (MEMS)', in *Proceedings of the 50th Electronic Components and Technology Conference*, IEEE, Piscataway, NJ, USA, pp. 666–675 (2000).
20. K.H.-L. Chau, S.R. Lewis, Y. Zhao, R.T. Howe, S.F. Bart and R.G. Marcheselli, 'An integrated force-balanced capacitive accelerometer for low-g applications', *Sensors and Actuators: Physical*, **A54**, 472–476 (1996).
21. C. Hierold, 'Intelligent CMOS sensors', in *Proceedings of the IEEE Micro Electro Mechanical Systems (MEMS) Conference*, IEEE, Piscataway, NJ, USA, pp. 1–6 (2000).
22. J.T. Butler, V.M. Bright, P.B. Chu and R.J. Saia, 'Adapting multichip module foundations for MEMS packaging', in *Proceedings of the IEEE International Conference on Multichip Modules and High-Density Packaging*, IEEE, Piscataway, NJ, USA, pp. 106–111 (1998).
23. M. Elwenspoek and R. Wiegerink, *Mechanical Microsensors*, Springer-Verlag, Berlin, Germany (2001).
24. G.R. Blackwell (Ed.), *The Electronic Packaging Handbook*, CRC Press, Boca Raton, FL, USA (2000).
25. N. Maluf, *An Introduction to Micromechanical System Engineering*, Artech House, Boston, MA, USA (2000).
26. L. Lin, 'MEMS post-packaging by localized heating and bonding', *IEEE Transactions: Advanced Packaging*, **23**, 608–616 (2000).
27. W. Nakayama, 'Thermal issues in Microsystems packaging', *IEEE Transactions: Advanced Packaging*, **23**, 602–607 (2000).
28. H.H. Oppermann, C. Kallmayer, C. Klein, R. Aschenbrenner and H. Reichl, 'Advanced Flip chip technologies in RF,

- Microwave and MEMS applications', *Proceedings of SPIE*, **4019**, 308–314 (2000).
29. S.J. Kim, Y.S. Kwon and H.Y. Lee H.Y., 'Silicon MEMS packages for coplanar MMICs', in *Proceedings of the 2000 Asia-Pacific Microwave Conference*, IEEE, Piscataway, NJ, USA pp. 17–20 (2000).
 30. H. Kusamitsu, Y. Morishita, K. Marushashi, M. Ito and K. Ohata, "The flip-chip bump interconnection for millimeter wave GaAs MMIC", *IEEE Transactions: Electronics Packaging and Manufacturing*, **22**, 23–28 (1999).
 31. R.D. Gerke, 'MEMS packaging', In *MEMS Reliability Assurance Guidelines for Space Applications*, B. Stark (Ed.), Publication 99-1, Jet Propulsion Laboratory, Pasadena, CA, USA, pp. 166–191 (1989). [available at <http://nppp.jpl.nasa.gov/docs/JPL%20PUB%2099-1H.pdf>].
 32. K. Takahashi, U. Sangawa, S. Fujita, M. Matsuo, T. Urabe, H. Ogura and H. Yubuki, 'Packaging using microelectromechanical technologies and planar components', *IEEE Transactions: Microwave Theory and Technology*, **49**, 2099–2104 (2001).
 33. J.T. Butler and V.M. Bright, 'An embedded overlay concept for microsystems packaging', *IEEE Transactions: Advanced Packaging*, **23**, 617–622 (2000).
 34. H. Reichal and V. Grosser, 'Overview and development trends in the field of MEMS packaging', in *Proceedings of the 14th IEEE International Conf on MEMS' 2001* IEEE, Piscataway, NJ, USA, pp. 1–5 (2001).
 35. K. Gilleo, 'Overview of new packages, materials and processes', in *Proceedings of the IEEE International Symposium on Advanced Packaging Materials*, IEEE, Piscataway, NJ, USA, pp. 1–5 (2001).
 36. A.R. Mirza, 'One micron precision wafer-level aligned bonding for interconnect, MEMS and packaging applications', in *Proceedings of the IEEE 2000 Electronic Components and Technology Conference*, IEEE, Piscataway, NJ, USA, pp. 676–680 (2000).
 37. M.P. Helsel, J.D. Berger, D.W. Wine and T.D. Osborn, 'Wafer scale packaging for a MEMS video scanner', in *Proceedings of the SPIE Symposium on MEMS Design, Fabrication, Characterization and Packaging*, Vol. 4407, U.F.W. Behringer and D.G. Uttachandani (Eds), SPIE, Bellingham, WA, USA, pp. 214–220 (2001).
 38. K. Gilleo, 'MEMS Packaging issues and materials', in *Proceedings of the IEEE International Symposium on Advanced Packaging: Processes, Properties and Interfaces*, IEEE, Piscataway, NJ, USA, pp. 1–5 (2001).
 39. B. Shivkumar and C.J. Kim, 'Microrivets for MEMS packaging: Concept, fabrication and strength testing', *Journal of Microelectromechanical Systems*, **6**, 217–225 (1997).
 40. L. Lin, 'Selective encapsulations of MEMS: micro channels, needles, resonators and electromechanical filters', *Ph.D. Dissertation*, University of California at Berkeley, Barkeley, CA, USA, (1993).
 41. Y.T. Cheng, L. Lin and K. Najafi, 'Localized silicon fusion and eutectic bonding for MEMS fabrication and packaging', *Journal of Microelectromechanical Systems*, **9**, 3–8 (2000).
 42. A.R. Mirza, 'Wafer level packaging technology for MEMS', in *Proceedings of the IEEE International Society Conference on Thermal Phenomena*, IEEE, Piscataway, NJ, USA, pp. 113–119 (2000).
 43. J. Laskey, 'Wafer bonding for silicon-on-insulator technologies', *Applied Physics Letters*, **48**, 78–80 (1986).
 44. Z. Li, Y. Hao, D. Zhang, T. Li and G. Wu, 'An SOI–MEMS technology using substrate layer and bonded glass as wafer level package', *Sensors and Actuators: Physical*, **A96**, 34–42 (2002).
 45. M. Shimbo, K. Furukawa, F. Fukuda and K. Tanzawa, 'Silicon-to-silicon direct bonding method', *Journal of Applied Physics Letters*, **60**, 2987–2989 (1986).
 46. Y.Y. Cheng, L. Lin and K. Najafi, 'A hermetic glass–silicon package formed using localized aluminum/silicon-glass bonding', *Journal of Microelectromechanical Systems*, **10**, 392–399 (2001).
 47. A.R. Mirza and A.A. Ayon, "Silicon wafer bonding", *IEEE Sensors*, 24–33 (December, 1998).
 48. P. Sandborn, R. Swaminathan and G. Subramanian, 'Test and evaluation of chip-to-chip attachment of MEMS devices', in *Proceedings of the IEEE 2000 Inter-Society conference on Thermal Phenomena*, IEEE, Piscataway, NJ, USA, pp. 133–140 (2000).
 49. H. Kahn, R. Ballarini, J. Bellante and A.H. Heuer, 'Fatigue failure in polysilicon not due to simple stress corrosion cracking', *Science*, **298**, 1215–1218 (2002).

13

Fabrication Examples of Smart Microsystems

13.1 INTRODUCTION

With the basic principles of sensor and actuators discussed in Part 2 and the fabrication technologies in earlier chapters in Part 4, the reader should be able to reasonably visualize fabrication approaches for most of the devices discussed in this book so far. This chapter endeavors to discuss case studies of some specific devices to widen their understanding.

Poly(vinylidene fluoride) (PVDF) is gaining acceptance as a good substitute for PZT in piezoelectric sensor applications. The first set of examples here looks at its application in structural health monitoring and in hydrophones. The design of a SAW-based accelerometer was discussed in Chapter 5. We address its fabrication in Section 13.3. Another SAW-based device, for liquid sensing, is discussed next. Chemical and biological sensing properties of carbon nanotubes are beginning to be understood by the community. Hence, an example based on this configuration is included in the next section. As discussed in Chapter 11, polymer-based fabrication approaches are gaining acceptance in several biomedical applications. A set of examples for fabricating microfluidic systems with polymeric materials is included as Section 13.5. Preliminary characterization set-ups and measured results are also included for each of these devices for a better appreciation.

13.2 PVDF TRANSDUCERS

Two examples based on PVDF films, one for the fabrication of a transducer for structural health monitoring and a sensor for hydrophone applications, are discussed in this section. In the second, we show how the addition of a PVDF film attached to the gate electrode of an FET can

result in various pressure-detecting sensors. Interdigital electrodes deposited on one side of a PVDF film can excite and detect surface-propagating acoustic waves. Hence, in the first example we demonstrate the construction of such a transducer.

13.2.1 PVDF-based transducer for structural health monitoring

Ensuring the structural integrity of equipment and aircraft is of great importance in aerospace industry to avoid catastrophic failures and to extend the life span of these expensive vehicles. Most of the maintenance and health monitoring schemes currently employed for large-area surfaces, such as aircraft wings and fuselages, are time consuming and hence very expensive. Schemes based on radiography, ultrasonics, eddy currents, liquid penetration and magnetic particles have been successfully used in the field for such applications. Of these, ultrasonic non-destructive testing offers immense possibility for a great deal of improvement to make the schemes less expensive, and less time consuming. In this proposed research work, we plan to develop a remotely readable, PVDF-based ultrasonic transducer for *in situ* health monitoring of aircraft structures.

Usually, ultrasonic inspection requires a bulky probe assembly, which is usually based on piezoelectric transducers, and should be scanned over the entire area to be tested. This is a particularly laborious process and is often limited by accessibility for some difficult-to-reach parts. These incorporate bulk longitudinal or shear wave propagation within the structure, which limits the area covered by a typical transducer. In contrast, guided Lamb waves offers great potential in the health monitoring of wide surface areas that have the possibility of having some defects [1]. Piezoelectric PVDF film is used to

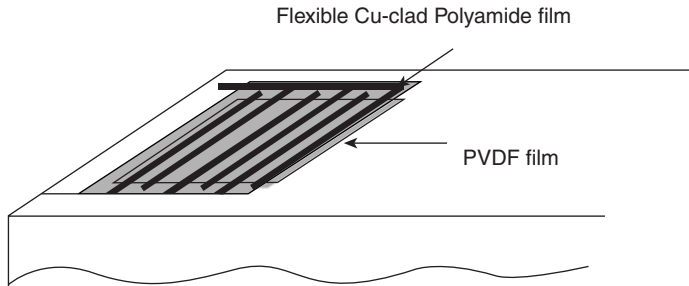


Figure 13.1 Transducer made of PVDF for structural health monitoring.

generate acoustic waves, which propagate as Lamb waves on the surface of the structure. PVDF film is thin, flexible and has a low impedance, wide frequency range and good sensitivity. Due to these characteristics, it can be coupled onto difficult-to-access structures or curved surfaces with little harm to the functions of the structure. In contrast conventional ultrasonic transducers typically consist of PZT material which has a tendency of being stiff and not suitable for places which are hard to access or of curved shape. An interdigitated pattern comprising of a flexible copper layer is deposited on top of the PVDF film [2].

For a simplified design procedure, the transducer may be considered as being attached to the plate, as shown in Figure 13.1 [3]. Recall that for a given structure Lamb waves have many antisymmetric and symmetric modes. The out-of-plane displacement across the thickness of the plate represents the wave propagation on the surface. Of these, the A1 mode is more sensitive to cracks located on the surface of the structure. In the case of a thin aluminum skin, defects (cracks) existing on the surface or just underneath the surface can be detected by using this scheme. Therefore, the PVDF IDT is designed to excite and receive the antisymmetric A1

Lamb wave mode. The frequency–thickness product (fd) corresponding to the maximum group velocity point on the dispersion curve is selected [2]. At a point of maximum group velocity of A1, wave propagation occurs without much dispersion. Once fd is decided, the operational frequency and hence the IDT finger spacing can be determined. Since the thickness of the structural member is usually known (0.8 mm in the case shown here), the operational frequency is estimated to be 3.145 MHz.

In order to make PVDF interdigital transducers, the interdigital electrodes must be prepared. A PVDF film from Measurement Specialties, Inc. is used here. A PVDF interdigital transducer is shown in Figure 13.2. Copper-clad polyamide film is patterned by standard lithographic process. Copper-deposited flexible polyamide film is then glued with PVDF film using ‘Future Glue^R’. This transducer is coupled to the aluminum plate, again using ‘Future Glue^R’, for a permanent mount on the structure. In order to supply a voltage to the IDT, these sets of fingers are connected to a voltage source. These ports are then covered with non-conducting tape to prevent an electrical short circuit between the finger electrodes.

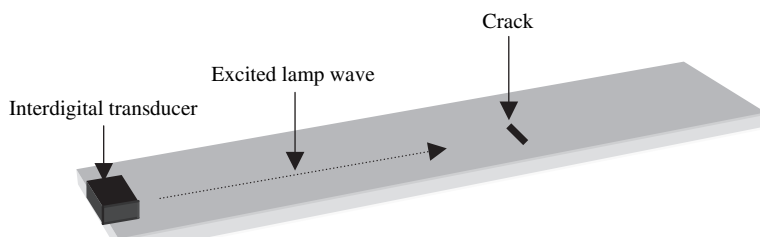


Figure 13.2 Schematic of a PVDF IDT (interdigital transducer) bonded onto an aluminum plate.

The most important design factor of an IDT is to decide the interdigital transducer finger spacing. To accommodate for the constructive interference of the acoustic waves excited by each pair of IDTs, the spacing between them is chosen to be constant at $\lambda/4$ (λ is the acoustic wavelength).

Guided waves are generated by the interdigital transducer with PVDF film. The transducer connected to a pulse-echo experimental set-up can detect the signal reflected from the crack as well as the edge of the aluminum plate. The self-calibrating technique employed here can relate the intensity of the reflected signal to the crack size. The sensed signal is represented as the product of the following factors:

$$F_{\text{cr}} = T(f)\alpha(f)S(f)R(f) \quad (13.1)$$

where F_{cr} is the Fourier transform coefficient of the signal from the cracks, $T(f)$ is the transmission coefficient of the transducer, $\alpha(f)$ is the attenuation coefficient, $S(f)$ is the scattering coefficient and $R(f)$ is the receiving coefficient of the transducer.

Since only one transducer is used in the pulse-echo experimental set-up, it is assumed that the factors T , α and R remain the same for all crack sizes. Therefore, the intensity of scattering for a given crack can be obtained as:

$$\frac{F_{\text{cr}}}{F_{\text{big_cr}}} = \frac{T(f)\alpha(f)S_{\text{cr}}(f)R(f)}{T(f)\alpha(f)S_{\text{big_cr}}(f)R(f)} = \frac{S_{\text{cr}}(f)}{S_{\text{big_cr}}(f)} = \frac{S_{\text{cr}}(f)}{X} \quad (13.2)$$

By means of the self-calibrating technique, the term $S_{\text{cr}}(f)$ is determined with respect to the measured

reference signal $S_{\text{big_cr}}(f)$ from the biggest crack in the same material. The algorithm needs further refinement to resolve when multiple cracks are present.

The relation between the intensity of scattering and the crack size is represented by Equation (13.2). The Fourier transform coefficient of the signal is a function of the intensity of scattering. Since the reflected signal from the crack is changing with respect to the size of the crack, its Fourier transform coefficient also changes, thus affecting the intensity of scattering.

The PVDF IDT launches a narrow acoustic wave beam. If the size of the crack is over the length of the IDT fingers, the amplitude of the reflected crack signal does not change much with increasing crack length. Therefore, the PVDF interdigital transducer is sensitive to detecting cracks only up to the overlapped finger length of the IDT. This means that if one has the purpose of searching in a narrow region for cracks, by adjusting the overlapped finger length of the IDT the width of the scanned region can be changed.

Studies indicate that the overlapped finger length of the interdigital transducer limits the maximum size of crack that can be detected. The finger length also determines the angle of dispersion. The expression for the dispersion angle is:

$$\gamma = \sin^{-1} \left(\frac{\lambda}{l} \right) \quad (13.3)$$

where γ is the angle of dispersion, λ is the wavelength and l is the overlapped finger length of the IDT.

The set-up for experimental studies uses a windows-based data-acquisition system (Figure 13.3). This is connected to the IDT attached to the aluminum plate specimen.

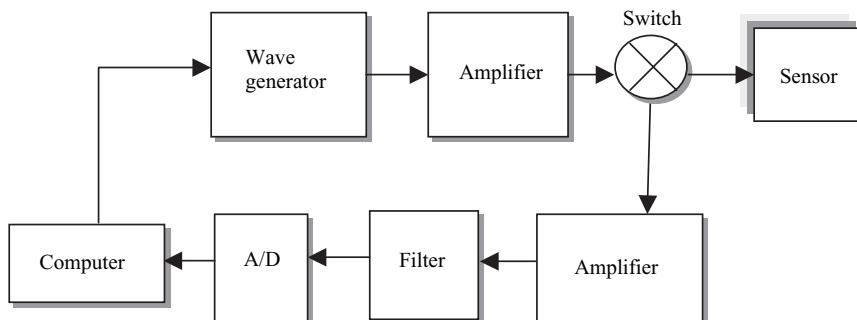


Figure 13.3 Block diagram of the experimental set-up.

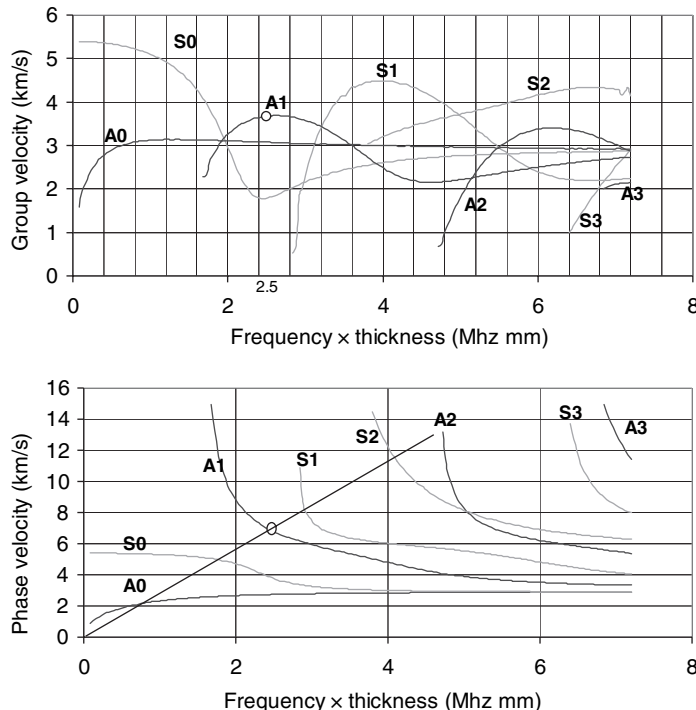


Figure 13.4 Dispersion curves for the specimen used in the measurements.

The specimen dimensions (as shown in Figure 13.2) are 91.5×15.3 cm and the crack is located 62.5 cm away from the transducer. The results presented in Figure 13.4 shows that the A1 modes are excited with the maximum group velocity. At an operational frequency of 3.145 MHz, both A1 and A0 modes are generated. It may also be noted that the velocities of the A1 and A0 modes are not very different at this frequency.

The reflected signals from the crack and the edge not only gives information about the location in the time domain but also is effective to determine the crack size in the frequency domain. Slots are cut through the aluminum sheet to emulate the cracks. In Figure 13.5, the measured time domain signals are presented for different crack sizes.

Since the reflected signal from the crack is changing with respect to the size of the crack, its Fourier transform coefficient also changes, thus affecting the intensity of scattering. These are plotted for different crack sizes in Figure 13.6. In order to verify the ability to detect surface defects, cracks are engraved with half the thickness of the aluminum plate. These results are comparable with the previously calibrated results. In Figure 13.6, the results of estimation of crack size are provided for cracks half

the thickness of the aluminum plate. These results indicate that piezoelectric PVDF film can be used to generate acoustic Lamb waves, which can be used to detect and estimate surface defects.

13.2.2 PVDF film for a hydrophone

A schematic of the device structure is shown in Figure 13.7 [4]. The device consists of a sensing part containing the PVDF film and an amplifying part made of an *n*-channel MOSFET with an extended aluminum gate. The basic structure is fabricated using a standard NMOS process. Transistors with larger *W/L* ratios are preferred in order to obtain a larger transconductance and better noise characteristics.

The operating principle of this device can be explained as follows. The incident acoustic signal initiates the charge redistribution on the surface of the PVDF film which in turn changes the charge on the gate of an *n*-type MOSFET. The shift in gate voltage is used to modulate the drain current in a common source configuration. The design of this sensor was described in Section 5.2. This hydrophone was fabricated using six photo mask levels.

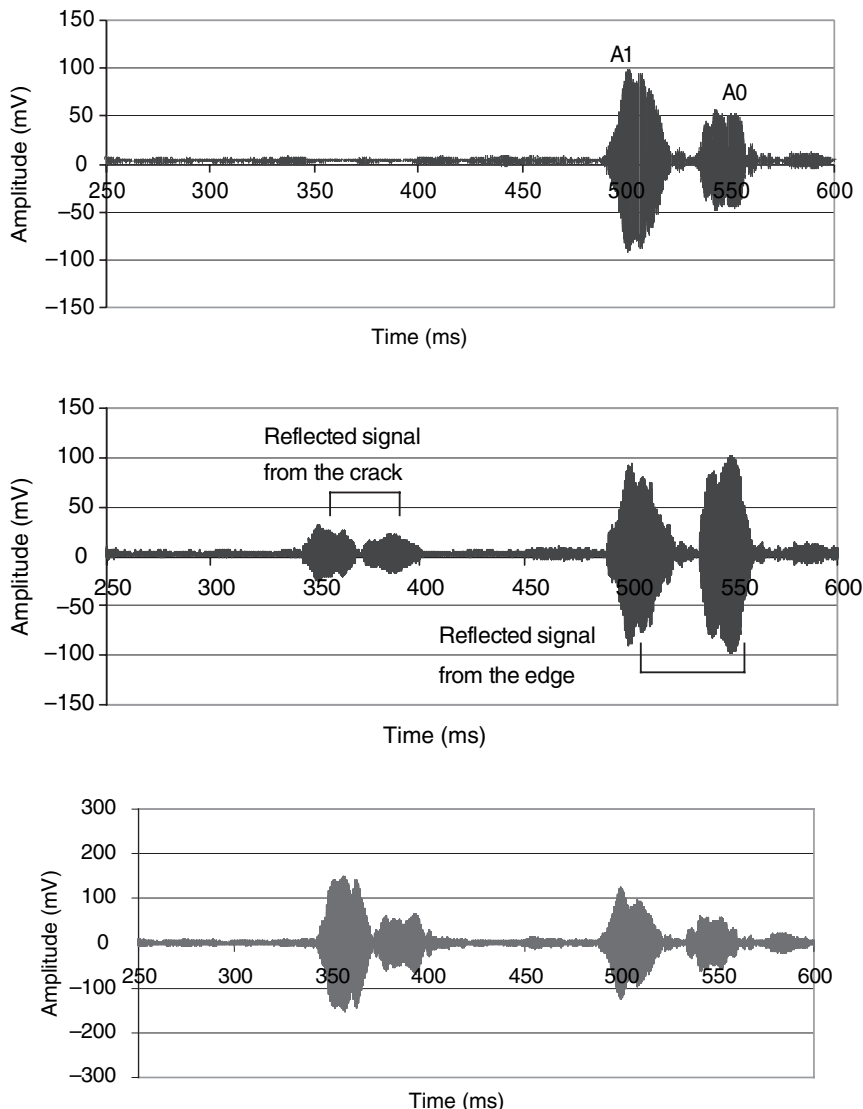


Figure 13.5 Reflected signals in the time-domain showing the presence and size of a crack in the specimen.

The fabrication process flow is shown in Figure 13.8 and is described in the following.

The starting substrate was a 2 in diameter, lightly doped *p*-type (100) silicon wafer. The first step to begin the fabrication was wafer cleaning, which is referred to as *residual cleaning agent* (RCA) cleaning. RCA cleaning is a standard process used in industry. The compositions of the RCA solutions are RCA1 ($H_2O:H_2O_2:NH_4OH = 600:150:100$) and RCA2 ($H_2O:H_2O_2:HCl = 700:150:100$). The purpose of RCA cleaning is

to remove the organic surface films, particles and alkali ions from the silicon wafer.

Next, a wet oxidation was performed at $1100\text{ }^\circ\text{C}$ for 3 h to grow a silicon dioxide layer of $\sim 1\text{ }\mu\text{m}$ on the surfaces of the silicon substrate to electrically isolate the devices from each other. As will be discussed later, the field oxide for the hydrophone devices should be quite thick in order to decrease the capacitance between the lower electrode of the PVDF sensing pad and the conductive silicon substrate.

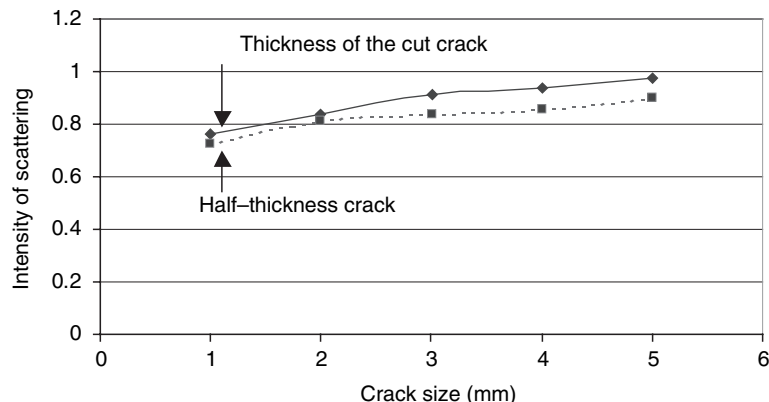


Figure 13.6 Fourier transform coefficients of the signals reflected from the crack plotted against the size of the crack.

The first lithography step was then performed to define the source and drain diffusion regions, followed by an etching to open the diffusion windows. Phosphorus was used as the n -type dopant. Thermal diffusion, consisting of predeposition and ‘drive-in’, was employed to form n^+ regions. Predeposition, as unlimited source diffusion, was carried out at 1000 °C for 25 min. Following an HF dip to remove the oxide grown during the predeposition step, ‘drive-in’ was performed at 1050 °C for 20 min without a phosphorus source. The purpose of ‘drive-in’ is to redistribute the dopant such that its concentration is more uniform. This diffusion was carried out in an oxygen atmosphere so that another layer of oxide was grown simultaneously on the wafer to protect the n^+ regions.

Gate windows were opened by the second lithography step and etching. Dry oxidation was then carried out at 950 °C for 47 min to grow the gate oxide with a thickness of 300 Å. Since the quality of the gate oxide was critical to the MOSFET’s performance, precautions were taken to get a high-quality gate oxide. First, during dry oxidation, some Cl was incorporated into the O₂ since chlorine can remove metal contamination by forming volatile metal compounds which are readily swept away from the tube. Therefore, the interface mobile oxide charge density can be reduced and a desirable threshold

voltage can be achieved. Oxide grown in a chloride ambient has a better interface with the underlying silicon and results in a higher breakdown voltage. Furthermore, after oxidation the wafer was annealed in a nitrogen ambient at the same temperature for 45 min to decrease the fixed charge density.

Then, contact windows were opened and a 2500 Å Al layer was evaporated onto the wafer and patterned as the contact metal for the MOSFET. The preparation of the SU-8 layer was performed after aluminum deposition and patterning for the MOSFET circuit and followed by aluminum deposition and patterning for the extended gate electrode. The thickness of the SU-8 layer was about 11 µm. Via holes through the SU-8 layer were developed by pure propylene glycol methyl acetate (PGMEA), which allows the connection to be made between the extended electrode and the gate of the MOSFET. Finally, a 110 µm thick PVDF film, supplied by Measurement Specialties, Inc., was glued onto the extended gate electrode by using a low-temperature silver epoxy.

In this process, however, one problem was encountered due to the thick SU-8 layer. Since the thickness of the SU-8 layer was 11 µm, while the thickness of the evaporated metal layer was only around 0.25 µm, it

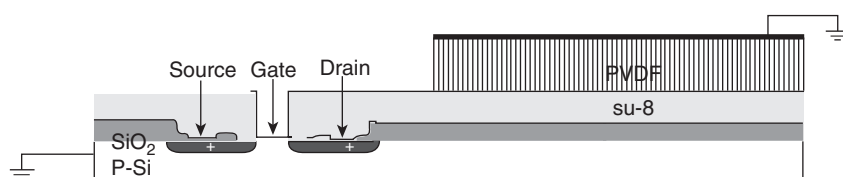


Figure 13.7 Cross-section of a PVDF-MOSFET hydrophone.

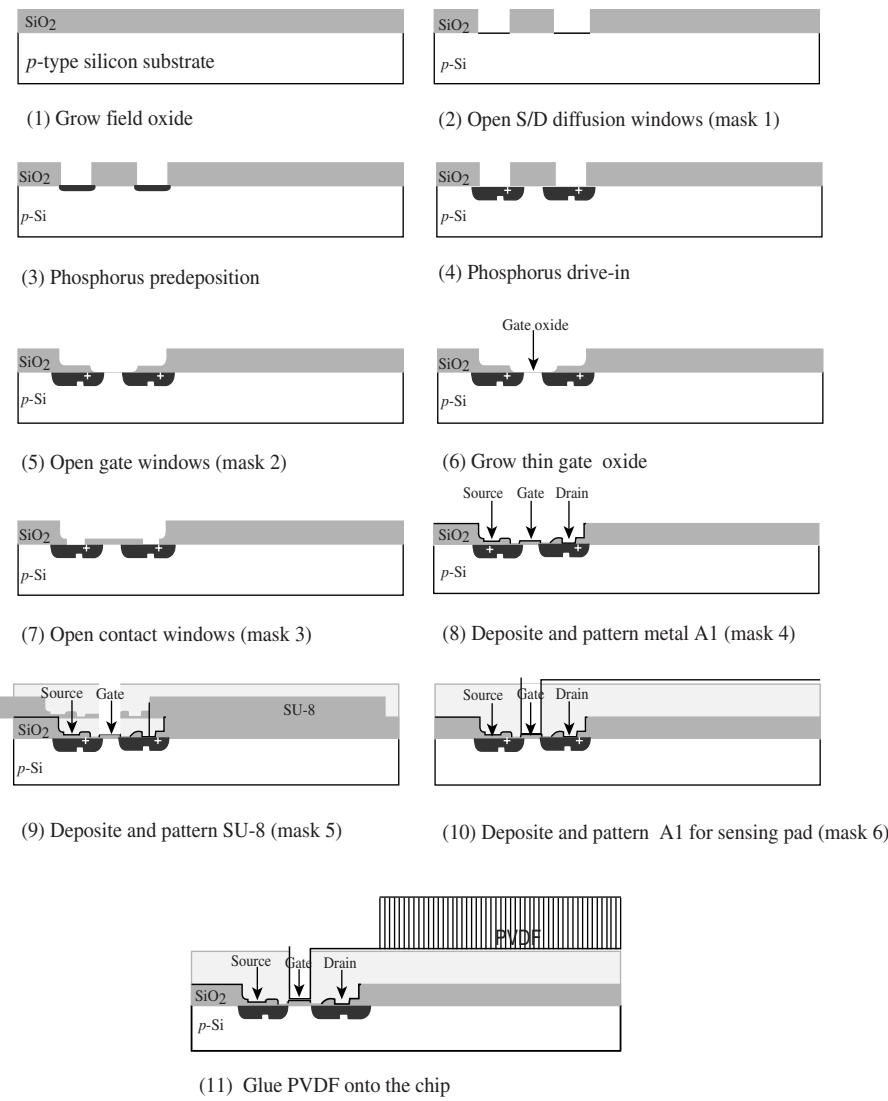


Figure 13.8 Process flow for a PVDF-based MEMS hydrophone.

turned out to be difficult to make the connection between the second metal layer with the first one through the via holes. Two means were used in the following steps to solve this problem. First, during the second metal-deposition step, the sample was rotated around the top of the evaporator by using a rotatable sample holder. Therefore, the sidewalls of the via holes could be covered with metal.

Secondly, in the following lithography step, a thick positive photoresist, AZ 4620, supplied by AZ Electronic Materials, was used to provide good step coverage over the already patterned features. In order to protect the

metal deposited on the sidewalls of the via holes, the resist was dispersed on the surface at a low spin speed. However, since this photoresist is much more viscous than the commonly used Shipley 1800 series photoresist, it is difficult to obtain a uniform layer of AZ 4620 at a low spin speed. After experimentation, it was found that a well-coated surface could be obtained by dispersing the photoresist at a spin speed of 2000 rpm.

The processing of AZ 4620 is very similar to that for normal positive photoresists, except that it requires longer times for soft bake and development. For a layer

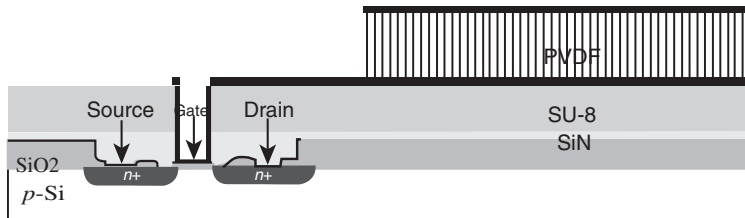


Figure 13.9 Cross-section of the hydrophone with passivation.

spin-coated at 2000 rpm with a thickness of 10 µm, both the soft bake and development times are about 3 min. The developer for this photoresist is a mixture of one part of AZ400K with four parts of deionized water.

After the PVDF is mounted onto the extended electrode of the device, the chip was glued onto a package and wire-bonded. Since the hydrophone is used for underwater acoustic signal detection, choosing the proper material as the encapsulant is very important. This material should be an insulator with its acoustic impedance close to that of water. In addition, this material is also expected to have excellent chemical as well as water resistance. One class of materials often used to transmit underwater sound signals are called *Rho-C* materials. The acoustic impedance of these *Rho-C* materials is quite close to that of water. Therefore, using these materials as the encapsulant can reduce the sound reflection at the water/encapsulant interface. To prepare the samples, the two components were first thoroughly mixed in the proper ratio for each material system. For Conthane EN-4/8, the ratio is 100 g Part A (EN-8) to 17.5 g Part B (EN-4), while for Conthane EN-1556, the ratio is 100 g Part A to 33 g Part B. In order to get rid of the bubbles generated during the mixing process, both materials were degassed under vacuum for about 4–5 min. Then, the mixtures were poured into two identical aluminum molds with an inner diameter of 6.35 cm and cured at 30 °C for more than 16 h until they solidified.

It has been found that the device encapsulated by *Rho-C* rubber loses its function after a few days (usually less than one week). The reason could be that the mobile ions penetrate through the SU-8 layer and contaminate the MOSFET. In order to protect the MOSFET from contamination, a SiN passivation layer was deposited and patterned right after the pattern of the first metal layer and followed by the spin-casting of the SU-8. Therefore, a total of seven masks was needed in the whole process. SiN is a good barrier material to most mobile ions and solvents. A cross-section of the final structure of the hydrophone device is shown in Figure 13.9.

The system used for the deposition of SiN is a Vactronic four-chamber plasma-enhanced chemical vapor deposition (PECVD) system. SiN (300 nm) was deposited at 250 °C with NH₃ flowing at a rate of 40 sccm (standard cubic centimeter per minute) and SiH₄ flowing at a rate of 4 sccm. The processing pressure is 500 m torr and the plasma power density is 16.5 mW/cm². After lithography, SiN was etched in a solution containing one part of BOE ('Buffered Oxide Etch') solution and three parts of deionized water.

The passivated devices were encapsulated by *Rho-C* rubber. No performance degradation was observed when the devices were examined after two weeks. This shows that SiN passivation is necessary and effective for increasing the reliability of the MOSFET.

The experimental set-up for the hydrophone is shown in Figure 13.10. The sensitivities of devices being developed with various configurations are listed in Table 13.1. MOS1 and MOS2 refer to two different W/L ratios, of 500 and 100, respectively. It can be seen from the data shown that the sensitivity of the hydrophone with MOS2 is improved by the SU-8 layer. With an 11 µm thick SU-8 layer, the average sensitivity improvement is about 15 dB.

In addition, it has also been observed that the noise level of the passivated device is lower than the unpassivated device. In the latter device, the MOSFET is in direct contact with the SU-8 layer, which is spin-coated from solution. Since it is very difficult to completely remove the solvent from the SU-8, the remaining solvent in the SU-8 may also contaminate the underneath MOSFET. Therefore, the unpassivated device generates more noise. This accounts for the improvement in sensitivity.

13.3 SAW ACCELEROMETER

In this section, the fabrication of a surface acoustic wave (SAW)-based accelerometer is described [5]. Please recall that the design of this device has already been discussed in Chapter 5 (Section 5.3).

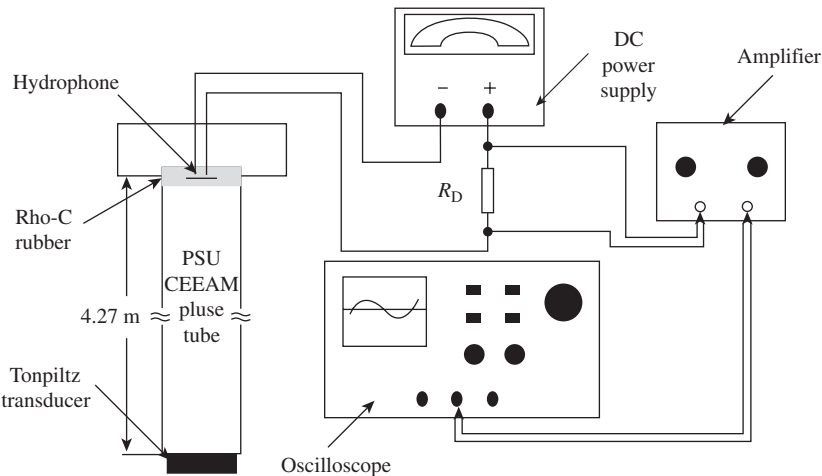


Figure 13.10 Experimental set-up for characterizing the hydrophone.

Table 13.1 Measured sensitivities of the hydrophones.

Frequency (kHz)	Sensitivity (dB)			
	Hydrophone with MOS1		Hydrophone with MOS2	
	Without SU-8	With SU-8	Without SU-8	With SU-8
4	-233.39	-233.81	-236.48	-223.25
5	-236.14	-234.067	-236.77	-224.6
6	-233.39	-233.073	-235.6	-222.7
7	-232.4	-232.84	-234.99	-219.54
8	-232.04	-230.31	-234.47	-220.33
9	-230.43	-229.07	-235.39	-216.83
10	-228.64	-228.71	-233.85	-217.23

This uses the Rayleigh wave, a type of surface wave in which the wave energy is almost completely confined within a distance of one wavelength above the substrate [6]. In this device, a conductive seismic mass is placed close to the substrate (at a distance of less than one acoustic wavelength). This serves to alter the electrical boundary conditions. The seismic mass consists of a micromachined polysilicon structure which incorporates reflectors and flexible beams. Details of the seismic mass and reflectors are shown in Figure 13.11.

The device functions as follows. An incoming electromagnetic wave at the IDT causes an RF electrical field between the transducer fingers. By the piezoelectric effect, mechanical deformations following the signal propagate along the substrate. The array of reflectors reflect

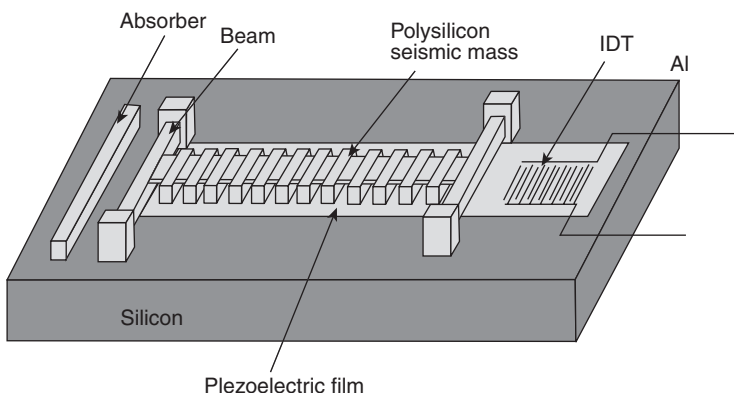


Figure 13.11 Schematic of an SAW-based accelerometer.

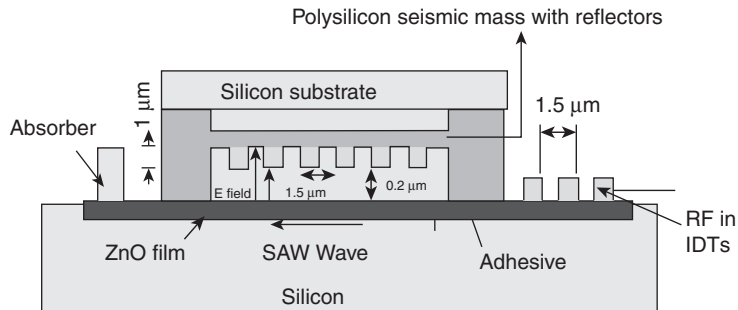


Figure 13.12 Design and dimensions of an SAW-based accelerometer.

this wave back to the IDT. The phase of the reflected wave is dependent on the position of the reflectors. If the position of the reflectors is altered, then the phase of the reflected wave is also changed. The reflectors are part of the seismic mass. In response to acceleration, the beam flexes, so causing the reflectors to move. This can be measured as a phase shift of the reflected wave. By calibrating the phase shift measured with respect to the acceleration, the device can be used as an acceleration sensor. Alternatively, the measurement can be done in the time domain, in which case the delay time of the reflection from the reflectors is used to sense the acceleration.

The basic elements of this device are the piezoelectric film on which the IDTs are patterned and a set of reflectors and a seismic mass bonded onto this. Silicon with a ZnO film was chosen as the SAW substrate. Figure 13.12 shows the design dimensions (mm) of the device. The metal deposition and etching techniques used to pattern the IDTs are standard in IC processing. Reflector arrays were fabricated using silicon micromachining techniques.

Flip-chip bonding was chosen in order to reduce the handling of the substrate and hence maintain the performance of the SAW substrate. These steps are detailed in the following paragraphs.

Figure 13.13 shows the various steps in the fabrication of the seismic mass. This can be realized by the sacrificial etching of silicon dioxide. The steps are outlined below:

- (1) A sacrificial oxide is thermally grown on the wafer.
- (2) Polysilicon (structural layer) is then deposited by LPCVD on the sacrificial layer. Polysilicon has good structural properties and is commonly used. This structural layer is thick enough (1 μm) to support itself. The polysilicon is patterned and etched with EDP.
- (3) The sacrificial layer is then etched with HF to finally release the seismic mass.
- (4) The seismic mass is now ready to be flip-chip bonded to the SAW substrate.

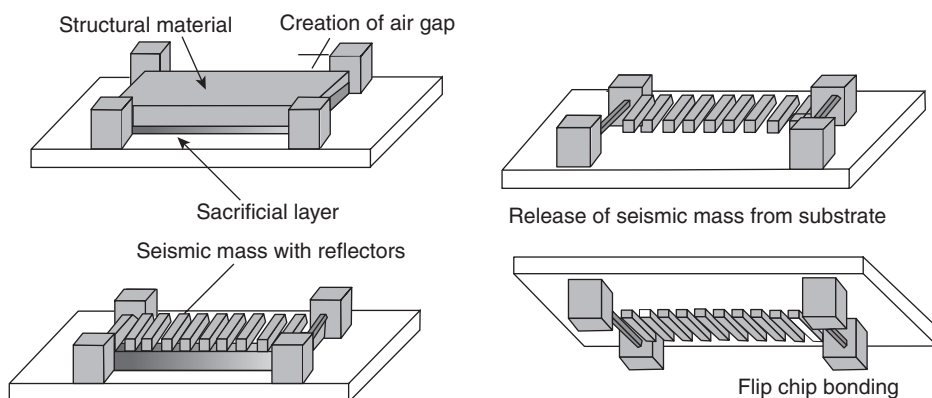


Figure 13.13 Fabrication of the seismic mass for an SAW-based accelerometer.

After the sacrificial oxide is removed in HF, the wafers are rinsed in deionized water and dried. The surface tension of the water under the structures pulls them down to the surface of the wafer, and in some cases causes them to stick (permanently). This problem can be avoided by using thick structural and sacrificial layers, and short structures.

The SAW device consists of a piezoelectric substrate on which the IDTs are patterned. The IDTs can be etched by using the lift-off technique. The thickness of the metal for the IDTs should be at least 2000 Å in order to make an adequate contact. A very thick layer of metal causes ‘mass-loading’ effects and is detrimental to the device performance. The metallization ratio used for the IDTs is 0.5. The number of IDTs and their apertures is chosen such that the IDTs have an impedance of 50 Ω.

The choice of the lithography method depends on the minimum feature size and adhesion of the selected metal to the piezoelectric substrate. Fabrication of the IDTs is essentially a single-mask process. For the lift-off technique, fabrication begins with standard photolithography using standard equipment like a wet bench, resist spinner, hotplates and an evaporator. The lithium niobate wafers are cleaned using acetone, isopropanol and trichloroethylene at about 60 °C for about 10 min. The wafers are then thoroughly rinsed in deionized (DI) water for about 5 min and subsequently heated at 125 °C (on a hot plate) for about 10 min to remove surface moisture. Upon cooling the wafer on a heat-sinking plate, Shipley 1813 photoresist is then spin coated (at 4000 rpm for 55 s) on the wafer after soaking the top face with an adhesion agent, hexamethyldisilazane (HMDS). The wafer is then heated at 125 °C for 2 min (soft-bake). The wafer is then exposed to UV light (15 mW/cm²) for 1.2 s, such that the regions of the resist that are exposed become soluble to the developer (DI water and MF312, in a 1:1 ratio). A negative mask (whereby the patterns on glass are set against a background of chrome) is used for this purpose. The wafer is developed until the sections that have been exposed to UV light (and therefore soluble) are etched away. The wafer was then hard-baked at 125 °C for 1.5 min. The patterned wafer was coated with 0.02 μm of chromium (to improve adhesion of gold to the substrate) using ‘e-gun evaporation’ and immediately coated with 0.12 μm of gold using thermal evaporation. The wafer was then submerged in acetone for lift-off.

If two wafers with surface oxide layers are hydrated in sulfuric and/or nitric acid and then brought into contact they will stick immediately. If these wafers are subsequently annealed at high temperatures, the resulting bond can be essentially perfect. The quality of the bond depends upon the type of oxides used, the temperature

and the cleanliness of the process. If the wafers can be annealed at 1000 °C, any common oxide (thermal, PSG, etc.) will do. This technique is often used in what is known as a ‘dissolved-wafer process’. Hence, this can be used for bonding the wafers with the IDTs and the seismic mass.

The fabrication of the spacer is a two-mask process. Four different wafers were processed to make one device, as each spacer height requires a separate wafer. The first step in the process was the creation of a spacer of the desired height. The next step is the fabrication of the reflector arrays. These two stages are described with the help of Figures 13.14 and 13.15. The basic steps in the process involves growth and patterning of an oxide mask, followed by dry etching of silicon by a plasma:

- (1) Four *p*-type silicon (100) wafers of resistivity between 2–5 Ω cm were used.
- (2) A 500 nm thick silicon dioxide is grown. This oxide layer is the mask for the dry etching.
- (3) The photoresist is spun onto the oxide layer. The resist is then baked to improve adhesion. The first mask is aligned with respect to the flat of the wafer and the photoresist is patterned. The oxide is then developed.
- (4) The silicon is dry-etched in a plasma. The four wafers are etched to different depths, namely 100 and 400 nm and 1 and 2 μm. This step results in the protected area being raised above the rest by the amounts indicated above. These raised regions are called *spacers*.
- (5) The wafers are cleaned and the oxide mask is then etched away. This completes fabrication of the spacers.

A view of the device after the above steps is shown in Figure 13.14.

The process steps in the fabrication of the reflector arrays are discussed next:

- (1) A thin layer (20 nm) of silicon dioxide is grown in preparation for ion implantation. This is done to make the reflectors more conductive with respect to the base of the wafer. Ion implantation uses accelerated ions to implant the surface with the desired dopant. This high-energy process causes damage to the surface. The implantation was done through a LPCVD oxide in order to reduce the surface damage as surface planarity of the reflector is desired.
- (2) Boron ions are implanted into the silicon wafer at 150 keV. The concentration of the dopant is 5 × 10¹⁵ cm⁻². Both the front and back of the wafer

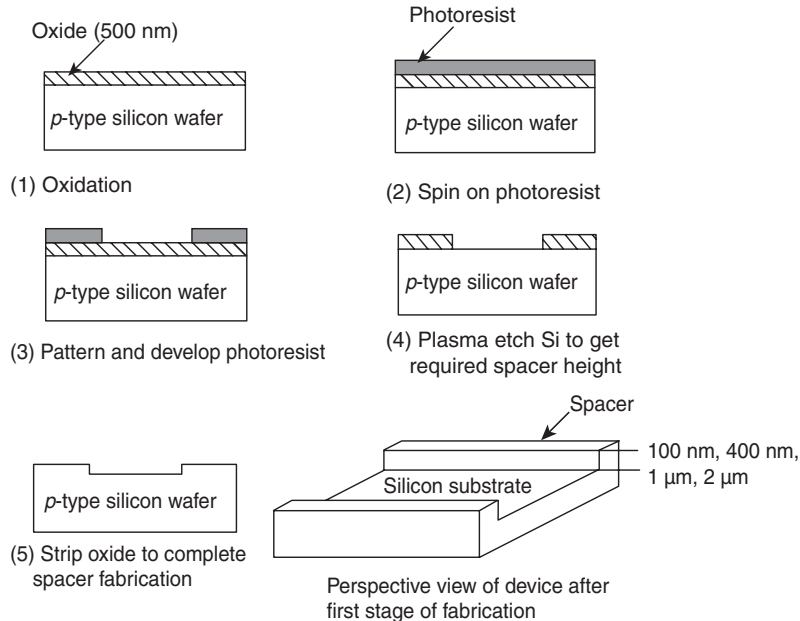


Figure 13.14 Fabrication of spacers for an SAW-based accelerometer.

are ion implanted. This dosage of ions will serve to make the doped region approximately ten times more conductive than the undoped region.

- (3) The wafers are then annealed to release any stress in the wafer. This is followed by plasma-enhanced chemical vapor deposition (PECVD) of a 1 μm thick oxide layer. This oxide layer will serve as the mask for the dry-etching step to follow.
- (4) The oxide is patterned and developed as described in the fabrication of the spacers. The second mask is aligned to alignment marks that were put down during the fabrication of the spacers. This will ensure that the spacers and the reflectors are properly aligned with respect to each other.
- (5) The silicon is dry-etched in plasma. The depth of the etch is 1 μm. This results in formation of reflectors 1 μm in thickness.
- (6) The back side of the wafer is sputtered with aluminum (0.6 μm) to allow grounding of the wafer.
- (7) The oxide is finally stripped from the front.

The completed set of reflectors is shown in Figure 13.15.

An array consisting of 200 reflectors is placed between the two IDTs. These reflectors cover nearly the entire space between the IDTs. The spacer height was 100 nm. This allows the reflectors to be placed 100 nm above the substrate on which the Rayleigh wave propagates.

Based on experimental studies it has been concluded that:

- (1) Purely electrical reflections due to the suspended array of reflectors can be detected.
- (2) The spacer is able to place the reflector array adequately close to the substrate, thus allowing the electric field to interact with the reflectors. This is achieved without perturbing the mechanical boundary conditions.
- (3) The reflection from the reflector array can be easily determined by using the reflection coefficient (S_{11}) measurement.

The device is characterized by using a network analyzer to measure the phase shift of the reflection coefficient at the IDT. A linear variation is obtained (see Figure 13.16) for the range of acceleration values studied here.

13.4 CHEMICAL AND BIOSENSORS

As a branch of *chemical sensors*, which convert a chemical or physical property of a specific analyte into a measurable signal proportional to the concentration of the analyte, *biosensors* employ a biological sensing system connected to a transducer to recognize biological

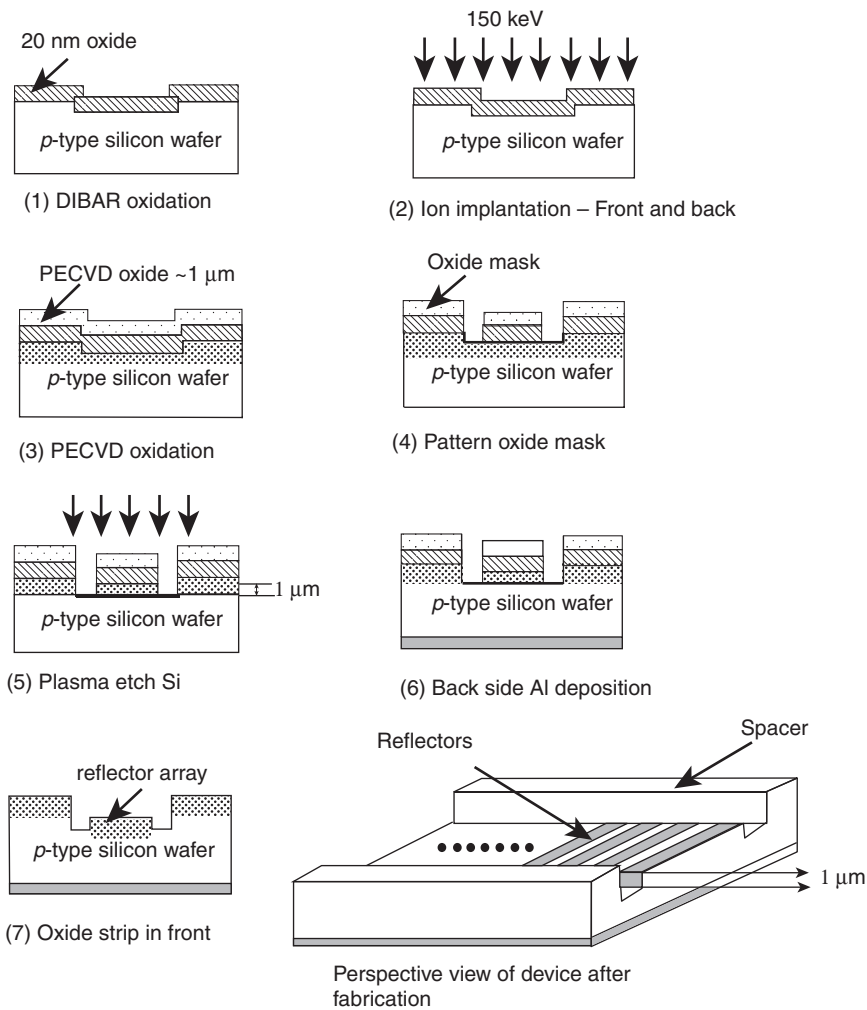


Figure 13.15 Fabrication steps for the reflectors in a SAW-based accelerometer.

analytes and to produce the measurable signal. Chemical and biological sensors can use different kinds of transducers based on the transduction principle. Hence, in this section a liquid sensor based on surface acoustic wave (SAW) principles and a glucose sensor that makes use of the special properties of carbon nanotubes are presented.

13.4.1 SAW-based smart tongue

The basic design principle of a ‘smart tongue’ that uses surface acoustic wave (SAW) principles has been described in Chapter 5. Several requirements should be taken into consideration in the design and fabrication of

this SH-SAW liquid sensor. First, the sizes of the devices has to be determined. In order to easily measure the delay time difference between the two delay lines of the SH-SAW device, long delay lines are desirable (large devices). However, the sensitivity and rise time due to thermal properties are improved with smaller devices. Secondly, the number of transducer fingers for the new devices had to be determined. The bandwidth of the sensor output is mainly dependent on this number [7]. Increasing the number of fingers decreases the bandwidth. On the other hand, in order to minimize the device capacitance, the number of fingers should be kept low. However, to minimize conversion losses, the number of

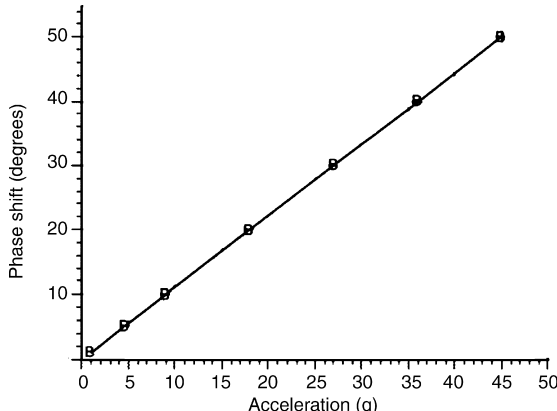


Figure 13.16 Measured results from the SAW-based accelerometer.

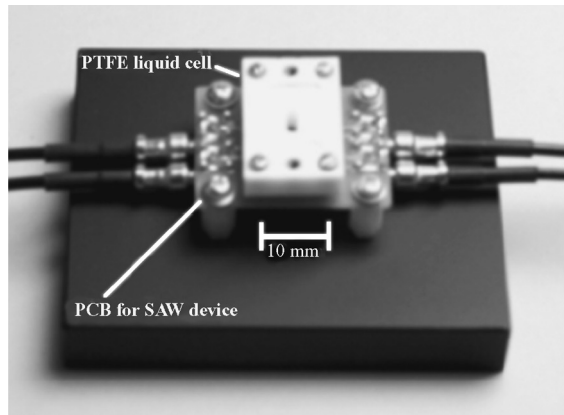


Figure 13.17 Assembled view of an SAW-based chemical liquid sensor.

fingers should be high and diffraction losses can be kept to a minimum when the aperture is large [8,9]. The maximum efficiency of coupling occurs when the width of the IDT fingers is equal to a quarter of the wavelength ($W = \lambda/4$) and for the waves to be generated over a distance L (between the centers of the IDTs), the requirement for the acoustic aperture is $W = \sqrt{L}\lambda$. Thus, by choosing the aperture and the number of finger pairs, the transducer can be matched to a given input line, thus giving a low insertion loss for the device. The maximum relative bandwidth over which the transducer can be matched is approximately proportional to $|K^2|$, the electromechanical coupling coefficient, and the optimum number of finger pairs N is proportional to $|(K^2)^{-1}|$ to allow the acoustic and electrical bandwidths to be made equal [7].

Any piezoelectric material, such as lithium niobate, lithium tantalite or quartz, could be used as a substrate. In order to integrate easily with solid-state electronics, silicon with a ZnO film or an Si/diamond/ZnO combination could also be used. However, to prove the concept of the usefulness of SAW-based device for this application, a low-loss material with a high electromechanical coupling coefficient was chosen. For efficient generation and detection of SAWs through the IDTs, a 128°YX LiNbO₃ crystalline wafer was chosen as the substrate since it is known to excite fewer bulk waves and has a very high electromechanical coupling coefficient.

These SAW-based sensors can be fabricated by the lift-off technique. This technique is adequate for a 60 MHz device that has a minimum feature size of about 7.5 μm . An initial layer of chromium is deposited as an adhesion promoter on the lithium niobate substrate prior to coating

with an additional layer of gold. The processed wafers are subsequently diced and the individual devices were mounted on a custom-designed PCB and below a PTFE cell (110 μl volume) that carries the liquid under test. The liquid cell is positioned accurately over the sensing area between the IDTs with the aid of guiding pins that fit into holes in the PCB and rests on the device without any sealant (Figure 13.17). This enables easy removal of the cell to clean the device and yet hold the liquid samples without leaking.

The experimental procedure for SH-SAW devices involves the measurement of both the phase velocity and attenuation of the SH-SAW signals propagating on the delay lines of the sensor. The set-up includes a signal generator, the SH-SAW sensor and a vector voltmeter (HP 8505A) (Figure 13.18). In this, an electrical signal is fed from the signal generator to the input IDTs; the amplitude ratio and phase difference between the input and output signals of each delay line were monitored by

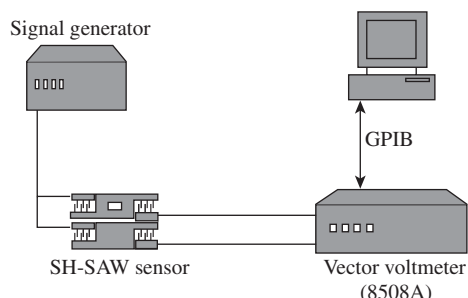


Figure 13.18 Experimental set-up for the SH-SAW-based characterization of liquids.

the vector voltmeter. The fractional velocity shift and attenuation change of the SH-SAW can be derived from the phase difference and the amplitude ratio, respectively [8].

All the experiments conducted in order to test and characterize the SAW devices were performed under controlled temperature conditions of $23 \pm 0.1^\circ\text{C}$ using a commercial ‘Dri-Bloc’ heater. Temperature characterization of the liquid sensors was performed and a linear dependence observed with temperature. After the initial characterization of the devices, experiments were conducted in order to discriminate between very different liquid samples (i.e. water, orange juice and milk) and, hence, confirm a ‘generic fingerprinting’ approach in which the need for biochemical-selective layers, normally used in liquid sensors, is eliminated. The experiments were performed by dispensing equal volumes ($50\text{ }\mu\text{l}$) of the different liquids into the micro cell using a clean, dry microliter syringe. The micro cell and devices were cleaned after each measurement using DI water and then dried. Results showing the discrimination of different liquid samples using the principal components analysis (PCA) technique, a linear, supervised, nonparametric pattern-recognition method used to discriminate between the different samples under test [10], are presented in Figure 13.19. The principal components in this case are derived by using four variables (sensor responses) measured using the vector voltmeter set-up, which are the attenuation and phase difference on the shorted and free delay lines. It has been shown in Chapter 5 that the measurements performed are directly related to the fractional change in phase velocity, $\Delta v/v$,

and attenuation change, $\Delta\alpha$. These parameters can be related to the measured parameters by

$$\frac{\Delta v}{v} = -\frac{1}{360} \frac{\lambda}{l} \Delta\phi$$

$$\Delta\alpha = C_b \frac{A}{l} \quad (13.4)$$

where l is the length of the delay line and C_b is a constant.

The fractional change in phase velocity and attenuation change are the result of perturbations of the SH-SAWs propagating on a substrate surface caused by mechanical and/or electrical properties of the liquid under test and, therefore, are functions of these properties. Thus, the above measured parameters can, in turn, be related to the viscosity, density, permittivity and conductivity of the liquid under test, via conductivity–permittivity charts [11].

13.4.2 CNT-based glucose sensor

Enzyme-immobilized sensors have found various important applications in many fields, such as clinical laboratories, fermentation processes and pollution monitoring. Within the area of biosensor research, immobilized enzyme-based electrode technology is stimulating active interest because of its ability to provide reliable, sensitive, accurate, easy-to-handle and low-cost probes. An enzyme electrode is a kind of electrochemical sensor obtained by immobilizing a thin layer of enzyme on the electrode. The concentration of the substrate (or the

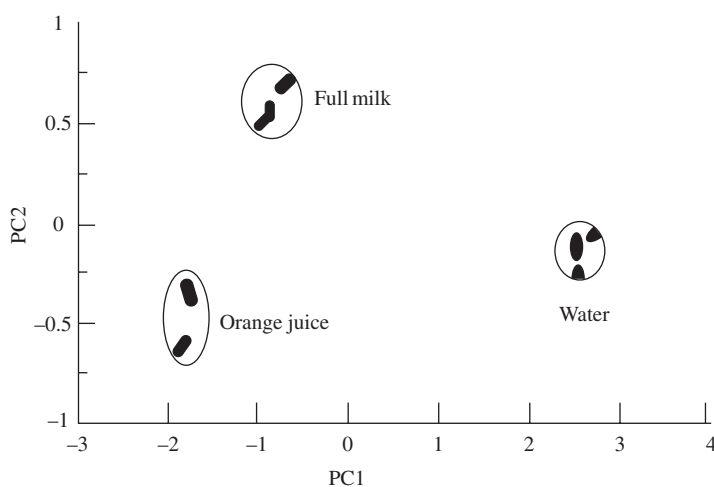


Figure 13.19 Principal component analysis for various liquids with an SAW-based device.

enzyme) can be associated to the electrochemical signal monitored potentiometrically or amperometrically.

It is expected that by reducing the electrode sizes from the microscale to the nanoscale will increase the detection sensitivity. Nanoscale materials, such as gold nanoelectrode ensembles, have proved to dramatically enhance electrochemical sensitivity over their larger-scale analogues [12,13]. As a new and interesting class of nanomaterials, carbon nanotubes (CNTs) were found to promote an electron transfer reaction when used as electrode materials. It has been demonstrated that CNTs reveal strong electrocatalytic activity and minimization of surface fouling onto electrochemical devices. Charge-transfer reactions at carbon nanotubes were found to occur at a faster rate than those at traditional carbon electrodes [14]. For SWCNTs, the electrical properties are sensitive to surface charge transfer and changes in the surrounding electrostatic environment as since every atom of them is on the surface, even simple adsorptions of certain molecules or polymers will significantly change the properties [15,16].

In this section, a recent effort on the fabrication of different functional carbon nanotube-based enzyme biosensors for glucose testing is presented. Multi-walled carbon nanotubes were synthesized by catalytic microwave chemical vapor deposition [17]. Purification was performed by acid treatment. Oxidized multi-walled carbon nanotubes (oCNT) were synthesized as described in Xie *et al.* [18].

Carbon nanotube-based electrodes were fabricated by the thick-film technique. Figure 13.20 presents a schematic diagram of a nanotube-based electrode structure. The silver conductive layers were fabricated using silver-derived paste prepared by the following procedure. Silver powder (2 g) was mixed with 1 g of 1,6-hexanediol

diacrylate and 0.1 g of ‘Darocur 1173’. The mixture was tape-cast on a PET transparency substrate under a mask. After removing the mask, the pattern on the substrate was UV-cured.

The graphite electrodes were fabricated by using a graphite-derived paste prepared by the following procedure. Graphite powder (1.2 g) was mixed thoroughly with 10 ml of isophorone solution containing 2% (w/v) PVC, 2% (v/v) DBE-4 and 2% (v/v) DBE-5 until a homogeneous paste was achieved. A 10 µL aliquot of this solution was then cast on the silver electrode surface of the sensor circle. The graphite electrodes were subsequently cured for 1 h (at 120 °C) and allowed to cool to room temperature. An insulator layer was then printed to cover most of the printed carbon strip, leaving a circle working area with a diameter of 5.1 mm and a contact area (on the opposite side). Glucose oxidase was immobilized onto the circular electrode by casting a 10 µL solution (0.05 M phosphate buffer solution (PBS), pH 7.0) containing 2 mg ml⁻¹ GOx and 0.5% Nafion and allowing it to evaporate at room temperature for 1 h. Subsequently, the surface was rinsed with doubly distilled water and stored at 4 °C.

The pCNT paste was prepared in a similar fashion to the graphite paste. To provide physical bonding of GOx, 0.18 g of pCNT powder was mixed thoroughly with 1.5 ml of isophorone solution containing 2% (w/v) PVC, 2% (v/v) DBE-4 and 2% (v/v) DBE-5 until a homogeneous paste was achieved. Then, 3 ml of DMF were added and the solution was ultrasonicated for 10 min. A 10 µL aliquot of this solution was cast on the silver electrode surface of the sensor circle. The pCNT electrodes were subsequently cured for 1 h (at 120 °C) and allowed to cool to room temperature. An insulator layer was then printed to cover most of the printed carbon strip, leaving a circle working area with a diameter of 5.1 mm and a contact area (on the opposite side). Glucose oxidase was immobilized onto the circle electrode by casting 10 µL of solution (0.05 M phosphate buffer, pH 7.0) containing 2 mg ml⁻¹ GOx and 0.5% Nafion and allowing it to evaporate at room temperature for 1 h. Subsequently, the surface was rinsed with doubly distilled water and stored at 4 °C.

Furthermore, aniline was electrochemically polymerized on the surface of a pCNT electrode. GOx (2 mg/ml) was immobilized by *in situ* polymerization of aniline (0.1 M aniline/0.2 M H₂SO₄/PBS) or by chemical immobilization. In the latter, 10 µL of a PBS solution of GOx, BSA and GA (2 mg/ml GOx, 4.2 mg/ml BSA and 0.2% GA) were placed on the electrode and allowed to react

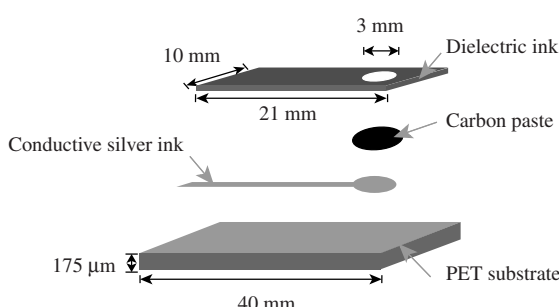


Figure 13.20 Configuration of a carbon nanotube-based electrode for glucose biosensing.

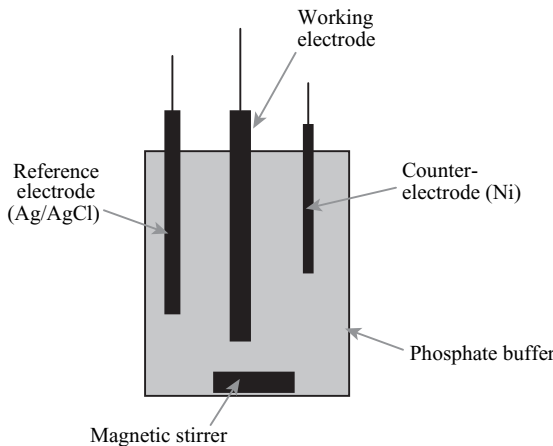


Figure 13.21 Schematic of a glucose-testing vessel.

for 12 h. Then, aniline (0.1 M aniline/0.2 M H₂SO₄/PBS) was electrochemically polymerized on the surface of a pCNT electrode containing chemically immobilized GO_x.

Then, 100 mg of PVA-oCNT were dispersed into 5 ml of PBS and ultrasonicated for 2 h. Next, 2 mg/ml of GO_x was added to the solution. A 10 µL aliquot of this solution was cast on the pCNT electrode surface of the sensor circle and allowed to evaporate for 12 h. Other electrodes were prepared by a similar procedure [19].

Measurements were carried out in a phosphate buffer (0.05 M, pH 7.0)-supporting electrolyte medium, using an ‘Accumet’ Ag/AgCl reference electrode (double junction, glass body) from Fisher Scientific. Cyclic voltammograms and chronoamperograms were recorded with a ‘Solartron’ SI 1280B electrochemical measurement unit. The working electrode, the Ag/AgCl reference electrode and nickel wire counter-electrode were inserted into a 20 ml beaker with a magnetic stirrer. Figure 13.21 shows a schematic diagram of the testing vessel.

Figure 13.22 compares cyclic voltammograms for glucose. These are expected to be similar to the cyclic voltammograms obtained for hydrogen peroxide. A graphite electrode without glucose shows a much lower current (Figure 13.22). The cyclic voltammograms of graphite electrodes, with or without glucose, in PBS buffer are compared in Figure 13.22(b). The current for the graphite electrode without glucose is much lower because of the non-addition of any Farady current due to reaction of glucose on the electrode. The oxidized current of ATPS-oCNT is also counteracted by the amino group of ATPS (Figure 13.22(c)).

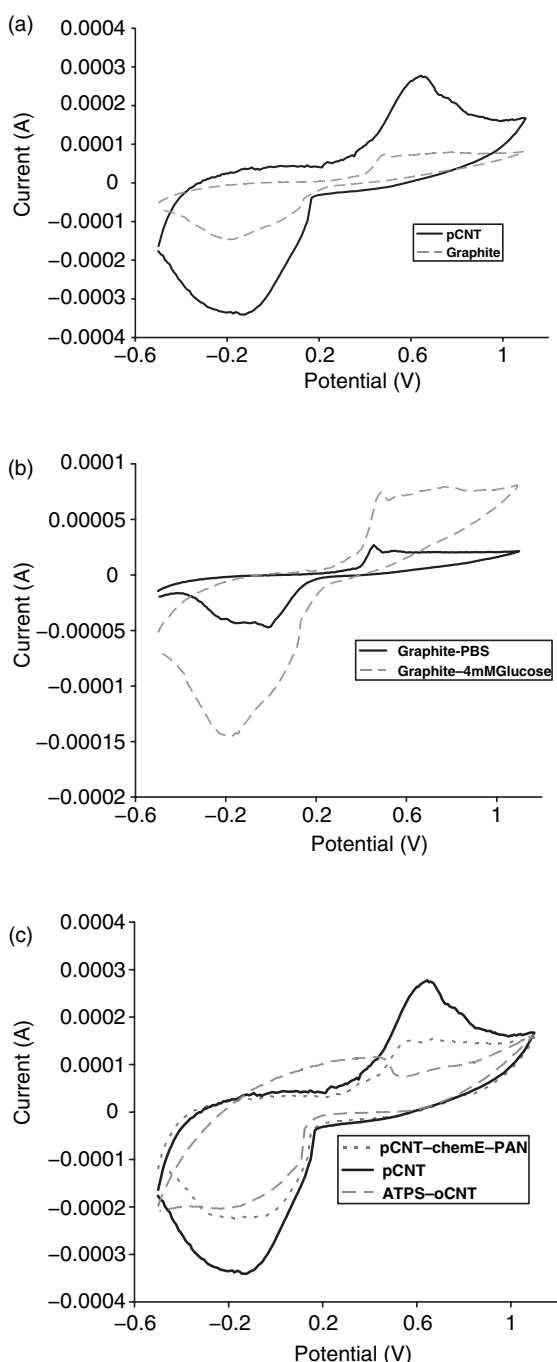


Figure 13.22 CV diagrams for using various electrode configurations for 4 mM glucose in phosphate buffer solutions (0.05 M, pH 7.0), at a scan rate of 50 mV/s.

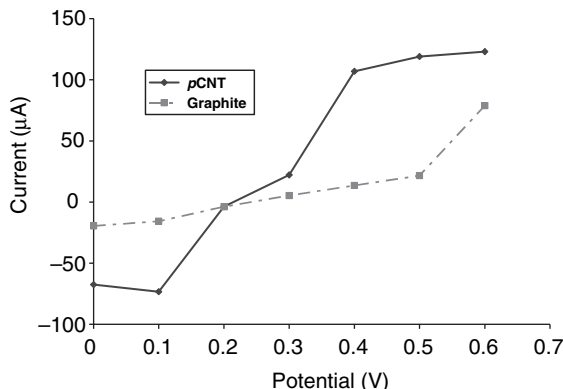


Figure 13.23 HDVs of *p*CNT and graphite in 4 mM Glucose phosphate buffer solutions (0.05 M, pH 7.0).

Figure 13.23 compares the hydrodynamic voltammograms (HDVs) for 4 mM of glucose at the *p*CNT-based microelectrode and the graphite-based device. The graphite/GOx electrode shows a low response to glucose at potentials lower than 0.5 V (vs. Ag/AgCl), while a gradual increase of the response is observed at higher potentials. The CNT/GOx microelectrode, in contrast, responds favorably to glucose over the entire (0.0–0.6 V) potential range. Significant oxidation and reduction currents, switching at around +0.20 V, are observed. The substantial lowering of the detection potential observed at the CNT-based microelectrode is coupled to significantly larger glucose signals.

Figure 13.24 compares the chronoamperograms of different types of CNT biosensors in 4 mM glucose

phosphate buffer solutions (0.05 M, pH 7.0). The *p*CNT electrode displays the highest current. The electrodes fabricated with functional materials, such as ATPS-*o*CNT and PVA-*o*CNT, also have good responses. Electrodes with physically immobilized GOx present higher currents than that with chemically immobilized GOx since chemical immobilization will destroy part of the activity of GOx (PVA-*o*CNT and *p*CNT-PAN). Electro-polymerized polyaniline can be applied as a diffusion barrier which dramatically decreased the current of the biosensor (*p*CNT-PAN).

This example shows that carbon nanotubes have potential applications as high performance electrodes for biosensor applications due to their high surface area, inertness, extraordinary conductivity, etc. For the optimization point of view, several nanotube-based electrodes were fabricated with different compositions and electrochemical testing in a three-electrode electrochemical cell was performed. A preliminary comparison showed that purified carbon nanotube-based electrodes exhibit a higher electrochemical activity than others.

13.5 POLYMERIC FABRICATION OF A MICROFLUIDIC SYSTEM

Polydimethylsiloxane (PDMS) is the preferred material for fabricating micro reactors, especially for biochemical applications, since it can replicate the fine features of sub-micron order. Figure 13.25 shows a schematic and a typical fabrication process of such a micro reactor [20]. These can be fabricated very easily via a micromolding process. A silicon wafer with a patterned SU-8 photo-

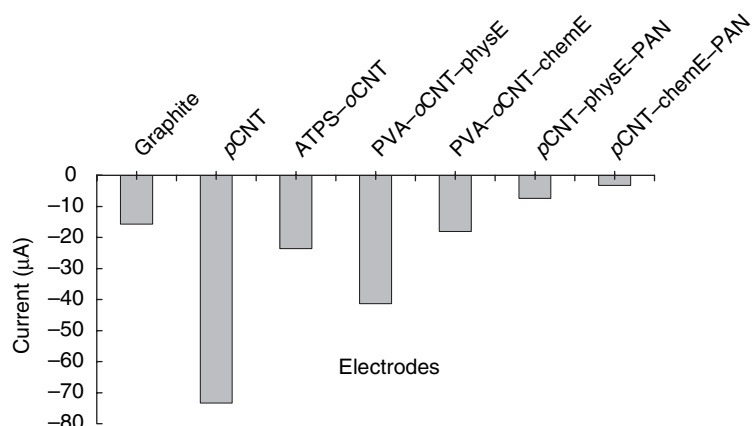


Figure 13.24 Chronoamperograms of different types of CNT biosensors in 4 mM glucose phosphate buffer solutions (0.05 M, pH 7.0).

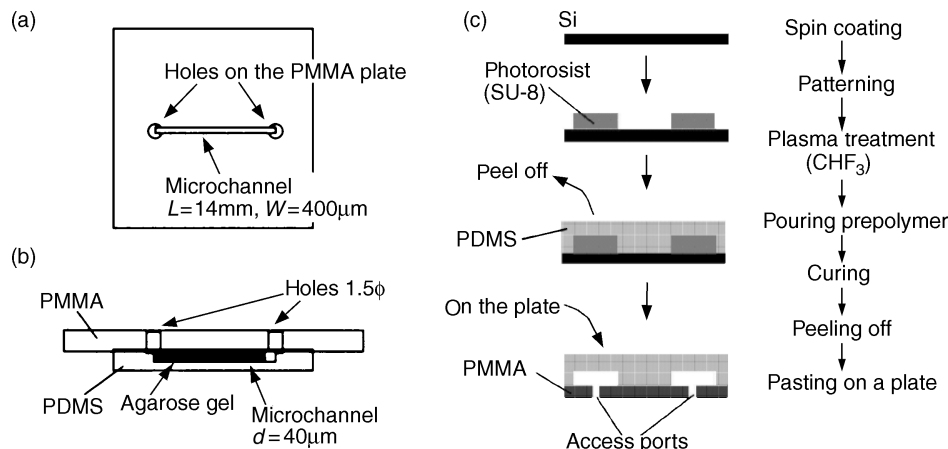


Figure 13.25 PDMS-based microchip: (a) top view; (b) cross-sectional view; (c) process flow [20]. Reprinted from Microelectronic Engineering, vol. 61–62, T. Fujii, PDMS-based microfluidic devices for biomedical applications, pp. 907–914, Copyright 2002, with permission from Elsevier

resist can be used as the ‘mold master’. After patterning, the prepolymer of PDMS is poured into the mold master and the cured PDMS is peeled off from the master to be pasted onto a flat plate of poly(methyl methacrylate) (PMMA) or glass on which access ports for introduction of the reagents and samples should be drilled in advance.

Another advantage of using PDMS in this context is attributed to its transparency to visible wavelengths, since fluorescent dyes are widely used for detection and quantification of molecules in most biochemical analyses. PDMS also has very good adhesion to flat surfaces. Functional devices with metal and/or oxide materials on a glass substrate can also be integrated with a PDMS–glass hybrid structure [20]. A PDMS–glass hybrid structure for cell-free protein synthesis is shown in Figure 13.26. For incubation of the reaction chamber, indium tin oxide (ITO) transparent electrodes are integrated in a multilayer glass substrate on which the PDMS chip with an array of reaction chambers is mounted. The activity of cell-free protein synthesis is dependent on the temperature. The two layers of integrated ITO electrodes could work as heater and temperature-sensing devices. The upper layer is used as a resistive temperature sensor while the lower layer is used as a heating device.

The concentration process is necessary for various chemical operations for both detection and purification. A basic design and the prototype of the micro-concentrator chip are shown in Figure 13.27 [21]. The chip consists of a micro reactor chamber divided by an ultrafiltration membrane and has an overall size of $8 \times 6 \times 8.5 \text{ mm}^3$. The lower part of the micro chamber

is filled with a high-concentration solution. A built-in photodiode at the bottom can detect changes in color and intensity caused by biochemical luminescence. The transparent nature of the UV-curable polymer structures enables such characterization. This device is useful in condensing protein to verify the concentration ability of biochemical reactions.

The optical transparency of UV-curable polymers can also facilitate isolation between the photo detector and the fluids under test, thus potentially enhancing the

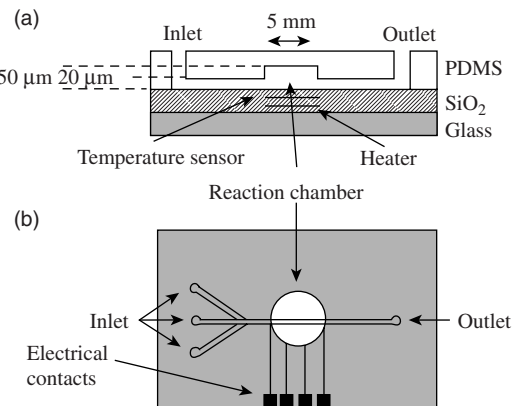


Figure 13.26 PDMS–glass hybrid structure for a single reactor in an array: (a) top view; (b) side view [20]. Reprinted from Microelectronic Engineering, vol. 61–62, T. Fujii, PDMS-based microfluidic devices for biomedical applications, pp. 907–914, Copyright 2002, with permission from Elsevier

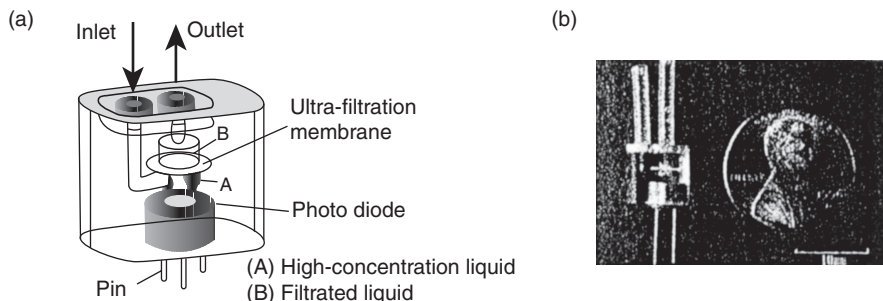


Figure 13.27 Polymer micro-concentrator chip: (a) schematic view; (b) photograph [21]. K. Ikuta, S. Maruo, T. Fujisawa, A. Yamada, ‘Micro concentrator with opto-sense micro reactor for biochemical IC chip family. 3D composite structure and experimental verification,’ IEEE Intern. Conf. Micro Electro Mechanical Systems, MEMS ’99, © 1999 IEEE

lifetime of the sensor [22]. Two such bioreactors are shown in Figure 13.28. In this *valveless design* of the reactor, the fluid flow is controlled by micro channels.

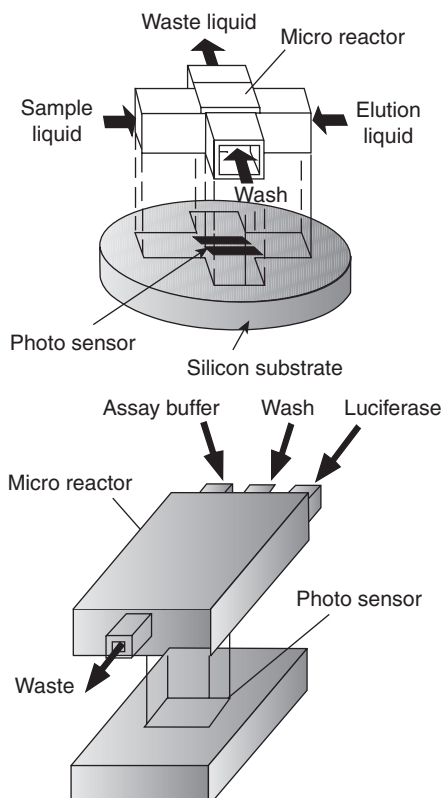


Figure 13.28 Designs of bioreactors integrated with a silicon-fabricated photo detector [22]. K. Ikuta, S. Maruo, Y. Fukaya, and T. Fujisawa, ‘Biochemical IC chip toward cell free DNA protein synthesis,’ Proc. IEEE Intern. Workshop on Micro Electro Mechanical Systems MEMS 98, 25–29, © 1998 IEEE

The polymer part is built by a microstereolithography technique such as the IH process (described in Chapter 11). The photodiode is first fabricated on a silicon wafer by conventional semiconductor processing which is later used as the substrate for the polymer structure.

REFERENCES

1. A. Sinha and A. Chandrakasan, ‘Dynamic power management in wireless sensor networks’, *IEEE Design and Testing of Computers*, **18**(2), 62–74 (March/April 2001).
2. G.J. Pottie and W.J. Kaiser, ‘Wireless integrated network sensors’, *Communications of the ACM*, **43**(5), 51–58 (2000).
3. J-S. Kim, K.J. Vinoy and V.K. Varadan, ‘Wireless health monitoring of cracks in structures with MEMS-IDT sensors’, *Proceedings of SPIE*, **4700**, 342–353 (2002).
4. B. Zhu and V.K. Varadan, ‘Integrated MOSFET-based hydrophone device for underwater applications’, *Proceedings of SPIE*, **4700**, 101–110 (2002).
5. V.K. Varadan, V.V. Varadan and H. Subramanian, ‘Fabrication, characterization and testing of wireless MEMS-IDT-based microaccelerometers’, *Sensors and Actuators: Physical*, **A90**, 7–19 (2001).
6. D.S. Ballantine Jr, R.M. White, S.J. Martin, A.J. Ricco, G.C. Frye, E.T. Zellers and H. Wohltjen, *Acoustic Wave Sensors – Theory, Design and Physico-Chemical Applications*, Academic Press, New York NY, USA (1997).
7. A.J. Pointon, ‘Piezoelectric devices’, *Proceedings of the IEE*, **129**, 298–307, (1982).
8. J.W. Gardner, V.K. Varadan and O.O. Awadelkarim, *Micro-sensors MEMS and Smart Devices*, John Wiley & Sons, Ltd, Chichester, UK (2001).
9. M. Thompson and D.C. Stone, *Surface-Launched Acoustic Wave Sensors*, John Wiley & Sons, Inc., New York, NY, USA (1997).
10. J.W. Gardner and P.N. Bartlett, *Electronic Noses: Principles and Applications*, Oxford University Press, Oxford, UK (1999).

11. M. Cole, G. Sehra, J.W. Gardner, and V.K. Varadan, 'Development of smart tongue devices for measurement of liquid properties', *IEEE Sensors Journal*, **4**, 543–550 (2004).
12. V.P. Menon and C.R. Martin, 'Fabrication and evaluation of nanoelectrode ensembles', *Analytical Chemistry*, **67**, 1920–1928 (1995).
13. C. R. Martin, 'Nanomaterials: a membrane-based synthetic approach', *Science*, **266**, 1961–1966 (1994).
14. P. J. Britto, K. S. V. Santhanam and P. M. Ajayan, 'Carbon nanotube electrode for oxidation of dopamine', *Bioelectrochemistry and Bioenergetics*, **41**, 121–125 (1996).
15. J. Kong, N.R. Franklin, C. Zhou, M. Chapline, S. Peng, K. Cho and H. Dai, 'Nanotube molecular wires as chemical sensors', *Science*, **287**, 622–625 (2000).
16. G. Collins, K. Bradley, M. Ishigami and A. Zettl, 'Extreme oxygen sensitivity of electronic properties of carbon nanotubes', *Science*, **287**, 1801–1804 (2000).
17. V.K. Varadan and J. Xie, 'Large-scale synthesis of multi-walled carbon nanotubes by microwave CVD', *Smart Materials and Structures*, **11**, 610–616 (2002).
18. J. Xie, N. Zhang, M. Guers and V.K. Varadan, 'Ultraviolet-curable polymers with chemically bonded carbon nanotubes for microelectromechanical system applications', *Smart Materials and Structures*, **11**, 575–580, (2002).
19. N. Zhang, J. Xie and V. K. Varadan, 'Functional carbon nanotube material-based enzyme biosensors for glucose sensing', *Proceedings of SPIE*, **5763**, 157–166 (2005).
20. T. Fujii, 'PDMS-based microfluidic devices for biomedical applications', *Microelectronics Engineering*, **61–62**, 907–914 (2002).
21. K. Ikuta, S. Maruo, T. Fujisawa and A. Yamada, 'Micro concentrator with opto-sense micro reactor for biochemical IC chip family. 3D composite structure and experimental verification', in *Proceedings of the IEEE MEMS'99 Conference*, IEEE, Piscataway, NJ, USA, pp. 376–381 (1999).
22. K. Ikuta, S. Maruo, Y. Fukaya and T. Fujisawa, 'Biochemical IC chip toward cell free DNA protein synthesis', in *Proceedings of the IEEE International Workshop: MEMS'98*, IEEE, Piscataway, NJ, USA, pp. 131–136 (1998).

Structural Health Monitoring Applications

14.1 INTRODUCTION

The study involving the monitoring, detection and arrest of the growth of flaws, such as cracks, constitutes what is universally termed as *Structural Health Monitoring* (SHM). SHM has four levels, which are the following: Level 1, confirming the presence of damage; Level 2, determination of the location, size and orientation of the damage; Level 3, assessing the severity of the damage; Level 4, controlling the growth of damage. Structural systems such as aircraft are quite complex, wherein there are several reasons that affect the structural integrity of the aerospace structure. The structural integrity of an aircraft is of paramount importance since any failure could be highly catastrophic, possibly leading to the loss of many lives. Hence, an early monitoring/warning system should be in place for notifying the impending failure of the system sufficiently early. These failures are normally caused by the presence of cracks, due to excessive vibrations, or due to the ‘flutter’ phenomenon caused by aeroelastic instability. Hence, it is necessary to find the regions of instability and place smart devices in these regions to detect and arrest these instabilities. These are shown in Figure 14.1. The figure also shows an exploded view of the engine where the sensors are placed for various functionalities.

Aircrafts are also composed of a variety of electronic, hydraulic and propulsion systems that have to withstand severe loading conditions. In addition, the whole system is highly ‘safety-critical’ and suffers degradation even when not being in service. Such complex systems thus require continuous monitoring and extended maintenance. Procedures for automated structural health and condition monitoring with high reliability, low cost and less power are therefore considerable. The monitoring of aircraft structures is nowadays still fully performed ‘on-

ground’ using *Non-Destructive Testing* (NDT) procedures according to prescribed instructions and after fixed service time intervals. It is generally well known in the NDT community that inspection redundancy can often improve the overall probability of detection of defects. In addition to bulk-wave, surface-wave and guided-wave ultrasonic NDT techniques, currently research is being pursued on a multi-technology program including MEMS devices and microwave NDT.

This chapter will address some aspects of crack detection using both bulk and microsensors, while the topic of vibration suppression and cabin noise control applications, which are also essential for enhancing the structural integrity of the structures, is addressed in the next chapter.

Civil engineering systems like building frames, trusses or bridges are a complex network of truss, rod, plate and shell elements. Their length scales may be larger than the aerospace structural components. The structural health monitoring of bridge structures for different moving loads is an area of great importance to increase the structural integrity of infrastructures and has been pursued in many countries. Damping of earthquake motions in structures is yet another area which has been taken up for active research in many seismically active countries. For such applications, smart devices derived from smart materials are extensively used. A schematic of a bridge structure showing the positions of smart sensors and actuators is shown in Figure 14.2. In this figure, we see that fiber-optic sensors are used essentially as sensing devices while PZT or Terfenol-D actuators are normally used for performing actuations such as vibration isolation and control.

The sensors and actuators used in these structures could be in the bulk form or thin-film form. With the availability of RF technology, wireless MEMS devices

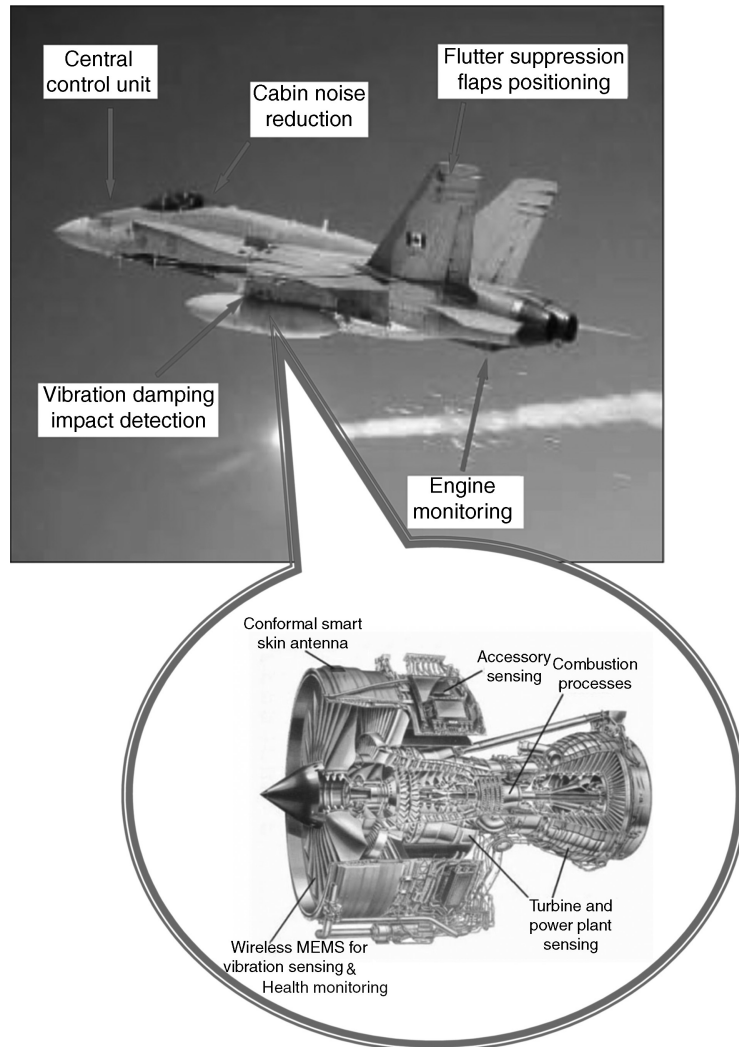


Figure 14.1 Location of smart devices in an aircraft.

are also currently being used extensively in sensing and actuator systems. In this chapter, a few examples of such wireless MEMS devices for structural health monitoring are given. In addition, two other examples of locating damage using bulk magnetostrictive and PZT sensors/actuators are provided. There also is a section devoted to vibration control in thin-walled box-beam structures which are traditionally used as aircraft structural components. Towards the end of this chapter, a section on the reduction of structure-borne cabin noise in helicopters is given. The examples given in this chapter only point to the variety of applications where one can use smart

materials. There are many more applications of smart materials and MEMS that are not covered in this book. However, the theoretical background given in this book will serve as a useful tool to handle such problems.

In this chapter, we will address Level 1, Level 3 and Level 4 of SHM. Level 3 will involve some correlation of damage parameters with fracture mechanics parameters such as *Stress Intensity Factors* (SIFs) or *Strain Energy Release Rates* (SERR). Level 1 will be demonstrated using both PZT as well as magnetostrictive sensors/actuators. Levels 3 and 4 will be demonstrated using only PZT sensors/actuators. In addition to the above,

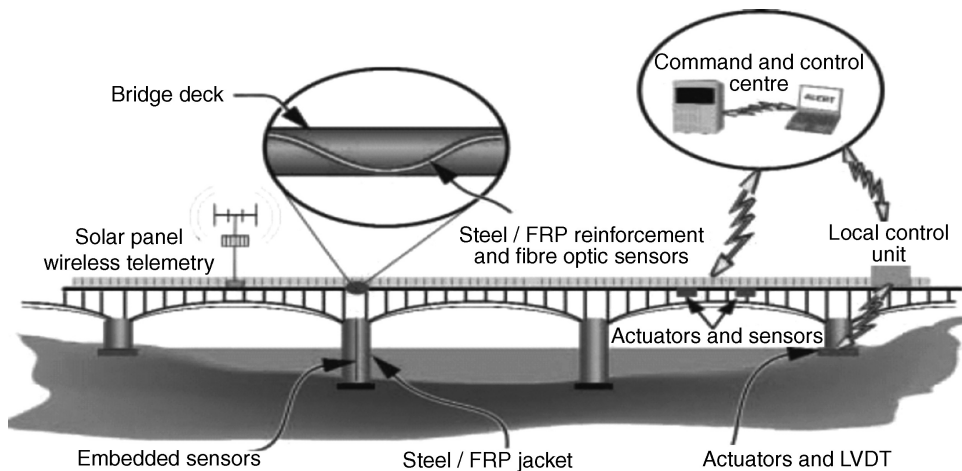


Figure 14.2 A schematic view of a ‘smart bridge’.

some of the latest technology on the usage of wireless MEMS devices for crack detection is discussed.

14.2 STRUCTURAL HEALTH MONITORING OF COMPOSITE WING-TYPE STRUCTURES USING MAGNETOSTRICTIVE SENSORS/ACTUATORS

In this section, the health monitoring concept is demonstrated both experimentally and numerically in a composite wing-type structure using magnetostrictive material patches. This falls under Level 1 of the SHM. The finite element model using the uncoupled magnetostrictive constitutive model (Chapter 8, Section 8.4.1), is used in the numerical simulation. The concept is based on the principle that the *open circuit voltage* (OCV) developed across a sensor due to an induced magnetic field in an actuator shows a change in its amplitude due to the presence of delaminations. Sensitivity studies are performed on two different structures, first on a 8-ply composite beam specimen and secondly on a 2-D tapered aircraft wing-type plate composite structure. The analysis is performed by varying the crack (delamination) size and location with respect to the location of the sensor and actuator patches. Both surface-mounted and embedded smart patch configurations are considered to study the effect of delamination on the OCV of the sensor over a wide range of actuating current frequencies. A horseshoe-type coil arrangement placed exactly over the magnetic patch is used to induce a magnetic field in the specimen. The *damage induced voltage* (DIV), which is the differ-

ence between the OCV across a sensor before and after the delamination, indicates the presence of damage. This voltage needs to be of the order of millivolts for meaningful measurement. Extensive experimentation is done on the beam system and the FE results are validated. Only FE simulation is done for 2-D models.

The most common form of failure of composites is the delamination of plies, which can grow rapidly and reduce the life of the structure. The main objective here is to detect the onset of delamination, so that corrective measures can be taken before it is too late to ‘salvage’ the structure. Traditionally, conventional non-destructive techniques (NDTs), such as ultrasonics, fractography, thermography or tomography, are extensively used to detect the presence of damage. However, these techniques require that the position of damage is known *a priori* and the region being inspected is readily accessible [1]. This limitation makes them very expensive for damage detection in aircraft or spacecraft structures which need frequent inspection. Therefore, an in-service damage detection (health monitoring) system is essential, which with built-in sensors can constantly monitor the integrity of the structure and also determine the location and extent of the damage.

Most methods available for damage detection do not use any smart material. The advantage of using smart materials is that they give an additional input in the form of an ‘interrogation signal’, which helps us in detecting damage more rapidly. These interrogating signals of practically any profile are easy to generate compared to mechanical signals. Most of the works reported have used piezoceramic sensors (PZT) for damage detection.

The advantage of using PZT sensors is that by passing a voltage in the PZT elements, strains are induced, even in the absence of external forces. These strains change rapidly with increasing delamination. This property is used to detect damages. A magnetostrictive material, such as Terfenol-D, until recently was thought off as an actuator material [2]. Compared to the PZT material, they offer a large ‘block force’ and a large ‘free strain’. In addition, they are available in the powder form, which makes them possible to be embedded in composites. Krishnamurthy *et al.* [3] was perhaps the first work reported on the properties of magnetostrictive particle layers that would make them useful for sensing purposes. Kumar and Krishnamurthy [4] demonstrated the use of a horseshoe-coil arrangement for creating the magnetic circuit, which is necessary for damage-sensing applications. The present study will use the above concept to demonstrate the effectiveness of a magnetostrictive material for damage-sensing purposes. Here, the health monitoring is based on the concept that when an AC current is passed to the actuation coil, it generates mechanical stress (strain). This stress changes not only with the change in delamination location, but also with its size. The change in stress produces a change in the magnetic flux and hence the voltage across the sensing coil. Measuring the change in the voltage (which is an easily measurable quantity compared to strains/stresses), before and after the delamination has taken place, will determine the condition of the structure.

14.2.1 Experimental study of a through-width delaminated beam specimen

Experiments are performed on a delaminated composite beam specimen. The delamination is assumed to be ‘through-width’. The experimental study required two sets of fabrications: (1) the fabrication of the magnetostrictive patch, which acts either as sensor or actuator, and (2) the fabrication and integration of a smart patch on a laminated composite beam. The smart patch is fabricated using a Terfenol-D powder, mixed in a matrix. The horseshoe coil magnet is mounted over a smart patch to generate the magnetic field and hence the mechanical strain. The aim of the experiment is to perform sensitivity studies to determine the effect of delamination size and location on the OCV across the sensing coil. Keeping this in mind, a number of experiments are designed on an 8-ply unidirectional laminated composite beam specimen of size $200\text{ mm} \times 24\text{ mm} \times 2.4\text{ mm}$. For these studies, both surface-bonded and embedded smart magnetostrictive patches are considered. The size of the smart patch is

made equal to $18\text{ mm} \times 8\text{ mm} \times 0.3\text{ mm}$. For a single patch collocated sensor-actuator configuration (see Figures 14.3(a) and 14.3(b)), the smart patch is introduced in the second layer. To study the effect of delamination size on the sensitivity of the response, three beam specimens with delamination sizes of 24 mm, 18 mm and 14 mm, located at 50 mm from the tip smart patch, are fabricated. For all of these cases, the delamination is introduced between the second and third layer. For the same collocated configuration, to study the effect of delamination location length-wise, five different specimens with delamination locations at 30 mm, 50 mm, 70 mm, 90 mm and 120 mm, respectively, from the sensor patch are fabricated. Here, the size of the delamination is made equal to 24 mm and they are again introduced between the second and third layer. For studying the depth-wise variation, five different beam specimens with delaminations at five different ply levels are fabricated. These delaminations are located length-wise at a distance of 50 mm from the smart patch. For studying the behavior of a non-collocated two-smart-patch configuration (see Figure 14.3(c)), a second smart patch of the same size is introduced in the second layer at a distance of 174 mm from the root. Three beam specimens with delamination of size 24 mm and located at 50 mm, 70 mm and 120 mm, respectively, from the second patch, are fabricated. All the composite beam specimens are fabricated using the hand ‘lay-up’ technique. After the fabrication process, the material properties of the patch are characterized and this is followed by experimentation. Figure 14.4 shows the laminate with the horseshoe coil and the overall experimental set-up.

The properties of the beam specimen and the smart patch are then estimated by using the principle of the Law of Mixtures. By knowing the volumes or mass fractions of the constituent materials, one can estimate the mechanical properties, as discussed in Chapter 6 (Section 6.2). The estimated material properties, using the Law of Mixtures, are given in Table 14.1. The magnetic circuit is established when an AC current is passed through the horseshoe coil arrangement. The horseshoe-type coil arrangement consists of two legs, one used as the sensing coil and the other for the purpose of actuation. This is mounted over the specimen with a small air gap for the flow of magnetic flux. Care is taken to position the open end tip of the horseshoe coil above the composite specimen to touch the ends of the embedded patch.

The experimental set-up (see Figure 14.4) consists of a signal generator, power amplifier, ampere meter power supply and a precision multimeter. An ampere meter is

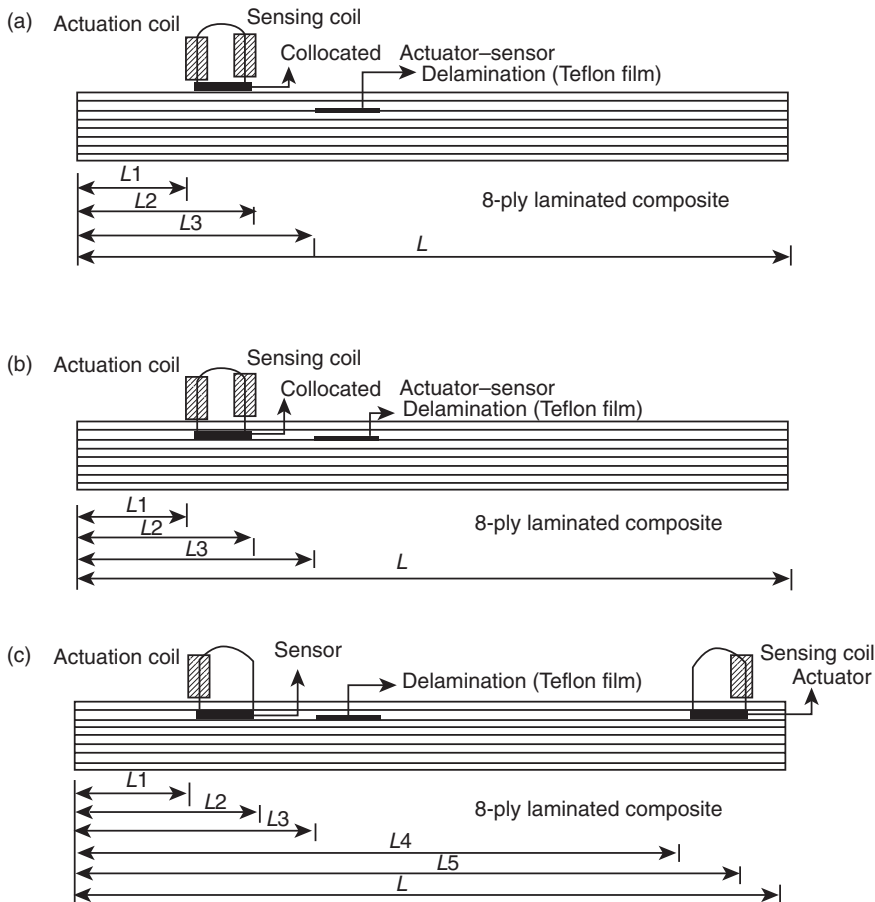


Figure 14.3 Laminated composite beam with (a) a surface-bonded patch, (b) a single embedded patch, and (c) two embedded patches: $L = 20\text{ cm}$; $L_1 = 2.3\text{ cm}$; $L_2 = 4.1\text{ cm}$; $L_3 = 6.1\text{ cm}$; $L_4 = 17.4\text{ cm}$; $L_5 = 19.2\text{ cm}$.

Table 14.1 Estimated material properties of the laminated composite and smart patch.

Property	Laminated composite	Smart patch
E_x (GPa)	53.48	32.7
E_y (GPa)	17.92	32.7
E_z (GPa)	17.92	32.7
G_{xy} (GPa)	8.92	12.57
G_{yz} (GPa)	8.92	12.57
G_{zx} (GPa)	3.44	12.57
ν_{xy}	0.25	0.3
ν_{yz}	0.25	0.3
ν_{xz}	0.34	0.3
ρ (Kg/m^3)	1500	2330

connected between the power amplifier and the actuation coil to measure the current value at the actuation end. The important parameters in this experiment are the applied current amplitude and its frequency. The actuation current signal generated (using a signal generator) is fed to the actuation coil through a power amplifier. The open circuit voltage (OCV) across the sensing coil is measured using a precision multimeter. This voltage is measured for different values of the actuation current and frequency. The same procedure is followed for every test, and the experimental results are discussed in the next section. Table 14.2 shows the parameters considered for the horseshoe coil configuration and the range of applied currents and frequencies used in the experimental work.

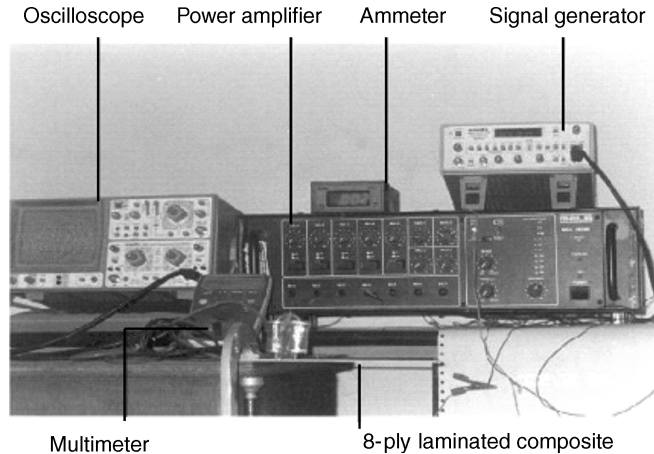


Figure 14.4 An overview of the experimental set-up for the laminate with a sensor.

14.2.2 Three-dimensional finite element modeling and analysis

The experimental results are verified using 3-D finite element simulation. The FE model assumes a linear behavior of the magnetostrictive material and hence an uncoupled linear constitutive model is used in numerical simulations. The coupling strains arising due to magneto-mechanical coupling are converted to block forces and ‘lumped’ onto the nodes containing the smart patch. The magnetostrictive material has the following constitutive laws. The first law is the *actuation* law, while the second is the *sensing* law:

$$\varepsilon = S^{(H)}\sigma + dH; \quad B = d\sigma + \mu^{(\sigma)}H \quad (14.1)$$

Table 14.2 Parameters of the horseshoe coil configuration and ranges of applied current and frequency.

Parameter of horseshoe coil configuration	Value
Number of turns in actuation coil	8000
Number of turns in sensing coil	7100
Air gap between the core and the laminate	0 mm
Diameter of the horseshoe core	3.6 mm
Length of the core	45 mm
Applied current frequency range	100 Hz–400 Hz
Applied current amplitude range	1 mA–4 mA
Magneto-mechanical coupling constant	$15 \times 10^{-6} \text{ mm/A}$

where ε is the induced strain, S is the material compliance measured at constant magnetic field H , σ is the induced stress, B is the magnetic flux density and μ is the permeability of the medium measured at constant H . The details of block force computation are given below. In the absence of mechanical forces, the strain and induced stress from the actuation law become:

$$\varepsilon(t) = dH(t); \quad \sigma(t) = E\varepsilon(t) = EdH(t) \quad (14.2)$$

where E is the Young’s modulus of the material.

If A is the cross-sectional area of the smart patch, the block force experienced by the smart patch due to the magnetic field intensity H is given by:

$$F(t) = EdA H(t) \quad (14.3)$$

The actuation current is an alternating current (I), which generates a magnetic flux (B) while passing through one arm of the horseshoe coil, also creating a magnetic field in the layer of smart patch, and this current varies sinusoidally with the time as $I(t) = I_0 \sin(Wt)$ where I_0 is the applied current amplitude and W is the applied current frequency. The magnetic field is related to the current by the expression $H(t) = n_a I(t)$, where n_a is the number of turns in the actuation coil. Using the above in Equation (14.3), the applied force can be written as:

$$F(t) = EdA I_0 n_a \sin(Wt) \quad (14.4)$$

The obtained force is applied as a concentrated force on the nodes of the patch in the longitudinal direction. This force will cause stress across the sensing coil. From this, the nodal finite element stresses can be computed. The *actual* stress is then calculated as:

$$\sigma_{\text{total}} = \sigma_{\text{nodal}} + \sigma_{\text{induced}} = \sigma_{\text{nodal}} + EdH \quad (14.5)$$

The sensing constitutive law (second part of Equation (14.1)), in the presence of a *pure* mechanical load will become $B = d\sigma_{\text{total}}$. Knowing the stresses from Equation (14.5), the flex density can be computed. Using this, the open circuit voltage can be computed from the relation:

$$V = -n_s A \frac{dB}{dt} \quad (14.6)$$

where n_s is the number of turns in the sensing coil.

The beam of size 200 mm \times 24 mm \times 2.4 mm is discretized using 1920 3-D brick elements. The total number of nodes in the model are 2499. The magnetostrictive patch is modeled using one 3-D brick element. The complete finite element model is shown in Figure 14.5. The beam is fixed at one end and the equivalent block force is applied in the longitudinal direction of the magnetostrictive patch – also shown in Figure 14.5.

Transient dynamic analysis using the ‘Newmark time-matching’ scheme is employed to compute the response histories. Stress histories are computed after ‘post-processing’ the displacement histories and subsequently using Equation (14.5). From the stress histories, the open circuit voltage is calculated for different times by using Equation (14.6). The AC current is applied over a frequency range of 100 Hz–400 Hz. The current amplitude is varied between 1 mA and 4 mA. In each case, the open circuit voltage (OCV) is measured and the damage-induced voltage (DIV), which is given by

$$\text{DIV} = \text{OCV}_d - \text{OCV}_h \quad (14.7)$$

is computed. Here, OCV_d is the OCV in a delaminated beam and OCV_h is the OCV in a healthy beam. All of the experimental results are validated with finite element results.

14.2.3 Composite beam with single smart patch

For the case of a beam with a surface-mounted patch, the delamination of size 24 mm is located between the second and the third layer at a distance of 50 mm from the tip of the sensor patch. OCV histories are obtained for

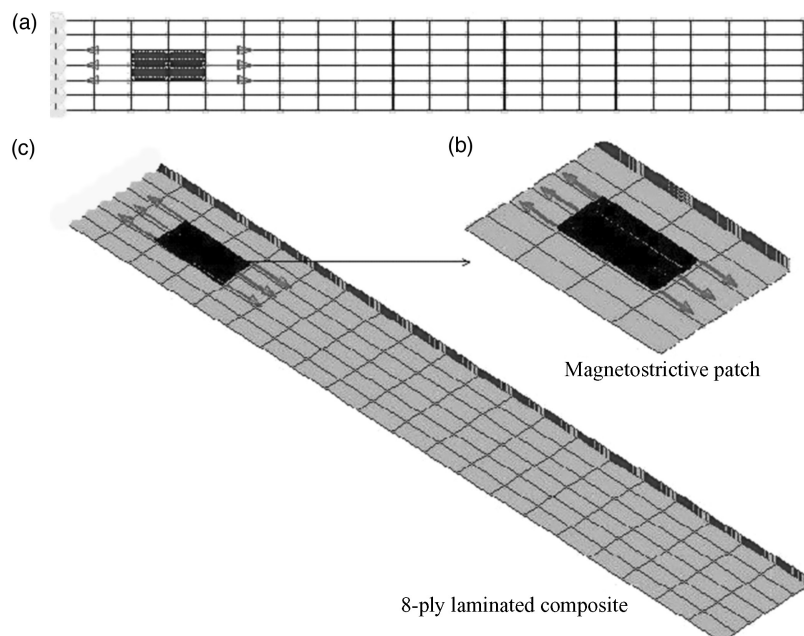


Figure 14.5 Three-dimensional finite-element model: (a) plan view; (b) enlarged isometric view of the smart patch; (c) isometric view of the complete model.

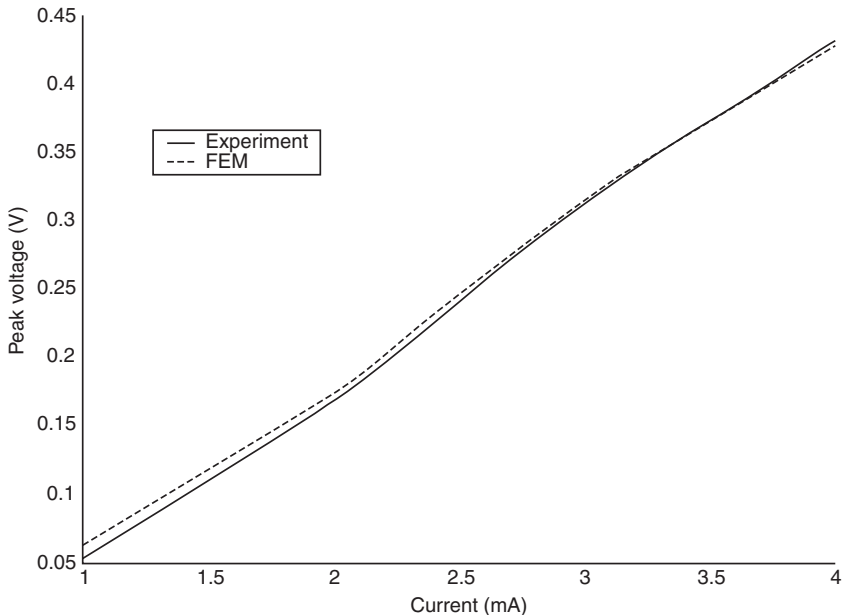


Figure 14.6 Comparison of experimental and FEM peak OCVs for a beam with a surface-bonded patch at a frequency of 100 Hz.

varying current amplitudes and frequencies. Figure 14.6 shows the peak voltage (OCV) as a function of the current amplitude for a current frequency of 100 Hz. We see from this figure that the OCV increases with

the current amplitude and there is excellent agreement with the results from the finite element prediction. Figure 14.7 shows the OCV and DIV time histories for the same delamination configuration at 200 Hz frequency.

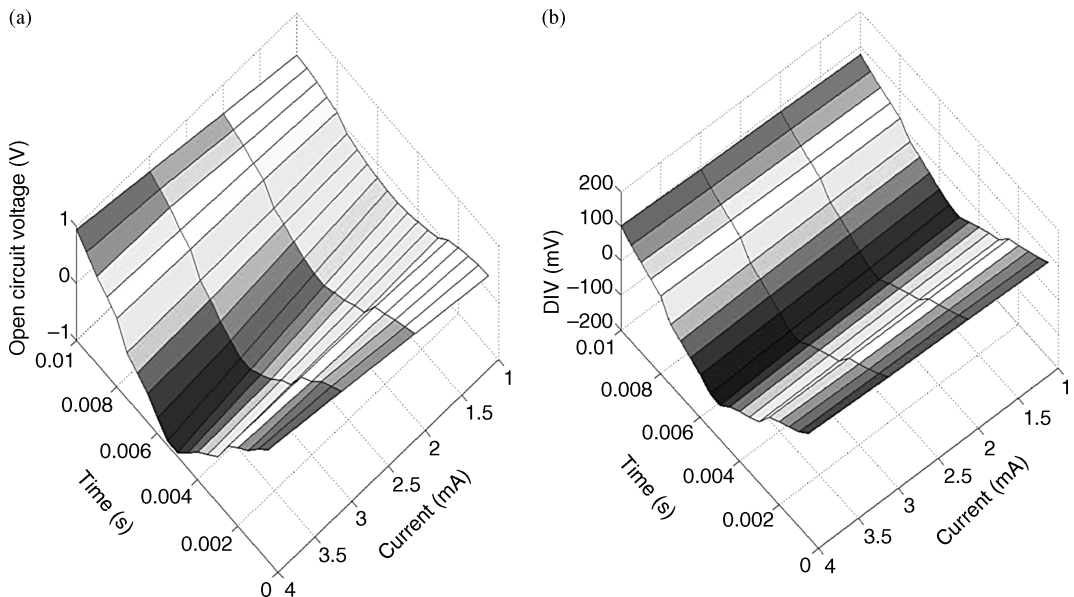


Figure 14.7 (a) OCV history and (b) DIV history of a surface-bonded patch as functions of the current amplitude at a frequency of 200 Hz.

Table 14.3 DIV data for an embedded single patch with a delamination size of 18 mm.

Frequency (Hz)	DIV (mV) (Experiment)				DIV (mV) (FEM)			
	1 mA	2 mA	3 mA	4 mA	1 mA	2 mA	3 mA	4 mA
100	45	58	72	87	46	57	71	87
200	54	68	82	99	53	66	80	98
300	64	79	94	112	65	78	92	109
400	76	91	107	126	75	89	104	121

This figure shows that the voltage history exhibits an inverted cosine profile. This is due to the presence of the time derivative for computing the magnetic flux intensity (B).

It is seen that the DIV is of the order of millivolts, which is easily measurable using normal instrumentation. The figure also shows that the DIV increases with increases in current amplitude and current frequency.

In the embedded smart patch case, three different sets of experiments are performed. In the first set, the delamination sizes are varied for a fixed location of 50 mm from the smart patch. Three different delamination sizes of 24 mm, 18 mm and 14 mm, respectively, are considered for the study. These delaminations are again introduced between the second and third layers and OCV histories are obtained for these specimens.

Tables 14.3 and 14.4 give the peak DIV values for 18 mm and 14 mm delaminations, computed from the peak OCV values of delaminated and ‘healthy’ beam specimens for different current frequencies and current amplitudes.

From these tables, we see that the magnitude of the DIV drops with the reduction in delamination size. This is to be expected since the smaller the delamination size, the smaller will be the change in the induced stress and hence the DIV will be smaller. As before, the DIV increases with the current frequency and amplitude.

The experimental results again match very well with the FEM computation.

In the second set of experiments on a single-patch collocated sensor–actuator configuration, the location of delamination was varied length-wise with respect to the smart patch for a fixed delamination size of 18 mm. OCV histories were obtained for five different locations of 30 mm, 50 mm, 70 mm, 90 mm and 120 mm from the smart patch. The peak value of the OCV was plotted as a function of the current amplitude and delamination location at a frequency of 100 Hz. The results are shown in Figure 14.8. We see from these plots that the peak value of the OCV increases with the current amplitude and as expected, the maximum value occurs near the sensor location.

In all of the above studies, both the actuation and sensing are performed at the same location. It would be interesting to know the sensor response when the actuator location is far away from the sensor location. This experimentation was performed by using two smart patches.

14.2.4 Composite beam with two smart patches

In this experiment, the second patch is introduced in the second layer of an 8-ply laminate specimen exactly in line and at a distance of 120 mm from the first patch.

Table 14.4 DIV data for an embedded single patch with a delamination size of 14 mm.

Frequency (Hz)	DIV (mV) (Experiment)				DIV (mV) (FEM)			
	1 mA	2 mA	3 mA	4 mA	1 mA	2 mA	3 mA	4 mA
100	32	44	57	71	30	42	54	68
200	41	53	66	83	38	52	62	81
300	50	64	78	95	48	61	76	95
400	62	76	90	108	59	73	91	110

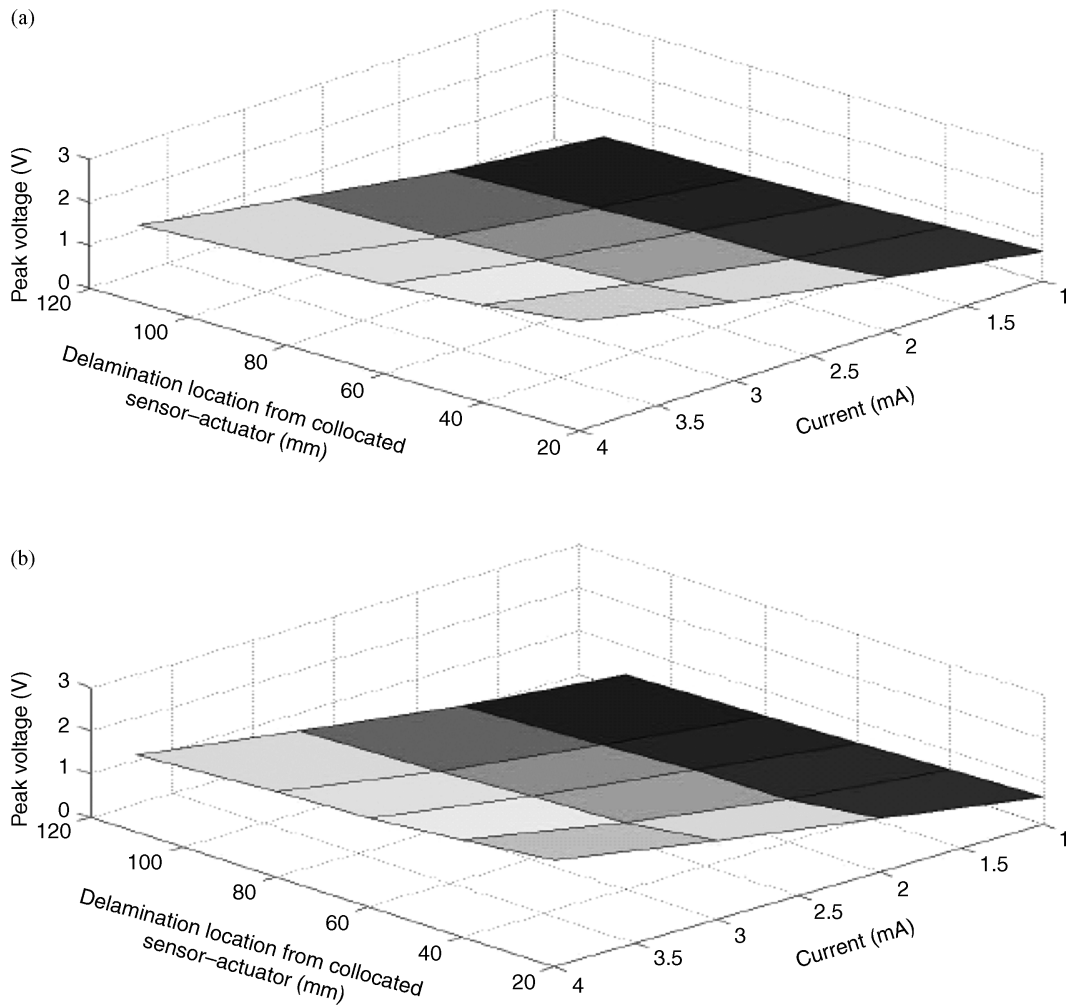


Figure 14.8 Peak OCV data for different delamination locations along the length of a laminated composite with an embedded single patch at a frequency of 100 Hz: (a) experimental; (b) FEM.

This patch is used as an actuator. The experiment is performed for three different delamination locations, length-wise at 50 mm (far from the sensor), 70 mm and 120 mm (close to the sensor) from the actuator patch. These distances also exactly correspond to the locations of delaminations for the single-patch-embedded collocated configuration, for which the experiments were performed previously. The size of delamination considered here is 18 mm. Tables 14.5 and 14.6 give the magnitudes of the peak DIVs for two different delamination locations. From these tables, we see that the DIV magnitudes are an order smaller than those predicted by the collocated configuration.

It is seen that if the delamination is very close to the sensor (Table 14.5), then peak DIVs are higher than in the case when the delamination is further away from the sensor (Table 14.6).

As in the single-patch case, the DIV increases with increases in the current amplitude and current frequency. This is because, in the collocated case the sensor and the actuator locations are at the same point. Due to this, the sensor experiences more strain and hence a greater open circuit voltage is induced in the sensing coil. In all of the above cases, the experimental results compare very well with the FE solutions. Hence, it can be concluded that the collocated sensor–actuator configuration predicts a

Table 14.5 DIV data for two embedded patches with a delamination at 50 mm from the actuator.

Frequency (Hz)	DIV (mV) (Experiment)				DIV (mV) (FEM)			
	1 mA	2 mA	3 mA	4 mA	1 mA	2 mA	3 mA	4 mA
100	0.3	0.5	0.7	0.9	0.4	0.5	0.6	0.8
200	0.4	0.6	0.8	1.0	0.4	0.6	0.7	0.9
300	0.5	0.7	0.8	1.1	0.5	0.7	0.7	1.1
400	0.5	0.8	0.9	1.2	0.6	0.8	0.8	1.2

Table 14.6 DIV data for two embedded patches with a delamination at 70 mm from the actuator.

Frequency (Hz)	DIV (mV) (Experiment)				DIV (mV) (FEM)			
	1 mA	2 mA	3 mA	4 mA	1 mA	2 mA	3 mA	4 mA
100	0.5	0.6	0.8	1.0	0.4	0.6	0.7	0.9
200	0.6	0.7	0.9	1.1	0.6	0.7	0.8	1.0
300	0.7	0.8	1.0	1.2	0.7	0.8	0.9	1.1
400	0.7	0.8	1.1	1.2	0.8	0.9	1.0	1.2

higher voltage compared to the non-collocated configuration. Many more parametric studies on this beam specimen for both single- and two-patch cases are reported in Saida *et al.* [5].

14.2.5 Two-dimensional wing-type plate structure

The above procedure of determining the presence of damage is next extended to a 2-D aircraft wing-type

plate structure. In this case, only an FE simulation is performed. The configuration of the structure with the location of sensors and actuators is shown in Figure 14.9. (All dimensions are given in millimeters). The configuration resembles that of a ‘delta wing’. The model has two sensor patches and a single actuator patch, as shown in the figure. The delamination is of a ‘rectangular type’, coming out from one of the edges, as shown in Figure 14.9.

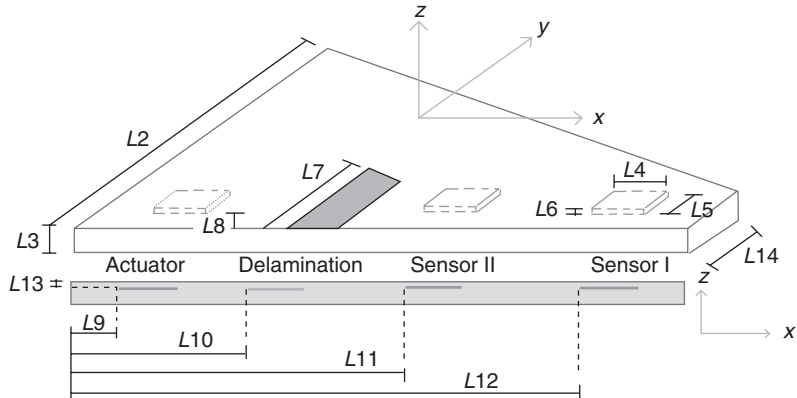


Figure 14.9 A delta-wing configuration showing locations of the sensors and actuators: L_1 , 1400 mm; L_2 , 800 mm; L_3 , 30 mm; L_4 , 20 mm; L_5 , 10 mm; L_6 , 0.3 mm; L_7 , 40 mm; L_8 , 20 mm; L_9 , 40 mm; L_{10} , 300 mm; L_{11} , 800 mm; L_{12} , 1340 mm; L_{13} , 0.3 mm; L_{14} , 200 mm.

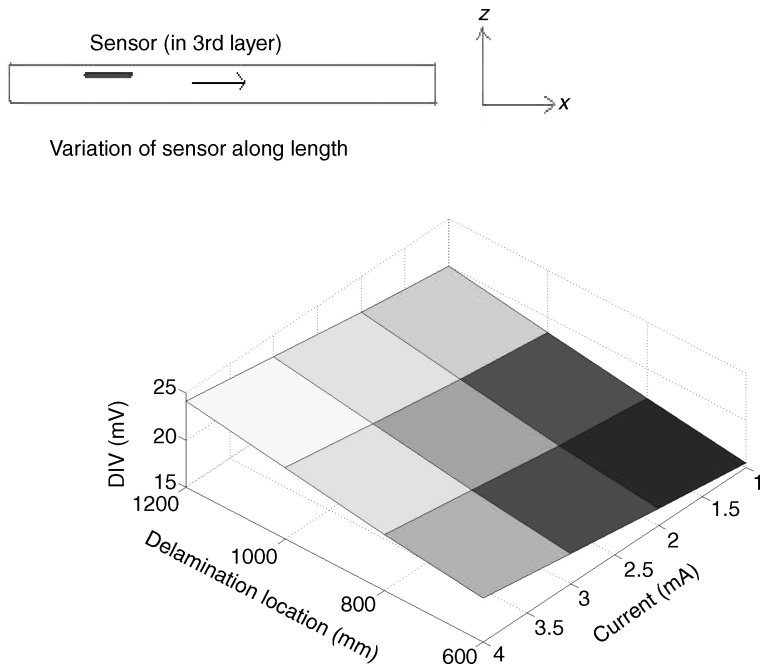


Figure 14.10 Peak DIV as a function of delamination location and current amplitude (sensor in the third layer).

As a first exercise, the sensor and actuator positions are fixed and the delamination location is varied along the length. The current amplitude is varied from 1 to 4 mA. The sensor is located in the third layer. The peak DIVs are plotted and these are shown in Figure 14.10. As in the 1-D case, for higher current amplitudes the DIV values are higher for all delamination locations. In addition, higher DIVs are obtained at locations closer to the actuator. Next, the actuator, delamination locations and Sensor-I locations are fixed and the Sensor-II location is varied, as shown in Figure 14.11. This figure shows the DIVs predicted by both Sensor-I and Sensor-II. When Sensor-II is very close to the actuator, it predicts a DIV as high as 45 mV. Note that this location is also quite close to the delamination location. Sensor-I predicts a lower DIV, as it is far away from both the delamination and actuator.

From these studies, it the use of Terfenol-D as a sensor material and its use in crack detection has been clearly demonstrated. It was also shown that the sensitivity of the sensor varied with the location of the delamination, and the locations of the actuator and sensor with respect to the delamination location.

14.3 ASSESSMENT OF DAMAGE SEVERITY AND HEALTH MONITORING USING PZT SENSORS/ACTUATORS

In this section, we will use a PZT actuator/sensor combination for the same purpose of detecting the presence of cracks. The principle of operation is very similar to the previous case of the magnetostrictive sensor/actuator combination. That is, by passing a voltage across the PZT actuator, it induces a strain in the structure, which changes the stress and hence the voltage across the PZT sensor. Measuring the voltage before and after the damage will confirm the presence of damage in the structure. However, our objective here is to establish the severity of the damage. This can be done if one determines the fracture parameters, such as the stress intensity factor (SIF) and strain energy release rate (SERR), and correlate these parameters with the output voltage across the sensor. If plots of the SIF or SERR with the sensor voltage for various damage configurations are available, by measuring the changes in the voltage across the sensor it will be possible to establish the severity of the flaw. The numerical model for this problem is done through a ‘self-sensing’ PZT finite element, as derived in Chapter 8.

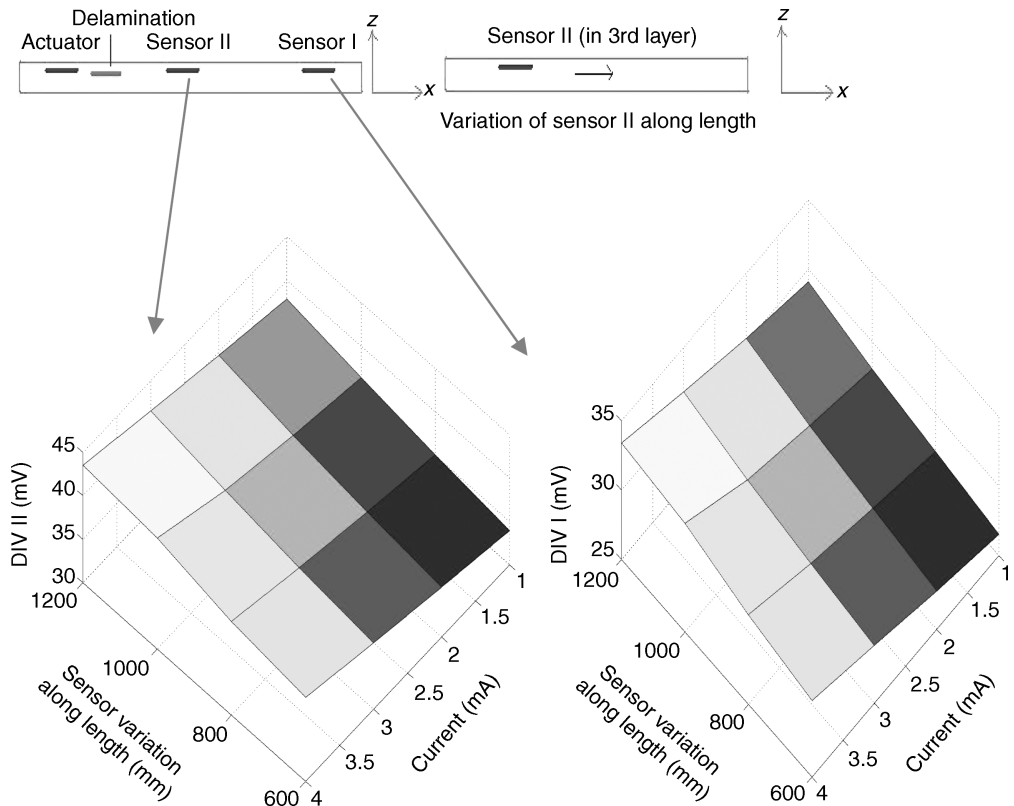


Figure 14.11 Peak DIVs in Sensors I and II for different locations of Sensor II as a function of current amplitude (Sensor II in the third layer).

The approach is demonstrated for both static and dynamic loading. The details of this work can be found in Sastry [6] and Sastry *et al.* [7].

First, we will introduce some basic definitions in *Linear Elastic Fracture Mechanics* (LEFM). It is well-known that if there is a crack in a body which is subjected to some loading, the stresses developed in the region surrounding the crack tip are nearly infinite. That is, the stress, $\sigma = \alpha K / \sqrt{r}$, where r is the radial distance measured from the crack tip and α is some constant. The parameter K is called the stress intensity factor (SIF). In fracture mechanics, one is mainly concerned in the region very close to the crack tip. Hence, it becomes more practical to deal with those parameters that are finite in the region close to the crack tip for quantifying the extent of fracture. In this context, the parameter K (SIF) can be used as it is always finite. Hence, the study of fracture mechanics always deals with the determination of the SIF, rather than the stress itself. Another

parameter that is commonly used in fracture studies is the strain energy release rate (SERR). This is defined as the energy required for closing the crack. If U is the strain energy and a is the crack length, then the SERR (G) is defined as:

$$G = \lim_{a \rightarrow 0} dU/da \quad (14.8)$$

The SERR is related to the SIF for an isotropic material structure in a plane-stress condition as $G = K^2/E$. Similar relations are available for composite structures. There are different ways to evaluate this parameter. The most common method of evaluating the SERR is via the ‘J-integral’ proposed by Rice [8]. This is a *line integral*. The improved form of this integral is called the ‘Equivalent Domain Integral’ (EDI), which is an *area integral* [9]. This form is now extensively used in fracture studies and is also used in this work. Such

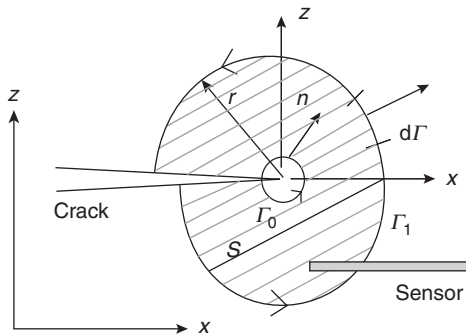


Figure 14.12 Schematic showing the J-integral contour.

an integral is evaluated over an area taken over a path taken far away from the crack tip, as shown in Figure 14.12.

In this figure, r is the radius of the contour path Γ_1 from the crack tip and n and m are the two outward normals from the contours Γ_0 and Γ_1 , respectively. If σ_{ij} is the 2-D stress field and U and T are the strain and kinetic energy, respectively, then the J-integral is given by:

$$G = J = \int_{S(\Gamma_0=0)} \left[\sigma_{ji} \frac{\partial u_i}{\partial x} \frac{\partial \eta}{\partial x_j} - (U + T) \frac{\partial \eta}{\partial x} + \rho \left(\ddot{u}_i \frac{\partial u_i}{\partial x} - \dot{u}_i \frac{\partial \dot{u}_i}{\partial x} \right) \right] dS \quad (14.9)$$

In the above equation, u_i , \dot{u}_i and \ddot{u}_i are the displacement, velocity and acceleration components in the two coordi-

nate directions and $\eta = r'/r$, where r' is the radius of the node of a particular element in the surface S .

The next important aspect in fracture mechanics is to know the modes of failure. There are three modes of failure, namely, the *Opening Mode* (Mode-I), *Shearing Mode* (Mode-II) and *Tearing Mode* (Mode-III). These are schematically shown in Figure 14.13. For 2-D problems, only Mode-I and Mode-II fractures are possible and hence the sensing of delamination will be carried out only under these two modes.

In this study, the FEM developed in Chapter 8 (Section 8.2) is used. Equation (8.30) gives the necessary FEM equation for the mechanical as well as the electrical degrees of freedom. These results are ‘post-processed’ to obtain the voltages as follows. We first assume that the surface charge vector $\{q\}$ remains constant with time due to an ‘open-circuit’ condition and in the present case it is assumed to be equal to zero. It is also assumed that there are no residual stresses and charges in the embedded piezoelectric patch. We can write the sensor equation as:

$$\{E_z\} = -[K_{EE}]^{-1}[K_{uE}]\{u\} \quad (14.10)$$

The voltage developed across each sensor due to the deformation-induced electric field $\{E_z\}$ acting in the z -direction is given by:

$$V_i = \sum_i E_{zi} \Delta z_i \quad (14.11)$$

The charge stored and the equivalent voltage are given by:

$$\bar{V} = \frac{\sum V_i Q_i}{\sum Q_i}; \quad Q = \int D_z t dx \quad (14.12)$$

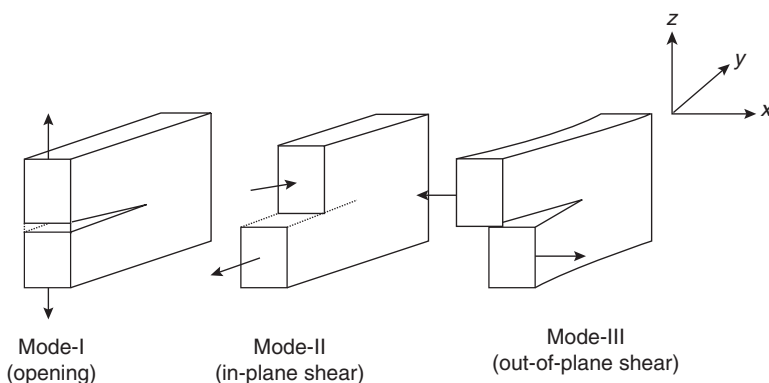


Figure 14.13 Three modes of fracture.

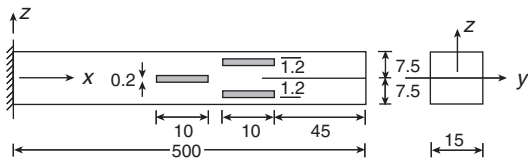


Figure 14.14 Schematic of the double-cantilever beam specimen (and dimensions (mm)) used for the numerical experiments.

All of the parameter definitions in the above equations have been defined earlier in Chapter 9. Numerical experiments are now performed to test the formulation. For this, the double cantilever beam (DCB) shown in Figure 14.14 is considered.

The model consists of a composite cantilever beam having an unidirectional (0^0) fiber orientation and made of graphite–epoxy laminates. Three patches of piezoelectric materials are embedded in between the composite layers. The first patch is placed exactly at the ‘mid-depth’ of the section at which the bending stresses due to the externally applied loads are at a minimum. The other two patches are placed away from the central patch and towards the free end of the beam and are also placed symmetrically about the central longitudinal axis of the beam. In this present study, the delamination is considered to occur along the central longitudinal axis at the ‘mid-depth’, which makes the beam specimen to act like a DCB. The central patch is placed ahead of the delamination crack tip. In the chosen configuration, the locations of the piezoelectric patches are fixed and the length of the delamination is varied from 25 mm to 50 mm from the free end. The material properties for the above beam are given in Table 14.7.

The FE model has 540 nodes and 440 elements (including the sensor patches), which gives an overall

system size of 1068×1068 . The above discretization is for a delamination length of 50 mm. The contour for computing the J-integral encompasses all three sensors and is symmetric about the delamination. The objective of keeping the location of the piezoelectric patches fixed is to study the effect of the strains developed in the piezoelectric material and the corresponding voltages generated on their surfaces as the tip of delamination approaches the piezoelectric patches. This will give a distinct correlation of the computed J-integral (hence, the SIF and other crack tip features) with the sensor output as the delamination grows towards the sensor group.

For sensing under Mode-I static loading, two static loads of 50 N are applied at the tip of the beam such that each load pulls each of the sublaminates to either side. Due to the symmetries of loading and geometry, the upper and lower sublaminates undergo the same amount of deformation and the symmetrical stress conditions prevail about the central longitudinal axis. About this axis, the stresses would be minimal, except at a certain region just ahead of the crack tip. Figure 14.15(a) shows the variation of the sensed voltage on the surface of the sensor patch placed at the ‘mid-depth’ and ahead of the crack tip. The abscissa shows the x -coordinate measured from the fixed end of the beam. When the delamination length of the beam is 25 mm, the effects of delamination and applied load upon the bending of the patch is minimal as the crack tip location is too far away to affect the flexural behavior of the patch and the sensed voltage distribution on its surface is almost constant. As the delamination length is increased and approaches towards the patch, a linear increment in the voltage across the surface from the far end and towards the crack tip can be observed in the figure. The same figure also shows an increase in the sensed voltage as the delamination length

Table 14.7 Material properties of the double-cantilever beam specimen used for the numerical experiments.

Material property	Graphite–epoxy beam	PZT
Young’s modulus, E_{11} (GPa)	150	63
Young’s modulus, $E_{22} = E_{33}$ (GPa)	9	63
Shear modulus, G_{12} (GPa)	7	24.2
Shear modulus, $G_{23} = G_{13}$ (GPa)	25	24.2
Poisson’s ratio, $\nu_{12} = \nu_{23} = \nu_{13}$	0.3	0.3
Mass density, ρ (kg/m^3)	1600	7600
Piezoelectric coefficient, $d_{31}(10^{-12} \text{ m/V})$	—	254
Piezoelectric coefficient, $d_{32}(10^{-12} \text{ m/V})$	—	254
Piezoelectric coefficient, $d_{33}(10^{-12} \text{ m/V})$	—	0
Relative permittivity, $\mu_{11}/\mu_0 = \mu_{22}/\mu_0 = \mu_{33}/\mu_0$	—	1500

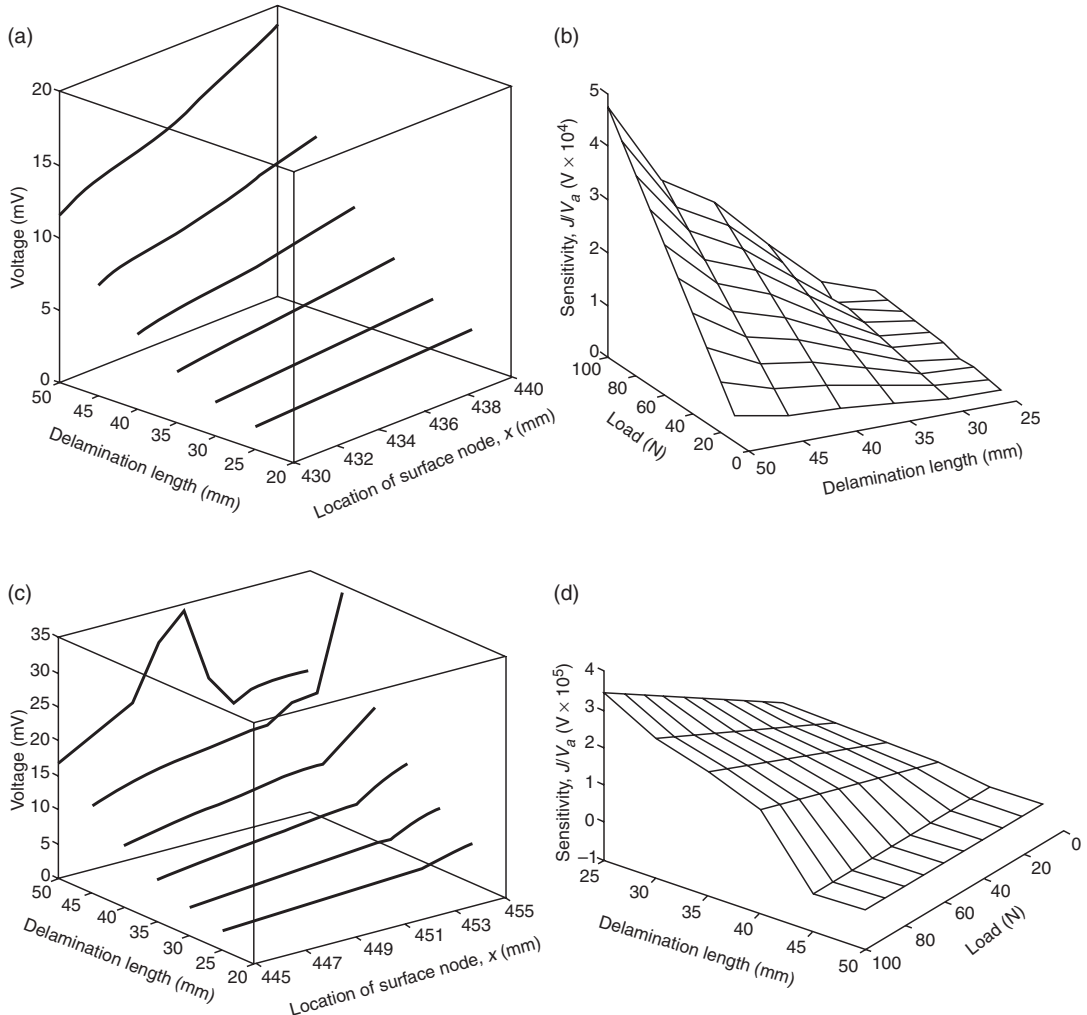


Figure 14.15 (a) Peak voltage generated in the central patch; (b) sensitivity in the central patch; (c) peak voltage generated in the lower patch; (d) sensitivity in the lower patch.

is increased, along with the distribution of voltage across the length of the patch. However, the effect of the intense crack tip stress fields approaching towards this sensor patch could not be captured. This is captured by the other two sensor patches.

As the load acts on the beam symmetrically on the geometrically symmetric DCB specimen (the delamination axis coinciding with the central longitudinal axis), the piezoelectric patches placed above and below the longitudinal axis undergo equal amounts of flexure. Due to this, symmetrical stress conditions prevail in these patches and equal amounts of voltage are generated in

these patches. Hence, the voltage distribution is shown only for the patch in the lower sublamine. Figure 14.15(c) shows the spatial distribution of the electric voltage along the length of the patch in the lower sublamine for various lengths of delamination and the abscissa is taken as the surface nodal x -coordinate from the fixed end. As can be observed from this figure, that when the delamination length is 25 mm, in which case the near end of the PZT patch is 20 mm away from the crack tip, the strains in the sensor patch seem to be almost uniform along the surface, except for a small length towards the near end of the crack tip.

As such, it can be inferred that the flexure of the beam is also causing flexure of the sensor patch. When the crack tip is made to approach the sensor patches in the sub-laminates, the effect of the crack tip stresses causing flexural strains in the PZT patches can also be observed to be causing non-uniform strains and voltages in the PZT patches. When the delamination length is 45 mm, the near end of the sensor patch lies just above and below the crack tip and the high-stress region near the crack tip is observed to be causing a phenomenal increase in the strains, as well as in the generated voltages in the sensor patches. When the delamination length is 50 mm, the mid-lengths of the patches lie above and below the crack tip. The high stresses at the crack tip mostly affect the mid-length region of the beam and a sudden jump in the generated voltage can be observed exactly at the mid-lengths of the sensor patches. The strains at the surface behind the crack tip again recede and thereby the voltage also recedes. Thus, the effect of the damage location upon the sensed voltage can be found and the sudden variation in the magnitude and profile of the surface voltage across the length of the sensor patches indicates a damage in the nearby regions.

Next, the sensitivity of the sensor, defined as the ratio of the J-integral to the average voltage generated by the sensor (J/V_a), is evaluated by computing the J-integral for each delamination length for different applied loads. The load is varied from 10 N to 100 N in increments of 10 N.

The average voltage generated is computed as a weighted average of all the values of voltage along the surface length of the piezoelectric patch. This is computed using Equation (14.12). The plots of these for the middle and bottom sensors are shown in Figures 14.15(b) and 14.15(c), respectively. When the delamination length is 50 mm, the J-integral value as well the value of average voltage shows a considerable increase, as a result of which the sensitivity value also shows a sudden increase in its value. The sensitivity is linear for various loads for a particular crack length and is piece-wise linear for various crack lengths under a particular load. For delamination lengths of 40 mm and 50 mm, the value of the J-integral and the average voltage show considerable increases as the sensor layers come very close to the high-stress crack-tip-surrounding zone. For the lower sensor patch, the nearest delamination tip case (50 mm delamination) is the most severe. For this case, the patch is highly sensitive only at the higher loading amplitude. However, the sensitivity is linear over the entire loading range.

Similar studies are performed for the Mode-II loading case. For this case, a loading of 100 N is applied at the tip of the beam such that the sublaminates slide upon each other in addition to undergoing bending deformation. In this case, the deformation field is not symmetrical as in the Mode-I loading case and as a result, the upper and lower patches will generate different voltages. Figures 14.16(a)

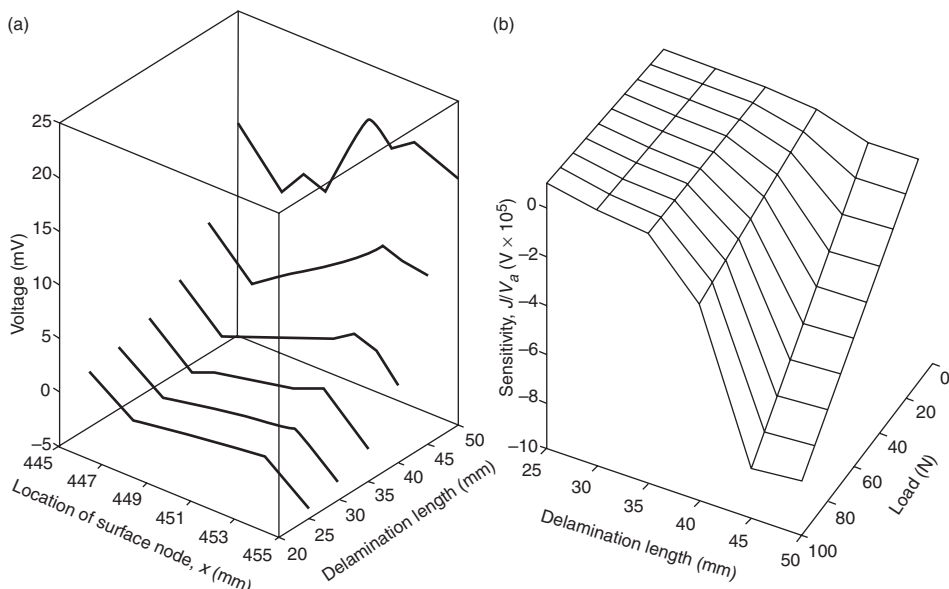


Figure 14.16 (a) Peak voltage generated and (b) sensitivity for the lower patch under Mode-II loading.

and 14.16(b) show the voltage generated and the sensitivity for the lower patch.

One can draw similar inferences as in the Mode-I loading cases. From these examples, we can conclude that the sensitivity measure not only confirms the presence of damage but also indicates its severity. Hence, this measure can be used in on-line SHM studies.

14.4 ACTUATION OF DCB SPECIMEN UNDER MODE-II DYNAMIC LOADING

The main objective of this section is study the effect of open-loop actuation to control or delay the growth of cracks. A crack is said to grow if the SIF reaches a threshold value with increases in the load. This problem falls under Level 4 of the SHM. The same configuration of the laminated composite DCB model with embedded piezoelectric sensor layers used in Section 14.3 for the purpose of sensing the crack tip stress fields is also considered here for distributed actuation to control the crack tip stresses. In this present study, the locations of the piezoelectric layers are taken as before; however, these layers are used for actuation purposes. The idea is to conduct a feasibility study for possible reduction of the strain energy release rate (SERR) with the application of counter-forces (due to smart actuation) to the developing crack tip stresses. This can be accomplished by applying a voltage to these piezoelectric actuator patches.

The time variation of the applied mechanical load is defined by $P(t) = P_0 \sin(\omega t)$ where $P_0 = 100\text{ N}$ and $\omega = 100\text{ Hz}$. The load is applied at the free end of the beam acting vertically downwards, thus allowing relative sliding of the sublaminates over each other, which forms a Mode-II type of loading. The SERR is estimated using the J-integral. In this present study, the energies associated with computation of the J-integral are considered from a domain of radius 1 mm. The applied mechanical load gives rise to a J-integral history, which is also periodic in nature. A sinusoidal voltage is then applied to the three embedded piezoelectric actuators as explained below. A positive voltage on the top surfaces and a negative voltage on the bottom surfaces of all of the three piezoelectric actuator layers is applied. The voltage is described by the function $V(t) = V_0 \sin(\omega t)$ and the same frequency of excitation is considered, that is, $\omega = 100\text{ Hz}$. The SIF in a Mode-II type of deformation is computed by using the formulae given by Bao *et al.* [10] and the computed SIF is normalized with $K_0 = P_{\max} \sqrt{a/bh}$, where a is the crack length and b and h are the breadth and thickness of the beam. The time history of the normalized K_{II} for various voltage amplitudes is shown in Figure 14.17.

As can be observed from this figure, the multiple peaks of the SIF values are reduced as V_0 is increased and a reduction of about 10–15% can be observed for $V_0 = 750\text{ V}$. The application of the voltage can be observed to be useful in generating the force required

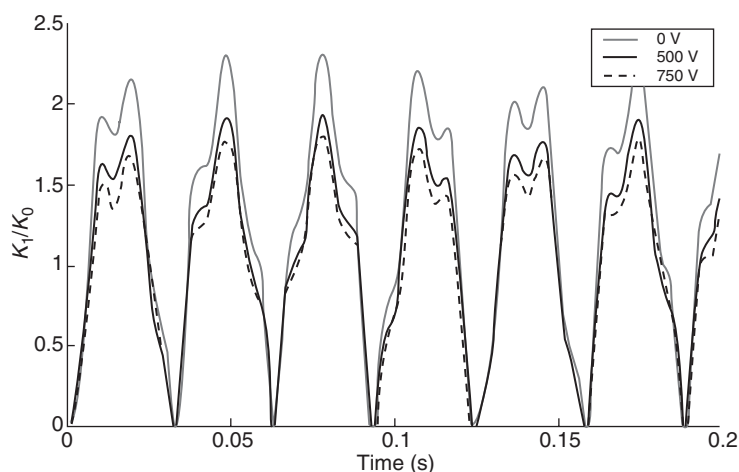


Figure 14.17 Normalized SIF for different voltage amplitudes.

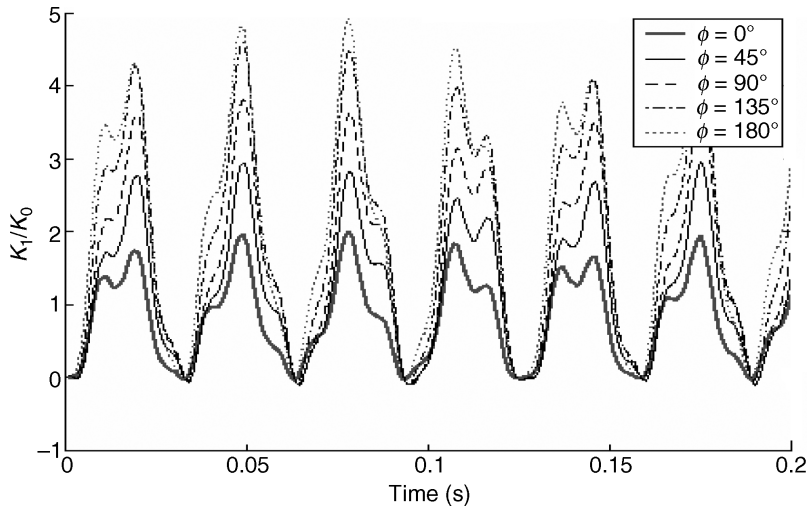


Figure 14.18 Normalized SIF for different phase angles.

to counteract the forces causing the growth of the delamination. It can also be observed that the linear increase in V_o results in a linear decrease in the crack tip stress values. As the deformations in the actuator layers have a direct effect on the local conditions near the crack tip, the mechanical strains developed in the region between the actuator and the crack faces cause the composite material to also undergo additional deformation in the opposite direction in order to satisfy the geometrical compatibility conditions and hence reducing the crack tip displacements. In this case, the voltage is applied in-phase with the mechanical load. It would be interesting to see what happens to the normalized SIF if the voltage and the mechanical load are out-of-phase. That is, the voltage variation is given by $V(t) = V_0 \sin(\omega t + \phi)$, where ϕ is the phase angle. This aspect is shown in Figure 14.18 for $V_o = 750$ V for a range of phase angles.

The plots show an increase in the SIF values for increases in the phase angles and for ϕ equal to 180° the SIF is almost doubled. Hence, it can be concluded that an increase in ϕ causes an increase in the SIF, thereby increasing the early risk of failure.

The examples used in this section show that it is indeed possible to delay the growth of the flaw by suitably designing a control system. Although this aspect was demonstrated using an open-loop control, a more practical and realistic way would be to design a closed-loop feedback control for wider applications and more robust performance.

14.5 WIRELESS MEMS-IDT MICROSENSORS FOR HEALTH MONITORING OF STRUCTURES AND SYSTEMS

The integration of MEMS, interdigital transducers (IDTs) and required microelectronics and conformal antennas to realize programmable, robust and low-cost passive microsensors suitable for many military structures and systems including aircraft and missiles is presented in this section. The technology is currently being applied to the structural health monitoring of critical aircraft components. The approach integrates acoustic emission, strain gauges, MEMS accelerometers, gyroscopes and vibration-monitoring devices with signal processing electronics to provide real-time indicators of incipient failure of aircraft components with a known history of catastrophic failure due to fracture. Micromachining offers the potential for fabricating a range of microsensors and MEMS for structural applications, including load, vibration and acoustics characterization and monitoring. Such microsensors are extremely small; they can be embedded into structural materials, can be mass-produced and are therefore potentially cheap. Additionally, a range of sensor types can be integrated onto a single chip with built-in electronics and an Application-Specific Integrated Circuit (ASIC), thus providing low-power microsystems. Smart sensors are being developed using standard microelectronics and micromachining in conjunction with wireless communication

systems suitable for condition monitoring of aircraft structures in-flight. A hybrid accelerometer and gyroscope in a single chip suitable for an inertial navigation system and other microsensors for health monitoring, condition-based maintenance of structures, drag sensing and control of aircraft, strain and deflection of structures and systems, etc. are discussed in this section.

The unique combination of technologies (microelectronics, MEMS and IDTs) results in novel conformal sensors that can be remotely sensed by a wireless communication system with the advantage of ‘no-power requirements’ at the sensor site (passive sensor). The sensors presented are simple in construction and easy to manufacture with existing silicon micromachining and stereolithography techniques. Programmable sensors can be achieved with ‘Split-finger’ IDTs as reflecting structures. If the IDTs are short-circuited or capacitively loaded, the wave propagates without any reflection, whereas in an open-circuit configuration, the IDTs reflect the incoming signal. Programmable accelerometers, gyroscopes, strain and deflection sensors, etc. can thus be achieved by using an external circuitry on a semiconductor chip using hybrid technology.

IDTs offer a simple and inexpensive means for sensing applications using surface acoustic waves (SAWs). The wave velocity and hence the oscillation frequency of a feedback loop containing an IDT device and a feedback amplifier are affected by changes in the mechanical or electrical boundary conditions in the wave path. Very small changes in the velocity can result in very repeatable frequency shifts since the stability of the oscillation frequency is extremely good. The device can also be attached to a conformal antenna and excited by a remote RF transceiver. The fidelity of the sensor and its high sensitivity are achieved by the five-orders-of-magnitude difference in wave speed between the acoustic signal and the RF signal. This mode of operation is particularly attractive because it is wireless and obviates the need for a local power supply. As the acoustic energy is confined to a thin near-surface region of the piezoelectric substrate, MEMS-IDT-based sensors are highly sensitive to surface perturbations of the propagation medium.

A set of IDT microsensors being developed for SHM is based on generating Lamb, Love or Rayleigh surface waves in structures. Lamb waves are 2-D counterparts of 1-D flexural and longitudinal waves. Lamb waves are proven to be useful for sensing impact damage, cracks, delamination, ‘*kissing bonds*’, corrosion and other health monitoring features of structures. Love waves are found to be ideal for detection of ice formation, and couple effectively with acoustic emission signals for monitoring

the onset of crack formation and propagation. Rayleigh waves are being used for sensing deflection, strain, temperature, humidity, pressure, acceleration and shock. These waves are generated by IDTs, either micromachined, etched or printed on special-cut piezoelectric wafers or on certain piezoelectric films deposited on silicon using standard microelectronics fabrication techniques and microstereolithography.

Wireless MEMS-IDT devices make use of both SAWs and traditional MEMS principles. MEMS-IDT-based microsensors possess typical advantages of MEMS sensors, including the additional benefits of robustness, excellent sensitivity, surface conformability and durability. Compared to conventional ones, these new sensors have a fewer number of moving mechanical parts, ultimately giving rise to inherent robustness and durability. Consequently, there is no electronics to balance or measure the movement of moving structures, which leads to even smaller micro devices.

Perhaps the major technical barrier to the acceptance of new developments in sensor technology is the need for wired communication between sensors and the electronics needed to drive them, as well as data-processing units. Retrofitting several sensors on an existing system and ‘hard-wiring’ all of the sensors is often impractical. Wires are prone to breakage and vandalism. Communication between moving and fixed systems is another case when ‘hard-wiring’ is difficult or sometimes impossible. Although advances have been made in wired communications, these complex assemblies are essentially similar to test hardware and present numerous reliability and maintainability limitations if implemented on a production scale. Cost effectiveness of sensor technology is also adversely affected by the physical complexities of moving to fixed system communications. Considering these limitations, development of a *wireless* means of communication, akin to telemetry, could have dramatic beneficial payoffs for the health monitoring of rotary and fixed-wing aircraft, machinery with fast moving parts, and all other applications that preclude wired sensors. The use of antennas for the telemetry of data from piezoelectric and other sensors, as well as wireless NDT using microwave probes, thus define a new era in practical NDT applications. It is now possible to use a wireless telemetry activation system at some distance from the structure containing the embedded transducer, and still obtain the pulsing and receiving characteristics to allow us to determine whether any changes are taking place in that material. The MEMS-IDT- and micro-comb-type sensors are most appropriate for this smart material application because of the simplicity in

size, manufacture and the overall capability and flexibility in being able to generate any mode and frequency of choice by way of controlling the various elements of the microsensors.

14.5.1 Description of technology

Microsensors are basically silicon, piezoelectric wafer or polymer devices that convert a mechanical signal into an electronic one using microelectronics technology. In smart structures, the electronic signal obtained from the sensors is amplified, conditioned and fed to ASIC chips. Using the intelligence in the electronics, the signal will be processed by the microprocessor and controller and then fed to the actuator. By using this type of integrated or smart sensor, one could achieve many actuation functions locally or remotely at different locations using wireless telemetry devices.

Many microsensors for SHM are based on the generation of Lamb waves, Love waves or Rayleigh waves. These waves can be generated by interdigital transducers (IDTs) either micromachined, etched or printed on special-cut piezoelectric wafers or on certain piezoelectric films deposited on silicon using standard microelectronics fabrication techniques. The IDT sensors can be integrated with MEMS using the recently developed techniques such as (a) micromechanics first and CMOS and microelectronics second, (b) CMOS and microelectronics first and micromechanics second, or (c) flip-chip bonding which result in a family of novel microsensors.

An MEMS-IDT device is usually a piezoelectric wafer with a set of interdigital transducers (IDTs) on its surface. The sensor principle is based on the fact that the wave-traveling time between the IDTs changes with variation in the physical variables. One of these IDTs acts as the device input and converts signal voltage variations into mechanical waves of the types mentioned above, based on the piezoelectric crystal-cut. The other IDT is employed as an output receiver to convert the mechanical waves back into output voltages. These devices are reciprocal in nature; as a result, signal voltages can be applied to either IDT with the same end result. To obtain a high sensitivity, MEMS-IDT sensors are usually constructed as electric oscillators using the IDT device as the frequency-control component. By accurately measuring the oscillation frequency, a small change of the physical variables can be detected by the sensors. A typical IDT oscillator sensor schematic is shown in Figure 14.19.

An amplifier connects two IDTs on a piezoelectric wafer so that oscillations result because of the feedback

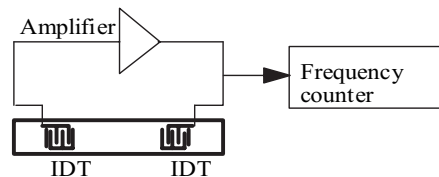


Figure 14.19 Schematic of an oscillator IDT sensor with a resonator.

of the waves propagating from one IDT to the other. The oscillation frequency satisfies the condition that the total phase shift of the loop equals 2π and varies with the wave velocity or the distance between the IDTs. The oscillator includes an amplifier and requires an electrical power supply and *cannot* be wireless. The operating frequency range of such devices is from ten MHz to a few GHz, which directly matches the frequency ranges of radios and radar. When an IDT is directly connected to an antenna, the waves can be excited remotely by electromagnetic waves. For remote wireless sensing, the receiving IDT can be replaced by a set of reflectors, as shown in Figure 14.20.

The reflectors can be programmed such that each sensor will have its own ‘bar code’ for identification. This kind of sensor identification is particularly attractive when many microsensors are used at various locations on an aircraft. The input IDT connects directly to a small antenna called the *device antenna*.

This antenna-IDT configuration is able to convert the microwave signal ‘from the air’ to an IDT signal on the wafer surface and vice versa. The reading system has a linear frequency modulated (FM) signal generator. A system antenna transmits the FM signals. The signals are received by the device antenna and converted by the antenna-IDT to waves propagating along the surface of the wafer and into the structure. The ‘echoes’ from the reflectors are picked up by the antenna-IDT and sent back to the system antenna. The ‘echo’ signals are delayed copies of the transmitted FM signal. The delay times mainly depend on the velocity of the waves and the distance between the IDT and the reflectors. A mixer, which takes the transmitted FM signal as the reference signal, outputs the signals of frequency difference between the echoes and the transmitted signals. Because the transmitted signal is linear frequency modulated, the frequency difference is proportional to the delay time. By using spectrum analysis technique like FFT, the two echo signals can be separated in the frequency domain since the delay times are different.

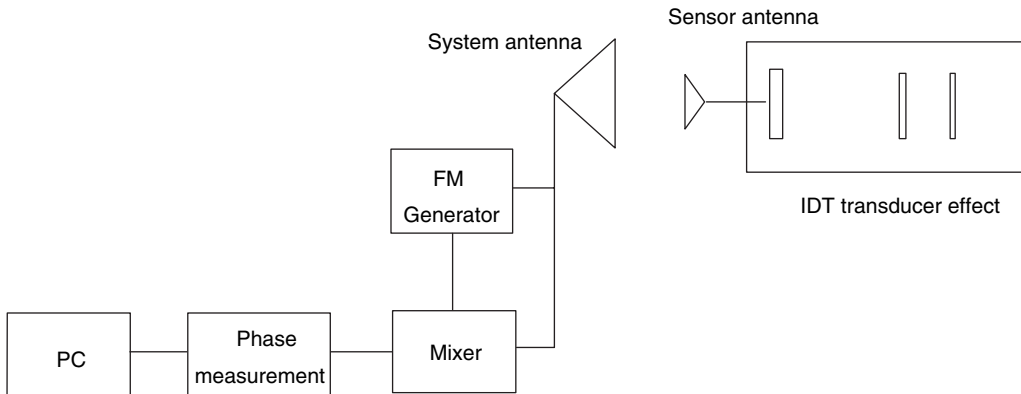


Figure 14.20 Schematic of a remote reading sensor system with a passive IDT sensor.

The MEMS substructure can be combined with the above IDT devices to conceive wireless-conformal sensors such as accelerometers, gyroscope etc. [11].

14.5.2 Wireless-telemetry systems

Figure 14.21 shows a typical layout of a transceiver telemetry system. This system operates in the range 905 to 925 MHz. The circuit operation is as follows. The signal is pulse-FM modulated. A pulser can synchronize the DC voltage ramp circuit, voltage-controlled oscillator (VCO) output and the A/D converter. During the pulse, the DC voltage ramp circuit would linearly

tune the VCO from 905 to 925 MHz. The VCO output is controlled by a diode switch, which is then amplified to 50 mW by a high-isolation amplifier. A coupler diverts a sample of the signal to the LO input of the mixer. A circulator sends the transmitted signal to the antenna and also sends the reflected signal through an automatic gain-control amplifier to the RF input of the mixer. A low-pass filter removes any noise and high-frequency signals. Next, the signal is digitized at 10 Msps and 10 bit resolution. A programmable DSP chip, such as the TI TMS320C3X, is used to extract delay information and compute the desired parameter. This is then output to an LCD.

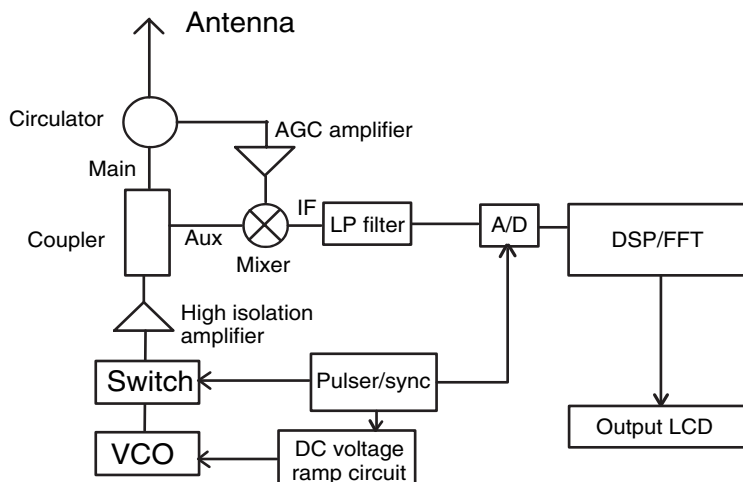


Figure 14.21 Schematic of a system for remote sensing applications.

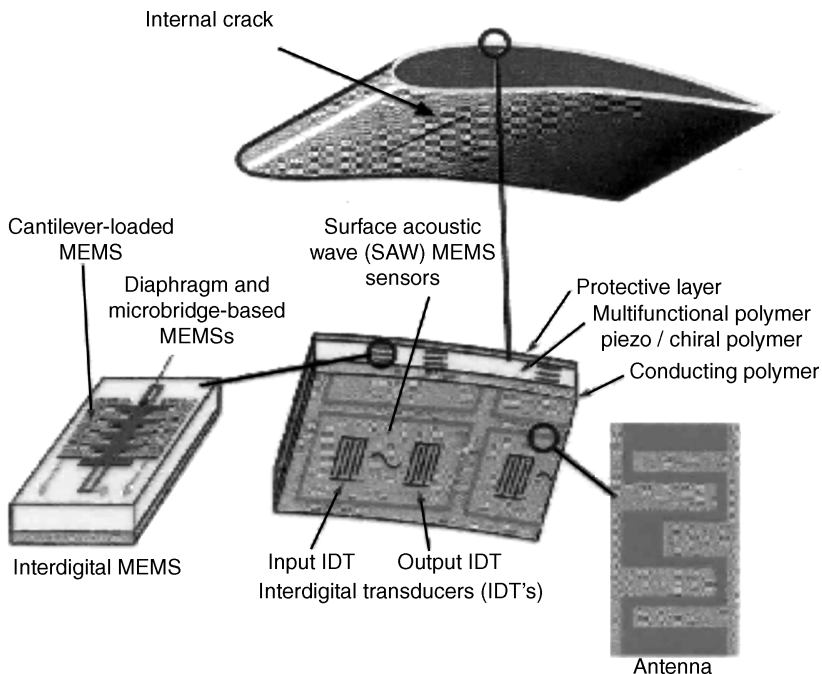


Figure 14.22 Surface-mounted microsensors confined in a thin layer for the health monitoring of aircraft structures.

14.5.2.1 Application of technology

For health monitoring of existing aircraft already in service, the sensor must be flush-mounted with a protective rain and sand erosion coating and should not affect the airfoil and aerodynamical design and structural integrity. A series of low-profile, MEMS-IDT- and micro-comb-type sensors can be surface mounted and protected by a thin UV-curable multifunctional polymer coating [11], as shown in Figure 14.22. The thickness of the coating is around $100\text{ }\mu\text{m}$, which will not affect the airfoil and aerodynamical design. The sensors can be used to generate a host of bulk, guided, Lamb and Love waves, as described above. These sensors could even be mounted inside the composite material during the fabrication process itself to advance the state-of-the-art of smart structure application and design for future aircraft. With availability of the dispersion curves associated with guided-wave analysis in both isotropic and anisotropic media [12–19], procedures for making use of the wave structure across the thickness of a composite material for enhanced defect detection and sensitivity analysis is now possible. As an example, if emphasis was directed towards the tiny cracks emanating from the outer

surface of the structure, one would select a mode and frequency from the dispersion curve that has maximum displacement and/or energy concentration on the surface of the structure. On the other hand, if one's primary goal was the detection of fairly large defects from the surface, midway through the thickness of the component or perhaps, defects emanating at the center of the structure, one would select a wave structure with maximum displacement and/or energy concentration at the center of the thickness of the component. Since the wave structure varies along the dispersion curves, computational procedures and the use of elasticity analysis can be used to select these points of interest.

A micro-comb-type sensor is made up of a number of fingers, say five to twenty, that are mounted with gaps between the elements and all made to oscillate in-phase by either shock excitation or a tone burst. Frequency variations can also be accomplished by using a shock-type excitation, followed by appropriate signal processing. Wireless telemetry which is custom-built with localized power and drive circuitry will result in a compact, remotely addressable system. A multiplexing arrangement is also possible, whereby a single spacing might be used to control the time-delay sequence in pulsing to allow us

to move to any point of choice on a dispersion curve to achieve a special wave-propagation characteristic desired for a particular application. Utilization of a comb makes multi-mode inspection possible, whereby defect detection and classification is simplified. Thus, it is ideal for multi-site damage detection. It is a well-known fact that redundancy in inspection can improve the overall probability of detection. Quite often, the features established from the multi-mode data collection procedures can then be used as input into a pattern-recognition program, or neural network, for further classification and implementation of a decision algorithm to assist in the material or composite material characterization and defect-characterization phase of the work effort. Research studies conducted to date indicate that the MEMS-IDT- and micro-comb-type sensors would work well for almost any materials and structures. A simple description of the approach used is given below.

Lamb-wave-based sensors Lamb waves have been proven to be useful for sensing impact damage cracks, delamination, ‘kissing bonds’ and corrosion. MEMS-IDTs for Lamb-wave generation are fabricated either on piezoelectric films deposited on silicon or on piezoelectric polymers by microstereolithography.

A micro-comb type sensor is made up of a number of such MEMS-IDT sensors that are mounted with gaps between the elements and are all made to oscillate in-phase by either shock excitation, a tone burst or an external antenna signal. In such a measurement system, the acoustic wave signals are generated on the surface by the application of an AC voltage across the IDT terminals. These acoustic signals travel along the surface of the body and are reflected by the edges as well as by any cracks that are formed in their propagation paths. These reflected signals could then be analyzed using wireless health monitoring systems. Additional components and systems are required to make the system ‘wireless’. The first step in this direction is on deciding how to reach the required electrical signals at the terminals of the IDT. In the block schematic shown in Figure 14.23, an amplitude-modulation scheme is proposed. Pulses of this amplitude-modulated carrier signal are transmitted by an antenna in the transmitter section of the readout unit. The modulation scheme is necessitated by the enormous size of the antenna if the HF signals were to be transmitted unmodulated. By using a conveniently higher carrier signal, the antenna size can be reduced. It would also enable the use of existing antennas on the structure itself (if available) for the

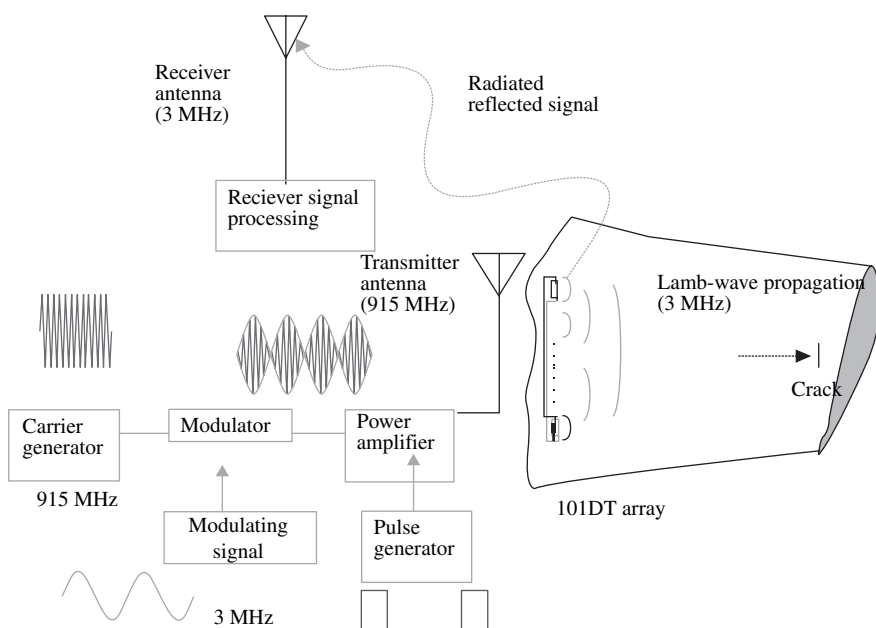


Figure 14.23 Wireless MEMS-IDT configuration for monitoring cracks.

secondary purpose of monitoring itself. Alternately, these can be located on a separate ground vehicle which would send out radio-frequency signals for exciting the IDTs attached to the monitored body. Amplitude modulation is a very common technique used for telecommunications, particularly in conventional AM broadcasting. Depending on the extent of surface area needed to be covered and the proximity for accessing the IDTs, these act as antennas for receiving these transmitted signals. This transmission path is similar to an AM broadcast system, where the transmitter antennas are much taller compared to the receiver antennas, which are barely visible. The ‘demodulation’ takes place at the transducer itself. The maximum frequency at which the PVDF transducer can respond is well below the transmitted radio frequencies. Hence, the acoustic signal on the surface is at the frequency of the modulating signals. These, in turn, get reflected by the edges and cracks and are re-transmitted by the IDT. A small receiving antenna (separate from the transmitter for improved isolation) picks up the signals, which contain information about the location and size of cracks and other damage. The receiver unit contains a pre-amplifier, filter banks and an oscilloscope or digitizing units for computer processing at a later stage. The results presented in Figure 14.24 are based on the A_1 (antisymmetric Mode 1 of the Lamb waves) modes excited at the maximum point of group velocity. At an operational frequency of 3.145 MHz, both A_1 and A_o (antisymmetric Mode 0) modes are generated. It may be noted that the difference between the group velocity of the A_1 and A_o modes is not too much. In Figures 14.24(a) and 14.24(b), the measured time-domain signals are presented for a structure with and without a crack, respectively. The reflected signal from the crack changes according to the crack size. It is shown that the intensity of scattering is closely related to the crack size. The reflected signals from the cracks and edge not only gives information about the location of cracks in the time domain

but is also effective in determining the crack size in the frequency domain.

Love-wave-based sensors Love waves are found to be ideal for detection of ice formation and couple effectively with acoustic emission signals for monitoring the onset of crack formation and propagation. The SAW that propagates on a 36° rotated Y -cut X -propagating LiTaO₃ (36YX.LT) is of a ‘leaky-type’ SH mode, which can detect the effects of mechanical properties, such as viscosity and mass loading, as well as those of the electrical properties. These microsensors use interdigital electrodes (IDEs) or IDTs to generate Love waves at the interface of the sensor surface and the surrounding medium. The sensors use a pair of devices; one serves as a reference, due to the mechanical loading, while the other measures the electrical properties via the phase velocity and attenuation information from the sensors. Acoustic emission (AE) sensors have been fabricated by using the Love-wave concept, as shown in Figure 14.25. Acoustic emission is the elastic energy being suddenly released when materials undergo deformation. It may be released from the propagation of cracks and/or delaminations, friction, leakage or microscopic deformation or transformation. Various studies have been performed during the past decades using AE for monitoring damage in aircraft structures [20–24]. Some of these studies report of having even applied AE for in-flight monitoring. This has, however, been limited to either monitoring an aircraft structure in a ‘rig-test’ performed on ground under simulated in-flight conditions or implementing an inertial loading apparatus with a prescribed test specimen in a flying aircraft.

Other studies have been performed by pressurizing the cabins of commercial aircraft fuselages for the detection of fatigue cracks, corrosion, cracked lap joints and cracks around rivets and in forging and wing slices. The sensors used are also ‘macrosize’. Thus, they are not suitable for ‘true’ in-flight testing. A ‘true’ in-flight AE sensor can be

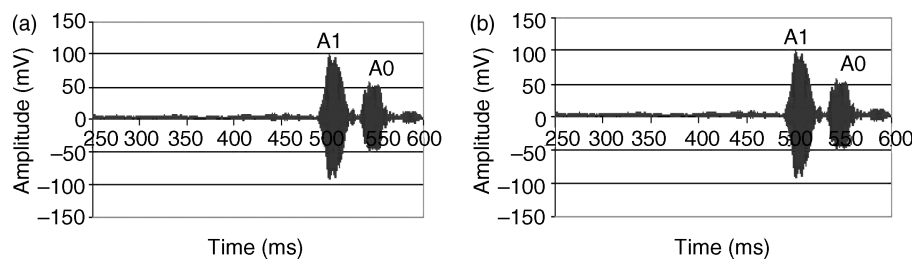


Figure 14.24 Reference tone-burst-signal data for (a) without a crack and (b) with a 2 mm crack.

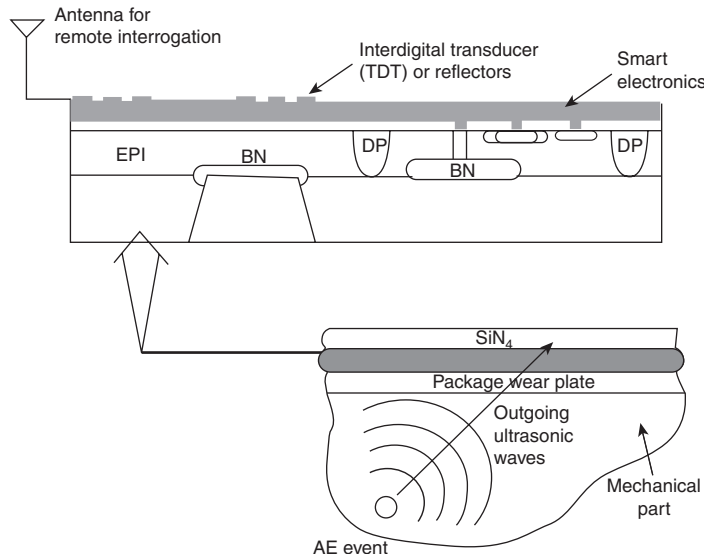


Figure 14.25 Schematic of an acoustic emission sensor fabricated by using the Love-wave concept.

conceived with a Love wave sensor, which will effectively couple with the shear component of the AE signal from the structure. This modulated signal can be read by smart electronics built into the sensor or by wireless means, as shown in Figure 14.25.

Rayleigh-wave-based sensors Rayleigh surface waves have been investigated for sensing deflection, strain, temperature, humidity, pressure and acceleration, and in highly sensitive gyroscopes for aircraft. Here, MEMS-IDT-based accelerometers, gyroscopes and strain sensing are described in detail.

14.5.2.2 MEMS-IDT accelerometers and gyroscopes

There is an emerging need for low cost and miniature accelerometers and gyroscopes for inertial navigation on a single chip. The inertial navigation system uses both gyroscopes and accelerometers to measure the state of motion of a target or a missile by sensing the changes in that state caused by acceleration. The required features in many of these applications are high precision, wide dynamic range and wide frequency range. Essentially, most accelerometers consist of a suspended seismic mass that is displaced by the measurand. Thus, the position of the seismic mass depends on the momentary acceleration sensed by the device. The design of a microsystem incorporating both an accelerometer and a gyroscope

on a single silicon chip is shown in Figure 14.26. This consists of (a) IDTs for generating SAWs and (b) a floating seismic mass for sensing acceleration and a perturbation mass array for sensing the gyroscope motion. Silicon with a ZnO film is chosen as the SAW substrate. The IDTs are sputtered on the substrate. The

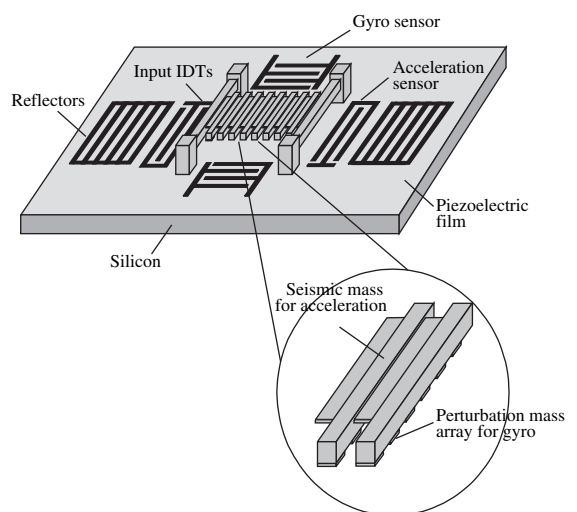


Figure 14.26 MEMS-IDT accelerometer and gyroscope on a single chip.

fabrication steps involve mask preparation, lithography and etching. The thickness of the metal for the IDTs should at least be 2000 Å in order to make an adequate contact. A very thick layer of metal causes mass loading effects and is detrimental to the device performance. The metallization ratio for the IDTs is 0.5. The fabrication of the seismic mass is realized by the sacrificial etching of silicon dioxide. The steps involved are as follows: (1) a sacrificial oxide is thermally grown on a second silicon wafer; (2) a polysilicon (structural layer) is then deposited by LPCVD onto the sacrificial layer – the polysilicon is patterned to form the seismic mass and etched with EDP; (3) the perturbation mass array for gyroscope sensing is deposited onto this seismic mass; (4) the sacrificial layer is then etched with HF to finally release the seismic mass and the perturbation mass array; (5) the seismic mass is then flip-chip bonded to the SAW silicon substrate. The floating reflectors (seismic mass) can move relative to the substrate and this displacement is proportional to the acceleration of the body the substrate is attached to. This displacement is then measured as a phase difference of the reflected acoustic wave, which can be calibrated to measure the acceleration. This phase shift can be detected at the accelerometer sensor port of the device [25]. It should also be noted that the strategically positioned metallic mass arrays on the underside of the seismic mass would change the coupling between the SAW at the gyroscope sensor port due to the rotation and ‘Coriolis force generation’. This is sensed as the rate information for gyroscope. When the electromagnetic signal is converted to an acoustic signal on the surface of a piezoelectric material, the wavelength is reduced by

a factor of 10^5 . This allows the dimensions in the realm of the acoustic wave devices to be compatible with integrated circuit technology. The main advantage of a single device for the measurement of angular rate, as well as the acceleration is the reduction in power requirements, signal processing electronics, weight and overall expenses for many commercial, military and space applications.

14.5.2.3 MEMS-IDT-based strain sensors

The MEMS-IDT strain sensor system is employed to study the deflection and strain of a ‘flex-beam beam’-type structure of a helicopter. The concept is based on the fact that the phase delay is changed because of the strain of the sensor substrate. The system consists of remotely readable passive MEMS sensors and a microwave-reading system. The phase difference is sensitive to the change in the delay times. The phase shift of the signal is then calibrated with that of the strain by using a simple cantilever beam model. This is an experiment that was performed on a scaled model of the ‘Sikorsky S-76A’ rotor blade, (see Varadan *et. al* [26]). First, the strain and the deflection were measured remotely by the antenna communicating with the sensors (via the built-in antenna) while the blades were stationary and then when the blades were rotating. The rotational speed is close to that of an actual helicopter. The results presented in Figure 14.27 are encouraging for further research.

In summary, the feature selection on health monitoring takes place from the physically based domains of guided

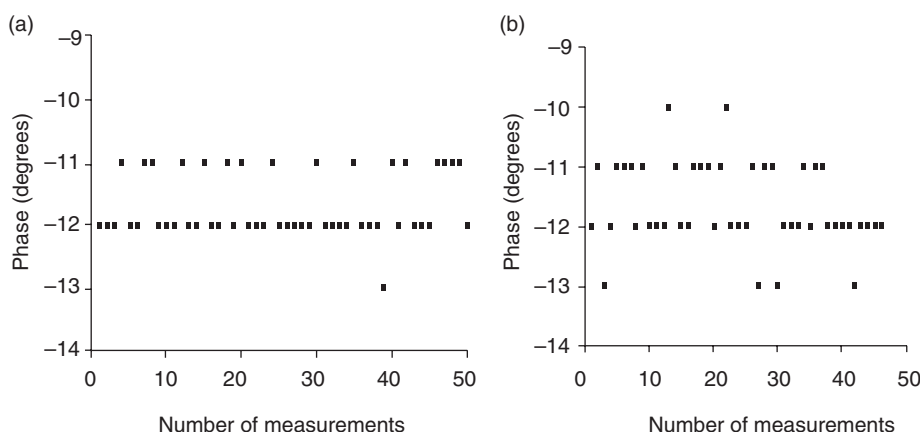


Figure 14.27 Phase shifts and number of strain measurements on a scaled model of a rotor blade: (a) static; (b) rotating.

waves, MEMS, microwaves, etc. The classification will use state-of-the-art artificial neural networks. This multi-technology approach to NDT vastly improves our ability to monitor the health of aircraft, civil structures and manufacturing processes. The goal, of course, is to finally develop a physically based *feature vector* for a complex system from which data fusion can be used in the development of a decision algorithm for the ‘criticality’ of system performance based on detection, classification and sizing. The feature vector that has been established with this multi-mode and multi-technology approach is rich and robust. Rather than filling in the elements of a feature vector with a long list of statistically or probabilistic-based features on a single-modality NDT approach in an attempt to solve the problem, the approach here with a multimode and multi-technology approach is to initially have tremendous sensitivity potential, hence improving the overall probability of detection and decision-algorithm performance potential.

Once the feature vector is completely formulated, the procedures for algorithm development follow traditional guidelines of pattern recognition whereby probability density function curves could be plotted to select the most useful features for the final input into a pattern recognition or neural net algorithm, hence establishing a decision function with appropriate weights for the physically based features selected. Thus, the multi-technology approach to health monitoring of systems and processes is not simply a set of disparate and complementary technologies, but rather a multi-scale inspection ability that can be combined together for a powerful new approach to NDT.

REFERENCES

- S.W. Doebling, C.R. Farrar, M.B. Prime and D.W. Shevitz, ‘Damage identification and health monitoring of structural and mechanical systems from changes in their vibration characteristics: A literature review’, Los Alamos National Laboratory, Report LA-13070-MS, Los Alamos, NM, USA (1996).
- B. Culshaw, *Smart Structures and Materials*, Artech House, Inc., Norwood, MA, USA (1996).
- A.V. Krishnamurthy, M. Anjanappa, Z. Wang, and X. Chen, ‘Sensing of delaminations in composite laminates using embedded magnetostrictive particle layers’, *Journal of Intelligent Material Systems and Structures*, **10**, 825–835 (1999).
- M. Kumar and A.V. Krishnamurthy, ‘Sensing of delaminations in smart composite laminates using a magnetostrictive particle layer and horseshoe coil arrangement’, *Journal of Aeronautical Society of India*, **52**, 19–25 (2000).
- E. Saida, G.N. Naik and S. Gopalakrishnan, ‘An experimental investigation of a smart laminated composite beam with a magnetostrictive patch for health monitoring applications’, *Structural Health Monitoring*, **2**, 273–292 (2003).
- C.V.S. Sastry, ‘Distributed sensing and actuation in delaminated smart composite structures’, *M.Sc. Thesis*, Indian Institute of Science, Bangalore, India (2002).
- C.V.S. Sastry, D. Roy Mahapatra, S. Gopalakrishnan and T.S. Ramamurthy, ‘Distributed sensing of static and dynamic fracture in self-sensing piezoelectric composites: finite element simulations’, *International Journal for Intelligent Materials and Systems*, **15**, 339–354 (2004).
- J. R. Rice, ‘A path-independent integral and the approximate analysis of strain concentration by notches and cracks’, *Journal of Applied Mechanics, Transactions of the ASME*, **35**, 379–386 (1968).
- L.B. Freund, *Dynamic Fracture Mechanics*, Cambridge University Press, Cambridge, UK (1990).
- G. Bao, S. Ho, Z. Suo and B. Fan, ‘The role of material orthotropy in fracture specimens for composites’, *International Journal of Solids and Structures*, **29**, 1105–1116 (1992).
- V.K. Varadan, V.V. Varadan and X.Q. Bao, ‘Integration of interdigital transducers, MEMS and antennas for smart structures’, *SPIE Proceedings*, **2722**, 95–106 (1996).
- V.K. Varadan and V.V. Varadan, *Smart Structures, MEMS and Smart Electronics for Aircraft*, AGARD-LS-205, (1996).
- V.K. Varadan and V.V. Varadan, ‘Microsensors, actuators, MEMS and electronics for smart structures’, in *Microlithography, Micromachining and Microfabrication*, P. Rai-Choudhury, (Ed.), SPIE and IEE Publications, (1997).
- H. Subramanian, V.K. Varadan, V.V. Varadan and M.J. Vellekoop, ‘Design and fabrication of wireless remotely readable MEMS based microaccelerometers’ *Smart Materials and Structures*, **6**, 730–738 (1997).
- V.K. Varadan, V.V. Varadan, X. BaÓ, S. Ramanathan and D. Piscotty, ‘Wireless-passive IDT microsensor’, *Smart Materials and Structures*, **6**, 745–751 (1997).
- V.K. Varadan, *Smart Electronics*, Eds. V.K. Varadan, **2448**, SPIE Press, Bellingham, WA, USA (1995).
- V.K. Varadan and P.J. McWhorter, *Smart Electronics and MEMS*, Eds. V.K. Varadan and P.J. McWhorter, **3046**, SPIE Press, Bellingham, WA, USA (1997).
- A. Hariz, V.K. Varadan and O. Reinhold, *Smart Electronics and MEMS*, Eds. A. Hariz, V.K. Varadan and O. Reinhold, **3242**, SPIE Press, Bellingham, WA, USA (1997).
- V.K. Varadan, P.J. McWhorter, R. Singer and M.J. Vellekoop, *Smart Electronics and MEMS*, Eds. V.K. Varadan, P.J. McWhorter, R. Singer and M.J. Vellekoop, **3641**, SPIE Press, Bellingham, WA, USA (1998).
- C.D. Bailey, ‘Acoustic emission for in-flight monitoring on aircraft structures’, *Materials Evaluation*, **34**, 165–171 (1976).
- C.M. Scala, ‘A semi-adaptive approach to in-flight monitoring using acoustic emission’, in *Proceedings of Review*

- of Progress in Quantitative NDE, (Eds), D.O. Thompson and D.E. Chimenti, 361–369 (1986).
- 22. J.M. Carlyle, ‘Acoustic emission testing the F-111’, *NDT-International*, **22**, 67–73 (1989).
 - 23. C.P. Fotos, ‘Acoustic emission technique tests aircraft integrity’, *Aviation Week and Space Technology*, **76** (August 28, 1989).
 - 24. S. McBride, M. Viner, M.D. Pollard, P.S. MacPhail, D. Bouwman and D.T. Peters, *Acoustic Emission Detection of Crack Presence and Crack Advance During Flight*, AGARD-CP-462, (1989).
 - 25. H. Subramanian, V.K. Varadan, V.V. Varadan and M.J. Vellakoop, ‘Design and fabrication of wireless remotely readable MEMS based microaccelerometers’, *Smart Materials and Structures*, **6**, 730–738 (1997).
 - 26. V.K. Varadan, V.V. Varadan, X. Bao, S. Ramanathan and D. Piscotty, ‘Wireless-passive IDT strain microsensor’, *Smart Materials and Structures*, **6**, 745–751(1997).

Vibration and Noise-Control Applications

15.1 INTRODUCTION

In this chapter, vibration and structure-borne noise-control applications are presented. For longevity of a structure, whether it is an aircraft wing, a building structure or a machine element, the amount of vibration it experiences should be reduced. Vibration reduction can normally be achieved passively by identifying the resonant conditions and suitably modifying the geometry of the structure such that the natural frequency of the system is far away from the driving frequency of the system. Alternatively, one can do a detailed analysis and identify the regions in a structure having high vibration levels and design suitable damping mechanisms to alleviate the vibrations. However, design constraints will always not allow any modification to the existing structure. In such cases, one has to look at other alternatives, such as adaptive technology, wherein the desired results can be achieved without any major design modification. Such methods of reducing vibrations are called *active* methods. One such methodology is by using smart materials.

The control of noise generated by vibration of structural members is yet another application where smart materials can be used. This application has great impact in increasing the structural integrity of the structure. Noise could be air-borne or structure-borne. Air-borne noises are generated due to the pressure difference caused by differential flow fields. One example of this is the aerodynamic noise generated by a moving aircraft or a helicopter. Structure-borne noise is generated by vibrating structural members. These members act as a conduit for the vibration (disturbance) to propagate within the structure and are responsible for ‘screeching’ or high-frequency noise. In other words, structure-borne noise and vibration goes ‘hand-in hand’. In such cases,

reducing the vibration levels will automatically reduce the structure-borne noise levels.

Smart materials, through their constitutive relations, can generate extra forces arising due to mechanical coupling. This extra force will essentially act as a *damping* force to alleviate vibration or noise in a structure. In this chapter, two case-studies are presented. In the first study, vibration levels in a thin-walled box beam are controlled using PZT sensors/actuators. In this study, two different control schemes (outlined in Chapter 9) are employed. In the second study, the reduction of high-frequency cabin noise caused by the jamming of gears in a gearbox of a helicopter is addressed. In this study, the Active Spectral Finite Element Model (ASFEM), again outlined in Chapter 9, is used.

15.2 ACTIVE VIBRATION CONTROL IN A THIN-WALLED BOX BEAM

Thin-walled constructions are extensively used in aircraft structural components due to their inherent advantages of high stiffness and low weight. They are also used in many steel structures, such as girders, bridges, scaffolds, etc. in civil constructions. The analysis of these structures is more complicated than the conventional structures. There are many secondary effects, such as warping, ovaling, etc., which are very important in their behavior. In addition, thin-walled structures in aircraft give coupled motions. That is, for example, bending motion will give rise to torsional motion or an axial load will give rise to bending motion. Megson [1] gives a complete overview of thin-walled structure behavior in aerospace and civil structures.

The thin-walled box beam FE formulation was studied in detail in Chapter 8 (Section 8.3). The details of this

Table 15.1 Material properties and dimensions of the glass–epoxy beam.

<i>Material properties</i>
$E_{11} = 23.69 \text{ GPa}$; $E_{22} = 7.63 \text{ GPa}$; $G_{12} = G_{13} = G_{23} = 3.37 \text{ GPa}$; $n_{12} = 0.26$, $\rho = 1985 \text{ kg/m}^3$
<i>Dimensions (in meters)</i>
Length (L) = 0.655; width ($2b$) = 0.057; depth ($2h$) = 0.019; ply thickness, t_p = 0.00025

can also be found in Mitra [2] and Mitra *et al.* [3]. In this section, we will use this element to design the necessary controller to suppress the vibration caused by multi-modal loading. The output from the designed controller is verified both experimentally and numerically (through the formulated FE). SEREP is used to reduce the FE model.

15.2.1 Test article and experimental set-up

A glass–epoxy composite box beam with two bimorph surface-mounted SP5H PZT patches is used for the experimental study of vibration suppression of the transverse bending modes. The PZT patches act as actuators, through which both the exciting electrical load and control signals are applied. Sensing is done through a Structcel 330 A (PCB Electronics, USA) accelerometer with a sensitivity of $20.4 \text{ mV/m}^2/\text{s}$. The material properties and dimensions of the box beam and PZT patches are given in Tables 15.1 and 15.2, respectively. The cantilever beam has a ply layup of $[0_3/90_2/0_3]$ on all four sides. A schematic diagram of this beam is shown in Figure 15.1. The vibration in the box beam is induced through a single patch of a PZT actuator by using an oscillator. The generated vibration is sensed through an accelerometer (Structcel 330 A, PCB Electronics, USA) with a sensitivity of 200 mV/g , which is then fed to the A/D converter after signal conditioning. The PI controller is implemented in the DSP-based vibration control card. The card is designed around the ADSP-2181 DSP. The sensed voltage is proportional to the acceleration of the

ADSP controller, which outputs the calculated control voltage through the D/A converter channels. The control voltage is amplified by a high-voltage amplifier and then fed into the PZT actuators for bending actuation to suppress the transverse vibration. The experimental set-up and its block diagram are given in Figures 15.2 and 15.3, respectively.

15.2.2 DSP-based vibration controller card

The DSP-based vibration controller card is developed for the implementation of a digital control system. The card is designed around ADSP-2181 DSP. This card also contains one ADC with an eight-channel inbuilt multiplexer, an eight-channel serial DAC, a UART and a ‘Boot flash’. Eight analog sensor signals from the input to card and eight analog channels are the outputs. The ADSP-2181 DSP from the analog devices has been chosen to implement vibration control laws and to acquire sensor inputs. This DSP features high-speed processing, single cycled instruction execution and multifunction instructions. The signal-conditioner analog sensor inputs are connected to respective ADCs. Prior to ADC sampling, all sensor inputs are filtered by a second-order Butterworth low-pass filter of 2 kHz cutoff frequency. Analog outputs (DAC outputs) are buffered and brought to a connector. One asynchronous serial channel is provided for downloading the ADSP-2181 programs and for debugging purposes. Eight general-purpose inputs/outputs of the DSP are also brought out to a berg stick connector. The DSP-based vibration controller

Table 15.2 Properties of the SP5H PZT actuators for the test specimen.

<i>Material properties</i>
E (Young’s modulus) = 62.0 GPa; n (Poisson’s ratio) = 0.31; thickness = 0.0005 m; density, ρ = 7400 kg/m ³
<i>Piezoelectric coefficients</i>
$d_{31} = d_{32} = -166 \times 10^{-12} \text{ m/V}$, $d_{33} = 300 \times 10^{-12} \text{ m/V}$

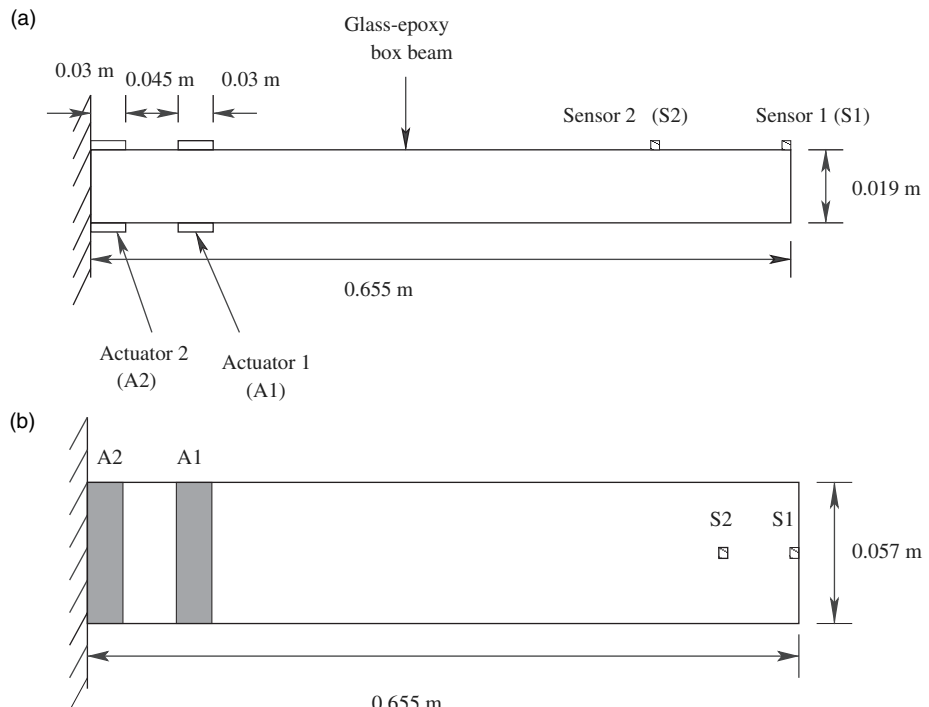


Figure 15.1 Test specimen with actuators and sensors: (a) side view; (b) plan view.

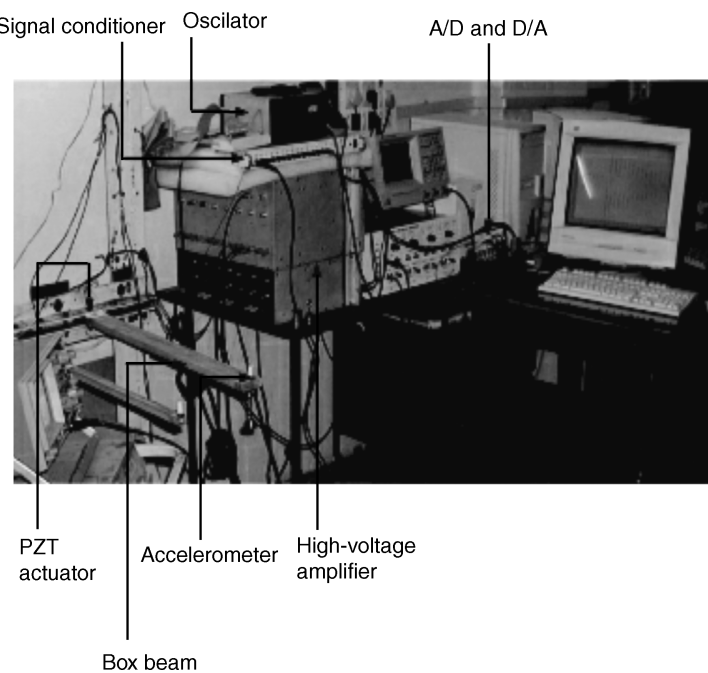


Figure 15.2 Experimental set-up.

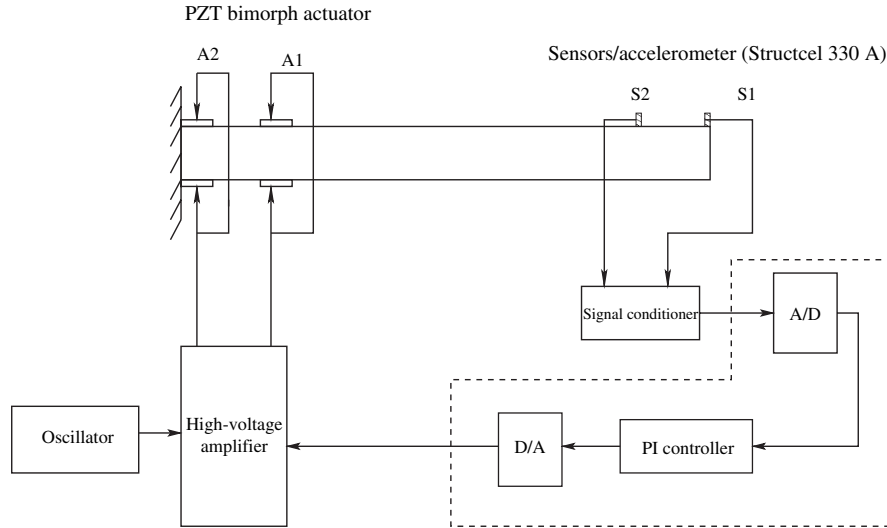


Figure 15.3 Block diagram of the experimental set-up.

card is shown by the block diagram in Figure 15.3 and the specifications are given in Tables 15.3, 15.4 and 15.5 for the digital interface, analog inputs and analog outputs, respectively.

15.2.3 Closed-loop feedback vibration control using a PI controller

The design methodology for the PI controller was explained in Chapter 9 (Section 9.4.1). Here, we will implement this controller to reduce the vibration in a

Table 15.3 Digital interface specifications of the DSP vibration-controller card (DSP ADSP 2181 KS-160).

Feature	Details
Operating frequency	40 MHz
Memory	Data 16×32 (on chip) Program 16×24 (on chip) Boot 64×8 (external) FP ROM
Serial channels	One RS 232 port
External ADC	AD 7891, 12 bit, 0–5 V
Digital inputs and outputs	8 ports
Power supply	5 V @ 1 A
Form factor	5.3 in \times 3.5 in

thin-walled box beam. First, the closed-loop responses using the PI controller are obtained experimentally by using an SISO and single-output-two-input system. The test specimen is excited in the transverse bending mode by applying a single-frequency sinusoidal voltage through the PZT actuators. The experimental results are correlated with the results simulated via state-space modeling. Here, the mass and stiffness matrix for the controller design are generated by using the superconvergent FE formulation for a thin-walled beam explained in Chapter 8 (Section 8.3). The SEREP technique explained in Chapter 9 (Section 9.4.3) was used to reduce the full system model to a 5×5 system. Next, multi-modal control of the transient response to impulse loading is

Table 15.4 Analog channel specifications for analog inputs.

Feature	Details
Number of channels	15
Voltage range	–5 V to +5 V
Frequency	0.5 Hz to 2 kHz
Signal conditioner	Second-order Butterworth filter; cut-off frequency at 2 kHz
Resolution	12 bit
Interface to DSP	Parallel

Table 15.5 Analog channel specifications for analog outputs.

Feature	Details
Number of channels	8 (buffered)
Voltage range	0 V to +5 V
Frequency	0.5 Hz to 2 kHz
Resolution	12 bit
Interface to DSP	Serial

investigated numerically by using the eigenstructure assignment technique. The state matrix [A] of size (10×10) of the beam considering five transverse bending modes and input matrix [B] of size (10×2) for the two actuator, A_1 and A_2 (shown in Figure 15.1(b)), are then obtained.

Vibration suppression is performed experimentally by a single and two PI controllers. In both cases, the tip acceleration is measured and the feedback is given as the proportional gain K_p multiplied by the tip acceleration \ddot{x}_{tip} (this is measured by the accelerometer sensor S_1 (see Figure 15.4) and the integral gain K_i multiplied by the velocity \dot{x}_{tip} obtained by integrating \ddot{x}_{tip} . In the first case,

using a single PI, a sinusoidal voltage having an amplitude of 95 V and a frequency of 34.5 Hz is applied through actuator 1 (A_1) (see Figure 15.1(b)) and the control signal is fed back through actuator 2 (A_2). In Figure 15.5(a), the experimental open-loop tip acceleration and the controlled tip acceleration with $K_p = 1.8$ and $K_i = 0.54$ are shown. These K_p and K_i values used in the experiment are obtained through tuning using the Ziegler–Nichols rule described in Chapter 9 (Section 9.4.1). The uncontrolled response has an amplitude of 1.88 V, which is reduced to 0.97 V in the controlled response. In this figure, 800 sample points with a sampling interval of 0.00025 s are shown. Figure 15.6(b) shows the corresponding simulated results with K_p and K_i , the same as that in the experiment. This figure shows the steady-state responses between 3.8 and 4.0 s and the time-step for numerical simulations is 0.0001 s. The simulated open- and closed-loop amplitudes are 1.93 V and 0.99 V, respectively, giving a net suppression of 48.7 %.

For a better attenuation, two PI controllers are implemented, with the control signal being applied to both the PZT patches, namely, actuators 1 and 2, respectively. The disturbance sinusoidal signal as described earlier is again applied through actuator 1. The gains used for the feedback to actuator 2 are $K_p^1 = 1.8$ and $K_i^1 = 0.27$

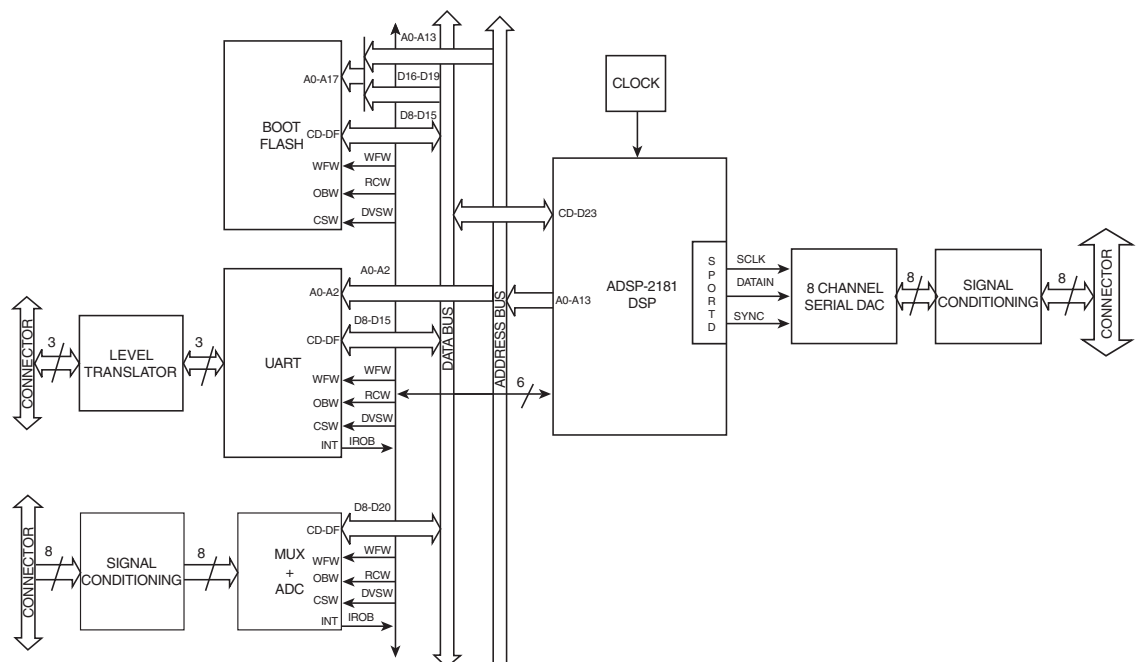


Figure 15.4 Block diagram of the DSP-based vibration-controller card.

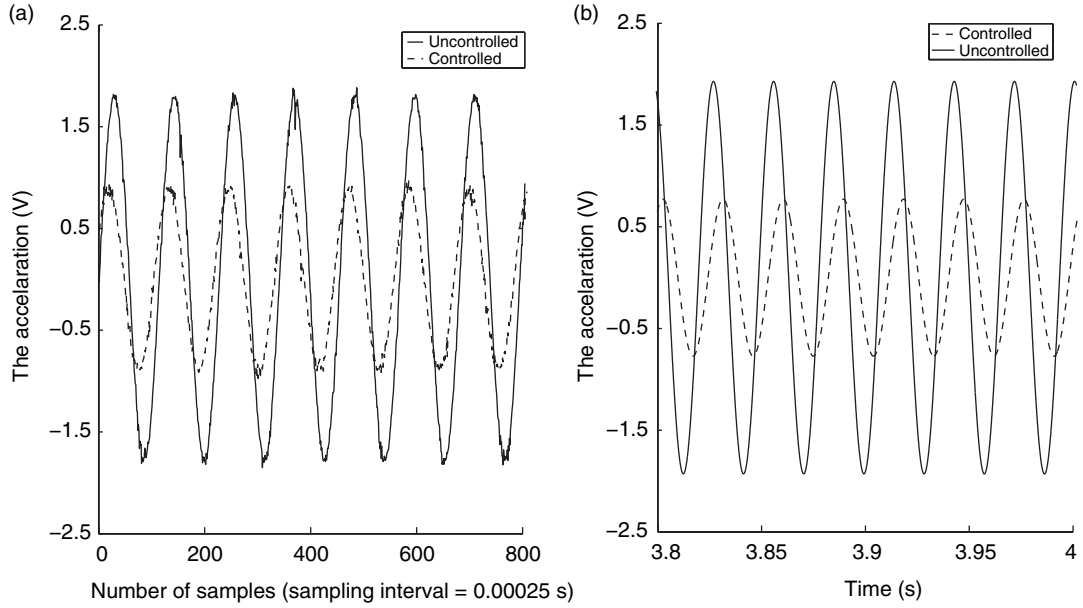


Figure 15.5 Uncontrolled and controlled responses of the box beam using a single PI controller: (a) experimental; (b) theoretical.

and that for actuator 1 are $K_p^2 = 5.4$ and $K_i^2 = 1.62$. Figure 15.6(a) shows the experimental open- and closed-loop tip acceleration data. The closed-loop amplitude is reduced to 0.31 V or 83.36 % vibration reduction.

The number of sample points plotted is 800 with a sampling interval of 0.00025 s. Figure 15.6(b) shows the simulated open- and closed-loop steady-state responses between 3.8 and 4.0 s with a time step of

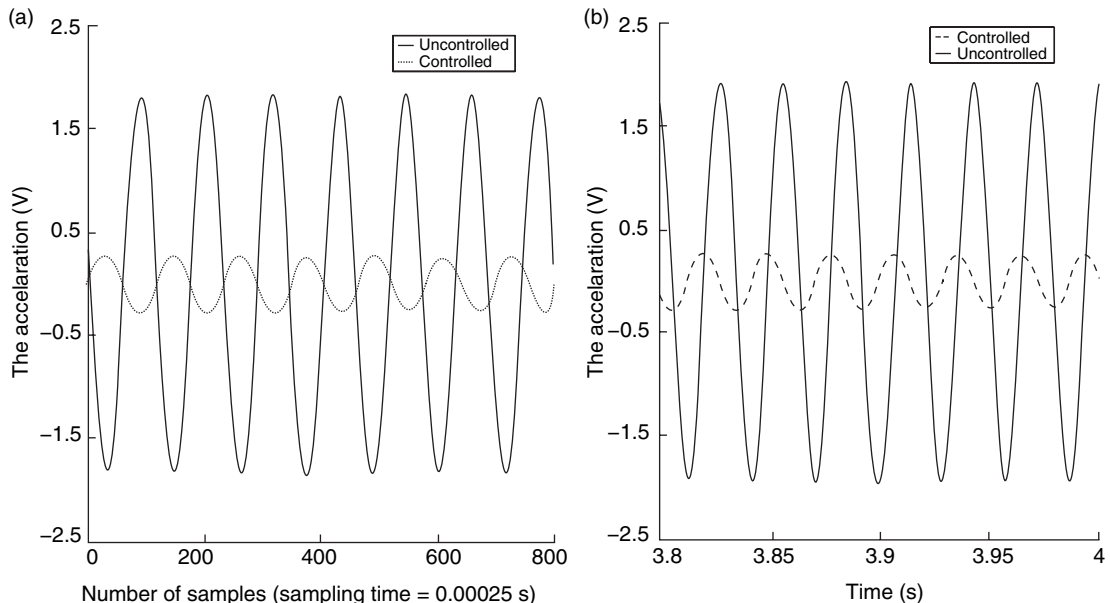


Figure 15.6 Uncontrolled and controlled responses of the box beam using two PI controllers: (a) experimental; (b) theoretical.

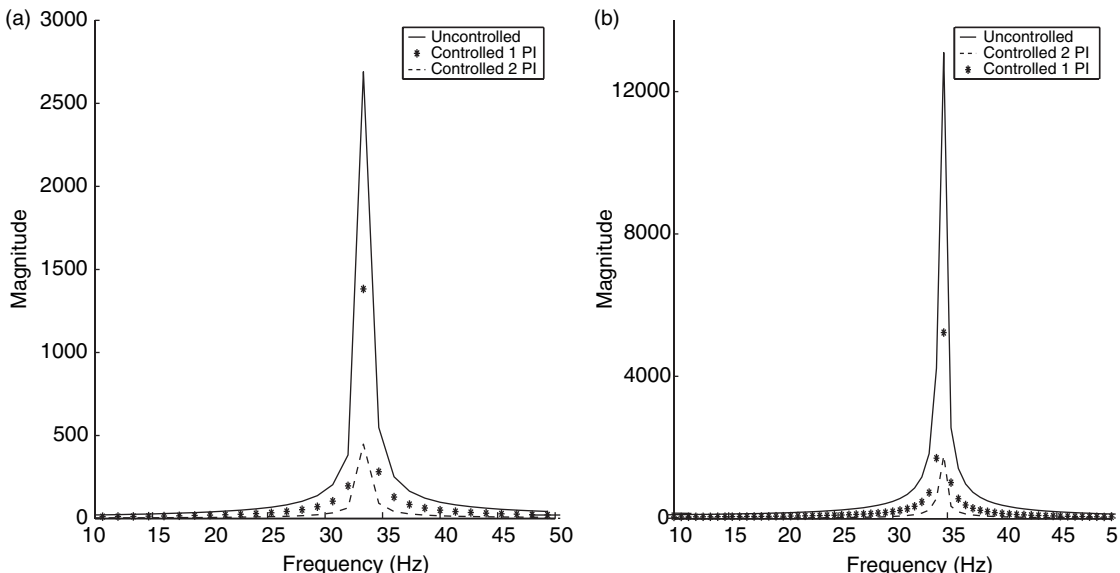


Figure 15.7 Uncontrolled and controlled responses of the box beam using PI controllers in the frequency domain: (a) experimental; (b) theoretical.

0.0001 s. The controlled response has an amplitude of 0.45 V and the reduction is 76.96 %. Figure 15.7 shows the open- and closed-loop responses using a single and two PI controllers in the frequency domain. From these experiments, we find that the formulated smart thin-walled beam element predicts excellent results under a control environment.

15.2.4 Multi-modal control of vibration in a box beam using eigenstructure assignment

The previous example dealt with only a single frequency excitation and hence only a single mode was controlled. In the next example, we will consider an example wherein a forcing function excites multiple modes. For this example, we will use the eigenstructure assignment technique to design the controller. The box beam test specimen, used in the earlier example, is now subjected to a unit voltage, the time history of which is the same as that shown in Figure 9.2. That is, the forcing function has a frequency content of 44 kHz. The load is applied through actuator A_1 (see Figure 15.1). The high-frequency content of the load will excite many transverse bending modes. The frequency response corresponding to this loading is shown in Figure 15.8, with the load history shown in the inset. As discussed earlier, for controller design, the model is reduced by using the

SEREP technique to contain only the first five of these transverse bending modes. As the first few modes contribute mainly to the total energy of the system, a suppression of these modes is expected to give satisfactory vibration reduction.

The eigenstructure assignment is applied to control the first two modes of the beam. The sensing is done through two accelerometers, and thus four state variables, which are the acceleration and velocity at two points, are measurable. Sensor 1 (S_1) is placed at the tip or at node 10 and sensor 2 (S_2) is placed at node 4, as shown in Figure 15.9. The feedback signal is given to actuator 1 (A_1) and actuator 2 (A_2). The system thus has four outputs and two inputs and four eigenvalues and eigenvectors can be assigned, as described in Chapter 9 (Section 9.4.2). The sampling time is taken as 0.001 s. The eigenvalues are assigned such that the damping ratio of the first two modes of the closed-loop system is 4 times that of the open-loop system. The eigenvectors for the first and second modes are specified such that the tip entries are 0.2 and 0.4 times those of the open-loop eigenvectors, respectively. The open-loop eigenvalues, λ_o , of the first-order system (Equation (9.9), Chapter 9), assigned eigenvalues, λ_a , and closed-loop eigenvalues, λ_c , in the form $\alpha \pm i\omega_d$, are given in Table 15.6, where $\alpha = \zeta\omega_n$, with ζ being the damping ratio, ω_n the natural frequencies (in rad/s) and

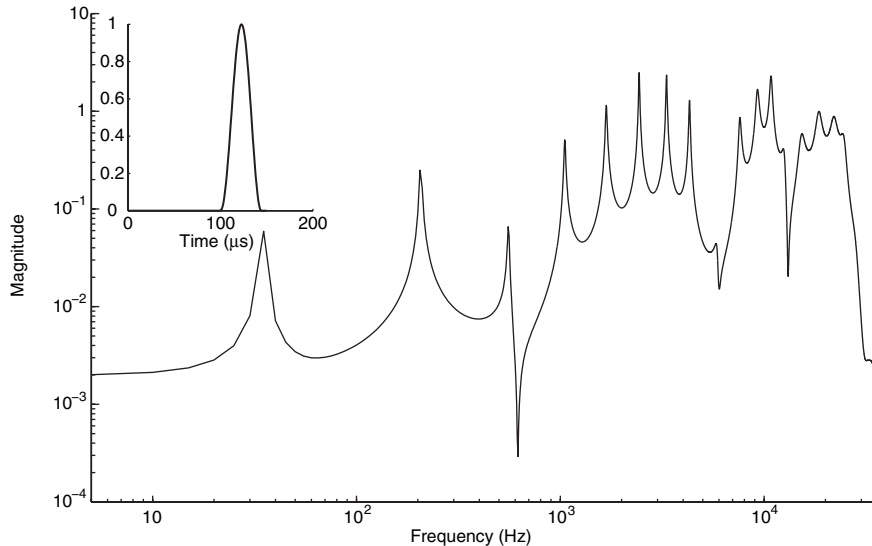


Figure 15.8 Frequency response of the tip displacement due to the impulse load and impulse load history (inset).

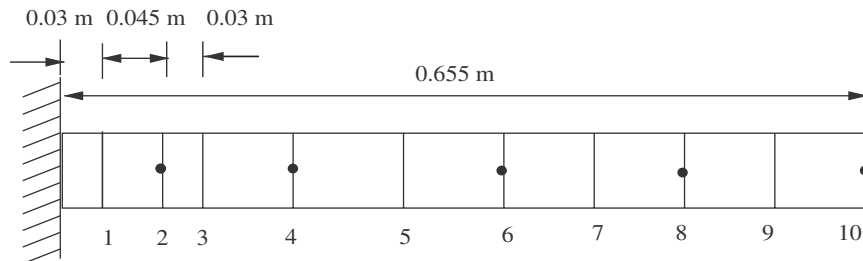


Figure 15.9 Experimental box beam showing the ten beam elements and nodes with master degrees of freedom (●).

$\omega_d = \omega_n \sqrt{1 - \zeta^2}$ the *damped* natural frequencies (in rad/s).

It can be seen that the first four λ_c values, corresponding to the first and second modes, are exactly equal to the λ_a and has a damping constant α four times that of λ_o .

The remaining six unassigned λ_c values are stable and α is increased in all cases. Hence, the overall response can be expected to be suppressed considerably. In Table 15.7, the corresponding ζ and ω_n (in Hz) are compared for the open- and closed-loop systems. Figure 15.10 shows the

Table 15.6 Open-loop and closed-loop eigenvalues.

Mode	Eigenvalues, $\alpha \pm i\omega_d$		
	Uncontrolled	Assigned	Controlled
1	$-1.87 \pm i216.5$	$-7.46 \pm i216.5$	$-7.46 \pm i216.5$
2	$-12.57 \pm i1298.0$	$-50.30 \pm i1298.0$	$-50.30 \pm i1298.0$
3	$-31.75 \pm i3497.2$	—	$-239.61 \pm i3489.0$
4	$-55.79 \pm i6605.7$	—	$-208.37 \pm i6588.7$
5	$-91.48 \pm i10557.0$	—	$-94.51 \pm i10554.0$

Table 15.7 Open-loop and closed-loop damping ratios and natural frequencies.

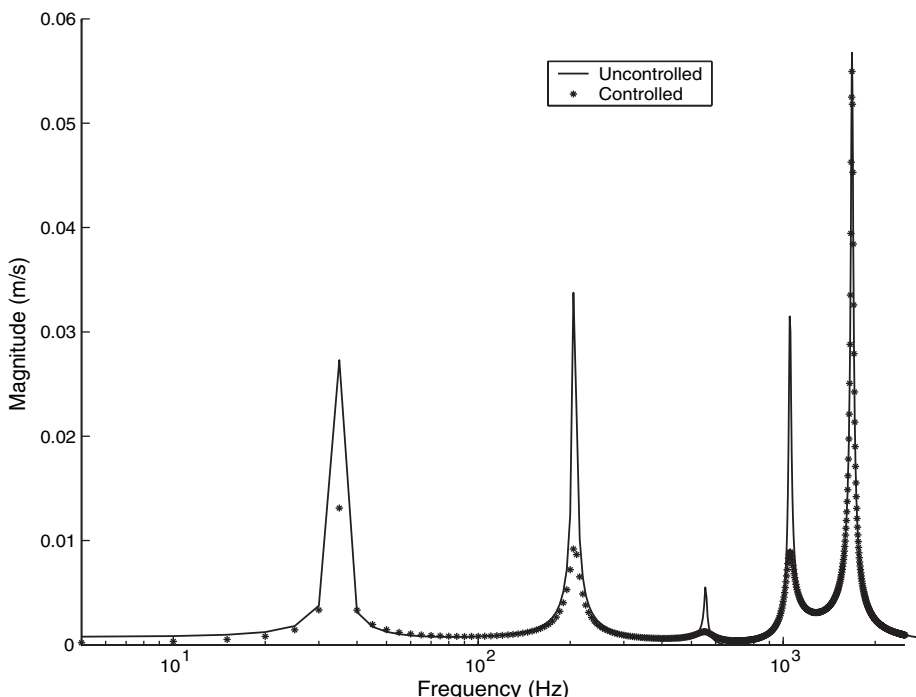
Mode	Damping ratio, ζ		Frequency, ω_n (Hz)	
	Uncontrolled	Controlled	Uncontrolled	Controlled
1	0.0086	0.0344	34.46	34.48
2	0.0097	0.0387	206.59	206.74
3	0.0091	0.0685	556.54	556.60
4	0.0084	0.0316	1051.00	1049.10
5	0.0087	0.0090	1679.30	1679.80

controlled and uncontrolled responses of the tip displacement due to a unit impulse load of duration 40 μ s applied to A_1 . The frequency responses of the tip displacement show considerable reductions in the 1 and 2 mode amplitudes. The unspecified 3rd and 4th modes are also damped considerably, while there is a small reduction in the 5th mode.

In summary, it has been effectively demonstrated that the use of PZT actuators coupled with the formulated smart FEM can be effectively used to control both single and multiple frequencies. A similar procedure can be applied to suppress bridge vibrations in civil structures or compressor vibrations in air-conditioning equipment.

15.3 ACTIVE NOISE CONTROL OF STRUCTURE-BORNE VIBRATION AND NOISE IN A HELICOPTER CABIN

In Chapter 9, we discussed the issues and possible solutions for dealing with the distributed actuator dynamics for broadband control. In this section, we focus on the issues and possible solutions to deal with the problem of controlling multiple-wave transmission in helicopter gear-box support struts fitted with Terfenol-D packaged actuators. The ASFEM (discussed in Chapter 9) is used for numerical simulation of the feedback control performance and the effect of the sensor–actuator configuration.

**Figure 15.10** Uncontrolled and controlled frequency responses of the tip displacement.

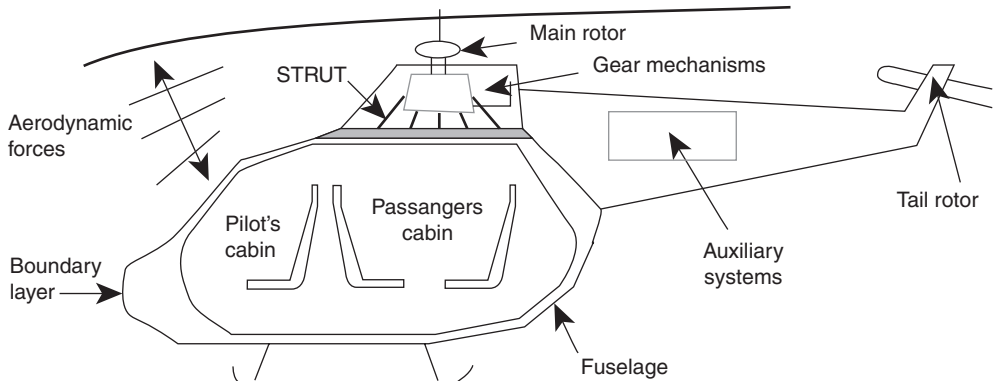


Figure 15.11 Schematic of a helicopter showing the sources of noise.

Helicopter cabin noise reduction has received considerable attention over the last two decades. With interior noise reduction, passenger comfort, as well as operational ease, can be improved, along with enhancement of structural fatigue life. The main rotor and the gearbox mechanisms serve as the main sources (see Figure 15.11) of persistent acoustic disturbances, while quick changes in gear-teeth movement and aero-elastic events associated with maneuver transitions can result in transient acoustic disturbances. In many helicopters, the entire gearbox assembly is mounted on a set of vertical and inclined struts [4,5]. The transient and persistent disturbances generated by the gearbox mechanisms, as well as the main rotor, are transmitted through the struts into the fuselage; this transmission is one of the main sources of structure-borne noise in a helicopter cabin. The frequency components associated with this noise are within the bandwidth extending up to 6 kHz [6,7].

Among many approaches pursued to realize cabin-noise reduction, the control of waves transmitted through the ‘noise paths’, such as struts, has been found to be viable. An early initiative in this regard is due to Westland Helicopters, Ltd. During the late 1980s, they demonstrated that considerable reduction of the average vibration level can be achieved by using an Active Control of Structural Response (ACSR) system at a blade-passing frequency of 17.5 Hz [4,5]. An electro-hydraulic actuator is used in this low-frequency application. The application of active wave control in the gearbox support strut at high frequencies was carried out in a major group effort as a part of the *Reduction of Helicopter Interior Noise* (RHINO) project. This project involved Westland Helicopters Ltd., Agusta and others [6]. As reported in this work, an actual helicopter strut was tested in a test-rig under realistic loading conditions.

A primary source in the form of a ‘shaker’ was used to excite the system at the upstream end-plate of the strut and a group of three secondary sources in the form of magnetostrictive actuators were mounted in-parallel to the strut. The choice of the driving voltage inputs (that is, amplitudes and phases) to the actuators was based on minimizing the sum of the squared responses, measured by six error sensors at the downstream end-plate. The location of the compliant ring for the secondary actuator group housing was chosen based on earlier studies on structural wave control in ducts and beams [7–9]. As reported in the study by Sutton *et al.* [6], an adaptive multiple-actuator feed-forward control scheme produced an energy attenuation of up to 40 dB at the downstream interface of the strut over different discrete frequencies in the range extending up to 1.25 kHz. The development of an *Active Noise Control* (ANC) system for the S-76 helicopter by the Sikorsky Aircraft Corporation has also been reported [10,11].

Although active-materials integrated finite struts have been used extensively in experimental studies of full-scale systems, related analytical efforts have primarily focused on infinite struts. Pelinescu and Balachandran [12] developed integrated mechanics models for finite struts and used them for open-loop studies of longitudinal and flexural wave transmission. In their models, the strut is treated as a homogeneous cylindrical waveguide and the actuators are also modeled as waveguides. In the related study by Ortell and Balachandran [13] these models are used to develop closed-loop schemes for control of flexural wave transmission. Although these studies represent progress towards analytical development of an integrated active system, in order to use them for realistic configurations the following features need to be taken into account in the modeling: (a) effects of

structural boundaries, joints and other local discontinuities that can be important in the high-frequency range, (b) steady state axial and transverse loading, and (c) coupling between the longitudinal and flexural waves. In addition, the developed models need to be amenable for establishing schemes for controlling wave transmission over a broad frequency range that includes multiple spectral peaks, as in the present problem. However, models of realistic systems inclusive of the above features are not amenable to analytical solutions. The efforts in this work are directed towards using the ASFEM to analyze and design the active strut system for optimal performance.

Apart from the ASFEM, other similar Fourier domain representations and the transfer-function concept have been developed [14,15]. These transfer-function-based methods were later extended to the adaptive control of structural waves for minimizing the transmitted power flow through a one-dimensional elastic member [16,17]. For distributed structural networks, the concept of *low authority control* (LAC) of traveling waves has also been developed and studied by using a feedback compensator [18]. However, the aspects of distributed sensing and actuation and issues, such as actuator dynamics, have not been addressed in the above studies based on the transfer-function concept. From the above mentioned studies, it is noted that as complexity in the structural geometry and applying the transfer function analysis increases, the control analysis involves extensive computation. On the other hand, the ASFEM can be efficient from a computational viewpoint due to its generalized matrix assembly procedure and easy ‘post-processing’.

15.3.1 Active strut system

Helicopter gearbox support struts can be idealized as monolithic cylindrical shells with appropriate end-sections to support the bearings. As reported in Sutton *et al.* [6], the ring frequency of the EH101 strut is typically 22.5 kHz. A high ring frequency is indicative of the dominance of torsional and warping modes in the overall response. Based on the disturbance frequency range, it was concluded in this study that the torsional motion is unlikely to be excited and that the resonances associated with warping motions are too high to affect the control performance significantly. Hence, for simplicity, only axial and flexural modes are considered in the model development following the analytical studies in Pelinescu and Balachandran [12].

The cylindrical strut is modeled as a beam with a ‘stiffness-equivalent’ solid cross-section. Terfenol-D rod-

type actuators, including the actuator housing, are considered to be mounted on either the strut ends or on the surface with the help of a rigid ring. In Roy Mahapatra [19], an accurate mechanics model of a uniform cylindrical strut/tube system is developed and was shown that a new propagating mode (radial mode) causing strong dispersiveness in other modes appears above the cut-off frequency of 8.5 kHz. However, this cut-off can be considered very high when compared to the major noise spectrum. In order to allow for the dynamic boundary conditions, the strut ends are considered to be under ‘dynamic reaction’ by the gearbox and fuselage interfaces. As noted in the study by Pelinescu and Balachandran [12], this configuration is an idealization made to suit the linear analysis.

In this case study, we have used a feedback scheme based on responses measured by downstream displacement or strain sensors. This model-based scheme requires accurate modeling of actuator-induced strain in the host structure to capture the ‘near-field’ effects. With a good model, it is believed that analysis and control design efforts may be carried out with a lower number of actuators than that required in the ‘feed-forward’ effort.

15.3.2 Numerical simulations

Following the work of Pelinescu and Balachandran [12], the finite-length strut considered is a 1.0 m long hollow cylindrical aluminum strut with a 7.62 cm outer diameter and a 6.35 cm inner diameter. Harmonic loads are applied at the strut ends in the longitudinal and transverse directions. As considered in Pelinescu and Balachandran [12], such dynamic loading represents a simplified model of a high-impedance gearbox reaction at one end and a reaction from the bearing at the fuselage interface. A cylindrical magnetostrictive actuator with a rod-shaped Terfenol-D core is chosen due to its high force capability. Such an actuator has its own housing and reaction mass [20]. These aspects can also be accurately modeled in the ASFEM if the effective stiffness and mass distributions are known for packaged actuators. Based on the strut geometry considered here and the loading conditions to be considered, it is known that the longitudinal motion is expected to contribute substantially to the total kinetic energy at the fuselage interface. The main objective of numerical simulation here is to reduce the total noise level of the structure-borne noise. For this to be accomplished, we need to control the transmitted waves at the strut-fuselage interface. With these points

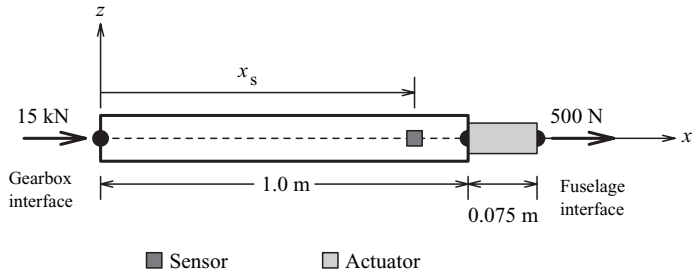


Figure 15.12 Schematic of an active strut for the control of longitudinal wave transmission.

in mind, the first case considered below has to do with the control of longitudinal-wave transmission.

15.3.2.1 Control of longitudinal-wave transmission

In Figure 15.12, an actuator located at the strut-fuselage interface is shown, along with a point velocity feedback sensor mounted at a distance x_s from the gearbox end of the strut. This system is described by two spectral elements, where one is an actuator element

and the other is a strut element. The results obtained in the uncontrolled and controlled cases are shown in Figure 15.13. With the actuator, the system resonances are shifted to lower frequencies and it appears that the magnitude of the frequency shift increases linearly with the mode number. A non-dimensional scalar velocity feedback gain, g , defined as:

$$g = \frac{\alpha\beta\gamma}{n_0 I_0 c_0} \quad (15.1)$$

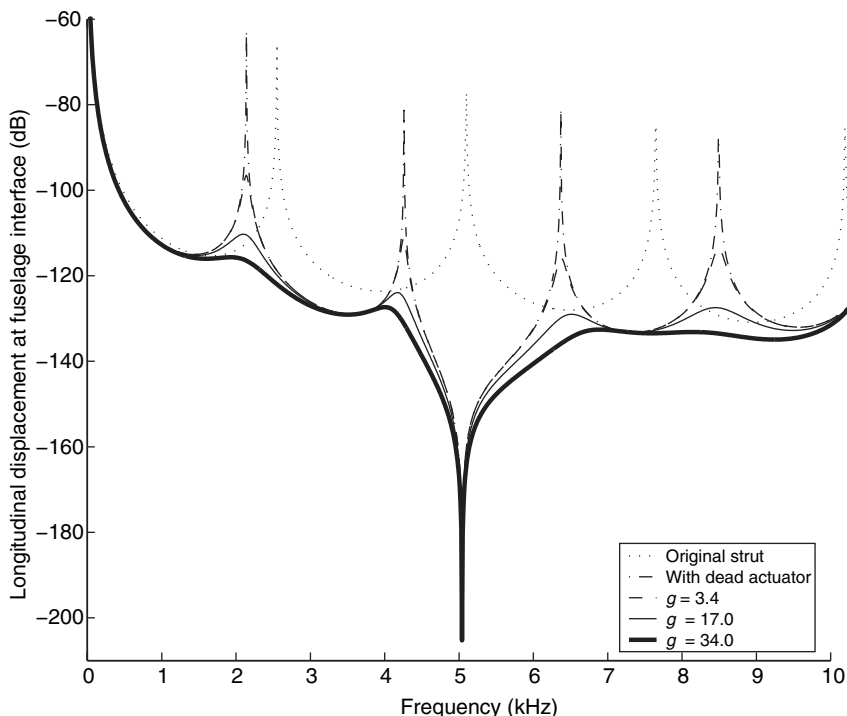


Figure 15.13 Longitudinal displacement at the strut-fuselage interface showing the controlled and uncontrolled responses for different control gains.

is used, where α and β are, respectively, the sensitivity parameters for the sensor and actuator, as discussed in Chapter 9 (Section 9.6.2), γ is the constant gain, n_0 is the number of specific turns in the actuator coil, I_0 is a nominal rms coil current and c_0 is the speed of sound in air. In all of the numerical studies conducted here, the values of the different quantities are $\alpha = 1$ and $\beta = 1$.

It is seen that the sensor–actuator collocated configuration (Figure 15.12) can be used to attain considerable displacement response attenuation throughout the frequency bandwidth of interest. A similar displacement response attenuation at targeted frequencies based on an analog feed-forward scheme for the same sensor–actuator configuration was reported in Pelinescu and Balachandran [12]. Since it may be difficult to exactly place the sensor at the actuator base, an alternate configuration is used wherein the sensor is placed away from the actuator base. The results obtained for the configurations, $x_s = 0.9\text{ m}$ and $x_s = 0.8\text{ m}$ for $g = 17.0$ (optimal in Figure 15.13), are shown in Figure 15.14, with $n_0 = 1 \times 10^6 \text{ m}^{-1}$, $I_0 = 1 \text{ rms}$ and $c_0 = 340 \text{ m/s}$. The sensor is located at the strut–fuselage interface (that is, $x_s = 1\text{ m}$) and the parameter g for velocity feedback is increased in the range from 3.4 to 34.

It is observed that $x_s = 0.9\text{ m}$ may be the most preferable sensor location, since for this choice the response close to the fourth-mode resonance location is completely suppressed. For the non-collocated case, $x_s = 0.8\text{ m}$, although there is the largest suppression at the frequency location close to the resonance of the second mode, while the suppression at the location close to the resonance of the fourth mode is not as good as that obtained for the case with $x_s = 0.9\text{ m}$. However, in this later case the suppression at the location near the resonance of the second mode is not as good as that obtained with $x_s = 0.8\text{ m}$.

In some designs, it may be necessary to use a group of actuators, rather than one actuator, to realize the required actuator force. Such actuator groups have been used in earlier work (e.g. [6]). In this study, the performances of three secondary magnetostrictive actuators in a group (hosted by a steel end-cap) was studied in an experimental arrangement. Input to the actuators was decided based on the measurement from one error sensor located on the upstream side of the actuator. The actuators were driven in-phase for controlling the longitudinal wave transmission through a strut and they were *not* driven in-phase for controlling

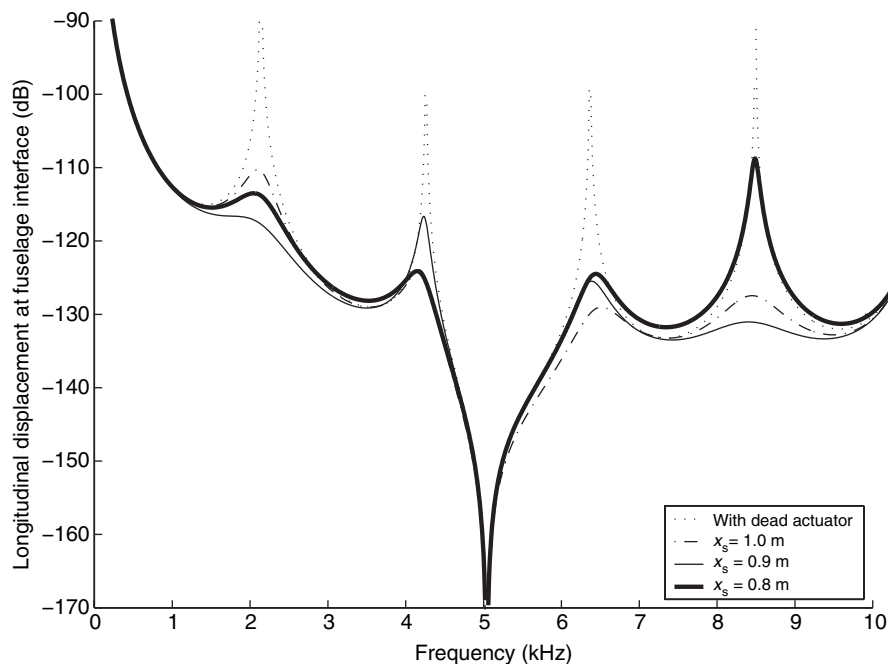


Figure 15.14 Longitudinal displacement at the strut–fuselage interface showing the controlled and uncontrolled responses for different sensor locations.

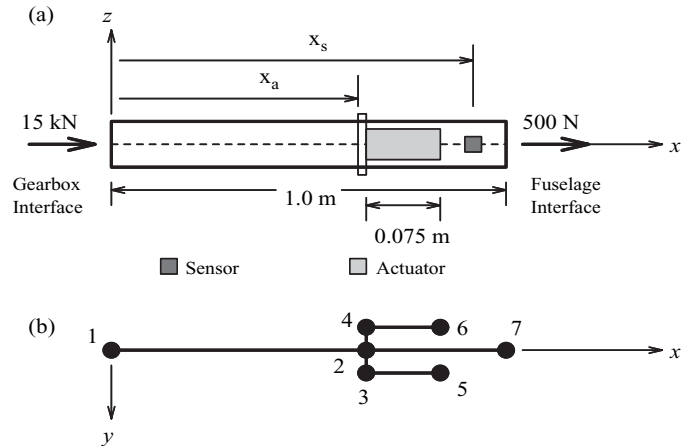


Figure 15.15 (a) Configuration of a strut with two intermediate actuators in a group and (b) spectral-element representation of the actuators, sensor, strut and base ring.

flexural wave transmission. To illustrate the applicability of the ASFEM for actuator group configurations, here the active strut illustrated in Figure 15.15(a) is considered.

There are two actuators in the actuator group here and these are represented by the spectral elements 3–5 and 4–6 in the modeling, as shown in Figure 15.15(b).

Apart from these two elements, the computational model consists of four other elements, which includes one sensor element (2–7) downstream of the actuators. The ‘base ring’ is modeled as a rigid link (4–2–3). Next, the results generated for this configuration with different actuator group locations x_a , with $x_s = 0.9$ m are shown in Figure 15.16.

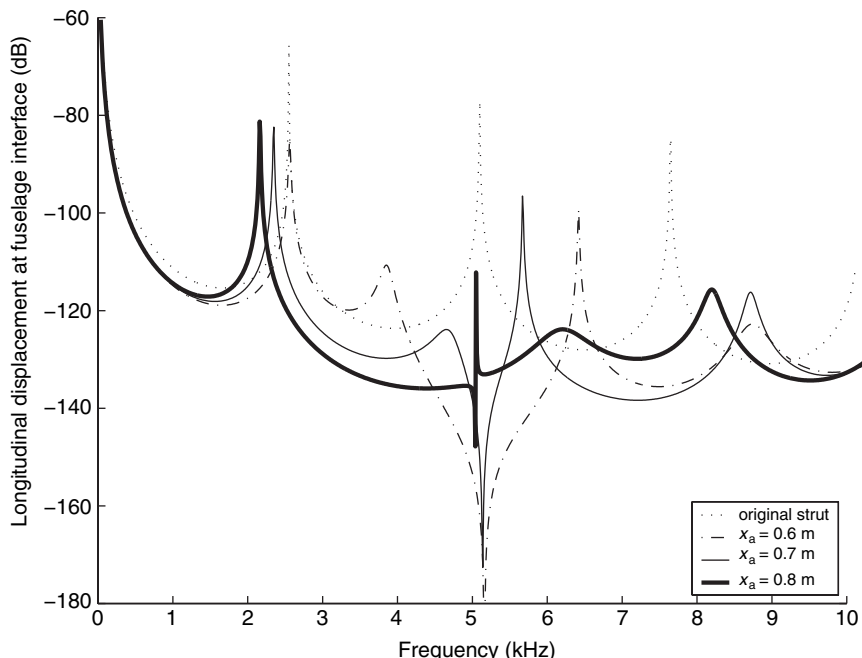


Figure 15.16 Longitudinal displacement at the strut–fuselage interface for different actuator group locations.

For each actuator, $g = 8.5$ (one half of the optimal value obtained previously for the one-actuator case) and both of the actuators receive identical inputs. In all cases, attenuation at the location close to the resonance of the first mode is considerable but less than that obtained at other frequency locations. In Figure 15.16, a zero (anti-resonance) is introduced into the closed-loop system (other zeros lie ‘towards infinity’ along the frequency axis and are fewer in number than the number of poles, meaning that the system is a realizable one) at a frequency close to the resonance frequency of the second mode (or pole) of the open-loop system. Interestingly, this corresponds to the second root-locus of the open-loop system transfer-function towards a closed-loop zero as the control effort is increased (meaning that the mode is a ‘stabilizable’ one). More parametric studies on this configuration can be found in Roy Mahapatra *et al.* [21].

15.3.2.2 Control of flexural-wave transmission

Figure 15.17 shows the active-strut configuration for control of the flexural-wave transmission where a single-transverse actuator is placed at x_a , as in Pelinescu and Balachandran [12], and a single-point velocity feedback sensor is placed downstream of the actuator.

In the study of Ortell and Balachandran [13] and also here, it was found that the introduction of single and multiple actuators alters the resonance of the system. Mechanically, therefore, the presence of a dead actuator may cause considerable change in the open-loop system due to the stiffness and inertia of the actuator. The spectral characteristics also suggest the presence of secondary axial–flexural coupled modes; these are due to scattering of the incident flexural wave, producing

additional longitudinal waves at the strut–actuator interface. This observation indicates the need for considering the dynamics of distributed actuation in similar broadband (multiple-tone) structural-control problems.

In Figure 15.18, the responses of the closed-loop system with different values of g are shown for $x_s = 0.6\text{ m}$ and, $x_a = 1.0\text{ m}$. Good attenuation is obtained at all frequency locations except for the first mode resonance close to 5 kHz. The locations of the zeros observed in the open-loop system also appear to be unchanged in the closed-loop cases. In Figure 15.18, the sensor is shifted away from the strut–fuselage interface to $x_s = 0.9\text{ m}$. The trends are similar to those seen in the context of Figure 15.19, except that few zeros disappear. The results are suggestive of the inability to achieve response attenuation at the location close to the first resonance location of the open-loop system. This indicates the requirement of an additional damping mechanism to absorb the ‘high energy’ that associates to the first mode. However, in most helicopters, such damping mechanisms already exist, along with elastomeric bearings to augment the performance.

15.3.2.3 Control of axial–flexural coupled wave transmission

One of the main objectives of the numerical study was coupled axial–flexural wave transmission. A two-actuator configuration chosen for this purpose is shown in Figure 15.20.

One of these actuators is inclined at an angle θ with respect to the longitudinal axis of the strut. Control inputs to both these actuators are based on a single-error sensor response. Based on the results presented in the earlier

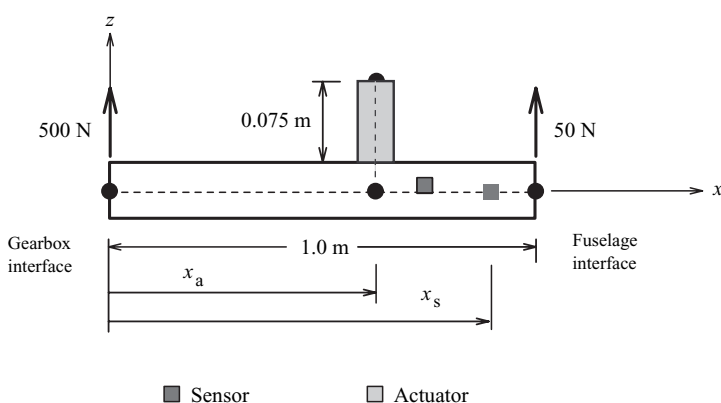


Figure 15.17 Configuration of an active strut for control of flexural wave transmission.

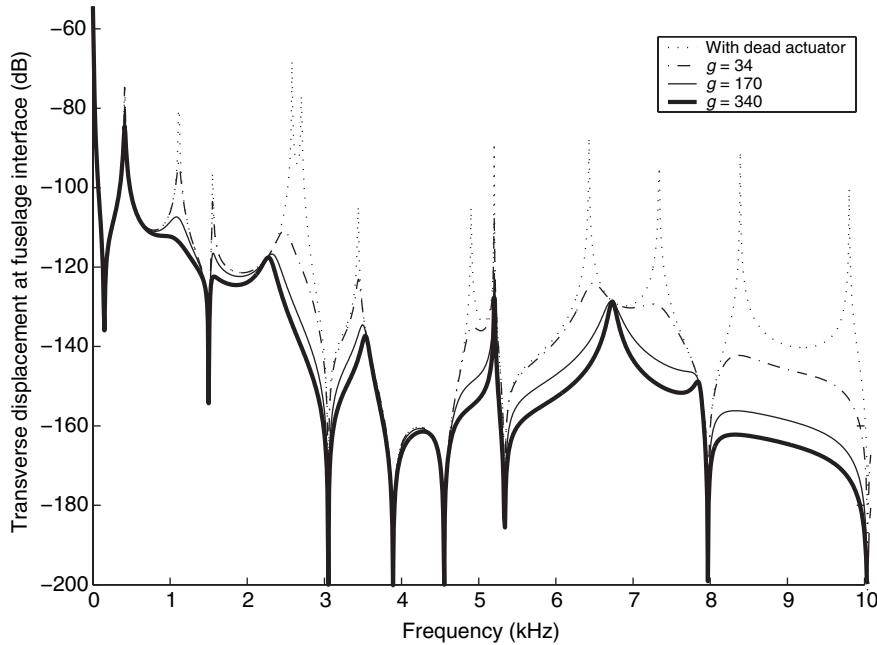


Figure 15.18 Transverse displacement responses at the fuselage interface for various gain-parameter values.

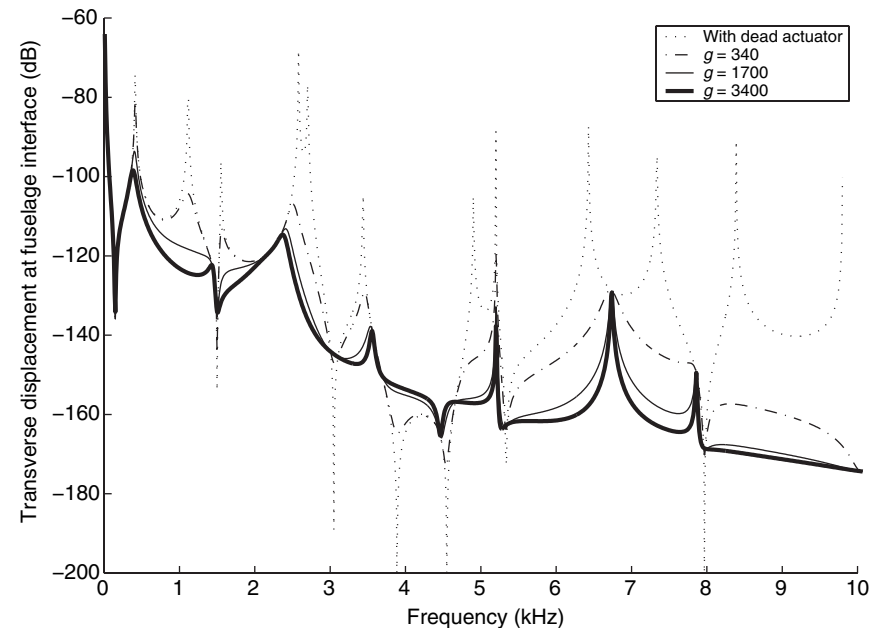


Figure 15.19 Transverse displacement responses at the fuselage interface for various gain-parameter values.

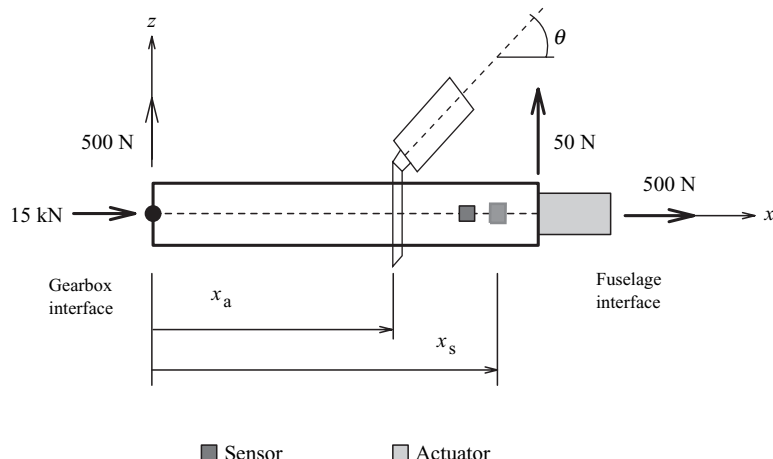


Figure 15.20 Configuration of an active strut for the control of axial–flexural waves.

sections, the sensor location is chosen to be $x_s = 0.9$ m, which was an ‘optimal’ location for the most number of axial and flexural modes. Uncontrolled and controlled longitudinal displacements at the strut–fuselage interface are plotted in Figure 15.21. The appearance of a number of secondary axial–flexural coupled modes can be seen in this figure. It can be noted that the additional secondary modes do not contribute significantly to the axial-

displacement response compared to those due to the primary modes. However, this is not the case for the flexural-displacement response, where the primary modal amplitudes are influenced considerably by the secondary coupled modes, leading to shifts in the locations of poles and zeros of the closed-loop system.

While constructing the closed-loop system, it is assumed that the sensor outputs corresponding to both

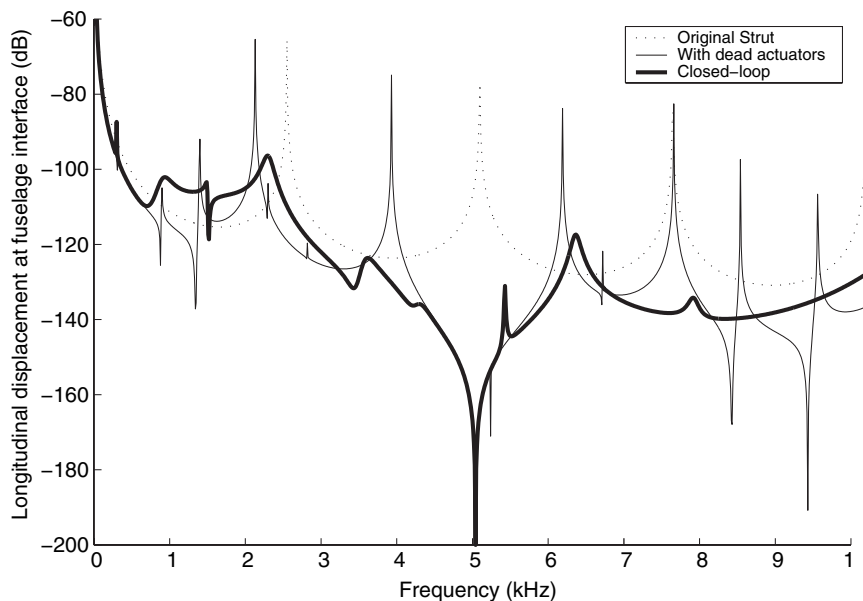


Figure 15.21 Longitudinal displacement responses at the fuselage interface for various gain-parameter values: $X_s = 0.9$ m; $X_a = 0.6$ m; $\theta = 90^\circ$.

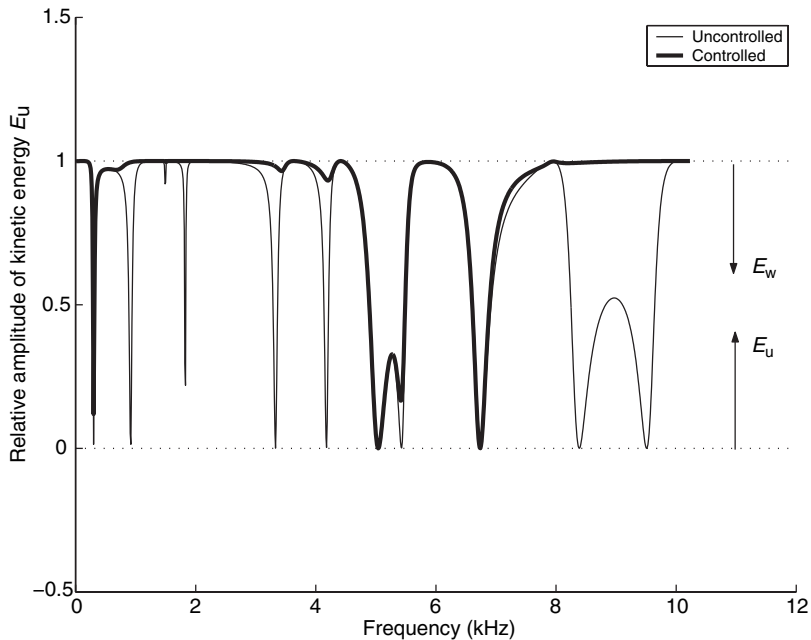


Figure 15.22 Distribution of kinetic energy between the longitudinal and transverse components at the fuselage interface for $\theta = 90^\circ$.

of the longitudinal and transverse forced-frequency responses are available from the chosen sensor location. The longitudinal and inclined actuators are driven based on these measured longitudinal and transverse responses, respectively. Among different sets of parametric values, considered for velocity feedback gains (g_u for the longitudinal actuator and g_w for the inclined actuator) and x_s , considered earlier for the control of axial and flexural waves separately, the best results were achieved for $g_u = 17.0$ and $g_w = 340.0$. From these results, it can be noted that with a constant gain velocity feedback scheme, an increase in effort to control the flexural waves leads to less attenuation in the longitudinal response.

The modeling efforts presented here may be used as a basis for carrying out the ‘path-treatment’ for helicopter cabin noise. In such cases, it is of interest to know the level of energy attenuation at the spatial location of interest; here, the strut–fuselage interface. The kinetic energy has contributions from longitudinal (primary) and transverse (secondary) motions. In order to analyze the distribution of total kinetic energy among its longitudinal and transverse components in the closed-loop system, Figure 15.22 is presented. Plots of the normalized spectra of the relative amplitudes of the kinetic energy, \hat{E}_u , for the longitudinal motions and \hat{E}_w , for the transverse

motions at the strut–fuselage interface are shown in this figure. The corresponding expressions are given by:

$$\hat{E}_u = \frac{|(\hat{u}_0)^2|}{|(\hat{u}_0)^2 + (\hat{w})^2|}; \quad \hat{E}_w = 1 - \hat{E}_u \quad (15.2)$$

where \hat{u}_0 and \hat{w} are the spectral amplitudes of the longitudinal and transverse displacements, respectively, at the strut–fuselage interface. From this figure, it can be said that the kinetic energy associated with the significant transverse modes is attenuated, except at the frequency locations close to the first transverse resonance mode and the other three modes associated with resonances near 5.2 and 6.8 kHz.

REFERENCES

1. T.H.G. Megson, *Linear Analysis of Thin Walled Elastic Structures*, Surrey University Press, Guildford, UK (1974).
2. Mira Mitra, Active vibration suppression of composite thin walled structures, *M.Sc. Thesis*, Indian Institute of Science, Bangalore, India (2003).
3. Mira Mitra, S. Gopalakrishnan and M. Seetharama Bhat, ‘Vibration control in a composite box beam with

- piezoelectric actuators', *Smart Structures and Materials*, **13**, 676–690 (2004).
4. A.E. Staple and D.M. Wells, 'The development and testing of an active control of structural response system for the EH101 helicopter', in *Proceedings of the 16th European Rotorcraft Forum*, pp. III.6.1.1–III.6.11 (1990).
 5. A.E. Staple and B.A. MacDonald, 'Active vibration control system', *US Patent*, 5 219 143 (1993).
 6. T.J. Sutton, S.J. Elliott, M.J. Brennan, K.H. Heron and D.A.C. Jessup, 'Active isolation of multiple structural waves on a helicopter gearbox support strut', *Journal of Sound and Vibration*, **205**, 81–101 (1997).
 7. P.A. Nelson and S.J. Elliott, *Active Control of Sound*, Academic Press, London, UK (1992).
 8. S.J. Elliott and L. Billet, 'Adaptive control of flexural waves propagating in a beam', *Journal of Sound and Vibration*, **163**, 295–310 (1993).
 9. M.J. Brennan, S.J. Elliott and R.J. Pennington, 'The dynamic coupling between piezoceramic actuators and a beam', *Journal of Acoustical Society of America*, **102**, 1931–1942 (1997).
 10. C.A. Yorker, Jr, J. Newington, W.A. Welsh, N. Haven and H. Sheehy, 'Helicopter active noise control system', *US Patent*, 5 310 137 (1994).
 11. T.A. Millot, W.A. Welsh, C.A. Yoerke, Jr, D.G. MacMartin and M.W. Davis, 'Flight test of an active gear-mesh noise control on the S-76 Aircraft', in *Proceedings of the 54th Annual Forum of the American Helicopter Society*, **1**, pp. 241–249 (1998).
 12. I. Pelinescu and B. Balachandran, 'Analytical study of active control of wave transmission through cylindrical struts', *Smart Materials and Structures*, **10**, 121–136 (2001).
 13. D. Ortell and B. Balachandran, 'Control of flexural wave transmission through struts', in *Proceedings of the SPIE Smart Structures and Materials Conference on Smart Structures and Integrated Systems*, **3985**, SPIE, Bellingham, WA, USA, pp. 76–85 (2000).
 14. A.H. von Flotow, 'Disturbance propagation in structural networks', *Journal of Sound and Vibration*, **106**, 433–450 (1986).
 15. D.W. Miller and A. von Flotow, 'A traveling wave approach to power flow in structural networks', *Journal of Sound and Vibration*, **128**, 145–162 (1989).
 16. J. Pan and C.H. Hansen, 'Active control of total vibratory power flow in a beam. I: physical system analysis', *Journal of Acoustical Society of America*, **89**, 200–209 (1991).
 17. P. Gardonio and S.J. Elliott, 'Active control of wave in a one-dimensional structure with scattering termination', *Journal of Sound and Vibration*, **192**, 701–730 (1996).
 18. A.H. von Flotow, 'Traveling wave control for large spacecraft structure', *Journal of Guidance and Control*, **9**, 462–468 (1986).
 19. D. Roy Mahapatra, 'Development of spectral finite element models for wave propagation studies, health monitoring and active control of waves in laminated composite structures', *Ph.D. Thesis*, Indian Institute of Science, Bangalore, India (2003).
 20. I. Pelinescu and B. Balachandran, 'Analytical and experimental investigations into active control of wave transmission through gearbox struts', in *Proceedings of the SPIE Smart Structures and Materials Conference on Smart Structures and Integrated Systems*, **3985**, SPIE, Bellingham, WA, USA, pp. 76–85 (2000).
 21. D. Roy Mahapatra, S. Gopalakrishnan and B. Balachandran, 'Active feedback control of multiple waves in helicopter gearbox support struts', *Smart Structures and Materials*, **10**, 1046–1058 (2001).

Index

- Absorber
 SAW accelerometer, 89, 334
 X-ray lithography, 277
 Vibration, 13, 82, 243
- Accelerometer
 Absorbers, 89, 334
 Applications of, 14, 15
 integrated with CMOS, 308
 with movable gate FET, 54
 with SAW IDT
 combined with gyroscope, 372
 design, 88
 fabrication, 333
- Acoustic
 admittance, 98
 aperture, 338
 emission sensor, 371
 impedance, 86, 332
 comparison of properties, 86
 PVDF, 60
 sensor, 57, 86
 wave, 57, 97
 Lamb wave, 326
 Love wave, 57
 sensor, 371
- Active control, 212
 Composite Beam, 248
- Active damping, 11
- Actuation law, 114, 187
- actuator dynamics
 Cantilever beam, 251
- Actuator (*see also* Transducers)
 applications of, 14, 15
 collocated with sensors, delamination, 356
 Comparison of schemes, 83
 Control strategies, 247
 definition of, 6
 in microfluidic systems, 100
 in smart systems, 7
 magnetostriuctive
- cantilever with, modeling of, 211
noise control in helicopter, 386
spectral element model of beam with, 213
- piezoelectric
 modeling of, 188, 189
 vibration control with, 378
- piezofiber composite
 modeling of, 212
 spectral element model of beam with, 213
- polymers for, 27
- PZT mounted beam, modeling of, 203
- Adaptive
 control, 387
 filter, 248
 structures, 216
 definition, 4
- Adhesion
 of sputtered thin films, 21
 comparison of curing schemes, 33
 properties of polymers, 282
- AMANDA process, 302
- Amorphous thin film, 49
- Amplifier
 charge preamplifier, in piezoelectric sensor, 86
 differential, in resonant sensor, 53
 high isolation, in wireless telemetry, 368
 MOSFET, in PVDF hydrophone, 87
 power amplifier, in structural health monitoring, 351
- Analogy, 64
- Anisotropic composite beam, wave equation for, 135
- Anisotropic
 etchants, 260, 269
 etching, 261, 271, 317
 nature
 composites, 118
 piezoelectric substrate, 58, 73
- Annealing
 after direct bonding, 262
 for ion implantation, 271
 interfacial stress, 314, 322

- Annealing (*continued*)
 rapid thermal, for stress relief, 308, 337
 solgel deposited films, 25
 sputtered films, 25
- Anodic bonding, 262
 comparison with other schemes, 321
 piezoresistive sensors, 50
- Anodization, pulse potential, 270
- APCVD (atmospheric pressure chemical vapor deposition), 266
- Area coordinates, 161
- Array
 of reflectors in SAW, 89, 334–336
 ball-grid, 316
 micro-mirror, 317
 of perturbation mass, 372
 of reaction chamber, 243
 of electrodes, 216
 of optical fibers, 286
- Assay buffer, 344
- Axisymmetric model, 213
- ball-grid array, 316
- bar element, Quadratic, 169, 170
- Beam
 element, FEM, 160
 exact solution, 160
 piezofiber composite Actuator, spectral element model, 213
 spectral element model piezofiber composite Actuator, 213
 as flexural waveguide, 134
 bending modes, 203, 378
 composite, 135, 140, 195
 active control of, 248
 PFC, 252
 piezoelectric bimorph, 195
 smart, 195, 196, 350
 Spectral element modeling, 215
 Terfenol-D, 210
- Euler–Bernoulli model, 215, 222
- isotropic, wave propagation in, 139
- laminated composite, wave equations for, 135
- modeling of, PZT Actuator, 203
- dispersion relation, 142
 spectrum relation, 142
- Bending
 mode wave, 144, 383
 moment, 215
 rigidity, 152
 stiffness, 128
 bimorph beam, 195
 modes in a beam, 203, 378
- bimorph beam, 195
 Bending, 195
 electrothermal, 80
 magnetostrictive, 211
 piezoelectric composite, 195, 378
 PVDF, 196, 202
- bimorph plate, 188
- Biomimetic materials, 5
- Bonding layer, 217
- Bonding, flip chip, 315
 hermetic, 317
- Boundary conditions, 91, 118, 149, 152
 in beams, 153, 252
 in coupled analysis, 210
 in FEM, 193, 199
 in spectral element modeling, 215
- Bragg grating, 52
- Cantilever beam, 202, 211
 distributed actuator, dynamics, 251
 dynamics, 244
- Cantilever rod, 181
- Cantilever, carbon nanotube, 228
- Capacitance
 analytical model of sensor, 216
 deflected diaphragm, 46
 gate, 55
 in electromechanical analogies, 64
 PZT, 218
- carbon nanotube
 composites, 35, 60
 Electrical Conductivity, 38
- Carrier mobility, 55, 88
- Carrier signal, 370
- ceramic, Composites, 23
- Ceramics, Deposition, 22, 268
- Channel, current density, 54
- Charge preamplifier, in piezoelectric sensor, 86
- Charge
 electromechanical analogy, 64
 generated in electrostrictive, 76
 generated in piezoelectric, 48, 73, 85, 97, 360
 stored in electrostatic actuator, 65
 in polymerization, 29, 30
- Classical finite difference technique, 150
- closed loop control, 10, 232, 384
- CNT sensor, CV diagrams, 341
- CNT, UV curable polymer composite, 39
- comparison
 bonding schemes, 321
 actuation schemes, 83
- Compliance, 63, 64
- Composite Beam, 135, 140, 195
 active control of, 248
 active control, 248
 laminated, 135, 140, 353
- composite
 smart beam, 195, 196, 350
 laminated, 120
 metal/polymer, 300
 piezoelectric, 191

- piezofiber, 212
 sensors, modeling, 212
 smart structure, 188, 192, 205
 anisotropic nature, 118
 carbon nanotube, 35, 60
 ceramic, 23
 structural health monitoring, 349
 Conductivity, Electrical, 18
 Electrical, of carbon nanotube, 38
 Conductivity, in liquid sensing, 99
 Conductivity, thermal, 18
 Control of cracks, open loop, 364
 Control strategies, actuator, 247
 vibration control, 247
 Control variable, 231
 Control
 Vibration with Piezoelectric actuator, 378
 closed loop, 10, 232, 384
 open loop, 9, 194, 232, 384
 open loop, cracks, 364
 active, 212
 Adaptive, 387
 Controllability, 238, 247
 Coriolis force, in SAW sensor, 373
 coupled analysis, Boundary conditions, 210
 Crack detection, 216, 273, 326, 349, 370
 Crack formation, in packages, 315
 Crack formation, in structures, 321, 362
 Crystal cut, piezoelectric, 57, 85, 367
 Crystal growth, silicon, 19, 260
 Crystal orientation, 20, 260, 271
 Crystal structure, 18, 81
 Current density, effect on electrodeposition, 296
 Current
 CV diagrams of CNT sensor, 341
 drain current in FET, 55, 87
 electromechanical analogy, 64
 in electromagnetic actuator, 69
 in electrostatic actuator, 67
 in electrostrictive actuator, 76
 CVD, 21, 39, 264, 332
 of dielectrics, 266

 Damping
 force, 157, 163, 231, 377
 matrix, 159, 164, 168, 171, 234, 242
 Data acquisition system, 327
 Data fusion, 374
 Delamination, actuator, collocated with sensors, 356
 Demolding, 297
 Deposition, 21
 of ceramics, 22, 268
 of metal, 20, 264
 of polymer thin films, 35, 59
 of Silicon, 263
 Electrochemical, 299
 Polysilicon, 268, 273
 Pulse laser, 35
 Silicon dioxide, 272, 273
 Silicon nitride, 331
 Sol-gel, 22, 25
 Thick film, 23
 Thin film, 22, 25, 263
 Diaphragm, 26, 46, 80, 101, 317
 capacitance, 46
 micro valve, 100
 Dielectric polarization, 74
 Dielectrics, CVD, 266
 Differential Amplifier, in resonant sensor, 53
 Dipole moment, 48, 59, 73
 Direct bonding, Annealing in, 262
 Direct electromechanical analogies, 64
 Dispersion angle, 327
 Dispersion relation, 129, 135, 182, 326, 369
 For beams, 142
 Divergence theorem, 113, 155
 Dopant selective etching, 260
 Double cantilever beam, 361
 Drain current in FET, 55, 87
 DRIE (deep reactive ion etching), 260
 Dry etching, 260

 Effective
 mass, 77
 stress, 217
 Eigen structure, 240, 381, 383
 Elastic
 constant, 48, 58, 75, 115, 124
 waves, 57
 Electrical conductivity, 18
 Electrochemical deposition, 299
 Electrochemical
 etching, 269
 fabrication, 296
 polymerization, 27, 282, 340
 Electrodeposition, 296
 Electrodynamic transducer, 70
 Electromagnetic transducer, 68
 Electromechanical analogies, 64
 Electromechanical coupling coefficient, 99, 338
 Electroplating, 21
 Electrostatic transducer, 64
 Electrostrictive transducer, 74
 Electrothermal actuator, 80
 Emission sensor, acoustic, 371
 Epitaxial deposition, 20
 Etch stop, 19, 260, 269, 270
 Electrochemical, 269
 Polycrystalline, 269
 Etchant, 260, 269
 anisotropic, 260, 269
 Anisotropic, properties, 269

- Etching, 254, 263
 - Anisotropic, 260, 261
- Eulerian
 - coordinates, 106
 - strain tensor, 108
- Eutectic bonding, 317, 318
- Evaporation, 21, 264
 - Metal, 21, 264, 289, 335
- Exact solution, 151, 160, 183
- Excimer laser, 290, 294
- Feedback
 - control, 232, 239, 248, 365, 380
 - gain, 251, 388
 - sensor, 250, 391
 - System, Block Diagram, 248, 327, 343, 378
- FEM, 115, 128, 145–185, 234
 - Superconvergent formulation, 147, 178, 380
- fiber optic gyro
 - Open loop configuration, 93
- Field Strength, 74, 78
- Finite Difference Method, 2
- Flexural Plate Waves, 57, 97
- Flexural waveguide with beam, 134
- Flip chip, bonding, 315
- Force balance, 65
- Force method, 145
- Force –Piezoelectric, 9
- Fourier Transform, 129, 182, 233, 243
- Friction, 36, 171, 371
- Gas damping, 53
- Gate capacitance, 55
- Hamilton principle, 135, 156, 192
- Helicopter noise control, Magnetostrictive actuator, 386
- Hermetic bonding, 317, 320
- Hermetic package, 312
- High aspect ratio
 - micro-fabrications, 288
 - micromachining, 301
 - microstructures, 8, 26, 257, 284, 290
- high isolation amplifier, in wireless telemetry, 368
- Hookean elastic solid, 114
- Hooke's law, 114
- Hot embossing, 289
- Hybrid processing, 8
- Hybrid technology, 366
- hydrophone, MOSFET Amplifier in, 87
- IDT accelerometer, 332, 372
- IDT accelerometer, 372
- Impact damage, 366, 370
- induced Strain, 12, 96, 195, 352
- Inductor, moving coil, 68
- Inertial
 - constants, 136, 202
- coupling, 136
- force, 55, 148, 242
- frame of reference, 92
- loading, 371
- navigation system, 366, 372
- sensors, 46, 321
- space, 92
- injection molding, Polycarbonate (PC), 291
- Interconnect, 308
- Interdigital transducers, 51, 326, 365
- interfacial stress, effect of annealing, 314, 322
- Inverse Transform, 131
- Ion implantation, Annealing for, 271
- Isoparametric elements, 167
- Isotropic
 - plasma etching, 26
 - solids, 118, 119
 - waveguide, 136
 - wet etching, 260
- Jacobian, 107, 165, 166, 170, 193
 - matrix, 167
 - transformation, 193
- J-integral, 360
- Lagrange equation, 158
- Lagrangian
 - coordinates, 109
 - strain tensor, 108
 - variable, 106
- Lamb wave, 326
- laminated, Composite beam, 135, 140, 353
- Lamination, Classical theory, 126
- Laser ablation, 25, 268, 290, 309, 317
- Laser and electrochemical etching, 26
- Laser, excimer, 290, 294
- Laser-Doppler effect, 51
- Lift off technique, 259
- LIGA, process, 8, 257, 269, 274
- linear time-invariant System, 240
- Liquid crystal display, 288
- liquid sensing, by Conductivity, 99
- Lithography, 257
 - masks in, 258
- Love wave, 57
 - sensor, 371
- Low pressure chemical vapor deposition (LPCVD), 266, 272, 321
- Lumped-element model
 - accelerometer, 88
 - for pressure sensor, 46
- Magneto-optic effect, 51
- Magnetostrictive actuator, 49, 78, 349
 - modeling of, 204
- Structural health monitoring with, 349

- Metal
 Deposition, 20, 264
 evaporation of, 21, 264, 289, 335
 sputtering of, 21
 metal/polymer composite, 300
 Metallo organic chemical vapor deposition (MOCVD), 21, 265
 Micro-channel, 344
 Microfabrication, electroplating, 21
 Microfluidic system, 342
 Actuation, 100
 Micromachining
 demolding in, 297
 Micromolding, 289
 in capillaries (MIMIC), 292
 micro-mirror array, 317
 Micro-nozzles, 29
 Micro-transfer molding, 291
 Minority carrier lifetime, 19
 Mobility analogies, 64
 MOCVD, 265
 model, axisymmetric, 213
 Modeling of
 carbon nanotubes, 35, 219, 340
 magnetostrictive actuator, 204
 piezofiber composite Actuator, 212
 PZT mounted beam actuator, 203
 piezoelectric actuator, 188, 189
 cantilever with Magnetostrictive actuator, 211
 Composite, sensors, 212
 Molding, Micro-transfer, 291
 Molecular beam epitaxy (MBE), 20
 Monolayers, self assembled, 223
 MOSFET Amplifier, in PVDF hydrophone, 87
 Movable gate FET, Accelerometer, 54
 Multichip modules (MCMs), 311
 multilayer packages, 315
 Nanocomposite, 39, 221
 n-channel MOSFET 55, 86, 328
 Negative resists, 258
 Nickel electroplating, 296
 Open loop, fiber optic gyro, 93
 open loop Control, 9, 194, 232, 384
 Operational amplifier, 54, 86
 optical fiber array, 286
 Optical, glucose sensors, 340
 Optimum damping, 82, 233
 Organic materials
 deposition methods for, 59, 266
 nonstandard, 21, 264
 patterning of, 31, 257, 259, 297, 330, 335
 Organic thin films, 35, 59
 Oxidation, 265
 processes, 266
 Packaging, 307–322
 Passivation, 50, 321, 332
 electrochemical, 269
 PCR, 240
 PDMS, 37, 289, 292
 Passive valve, 100
 PDMS (polydimethylsiloxane) process
 critical dimensions in, 260
 line width in, 258, 287, 295
 profiles in, 37
 reactors for, 343
 Passivation, 37, 289, 292
 Permalloy
 electroplating of, 21, 282, 290, 296–298, 300
 Permanent magnets, 22
 perturbation mass, 372
 PFC Beam, 252
 Phase modulation, 93
 Phospho silicate, 274, 307, 318
 Phosphosilicate glass thin films, 274, 307
 Photo electrochemical (PEC) etching, 8
 Photoforming process, 9, 293
 Photolithography, 14, 287, 289
 Photoresist, 258
 as masking layer for implant, 272
 deposition of, 31, 290, 335
 spin casting of, 332
 SU-8, 263, 332, 342
 electron-beam, 258
 negative, 258
 patterning, 31
 positive, 258, 331
 removal of, 297
 Physical vapor deposition, 21, 264
 PID control, 239, 240
 Piezoelectric actuator, 364
 modeling of, 188, 189
 vibration control with, 378
 bimorph, 195
 bimorph, composite, Beam, 195
 Piezoelectric coefficient, 85, 187
 Piezoelectric composite, 191
 Piezoelectric effect, 12, 333
 Piezoelectric material, 4, 11, 48, 57, 77, 89, 187, 249, 338
 Piezoelectric
 sensor, charge preamplifier, in, 86
 substrate, anisotropic nature, 58, 73
 transducer, 73
 Crystal cut, 57, 85, 367
 Piezoelectricity, 12, 48, 59, 195
 Piezofiber composite Actuator
 modeling of, 212
 spectral element model of beam with, 213
 Piezoresistive pressure sensor, 94, 267
 Piezoresistive sensors, anodic bonding, 50
 Planarization, 298, 308

- Plane stress, 120, 127, 136, 189, 359
 Plasma enhanced chemical vapor deposition (PECVD), 272, 332, 336
 Plasma etching, 26, 260, 269, 272
 Plasma
 in dry etching processes, 260
 reactors for, 265, 272, 274
 as etchants, 26, 260, 269, 272, 289, 321
 etch rates, 260, 269
 in deposition techniques, 263, 266, 332
 ionization of, 260
 Plastics
 PMMA (poly(methylmethacrylate)), 18, 277, 343
 Polycarbonate (PC), in injection molding, 291
 PDMS process in x-ray lithography, 275
 Polyethylene (PE), in injection molding, 289, 291
 PMMA (poly(methylmethacrylate)), 18, 277, 343
 Point load, 178, 179, 192
 Poisson equation, 118
 Polarization, dielectric, 74
 Polycarbonate (PC), in injection molding, 291
 Polycrystalline silicon, 8, 273
 as etch mask for KOH, 260
 as etch stop, 269
 as masking layer for implant, 317
 CVD of, 273
 etch rate in KOH, 269
 mechanical properties of, 19
 PDMS process in x-ray lithography, 275
 Polyimide, 60
 polymer thin films, Deposition, 35, 59
 polymerization, Electrochemical, 27, 282, 340
 Polymers
 actuator for, 27
 Polyoxymethylene (paM) resist, 291
 properties, 282
 Polysilicon, 50, 54, 62, 80, 89, 263, 266, 268, 272, 273, 274
 deposition, 268, 273
 Polystyrene, 36
 Polyvinylidene, 86, 102
 Positive Photoresist, 258, 331
 power amplifier, in structural health monitoring, 351
 Principle of Potential energy, 154
 Principle of Virtual Work, 115, 147, 254
 Projection operator, 244
 Projection, 8, 112, 284, 285
 Proof mass, 53, 54
 properties of polymers, 282
 Proportional damping, 159
 Proportional, 296, 336
 Protein synthesis, 343, 344
 Proximity printing, 275
 Pulse laser deposition, 35
 pulse potential anodization, 270
 PVC, 2, 36, 340
 PVD, 21, 264, 302
 Pyrex, 50
 PZT mounted beam actuator, modeling of, 203
 PZT, Capacitance, 218
 Q_matrix, 126
 Quadratic bar element, 169, 170
 Quadratic functional, 152
 Quadratic rod element, 165
 Quadrature, 166, 179
 Quantum-well spectrum, 51
 Quartzite, 19
 Radial-flow, 266
 Radiation, 24, 29
 Radical-generating photoinitiator, 33
 Rain monitors, 14
 Rapid thermal annealing (RTA), 307
 Rare earth elements, 5
 Rate of formation, 33
 Reaction chamber, 243
 Rectangular element, FEM, 160
 Rectangular grid, 106
 Refractive index, 92
 Refractory material, 21
 Residual stress, 51, 91, 273, 360
 Resistance change, 50, 95
 Resistive heating, 82
 Resonant frequency, 100, 233, 320
 resonant sensor, differential amplifier in, 53
 Resonator, 14, 53, 68, 323, 367
 Rod element, FEM, 160
 rod, cantilever, 181
 Root locus, 237, 238, 239, 248, 391
 Rotation rate, 14, 15, 52, 92
 Rotational Inertia, 140, 215
 Sacrificial layer, 26, 271–277
 Sagnac effect, 51, 92
 SAW accelerometer, 332, 372
 combined with gyroscope, 372
 design, 88
 fabrication, 333
 SCREAM, 26, 269, 271
 Screen printing, 314
 Second-order system, 135, 161, 232, 237
 Self assembled monolayer, 223
 Sensitivity analysis, 369
 Shape memory alloy (SMA), 3, 5, 22, 81
 Shape memory alloy (SMA), in thermal actuators, 81
 Shape memory, applications of, 14
 Shape memory, effect, 81
 Shape memory, phase transformation, 3, 81
 Shape memory, stress-induced martensite, 81
 Shell
 CNT, 38, 221
 finite element, 203

- thermal, 313
- Shipley, 331, 335
- Silica, 27, 52
- Silicon dioxide, 260, 271, 313, 334, 373
 - deposition, 272, 273
- Silicon
 - growth, 19–20
 - hardness, 19
 - in micromachining, 110–111
 - nitride deposition, 331
 - [100] orientation, 19, 261, 269
 - [110] orientation, 261, 269
 - crystalline, 8, 19, 26, 257, 269
 - deep reactive ion etching, 260
 - deposition and etching of, 263
 - lattice planes in, 296
 - mechanical properties of, 17, 19, 21, 33
 - orientation of, 19, 261, 269
 - oxidation of, 265
 - physical/chemical etching, 260, 269, 271
 - piezoresistivity, 50
 - residual stress, 51, 91, 273
 - resists in, 258
 - Single crystal silicon, 268, 271
 - Wet etching, 260
 - silicon-on-insulator, 262, 318
- Single crystal silicon, 268, 271
- slotted-quartz, 256, 266
- SMA, Crystal structure, 81
- Smart composite beam, 195, 196, 350
- smart structure, Composite, 188, 192, 205
- Smart systems, Actuator, 7
- solgel deposited films, Annealing, 25
- Sol-gel deposition, 22, 25
- Space-charge density, 87
- Sparse matrix, 173
- Spectral element model of beam
 - with piezofiber composite Actuator, 213
 - with magnetostrictive actuator, 213
 - Boundary conditions, 215
 - composite beam, 215
- Spectrum relation, 129, 135, 139
- spin casting, 332
- Spring-mass-damper system, 233, 236
- sputtered films, Annealing, 25
- sputtered thin films, Adhesion of, 21
- Sputtering, Metal, 21
- Stability analysis, 239
- State equations, 234, 236
- State variables, 65, 71, 76, 81, 234
- Stiction, 313
- Stiffness coefficients, 124, 137, 183, 199, 252
- stiffness, bending, 128
- Strain energy, 135, 147, 162, 197
- Stress gradient, 164
- stress relief, by rapid thermal annealing, 308, 337
- Stress
 - normal, 112
 - principal, 111
 - residual, 51, 91, 273
- Stress-induced martensite, 81
- Structural health monitoring
 - with Magnetostrictive transducer, 349
 - power amplifier in, 351
- Structure, modeling of, for control, 189, 248
- SU-8
 - resist, 263, 332, 342
 - Spin casting, 332
- Surface micromachining, 8, 26, 271–275
- Surface tension, 273, 335
- Synchrotron radiation, 275
- System architecture, 8
- System, linear time-invariant, 240
- System, linear, 232, 237
- Terfenol-D, composite, 210
- Thermal annealing, 262, 314
- Thermal
 - Conductivity, 18
 - evaporation, 318
- Thermal expansion coefficient, 51, 80, 82, 314, 316
- Thermal stress, 314
- Thick film deposition, 23
- Thick films, 23
- Thin film deposition, 22, 25, 263
- Thin film multilayer packages, 315
- Thin film sensors, 216
- thin films, sputtering, adhesion of, 21
- Transconductance, 87, 328
- Transducer
 - comb type electrostatic, 68
 - Electrodynamic, 70
 - Electromagnetic, 68
 - electrostatic, 64
 - Electrostrictive, 74
 - Electrothermal, 80
 - Magnetostrictive, 74
 - Structural health monitoring with, 349
 - piezoelectric, 73
- Transduction factor, 67, 72, 76, 80
- transition temperatures, 77, 291
- Triangular element, FEM, 160, 161
- Tuned system, 286
- Tungsten, 21, 264, 273, 307
- Ultrasonic actuators, 15
- Ultrasonic energy, 312
- Ultrasonic NDT techniques, 325, 348
- Ultrasonic probe, 39
- Ultrasonic transducer, 7, 73, 325, 326
- Ultrasonic wire bonding, 313
- Ultrasoundicated, 340, 341

- Ultraviolet irradiation, 27, 282
Ultraviolet light, 31
Undercut etching of channels, 274
Undercut of the mask, 272
Unit feed back, 239
Unit gate area, 55
Unmanned carriage system, 13
Unstable system, 237, 239
UV curable polymers, 8, 27, 263, 281
UV curable polymers, with CNT, 39
UV, 258, 291
- Vacuum Pressure reservoir, 21, 24, 50, 264
Valence band, 18, 38
Vapor phase etching, 310
Variational methods, 145
Velocity feedback, 251, 394
Velocity of sound, 57, 67, 89
Very low pressure chemical vapor deposition (VLPCVD), 265
Vibration absorber, 13, 82, 243
- Virtual work, 114, 154
Viscoelasticity, 105
- Wafer bonding, 261, 317–320, 335
wave equation for
 anisotropic composite beam, 135
 laminated composite beam, 135
wave propagation in
 composite beam, 143
 isotropic beam, 139
Wet bench, 3, 35
Wet chemical etchant, 271
Wet etching, 50, 260, 269, 310, 317
Wet oxidation, 329
Wetting action, 316
Wheatstone bridge, 45, 50, 95
Wire bonding, 310
Work, virtual, 114, 154
- x-ray lithography, 275

